Gamma-Ray Bursts

Contents

1 Topics

- GRB classification in different families with different progenitor systems.

- "Genuine short" GRBs: Possible identifications and selection effects

- The observed spectra of the P-GRBs

- GRB prompt emission spectra below 5 keV: challenges for future missions

- Interpretation of the ultra high energy emission from GRBs observed by Fermi, AGILE and MAGIC

- Analysis of different families of progenitors for GRBs with different energetics

- GRBs at redshift $z > 6$

- GRBs originating from a multiple collapse

- Prompt emission: the clumpiness of CBM

- Microphysical description of the interaction between the fireshell and the CBM

- Emission from newly born neutron stars, or "neo neutron stars".

- Induced Gravitational Collapse process for GRBs associated with supernovae.

- Redshift estimators for GRBs with no measured redshift.

- Binary Driven Hypernovae (BdHNe) as progenitor of GRBs via Induced Gravitational Collapse.

- GRB light curves as composed of different episodes.

- "Cosmic Matrix" for GRBs.

- GRB X-Ray Flares and Gamma-Ray Flares.

- GRB afterglow theory consistent with the mildly relativistic velocities inferred from the observations.

- Extended thermal emission components in GRBs.

- GRBs from merging white dwarfs.

- "Inner engine" of GRB emission.

- Quantized emission in GRBs.

2 Participants

2.1 ICRANet participants

- David Arnett
- Carlo Luciano Bianco
- Massimo Della Valle
- Li Liang
- Rahim Moradi
- Jorge Armando Rueda Hernandez
- Remo Ruffini
- Narek Sahakyan
- Gregory Vereshchagin
- Yu Wang
- She-Sheng Xue

2.2 Past collaborators

- Andrey Baranov
- Maria Grazia Bernardini (OAB, Italy)
- Joao Braga (INPE, Brazil)
- Sabrina Casanova (MPIK, Germany)

- Letizia Caito

- Pascal Chardonnet (Université de Savoie, France)

- Guido Chincarini (Università di Milano "Bicocca", Italy)

- Demetrios Christodoulou (ETH Zurich, Switzerland)

- Alessandra Corsi (INAF-IASF Roma, Italy)

- Valeri Chechetkin

- Maria Giovanna Dainotti

- Thibault Damour (IHES, France)

- Maxime Enderli

- Walter Ferrara

- Federico Fraschetti (CEA Saclay, France)

- Roberto Guida

- Vahe Gurzadyan (Yerevan Physics Institute, Armenia)

- Wen-Biao Han

- Milos Kovacevic

- Massimiliano Lattanzi (Oxford Astrophysics, UK)

- Vincenzo Liccardo

- Hendrik Ludwig

- Marco Muccino

- Nino Panagia

- Barbara Patricelli (Pisa University, Italy)

- Elena Pian

- Giovanni Battista Pisani

- Giuliano Preparata (Università di Milano, Italy)

- Daria Primorac

- Jay D. Salmonson (Livermore Lab, USA)

- Vineeth Valsan

- Jim Wilson (Livermore Lab, USA)

2.3 Ongoing collaborations

- Alexey Aksenov (ITEP, Russia)

- Lorenzo Amati (INAF-IASF Bologna, Italy)

- Ulisses Barres de Almeida (CBPF, Brazil)

- Laura Marcela Becerra Bayona (Universidad Industrial de Santander, Colombia)

- Riccardo Belvedere (ICRANet-Rio, Brazil)

- Sandip Kumar Chakrabarti (S.N. Bose National Centre and Indian Centre for Space Physics, India)

- Christian Cherubini (Università Campus Biomedico, Italy)

- Alessandro Chieffi (INAF-IASF Roma, Italy)

- Stefano Covino (OAB, Italy)

- Gustavo de Barros (UFRJ, Brazil)

- Simonetta Filippi (Università Campus Biomedico, Italy)

- Filippo Frontera (Università di Ferrara, Italy)

- Chris Fryer (Los Alamos National Laboratories, USA).

- Dafne Guetta (OAR, Italy)

- Cristiano Guidorzi (OAB, Italy)

- Stanislav Kelner (MEPhI, Russia, and MPIK, Germany)

- Marco Limongi (OAR, Italy)

- Clovis Maia (University of Brasilia, Brazil)

- Vanessa Mangano (INAF-IASF Palermo, Italy)

- Grant Mathews (University of Notre Dame, USA)

- Ana Virginia Penacchioni (INPE, Brazil)

- Luis Juracy Rangel Lemos (Fundação Universidade Federal do Tocantins, Brazil)

- Felix Ryde (KTH Royal Institute of Technology, Stockholm, Sweden)

- Soroush Shakeri (Isfahan University of Technology, Iran)

- Ivan Siutsou (ICRANet-Rio, Brazil)

- Bing Zhang (University of Nevada, USA)

- Susanna Vergani (Dunsink Observatory, Ireland)

- Francesco Vissani (INFN, Italy)

- Elena Zaninoni (ICRANet-Rio, Brazil)

2.4 Students

- Yerlan Aimuratov (IRAP PhD, Kazakhstan)

- Stefano Campion (IRAP PhD, Italy)

- Yen-Chen Chen (IRAP-PhD, China-Taiwan)

- Mile Karlika (IRAP PhD, Croatia)

- Ronaldo V. Lobato (IRAP-PhD, Brazil)

- J. David Melon Fuksman (IRAP PhD, Argentina)

- Jose Fernando Rodriguez Ruiz (IRAP PhD, Colombia)

3 Selected publications before 2005

3.1 Refereed journals

1. D. Christodoulou, R. Ruffini; "Reversible Transformations of a Charged Black Hole"; Physical Review D, 4, 3552 (1971).

   A formula is derived for the mass of a black hole as a function of its "irreducible mass", its angular momentum, and its charge. It is shown that 50% of the mass of an extreme charged black hole can be converted into energy as contrasted with 29% for an extreme rotating black hole.

2. T. Damour, R. Ruffini; "Quantum electrodynamical effects in Kerr-Newman geometries"; Physical Review Letters, 35, 463 (1975).

   Following the classical approach of Sauter, of Heisenberg and Euler and of Schwinger the process of vacuum polarization in the field of a "bare" Kerr-Newman geometry is studied. The value of the critical strength of the electromagnetic fields is given together with an analysis of the feedback of the discharge on the geometry. The relevance of this analysis for current astrophysical observations is mentioned.

3. G. Preparata, R. Ruffini, S.-S. Xue; "The dyadosphere of black holes and gamma-ray bursts"; Astronomy & Astrophysics, 338, L87 (1999).

   The "dyadosphere" has been defined as the region outside the horizon of a black hole endowed with an electromagnetic field (abbreviated to EMBH for "electromagnetic black hole") where the electromagnetic field exceeds the critical value, predicted by Heisenberg & Euler for $e^{\pm}$ pair production. In a very short time ($\sim O(\hbar/mc^2)$) a very large number of pairs is created there. We here give limits on the EMBH parameters leading to a Dyadosphere for $10 M_\odot$ and $10^5 M_\odot$ EMBH's, and give as well the pair densities as functions of the radial coordinate. We here assume that the pairs reach thermodynamic equilibrium

with a photon gas and estimate the average energy per pair as a function of the EMBH mass. These data give the initial conditions for the analysis of an enormous pair-electromagnetic-pulse or "P.E.M. pulse" which naturally leads to relativistic expansion. Basic energy requirements for gamma ray bursts (GRB), including GRB971214 recently observed at z=3.4, can be accounted for by processes occurring in the dyadosphere. In this letter we do not address the problem of forming either the EMBH or the dyadosphere: we establish some inequalities which must be satisfied during their formation process.

4. R. Ruffini, J.D. Salmonson, J.R. Wilson, S.-S. Xue; "On the pair electromagnetic pulse of a black hole with electromagnetic structure"; Astronomy & Astrophysics, 350, 334 (1999).

   We study the relativistically expanding electron-positron pair plasma formed by the process of vacuum polarization around an electromagnetic black hole (EMBH). Such processes can occur for EMBH's with mass all the way up to $6 \times 10^5 M_\odot$. Beginning with a idealized model of a Reissner-Nordstrom EMBH with charge to mass ratio $\xi = 0.1$, numerical hydrodynamic calculations are made to model the expansion of the pair-electromagnetic pulse (PEM pulse) to the point that the system is transparent to photons. Three idealized special relativistic models have been compared and contrasted with the results of the numerically integrated general relativistic hydrodynamic equations. One of the three models has been validated: a PEM pulse of constant thickness in the laboratory frame is shown to be in excellent agreement with results of the general relativistic hydrodynamic code. It is remarkable that this precise model, starting from the fundamental parameters of the EMBH, leads uniquely to the explicit evaluation of the parameters of the PEM pulse, including the energy spectrum and the astrophysically unprecedented large Lorentz factors (up to 6×10^3 for a $10^3 M_\odot$ EMBH). The observed photon energy at the peak of the photon spectrum at the moment of photon decoupling is shown to range from 0.1 MeV to 4 MeV as a function of the EMBH mass. Correspondingly the total energy in photons is in the range of 10^{52} to 10^{54} ergs, consistent with observed gamma-ray bursts. In these computations we neglect the presence of baryonic matter which will be the subject of forthcoming publications.

5. R. Ruffini, J.D. Salmonson, J.R. Wilson, S.-S. Xue; "On the pair-electro magnetic pulse from an electromagnetic black hole surrounded by a baryonic remnant"; Astronomy & Astrophysics, 359, 855 (2000).

   The interaction of an expanding Pair-Electromagnetic pulse (PEM pulse) with

a shell of baryonic matter surrounding a Black Hole with electromagnetic structure (EMBH) is analyzed for selected values of the baryonic mass at selected distances well outside the dyadosphere of an EMBH. The dyadosphere, the region in which a super critical field exists for the creation of e+e- pairs, is here considered in the special case of a Reissner-Nordstrom geometry. The interaction of the PEM pulse with the baryonic matter is described using a simplified model of a slab of constant thickness in the laboratory frame (constant-thickness approximation) as well as performing the integration of the general relativistic hydrodynamical equations. Te validation of the constant-thickness approximation, already presented in a previous paper Ruffini et al. (1999) for a PEM pulse in vacuum, is here generalized to the presence of baryonic matter. It is found that for a baryonic shell of mass-energy less than 1% of the total energy of the dyadosphere, the constant-thickness approximation is in excellent agreement with full general relativistic computations. The approximation breaks down for larger values of the baryonic shell mass, however such cases are of less interest for observed Gamma Ray Bursts (GRBs). On the basis of numerical computations of the slab model for PEM pulses, we describe (i) the properties of relativistic evolution of a PEM pulse colliding with a baryonic shell; (ii) the details of the expected emission energy and observed temperature of the associated GRBs for a given value of the EMBH mass; $10^3 M_\odot$, and for baryonic mass-energies in the range 10^{-8} to 10^{-2} the total energy of the dyadosphere.

6. C.L. Bianco, R. Ruffini, S.-S. Xue; "The elementary spike produced by a pure e+e- pair-electromagnetic pulse from a Black Hole: The PEM Pulse"; Astronomy & Astrophysics, 368, 377 (2001).

In the framework of the model that uses black holes endowed with electromagnetic structure (EMBH) as the energy source, we study how an elementary spike appears to the detectors. We consider the simplest possible case of a pulse produced by a pure e^+e^- pair-electro-magnetic plasma, the PEM pulse, in the absence of any baryonic matter. The resulting time profiles show a *Fast-Rise-Exponential-Decay* shape, followed by a power-law tail. This is obtained without any special fitting procedure, but only by fixing the energetics of the process taking place in a given EMBH of selected mass, varying in the range from 10 to 10^3 $M_\odot$ and considering the relativistic effects to be expected in an electron-positron plasma gradually reaching transparency. Special attention is given to the contributions from all regimes with Lorentz γ factor varying from $\gamma = 1$ to $\gamma = 10^4$ in a few hundreds of the PEM pulse travel time. Although the

main goal of this paper is to obtain the elementary spike intensity as a function of the arrival time, and its observed duration, some qualitative considerations are also presented regarding the expected spectrum and on its departure from the thermal one. The results of this paper will be comparable, when data will become available, with a subfamily of particularly short GRBs not followed by any afterglow. They can also be propedeutical to the study of longer bursts in presence of baryonic matter currently observed in GRBs.

7. R. Ruffini, C.L. Bianco, P. Chardonnet, F. Fraschetti, S.-S. Xue; "Relative spacetime transformations in Gamma-Ray Bursts"; The Astrophysical Journal, 555, L107 (2001).

   The GRB 991216 and its relevant data acquired from the BATSE experiment and RXTE and Chandra satellites are used as a prototypical case to test the theory linking the origin of gamma ray bursts (GRBs) to the process of vacuum polarization occurring during the formation phase of a black hole endowed with electromagnetic structure (EMBH). The relative space-time transformation paradigm (RSTT paradigm) is presented. It relates the observed signals of GRBs to their past light cones, defining the events on the worldline of the source essential for the interpretation of the data. Since GRBs present regimes with unprecedently large Lorentz γ factor, also sharply varying with time, particular attention is given to the constitutive equations relating the four time variables: the comoving time, the laboratory time, the arrival time at the detector, duly corrected by the cosmological effects. This paradigm is at the very foundation of any possible interpretation of the data of GRBs.

8. R. Ruffini, C.L. Bianco, P. Chardonnet, F. Fraschetti, S.-S. Xue; "On the interpretation of the burst structure of Gamma-Ray Bursts"; The Astrophysical Journal, 555, L113 (2001).

   Given the very accurate data from the BATSE experiment and RXTE and Chandra satellites, we use the GRB 991216 as a prototypical case to test the EMBH theory linking the origin of the energy of GRBs to the electromagnetic energy of black holes. The fit of the afterglow fixes the only two free parameters of the model and leads to a new paradigm for the interpretation of the burst structure, the IBS paradigm. It leads as well to a reconsideration of the relative roles of the afterglow and burst in GRBs by defining two new phases in this complex phenomenon: a) the injector phase, giving rise to the proper-GRB (P-GRB), and b) the beam-target phase, giving rise to the extended afterglow peak emission (E-APE) and to the afterglow. Such differentiation leads to a

natural possible explanation of the bimodal distribution of GRBs observed by BATSE. The agreement with the observational data in regions extending from the horizon of the EMBH all the way out to the distant observer confirms the uniqueness of the model.

9. R. Ruffini, C.L. Bianco, P. Chardonnet, F. Fraschetti, S.-S. Xue; "On a possible Gamma-Ray Burst-Supernova time sequence"; The Astrophysical Journal, 555, L117 (2001).

The data from the Chandra satellite on the iron emission lines in the afterglow of GRB 991216 are used to give further support for the EMBH theory, which links the origin of the energy of GRBs to the extractable energy of electromagnetic black holes (EMBHs), leading to an interpretation of the GRB-supernova correlation. Following the relative space-time transformation (RSTT) paradigm and the interpretation of the burst structure (IBS) paradigm, we introduce a paradigm for the correlation between GRBs and supernovae. The following sequence of events is shown as kinematically possible and consistent with the available data: a) the GRB-progenitor star P_1 first collapses to an EMBH, b) the proper GRB (P-GRB) and the peak of the afterglow (E-APE) propagate in interstellar space until the impact on a supernova-progenitor star P_2 at a distance $\leq 2.69 \times 10^{17}$ cm, and they induce the supernova explosion, c) the accelerated baryonic matter (ABM) pulse, originating the afterglow, reaches the supernova remnants 18.5 hours after the supernova explosion and gives rise to the iron emission lines. Some considerations on the dynamical implementation of the paradigm are presented. The concept of induced supernova explosion introduced here specifically for the GRB-supernova correlation may have more general application in relativistic astrophysics.

10. R. Ruffini, C.L. Bianco, P. Chardonnet, F. Fraschetti, S.-S. Xue; "On the physical processes which lie at the bases of time variability of GRBs"; Il Nuovo Cimento B, 116, 99 (2001).

The relative-space-time-transformation (RSTT) paradigm and the interpretation of the burst-structure (IBS) paradigm are applied to probe the origin of the time variability of GRBs. Again GRB 991216 is used as a prototypical case, thanks to the precise data from the CGRO, RXTE and Chandra satellites. It is found that with the exception of the relatively inconspicuous but scientifically very important signal originating from the initial "proper gamma ray burst" (P-GRB), all the other spikes and time variabilities can be explained by the interaction of the accelerated-baryonic-matter pulse with inhomogeneities in the

interstellar matter. This can be demonstrated by using the RSTT paradigm as well as the IBS paradigm, to trace a typical spike observed in arrival time back to the corresponding one in the laboratory time. Using these paradigms, the identification of the physical nature of the time variablity of the GRBs can be made most convincingly. It is made explicit the dependence of a) the intensities of the afterglow, b) the spikes amplitude and c) the actual time structure on the Lorentz gamma factor of the accelerated-baryonic-matter pulse. In principle it is possible to read off from the spike structure the detailed density contrast of the interstellar medium in the host galaxy, even at very high redshift.

11. R. Ruffini, C.L. Bianco, P. Chardonnet, F. Fraschetti, S.-S. Xue; "On the structures in the afterglow peak emission of gamma ray bursts"; The Astrophysical Journal, 581, L19 (2002).

    Using GRB 991216 as a prototype, it is shown that the intensity substructures observed in what is generally called the "prompt emission" in gamma ray bursts (GRBs) do originate in the collision between the accelerated baryonic matter (ABM) pulse with inhomogeneities in the interstellar medium (ISM). The initial phase of such process occurs at a Lorentz factor $\gamma \sim 310$. The crossing of ISM inhomogeneities of sizes $\Delta R \sim 10^{15}$ cm occurs in a detector arrival time interval of ~ 0.4 s implying an apparent superluminal behavior of $\sim 10^5 c$. The long lasting debate between the validity of the external shock model vs. the internal shock model for GRBs is solved in favor of the first.

12. R. Ruffini, C.L. Bianco, P. Chardonnet, F. Fraschetti, S.-S. Xue; "On the structure of the burst and afterglow of Gamma-Ray Bursts I: the radial approximation"; International Journal of Modern Physics D, 12, 173 (2003).

    We have recently proposed three paradigms for the theoretical interpretation of gamma-ray bursts (GRBs). (1) The relative space-time transformation (RSTT) paradigm emphasizes how the knowledge of the entire world-line of the source from the moment of gravitational collapse is a necessary condition in order to interpret GRB data. (2) The interpretation of the burst structure (IBS) paradigm differentiates in all GRBs between an injector phase and a beam-target phase. (3) The GRB-supernova time sequence (GSTS) paradigm introduces the concept of *induced supernova explosion* in the supernovae-GRB association. In the introduction the RSTT and IBS paradigms are enunciated and illustrated using our theory based on the vacuum polarization process occurring around an electromagnetic black hole (EMBH theory). The results are summarized

using figures, diagrams and a complete table with the space-time grid, the fundamental parameters and the corresponding values of the Lorentz gamma factor for GRB 991216 used as a prototype. In the following sections the detailed treatment of the EMBH theory needed to understand the results of the three above letters is presented. We start from the considerations on the dyadosphere formation. We then review the basic hydrodynamic and rate equations, the equations leading to the relative space-time transformations as well as the adopted numerical integration techniques. We then illustrate the five fundamental eras of the EMBH theory: the self acceleration of the e^+e^- pair-electromagnetic plasma (PEM pulse), its interaction with the baryonic remnant of the progenitor star, the further self acceleration of the e^+e^- pair-electroma--gnetic radiation and baryon plasma (PEMB pulse). We then study the approach of the PEMB pulse to transparency, the emission of the proper GRB (P-GRB) and its relation to the "short GRBs". Particular attention is given to the free parameters of the theory and to the values of the thermodynamical quantities at transparency. Finally the three different regimes of the afterglow are described within the fully radiative and radial approximations: the ultrarelativistic, the relativistic and the nonrelativistic regimes. The best fit of the theory leads to an unequivocal identification of the "long GRBs" as extended emission occurring at the afterglow peak (E-APE). The relative intensities, the time separation and the hardness ratio of the P-GRB and the E-APE are used as distinctive observational test of the EMBH theory and the excellent agreement between our theoretical predictions and the observations are documented. The afterglow power-law indexes in the EMBH theory are compared and contrasted with the ones in the literature, and no beaming process is found for GRB 991216. Finally, some preliminary results relating the observed time variability of the E-APE to the inhomogeneities in the interstellar medium are presented, as well as some general considerations on the EMBH formation. The issue of the GSTS paradigm will be the object of a forthcoming publication and the relevance of the iron-lines observed in GRB 991216 is shortly reviewed. The general conclusions are then presented based on the three fundamental parameters of the EMBH theory: the dyadosphere energy, the baryonic mass of the remnant, the interstellar medium density. An in depth discussion and comparison of the EMBH theory with alternative theories is presented as well as indications of further developments beyond the radial approximation, which will be the subject of paper II in this series. Future needs for specific GRB observations are outlined.

13. R. Ruffini, C.L. Bianco, P. Chardonnet, F. Fraschetti, V. Gurzadyan, S.-S. Xue; "On the instantaneous spectrum of gamma ray bursts"; International Journal of Modern Physics D, 13, 843 (2004).

A theoretical attempt to identify the physical process responsible for the afterglow emission of Gamma-Ray Bursts (GRBs) is presented, leading to the occurrence of thermal emission in the comoving frame of the shock wave giving rise to the bursts. The determination of the luminosities and spectra involves integration over an infinite number of Planckian spectra, weighted by appropriate relativistic transformations, each one corresponding to a different viewing angle in the past light cone of the observer. The relativistic transformations have been computed using the equations of motion of GRBs within our theory, giving special attention to the determination of the equitemporal surfaces. The only free parameter of the present theory is the "effective emitting area" in the shock wave front. A self consistent model for the observed hard-to-soft transition in GRBs is also presented. When applied to GRB 991216 a precise fit $\left(\chi^2 \simeq 1.078\right)$ of the observed luminosity in the 2–10 keV band is obtained. Similarly, detailed estimates of the observed luminosity in the 50–300 keV and in the 10–50 keV bands are obtained.

3.2 Conference proceedings

1. R. Ruffini; "Beyond the critical mass: The dyadosphere of black holes"; in "Black Holes and High Energy Astrophysics", H. sato, N. Sugiyama, Editors; p. 167; Universal Academy Press (Tokyo, Japan, 1998).

The "dyadosphere" (from the Greek word "duas-duados" for pairs) is here defined as the region outside the horizon of a black hole endowed with an electromagnetic field (abbreviated to EMBH for "electromagnetic black hole") where the electromagnetic field exceeds the critical value, predicted by Heisenberg and Euler for e^+e^- pair production. In a very short time ($\sim O(\hbar/mc^2)$), a very large number of pairs is created there. I give limits on the EMBH parameters leading to a Dyadosphere for $10M_\odot$ and $10^5M_\odot$ EMBH's, and give as well the pair densities as functions of the radial coordinate. These data give the initial conditions for the analysis of an enormous pair-electromagnetic-pulse or "PEM-pulse" which naturally leads to relativistic expansion. Basic energy requirements for gamma ray bursts (GRB), including GRB971214 recently observed at $z = 3.4$, can be accounted for by processes occurring in the dyado-

sphere.

2. R. Ruffini, C.L. Bianco, P. Chardonnet, F. Fraschetti, L. Vitagliano, S.-S. Xue; "New perspectives in physics and astrophysics from the theoretical understanding of Gamma-Ray Bursts"; in "COSMOLOGY AND GRAVITATION: Xth Brazilian School of Cosmology and Gravitation; 25th Anniversary (1977-2002)", Proceedings of the Xth Brazilian School on Cosmology and Gravitation, Mangaratiba, Rio de Janeiro (Brazil), July - August 2002, M. Novello, S.E. Perez Bergliaffa, Editors; AIP Conference Proceedings, 668, 16 (2003).

If due attention is given in formulating the basic equations for the Gamma-Ray Burst (GRB) phenomenon and in performing the corresponding quantitative analysis, GRBs open a main avenue of inquiring on totally new physical and astrophysical regimes. This program is very likely one of the greatest computational efforts in physics and astrophysics and cannot be actuated using shortcuts. A systematic approach is needed which has been highlighted in three basic new paradigms: the relative space-time transformation (RSTT) paradigm, the interpretation of the burst structure (IBS) paradigm, the GRB-supernova time sequence (GSTS) paradigm. From the point of view of fundamental physics new regimes are explored: (1) the process of energy extraction from black holes; (2) the quantum and general relativistic effects of matter-antimatter creation near the black hole horizon; (3) the physics of ultrarelativisitc shock waves with Lorentz gamma factor $\gamma > 100$. From the point of view of astronomy and astrophysics also new regimes are explored: (i) the occurrence of gravitational collapse to a black hole from a critical mass core of mass $M \gtrsim 10 M_\odot$, which clearly differs from the values of the critical mass encountered in the study of stars "catalyzed at the endpoint of thermonuclear evolution" (white dwarfs and neutron stars); (ii) the extremely high efficiency of the spherical collapse to a black hole, where almost 99.99% of the core mass collapses leaving negligible remnant; (iii) the necessity of developing a fine tuning in the final phases of thermonuclear evolution of the stars, both for the star collapsing to the black hole and the surrounding ones, in order to explain the possible occurrence of the "induced gravitational collapse". New regimes are as well encountered from the point of view of nature of GRBs: (I) the basic structure of GRBs is uniquely composed by a proper-GRB (P-GRB) and the afterglow; (II) the long bursts are then simply explained as the peak of the afterglow (the E-APE) and their observed time variability is explained in terms of inhomogeneities in the interstellar medium (ISM); (III) the short bursts are

identified with the P-GRBs and the crucial information on general relativistic and vacuum polarization effects are encoded in their spectra and intensity time variability. A new class of space missions to acquire information on such extreme new regimes are urgently needed.

3. R. Ruffini, C.L. Bianco, P. Chardonnet, F. Fraschetti, S.-S. Xue; "The EMBH Model in GRB 991216 and GRB 980425"; in Proceedings of "Third Rome Workshop on Gamma-Ray Burst in the Afterglow Era", 17-20 September 2002; M. Feroci, F. Frontera, N. Masetti, L. Piro, Editors; ASP Conference Series, 312, 349 (2004).

This is a summary of the two talks presented at the Rome GRB meeting by C.L. Bianco and R. Ruffini. It is shown that by respecting the Relative Space-Time Transformation (RSTT) paradigm and the Interpretation of the Burst Structure (IBS) paradigm, important inferences are possible: a) in the new physics occurring in the energy sources of GRBs, b) on the structure of the bursts and c) on the composition of the interstellar matter surrounding the source.

4. M.G. Bernardini, C.L. Bianco, P. Chardonnet, F. Fraschetti, R. Ruffini, S.-S. Xue; "A New Astrophysical 'Triptych': GRB030329/SN2003dh/ URCA-2"; in "GAMMA-RAY BURSTS: 30 YEARS OF DISCOVERY", Proceedings of the Los Alamos "Gamma Ray Burst Symposium", Santa Fe, New Mexico, 8 – 12 September 2003, E.E. Fenimore, M. Galassi, Editors; AIP Conference Proceedings, 727, 312 (2004).

We analyze the data of the Gamma-Ray Burst/Supernova GRB030329/ SN2003dh system obtained by HETE-2, R-XTE, XMM and VLT within our theory for GRB030329. By fitting the only three free parameters of the EMBH theory, we obtain the luminosity in fixed energy bands for the prompt emission and the afterglow. Since the Gamma-Ray Burst (GRB) analysis is consistent with a spherically symmetric expansion, the energy of GRB030329 is $E = 2.1 \times 10^{52}$ erg, namely $\sim 2 \times 10^3$ times larger than the Supernova energy. We conclude that either the GRB is triggering an induced-supernova event or both the GRB and the Supernova are triggered by the same relativistic process. In no way the GRB can be originated from the supernova. We also evidence that the XMM observations, much like in the system GRB980425/SN1998bw, are not part of the GRB afterglow, as interpreted in the literature, but are associated to the Supernova phenomenon. A dedicated campaign of observations is needed to confirm the nature of this XMM source as a newly born neutron star cooling by generalized URCA processes.

5. F. Fraschetti, M.G. Bernardini, C.L. Bianco, P. Chardonnet, R. Ruffini, S.-S. Xue; "The GRB980425-SN1998bw Association in the EMBH Model"; in "GAMMA-RAY BURSTS: 30 YEARS OF DISCOVERY", Proceedings of the Los Alamos "Gamma Ray Burst Symposium", Santa Fe, New Mexico, 8 – 12 September 2003, E.E. Fenimore, M. Galassi, Editors; AIP Conference Proceedings, 727, 424 (2004).

Our GRB theory, previously developed using GRB 991216 as a prototype, is here applied to GRB 980425. We fit the luminosity observed in the 40–700 keV, 2–26 keV and 2–10 keV bands by the BeppoSAX satellite. In addition the supernova SN1998bw is the outcome of an "induced gravitational collapse" triggered by GRB 980425, in agreement with the GRB-Supernova Time Sequence (GSTS) paradigm. A further outcome of this astrophysically exceptional sequence of events is the formation of a young neutron star generated by the SN1998bw event. A coordinated observational activity is recommended to further enlighten the underlying scenario of this most unique astrophysical system.

6. A. Corsi, M.G. Bernardini, C.L. Bianco, P. Chardonnet, F. Fraschetti, R. Ruffini, S.-S. Xue; "GRB 970228 Within the EMBH Model"; in "GAMMA-RAY BURSTS: 30 YEARS OF DISCOVERY", Proceedings of the Los Alamos "Gamma Ray Burst Symposium", Santa Fe, New Mexico, 8 – 12 September 2003, E.E. Fenimore, M. Galassi, Editors; AIP Conference Proceedings, 727, 428 (2004).

We consider the gamma-ray burst of 1997 February 28 (GRB 970228) within the ElectroMagnetic Black Hole (EMBH) model. We first determine the value of the two free parameters that characterize energetically the GRB phenomenon in the EMBH model, that is to say the dyadosphere energy, $E_{dya} = 5.1 \times 10^{52}$ ergs, and the baryonic remnant mass M_B in units of E_{dya}, $B = M_B c^2 / E_{dya} = 3.0 \times 10^{-3}$. Having in this way estimated the energy emitted during the beam-target phase, we evaluate the role of the InterStellar Medium (ISM) number density (n_{ISM}) and of the ratio $\mathcal{R}$ between the effective emitting area and the total surface area of the GRB source, in reproducing the observed profiles of the GRB 970228 prompt emission and X-ray (2-10 keV energy band) afterglow. The importance of the ISM distribution three-dimensional treatment around the central black hole is also stressed in this analysis.

4 Publications (2005–2021)

4.1 Refereed journals

1. R. Ruffini, C.L. Bianco, P. Chardonnet, F. Fraschetti, V. Gurzadyan, S.-S. Xue; "Emergence of a filamentary structure in the fireball from GRB spectra"; International Journal of Modern Physics D, 14, 97 (2005).

   It is shown that the concept of a fireball with a definite filamentary structure naturally emerges from the analysis of the spectra of Gamma-Ray Bursts (GRBs). These results, made possible by the recently obtained analytic expressions of the equitemporal surfaces in the GRB afterglow, depend crucially on the single parameter R describing the effective area of the fireball emitting the X-ray and gamma-ray radiation. The X-ray and gamma-ray components of the afterglow radiation are shown to have a thermal spectrum in the co-moving frame of the fireball and originate from a stable shock front described self-consistently by the Rankine-Hugoniot equations. Precise predictions are presented on a correlation between spectral changes and intensity variations in the prompt radiation verifiable, e.g., by the Swift and future missions. The highly variable optical and radio emission depends instead on the parameters of the surrounding medium. The GRB 991216 is used as a prototype for this model.

2. R. Ruffini, M.G. Bernardini, C.L. Bianco, P. Chardonnet, F. Fraschetti, V. Gurzadyan, M. Lattanzi, L. Vitagliano, S.-S. Xue; "Extracting energy from black holes: 'long' and 'short' GRBs and their astrophysical settings"; Il Nuovo Cimento C, 28, 589 (2005).

   The introduction of the three interpretational paradigms for Gamma-Ray Bursts (GRBs) and recent progress in understanding the X- and gamma-ray luminosity in the afterglow allow us to make assessments about the astrophysical settings of GRBs. In particular, we evidence the distinct possibility that some GRBs occur in a binary system. This subclass of GRBs manifests itself in a "tryptich": one component formed by the collapse of a massive star to a black

hole, which originates the GRB; a second component by a supernova and a third one by a young neutron star born in the supernova event. Similarly, the understanding of the physics of quantum relativistic processes during the gravitational collapse makes possible precise predictions about the structure of short GRBs.

3. M.G. Bernardini, C.L. Bianco, P. Chardonnet, F. Fraschetti, R. Ruffini, S.-S. Xue; "Theoretical interpretation of luminosity and spectral properties of GRB 031203"; The Astrophysical Journal, 634, L29 (2005).

The X-ray and gamma-ray observations of the source GRB 031203 by INTE-GRAL are interpreted within our theoretical model. In addition to a complete spacetime parameterization of the GRB, we specifically assume that the after-glow emission originates from a thermal spectrum in the comoving frame of the expanding baryonic matter shell. By determining the two free parameters of the model and estimating the density and filamentary structure of the ISM, we reproduce the observed luminosity in the 20-200 keV energy band. As in previous sources, the prompt radiation is shown to coincide with the peak of the afterglow, and the luminosity substructure is shown to originate in the fil-amentary structure of the ISM. We predict a clear hard-to-soft behavior in the instantaneous spectra. The time-integrated spectrum over 20 s observed by INTEGRAL is well fitted. Despite the fact that this source has been considered "unusual", it appears to us to be a normal low-energy GRB.

4. R. Ruffini, M.G. Bernardini, C.L. Bianco, P. Chardonnet, F. Fraschetti, S.-S. Xue; Evidence for isotropic emission in GRB991216; Advances in Space Research, 38, 1291 (2006).

The issue of the possible presence or absence of jets in GRBs is here re-examined for GRB991216. We compare and contrast our theoretically predicted after-glow luminosity in the 2–10 keV band for spherically symmetric versus jetted emission. At these wavelengths the jetted emission can be excluded and data analysis confirms spherical symmetry. These theoretical fits are expected to be improved by the forthcoming data of the Swift mission.

5. R. Ruffini, M.G. Bernardini, C.L. Bianco, P. Chardonnet, F. Fraschetti, R. Guida, S.-S. Xue; "GRB 050315: A step toward understanding the uniqueness of the overall GRB structure"; The Astrophysical Journal, 645, L109 (2006).

Using the Swift data of GRB 050315, we are making progress toward understanding the uniqueness of our theoretically predicted gamma-ray burst (GRB) structure, which is composed of a proper GRB (P-GRB), emitted at the transparency of an electron-positron plasma with suitable baryon loading, and an afterglow comprising the so-called prompt emission due to external shocks. Thanks to the Swift observations, the P-GRB is identified, and for the first time we can theoretically fit detailed light curves for selected energy bands on a continuous timescale ranging over 106 s. The theoretically predicted instantaneous spectral distribution over the entire afterglow is presented, confirming a clear hard-to-soft behavior encompassing, continuously, the "prompt emission" all the way to the latest phases of the afterglow.

6. C.L. Bianco, L. Caito, R. Ruffini; "Theoretical interpretation of GRB 011121"; Il Nuovo Cimento B, 121, 1441 (2006).

   GRB011121 is analyzed as a prototype to understand the "flares" recently observed by Swift in the afterglow of many GRB sources. Detailed theoretical computation of the GRB011121 light curves in selected energy bands are presented and compared and contrasted with observational BeppoSAX data.

7. R. Ruffini, M.G. Bernardini, C.L. Bianco, P. Chardonnet, F. Fraschetti, R. Guida, S.-S. Xue; "GRB 050315: A step toward the uniqueness of the overall GRB structure"; Il Nuovo Cimento B, 121, 1367 (2006).

   Using the *Swift* data of GRB 050315, we progress on the uniqueness of our theoretically predicted Gamma-Ray Burst (GRB) structure as composed by a proper-GRB (P-GRB), emitted at the transparency of an electron-positron plasma with suitable baryon loading, and an afterglow comprising the so called "prompt emission" as due to external shocks. Thanks to the *Swift* observations, we can theoretically fit detailed light curves for selected energy bands on a continuous time scale ranging over 10^6 seconds. The theoretically predicted instantaneous spectral distribution over the entire afterglow confirms a clear hard-to-soft behavior encompassing, continuously, the "prompt emission" all the way to the latest phases of the afterglow. Consequences of the instrumental threshold on the definition of "short" and "long" GRBs are discussed.

8. M.G. Bernardini, C.L. Bianco, L. Caito, P. Chardonnet, A. Corsi, M.G. Dainotti, F. Fraschetti, R. Guida, R. Ruffini, S.-S. Xue; GRB970228 as a prototype for short GRBs with afterglow; Il Nuovo Cimento B, 121, 1439 (2006).

GRB970228 is analyzed as a prototype to understand the relative role of short GRBs and their associated afterglows, recently observed by Swift and HETE-II. Detailed theoretical computation of the GRB970228 light curves in selected energy bands are presented and compared with observational BeppoSAX data.

9. M.G. Dainotti, M.G. Bernardini, C.L. Bianco, L. Caito, R. Guida, R. Ruffini; "GRB060218 and GRBs associated with Supernovae Ib/c"; Astronomy & Astrophysics, 471, L29 (2007).

Context: The *Swift* satellite has given continuous data in the range 0.3–150 keV from 0 s to 10^6 s for GRB060218 associated with SN2006aj. This Gamma-Ray Burst (GRB) which has an unusually long duration ($T_{90} \sim 2100$ s) fulfills the Amati relation. These data offer the opportunity to probe theoretical models for GRBs connected with Supernovae (SNe).

Aims: We plan to fit the complete γ- and X-ray light curves of this long duration GRB, including the prompt emission, in order to clarify the nature of the progenitors and the astrophysical scenario of the class of GRBs associated with SNe Ib/c.

Methods: We apply our "fireshell" model based on the formation of a black hole, giving the relevant references. It is characterized by the precise equations of motion and equitemporal surfaces and by the role of thermal emission.

Results: The initial total energy of the electron-positron plasma $E_{e\pm}^{tot} = 2.32 \times 10^{50}$ erg has a particularly low value, similar to the other GRBs associated with SNe. For the first time, we observe a baryon loading $B = 10^{-2}$ which coincides with the upper limit for the dynamical stability of the fireshell. The effective CircumBurst Medium (CBM) density shows a radial dependence $n_{cbm} \propto r^{-\alpha}$ with $1.0 \lesssim \alpha \lesssim 1.7$ and monotonically decreases from 1 to 10^{-6} particles/cm^3. This behavior is interpreted as being due to a fragmentation in the fireshell. Analogies with the fragmented density and filling factor characterizing Novae are outlined. The fit presented is particularly significant in view of the complete data set available for GRB060218 and of the fact that it fulfills the Amati relation.

Conclusions: We fit GRB060218, usually considered as an X-Ray Flash (XRF), as a "canonical GRB" within our theoretical model. The smallest possible black hole, formed by the gravitational collapse of a neutron star in a binary system, is consistent with the especially low energetics of the class of GRBs associated with SNe Ib/c. We provide the first evidence for a fragmentation in the fireshell. This fragmentation is crucial in explaining both the unusually large T_{90} and the consequently inferred abnormally low value of the CBM effective

density.

10. M.G. Bernardini, C.L. Bianco, L. Caito, M.G. Dainotti, R. Guida, R. Ruffini; "GRB970228 and a class of GRBs with an initial spikelike emission"; Astronomy & Astrophysics, 474, L13 (2007).

Context: The discovery by *Swift* and HETE-2 of an afterglow emission associated possibly with short GRBs opened the new problematic of their nature and classification. This issue has been further enhanced by the observation of GRB060614 and by a new analysis of the BATSE catalog which led to the identification of a new class of GRBs with "an occasional softer extended emission lasting tenths of seconds after an initial spikelike emission".

Aims: We plan a twofold task: a) to fit this new class of "hybrid" sources within our "canonical GRB" scenario, where all GRBs are generated by a "common engine" (i.e. the gravitational collapse to a black hole); b) to propose GRB970228 as the prototype of the above mentioned class, since it shares the same morphology and observational features.

Methods: We analyze *Beppo*SAX data on GRB970228 within the "fireshell" model and we determine the parameters describing the source and the CircumBurst Medium (CBM) needed to reproduce its light curves in the 40–700 keV and 2–26 keV energy bands.

Results: We find that GRB970228 is a "canonical GRB", like e.g. GRB050315, with the main peculiarity of a particularly low average density of the CBM $\langle n_{cbm} \rangle \sim 10^{-3}$ particles/cm^3. We also simulate the light curve corresponding to a rescaled CBM density profile with $\langle n_{cbm} \rangle = 1$ particle/cm^3. From such a comparison it follows that the total time-integrated luminosity is a faithful indicator of the nature of GRBs, contrary to the peak luminosity which is merely a function of the CBM density.

Conclusions: We call attention on discriminating the short GRBs between the "genuine" and the "fake" ones. The "genuine" ones are intrinsically short, with baryon loading $B \lesssim 10^{-5}$, as stated in our original classification. The "fake" ones, characterized by an initial spikelike emission followed by an extended emission lasting tenths of seconds, have a baryon loading $10^{-4} \lesssim B \leq 10^{-2}$. They are observed as such only due to an underdense CBM consistent with a galactic halo environment which deflates the afterglow intensity.

11. R. Guida, M.G. Bernardini, C.L. Bianco, L. Caito, M.G. Dainotti, R. Ruffini; "The Amati relation in the "fireshell" model"; Astronomy & Astrophysics, 487, L37 (2008).

Context: The cosmological origin of gamma-ray bursts (GRBs) has been firmly established, with redshifts up to $z = 6.29$. They are possible candidates for use as "distance indicators" for testing cosmological models in a redshift range hardly achievable by other cosmological probes. Asserting the validity of the empirical relations among GRB observables is now crucial for their calibration. *Aims*: Motivated by the relation proposed by Amati and collaborators, we look within the "fireshell" model for a relation between the peak energy E_p of the νF_ν total time-integrated spectrum of the afterglow and the total energy of the afterglow E_{aft}, which in our model encompasses and extends the prompt emission.

Methods: The fit within the fireshell model, as for the "canonical" GRB050315, uses the complete arrival time coverage given by the Swift satellite. It is performed simultaneously, self-consistently, and recursively in the four BAT energy bands (15–25 keV, 25–50 keV, 50–100 keV, and 100-150 keV), as well as in the XRT one (0.2–10 keV). It uniquely determines the two free parameters characterizing the GRB source, the total energy $E_{tot}^{e^\pm}$ of the $e^\pm$ plasma and its baryon loading B, as well as the effective CircumBurst Medium (CBM) distribution. We can then build two sets of "gedanken" GRBs varying the total energy of the electron-positron plasma $E_{tot}^{e^\pm}$ and keeping the same baryon loading B of GRB050315. The first set assumes the one obtained in the fit of GRB050315 for the effective CBM density. The second set assumes instead a constant CBM density equal to the average value of the GRB050315 prompt phase.

Results: For the first set of "gedanken" GRBs we find a relation $E_p \propto (E_{aft})^a$, with $a = 0.45 \pm 0.01$, whose slope strictly agrees with the Amati one. Such a relation, in the limit $B \to 10^{-2}$, coincides with the Amati one. Instead, no correlation is found in the second set of "gedanken" GRBs.

Conclusions: Our analysis excludes the proper GRB (P-GRB) from the prompt emission, extends all the way to the latest afterglow phases, and is independent of the assumed cosmological model, since all "gedanken" GRBs are at the same redshift. The Amati relation, on the other hand, includes the P-GRB, focuses only on the prompt emission, being therefore influenced by the instrumental threshold that fixes the end of the prompt emission, and depends on the assumed cosmology. This might explain the intrinsic scatter observed in the Amati relation.

12. L. Caito, M.G. Bernardini, C.L. Bianco, M.G. Dainotti, R. Guida, R. Ruffini; "GRB060614: a "fake" short GRB from a merging binary system"; Astronomy & Astrophysics, 489, 501 (2009).

Context: GRB060614 observations by VLT and by Swift have infringed the traditionally accepted gamma-ray burst (GRB) collapsar scenario that purports the origin of all long duration GRBs from supernovae (SN). GRB060614 is the first nearby long duration GRB clearly not associated with a bright Ib/c SN. Moreover, its duration ($T_{90} \sim 100$ s) makes it hardly classifiable as a short GRB. It presents strong similarities with GRB970228, the prototype of a new class of "fake" short GRBs that appear to originate from the coalescence of binary neutron stars or white dwarfs spiraled out into the galactic halo. *Aims*: Within the "canonical" GRB scenario based on the "fireshell" model, we test if GRB060614 can be a "fake" or "disguised" short GRB. We model the traditionally termed "prompt emission" and discriminate the signal originating from the gravitational collapse leading to the GRB from the process occurring in the circumburst medium (CBM). *Methods*: We fit GRB060614 light curves in Swift's BAT ($15 - 150$ keV) and XRT ($0.2 - 10$ keV) energy bands. Within the fireshell model, light curves are formed by two well defined and different components: the proper-GRB (P-GRB), emitted when the fireshell becomes transparent, and the extended afterglow, due to the interaction between the leftover accelerated baryonic and leptonic shell and the CBM. *Results*: We determine the two free parameters describing the GRB source within the fireshell model: the total $e^{\pm}$ plasma energy ($E_{tot}^{e^{\pm}} = 2.94 \times 10^{51}$erg) and baryon loading ($B = 2.8 \times 10^{-3}$). A small average CBM density $\sim 10^{-3}$ particles/cm^3 is inferred, typical of galactic halos. The first spikelike emission is identified with the P-GRB and the following prolonged emission with the extended afterglow peak. We obtain very good agreement in the BAT ($15 - 150$ keV) energy band, in what is traditionally called "prompt emission", and in the XRT ($0.2 - 10$ keV) one. *Conclusions*: The *anomalous* GRB060614 finds a natural interpretation within our canonical GRB scenario: it is a "disguised" short GRB. The total time-integrated extended afterglow luminosity is greater than the P-GRB one, but its peak luminosity is smaller since it is deflated by the peculiarly low average CBM density of galactic halos. This result points to an old binary system, likely formed by a white dwarf and a neutron star, as the progenitor of GRB060614 and well justifies the absence of an associated SN Ib/c. Particularly important for further studies of the final merging process are the temporal structures in the P-GRB down to 0.1 s.

13. M.G. Bernardini, C.L. Bianco, L. Caito, M.G. Dainotti, R. Guida, R. Ruffini; "GRB970228 in the "canonical GRB" scenario"; Journal of the Korean Physical Society, 56, 1575 (2010).

Within the "fireshell" model, we define a "canonical GRB" light curve with two sharply different components: the proper-GRB (P-GRB), emitted when the optically thick fireshell of an electron-positron plasma originating from the phenomenon reaches transparency, and the afterglow, emitted due to the collision between the remaining optically thin fireshell and the circumburst medium (CBM). On the basis of the recent understanding of GRB970228 as the prototype for a new class of GRBs with "an occasional softer extended emission lasting tenths of seconds after an initial spikelike emission", we outline our "canonical GRB" scenario, originating from the gravitational collapse to a black hole, with special emphasis on the discrimination between "genuine" and "fake" short GRBs. Furthermore, we investigate how the GRB970228 analysis provides a theoretical explanation for the apparent absence of such a correlation for the GRBs belonging to this new class.

14. L. Caito, M.G. Bernardini, C.L. Bianco, M.G. Dainotti, R. Guida, R. Ruffini; "GRB060614: a preliminary result"; Journal of the Korean Physical Society, 56, 1579 (2010).

The explosion of GRB 060614 produced a deep break in the GRB scenario and opened new horizons of investigation because it can't be traced back to any traditional scheme of classification. In fact, it manifests peculiarities both of long bursts and of short bursts, and above all, it is the first case of a long-duration near GRB without any bright Ib/c associated Supernova. We will show that, in our canonical GRB scenario, this "anomalous" situation finds a natural interpretation and allows us to discuss a possible variation in the traditional classification scheme, introducing a distinction between "genuine" and "fake" short bursts.

15. M.G. Dainotti, M.G. Bernardini, C.L. Bianco, L. Caito, R. Guida, R. Ruffini; "The astrophysical trypthic: GRB, SN and URCA can be extended to GRB060218?"; Journal of the Korean Physical Society, 56, 1588 (2010).

The *Swift* satellite has given continuous data in the range 0.3–150 keV from 0 s to 10^6 s for GRB060218 associated with SN2006aj. This GRB is the fourth GRB spectroscopically associated with SNe after the cases of GRB980425-SN1998bw, GRB031203-SN2003lw, GRB 030329-SN2003dh. It has an unusually long duration ($T_{90} \sim 2100$ s). These data offer the opportunity to probe theoretical models for Gamma-Ray Bursts (GRBs) connected with Supernovae (SNe). We plan to fit the complete γ- and X-ray light curves of this long duration GRB,

including the prompt emission, in order to clarify the nature of the progenitors and the astrophysical scenario of the class of GRBs associated to SNe Ib/c. We apply our "fireshell" model based on the formation of a black hole, giving the relevant references. The initial total energy of the electron-positron plasma $E_{e\pm}^{tot} = 2.32 \times 10^{50}$ erg has a particularly low value similarly to the other GRBs associated with SNe. For the first time we observe a baryon loading $B = 10^{-2}$ which coincides with the upper limit for the dynamical stability of the fireshell. The effective CircumBurst Medium (CBM) density shows a radial dependence $n_{cbm} \propto r^{-\alpha}$ with $1.0 \lesssim \alpha \lesssim 1.7$ and monotonically decreases from 1 to 10^{-6} particles/cm^3. Such a behavior is interpreted as due to a fragmentation in the fireshell. Such a fragmentation is crucial in explaining both the unusually large T_{90} and the consequently inferred abnormal low value of the CBM effective density. We fit GRB060218, usually considered as an X-Ray Flash (XRF), as a "canonical GRB" within our theoretical model. The smallest possible black hole, formed by the gravitational collapse of a neutron star in a binary system, is consistent with the especially low energetics of the class of GRBs associated with SNe Ib/c. We present the URCA process and the connection between the GRBs associated with SNe extended also to the case of GRB060218.

16. L. Izzo, M.G. Bernardini, C.L. Bianco, L. Caito, B. Patricelli, R. Ruffini; "GRB 090423 at Redshift 8.1: a Theoretical Interpretation"; Journal of the Korean Physical Society, 57, 551 (2010).

   GRB 090423 is the farthest gamma ray burst ever observed, with a redshift of about 8.1. We present within the fireshell scenario a complete analysis of this GRB. We model the prompt emission and the first rapid flux decay of the afterglow emission as being to the canonical emission of the interaction in the interval $0 \leq t \leq 440$ s by using accelerated baryonic matter with the circumburst medium. After the data reduction of the Swift data in the BAT (15 - 150 keV) and XRT (0.2 - 10 keV) energy bands, we interpret the light curves and the spectral distribution in the context of the fireshell scenario. We also confirm in this source the existence of a second component, a plateau phase, as being responsible for the late emission in the X-ray light curve. This extra component originates from the fact that the ejecta have a range of the bulk Lorentz Γ factor, which starts to interact each other ejecta at the start of the plateau phase.

17. L. Caito, L. Amati, M.G. Bernardini, C.L. Bianco, G. De Barros, L. Izzo, B. Patricelli, R. Ruffini; "GRB 071227: an additional case of a disguised

short burst"; Astronomy & Astrophysics, 521, A80 (2010).

Context: Observations of gamma-ray bursts (GRBs) have shown an hybridization between the two classes of long and short bursts. In the context of the fireshell model, the GRB light curves are formed by two different components: the *proper* GRB (P-GRB) and the extended afterglow. Their relative intensity is linked to the fireshell baryon loading B. The GRBs with P-GRB predominance are the short ones, the remainders are long. A new family of *disguised* short bursts has been identified: long bursts with a protracted low instantaneous luminosity due to a low density CircumBurst Medium (CBM). In the 15–150 keV energy band GRB 071227 exhibits a short duration (about 1.8s) spike-like emission followed by a very soft extended tail up to one hundred seconds after the trigger. It is a faint ($E_{iso} = 5.8 \times 10^{50}$) nearby GRB ($z = 0.383$) that does not have an associated type Ib/c bright supernova (SN). For these reasons, GRB 071227 has been classified as a short burst not fulfilling the Amati relation holding for long burst. *Aims:* We check the classification of GRB 071227 provided by the fireshell model. In particular, we test whether this burst is another example of a *disguised* short burst, after GRB 970228 and GRB 060614, and, for this reason, whether it fulfills the Amati relation. *Methods:* We simulate GRB 071227 light curves in the *Swift* BAT 15–50 keV bandpass and in the XRT (0.3–10 keV) energy band within the fireshell model. *Results:* We perform simulations of the tail in the 15–50 keV bandpass, as well as of the first part of the X-ray afterglow. This infers that: $E_{tot}^{e^\pm} = 5.04 \times 10^{51}$ erg, $B = 2.0 \times 10^{-4}$, $E_{P-GRB}/E_{aft} \sim 0.25$, and $\langle n_{cbm} \rangle = 3.33$ particles/cm^3. These values are consistent with those of "long duration" GRBs. We interpret the observed energy of the first hard emission by identifying it with the P-GRB emission. The remaining long soft tail indeed fulfills the Amati relation. *Conclusions:* Previously classified as a short burst, GRB 071227 on the basis of our analysis performed in the context of the fireshell scenario represents another example of a *disguised* short burst, after GRB 970228 and GRB 060614. Further confirmation of this result is that the soft tail of GRB 071227 fulfills the Amati relation.

18. M.G. Bernardini, C.L. Bianco, L. Caito, L. Izzo, B. Patricelli, R. Ruffini; "Analysis of GRB060607A within the fireshell model: prompt emission, X-ray flares and late afterglow phase"; Astronomy & Astrophysics, submitted to.

Context: GRB060607A is a very distant ($z = 3.082$) and energetic event ($E_{iso} \sim 10^{53}$ erg). Its main peculiarity is that the peak of the near-infrared (NIR) af-

terglow has been observed with the REM robotic telescope. This NIR peak has been interpreted as the afterglow onset within the fireball forward shock model, and the initial Lorentz gamma factor of the emitting system has been inferred. *Aims*: We analyze GRB060607A within the fireshell model. We emphasize the central role of the prompt emission in determining the initial Lorentz gamma factor of the extended afterglow and we interpret the X-ray flares as produced by the interaction of the optically thin fireshell with overdense CircumBurst Medium (CBM) clumps. *Methods*: We deal only with the Swift BAT and XRT observations, that are the basic contribution to the GRB emission and that are neglected in the treatment adopted in the current literature. The numerical modeling of the fireshell dynamics allows to calculate all its characteristic quantities, in particular the exact value of the Lorentz gamma factor at the transparency. *Results*: We show that the theoretically computed prompt emission light curves are in good agreement with the observations in all the *Swift* BAT energy bands as well as the spectra integrated over different time intervals. The flares observed in the decaying phase of the X-ray afterglow are also reproduced by the same mechanism, but in a region in which the typical dimensions of the clumps are smaller than the visible area of the fireshell and most energy lies in the X-ray band due to the hard-to-soft evolution. *Conclusions*: We show that it is possible to obtain flares with $\Delta t/t$ compatible with the observations when the three-dimensional structure of the CBM clumps is duly taken into account. We stop our analysis at the beginning of the X-ray plateau phase, since we suppose this originates from the instabilities developed in the collision between different subshells within a structured fireshell.

19. G. de Barros, M. G. Bernardini, C.L. Bianco, L. Caito, L. Izzo, B. Patricelli, R. Ruffini; "On the nature of GRB 050509b: a disguised short GRB"; Astronomy & Astrophyscs, 529, A130 (2011)

Context: GRB 050509b, detected by the *Swift* satellite, is the first case where an X-ray afterglow has been observed associated with a short gamma-ray burst (GRB). Within the fireshell model, the canonical GRB light curve presents two different components: the proper-GRB (P-GRB) and the extended afterglow. Their relative intensity is a function of the fireshell baryon loading parameter B and of the CircumBurst Medium (CBM) density (n_{CBM}). In particular, the traditionally called short GRBs can be either "genuine" short GRBs (with $B \lesssim 10^{-5}$, where the P-GRB is energetically predominant) or "disguised" short GRBs (with $B \gtrsim 3.0 \times 10^{-4}$ and $n_{CBM} \ll 1$, where the extended afterglow is energetically predominant). *Aims*: We verify whether GRB 050509b can be clas-

sified as a "genuine" short or a "disguised" short GRB, in the fireshell model. *Methods*: We investigate two alternative scenarios. In the first, we start from the assumption that this GRB is a "genuine" short burst. In the second attempt, we assume that this GRB is a "disguised" burst. *Results*: If GRB 050509b were a genuine short GRB, there should initially be very hard emission which is ruled out by the observations. The analysis that assumes that this is a disguised short GRB is compatible with the observations. The theoretical model predicts a value of the extended afterglow energy peak that is consistent with the Amati relation. *Conclusions*: GRB 050509b cannot be classified as a "genuine" short GRB. The observational data are consistent with a "disguised" short GRB classification, i.e., a long burst with a weak extended afterglow "deflated" by the low density of the CBM. We expect that all short GRBs with measured redshifts are disguised short GRBs because of a selection effect: if there is enough energy in the afterglow to measure the redshift, then the proper GRB must be less energetic than the afterglow. The Amati relation is found to be fulfilled only by the extended afterglow excluding the P-GRB.

20. L. Caito, M.G. Bernardini, C.L. Bianco, L. Izzo, B. Patricelli, R. Ruffini; "GRB 071227: another disguised short burst"; International Journal of Modern Physics D, 20, 1931 (2011).

    Observations of Gamma-ray Bursts (GRBs) put forward in the recent years have revealed, with increasing evidence, that the historical classification between long and short bursts has to be revised. Within the Fireshell scenario, both short and long bursts are canonical bursts, consisting of two different phases. First, a Proper-GRB (P-GRB), that is the emission of photons at the transparency of the fireshell. Then, the Extended Afterglow, multiwavelength emission due to the interacion of the baryonic remnants of the fireshell with the CircumBurst Medium (CBM). We discriminate between long and short bursts by the amount of energy stored in the first phase with respect to the second one. Within the Fireshell scenario, we have introduced a third intermediate class: the disguised GRBs. They appear like short bursts, because their morphology is characterized by a first, short, hard episode and a following deflated tail, but this last part — coincident with the peak of the afterglow — is energetically predominant. The origin of this peculiar kind of sources is inferred to a very low average density of the environment (of the order of 10^{-3}). After GRB 970228 and GRB 060614, we find in GRB 071227 a third example of disguised burst.

21. L. Izzo, M.G. Bernardini, C.L. Bianco, L. Caito, B. Patricelli, L.J. Rangel Lemos, R. Ruffini; "GRB 080916C and the high-energy emission in the fireshell scenario"; International Journal of Modern Physics D, 20, 1949 (2011).

In this paper we discuss a possible explanation for the high energy emission (up to $\sim$ GeV) seen in GRB 080916C. We propose that the GeV emission is originated by the collision between relativistic baryons in the fireshell after the transparency and the nucleons located in molecular clouds near the burst site. This collision should give rise pion production, whose immediate decay provides high energy photons, neutrinos and leptons. Using a public code (SYBILL) we simulate these relativistic collisions in their simple form, so that we can draw our preliminar results in this paper. We will present moreover our hypothesis that the delayed onset of this emission identifies in a complete way the P-GRB emission.

22. B. Patricelli, M.G. Bernardini, C.L. Bianco, L. Caito, L. Izzo, R. Ruffini, G. Vereshchagin; "A new spectral energy distribution of photons in the fireshell model of GRBs"; International Journal of Modern Physics D, 20, 1983 (2011).

The analysis of various Gamma-Ray Bursts (GRBs) having a low energetics (an isotropic energy $E_{iso} \lesssim 10^{53}$ ergs) within the fireshell model has shown how the $N(E)$ spectrum of their prompt emission can be reproduced in a satisfactory way by a convolution of thermal spectra. Nevertheless, from the study of very energetic bursts ($E_{iso} \lesssim 10^{54}$ ergs) such as, for example, GRB 080319B, some discrepancies between the numerical simulations and the observational data have been observed. We investigate a different spectrum of photons in the comoving frame of the fireshell in order to better reproduce the spectral properties of GRB prompt emission within the fireshell model. We introduce a phenomenologically modified thermal spectrum: a thermal spectrum characterized by a different asymptotic power-law index in the low energy region. Such an index depends on a free parameter α, so that the pure thermal spectrum corresponds to the case $\alpha = 0$. We test this spectrum by comparing the numerical simulations with the observed prompt emission spectra of various GRBs. From this analysis it has emerged that the observational data can be correctly reproduced by assuming a modified thermal spectrum with $\alpha = -1.8$.

23. A.V. Penacchioni, R. Ruffini, L. Izzo, M. Muccino, C.L. Bianco, L. Caito, B. Patricelli, L. Amati; "Evidence for a proto-black hole and a double

astrophysical component in GRB 101023"; Astronomy & Astrophysics, 538, A58 (2012).

Context: It has been recently shown that GRB 090618, observed by AGILE, Coronas Photon, Fermi, Konus, Suzaku and Swift, is composed of two very different components: episode 1, lasting 50 s, shows a thermal plus power-law spectrum with a characteristic temperature evolving in time as a power law; episode 2 (the remaining 100 s) is a canonical long GRB. We have associated episode 1 to the progenitor of a collapsing bare core leading to the formation of a black hole: what was defined as a "proto black hole". *Aims*: In precise analogy with GRB 090618 we aim to analyze the 89s of the emission of GRB 101023, observed by Fermi, Gemini, Konus and Swift, to see if there are two different episodes: the first one presenting a characteristic black-body temperature evolving in time as a broken power law, and the second one consistent with a canonical GRB. *Methods*: To obtain information on the spectra, we analyzed the data provided by the GBM detector onboard the Fermi satellite, and we used the heasoft package XSPEC and RMFIT to obtain their spectral distribution. We also used the numerical code GRBsim to simulate the emission in the context of the fireshell scenario for episode 2. *Results*: We confirm that the first episode can be well fit by a black body plus power-law spectral model. The temperature changes with time following a broken power law, and the photon index of the power-law component presents a soft-to-hard evolution. We estimate that the radius of this source increases with time with a velocity of $1.5 \times 10^4 km/s$. The second episode appears to be a canonical GRB. By using the Amati and the Atteia relations, we determined the cosmological redshift, $z \sim 0.9 \pm 0.084(stat.) \pm 0.2(sys.)$. The results of GRB 090618 are compared and contrasted with the results of GRB 101023. Particularly striking is the scaling law of the soft X-ray component of the afterglow. *Conclusions*: We identify GRB 090618 and GRB 101023 with a new family of GRBs related to a single core collapse and presenting two astrophysical components: a first one related to the proto-black hole prior to the process of gravitational collapse (episode 1), and a second one, which is the canonical GRB (episode 2) emitted during the formation of the black hole. For the first time we are witnessing the process of a black hole formation from the instants preceding the gravitational collapse up to the GRB emission. This analysis indicates progress towards developing a GRB distance indicator based on understanding the P-GRB and the prompt emission, as well as the soft X-ray behavior of the late afterglow.

24. R. Negreiros, R. Ruffini, C. L. Bianco, J. A. Rueda; "Cooling of young

neutron stars in GRB associated to supernovae"; Astronomy & Astrophysics, 540, A12 (2012).

Context: The traditional study of neutron star cooling has been generally applied to quite old objects such as the Crab Pulsar (957 years) or the central compact object in Cassiopeia A (330 years) with an observed surface temperature $\sim 10^6$ K. However, recent observations of the late ($t = 10^8$–10^9 s) emission of the supernovae (SNe) associated to GRBs (GRB-SN) show a distinctive emission in the X-ray regime consistent with temperatures $\sim 10^7$–10^8 K. Similar features have been also observed in two Type Ic SNe SN 2002ap and SN 1994I that are not associated to GRBs. *Aims*: We advance the possibility that the late X-ray emission observed in GRB-SN and in isolated SN is associated to a hot neutron star just formed in the SN event, here defined as a neo-neutron star. *Methods*: We discuss the thermal evolution of neo-neutron stars in the age regime that spans from ~ 1 minute (just after the proto-neutron star phase) all the way up to ages < 10–100 yr. We examine critically the key factor governing the neo-neutron star cooling with special emphasis on the neutrino emission. We introduce a phenomenological heating source, as well as new boundary conditions, in order to mimic the high temperature of the atmosphere for young neutron stars. In this way we match the neo-neutron star luminosity to the observed late X-ray emission of the GRB-SN events: URCA-1 in GRB980425-SN1998bw, URCA-2 in GRB030329-SN2003dh, and URCA-3 in GRB031203-SN2003lw. *Results*: We identify the major role played by the neutrino emissivity in the thermal evolution of neo-neutron stars. By calibrating our additional heating source at early times to $\sim 10^{12}$–10^{15} erg/g/s, we find a striking agreement of the luminosity obtained from the cooling of a neo-neutron stars with the prolonged ($t = 10^8$–10^9 s) X-ray emission observed in GRB associated with SN. It is therefore appropriate a revision of the boundary conditions usually used in the thermal cooling theory of neutron stars, to match the proper conditions of the atmosphere at young ages. The traditional thermal processes taking place in the crust might be enhanced by the extreme high-temperature conditions of a neo-neutron star. Additional heating processes that are still not studied within this context, such as e^+e^- pair creation by overcritical fields, nuclear fusion, and fission energy release, might also take place under such conditions and deserve further analysis. *Conclusions*: Observation of GRB-SN has shown the possibility of witnessing the thermal evolution of neo-neutron stars. A new campaign of dedicated observations is recommended both of GRB-SN and of isolated Type Ic SN.

25. L. Izzo, R. Ruffini, A.V. Penacchioni, C.L. Bianco, L. Caito, S.K. Chakrabarti, J.A. Rueda, A. Nandi, B. Patricelli; "A double component in GRB 090618: a proto-black hole and a genuinely long gamma-ray burst"; Astronomy & Astrophysics, 543, A10 (2012).

Context: The joint X-ray and gamma-ray observations of GRB 090618 by very many satellites offer an unprecedented possibility of testing crucial aspects of theoretical models. In particular, they allow us to test (a) in the process of gravitational collapse, the formation of an optically thick e+e.-baryon plasma self-accelerating to Lorentz factors in the range $200 < \Gamma < 3000$; (b) its transparency condition with the emission of a component of 10^{53-54} baryons in the TeV region and (c) the collision of these baryons with the circumburst medium (CBM) clouds, characterized by dimensions of 10^{15-16} cm. In addition, these observations offer the possibility of testing a new understanding of the thermal and power-law components in the early phase of this GRB. *Aims*: We test the fireshell model of GRBs in one of the closest ($z = 0.54$) and most energetic ($E_{iso} = 2.90 \times 10^{53}$ erg) GRBs, namely GRB 090618. It was observed at ideal conditions by several satellites, namely *Fermi*, *Swift*, Konus-WIND, AGILE, RT-2, and Suzaku, as well as from on-ground optical observatories. *Methods*: We analyzed the emission from GRB 090618 using several spectral models, with special attention to the thermal and power-law components. We determined the fundamental parameters of a canonical GRB within the context of the fireshell model, including the identification of the total energy of the e^+e^- plasma, E_{tot}^{e+e-}, the proper GRB (P-GRB), the baryon load, the density and structure of the CBM. *Results*: We find evidence of the existence of two different episodes in GRB 090618. The first episode lasts 50 s and is characterized by a spectrum consisting of a thermal component, which evolves between $kT = 54$ keV and $kT = 12$ keV, and a power law with an average index $\gamma = 1.75 \pm 0.04$. The second episode, which lasts for ~ 100 s, behaves as a canonical long GRB with a Lorentz gamma factor at transparency of $\Gamma = 495$, a temperature at transparency of 29.22 keV and with a characteristic size of the surrounding clouds of $R_{cl} \sim 10^{15-16}$ cm and masses of $\sim 10^{22-24}$ g. *Conclusions*: We support the recently proposed two-component nature of GRB 090618, namely, episode 1 and episode 2, with a specific theoretical analysis. We furthermore illustrate that episode 1 cannot be considered to be either a GRB or a part of a GRB event, but it appears to be related to the progenitor of the collapsing bare core, leading to the formation of the black hole, which we call a "proto-black hole". Thus, for the first time, we are witnessing the process of formation of a black

hole from the phases just preceding the gravitational collapse all the way up to the GRB emission.

26. B. Patricelli, M.G. Bernardini, C.L. Bianco, L. Caito, G. De Barros, L. Izzo, R. Ruffini, G.V. Vereshchagin; "Analysis of GRB 080319B and GRB 050904 within the Fireshell Model: Evidence for a Broader Spectral Energy Distribution"; The Astrophysical Journal, 756, 16 (2012).

The observation of GRB 080319B, with an isotropic energy $E_{iso} = 1.32 \times 10^{54}$ erg, and GRB 050904, with $E_{iso} = 1.04 \times 10^{54}$ erg, offers the possibility of studying the spectral properties of the prompt radiation of two of the most energetic Gamma Ray Bursts (GRBs). This allows us to probe the validity of the fireshell model for GRBs beyond 10^{54} erg, well outside the energy range where it has been successfully tested up to now (10^{49}–10^{53} erg). We find that in the low energy region, the prompt emission spectra observed by *Swift* BAT reveals more power than theoretically predicted. The opportunities offered by these observations to improve the fireshell model are outlined in this paper. One of the distinguishing features of the fireshell model is that it relates the observed GRB spectra to the spectrum in the comoving frame of the fireshell. Originally, a fully radiative condition and a comoving thermal spectrum were adopted. An additional power-law in the comoving thermal spectrum is required due to the discrepancy of the theoretical and observed light curves and spectra in the fireshell model for GRBs 080319B and 050904. A new phenomenological parameter α is correspondingly introduced in the model. We perform numerical simulations of the prompt emission in the *Swift* BAT bandpass by assuming different values of α within the fireshell model. We compare them with the GRB 080319B and GRB 050904 observed time-resolved spectra, as well as with their time-integrated spectra and light curves. Although GRB 080319B and GRB 050904 are at very different redshifts (z=0.937 and z=6.29 respectively), a value of $\alpha = -1.8$ leads for both of them to a good agreement between the numerical simulations and the observed BAT light curves, time-resolved and time-integrated spectra. Such a modified spectrum is also consistent with the observations of previously analyzed less energetic GRBs and reasons for this additional agreement are given. Perspectives for future low energy missions are outlined.

27. M. Muccino, R. Ruffini, C.L. Bianco, L. Izzo, A.V. Penacchioni; "GRB 090227B: The missing link between the genuine short and long GRBs"; The Astrophysical Journal, 763, 125 (2013).

The time-resolved spectral analysis of GRB 090227B, made possible by the *Fermi*-GBM data, allows to identify in this source the missing link between the genuine short and long GRBs. Within the Fireshell model of the Gamma-Ray Bursts (GRBs) we predict genuine short GRBs: bursts with the same inner engine of the long bursts but endowed with a severely low value of the Baryon load, $B \lesssim 5 \times 10^{-5}$. A first energetically predominant emission occurs at the transparency of the e^+e^- plasma, the Proper-GRB (P-GRB), followed by a softer emission, the extended afterglow. The typical separation between the two emissions is expected to be of the order of $10^{-3} - 10^{-2}$ s. We identify the P-GRB of GRB 090227B in the first 96 ms of emission, where a thermal component with the temperature $kT = (517 \pm 28)$ keV and a flux comparable with the non thermal part of the spectrum is observed. This non thermal component as well as the subsequent emission, where there is no evidence for a thermal spectrum, is identified with the extended afterglow. We deduce a theoretical cosmological redshift $z = 1.61 \pm 0.14$. We then derive the total energy $E^{tot}_{e^+e^-} = (2.83 \pm 0.15) \times 10^{53}$ ergs, the Baryon load $B = (4.13 \pm 0.05) \times 10^{-5}$, the Lorentz Γ factor at transparency $\Gamma_{tr} = (1.44 \pm 0.01) \times 10^4$, and the intrinsic duration $\Delta t' \sim 0.35$ s. We also determine the average density of the CircumBurst Medium (CBM), $\langle n_{CBM} \rangle = (1.90 \pm 0.20) \times 10^{-5}$ particles/cm^3. There is no evidence of beaming in the system. In view of the energetics and of the Baryon load of the source, as well as of the low interstellar medium and of the intrinsic time scale of the signal, we identify the GRB progenitor as a binary neutron star. From the recent progress in the theory of neutron stars, we obtain masses of the stars $m_1 = m_2 = 1.34 M_\odot$ and their corresponding radii $R_1 = R_2 = 12.24$ km and thickness of their crusts ~ 0.47 km, consistent with the above values of the Baryon load, of the energetics and of the time duration of the event.

28. A.V. Penacchioni, R. Ruffini, C.L. Bianco, L. Izzo, M. Muccino, G.B. Pisani, J.A. Rueda; "GRB 110709B in the induced gravitational collapse paradigm"; Astronomy & Astrophysics, 551, A133 (2013).

Context: GRB 110709B is the first source for which *Swift* BAT triggered twice, with a time separation of ~ 10 minutes. The first emission (called here Episode 1) goes from 40 s before the first trigger up to 60 s after it. The second emission (hereafter Episode 2) goes from 35 s before the second trigger to 100 s after it. These features reproduce the ones of GRB 090618, which has been recently interpreted within the Induced Gravitational Collapse paradigm (IGC). In line with this paradigm we assume the progenitor to be a close binary system composed of a core of an evolved star and a Neutron Star (NS). The evolved star

explodes as a Supernova (SN) and ejects material that is partially accreted by the NS. We identify this process with Episode 1. The accretion process brings the NS over its critical mass, thus gravitationally collapsing to a BH. This process leads to the GRB emission, Episode 2. The double trigger has given for the first time the possibility to have a coverage of the X-ray emission observed by XRT both prior to and during the prompt phase of GRB 110709B. *Aims*: We analyze the spectra and time variability of Episode 1 and 2 and compute the relevant parameters of the binary progenitor, as well as the astrophysical parameters both in the SN and the GRB phase in the IGC paradigm. *Methods*: We perform a time-resolved spectral analysis of Episode 1 by fitting the spectrum with a blackbody (BB) plus a power-law (PL) spectral model. From the BB fluxes and temperatures of Episode 1 and the luminosity distance d_L, we evaluate the evolution with time of the radius of the BB emitter, associated here to the evolution of the SN ejecta. We analyze Episode 2 within the Fireshell model, identifying the Proper-GRB (P-GRB) and simulating the light curve and spectrum. We establish the redshift to be $z = 0.75$, following the phenomenological methods by Amati, by Yonetoku and by Grupe, and our analysis of the late X-ray afterglow. It is most remarkable that the determination of the cosmological redshift on the ground of the scaling of the late X-ray afterglow, already verified in GRB 090618 and GRB 101023, is again verified by this analysis. *Results*: We find for Episode 1 a temperature of the BB component that evolves with time following a broken PL, with the slope of the PL at early times $\alpha = 0$ (constant function) and the slope of the PL at late times $\beta = -4 \pm 2$. The break occurs at $t = 41.21$ s. The total energy of Episode 1 is $E_{iso}^{(1)} = 1.42 \times 10^{53}$ erg. The total energy of Episode 2 is $E_{iso}^{(2)} = 2.43 \times 10^{52}$ erg. We find at transparency a Lorentz factor $\Gamma \sim 1.73 \times 10^2$, laboratory radius of 6.04×10^{13} cm, P-GRB observed temperature $kT_{P-GRB} = 12.36$ keV, baryon load $B = 5.7 \times 10^{-3}$ and P-GRB energy of $E_{P-GRB} = 3.44 \times 10^{50}$ erg. We find a remarkable coincidence of the cosmological redshift by the scaling of the XRT data and with three other phenomenological methods. *Conclusions*: We interpret GRB 110709B as a member of the IGC sources, together with GRB 970828, GRB 090618 and GRB 101023. The existence of the XRT data during the prompt phase of the emission of GRB 110709B (Episode 2) offers an unprecedented tool for improving the diagnostic of GRBs emission.

29. G.B. Pisani, L. Izzo, R. Ruffini, C.L. Bianco, M. Muccino, A.V. Penacchioni, J.A. Rueda, Y. Wang; "Novel distance indicator for gamma-ray bursts associated with supernovae"; Astronomy & Astrophysics, 552,

L5 (2013).

Context: In recent years it has been proposed that the temporal coincidence of a Gamma Ray Burst (GRB) and a type Ib/c supernova (SN) can be explained by the concept of Induced Gravitational Collapse (IGC) of a Neutron Star (NS) to a Black Hole (BH) by accretion of matter ejected by a SN Ib/c. This scenario reveals a possible common behavior in the late time X-ray emission of this subclass of GRBs. *Aims*: We want to test if such a common behavior can actually be present in the sources belonging to this GRB sub-class and if this may lead to a redshift estimator for these sources. *Methods*: We build a sample of GRBs belonging to this sub-class, and we rescale the X-ray light curves of all of them both in time and in flux to a common cosmological redshift. *Results*: We found that the X-ray light curves of all the GRBs of the sample with a measured redshift present a common late time behavior when rescaled to a common redshift $z = 1$. We then use this result to estimate the redshift of the GRBs of the sample with no measured redshift. *Conclusions*: The common behavior in the late decay of the X-ray light curves of the GRBs of the sample points to a common physical mechanism in this particular phase of the GRB emission, possibly related to the SN process. This scenario may represent an invaluable tool to estimate the redshift of GRBs belonging to this sub-class of events. More GRBs are therefore needed in order to enlarge the subclass and to make more stringent constraints on the redshift estimates performed with this method for GRBs pertaining to this class.

30. C.L. Bianco, M. G. Bernardini, L. Caito, G. De Barros, L. Izzo, M. Muc-cino, B. Patricelli, A.V. Penacchioni, G.B. Pisani, R. Ruffini; "The canonical GRB scenario"; Il Nuovo Cimento C, 36 s01, 21 (2013).

The canonical GRB scenario implied by the fireshell model is briefly summarized.

31. A.V. Penacchioni, R. Ruffini, L. Izzo, M. Muccino, C.L. Bianco, L. Caito, B. Patricelli; "Evidences for a double component in the emission of GRB 101023"; Il Nuovo Cimento C, 36 s01, 117 (2013).

In this work we present the results of the analysis of GRB 101023 in the fireshell scenario. Its redshift is not known, so we attempted to infer it from the Amati Relation, obtaining $z = 0.9$. Its light curve presents a double emission, which makes it very similar to the already studied GRB 090618. We called each part Episode 1 and Episode 2. We performed a time-resolved spectral

analysis with RMFIT using different spectral models, and fitted the light curve with a numerical code integrating the fireshell equations of motion. We used Fermi GBM data to build the light curve, in particular the second NaI detector, in the range (8.5–1000 keV). We considered different hypotheses regarding which part of the light curve could be the GRB and performed the analysis of all of them. We noticed a great variation of the temperature with time in the first episode, as well as almost no variation of the progenitor radius. We found that the first emission does not match the requirements for a GRB, while the second part perfectly agrees with being a canonical GRB, with a P-GRB lasting 4 s.

32. M. Muccino, R. Ruffini, C.L. Bianco, L. Izzo, A.V. Penacchioni, G.B. Pisani; "GRB 090510: A Disguised Short Gamma-Ray Burst with the Highest Lorentz Factor and Circumburst Medium"; The Astrophysical Journal, 772, 62 (2013).

GRB 090510, observed both by Fermi and AGILE satellites, is the first bright short-hard Gamma-Ray Burst (GRB) with an emission from the keV up to the GeV energy range. Within the Fireshell model, we interpret the faint precursor in the light curve as the emission at the transparency of the expanding e^+e^- plasma: the Proper-GRB (P-GRB). From the observed isotropic energy we assume a total plasma energy $E_{e^+e^-}^{tot} = (1.10 \pm 0.06) \times 10^{53}$ erg and derive a Baryon load $B = (1.45 \pm 0.28) \times 10^{-3}$ and a Lorentz factor at transparency $\Gamma_{tr} = (6.7 \pm 1.6) \times 10^2$. The main emission ~ 0.4s after the initial spike is interpreted as the extended afterglow, due to the interaction of the ultrarelativistic baryons with the CircumBurst Medium (CBM). Using the condition of fully radiative regime, we infer a CBM average spherically symmetric density of $\langle n_{CBM} \rangle = (1.85 \pm 0.14) \times 10^3$ particles/cm^3, one of the highest found in the Fireshell model. The value of the filling factor, $1.5 \times 10^{-10} \leq \mathcal{R} \leq 3.8 \times 10^{-8}$, leads to the estimate of filaments with densities $n_{fil} = n_{CBM}/\mathcal{R} \approx (10^6 - 10^{14})$ particles/cm^3. The sub-MeV and the MeV emissions are well reproduced. When compared to the canonical GRBs with $\langle n_{CBM} \rangle \approx 1$ particles/cm^3 and to the disguised short GRBs with $\langle n_{CBM} \rangle \approx 10^{-3}$ particles/cm^3, the case of GRB 090510 leads to the existence of a new family of bursts exploding in an over-dense galactic region with $\langle n_{CBM} \rangle \approx 10^3$ particles/cm^3. The joint effect of the high Γ_{tr} and the high density compresses in time and "inflates" in intensity the extended afterglow, making it appear as a short burst, which we here define as "disguised short GRB by excess". The determination of the above parameters values may represent an important step towards the explanation

of the GeV emission.

33. R. Ruffini, M. Muccino, C.L. Bianco, M. Enderli, L. Izzo, M. Kovacevic, A.V. Penacchioni, G.B. Pisani, J.A. Rueda, Y. Wang; "On Binary Driven Hypernovae and their nested late X-ray emission"; Astronomy & Astrophysics, 565, L10 (2014).

Context: The induced gravitational collapse (IGC) paradigm addresses the very energetic (10^{52}–10^{54} erg) long gamma-ray bursts (GRBs) associated to supernovae (SNe). Unlike the traditional "collapsar" model, an evolved FeCO core with a companion neutron star (NS) in a tight binary system is considered as the progenitor. This special class of sources, here named "binary driven hypernovae" (BdHNe), presents a composite sequence composed of four different episodes with precise spectral and luminosity features.

Aims: We first compare and contrast the steep decay, the plateau, and the power-law decay of the X-ray luminosities of three selected BdHNe (GRB 060729, GRB 061121, and GRB 130427A). Second, to explain the different sizes and Lorentz factors of the emitting regions of the four episodes, for definiteness, we use the most complete set of data of GRB 090618. Finally, we show the possible role of r-process, which originates in the binary system of the progenitor.

Methods: We compare and contrast the late X-ray luminosity of the above three BdHNe. We examine correlations between the time at the starting point of the constant late power-law decay t_a^*, the average prompt luminosity $\langle L_{iso} \rangle$, and the luminosity at the end of the plateau L_a. We analyze a thermal emission ($\sim$ 0.97–0.29 keV), observed during the X-ray steep decay phase of GRB 090618.

Results: The late X-ray luminosities of the three BdHNe, in the rest-frame energy band 0.3–10 keV, show a precisely constrained "nested" structure. In a space-time diagram, we illustrate the different sizes and Lorentz factors of the emitting regions of the three episodes. For GRB 090618, we infer an initial dimension of the thermal emitter of $\sim 7 \times 10^{12}$ cm, expanding at $\Gamma \approx 2$. We find tighter correlations than the Dainotti-Willingale ones.

Conclusions: We confirm a constant slope power-law behavior for the late X-ray luminosity in the source rest frame, which may lead to a new distance indicator for BdHNe. These results, as well as the emitter size and Lorentz factor, appear to be inconsistent with the traditional afterglow model based on synchrotron emission from an ultra-relativistic ($\Gamma \sim 10^2$–10^3) collimated jet outflow. We argue, instead, for the possible role of r-process, originating in the binary system, to power the mildly relativistic X-ray source.

34. R. Ruffini, L. Izzo, M. Muccino, G.B. Pisani, J.A. Rueda, Y. Wang, C. Barbarino, C.L. Bianco, M. Enderli, M. Kovacevic; "Induced gravitational collapse at extreme cosmological distances: the case of GRB 090423"; Astronomy & Astrophysics, 569, A39 (2014).

    Context: The induced gravitational collapse (IGC) scenario has been introduced in order to explain the most energetic gamma ray bursts (GRBs), $E_{iso} = 10^{52} - 10^{54}$ erg, associated with type Ib/c supernovae (SNe). It has led to the concept of binary-driven hypernovae (BdHNe) originating in a tight binary system composed by a FeCO core on the verge of a SN explosion and a companion neutron star (NS). Their evolution is characterized by a rapid sequence of events: 1) The SN explodes, giving birth to a new NS (νNS). The accretion of SN ejecta onto the companion NS increases its mass up to the critical value; 2) The consequent gravitational collapse is triggered, leading to the formation of a black hole (BH) with GRB emission; 3) A novel feature responsible for the emission in the GeV, X-ray, and optical energy range occurs and is characterized by specific power-law behavior in their luminosity evolution and total spectrum; 4) The optical observations of the SN then occurs.
    Aims: We investigate whether GRB 090423, one of the farthest observed GRB at $z = 8.2$, is a member of the BdHN family.
    Methods: We compare and contrast the spectra, the luminosity evolution, and the detectability in the observations by *Swift* of GRB 090423 with the corresponding ones of the best known BdHN case, GRB 090618.
    Results: Identification of constant slope power-law behavior in the late X-ray emission of GRB 090423 and its overlapping with the corresponding one in GRB 090618, measured in a common rest frame, represents the main result of this article. This result represents a very significant step on the way to using the scaling law properties, proven in Episode 3 of this BdHN family, as a cosmological standard candle.
    Conclusions: Having identified GRB 090423 as a member of the BdHN family, we can conclude that SN events, leading to NS formation, can already occur already at $z = 8.2$, namely at 650 Myr after the Big Bang. It is then possible that these BdHNe originate stem from 40-60 $M_\odot$ binaries. They are probing the Population II stars after the completion and possible disappearance of Population III stars.

35. M. Muccino, C.L. Bianco, L. Izzo, Y. Wang, M. Enderli, M. Kovacevic, G.B. Pisani, A.V. Penacchioni, R. Ruffini; "The Genuine Short GRB 090227B and the Disguised by Excess GRB 090510"; Gravitation and

Cosmology, 20, 197 (2014).

GRB 090227B and GRB 090510, traditionally classified as short gamma-ray Bursts (GRBs), indeed originate from different systems. For GRB 090227B we inferred a total energy of the e^+e^- plasma $E^{tot}_{e^+e^-} = (2.83 \pm 0.15) \times 10^{53}$ erg, a baryon load of $B = (4.1 \pm 0.05) \times 10^{-5}$, and a CircumBurst Medium (CBM) average density $\langle n_{CBM} \rangle = (1.90 \pm 0.20) \times 10^{-5}$ cm^{-3}. From these results we have assumed the progenitor of this burst to be a symmetric neutron stars (NSs) merger with masses $m = 1.34 M_\odot$, radii $R = 12.24$ km. GRB 090510, instead, has $E^{tot}_{e^+e^-} = (1.10 \pm 0.06) \times 10^{53}$ erg, $B = (1.45 \pm 0.28) \times 10^{-3}$, implying a Lorentz factor at transparency of $\Gamma = (6.7 \pm 1.7) \times 10^2$, which are characteristic of the long GRB class, and a very high CBM density, $\langle n_{CBM} \rangle = (1.85 \pm 0.14) \times 10^3$ cm^{-3}. The joint effect of the high values of Γ and of $\langle n_{CBM} \rangle$ compresses in time and "inflates" in intensity in an extended afterglow, making appear GRB 090510 as a short burst, which we here define as "disguised short GRB by excess" occurring an overdense region with 10^3 cm^{-3}.

36. M. Muccino, C.L. Bianco, L. Izzo, Y. Wang, M. Enderli, G.B. Pisani, A.V. Penacchioni, R. Ruffini; "Two short bursts originating from different astrophysical systems: The genuine short GRB 090227B and the disguised short GRB 090510 by excess"; Journal of the Korean Physical Society, 65, 865 (2014).

GRB 090227B and GRB 090510 are two gamma-ray bursts (GRBs) traditionally classified as short bursts. The major outcome of our analysis is that they indeed originate from different systems. In the case of GRB 090227B, from the inferred values of the total energy of the e^+e^- plasma, $E^{tot}_{e^+e^-} = (2.83 \pm 0.15) \times 10^{53}$ erg, the engulfed baryonic mass M_B, expressed as $B = M_B c^2 / E^{tot}_{e^+e^-} = (4.1 \pm 0.05) \times 10^{-5}$, and the circumburst medium (CBM) average density, $\langle n_{CBM} \rangle = (1.90 \pm 0.20) \times 10^{-5}$ cm^{-3}, we have assumed the progenitor of this burst to be a symmetric neutron star (NS) merger with masses $m = 1.34 M_\odot$, radii $R = 12.24$ km, and crustal thicknesses of ~ 0.47 km. In the case of GRB 090510, we have derived the total plasma energy, $E^{tot}_{e^+e^-} = (1.10 \pm 0.06) \times 10^{53}$ erg, the Baryon load, $B = (1.45 \pm 0.28) \times 10^{-3}$, and the Lorentz factor at transparency, $\Gamma = (6.7 \pm 1.7) \times 10^2$, which are characteristic of the long GRB class, as well as a very high CBM density, $\langle n_{CBM} \rangle = (1.85 \pm 0.14) \times 10^3$ cm^{-3}. The joint effect of the high values of Γ and $\langle n_{CBM} \rangle$ compresses in time and "inflates" in intensity the extended afterglow, making GRB 090510 appear to be a short burst, which we here define as a "disguised short GRB by excess", occurring

in an overdense region with 10^3 cm^{-3}.

37. R. Ruffini, Y. Wang, M. Kovacevic, C.L. Bianco, M. Enderli, M. Muccino, A.V. Penacchioni, G.B. Pisani, J. Rueda; "GRB 130427A and SN 2013cq: A Multi-wavelength Analysis of An Induced Gravitational Collapse Event"; The Astrophysical Journal, 798, 10 (2015).

We have performed our data analysis of the observations by *Swift*, *NuStar* and *Fermi* satellites in order to probe the induced gravitational collapse (IGC) paradigm for GRBs associated with supernovae (SNe), in the "terra incognita" of GRB 130427A. We compare and contrast our data analysis with those in the literature. We have verified that the GRB 130427A conforms to the IGC paradigm by examining the power law behavior of the luminosity in the early 10^4 s of the XRT observations. This has led to the identification of the four different episodes of the "binary driven hypernovae" (BdHNe) and to the prediction, on May 2, 2013, of the occurrence of SN 2013cq, duly observed in the optical band on May 13, 2013. The exceptional quality of the data has allowed the identification of novel features in *Episode 3* including: a) the confirmation and the extension of the existence of the recently discovered "nested structure" in the late X-ray luminosity in GRB 130427A, as well as the identification of a spiky structure at 10^2 s in the cosmological rest-frame of the source; b) a power law emission of the GeV luminosity light curve and its onset at the end of *Episode 2*; c) different Lorentz Γ factors for the emitting regions of the X-ray and GeV emissions in this *Episode 3*. These results make it possible to test the details of the physical and astrophysical regimes at work in the BdHNe: 1) a newly born neutron star and the supernova ejecta, originating in *Episode 1*, 2) a newly formed black hole originating in *Episode 2*, and 3) the possible interaction among these components, observable in the standard features of *Episode 3*.

38. M. Muccino, R. Ruffini, C.L. Bianco, M. Enderli, M. Kovacevic, L. Izzo, A.V. Penacchioni, G.B. Pisani, J.A. Rueda, Y. Wang; "On binary driven hypernovae and their nested late X-ray emission"; Astronomy Reports, 59, 581 (2015).

The induced gravitational collapse (IGC) paradigm addresses energetic (10^{52}–10^{54} erg), long gamma-ray bursts (GRBs) associated to supernovae (SNe) and proposes as their progenitors tight binary systems composed of an evolved FeCO core and a companion neutron star (NS). Their emission is characterized by four specific episodes: Episode 1, corresponding to the on-set of the FeCO

SN explosion and the accretion of the ejecta onto the companion NS; Episode 2, related the collapse of the companion NS to a black hole (BH) and to the emission of a long GRB; Episode 3, observed in X-rays and characterized by a steep decay, a plateau phase and a late power-law decay; Episode 4, corresponding to the optical SN emission due to the ^{56}Ni decay. We focus on Episode 3 and we show that, from the thermal component observed during the steep decay of the prototype GRB 090618, the emission region has a typical dimension of $\sim 10^{13}$ cm, which is inconsistent with the typical size of the emitting region of GRBs, e.g., $\sim 10^{16}$ cm. We propose, therefore, that the X-ray afterglow emission originates from a spherically symmetric SN ejecta expanding at $\Gamma \sim 2$ or, possibly, from the accretion onto the newly formed black hole, and we name these systems "binary driven hypernovae" (BdHNe). This interpretation is alternative to the traditional afterglow model based on the GRB synchrotron emission from a collimated jet outflow, expanding at ultra-relativistic Lorentz factor of $\Gamma \sim 10^2 - 10^3$ and originating from the collapse of a single object. We show then that the rest-frame energy band 0.3–10 keV X-ray luminosities of three selected BdHNe, GRB 060729, GRB 061121, and GRB 130427A, evidence a precisely constrained "nested" structure and satisfy precise scaling laws between the average prompt luminosity, $< L_{iso} >$, and the luminosity at the end of the plateau, L_a, as functions of the time at the end of the plateau. All these features extend the applicability of the "cosmic candle" nature of Episode 3. The relevance of r-process in fulfilling the demanding scaling laws and the nested structure are indicated.

39. R. Ruffini, J.A. Rueda, C. Barbarino, C. L. Bianco, H. Dereli, M. Enderli, L. Izzo, M. Muccino, A.V. Penacchioni, G.B. Pisani, Y. Wang; "Induced Gravitational Collapse in the BATSE era: the case of GRB 970828"; Astronomy Reports, 59, 626 (2015).

Following the recently established "Binary-driven HyperNova" (BdHN) paradigm, we here interpret GRB 970828 in terms of the four episodes typical of such a model. The "Episode 1", up to 40 s after the trigger time t_0, with a time varying thermal emission and a total energy of $E_{iso,1st} = 2.60 \times 10^{53}$ erg, is interpreted as due to the onset of an hyper-critical accretion process onto a companion neutron star, triggered by the companion star, an FeCO core approaching a SN explosion. The "Episode 2", observed up t_0+90 s, is interpreted as a canonical gamma ray burst, with an energy of $E_{tot}^{e^+e^-} = 1.60 \times 10^{53}$ erg, a baryon load of $B = 7 \times 10^{-3}$ and a bulk Lorentz factor at transparency of $\Gamma = 142.5$. From this Episode 2, we infer that the GRB exploded in an environment with a large av-

erage particle density $\langle n \rangle \approx 10^3$ particles/cm^3 and dense clouds characterized by typical dimensions of $(4 \div 8) \times 10^{14}$ cm and $\delta n/n \sim 10$. The "Episode 3" is identified from t_0+90 s all the way up to 10^{5-6} s: despite the paucity of the early X-ray data, typical in the BATSE, pre-Swift era, we find extremely significant data points in the late X-ray afterglow emission of GRB 970828, which corresponds to the ones observed in all BdHNe sources. The "Episode 4", related to the Supernova emission, does not appear to be observable in this source, due to the presence of darkening from the large density of the GRB environment, also inferred from the analysis of the Episode 2.

40. Y. Wang, R. Ruffini, M. Kovacevic, C.L. Bianco, M. Enderli, M. Muccino, A.V. Penacchioni, G.B. Pisani, J.A. Rueda; "Predicting supernova associated to gamma-ray burst 130427a"; Astronomy Reports, 59, 667 (2015).

Binary systems constituted by a neutron star and a massive star are not rare in the universe. The Induced Gravitational Gamma-ray Burst (IGC) paradigm interprets Gamma-ray bursts as the outcome of a neutron star that collapses into a black hole due to the accretion of the ejecta coming from its companion massive star that underwent a supernova event. GRB 130427A is one of the most luminous GRBs ever observed, of which isotropic energy exceeds 10^{54} erg. And it is within one of the few GRBs obtained optical, X-ray and GeV spectra simultaneously for hundreds of seconds, which provides an unique opportunity so far to understand the multi-wavelength observation within the IGC paradigm, our data analysis found low Lorentz factor blackbody emission in the Episode 3 and its X-ray light curve overlaps typical IGC Golden Sample, which comply to the IGC mechanisms. We consider these findings as clues of GRB 130427A belonging to the IGC GRBs. We predicted on GCN the emergence of a supernova on May 2, 2013, which was later successfully detected on May 13, 2013.

41. R. Ruffini, M. Muccino, M. Kovacevic, F.G. Oliveira, J.A. Rueda, C.L. Bianco, M. Enderli, A.V. Penacchioni, G.B. Pisani, Y. Wang, E. Zaninoni; "GRB 140619B: a short GRB from a binary neutron star merger leading to black hole formation"; The Astrophysical Journal, 808, 190 (2015).

We show the existence of two families of short GRBs, both originating from the merger of binary neutron stars (NSs): family-1 with $E_{iso} < 10^{52}$ erg, leading to a massive NS as the merged core, and family-2 with $E_{iso} > 10^{52}$ erg, leading to a black hole (BH). Following the identification of the prototype

GRB 090227B, we present the details of a new example of family-2 short burst: GRB 140619B. From the spectral analysis of the early ~ 0.2 s, we infer an observed temperature $kT = (324 \pm 33)$ keV of the e^+e^--plasma at transparency (P-GRB), a theoretically derived redshift $z = 2.67 \pm 0.37$, a total burst energy $E_{e^+e^-}^{tot} = (6.03 \pm 0.79) \times 10^{52}$ erg, a rest-frame peak energy $E_{p,i} = 4.7$ MeV, and a baryon load $B = (5.52 \pm 0.73) \times 10^{-5}$. We also estimate the corresponding emission of gravitational waves. Two additional examples of family-2 short bursts are identified: GRB 081024B and GRB 090510, remarkable for its well determined cosmological distance. We show that marked differences exist in the nature of the afterglows of these two families of short bursts: family-2 bursts, leading to BH formation, consistently exhibit high energy emission following the P-GRB emission; family-1 bursts, leading to the formation of a massive NS, should never exhibit high energy emission. We also show that both the families fulfill an $E_{p,i}$–E_{iso} relation with slope $\gamma = 0.59 \pm 0.07$ and a normalization constant incompatible with the one for long GRBs. The observed rate of such family-2 events is $\rho_0 = \left(2.1^{+2.8}_{-1.4}\right) \times 10^{-4} \mathrm{Gpc}^{-3}\mathrm{yr}^{-1}$.

42. R. Ruffini, Y. Aimuratov, C.L. Bianco, M. Enderli, M. Kovacevic, R. Moradi, M. Muccino, A.V. Penacchioni, G.B. Pisani, J.A. Rueda, Y. Wang; "Induced gravitational collapse in FeCO Core-Neutron star binaries and Neutron star-Neutron star binary mergers"; International Journal of Modern Physics A, 30, 1545023 (2015).

We review the recent progress in understanding the nature of gamma-ray bursts (GRBs). The occurrence of GRB is explained by the Induced Gravitational Collapse (IGC) in FeCO Core-Neutron star binaries and Neutron star-Neutron star binary mergers, both processes occur within binary system progenitors. Making use of this most unexpected new paradigm, with the fundamental implications by the neutron star (NS) critical mass, we find that different initial configurations of binary systems lead to different GRB families with specific new physical predictions confirmed by observations.

43. R. Ruffini, M. Muccino, Y. Aimuratov, C.L. Bianco, C. Cherubini, M. Enderli, M. Kovacevic, R. Moradi, A.V. Penacchioni, G.B. Pisani, J.A. Rueda, Y. Wang; "GRB 090510: A genuine short-GRB from a binary neutron star coalescing into a Kerr-Newman black hole"; The Astrophysical Journal, 831, 178 (2016).

In a new classification of merging binary neutron stars (NSs) we separate short gamma-ray bursts (GRBs) in two sub-classes. The ones with $E_{iso} \lesssim 10^{52}$ erg

coalesce to form a massive NS and are indicated as short gamma-ray flashes (S-GRFs). The hardest, with $E_{iso} \gtrsim 10^{52}$ erg, coalesce to form a black hole (BH) and are indicated as genuine short-GRBs (S-GRBs). Within the fireshell model, S-GRBs exhibit three different components: the P-GRB emission, observed at the transparency of a self-accelerating baryon-e^+e^- plasma; the prompt emission, originating from the interaction of the accelerated baryons with the circumburst medium; the high-energy (GeV) emission, observed after the P-GRB and indicating the formation of a BH. GRB 090510 gives the first evidence for the formation of a Kerr BH or, possibly, a Kerr-Newman BH. Its P-GRB spectrum can be fitted by a convolution of thermal spectra whose origin can be traced back to an axially symmetric dyadotorus. A large value of the angular momentum of the newborn BH is consistent with the large energetics of this S-GRB, which reach in the 1–10000 keV range $E_{iso} = (3.95 \pm 0.21) \times 10^{52}$ erg and in the 0.1–100 GeV range $E_{LAT} = (5.78 \pm 0.60) \times 10^{52}$ erg, the most energetic GeV emission ever observed in S-GRBs. The theoretical redshift $z_{th} = 0.75 \pm 0.17$ that we derive from the fireshell theory is consistent with the spectroscopic measurement $z = 0.903 \pm 0.003$, showing the self-consistency of the theoretical approach. All S-GRBs exhibit GeV emission, when inside the *Fermi*-LAT field of view, unlike S-GRFs, which never evidence it. The GeV emission appears to be the discriminant for the formation of a BH in GRBs, confirmed by their observed overall energetics.

44. Ruffini, R.; Rueda, J. A.; Muccino, M.; Aimuratov, Y.; Becerra, L. M.; Bianco, C. L.; Kovacevic, M.; Moradi, R.; Oliveira, F. G.; Pisani, G. B.; Wang, Y.; On the classification of GRBs and their occurrence rates; The Astrophysical Journal, 832, 136 (2016).

There is mounting evidence for the binary nature of the progenitors of gamma-ray bursts (GRBs). For a long GRB, the induced gravitational collapse (IGC) paradigm proposes as progenitor, or "in-state", a tight binary system composed of a carbon-oxygen core (CO_{core}) undergoing a supernova (SN) explosion which triggers hypercritical accretion onto a neutron star (NS) companion. For a short GRB, a NS-NS merger is traditionally adopted as the progenitor. We divide long and short GRBs into two sub-classes, depending on whether or not a black hole (BH) is formed in the merger or in the hypercritical accretion process exceeding the NS critical mass. For long bursts, when no BH is formed we have the sub-class of X-ray flashes (XRFs), with isotropic energy $E_{iso} \lesssim 10^{52}$ erg and rest-frame spectral peak energy $E_{p,i} \lesssim 200$ keV. When a BH is formed we have the sub-class of binary-driven hypernovae (BdHNe),

with $E_{iso} \gtrsim 10^{52}$ erg and $E_{p,i} \gtrsim 200$ keV. In analogy, short bursts are similarly divided into two sub-classes. When no BH is formed, short gamma-ray flashes (S-GRFs) occur, with $E_{iso} \lesssim 10^{52}$ erg and $E_{p,i} \lesssim 2$ MeV. When a BH is formed, the authentic short GRBs (S-GRBs) occur, with $E_{iso} \gtrsim 10^{52}$ erg and $E_{p,i} \gtrsim 2$ MeV. We give examples and observational signatures of these four sub-classes and their rate of occurrence. From their respective rates it is possible that "in-states" of S-GRFs and S-GRBs originate from the "out-states" of XRFs. We indicate two additional progenitor systems: white dwarf-NS and BH-NS. These systems have hybrid features between long and short bursts. In the case of S-GRBs and BdHNe evidence is given of the coincidence of the onset of the high energy GeV emission with the birth of a Kerr BH.

45. Becerra, L.; Bianco, C. L.; Fryer, C. L.; Rueda, J. A.; Ruffini, R.; On the induced gravitational collapse scenario of gamma-ray bursts associated with supernovae; The Astrophysical Journal, 833, 107 (2016).

    Following the induced gravitational collapse (IGC) paradigm of gamma-ray bursts (GRBs) associated with type Ib/c supernovae, we present numerical simulations of the explosion of a carbon-oxygen (CO) core in a binary system with a neutron-star (NS) companion. The supernova ejecta trigger a *hypercritical* accretion process onto the NS thanks to a copious neutrino emission and the trapping of photons within the accretion flow. We show that temperatures 1–10 MeV develop near the NS surface, hence electron-positron annihilation into neutrinos becomes the main cooling channel leading to accretion rates 10^{-9}–10^{-1} $M_\odot$ s^{-1} and neutrino luminosities 10^{43}–10^{52} erg s^{-1} (the shorter the orbital period the higher the accretion rate). We estimate the maximum orbital period, $P_{\max}$, as a function of the NS initial mass, up to which the NS companion can reach by hypercritical accretion the critical mass for gravitational collapse leading to black-hole (BH) formation. We then estimate the effects of the accreting and orbiting NS companion onto a novel geometry of the supernova ejecta density profile. We present the results of a 1.4×10^7 particle simulation which show that the NS induces accentuated asymmetries in the ejecta density around the orbital plane. We elaborate on the observables associated with the above features of the IGC process. We apply this framework to specific GRBs: we find that X-ray flashes (XRFs) and binary-driven hypernovae (BdHNe) are produced in binaries with $P > P_{\max}$ and $P < P_{\max}$, respectively. We analyze in detail the case of XRF 060218.

46. Pisani, G. B.; Ruffini, R.; Aimuratov, Y.; Bianco, C. L.; Kovacevic, M.;

Moradi, R.; Muccino, M.; Penacchioni, A. V.; Rueda, J. A.; Shakeri, S.; Wang, Y.; On the universal late X-ray emission of binary-driven hypernovae and its possible collimation; The Astrophysical Journal, 833, 159 (2016).

It has been previously discovered a universal power-law behaviour of the late X-ray emission (LXRE) of a "golden sample" (GS) of six long energetic GRBs, when observed in the rest-frame of the source. This remarkable feature, independent on the different isotropic energy (E_{iso}) of each GRB, has been used to estimate the cosmological redshift of some long GRBs. This analysis is here extended to a new class of 161 long GRBs, all with $E_{iso} > 10^{52}$ erg. These GRBs are indicated as binary-driven hypernovae (BdHNe) in view of their progenitors: a tight binary systems composed of a carbon-oxigen core (CO_{core}) and a neutron star (NS) undergoing an induced gravitational collapse (IGC) to a black hole (BH) triggered by the CO_{core} explosion as a supernova (SN). We confirm the universal behaviour of the LXRE for the "enlarged sample" (ES) of 161 BdHNe observed up to the end of 2015, assuming a double-cone emitting region. We obtain a distribution of half-opening angles peaking at $\theta = 17.62°$, with mean value $30.05°$, and a standard deviation $19.65°$. This, in turn, leads to the possible establishment of a new cosmological candle. Within the IGC model, such universal LXRE behaviour is only indirectly related to the GRB and originates from the SN ejecta, of a standard constant mass, being shocked by the GRB emission. The fulfillment of the universal relation in the LXRE and its independence of the prompt emission, further confirmed in this article, establishes a crucial test for any viable GRB model.

47. Y. Aimuratov, R. Ruffini, M. Muccino, C.L. Bianco, A.V. Penacchioni, G.B. Pisani, D. Primorac, J.A. Rueda, Y. Wang; GRB 081024B and GRB 140402A: Two Additional Short GRBs from Binary Neutron Star Mergers; The Astrophysical Journal, 844, 83 (2017).

Theoretical and observational evidences have been recently gained for a two-fold classification of short bursts: 1) short gamma-ray flashes (S-GRFs), with isotropic energy $E_{iso} < 10^{52}$ erg and no BH formation, and 2) the authentic short gamma-ray bursts (S-GRBs), with isotropic energy $E_{iso} > 10^{52}$ erg evidencing a BH formation in the binary neutron star merging process. The signature for the BH formation consists in the on-set of the high energy (0.1–100 GeV) emission, coeval to the prompt emission, in all S-GRBs. No GeV emission is expected nor observed in the S-GRFs. In this paper we present

two additional S-GRBs, GRB 081024B and GRB 140402A, following the already identified S-GRBs, i.e., GRB 090227B, GRB 090510 and GRB 140619B. We also return on the absence of the GeV emission of the S-GRB 090227B, at an angle of 71º from the *Fermi*-LAT boresight. All the correctly identified S-GRBs correlate to the high energy emission, implying no significant presence of beaming in the GeV emission. The existence of a common power-law behavior in the GeV luminosities, following the BH formation, when measured in the source rest-frame, points to a commonality in the mass and spin of the newly-formed BH in all S-GRBs.

48. J.A. Rueda, Y. Aimuratov, U. Barres de Almeida, L.M. Becerra, C.L. Bianco, C. Cherubini, S. Filippi, M. Karlica, M. Kovacevic, J.D. Melon Fuksman, R. Moradi, M. Muccino, A.V. Penacchioni, G.B. Pisani, D. Primorac, R. Ruffini, N. Sahakyan, S. Shakeri, Y. Wang; The binary systems associated with short and long gamma-ray bursts and their detectability; International Journal of Modern Physics D, 26, 1730016 (2017).

    Short and long-duration gamma-ray bursts (GRBs) have been recently subclassified into seven families according to the binary nature of their progenitors. For short GRBs, mergers of neutron star binaries (NS–NS) or neutron star-black hole binaries (NS-BH) are proposed. For long GRBs, the induced gravitational collapse (IGC) paradigm proposes a tight binary system composed of a carbon–oxygen core (COcore) and a NS companion. The explosion of the COcore as supernova (SN) triggers a hypercritical accretion process onto the NS companion which might reach the critical mass for the gravitational collapse to a BH. Thus, this process can lead either to a NS-BH or to NS–NS depending on whether or not the accretion is sufficient to induce the collapse of the NS into a BH. We shall discuss for the above compact object binaries: (1) the role of the NS structure and the equation-of-state on their final fate; (2) their occurrence rates as inferred from the X and gamma-ray observations; (3) the expected number of detections of their gravitational wave (GW) emission by the Advanced LIGO interferometer.

49. R. Ruffini, Y. Aimuratov, L.M. Becerra, C.L. Bianco, M. Karlica, M. Kovacevic, J.D. Melon Fuksman, R. Moradi, M. Muccino, A.V. Penacchioni, G.B. Pisani, D. Primorac, J.A. Rueda, S. Shakeri, G.V. Vereshchagin, Y. Wang, S.-S. Xue; The cosmic matrix in the 50th anniversary of relativistic astrophysics; International Journal of Modern Physics D, 26, 1730019 (2017).

Our concept of induced gravitational collapse (IGC paradigm) starting from a supernova occurring with a companion neutron star, has unlocked the understanding of seven different families of gamma ray bursts (GRBs), indicating a path for the formation of black holes in the universe. An authentic laboratory of relativistic astrophysics has been unveiled in which new paradigms have been introduced in order to advance knowledge of the most energetic, distant and complex systems in our universe. A novel cosmic matrix paradigm has been introduced at a relativistic cosmic level, which parallels the concept of an S-matrix introduced by Feynmann, Wheeler and Heisenberg in the quantum world of microphysics. Here the "in" states are represented by a neutron star and a supernova, while the "out" states, generated within less than a second, are a new neutron star and a black hole. This novel field of research needs very powerful technological observations in all wavelengths ranging from radio through optical, X-ray and gamma ray radiation all the way up to ultra-high-energy cosmic rays.

50. R. Ruffini, Y. Wang, Y. Aimuratov, U. Barres de Almeida, L.M. Becerra, C.L. Bianco, Y.C. Chen, M. Karlica, M. Kovacevic, L. Li, J.D. Melon Fuksman, R. Moradi, M. Muccino, A.V. Penacchioni, G.B. Pisani, D. Primorac, J.A. Rueda, S. Shakeri, G.V. Vereshchagin, S.-S. Xue; Early X-Ray Flares in GRBs; The Astrophysical Journal, 852, 53 (2018).

We analyze the early X-ray flares in the GRB "flare-plateau-afterglow" (FPA) phase observed by Swift-XRT. The FPA occurs only in one of the seven GRB subclasses: the binary-driven hypernovae (BdHNe). This subclass consists of long GRBs with a carbon-oxygen core and a neutron star (NS) binary companion as progenitors. The hypercritical accretion of the supernova (SN) ejecta onto the NS can lead to the gravitational collapse of the NS into a black hole. Consequently, one can observe a GRB emission with isotropic energy $E_{iso} \gtrsim 10^{52}$ erg, as well as the associated GeV emission and the FPA phase. Previous work had shown that gamma-ray spikes in the prompt emission occur at $\sim 10^{15}$–10^{17} cm with Lorentz gamma factor $\Gamma \sim 10^2$–10^3. Using a novel data analysis we show that the time of occurrence, duration, luminosity and total energy of the X-ray flares correlate with E_{iso}. A crucial feature is the observation of thermal emission in the X-ray flares that we show occurs at radii $\sim 10^{12}$ cm with $\Gamma \lesssim 4$. These model independent observations cannot be explained by the "fireball" model, which postulates synchrotron and inverse Compton radiation from a single ultra relativistic jetted emission extending from the prompt to the late afterglow and GeV emission phases. We show that

in BdHNe a collision between the GRB and the SN ejecta occurs at $\simeq 10^{10}$ cm reaching transparency at $\sim 10^{12}$ cm with $\Gamma \lesssim 4$. The agreement between the thermal emission observations and these theoretically derived values validates our model and opens the possibility of testing each BdHN episode with the corresponding Lorentz gamma factor.

51. R. Ruffini, J. Rodriguez, M. Muccino, J.A. Rueda, Y. Aimuratov, U. Barres de Almeida, L.M. Becerra, C.L. Bianco, C. Cherubini, S. Filippi, D. Gizzi, M. Kovacevic, R. Moradi, F.G. Oliveira, G.B. Pisani, Y. Wang; On the Rate and on the Gravitational Wave Emission of Short and Long GRBs; The Astrophysical Journal, 859, 30 (2018).

    On the ground of the large number of gamma-ray bursts (GRBs) detected with cosmological redshift, we classified GRBs in seven subclasses, all with binary progenitors which emit gravitational waves (GWs). Each binary is composed of combinations of carbon-oxygen cores (COcore), neutron stars (NSs), black holes (BHs), and white dwarfs (WDs). The long bursts, traditionally assumed to originate from a BH with an ultrarelativistic jetted emission, not emitting GWs, have been subclassified as (I) X-ray flashes (XRFs), (II) binary-driven hypernovae (BdHNe), and (III) BH-supernovae (BH-SNe). They are framed within the induced gravitational collapse paradigm with a progenitor COcore-NS/BH binary. The SN explosion of the COcore triggers an accretion process onto the NS/BH. If the accretion does not lead the NS to its critical mass, an XRF occurs, while when the BH is present or formed by accretion, a BdHN occurs. When the binaries are not disrupted, XRFs lead to NS-NS and BdHNe lead to NS-BH. The short bursts, originating in NS-NS, are subclassified as (IV) short gamma-ray flashes (S-GRFs) and (V) short GRBs (S-GRBs), the latter when a BH is formed. There are (VI) ultrashort GRBs (U-GRBs) and (VII) gamma-ray flashes (GRFs) formed in NS-BH and NS-WD, respectively. We use the occurrence rate and GW emission of these subclasses to assess their detectability by Advanced LIGO-Virgo, eLISA, and resonant bars. We discuss the consequences of our results in view of the announcement of the LIGO/Virgo Collaboration of the source GW 170817 as being originated by an NS-NS.

52. J.A. Rueda, R. Ruffini, Y. Wang, Y. Aimuratov, U. Barres de Almeida, C.L. Bianco, Y.-C. Chen, R.V. Lobato, C. Maia, D. Primorac, R. Moradi, J. Rodriguez; GRB 170817A-GW170817-AT 2017gfo and the observations of NS-NS, NS-WD and WD-WD mergers; Journal of Cosmology and Astroparticle Physics, 10, 006 (2018).

The LIGO-Virgo Collaboration has announced the detection of GW170817 and has associated it with GRB 170817A . These signals have been followed after 11 hours by the optical and infrared emission of AT 2017gfo. The origin of this complex phenomenon has been attributed to a neutron star-neutron star (NS-NS) merger. In order to probe this association we confront our current understanding of the gravitational waves and associated electromagnetic radiation with four observed GRBs originating in binaries composed of different combinations NSs and white dwarfs (WDs). We consider 1) GRB 090510 the prototype of NS-NS merger leading to a black hole (BH); 2) GRB 130603B the prototype of a NS-NS merger leading to massive NS (MNS) with an associated kilonova; 3) GRB 060614 the prototype of a NS-WD merger leading to a MNS with an associated kilonova candidate; 4) GRB 170817A the prototype of a WD-WD merger leading to massive WD with an associated AT 2017gfo-like emission. None of these systems support the above mentioned association. The clear association between GRB 170817A and AT 2017gfo has led to introduce a new model based on a new subfamily of GRBs originating from WD-WD mergers. We show how this novel model is in agreement with the exceptional observations in the optical, infrared, X- and gamma-rays of GRB 170817A-AT 2017gfo.

53. R. Ruffini, M. Karlica, N. Sahakyan, J.A. Rueda, Y. Wang, G.W. Mathews, C.L. Bianco, M. Muccino; A GRB Afterglow Model Consistent with Hypernova Observations; The Astrophysical Journal, 869, 101 (2018).

We describe the afterglows of the long gamma-ray-burst (GRB) 130427A within the context of a binary-driven hypernova. The afterglows originate from the interaction between a newly born neutron star (νNS), created by an Ic supernova (SN), and a mildly relativistic ejecta of a hypernova (HN). Such an HN in turn results from the impact of the GRB on the original SN Ic. The mildly relativistic expansion velocity of the afterglow ($\Gamma \sim 3$) is determined, using our model-independent approach, from the thermal emission between 196 and 461 s. The power law in the optical and X-ray bands of the afterglow is shown to arise from the synchrotron emission of relativistic electrons in the expanding magnetized HN ejecta. Two components contribute to the injected energy: the kinetic energy of the mildly relativistic expanding HN and the rotational energy of the fast-rotating highly magnetized ?NS. We reproduce the afterglow in all wavelengths from the optical (10^{14} Hz) to the X-ray band (10^{19} Hz) over times from 604 s to 5.18×10^6 s relative to the Fermi-GBM trigger. Initially, the emission is dominated by the loss of kinetic energy of the HN component.

After 10^5 s the emission is dominated by the loss of rotational energy of the νNS, for which we adopt an initial rotation period of 2 ms and a dipole plus quadrupole magnetic field of $\lesssim 7 \times 10^{12}$ G or $\sim 10^{14}$ G. This scenario with a progenitor composed of a COcore and an NS companion differs from the traditional ultra-relativistic-jetted treatments of the afterglows originating from a single black hole.

54. R. Ruffini, L.M. Becerra, C.L. Bianco, Y.-C. Chen, M. Karlica, M. Kovacevic, J.D. Melon Fuksman, R. Moradi, M. Muccino, G.B. Pisani, D. Primorac, J.A. Rueda, G.V. Vereshchagin, Y. Wang, S.-S. Xue; On the ultra-relativistic Prompt Emission (UPE), the Hard and Soft X-ray Flares, and the extended thermal emission (ETE) in GRB 151027A; The Astrophysical Journal, 869, 151 (2018).

We analyze GRB 151027A within the binary-driven hypernova approach, with a progenitor of a carbon–oxygen core on the verge of a supernova (SN) explosion and a binary companion neutron star (NS). The hypercritical accretion of the SN ejecta onto the NS leads to its gravitational collapse into a black hole (BH), to the emission of the gamma-ray burst (GRB), and to a copious e+e- plasma. The impact of this e+e- plasma on the SN ejecta explains the early soft X-ray flare observed in long GRBs. Here, we apply this approach to the ultra-relativistic prompt emission (UPE) and to the hard X-ray flares. We use GRB 151027A as a prototype. From the time-integrated and the time-resolved analysis, we identify a double component in the UPE and confirm its ultra-relativistic nature. We confirm the mildly relativistic nature of the soft X-ray flare, of the hard X-ray flare, and of the extended thermal emission (ETE). We show that the ETE identifies the transition from an SN to a hypernova (HN). We then address the theoretical justification of these observations by integrating the hydrodynamical propagation equations of the e+e- into the SN ejecta, with the latter independently obtained from 3D smoothed particle hydrodynamics simulations. We conclude that the UPE, the hard X-ray flare, and the soft X-ray flare do not form a causally connected sequence. Within our model, they are the manifestation of the same physical process of the BH formation as seen through different viewing angles, implied by the morphology and the ~ 300 s rotation period of the HN ejecta.

55. R. Moradi, R. Ruffini, C.L. Bianco, Y.-C. Chen, M. Karlica, J.D. Melon Fuksman, D. Primorac, J.A. Rueda, S. Shakeri, Y. Wang, S.-S. Xue; Relativistic Behavior and Equitemporal Surfaces in Ultra-Relativistic Prompt

Emission Phase of Gamma-Ray Bursts; Astronomy Reports, 62, 905 (2018).

In this work we study a role of baryon load and interstellar medium density to explain the nature of peaks in the ultra-relativistic prompt emission (UPE) phase of Gamma-ray Bursts (GRBs). We study the behavior of their Γ Lorenz factor fromthe moment of transparency all the way up to interstellar medium. We finally study the characteristic of equitemporal surfaces in the UPE phase.

56. D. Primorac, M. Muccino, R. Moradi, Y. Wang, J.D. Melon Fuksman, R. Ruffini, C.L. Bianco, J.A. Rueda; Structure of the Prompt Emission of GRB 151027A Within the Fireshell Model; Astronomy Reports, 62, 933 (2018).

Long gamma-ray burst GRB 151027A was observed by all three detectors on-board the Swift spacecraft, and many more, including MAXI, Konus-Wind and Fermi GBM/LAT instruments. This revealed a complex structure of the prompt and afterglow emission, consisting of a double-peak gammaray prompt with a quiescent period and a HRF/SXF within the X-ray afterglow, together with multiple BB components seen within the time-resolved spectral analysis. These features, within the fireshell model, are interpreted as the manifestation of the same physical process viewed at different angles with respect to the HN ejecta. Here we present the time-resolved and time-integrated spectral analysis used to determine the energy of the e-e+ plasma E_{tot} and the baryon load B. These quantities describe the dynamics of the fireshell up to the transparency point. We proceed with the light-curve simulation from which CBM density values and its inhomogeneities are deduced. We also investigate the properties of GRB 140206A, whose prompt emission exhibits a similar structure.

57. Y. Wang, J.A. Rueda, R. Ruffini, C.L. Bianco, L.M. Becerra, L. Li, M. Karlica; Two Predictions of Supernova: GRB 130427A/SN 2013cq and GRB 180728A/SN 2018fip; The Astrophysical Journal, 874, 39 (2019).

On 2018 July 28, GRB 180728A triggered *Swift* satellites and, soon after the determination of the redshift, we identified this source as a type II binary-driven hypernova (BdHN II) in our model. Consequently, we predicted the appearance time of its associated supernova (SN), which was later confirmed as SN 2018fip. A BdHN II originates in a binary composed of a carbon-oxygen core (CO_{core}) undergoing SN, and the SN ejecta hypercritically accrete onto a companion neutron star (NS). From the time of the SN shock breakout to the time when the hypercritical accretion starts, we infer the binary separation

$\simeq 3 \times 10^{10}$ cm. The accretion explains the prompt emission of isotropic energy $\simeq 3 \times 10^{51}$ erg, lasting ~ 10 s, and the accompanying observed blackbody emission from a thermal convective instability bubble. The new neutron star (νNS) originating from the SN powers the late afterglow from which a νNS initial spin of 2.5 ms is inferred. We compare GRB 180728A with GRB 130427A, a type I binary-driven hypernova (BdHN I) with isotropic energy $> 10^{54}$ erg. For GRB 130427A we have inferred an initially closer binary separation of $\simeq 10^{10}$ cm, implying a higher accretion rate leading to the collapse of the NS companion with consequent black hole formation, and a faster, 1 ms spinning νNS. In both cases, the optical spectra of the SNe are similar, and not correlated to the energy of the gamma-ray burst. We present three-dimensional smoothed-particle-hydrodynamic simulations and visualisations of the BdHNe I and II.

58. J.A. Rueda, R. Ruffini, Y. Wang, C.L. Bianco, J.M. Blanco-Iglesias, M. Karlica, P. Lorén-Aguilar, R. Moradi, N. Sahakyan; Electromagnetic emission of white dwarf binary mergers; Journal of Cosmology and Astroparticle Physics, 03, 044 (2019).

It has been recently proposed that the ejected matter from white dwarf (WD) binary mergers can produce transient, optical and infrared emission similar to the "kilonovae" of neutron star (NS) binary mergers. To confirm this we calculate the electromagnetic emission from WD-WD mergers and compare with kilonova observations. We simulate WD-WD mergers leading to a massive, fast rotating, highly magnetized WD with an adapted version of the smoothed-particle-hydrodynamics (SPH) code Phantom. We thus obtain initial conditions for the ejecta such as escape velocity, mass and initial position and distribution. The subsequent thermal and dynamical evolution of the ejecta is obtained by integrating the energy-conservation equation accounting for expansion cooling and a heating source given by the fallback accretion onto the newly-formed WD and its magneto-dipole radiation. We show that magnetospheric processes in the merger can lead to a prompt, short gamma-ray emission of up to $\approx 10^{46}$ erg in a timescale of 0.1–1 s. The bulk of the ejecta initially expands non-relativistically with velocity 0.01 c and then it accelerates to 0.1 c due to the injection of fallback accretion energy. The ejecta become transparent at optical wavelengths around ~ 7 days post-merger with a luminosity 10^{41}–10^{42} erg s^{-1}. The X-ray emission from the fallback accretion becomes visible around ~ 150–200 day post-merger with a luminosity of 10^{39} erg s^{-1}. We also predict the post-merger time at which the central WD should appear as a pulsar depending on the value of the magnetic field and rotation period.

59. J.A. Rueda, R. Ruffini, Y. Wang; Induced Gravitational Collapse, Binary-Driven Hypernovae, Long Gramma-ray Bursts and Their Connection with Short Gamma-ray Bursts; Universe, 5, 110 (2019).

There is increasing observational evidence that short and long Gamma-ray bursts (GRBs) originate in different subclasses, each one with specific energy release, spectra, duration, etc, and all of them with binary progenitors. The binary components involve carbon-oxygen cores (CO_{core}), neutron stars (NSs), black holes (BHs), and white dwarfs (WDs). We review here the salient features of the specific class of binary-driven hypernovae (BdHNe) within the induced gravitational collapse (IGC) scenario for the explanation of the long GRBs. The progenitor is a CO_{core}-NS binary. The supernova (SN) explosion of the CO_{core}, producing at its center a new NS (νNS), triggers onto the NS companion a hypercritical, i.e., highly super-Eddington accretion process, accompanied by a copious emission of neutrinos. By accretion the NS can become either a more massive NS or reach the critical mass for gravitational collapse with consequent formation of a BH. We summarize the results on this topic from the first analytic estimates in 2012 all the way up to the most recent three-dimensional (3D) smoothed-particle-hydrodynamics (SPH) numerical simulations in 2018. Thanks to these results it is by now clear that long GRBs are richer and more complex systems than thought before. The SN explosion and its hypercritical accretion onto the NS explain the X-ray precursor. The feedback of the NS accretion, the NS collapse and the BH formation produce asymmetries in the SN ejecta, implying the necessity of a 3D analysis for GRBs. The newborn BH, the surrounding matter and the magnetic field inherited from the NS, comprises the *inner engine* from which the GRB electron-positron (e^+e^-) plasma and the high-energy emission are initiated. The impact of the e^+e^- on the asymmetric ejecta transforms the SN into a hypernova (HN). The dynamics of the plasma in the asymmetric ejecta leads to signatures depending on the viewing angle. This explains the ultrarelativistic prompt emission in the MeV domain and the mildly-relativistic flares in the early afterglow in the X-ray domain. The feedback of the νNS pulsar-like emission on the HN explains the X-ray late afterglow and its power-law regime. All of the above is in contrast with a simple GRB model attempting to explain the entire GRB with the kinetic energy of an ultrarelativistic jet extending through all of the above GRB phases, as traditionally proposed in the "collapsar-fireball" model. In addition, BdHNe in their different flavors lead to νNS-NS or νNS-BH binaries. The gravitational wave emission drives these binaries to merge

producing short GRBs. It is thus established a previously unthought interconnection between long and short GRBs and their occurrence rates. This needs to be accounted for in the cosmological evolution of binaries within population synthesis models for the formation of compact-object binaries.

60. R. Ruffini, J.D. Melon Fuksman, G.V. Vereshchagin; On the role of a cavity in the hypernova ejecta of GRB 190114C; The Astrophysical Journal, 883, 191 (2019).

Within the binary-driven hypernova I (BdHN I) scenario, the gamma-ray burst GRB190114C originates in a binary system composed of a massive carbon-oxygen core (CO_{core}), and a binary neutron star (NS) companion. As the CO_{core} undergoes a supernova explosion with the creation of a new neutron star (νNS), hypercritical accretion occurs onto the companion binary neutron star until it exceeds the critical mass for gravitational collapse. The formation of a black hole (BH) captures 10^{57} baryons by enclosing them within its horizon, and thus a cavity of approximately 10^{11} cm is formed around it with initial density 10^{-7} g/cm^3. A further depletion of baryons in the cavity originates from the expansion of the electron-positron-photon ($e^+e^-\gamma$) plasma formed at the collapse, reaching a density of 10^{-14} g/cm^3 by the end of the interaction. It is demonstrated here using an analytical model complemented by a hydrodynamical numerical simulation that part of the $e^+e^-\gamma$ plasma is reflected off the walls of the cavity. The consequent outflow and its observed properties are shown to coincide with the featureless emission occurring in a time interval of duration t_{rf}, measured in the rest frame of the source, between 11 and 20 s of the GBM observation. Moreover, similar features of the GRB light curve were previously observed in GRB 090926A and GRB 130427A, all belonging to the BdHN I class. This interpretation supports the general conceptual framework presented in R. Ruffini et al. and guarantees that a low baryon density is reached in the cavity, a necessary condition for the operation of the "*inner engine*" of the GRB presented in an accompanying article.

61. R. Ruffini, R. Moradi, J.A. Rueda, L.M. Becerra, C.L. Bianco, C. Cherubini, S. Filippi, Y.C. Chen, M. Karlica, N. Sahakyan, Y. Wang, S.-S. Xue; On the GeV Emission of the Type I BdHN GRB 130427A; The Astrophysical Journal, 886, 82 (2019).

We propose that the *inner engine* of a type I binary-driven hypernova (BdHN) is composed of a Kerr black hole (BH) in a non-stationary state, embedded in a uniform magnetic field B_0 aligned with the BH rotation axis, and surrounded

by an ionized plasma of extremely low density of 10^{-14} g cm^{-3}. Using GRB 130427A as a prototype we show that this *inner engine* acts in a sequence of *elementary impulses*. Electrons are accelerated to ultra-relativistic energy near the BH horizon and, propagating along the polar axis, $\theta = 0$, they can reach energies of $\sim 10^{18}$ eV, and partially contribute to ultra-high energy cosmic rays (UHECRs). When propagating with $\theta \neq 0$ through the magnetic field B_0 they give origin by synchrotron emission to GeV and TeV radiation. The mass of BH, $M = 2.3 M_\odot$, its spin, $\alpha = 0.47$, and the value of magnetic field $B_0 = 3.48 \times 10^{10}$ G, are determined self-consistently in order to fulfill the energetic and the transparency requirement. The repetition time of each elementary impulse of energy $\mathcal{E} \sim 10^{37}$ erg, is $\sim 10^{-14}$ s at the beginning of the process, then slowly increasing with time evolution. In principle, this "*inner engine*" can operate in a GRB for thousands of years. By scaling the BH mass and the magnetic field the same "*inner engine*" can describe active galactic nuclei (AGN).

62. L. Li; Thermal Components in Gamma-ray Bursts. II. Constraining the Hybrid Jet Model; The Astrophysical Journal, 894, 100 (2020).

In explaining the physical origin of the jet composition of gamma-ray bursts (GRBs), a more general picture, i.e. the hybrid jet model (which introduced another magnetization parameter σ_0 on the basis of the traditional fireball model), has been well studied in Gao & Zhang. However, it still has not yet been applied to a large GRB sample. Here, we first employ the "top-down" approach of Gao & Zhang to diagnose the photosphere properties at the central engine to see how the hybrid model can account for the observed data as well, through applying a *Fermi* GRB sample (eight bursts) with the detected photosphere component, as presented in Li (our Paper I). We infer all physical parameters of a hybrid problem with three typical values of the radius of the jet base ($r_0 = 10^7$, 10^8, and 10^9 cm). We find that the dimensionless entropy for all the bursts shows $\eta \gg 1$ while the derived $(1+\sigma_0)$ for five bursts (GRB 081224, GRB 110721A, GRB 090719, GRB 100707, and GRB 100724) is larger than unity, indicating that in addition to a hot fireball component, another cold Poynting-flux component may also play an important role. Our analysis also shows that in a few time bins for all r_0 in GRB 081224 and GRB 110721A, the magnetization parameter at $\sim 10^{15}$cm $(1+\sigma_{r15})$ is greater than unity, which implies that internal-collision-induced magnetic reconnection and turbulence may be the mechanism to power the nonthermal emission, rather than internal shocks. We conclude that the majority of bursts (probably all) can be well explained by the hybrid jet problem.

63. J.A. Rueda, R. Ruffini, M. Karlica, R. Moradi, Y. Wang; Magnetic fields and afterglows of bdhne: inferences from grb 130427a, grb 160509a, grb 160625b, grb 180728a, and grb 190114c; The Astrophysical Journal, 893, 148 (2020).

GRB 190114C is the first binary-driven hypernova (BdHN) fully observed from the initial supernova appearance to the final emergence of the optical SN signal. It offers an unprecedented testing ground for the BdHN theory and it is here determined and further extended to additional gamma-ray bursts (GRBs). BdHNe comprise two subclasses of long GRBs with progenitors a binary system composed of a carbon-oxygen star (CO_{core}) and a neutron star (NS) companion. The CO_{core} explodes as a SN leaving at its center a newborn NS (νNS). The SN ejecta hypercritically accretes both on the νNS and the NS companion. BdHNe I are the tightest binaries where the accretion leads the companion NS to gravitational collapse into a black hole (BH). In BdHN II the accretion onto the NS is lower, so there is no BH formation. We observe the same structure of the afterglow for GRB 190114C and other selected examples of BdHNe I (GRB 130427A, GRB 160509A, GRB 160625B) and for BdHN II (GRB 180728A). In all the cases the explanation of the afterglow is reached via the synchrotron emission powered by the νNS: their magnetic fields structures and their spin are determined. For BdHNe I, we discuss the properties of the magnetic field embedding the newborn BH, inherited from the collapsed NS and amplified during the gravitational collapse process, and surrounded by the SN ejecta.

64. J.A. Rueda, R. Ruffini; The blackholic quantum; European Physical Journal C, 80, 300 (2020).

We show that the high-energy emission of GRBs originates in the *inner engine*: a Kerr black hole (BH) surrounded by matter and a magnetic field B_0. It radiates a sequence of discrete events of particle acceleration, each of energy $\mathcal{E} = \hbar\,\Omega_{eff}$, the *blackholic quantum*, where $\Omega_{eff} = 4(m_{Pl}/m_n)^8 (c\,a/G\,M)(B_0^2/\rho_{Pl})\Omega_+$. Here M, $a = J/M$, $\Omega_+ = c^2 \partial M/\partial J = (c^2/G)\,a/(2Mr_+)$ and r_+ are the BH mass, angular momentum per unit mass, angular velocity and horizon; m_n is the neutron mass, m_{Pl}, $\lambda_{Pl} = \hbar/(m_{Pl}c)$ and $\rho_{Pl} = m_{Pl}c^2/\lambda_{Pl}^3$, are the Planck mass, length and energy density. Here and in the following use CGS-Gaussian units. The timescale of each process is $\tau_{el} \sim \Omega_+^{-1}$, along the rotation axis, while it is much shorter off-axis owing to energy losses such as synchrotron radiation. We show an analogy with the Zeeman and Stark effects, properly scaled from microphysics to macrophysics, that allows us to define the *BH magneton*,

$\mu_{\rm BH} = (m_{\rm Pl}/m_n)^4 (c\,a/G\,M)e\,\hbar/(Mc)$. We give quantitative estimates for GRB 130427A adopting $M = 2.3\,M_\odot$, $c\,a/(G\,M) = 0.47$ and $B_0 = 3.5 \times 10^{10}$ G. Each emitted *quantum*, $\mathcal{E} \sim 10^{37}$ erg, extracts only 10^{-16} times the BH rotational energy, guaranteeing that the process can be repeated for thousands of years. The *inner engine* can also work in AGN as we here exemplified for the supermassive BH at the center of M87.

65. B. Zhang, Y. Wang, L. Li; Dissecting the Energy Budget of a Gamma-Ray Burst Fireball; The Astrophysical Journal Letters, 909, L3 (2021)

66. L. Li, B. Zhang; Testing the High-latitude Curvature Effect of Gamma-Ray Bursts with Fermi Data: Evidence of Bulk Acceleration in Prompt Emission; The Astrophysical Journal Supplement Series, 253, 43 (2021)

67. L. Li, F. Ryde, A. Pe'er, H.-F. Yu, Z. Acuner; The Astrophysical Journal Supplement Series; 254, 35 (2021)

68. Y. Wang; Do All Long-duration Gamma-Ray Bursts Emit GeV Photons?; The Astrophysical Journal, 913, 86 (2021)

69. L. Li; Searching for Observational Evidence for Binary Star Systems in Gamma-ray Bursts; Astronomy Reports, 65, 973 (2021)

70. Y. Wang; Gamma-Ray Burst from Binary Star: Neutron Star and Carbon–Oxygen Core; Astronomy Reports, 65, 1077 (2021)

71. R. Ruffini; Discovery of the Moment of Formation of the Black Hole in GRB 190114C; Astronomy Reports, 65, 1030 (2021)

72. R. Ruffini, R. Moradi, J.A. Rueda, L. Li, N. Sahakyan, Y.-C. Chen, Y. Wang, Y. Aimuratov, L. Becerra, C.L. Bianco, C. Cherubini, S. Filippi, M. Karlica, G.J. Mathews, M. Muccino, G.B. Pisani, S.-S. Xue; The morphology of the X-ray afterglows and of the jetted GeV emission in long GRBs; Monthly Notices of the Royal Astronomical Society, 504, 5301 (2021)

73. R. Moradi, J.?A. Rueda, R. Ruffini, Liang Li, C.?L. Bianco, S. Campion, C. Cherubini, S. Filippi, Y. Wang, and S.?S. Xue; Nature of the ultrarelativistic prompt emission phase of GRB 190114C; Phys. Rev. D, 104, 063043 (2021)

74. R. Moradi, J.A. Rueda, R. Ruffini and Y. Wang; The newborn black hole in GRB 191014C proves that it is alive; Astronomy & Astrophysics, 649, A75 (2021)

4.2 Conference proceedings

1. R. Ruffini, M.G. Bernardini, C.L. Bianco, P. Chardonnet, F. Fraschetti, V. Gurzadyan, L. Vitagliano, S.-S. Xue; "The Blackholic energy: long and short Gamma-Ray Bursts (New perspectives in physics and astrophysics from the theoretical understanding of Gamma-Ray Bursts, II)"; in Proceedings of the XIth Brazilian School on Cosmology and Gravitation, Mangaratiba, Rio de Janeiro (Brazil), July – August 2004, M. Novello, S.E. Perez Bergliaffa, Editors; AIP Conference Proceedings, 782, 42 (2005).

We outline the confluence of three novel theoretical fields in our modeling of Gamma-Ray Bursts (GRBs): 1) the ultrarelativistic regime of a shock front expanding with a Lorentz gamma factor ~ 300; 2) the quantum vacuum polarization process leading to an electron-positron plasma originating the shock front; and 3) the general relativistic process of energy extraction from a black hole originating the vacuum polarization process. There are two different classes of GRBs: the long GRBs and the short GRBs. We here address the issue of the long GRBs. The theoretical understanding of the long GRBs has led to the detailed description of their luminosities in fixed energy bands, of their spectral features and made also possible to probe the astrophysical scenario in which they originate. We are specially interested, in this report, to a subclass of long GRBs which appear to be accompanied by a supernova explosion. We are considering two specific examples: GRB980425/SN1998bw and GRB030329/SN2003dh. While these supernovae appear to have a standard energetics of 10^{49} ergs, the GRBs are highly variable and can have energetics $10^4 – 10^5$ times larger than the ones of the supernovae. Moreover, many long GRBs occurs without the presence of a supernova. It is concluded that in no way a GRB can originate from a supernova. The precise theoretical understanding of the GRB luminosity we present evidence, in both these systems, the existence of an independent component in the X-ray emission, usually interpreted in the current literature as part of the GRB afterglow. This component has been observed by Chandra and XMM to have a strong decay on scale of months. We have named here these two sources respectively URCA-1 and

URCA-2, in honor of the work that George Gamow and Mario Shoenberg did in 1939 in this town of Urca identifying the basic mechanism, the Urca processes, leading to the process of gravitational collapse and the formation of a neutron star and a supernova. The further hypothesis is considered to relate this X-ray source to a neutron star, newly born in the Supernova. This hypothesis should be submitted to further theoretical and observational investigation. Some theoretical developments to clarify the astrophysical origin of this new scenario are outlined. We turn then to the theoretical developments in the short GRBs: we first report some progress in the understanding the dynamical phase of collapse, the mass-energy formula and the extraction of blackholic energy which have been motivated by the analysis of the short GRBs. In this context progress has also been accomplished on establishing an absolute lower limit to the irreducible mass of the black hole as well as on some critical considerations about the relations of general relativity and the second law of thermodynamics. We recall how this last issue has been one of the most debated in theoretical physics in the past thirty years due to the work of Bekenstein and Hawking. Following these conceptual progresses we analyze the vacuum polarization process around an overcritical collapsing shell. We evidence the existence of a separatrix and a dyadosphere trapping surface in the dynamics of the electron-positron plasma generated during the process of gravitational collapse. We then analyze, using recent progress in the solution of the Vlasov-Boltzmann-Maxwell system, the oscillation regime in the created electron-positron plasma and their rapid convergence to a thermalized spectrum. We conclude by making precise predictions for the spectra, the energy fluxes and characteristic time-scales of the radiation for short-bursts. If the precise luminosity variation and spectral hardening of the radiation we have predicted will be confirmed by observations of short-bursts, these systems will play a major role as standard candles in cosmology. These considerations will also be relevant for the analysis of the long-bursts when the baryonic matter contribution will be taken into account.

2. R. Ruffini, M.G. Bernardini, C.L. Bianco, P. Chardonnet, F. Fraschetti, V. Gurzadyan, L. Vitagliano, S.-S. Xue; "Black hole physics and astrophysics: The GRB-Supernova connection and URCA-1 – URCA-2"; in Proceedings of the Tenth Marcel Grossmann Meeting on General Relativity, Rio de Janeiro, Brazil, July 2003, M. Novello, S.E. Perez-Bergliaffa, Editors; p. 369; World Scientific, (Singapore, 2006).

We outline the confluence of three novel theoretical fields in our modeling

of Gamma-Ray Bursts (GRBs): 1) the ultrarelativistic regime of a shock front expanding with a Lorentz gamma factor ~ 300; 2) the quantum vacuum polarization process leading to an electron-positron plasma originating the shock front; and 3) the general relativistic process of energy extraction from a black hole originating the vacuum polarization process. There are two different classes of GRBs: the long GRBs and the short GRBs. We here address the issue of the long GRBs. The theoretical understanding of the long GRBs has led to the detailed description of their luminosities in fixed energy bands, of their spectral features and made also possible to probe the astrophysical scenario in which they originate. We are specially interested, in this report, to a subclass of long GRBs which appear to be accompanied by a supernova explosion. We are considering two specific examples: GRB980425/SN1998bw and GRB030329/SN2003dh. While these supernovae appear to have a standard energetics of 10^{49} ergs, the GRBs are highly variable and can have energetics 10^4 – 10^5 times larger than the ones of the supernovae. Moreover, many long GRBs occurs without the presence of a supernova. It is concluded that in no way a GRB can originate from a supernova. The precise theoretical understanding of the GRB luminosity we present evidence, in both these systems, the existence of an independent component in the X-ray emission, usually interpreted in the current literature as part of the GRB afterglow. This component has been observed by Chandra and XMM to have a strong decay on scale of months. We have named here these two sources respectively URCA-1 and URCA-2, in honor of the work that George Gamow and Mario Shoenberg did in 1939 in this town of Urca identifying the basic mechanism, the Urca processes, leading to the process of gravitational collapse and the formation of a neutron star and a supernova. The further hypothesis is considered to relate this X-ray source to a neutron star, newly born in the Supernova. This hypothesis should be submitted to further theoretical and observational investigation. Some theoretical developments to clarify the astrophysical origin of this new scenario are outlined.

3. M.G. Bernardini, C.L. Bianco, P. Chardonnet, F. Fraschetti, R. Ruffini, S.-S. Xue; "General features of GRB 030329 in the EMBH model"; in Proceedings of the Tenth Marcel Grossmann Meeting on General Relativity, Rio de Janeiro, Brazil, July 2003, M. Novello, S.E. Perez-Bergliaffa, Editors; p. 2459; World Scientific, (Singapore, 2006).

GRB 030329 is considered within the EMBH model. We determine the three free parameters and deduce its luminosity in given energy bands comparing

it with the observations. The observed substructures are compared with the predictions of the model: by applying the result that substructures observed in the extended afterglow peak emission (E-APE) do indeed originate in the collision of the accelerated baryonic matter (ABM) pulse with the inhomogeneities in the interstellar medium around the black-hole, masks of density inhomogeneities are considered in order to reproduce the observed temporal substructures. The induced supernova concept is applied to this system and the general consequences that we are witnessing are the formation of a cosmological thriptych of a black hole originating the GRB 030329, the supernova SN2003dh and a young neutron star. Analogies to the system GRB 980425–SN1998bw are outlined.

4. R. Ruffini, M.G. Bernardini, C.L. Bianco, P. Chardonnet, A. Corsi, F. Fraschetti, S.-S. Xue; "GRB 970228 and its associated Supernova in the EMBH model"; in Proceedings of the Tenth Marcel Grossmann Meeting on General Relativity, Rio de Janeiro, Brazil, July 2003, M. Novello, S.E. Perez-Bergliaffa, Editors; p. 2465; World Scientific, (Singapore, 2006).

   The γ-ray burst of 1997 February 28 is analyzed within the Electromagnetic Black Hole model. We first estimate the value of the total energy deposited in the dyadosphere, E_{dya}, and the amount of baryonic matter left over by the EMBH progenitor star, $B = M_B c^2 / E_{dya}$. We then consider the role of the interstellar medium number density n_{ISM} and of the ratio R between the effective emitting area and the total surface area of the γ-ray burst source, in reproducing the prompt emission and the X-ray afterglow of this burst. Some considerations are also done concerning the possibility of explaining, within the theory, the observed evidence for a supernova in the optical afterglow.

5. F. Fraschetti, M.G. Bernardini, C.L. Bianco, P. Chardonnet, R. Ruffini, S.-S. Xue; "Inferences on the ISM structure around GRB980425 and GRB980425-SN1998bw association in the EMBH Model"; in Proceedings of the Tenth Marcel Grossmann Meeting on General Relativity, Rio de Janeiro, Brazil, July 2003, M. Novello, S.E. Perez-Bergliaffa, Editors; p. 2451; World Scientific, (Singapore, 2006).

   We determine the four free parameters within the EMBH model for GRB 980425 and deduce its luminosity in given energy bands, its spectra and its time variability in the prompt radiation. We compute the basic kinematical parameters of GRB 980425. In the extended afterglow peak emission the Lorentz γ factor is lower than the critical value 150 which has been found in Ruffini et al. (2002)

to be necessary in order to perform the tomography of the ISM surrounding the GRB as suggested by Dermer & Mitman (1999). The detailed structure of the density inhomogeneities as well as the effects of radial apparent superluminal effects are evaluated within the EMBH model. Under the assumption that the energy distribution of emitted radiation is thermal in the comoving frame, time integrated spectra of EMBH model for prompt emission are computed. The induced supernova concept is applied to this system and general consequences on the astrophysical and cosmological scenario are derived.

6. R. Ruffini, M.G. Bernardini, C.L. Bianco, P. Chardonnet, F. Fraschetti, R. Guida, S.-S. Xue; "GRB 050315: A step in the proof of the uniqueness of the overall GRB structure"; in "GAMMA-RAY BURSTS IN THE SWIFT ERA: Sixteenth Maryland Astrophysics Conference", Washington, DC, USA, November 29th – December 2nd 2005, Stephen S. Holt, Neil Gehrels, John A. Nousek, Editors; AIP Conference Proceedings, 836, 103 (2006).

Using the Swift data of GRB 050315, we progress in proving the uniqueness of our theoretically predicted Gamma-Ray Burst (GRB) structure as composed by a proper-GRB, emitted at the transparency of an electron-positron plasma with suitable baryon loading, and an afterglow comprising the "prompt radiation" as due to external shocks. Detailed light curves for selected energy bands are theoretically fitted in the entire temporal region of the Swift observations ranging over 10^6 seconds.

7. R. Ruffini, M.G. Bernardini, C.L. Bianco, P. Chardonnet, F. Fraschetti, S.-S. Xue; "Theoretical Interpretation of GRB 031203 and URCA-3"; in "Relativistic Astrophysics and Cosmology - Einstein's Legacy", B. Aschenbach, V. Burwitz, G. Hasinger, B. Leibundgut, Editors; Springer-Verlag (2007).

8. R. Ruffini, M.G. Bernardini, C.L. Bianco, L. Caito, P. Chardonnet, M.G. Dainotti, F. Fraschetti, R. Guida, M. Rotondo, G. Vereshchagin, L. Vita-gliano, S.-S. Xue; "The Blackholic energy and the canonical Gamma-Ray Burst"; in Proceedings of the XIIth Brazilian School on Cosmology and Gravitation, Mangaratiba, Rio de Janeiro (Brazil), September 2006, M. Novello, S.E. Perez Bergliaffa, Editors; AIP Conference Proceedings, 910, 55 (2007).

Gamma-Ray Bursts (GRBs) represent very likely "the" most extensive computational, theoretical and observational effort ever carried out successfully in physics and astrophysics. The extensive campaign of observation from space based X-ray and γ-ray observatory, such as the *Vela*, CGRO, BeppoSAX, HETE-II, INTEGRAL, *Swift*, R-XTE, *Chandra*, XMM satellites, have been matched by complementary observations in the radio wavelength (e.g. by the VLA) and in the optical band (e.g. by VLT, Keck, ROSAT). The net result is unprecedented accuracy in the received data allowing the determination of the energetics, the time variability and the spectral properties of these GRB sources. The very fortunate situation occurs that these data can be confronted with a mature theoretical development. Theoretical interpretation of the above data allows progress in three different frontiers of knowledge: **a)** the ultrarelativistic regimes of a macroscopic source moving at Lorentz gamma factors up to ~ 400; **b)** the occurrence of vacuum polarization process verifying some of the yet untested regimes of ultrarelativistic quantum field theories; and **c)** the first evidence for extracting, during the process of gravitational collapse leading to the formation of a black hole, amounts of energies up to 10^{55} ergs of blackholic energy — a new form of energy in physics and astrophysics. We outline how this progress leads to the confirmation of three interpretation paradigms for GRBs proposed in July 2001. Thanks mainly to the observations by *Swift* and the optical observations by VLT, the outcome of this analysis points to the existence of a "canonical" GRB, originating from a variety of different initial astrophysical scenarios. The communality of these GRBs appears to be that they all are emitted in the process of formation of a black hole with a negligible value of its angular momentum. The following sequence of events appears to be canonical: the vacuum polarization process in the dyadosphere with the creation of the optically thick self accelerating electron-positron plasma; the engulfment of baryonic mass during the plasma expansion; adiabatic expansion of the optically thick "fireshell" of electron-positron-baryon plasma up to the transparency; the interaction of the accelerated baryonic matter with the interstellar medium (ISM). This leads to the canonical GRB composed of a proper GRB (P-GRB), emitted at the moment of transparency, followed by an extended afterglow. The sole parameters in this scenario are the total energy of the dyadosphere E_{dya}, the fireshell baryon loading M_B defined by the dimensionless parameter $B \equiv M_B c^2 / E_{dya}$, and the ISM filamentary distribution around the source. In the limit $B \to 0$ the total energy is radiated in the P-GRB with a vanishing contribution in the afterglow. In this limit, the canonical GRBs explain as well the short GRBs. In these lecture notes we systematically

outline the main results of our model comparing and contrasting them with the ones in the current literature. In both cases, we have limited ourselves to review already published results in refereed publications. We emphasize as well the role of GRBs in testing yet unexplored grounds in the foundations of general relativity and relativistic field theories.

9. R. Ruffini, M.G. Bernardini, C.L. Bianco, L. Caito, P. Chardonnet, M.G. Dainotti, F. Fraschetti, R. Guida, G. Vereshchagin, S.-S. Xue; "The role of GRB 031203 in clarifying the astrophysical GRB scenario"; in Proceedings of the 6th Integral Workshop - The Obscured Universe, Moscow, (Russia), July 2006, S. Grebenev, R. Sunyaev, C. Winkler, A. Parmar, L. Ouwehand, Editors; ESA Special Publication, SP-622, 561 (2007).

The luminosity and the spectral distribution of the afterglow of GRB 031203 have been presented within our theoretical framework, which envisages the GRB structure as composed by a proper-GRB, emitted at the transparency of an electron-positron plasma with suitable baryon loading, and an afterglow comprising the "prompt emission" as due to external shocks. In addition to the GRB emission, there appears to be a prolonged soft X-Ray emission lasting for 10^6–10^7 seconds followed by an exponential decay. This additional source has been called by us URCA-3. It is urgent to establish if this component is related to the GRB or to the Supernova (SN). In this second case, there are two possibilities: either the interaction of the SN ejecta with the interstellar medium or, possibly, the cooling of a young neutron star formed in the SN 2003lw process. The analogies and the differences between this triptych GRB 031203 / SN 2003lw / URCA-3 and the corresponding ones GRB 980425 / SN 1998bw / URCA-1 and GRB 030329 / SN 2003dh / URCA-2, as well as GRB 060218 / SN 2006aj are discussed.

10. M.G. Bernardini, C.L. Bianco, L. Caito, M.G. Dainotti, R. Guida, R. Ruffini; "GRB970228 and the class of GRBs with an initial spikelike emission: do they follow the Amati relation?"; in Relativistic Astrophysics – Proceedings of the 4th Italian-Sino Workshop, Pescara (Italy), July 2007, C.L. Bianco, S.-S. Xue, Editors; AIP Conference Proceedings, 966, 7 (2008).

On the basis of the recent understanding of GRB050315 and GRB060218, we return to GRB970228, the first Gamma-Ray Burst (GRB) with detected afterglow. We proposed it as the prototype for a new class of GRBs with "an occasional softer extended emission lasting tenths of seconds after an initial spikelike emission". Detailed theoretical computation of the GRB970228 light

curves in selected energy bands for the prompt emission are presented and compared with observational *Beppo*SAX data. From our analysis we conclude that GRB970228 and likely the ones of the above mentioned new class of GRBs are "canonical GRBs" have only one peculiarity: they exploded in a galactic environment, possibly the halo, with a very low value of CBM density. Here we investigate how GRB970228 unveils another peculiarity of this class of GRBs: they do not fulfill the "Amati relation". We provide a theoretical explanation within the fireshell model for the apparent absence of such correlation for the GRBs belonging to this new class.

11. C.L. Bianco, M.G. Bernardini, L. Caito, M.G. Dainotti, R. Guida, R. Ruffini; "The "Fireshell" Model and the "Canonical" GRB Scenario; in Relativistic Astrophysics – Proceedings of the 4th Italian-Sino Workshop, Pescara (Italy), July 2007, C.L. Bianco, S.-S. Xue, Editors; AIP Conference Proceedings, 966, 12 (2008).

In the "fireshell" model we define a "canonical GRB" light curve with two sharply different components: the Proper-GRB (P-GRB), emitted when the optically thick fireshell of electron-positron plasma originating the phenomenon reaches transparency, and the afterglow, emitted due to the collision between the remaining optically thin fireshell and the CircumBurst Medium (CBM). We outline our "canonical GRB" scenario, originating from the gravitational collapse to a black hole, with a special emphasis on the discrimination between "genuine" and "fake" short GRBs.

12. L. Caito, M.G. Bernardini, C.L. Bianco, M.G. Dainotti, R. Guida, R. Ruffini; "GRB 060614: A Progress Report"; in Relativistic Astrophysics – Proceedings of the 4th Italian-Sino Workshop, Pescara (Italy), July 2007, C.L. Bianco, S.-S. Xue, Editors; AIP Conference Proceedings, 966, 16 (2008).

The explosion of GRB 060614, detected by the Swift satellite, produced a deep break in the GRB scenario opening new horizons of investigation, because it can't be traced back to any traditional scheme of classification. In fact, it manifests peculiarities both of long bursts and of short bursts. Above all, it is the first case of long duration near GRB without any bright Ib/c associated Supernova. We will show that, in our canonical GRB scenario, this "anomalous" situation finds a natural interpretation and allows us to discuss a possible variation to the traditional classification scheme, introducing the distinction between "genuine" and "fake" short bursts.

13. M.G. Dainotti, M.G. Bernardini, C.L. Bianco, L. Caito, R. Guida, R. Ruffini; "GRB 060218 and the Binaries as Progenitors of GRB-SN Systems"; in Relativistic Astrophysics – Proceedings of the 4th Italian-Sino Workshop, Pescara (Italy), July 2007, C.L. Bianco, S.-S. Xue, Editors; AIP Conference Proceedings, 966, 25 (2008).

We study the Gamma-Ray Burst (GRB) 060218: a particularly close source at $z = 0.033$ with an extremely long duration, namely $T_{90} \sim 2000$ s, related to SN 2006aj. This source appears to be a very soft burst, with a peak in the spectrum at 4.9 keV, therefore interpreted as an X-Ray Flash (XRF). It fullfills the Amati relation. I present the fitting procedure, which is time consuming. In order to show its sensitivity I also present two examples of fits with the same value of B and different value of $E_{e\pm}^{tot}$. We fit the X- and γ-ray observations by *Swift* of GRB 060218 in the 0.1–150 keV energy band during the entire time of observations from 0 all the way to 10^6 s within a unified theoretical model. The free parameters of our theory are only three, namely the total energy $E_{e\pm}^{tot}$ of the $e^{\pm}$ plasma, its baryon loading $B \equiv M_B c^2 / E_{e\pm}^{tot}$, as well as the CircumBurst Medium (CBM) distribution. We justify the extremely long duration of this GRB by a total energy $E_{e\pm}^{tot} = 2.32 \times 10^{50}$ erg, a very high value of the baryon loading $B = 1.0 \times 10^{-2}$ and the effective CircumBurst Medium (CBM) density which shows a radial dependence $n_{cbm} \propto r^{-\alpha}$ with $1.0 \leq \alpha \leq 1.7$ and monotonically decreases from 1 to 10^{-6} particles/cm^3. We recall that this value of the B parameter is the highest among the sources we have analyzed and it is very close to its absolute upper limit expected. By our fit we show that there is no basic differences between XRFs and more general GRBs. They all originate from the collapse process to a black hole and their difference is due to the variability of the three basic parameters within the range of full applicability of the theory. We also think that the smallest possible black hole, formed by the gravitational collapse of a neutron star in a binary system, is consistent with the especially low energetics of the class of GRBs associated with SNe Ib/c.

14. R. Guida, M.G. Bernardini, C.L. Bianco, L. Caito, M.G. Dainotti, R. Ruffini; "The Amati Relation within the Fireshell Model"; in Relativistic Astrophysics – Proceedings of the 4th Italian-Sino Workshop, Pescara (Italy), July 2007, C.L. Bianco, S.-S. Xue, Editors; AIP Conference Proceedings, 966, 46 (2008).

In this work we show the existence of a spectral-energy correlation within our "fireshell" model for GRBs. The free parameters of the model are the total

energy $E^{e\pm}_{tot}$ of the $e^\pm$ plasma and its baryon loading $B \equiv M_B\,c^2/E^{e\pm}_{tot}$, characterizing the source, and the parameters describing the effective CircumBurst medium (CBM) distribution, namely its particle number density ρ and its effective emitting area R. We build a sample of pseudo-GRBs, i.e. a set of theoretically simulated light curves, varying the total energy of the electron-positron plasma $E^{e\pm}_{tot}$ and keeping the same baryon loading; the parametrization used to describe the distribution of the CircumBurst medium is the same as well for all the pseudo-GRBs. The values of these parameters (B, ρ and R) used in this work are equal to the ones assumed to fit GRB050315, a *Swift* burst representing a good example of what in the literature has been addressed as "canonical light curve". For each GRB of the sample we calculate the νF_ν spectrum integrating the theoretically computed light curve over the total time, namely from our T_0, the end of the Proper-GRB (P-GRB), up to the end of our afterglow phase, when the fireshell Lorentz gamma factor is close to unity; we exclude the P-GRB from this spectral computation because, following our "canonical" GRB scenario, this component of the GRB emission is physically different from the other component, that is our afterglow component, so one should take care in no mixing them. We find that the maximum of this spectrum, that is the observed peak energy $E_{p,tot}$, correlates with the initial electron-positron plasma energy $E^{e\pm}_{tot}$ in a way very similar to the Amati one: $E_{p,tot} \propto (E^{e\pm}_{tot})^{0.5}$.

15. R. Guida, M.G. Bernardini, C.L. Bianco, L. Caito, M.G. Dainotti, R. Ruffini; "Theoretical interpretation of the Amati relation within the fireshell model"; in GAMMA-RAY BURSTS 2007: Proceedings of the Santa Fe Conference, Santa Fe (NM, USA), November 2007, M. Galassi, D. Palmer, E. Fenimore, Editors; AIP Conference Proceedings, 1000, 60 (2008).

    We discuss within our theoretical "fireshell" model for Gamma-Ray Bursts (GRBs) the theoretical interpretation of the phenomenological correlation between the isotropic-equivalent radiated energy of the prompt emission E_{iso} and the cosmological rest-frame νF_ν spectrum peak energy E_p observed by Amati and collaborators. Possible reasons for some of the outliers of this relation are given.

16. L. Caito, M.G. Bernardini, C.L. Bianco, M.G. Dainotti, R. Guida, R. Ruffini; "GRB 060614: a Fake Short Gamma-Ray Burst"; in GAMMA-RAY BURSTS 2007: Proceedings of the Santa Fe Conference, Santa Fe (NM, USA), November 2007, M. Galassi, D. Palmer, E. Fenimore, Editors; AIP Conference Proceedings, 1000, 301 (2008).

The explosion of GRB 060614 produced a deep break in the GRB scenario and opened new horizons of investigation because it can't be traced back to any traditional scheme of classification. In fact, it manifests peculiarities both of long bursts and of short bursts and, above all, it is the first case of long duration near GRB without any bright Ib/c associated Supernova. We will show that, in our canonical GRB scenario, this "anomalous" situation finds a natural interpretation and allows us to discuss a possible variation to the traditional classification scheme, introducing the distinction between "genuine" and "fake" short bursts.

17. C.L. Bianco, M.G. Bernardini, L. Caito, M.G. Dainotti, R. Guida, R. Ruffini; "Short and canonical GRBs"; in GAMMA-RAY BURSTS 2007: Proceedings of the Santa Fe Conference, Santa Fe (NM, USA), November 2007, M. Galassi, D. Palmer, E. Fenimore, Editors; AIP Conference Proceedings, 1000, 305 (2008).

Within the "fireshell" model for the Gamma-Ray Bursts (GRBs) we define a "canonical GRB" light curve with two sharply different components: the Proper-GRB (P-GRB), emitted when the optically thick fireshell of electron-positron plasma originating the phenomenon reaches transparency, and the afterglow, emitted due to the collision between the remaining optically thin fireshell and the CircumBurst Medium (CBM). We outline our "canonical GRB" scenario, with a special emphasis on the discrimination between "genuine" and "fake" short GRBs.

18. C.L. Bianco, M.G. Bernardini, L. Caito, M.G. Dainotti, R. Guida, R. Ruffini, G. Vereshchagin, S.-S. Xue; "The Equations of motion of the "fireshell""; in OBSERVATIONAL EVIDENCE FOR BLACK HOLES IN THE UNIVERSE: Proceedings of the 2nd Kolkata Conference, Kolkata (India), February 2008, S.K. Chakrabarti, A.S. Majumdar, Editors; AIP Conference Proceedings, 1053, 259 (2008).

The Fireshell originating a Gamma-Ray Burst (GRB) encompasses an optically thick regime followed by an optically thin one. In the first one the fireshell self-accelerates from a Lorentz gamma factor equal to 1 all the way to 200-300. The physics of this system is based on the continuous annihilation of electron-positron pairs in an optically thick e^+e^- plasma with a small baryon loading. In the following regime, the optically thin fireshell, composed by the baryons left over after the transparency point, ballistically expands into the Circum-Burst Medium (CBM). The dynamics of the fireshell during both regimes will

be analyzed. In particular we will re-examine the validity of the constant-index power-law relation between the fireshell Lorentz gamma factor and its radial coordinate, usually adopted in the current literature on the grounds of an "ultrarelativistic" approximation. Such expressions are found to be mathematically correct but only approximately valid in a very limited range of the physical and astrophysical parameters and in an asymptotic regime which is reached only for a very short time, if any.

19. M.G. Bernardini, C.L. Bianco, L. Caito, M.G. Dainotti, R. Guida, R. Ruffini; "The "Canonical" GRBs within the fireshell model"; in OBSERVATIONAL EVIDENCE FOR BLACK HOLES IN THE UNIVERSE: Proceedings of the 2nd Kolkata Conference, Kolkata (India), February 2008, S.K. Chakrabarti, A.S. Majumdar, Editors; AIP Conference Proceedings, 1053, 267 (2008).

Within the fireshell model we define a "canonical" GRB light curve with two sharply different components: the Proper-GRB (P-GRB), emitted when the optically thick fireshell of electron-positron plasma originating the phenomenon reaches transparency, and the afterglow, emitted due to the collision between the remaining optically thin fireshell and the CircumBurst Medium (CBM). On the basis of the recent understanding of GRB970228 as the prototype for a new class of GRBs with "an occasional softer extended emission lasting tenths of seconds after an initial spikelike emission" we outline our "canonical" GRB scenario, originating from the gravitational collapse to a black hole, with a special emphasis on the discrimination between short GRBs and the ones appearing as such due to their peculiar astrophysical setting.

20. M.G. Dainotti, M.G. Bernardini, C.L. Bianco, L. Caito, R. Guida, R. Ruffini; "GRB 060218: the density mask and its peculiarity compared to the other sources"; in OBSERVATIONAL EVIDENCE FOR BLACK HOLES IN THE UNIVERSE: Proceedings of the 2nd Kolkata Conference, Kolkata (India), February 2008, S.K. Chakrabarti, A.S. Majumdar, Editors; AIP Conference Proceedings, 1053, 283 (2008).

The Swift satellite has given continuous data in the range 0.3–150 keV from 0 s to 106 s for GRB060218 associated with SN2006aj. It has an unusually long duration ($T_{90} \sim 2100$ s). We plan to fit the complete γ- and X-ray light curves of this long duration GRB, including the prompt emission and we give peculiar attention to the afterglow lightcurve in order to better constrain the density mask. We apply our "fireshell" model based on the formation of a black hole, giving the relevant references. The initial total energy of the electron-positron

plasma $E_{e\pm}^{tot} == 2.32 \times 10^{50}$ erg has a particularly low value similarly to the other GRBs associated with SNe. For the first time we observe a baryon loading $B = 10^{-2}$ which coincides with the upper limit for the dynamical stability of the fireshell. The effective CircumBurst Medium (CBM) density shows a radial dependence $n_{cbm} \propto r^{-a}$ with $1.0 \leq a \leq 1.7$ and monotonically decreases from 1 to 10^{-6} particles/cm^3. Such a behavior is interpreted as due to a fragmentation in the fireshell. Such a fragmentation is crucial in explaining both the unusually large T_{90} and the consequently inferred abnormal low value of the CBM effective density. We present the comparison between the density mask of this source and the ones of a normal GRB 050315 and a fake short, GRB 970228, making some assumptions on the CBM behaviour in the surrounding of the Black hole.

21. L. Caito, M.G. Bernardini, C.L. Bianco, M.G. Dainotti, R. Guida, R. Ruffini; "GRB 060614 in the canonical fireshell model"; in OBSERVATIONAL EVIDENCE FOR BLACK HOLES IN THE UNIVERSE: Proceedings of the 2nd Kolkata Conference, Kolkata (India), February 2008, S.K. Chakrabarti, A.S. Majumdar, Editors; AIP Conference Proceedings, 1053, 291 (2008).

    Gamma-Ray Burst (GRB) 060614 is the first nearby long duration GRB clearly not associated to any bright Ib/c Supernova. The explosion of this burst undermines one of the fundamental assumptions of the standard scenario and opens new horizons and hints of investigation. GRB 060614, hardly classifiable as a short GRB, is not either a "typical" long GRB since it occurs in a low star forming region. Moreover, it presents deep similarities with GRB 970228, which is the prototype of the "fake" short bursts, or better canonical GRBs disguised as short ones. Within the "fireshell" model, we test if this "anomalous" source can be a disguised short GRB.

22. L.J. Rangel Lemos, S. Casanova, R. Ruffini, S.S. Xue; "Fermi's approach to the study of pp interactions"; in OBSERVATIONAL EVIDENCE FOR BLACK HOLES IN THE UNIVERSE: Proceedings of the 2nd Kolkata Conference, Kolkata (India), February 2008, S.K. Chakrabarti, A.S. Majumdar, Editors; AIP Conference Proceedings, 1053, 275 (2008).

    The physics of hadronic interactions found much difficulties for explain the experimental data. In this work we study the approach of Fermi (1950) about the multiplicity of pions emitted in pp interactions and in follow we compare with the modern approach

23. R. Ruffini, A.G. Aksenov, M.G. Bernardini, C.L. Bianco, L. Caito, M.G. Dainotti, G. De Barros, R. Guida, G.V. Vereshchagin, S.-S. Xue; "The canonical Gamma-Ray Bursts and their 'precursors'"; in 2008 NAN-JING GAMMA-RAY BURST CONFERENCE, Proceedings of the 2008 Nanjing Gamma-Ray Burst Conference, Nanjing (China), June 2008, Y.-F. Huang, Z.-G. Dai, B. Zhang, Editors; AIP Conference Proceedings, 1065, 219 (2008).

The fireshell model for Gamma-Ray Bursts (GRBs) naturally leads to a canonical GRB composed of a proper-GRB (P-GRB) and an afterglow. P-GRBs, introduced by us in 2001, are sometimes considered "precursors" of the main GRB event in the current literature. We show in this paper how the fireshell model leads to the understanding of the structure of GRBs, with precise estimates of the time sequence and intensities of the P-GRB and the of the afterglow. It leads as well to a natural classification of the canonical GRBs which overcomes the traditional one in short and long GRBs.

24. M.G. Bernardini, C.L. Bianco, L. Caito, M.G. Dainotti, R. Guida, R. Ruffini; "Preliminary analysis of GRB060607A within the fireshell model"; in 2008 NANJING GAMMA-RAY BURST CONFERENCE; Proceedings of the 2008 Nanjing Gamma-Ray Burst Conference, Nanjing (China), June 2008, Y.-F. Huang, Z.-G. Dai, B. Zhang, Editors; AIP Conference Proceedings, 1065, 227 (2008).

GRB060607A is a very distant ($z = 3.082$) and energetic event ($E_{iso} \sim 10^{53}$ erg). Its main peculiarity is that the peak of the near-infrared afterglow has been observed with the REM robotic telescope, allowing to infer the initial Lorentz gamma factor of the emitting system. We present a preliminary analysis of the spectra and light curves of GRB060607A prompt emission within the fireshell model. We show that the N(E) spectrum of the prompt emission, whose behavior is usually described as "simple power-law", can also be fitted in a satisfactory way by a convolution of thermal spectra as predicted by the model we applied. The theoretical time-integrated spectrum of the prompt emission as well as the light curves in the BAT and XRT energy band are in good agreement with the observations, enforcing the plausibility of our approach. Furthermore, the initial value of Lorentz gamma factor we predict is compatible with the one deduced from the REM observations.

25. C.L. Bianco, M.G. Bernardini, L. Caito, M.G. Dainotti, R. Guida, R. Ruffini; "The "fireshell" model and the "canonical GRB" scenario"; in 2008 NAN-

JING GAMMA-RAY BURST CONFERENCE; Proceedings of the 2008 Nanjing Gamma-Ray Burst Conference, Nanjing (China), June 2008, Y.-F. Huang, Z.-G. Dai, B. Zhang, Editors; AIP Conference Proceedings, 1065, 223 (2008).

The Swift observation of GRB 060614, as well as the catalog analysis by Norris & Bonnell (2006), opened the door "on a new Gamma-Ray Bursts (GRBs) classification scheme that straddles both long and short bursts" (Gehrels et al. 2006). Within the "fireshell" model for the Gamma-Ray Bursts (GRBs) we define a "canonical GRB" light curve with two sharply different components: the Proper-GRB (P-GRB), emitted when the optically thick fireshell of electron-positron plasma originating the phenomenon reaches transparency, and the afterglow, emitted due to the collision between the remaining optically thin fireshell and the CircumBurst Medium (CBM). We here outline our "canonical GRB" scenario, which implies three different GRB classes: the "genuine" short GRBs, the "fake" or "disguised" short GRBs and the other (so-called "long") GRBs. We also outline some implications for the theoretical interpretation of the Amati relation.

26. G. De Barros, M.G. Bernardini, C.L. Bianco, L. Caito, M.G. Dainotti, R. Guida, R. Ruffini; "Is GRB 050509b a "genuine" short GRB?"; in 2008 NANJING GAMMA-RAY BURST CONFERENCE; Proceedings of the 2008 Nanjing Gamma-Ray Burst Conference, Nanjing (China), June 2008, Y.-F. Huang, Z.-G. Dai, B. Zhang, Editors; AIP Conference Proceedings, 1065, 231 (2008).

Within our "fireshell" model we introduced a "canonical" GRB scenario which differentiates physically the "proper GRB" (P-GRB) emission when photons decouple, and the afterglow emission due to interaction of the accelerated baryons with the CircumBurst Medium (CBM). The ratio between energetics of the two components is ruled by the baryon loading of the fireshell. We here analyse the possibility that GRB050509b is the first case of a "genuine" short GRB the ones with smaller baryon loading. In such a case, the GRB050509b "prompt emission" would be dominated by the "proper GRB" and, moreover, the P-GRB total energy would be greater than the afterglow one. Our fit of the afterglow data and of the P-GRB energetics indicates that this source present the smallest baryon loading we ever encountered so far, being on the order of 10^{-4}.

27. G. De Barros, A.G. Aksenov, C.L. Bianco, R. Ruffini, G.V. Vereshchagin;

"Fireshell versus Fireball scenarios"; in 2008 NANJING GAMMA-RAY BURST CONFERENCE; Proceedings of the 2008 Nanjing Gamma-Ray Burst Conference, Nanjing (China), June 2008, Y.-F. Huang, Z.-G. Dai, B. Zhang, Editors; AIP Conference Proceedings, 1065, 234 (2008).

We revisit Cavallo and Rees classification based on the analysis of initial conditions in electron-positron-photon plasma which appears suddenly around compact astrophysical objects and gives origin to GRBs. These initial conditions were recently studied in [1,2] by numerical integration of relativistic Boltzmann equations with collision integrals, including binary and triple interactions between particles. The main conclusion is that the pair plasma in GRB sources quickly reaches thermal equilibrium well before its expansion starts. In light of this work we comment on each of the four scenarios proposed by Cavallo and Rees and discuss their applicability to describe evolution of GRB sources.

28. M.G. Bernardini, C.L. Bianco, L. Caito, M.G. Dainotti, R. Guida, R. Ruffini; "GRB970228 as a prototype for the class of GRBs with an initial spike-like emission"; in Proceedings of the Eleventh Marcel Grossmann Meeting on General Relativity, Berlin, Germany, July 2006, H. Kleinert, R.T. Jantzen, Editors; World Scientific, (Singapore, 2008).

We interpret GRB970228 prompt emission within our "canonical" GRB scenario, identifying the initial spikelike emission with the Proper-GRB (P-GRB) and the following bumps with the afterglow peak emission. Furthermore, we emphasize the necessity to consider the "canonical" GRB as a whole due to the highly non-linear nature of the model we applied.

29. M.G. Bernardini, C.L. Bianco, L. Caito, M.G. Dainotti, R. Guida, R. Ruffini; "GRB980425 and the puzzling URCA1 emission"; in Proceedings of the Eleventh Marcel Grossmann Meeting on General Relativity, Berlin, Germany, July 2006, H. Kleinert, R.T. Jantzen, Editors; World Scientific, (Singapore, 2008).

We applied our "fireshell" model to GRB980425 observational data, reproducing very satisfactory its prompt emission. We use the results of our analysis to provide a possible interpretation for the X-ray emission of the source S1. The effect on the GRB analysis of the lack of data in the pre-Swift observations is also outlined.

30. C.L. Bianco, M.G. Bernardini, L. Caito, P. Chardonnet, M.G. Dainotti,

F. Fraschetti, R. Guida, R. Ruffini, S.-S. Xue; "Theoretical interpretation of 'long' and 'short' GRBs"; in Proceedings of the Eleventh Marcel Grossmann Meeting on General Relativity, Berlin, Germany, July 2006, H. Kleinert, R.T. Jantzen, Editors; World Scientific, (Singapore, 2008).

Within the "fireshell" model we define a "canonical GRB" light curve with two sharply different components: the Proper-GRB (P-GRB), emitted when the optically thick fireshell of electron-positron plasma originating the phenomenon reaches transparency, and the afterglow, emitted due to the collision between the remaining optically thin fireshell and the CircumBurst Medium (CBM). We here present the consequences of such a scenario on the theoretical interpretation of the nature of "long" and "short" GRBs.

31. C.L. Bianco, M.G. Bernardini, P. Chardonnet, F. Fraschetti, R. Ruffini, S.-S. Xue; "Theoretical interpretation of luminosity and spectral properties of GRB 031203"; in Proceedings of the Eleventh Marcel Grossmann Meeting on General Relativity, Berlin, Germany, July 2006, H. Kleinert, R.T. Jantzen, Editors; World Scientific, (Singapore, 2008).

We show how an emission endowed with an instantaneous thermal spectrum in the co-moving frame of the expanding fireshell can reproduce the time-integrated GRB observed non-thermal spectrum. An explicit example in the case of GRB 031203 is presented.

32. C.L. Bianco, R. Ruffini; "The 'Fireshell' model in the Swift era"; in Proceedings of the Eleventh Marcel Grossmann Meeting on General Relativity, Berlin, Germany, July 2006, H. Kleinert, R.T. Jantzen, Editors; World Scientific, (Singapore, 2008).

We here re-examine the validity of the constant-index power-law relation between the fireshell Lorentz gamma factor and its radial coordinate, usually adopted in the current Gamma-Ray Burst (GRB) literature on the grounds of an "ultrarelativistic" approximation. Such expressions are found to be mathematically correct but only approximately valid in a very limited range of the physical and astrophysical parameters and in an asymptotic regime which is reached only for a very short time, if any.

33. L. Caito, M.G. Bernardini, C.L. Bianco, M.G. Dainotti, R. Guida, R. Ruffini; "Theoretical interpretation of GRB011121"; in Proceedings of the Eleventh Marcel Grossmann Meeting on General Relativity, Berlin, Germany, July

2006, H. Kleinert, R.T. Jantzen, Editors; World Scientific, (Singapore, 2008).

GRB 011121, detected by the BeppoSAX satellite, is studied as a prototype to understand the presence of flares observed by Swift in the afterglow of many GRB sources. Detailed theoretical analysis of the GRB 011121 light curves in selected energy bands are presented and compared with observational data. An interpretation of the flare of this source is provided by the introduction of the three-dimensional structure of the CircumBurst Medium(CBM).

34. M.G. Dainotti, M.G. Bernardini, C.L. Bianco, L. Caito, R. Guida, R. Ruffini; "On GRB 060218 and the GRBs related to Supernovae Ib/c"; in Proceedings of the Eleventh Marcel Grossmann Meeting on General Relativity, Berlin, Germany, July 2006, H. Kleinert, R.T. Jantzen, Editors; World Scientific, (Singapore, 2008).

We study the Gamma-Ray Burst (GRB) 060218: a particularly close source at $z = 0.033$ with an extremely long duration, namely $T_{90} \sim 2000$ s, related to SN 2006aj. This source appears to be a very soft burst, with a peak in the spectrum at 4.9 keV, therefore interpreted as an X-Ray Flash (XRF) and it obeys to the Amati relation. We fit the X- and γ-ray observations by Swift of GRB 060218 in the 0.1–150 keV energy band during the entire time of observations from 0 all the way to 106 s within a unified theoretical model. The details of our theoretical analysis have been recently published in a series of articles. The free parameters of the theory are only three, namely the total energy $E_{e\pm}^{tot}$ of the $e^{\pm}$ plasma, its baryon loading $B = M_B c^2 / E_{e\pm}^{tot}$, as well as the CircumBurst Medium (CBM) distribution. We fit the entire light curve, including the prompt emission as an essential part of the afterglow. We recall that this value of the B parameter is the highest among the sources we have analyzed and it is very close to its absolute upper limit expected. We successfully make definite predictions about the spectral distribution in the early part of the light curve, exactly we derive the instantaneous photon number spectrum N(E) and we show that although the spectrum in the co-moving frame of the expanding pulse is thermal, the shape of the final spectrum in the laboratory frame is clearly non thermal. In fact each single instantaneous spectrum is the result of an integration of thousands of thermal spectra over the corresponding EQuiTemporal Surfaces (EQTS). By our fit we show that there is no basic differences between XRFs and more general GRBs. They all originate from the collapse process to a black hole and their difference is due to the variability of the three basic parameters within

the range of full applicability of the theory.

35. R. Guida, M.G. Bernardini, C.L. Bianco, L. Caito, M.G. Dainotti, R. Ruffini; "Theoretical interpretation of GRB060124"; in Proceedings of the Eleventh Marcel Grossmann Meeting on General Relativity, Berlin, Germany, July 2006, H. Kleinert, R.T. Jantzen, Editors; World Scientific, (Singapore, 2008).

We show the preliminary results of the application of our "fireshell" model to GRB060124. This source is very peculiar because it is the first event for which both the prompt and the afterglow emission were observed simultaneously by the three Swift instruments: BAT (15 - 350 keV), XRT (0,2 - 10 keV) and UVOT (170 - 650 nm), due to the presence of a precursor ~ 570 s before the main burst. We analyze GRB060124 within our "canonical" GRB scenario, identifying the precursor with the P-GRB and the prompt emission with the afterglow peak emission. In this way we reproduce correctly the energetics of both these two components. We reproduce also the observed time delay between the precursor (P-GRB) and the main burst. The effect of such a time delay in our model will be discussed.

36. R. Ruffini, M.G. Bernardini, C.L. Bianco, L. Caito, P. Chardonnet, C. Cherubini, M.G. Dainotti, F. fraschetti, A. Geralico, R. Guida, B. Patricelli, M. Rotondo, J. Rueda Hernandez, G. Vereshchagin, S.-S. Xue; "Gamma-Ray Bursts"; in Proceedings of the Eleventh Marcel Grossmann Meeting on General Relativity, Berlin, Germany, July 2006, H. Kleinert, R.T. Jantzen, Editors; World Scientific, (Singapore, 2008).

We show by example how the uncoding of Gamma-Ray Bursts (GRBs) offers unprecedented possibilities to foster new knowledge in fundamental physics and in astrophysics. After recalling some of the classic work on vacuum polarization in uniform electric fields by Klein, Sauter, Heisenberg, Euler and Schwinger, we summarize some of the efforts to observe these effects in heavy ions and high energy ion collisions. We then turn to the theory of vacuum polarization around a Kerr-Newman black hole, leading to the extraction of the blackholic energy, to the concept of dyadosphere and dyadotorus, and to the creation of an electron-positron-photon plasma. We then present a new theoretical approach encompassing the physics of neutron stars and heavy nuclei. It is shown that configurations of nuclear matter in bulk with global charge neutrality can exist on macroscopic scales and with electric fields close to the

critical value near their surfaces. These configurations may represent an initial condition for the process of gravitational collapse, leading to the creation of an electron-positron-photon plasma: the basic self-accelerating system explaining both the energetics and the high energy Lorentz factor observed in GRBs. We then turn to recall the two basic interpretational paradigms of our GRB model: 1) the Relative Space-Time Transformation (RSTT) paradigm and 2) the Interpretation of the Burst Structure (IBS) paradigm. These paradigms lead to a "canonical" GRB light curve formed from two different components: a Proper-GRB (P-GRB) and an extended afterglow comprising a raising part, a peak, and a decaying tail. When the P-GRB is energetically predominant we have a "genuine" short GRB, while when the afterglow is energetically predominant we have a so-called long GRB or a "fake" short GRB. We compare and contrast the description of the relativistic expansion of the electron-positron plasma within our approach and within the other ones in the current literature. We then turn to the special role of the baryon loading in discriminating between "genuine" short and long or "fake" short GRBs and to the special role of GRB 991216 to illustrate for the first time the "canonical" GRB bolometric light curve. We then propose a spectral analysis of GRBs, and proceed to some applications: GRB 031203, the first spectral analysis, GRB 050315, the first complete light curve fitting, GRB 060218, the first evidence for a critical value of the baryon loading, GRB 970228, the appearance of "fake" short GRBs. We finally turn to the GRB-Supernova Time Sequence (GSTS) paradigm: the concept of induced gravitational collapse. We illustrate this paradigm by the systems GRB 980425 / SN 1998bw, GRB 030329 / SN 2003dh, GRB 031203 / SN 2003lw, GRB 060218 / SN 2006aj, and we present the enigma of the URCA sources. We then present some general conclusions.

37. R. Ruffini, A.G. Aksenov, M.G. Bernardini, C.L. Bianco, L. Caito, M.G. Dainotti, G. De Barros, R. Guida, G. Vereshchagin, S.-S. Xue; "The canonical Gamma-Ray Bursts: long, 'fake'-'disguised' and 'genuine' short bursts; in PROBING STELLAR POPULATIONS OUT TO THE DISTANT UNIVERSE: CEFALU 2008, Proceedings of the International Conference; Cefalù (Italy), September 2008, G. Giobbi, A. Tornambe, G. Raimondo, M. Limongi, L. A. Antonelli, N. Menci, E. Brocato, Editors; AIP Conference Proceedings, 1111, 325 (2009).

The Gamma-Ray Bursts (GRBs) offer the unprecedented opportunity to observe for the first time the blackholic energy extracted by the vacuum polarization during the process of gravitational collapse to a black hole leading to

the formation of an electron-positron plasma. The uniqueness of the Kerr-Newman black hole implies that very different processes originating from the gravitational collapse a) of a single star in a binary system induced by the companion, or b) of two neutron stars, or c) of a neutron star and a white dwarf, do lead to the same structure for the observed GRB. The recent progress of the numerical integration of the relativistic Boltzmann equations with collision integrals including 2-body and 3-body interactions between the particles offer a powerful conceptual tool in order to differentiate the traditional "fireball" picture, an expanding hot cavity considered by Cavallo and Rees, as opposed to the "fireshell" model, composed of an internally cold shell of relativistically expanding electron-positron-baryon plasma. The analysis of the fireshell naturally leads to a canonical GRB composed of a proper-GRB and an extended afterglow. By recalling the three interpretational paradigms for GRBs we show how the fireshell model leads to an understanding of the GRB structure and to an alternative classification of short and long GRBs.

38. M.G. Bernardini, M.G. Dainotti, C.L. Bianco, L. Caito, R. Guida, R. Ruffini; "Prompt emission and X-ray flares: the case of GRB 060607 A"; in PROBING STELLAR POPULATIONS OUT TO THE DISTANT UNIVERSE: CEFALU 2008, Proceedings of the International Conference; Cefalù (Italy), September 2008, G. Giobbi, A. Tornambe, G. Raimondo, M. Limongi, L. A. Antonelli, N. Menci, E. Brocato, Editors; AIP Conference Proceedings, 1111, 383 (2009).

GRB 060607A is a very distant and energetic event. Its main peculiarity is that the peak of the near-infrared (NIR) afterglow has been observed with the REM robotic telescope, allowing to estimate the initial Lorentz gamma factor within the fireball forward shock model. We analyze GRB 060607A within the fireshell model. The initial Lorentz gamma factor of the fireshell can be obtained adopting the exact solutions of its equations of motion, dealing only with the BAT and XRT observations, that are the basic contribution to the afterglow emission, up to a distance from the progenitor $r \sim 10^{18}$ cm. According to the "canonical GRB" scenario we interpret the whole prompt emission as the peak of the afterglow emission, and we show that the observed temporal variability of the prompt emission can be produced by the interaction of the fireshell with overdense CircumBurst Medium (CBM) clumps. This is indeed the case also of the X-ray flares which are present in the early phases of the afterglow light curve.

39. C.L. Bianco, M.G. Bernardini, L. Caito, M.G. Dainotti, R. Guida, R. Ruffini; "The 'fireshell' model and the 'canonical GRB' scenario. Implications for the Amati relation"; in PROBING STELLAR POPULATIONS OUT TO THE DISTANT UNIVERSE: CEFALU 2008, Proceedings of the International Conference; Cefalù (Italy), September 2008, G. Giobbi, A. Tornambe, G. Raimondo, M. Limongi, L. A. Antonelli, N. Menci, E. Brocato, Editors; AIP Conference Proceedings, 1111, 587 (2009).

Within the "fireshell" model for GRBs we define a "canonical GRB" light curve with two sharply different components: the Proper-GRB (P-GRB), emitted when the optically thick fireshell reaches transparency, and the extended afterglow, emitted due to the collision between the remaining optically thin fireshell and the CircumBurst Medium (CBM). We here outline our "canonical GRB" scenario, which implies three different GRB classes: the "genuine" short GRBs, the "fake" or "disguised" short GRBs and the other (so-called "long") GRBs. We will also outline the corresponding implications for the Amati relation, which are opening its use for cosmology.

40. R. Ruffini, A.G. Aksenov, M.G. Bernardini, C.L. Bianco, L. Caito, P. Chardonnet, M.G. Dainotti, G. De Barros, R. Guida, L. Izzo, B. Patricelli, L.J. Rangel Lemos, M. Rotondo, J.A. Rueda Hernandez, G. Vereshchagin, S.-S. Xue; "The Blackholic energy and the canonical Gamma-Ray Burst IV: the 'long', 'genuine short' and 'fake – disguised short' GRBs"; in Proceedings of the XIIIth Brazilian School on Cosmology and Gravitation, Mangaratiba, Rio de Janeiro (Brazil), July-August 2008, M. Novello, S.E. Perez Bergliaffa, Editors; AIP Conference Proceedings, 1132, 199 (2009).

We report some recent developments in the understanding of GRBs based on the theoretical framework of the "fireshell" model, already presented in the last three editions of the "Brazilian School of Cosmology and Gravitation". After recalling the basic features of the "fireshell model", we emphasize the following novel results: 1) the interpretation of the X-ray flares in GRB afterglows as due to the interaction of the optically thin fireshell with isolated clouds in the CircumBurst Medium (CBM); 2) an interpretation as "fake - disguised" short GRBs of the GRBs belonging to the class identified by Norris & Bonnell; we present two prototypes, GRB 970228 and GRB 060614; both these cases are consistent with an origin from the final coalescence of a binary system in the halo of their host galaxies with particularly low CBM density $n_{cbm} \sim 10^{-3}$

particles/cm^3; 3) the first attempt to study a genuine short GRB with the analysis of GRB 050509B, that reveals indeed still an open question; 4) the interpretation of the GRB-SN association in the case of GRB 060218 via the "induced gravitational collapse" process; 5) a first attempt to understand the nature of the "Amati relation", a phenomenological correlation between the isotropic-equivalent radiated energy of the prompt emission E_{iso} with the cosmological rest-frame νF_ν spectrum peak energy $E_{p,i}$. In addition, recent progress on the thermalization of the electron-positron plasma close to their formation phase, as well as the structure of the electrodynamics of Kerr-Newman Black Holes are presented. An outlook for possible explanation of high-energy phenomena in GRBs to be expected from the AGILE and the Fermi satellites are discussed. As an example of high energy process, the work by Enrico Fermi dealing with ultrarelativistic collisions is examined. It is clear that all the GRB physics points to the existence of overcritical electrodynamical fields. In this sense we present some progresses on a unified approach to heavy nuclei and neutron stars cores, which leads to the existence of overcritical fields under the neutron star crust.

41. A.G. Aksenov, M.G. Bernardini, C.L. Bianco, L. Caito, C. Cherubini, G. De Barros, A. Geralico, L. Izzo, F.A. Massucci, B. Patricelli, M. Rotondo, J.A. Rueda Hernandez, R. Ruffini, G. Vereshchagin, S.-S. Xue; "The fireshell model for Gamma-Ray Bursts"; in The Shocking Universe, Proceedings of the conference held in Venice (Italy), September 2009, G. Chincarini, P. D'Avanzo, R. Margutti, R. Salvaterra, Editors; SIF Conference Proceedings, 102, 451 (2010).

    The fireshell model for GRBs is briefly outlined, and the currently ongoing developments are summarized.

42. M.G. Bernardini, C.L. Bianco, L. Caito, L. Izzo, B. Patricelli, R. Ruffini; "The end of the prompt emission within the fireshell model"; in The Shocking Universe, Proceedings of the conference held in Venice (Italy), September 2009, G. Chincarini, P. D'Avanzo, R. Margutti, R. Salvaterra, Editors; SIF Conference Proceedings, 102, 489 (2010)

    The shallow decay emission, revealed by the Swift satellite in the X-ray afterglow of a good sample of bursts, is a puzzle. Within the fireshell model it has been recently proposed an alternative explanation: if we assume that after the prompt phase the system has a range of Lorentz factors, the plateau phase is simply the product of the injection of slower material into the fireshell. This

injection produces a modification both in the dynamics of the fireshell and in the spectrum of the emitted radiation. We postulate that this spread in the fireshell Lorentz factor occurs when the fireshell becomes transparent and do not depend on a prolonged activity of the central engine. The aim of this paper is to characterize dynamically the system in order to understand the nature of that material.

43. L. Izzo, M.G. Bernardini, C.L. Bianco, L. Caito, B. Patricelli, R. Ruffini; "GRB 090423 in the fireshell scenario"; in The Shocking Universe, Proceedings of the conference held in Venice (Italy), September 2009, G. Chincarini, P. D'Avanzo, R. Margutti, R. Salvaterra, Editors; SIF Conference Proceedings, 102, 537 (2010).

44. B. Patricelli, M.G. Bernardini, C.L. Bianco, L. Caito, L. Izzo, R. Ruffini, G. Vereshchagin; "A new spectral energy distribution of photons in the fireshell model of GRBs"; in The Shocking Universe, Proceedings of the conference held in Venice (Italy), September 2009, G. Chincarini, P. D'Avanzo, R. Margutti, R. Salvaterra, Editors; SIF Conference Proceedings, 102, 559 (2010).

The fireshell model of Gamma Ray Bursts (GRBs) postulates that the emission process is thermal in the comoving frame of the fireshell, but this is just a first approximation. We investigate a different spectrum of photons in the comoving frame in order to better reproduce the observed spectral properties of GRB prompt emission. We introduce a modified thermal spectrum whose low energy slope depends on an index α, left as a free parameter. We test it by comparing the numerical simulations with observed BAT spectra integrated over different intervals of time. We find that the observational data can be correctly reproduced by assuming $\alpha = -1.8$.

45. C.L. Bianco, M.G. Bernardini, L. Caito, G. De Barros, L. Izzo, B. Patricelli, R. Ruffini; "Disguised Short Bursts and the Amati Relation"; in Deciphering the ancient universe with Gamma-Ray Bursts, Proceedings of the conference held in Kyoto (Japan), April 2010, N. Kawai, S. Nagataki, Editors; AIP Conference Proceedings, 1279, 299 (2010).

The class of "Disguised short" GRBs implied by the fireshell scenario is presented, with special emphasis on the implications for the Amati relation.

46. L. Izzo, M.G. Bernardini, C.L. Bianco, L. Caito, B. Patricelli, L.J. Rangel Lemos, R. Ruffini; "On GRB 080916C and GRB 090902B observed by the

Fermi satellite"; in Deciphering the ancient universe with Gamma-Ray Bursts, Proceedings of the conference held in Kyoto (Japan), April 2010, N. Kawai, S. Nagataki, Editors; AIP Conference Proceedings, 1279, 343 (2010).

We propose a possible explanation, in the context of the Fireshell scenario, for the high-energy emission observed in GRB 080916C and GRB 090902B. The physical process underlying this emission consists mainly in the interaction of the baryon in the Fireshell with some high-density region around the burst site. Moreover we associate the observed delay of the onset of the high-energy emission as due to the P-GRB emission.

47. B. Patricelli, M.G. Bernardini, C.L. Bianco, L. Caito, G. De Barros, L. Izzo, R. Ruffini; "Black Holes in Gamma Ray Bursts"; in Deciphering the ancient universe with Gamma-Ray Bursts, Proceedings of the conference held in Kyoto (Japan), April 2010, N. Kawai, S. Nagataki, Editors; AIP Conference Proceedings, 1279, 406 (2010).

Within the fireshell model, Gamma Ray Bursts (GRBs) originate from an optically thick $e^{\pm}$ plasma created by vacuum polarization process during the formation of a Black Hole (BH). Here we briefly recall the basic features of this model, then we show how it is possible to interpret GRB observational properties within it. In particular we present, as a specific example, the analysis of GRB 050904 observations of the prompt emission light curve and spectrum in the Swift BAT energy band (15-150 keV).

48. M.G. Bernardini, C.L. Bianco, L. Caito, M.G. Dainotti, R. Guida, R. Ruffini; "The GRB classification within the "fireshell" model: short, long and "fake" short GRBs"; in Proceedings of the 3rd Stueckelberg Workshop on Relativistic Field Theories, Pescara, Italy, July 2008, N. Carlevaro, R. Ruffini, G.V. Vereshchagin, Editors; Cambridge Scientific Publishers, (UK, 2011).

49. C.L. Bianco, M.G. Bernardini, L. Caito, M.G. Dainotti, R. Guida, R. Ruffini, G.V. Vereshchagin, S.-S. Xue; "Equations of motion of the "fireshell""; in Proceedings of the 3rd Stueckelberg Workshop on Relativistic Field Theories, Pescara, Italy, July 2008, N. Carlevaro, R. Ruffini, G.V. Vereshchagin, Editors; Cambridge Scientific Publishers, (UK, 2011).

50. L. Caito, M.G. Bernardini, C.L. Bianco, M.G. Dainotti, R. Guida, R. Ruffini; "GRB 060614: another example of "fake" short burst from a merging

binary system"; in Proceedings of the 3rd Stueckelberg Workshop on Relativistic Field Theories, Pescara, Italy, July 2008, N. Carlevaro, R. Ruffini, G.V. Vereshchagin, Editors; Cambridge Scientific Publishers, (UK, 2011).

51. G. De Barros, M.G. Bernardini, C.L. Bianco, L. Caito, R. Guida, R. Ruffini; "Analysis of GRB 050509b"; in Proceedings of the 3rd Stueckelberg Workshop on Relativistic Field Theories, Pescara, Italy, July 2008, N. Carlevaro, R. Ruffini, G.V. Vereshchagin, Editors; Cambridge Scientific Publishers, (UK, 2011).

52. R. Ruffini, L. Izzo, A.V. Penacchioni, C.L. Bianco, L. Caito, S.K. Chakrabarti, A. Nandi; "GRB 090618: a possible case of multiple GRB?"; in Proceedings of the 25th Texas Symposium on Relativistic Astrophysics, held in Heidelberg (Germany), December 2010, F.M. Rieger, C. van Eldik, W. Hofmann, Editors; PoS(Texas2010), 101.

53. L.J. Rangel Lemos, C.L. Bianco, H.J. Mosquera Cuesta, J.A. Rueda, R. Ruffini; "Luminosity function of BATSE GRBs dominated by extended afterglow"; in Proceedings of the 25th Texas Symposium on Relativistic Astrophysics, held in Heidelberg (Germany), December 2010, F.M. Rieger, C. van Eldik, W. Hofmann, Editors; PoS(Texas2010), 204.

54. R. Ruffini, A.G. Aksenov, M.G. Bernardini, C.L. Bianco, L. Caito, P. Chardonnet, M.G. Dainotti, G. De Barros, R. Guida, L. Izzo, B. Patricelli, L.J. Rangel Lemos, M. Rotondo, J.A. Rueda Hernandez, G. Vereshchagin, She-Sheng Xue; "Black Holes Energetics and GRBs"; in The Sun, the Stars, the Universe and General Relativity: Proceedings of Sobral 2009; S.E. Perez Bergliaffa, M. Novello , R. Ruffini, Editors; Cambridge Scientific Publishers (UK, 2011).

55. C.L. Bianco, L. Amati, M.G. Bernardini, L. Caito, G. De Barros, L. Izzo, B. Patricelli, R. Ruffini; "The class of 'disguised' short GRBs and its implications for the Amati relation"; in GRBs as probes - from the progenitors environment to the high redshift Universe, Proceedings of the conference held in Como (Italy), May 2011, S. Campana, P. D'Avanzo, A. Melandri, Editors; Mem. S.A.It. Suppl., 21, 139 (2012).

56. A.V. Penacchioni, R. Ruffini, L. Izzo, M. Muccino, C.L. Bianco, L. Caito, B. Patricelli; "Evidences for a double component in the emission of GRB

101023"; in GRBs as probes - from the progenitors environment to the high redshift Universe, Proceedings of the conference held in Como (Italy), May 2011, S. Campana, P. D'Avanzo, A. Melandri, Editors; Mem. S.A.It. Suppl., 21, 230 (2012).

57. M.G. Bernardini, C.L. Bianco, L. Caito, L. Izzo, B. Patricelli, R. Ruffini; "The X-Ray Flares of GRB 060607A within the Fireshell Model"; in Proceedings of the Twelfth Marcel Grossmann Meeting on General Relativity, Paris, France, July 2009, T. Damour, R.T. Jantzen, R. Ruffini, Editors; World Scientific, (Singapore, 2012).

58. L. Izzo, M.G. Bernardini, C.L. Bianco, L. Caito, B. Patricelli, R. Ruffini; "GRB 090423 in the Fireshell Scenario: A Canonical GRB at Redshift 8.2"; in Proceedings of the Twelfth Marcel Grossmann Meeting on General Relativity, Paris, France, July 2009, T. Damour, R.T. Jantzen, R. Ruffini, Editors; World Scientific, (Singapore, 2012).

59. B. Patricelli, M.G. Bernardini, C.L. Bianco, L. Caito, L. Izzo, R. Ruffini, G.V. Vereshchagin; "A New Spectral Energy Distribution of Photons in the Fireshell Model of GRBs"; in Proceedings of the Twelfth Marcel Grossmann Meeting on General Relativity, Paris, France, July 2009, T. Damour, R.T. Jantzen, R. Ruffini, Editors; World Scientific, (Singapore, 2012).

60. C.L. Bianco, M.G. Bernardini, L. Caito, G. De Barros, L. Izzo, M. Muccino, B. Patricelli, A.V. Penacchioni, G.B. Pisani, R. Ruffini; "Needs for a new GRB classification following the fireshell model: "genuine short", "disguised short" and "long" GRBs"; in Proceedings of the Gamma-Ray Bursts 2012 Conference, held in Munich (Germany), May 2012, A. Rau, J. Greiner, Editors; PoS(GRB 2012), 043.

61. A.V. Penacchioni, G.B. Pisani, R. Ruffini, C.L. Bianco, L. Izzo, M. Muccino; "The proto-black hole concept in GRB 101023 and its possible extension to GRB 110709B"; in Proceedings of the Gamma-Ray Bursts 2012 Conference, held in Munich (Germany), May 2012, A. Rau, J. Greiner, Editors; PoS(GRB 2012), 042.

62. B. Patricelli, M.G. Bernardini, C.L. Bianco, L. Caito, L. Izzo, R. Ruffini; "GRB 050904: The study of a high redshift GRB within the Fireshell Model"; in Proceedings of the Twelfth Marcel Grossmann Meeting on

General Relativity, Paris, France, July 2009, T. Damour, R.T. Jantzen, R. Ruffini, Editors; World Scientific, (Singapore, 2012).

63. L. Izzo, G.B. Pisani, M. Muccino, J.A. Rueda, Y.Wang, C.L. Bianco, A.V. Penacchioni, R. Ruffini; "A common behavior in the late X-ray afterglow of energetic GRB-SN systems"; EAS Publications Series, Volume 61, 595-597 (2013).

64. R. Ruffini; "Black Holes, Supernovae and Gamma Ray Bursts"; in Proceedings of the Thirteenth Marcel Grossmann Meeting on General Relativity, Stockholm, Sweden, July 2012, R.T. Jantzen, K. Rosquist, R. Ruffini, Editors; World Scientific, (Singapore, 2015).

65. M. Muccino, R. Ruffini, C.L. Bianco, L. Izzo, A.V. Penacchioni, G.B. Pisani; "GRB 090227B: The missing link between the genuine short and long GRBs"; in Proceedings of the Thirteenth Marcel Grossmann Meeting on General Relativity, Stockholm, Sweden, July 2012, R.T. Jantzen, K. Rosquist, R. Ruffini, Editors; World Scientific, (Singapore, 2015).

66. A.V. Penacchioni, R. Ruffini, C.L. Bianco, L. Izzo, M. Muccino, G.B. Pisani, J.A. Rueda; "The family of the Induced Gravitational Collapse scenario: The case of GRB 110709B"; in Proceedings of the Thirteenth Marcel Grossmann Meeting on General Relativity, Stockholm, Sweden, July 2012, R.T. Jantzen, K. Rosquist, R. Ruffini, Editors; World Scientific, (Singapore, 2015).

67. A.V. Penacchioni, R. Ruffini, C.L. Bianco, L. Izzo, M. Muccino, G.B. Pisani; "GRB 111228, analysis within the Induced Gravitational Collapse scenario and association with a supernova"; in Proceedings of the Thirteenth Marcel Grossmann Meeting on General Relativity, Stockholm, Sweden, July 2012, R.T. Jantzen, K. Rosquist, R. Ruffini, Editors; World Scientific, (Singapore, 2015).

68. G.B. Pisani, L. Izzo, R. Ruffini, C.L. Bianco, M. Muccino, A.V. Penacchioni, J.A. Rueda, Y. Wang; "On a novel distance indicator for Gamma-Ray Bursts associated with supernovae"; in Proceedings of the Thirteenth Marcel Grossmann Meeting on General Relativity, Stockholm, Sweden, July 2012, R.T. Jantzen, K. Rosquist, R. Ruffini, Editors; World Scientific, (Singapore, 2015).

69. M. Muccino, R. Ruffini, C.L. Bianco, L. Izzo, A.V. Penacchioni, G.B. Pisani; "GRB 090510, explosion of a GRB in the highest circumburst medium even inferred: a disguised short GRB"; in Proceedings of the Thirteenth Marcel Grossmann Meeting on General Relativity, Stockholm, Sweden, July 2012, R.T. Jantzen, K. Rosquist, R. Ruffini, Editors; World Scientific, (Singapore, 2015).

70. L. Izzo, G.B. Pisani, M. Muccino, R. Ruffini, C.L. Bianco, M. Enderli, Y. Wang; "Hints for a physically based GRB distance indicator"; in Proceedings of the Thirteenth Marcel Grossmann Meeting on General Relativity, Stockholm, Sweden, July 2012, R.T. Jantzen, K. Rosquist, R. Ruffini, Editors; World Scientific, (Singapore, 2015).

71. R. Ruffini, Y. Aimuratov, V. Belinski, C.L. Bianco, M. Enderli, L. Izzo, M. Kovacevic, G.J. Mathews, R. Moradi, M. Muccino, A.V. Penacchioni, G.B. Pisani, J.A. Rueda, G.V. Vereshchagin, Y. Wang, S.-S. Xue; Cosmic matrix in the jubilee of relativistic astrophysics; in THE SECOND ICRANET CÉSAR LATTES MEETING: Supernovae, Neutron Stars and Black Holes, Proceedings of the conference held in Rio de Janeiro – Niterói – João Pessoa – Recife – Fortaleza (Brazil), 13-22 April 2015, U. Barres de Almeida, P. Chardonnet, R. Picanco Negreiros, J. Rueda, R. Ruffini, G. Vereshchagin, C. Zen Vasconcellos, Editors; AIP Conference Proceedings, 1693, 020001 (2015).

72. L. Becerra, C.L. Bianco, F. Cipolletta, M. Enderli, C.L. Fryer, L. Izzo, M. Kovacevic, R. Camargo Rodrigues de Lima, M. Muccino, F.G. de Oliveira, A.V. Penacchioni, G.B. Pisani, J.A. Rueda, R. Ruffini, Y. Wang, E. Zaninoni; Black holes, neutron stars and supernovae within the induced gravitational collapse paradigm for GRBs; in THE SECOND ICRANET CÉSAR LATTES MEETING: Supernovae, Neutron Stars and Black Holes, Proceedings of the conference held in Rio de Janeiro – Niterói – João Pessoa – Recife – Fortaleza (Brazil), 13-22 April 2015, U. Barres de Almeida, P. Chardonnet, R. Picanco Negreiros, J. Rueda, R. Ruffini, G. Vereshchagin, C. Zen Vasconcellos, Editors; AIP Conference Proceedings, 1693, 020002 (2015).

73. L.J. Rangel Lemos, C.L. Bianco, R. Ruffini; Applying the luminosity function statistics in the fireshell model; in THE SECOND ICRANET CÉSAR LATTES MEETING: Supernovae, Neutron Stars and Black Holes,

Proceedings of the conference held in Rio de Janeiro – Niterói – João Pessoa – Recife – Fortaleza (Brazil), 13-22 April 2015, U. Barres de Almeida, P. Chardonnet, R. Picanco Negreiros, J. Rueda, R. Ruffini, G. Vereshchagin, C. Zen Vasconcellos, Editors; AIP Conference Proceedings, 1693, 070004 (2015).

74. J.A. Rueda, R. Ruffini, J.F. Rodriguez, M. Muccino, Y. Aimuratov, U. Barres de Almeida, L.M. Becerra, C.L. Bianco, C. Cherubini, S. Filippi, M. Kovacevic, R. Moradi, G.B. Pisani, Y. Wang; The binary progenitors of short and long GRBs and their gravitational-wave emission; EPJ Web of Conferences, 168, 01006 (2018).

75. M. Muccino, R. Ruffini, Y. Aimuratov, L.M. Becerra, C.L. Bianco, M. Karlika, M. Kovacevic, J.D. Melon Fuksman, R. Moradi, A.V. Penacchioni, G.B. Pisani, D. Primorac, J.A. Rueda, S. Shakeri, G.V. Vereshchagin, S.-S. Xue, Y. Wang; What can we learn from GRBs?; EPJ Web of Conferences, 168, 01015 (2018).

76. L.M. Becerra, C.L. Bianco, C. Fryer, J.A. Rueda, R. Ruffini; On the Induced Gravitational Collapse; EPJ Web of Conferences, 168, 02005 (2018).

77. G.B. Pisani, R. Ruffini, Y. Aimuratov, C.L. Bianco, M. Karlika, M. Kovacevic, R. Moradi, M. Muccino, A.V. Penacchioni, D. Primorac, J.A. Rueda, Y. Wang; The first ICRANet catalog of Binary-Driven Hypernovae; EPJ Web of Conferences, 168, 04002 (2018).

78. D. Primorac, R. Ruffini, G.B. Pisani, Y. Aimuratov, C.L. Bianco, M. Karlika, J.D. Melon Fuksman, R. Moradi, M. Muccino, A.V. Penacchioni, J.A. Rueda, Y. Wang; GRB 110731A within the IGC paradgm; EPJ Web of Conferences, 168, 04008 (2018).

79. J.D. Melon Fuksman, L.M. Becerra, C.L. Bianco, M. Karlika, M. Kovacevic, R. Moradi, M. Muccino, G.B. Pisani, D. Primorac, J.A. Rueda, R. Ruffini, G.V. Vereshchagin, Y. Wang; Evolution of an electron-positron plasma produced by induced gravitational collapse in binary-driven hypernovae; EPJ Web of Conferences, 168, 04009 (2018).

Dissecting the Energy Budget of a Gamma-Ray Burst Fireball

Bing Zhang[1] , Yu Wang[2,3,4], and Liang Li[2,3,4]

[1] Department of Physics and Astronomy, University of Nevada Las Vegas, Las Vegas, NV 89154 USA; zhang@physics.unlv.edu
[2] ICRANet, Piazza della Repubblica 10, I-65122 Pescara, Italy
[3] INAF—Osservatorio Astronomico d'Abruzzo, Via M. Maggini snc, I-64100, Teramo, Italy
[4] Dip. di Fisica and ICRA, Sapienza Universita di Roma, Piazzale Aldo Moro 5, I-00185 Rome, Italy

Abstract

The jet composition and radiative efficiency of gamma-ray bursts (GRBs) are poorly constrained from the data. If the jet composition is matter-dominated (i.e., a fireball), the GRB prompt emission spectra would include a dominant thermal component originating from the fireball photosphere and a nonthermal component presumably originating from internal shocks whose radii are greater than the photosphere radius. We propose a method to directly dissect the GRB fireball energy budget into three components and measure their values by combining the prompt emission and early afterglow data. The measured parameters include the initial dimensionless specific enthalpy density (η), bulk Lorentz factors at the photosphere radius (Γ_{ph}) and before fireball deceleration (Γ_0), the amount of mass loading (M), and the GRB radiative efficiency (η_γ). All the parameters can be derived from the data for a GRB with a dominant thermal spectral component, a deceleration bump feature in the early afterglow lightcurve, and a measured redshift. The results only weakly depend on the density n of the interstellar medium when the composition $\mathcal{Y}$ parameter (typically unity) is specified.

Unified Astronomy Thesaurus concepts: Gamma-ray bursts (629); Relativistic fluid dynamics (1389)

1. Introduction

The jet composition of the gamma-ray bursts (GRBs) has been subject to debate (Kumar & Zhang 2015; Pe'er 2015; Zhang 2018). The GRB prompt emission spectra can in principle help to diagnose the jet composition: the existence of a bright thermal component would support a matter-dominated fireball (Mészáros & Rees 2000), while the nondetection of such a component may suggest the dominance of a Poynting flux in the jet composition (Zhang & Pe'er 2009).[5] Broadband observations with GRB detectors, especially with the Gamma-ray Burst Monitor and Large Area Telescope on board the Fermi Gamma-Ray Space Telescope, have collected rich data, which suggest that the GRB jet composition is likely diverse. Whereas some GRBs (e.g., GRB 090902B, Abdo et al. 2009a; Ryde et al. 2010; Pe'er et al. 2012, see Ryde 2005; Ryde & Pe'er 2009; Li 2019b for systematic searches) are consistent with being fireballs, a good fraction of bursts are consistent with not having a thermal component (e.g., GRBs 080916C, 130606B, and many others; Abdo et al. 2009b; Zhang et al. 2011, 2016; Oganesyan et al. 2017; Ravasio et al. 2019; Burgess et al. 2020). "Intermediate" GRBs with a dominant nonthermal component and a subdominant thermal component have been discovered (e.g., GRB 100724B, GRB 110721A and several others; Guiriec et al. 2011, 2015; Axelsson et al. 2012), which may be understood within the framework of "hybrid" jets, i.e., the composition is a mixture of a matter component and a Poynting-flux component (Gao & Zhang 2015; Li 2020). Some bursts (e.g., GRB 160625B) displayed a significant change of jet composition among different emission episodes within the same GRB (Zhang et al. 2018; Li 2019a), which may be consistent with some central engine models (e.g., Metzger et al. 2011). Different jet compositions may imply different

energy dissipation (shocks versus magnetic reconnection) and radiation (quasi-thermal versus synchrotron) mechanisms.

Another interesting subject related to the GRB prompt emission mechanism is the radiative efficiency of a burst, which may be defined as (Lloyd-Ronning & Zhang 2004)

$$\eta_\gamma \equiv \frac{E_\gamma}{E_{tot}} = \frac{E_\gamma}{E_\gamma + E_k} = \frac{L_\gamma}{L_{w,0}}, \quad (1)$$

where E_γ, E_k, and E_{tot} are isotropic-equivalent gamma-ray energy, afterglow kinetic energy, and total energy, respectively, and L_γ and $L_{w,0}$ are the isotropic-equivalent average gamma-ray luminosity and total wind luminosity at the central engine, respectively. Considering beaming correction would lead to the same results, since all the energy/luminosity terms are multiplied by the same beaming factor f_b, which is not considered in the discussion below. The E_γ value can be well measured from the data as long as the fluence is well measured and redshift is known. The E_k term, on the other hand, is usually estimated from the afterglow data through modeling. Its value depends on many uncertain shock microphysics parameters, mostly ϵ_e (Freedman & Waxman 2001), but also ϵ_B and electron spectral index p as well (Zhang et al. 2007; Wang et al. 2015). As a result, the derived GRB radiative efficiency has been subject to large uncertainties, ranging from below 10% to more than 90% (Zhang et al. 2007; Wang et al. 2015; Beniamini et al. 2015; Li et al. 2018).

The bulk Lorentz factor Γ of a GRB, which is related to the kinetic energy of the outflow, has been estimated using various methods. The maximum photon energy of prompt emission may be used to set a lower limit on Γ (e.g., Baring & Harding 1997; Lithwick & Sari 2001). However, a precise measurement cannot be made since the maximum energy also depends on emission radius, which is not well constrained
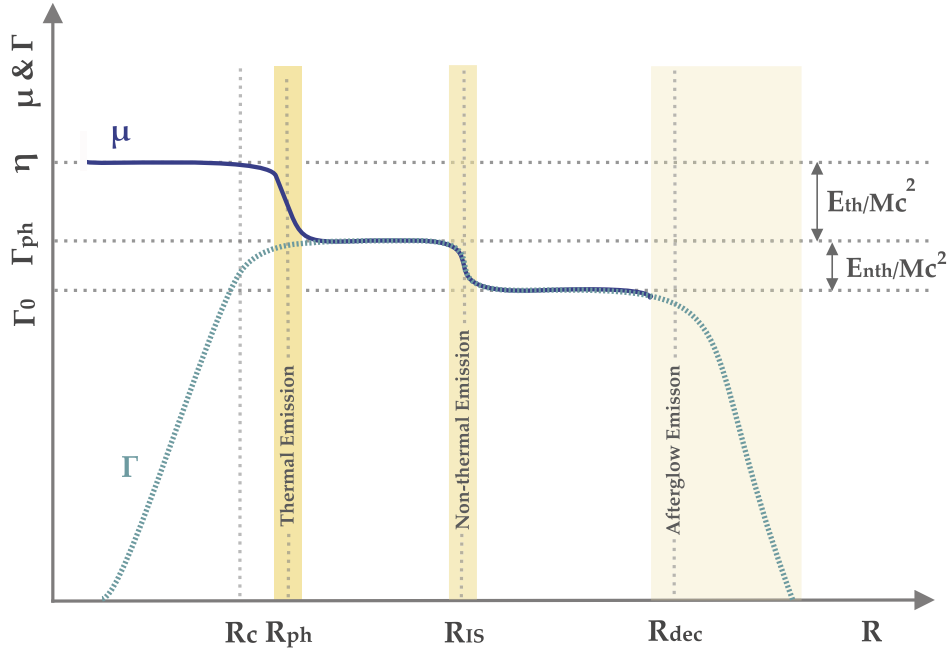

Figure 1. An indicative description of the evolution of μ and Γ in a GRB fireball. Both axes are in logarithmic scales. In reality, internal shocks may spread in a wide range of radii.

(Gupta & Zhang 2008).[6] Two other methods can give better estimates of Γ. The first makes use of the early afterglow lightcurve data. If a well-defined bump is identified in the early afterglow lightcurve, it can be interpreted as the fireball deceleration time. The Lorentz factor before deceleration (which we call Γ_0 in the rest of the paper) can be estimated (Rees & Mészáros 1992; Mészáros & Rees 1993; Sari & Piran 1999), which depends on E_k and the medium density parameter (i.e., n for the constant medium model and A_* for the wind model). Again E_k needs to be estimated from the afterglow data or from the prompt emission data assuming an efficiency parameter. Alternatively, if a strong thermal component is measured from the GRB prompt emission spectrum, one can estimate the Lorentz factor at the photosphere radius (which we call Γ_{ph} in the rest of the paper) based on the standard fireball photosphere model (Pe'er et al. 2007). The GRB efficiency again needs to be assumed in order to perform the estimate. This simple method relies on the assumption of a matter-dominated jet composition. For more general hybrid-jet models, more complicated diagnoses are needed (Gao & Zhang 2015). Observationally, the Γ values derived from the afterglow deceleration method (Liang et al. 2010; Lü et al. 2012; Ghirlanda et al. 2018) is somewhat smaller than those derived using other methods (Racusin et al. 2009; Pe'er et al. 2015).

In this paper, we propose a new method to diagnose fireball parameters by combining the deceleration and photosphere methods. We show that with adequate observations, one can measure several fireball parameters related to the energy budgets. In particular, the efficiency parameter that has to be assumed in previous methods can be directly measured. The

method is introduced in Section 2. Some examples are presented in Section 3. The results are summarized in Section 4 with some discussion.

2. The Method

2.1. Energy Budget Decomposition

Very generally, the effective energy per baryon at the central engine can be defined by the parameter

$$\mu_0 \equiv \eta(1 + \sigma_0) \simeq \eta, \qquad (2)$$

where $\eta \equiv (n_{w,0}m_pc^2 + e_0 + p_0)/(n_{w,0}m_pc^2) = 1 + \hat{\gamma}e_0/(n_{w,0}m_pc^2)$, σ_0, $n_{w,0}$, e_0, and p_0 are the dimensionless specific enthalpy density (also called dimensionless entropy in the literature, e.g., Mészáros & Rees 2000), the magnetization parameter, number density, internal energy density, and pressure of the fireball wind at the central engine, respectively, and $\hat{\gamma} = 4/3$ is the adiabatic index for a relativistic fireball with $\eta \gg 1$. The last approximation in Equation (2) applies to a pure fireball with $\sigma_0 \simeq 0$, which is the regime discussed in this paper. During the subsequent evolution of the fireball, the effective energy per baryon can be defined by

$$\mu = \Gamma(R)\Theta(R), \qquad (3)$$

which is conserved unless radiation is leaked out from the fireball. Here $\Gamma(R)$ is the bulk Lorentz factor of the fireball as a function of the radius R from the central engine, and $\Theta(R) = 1 + \hat{\gamma}e(R)/[n_w(R)m_pc^2]$ is the dimensionless specific enthalpy density as a function of R. Figure 1 shows a cartoon picture of the evolution of μ (only up to the deceleration radius R_{dec}, beyond which it is no longer of interest) and Γ (throughout the acceleration, coasting, dissipation, and deceleration phases) as a function of R. One can see that before the deceleration radius, the μ parameter undergoes two significant

---
[6] Most work made use of the variability timescale to estimate the emission radius, but the estimate is only relevant for the internal shock model but does not apply to photosphere (e.g., Rees & Mészáros 2005) or magnetic dissipation (e.g., Mészáros & Rees 1997; Lyutikov & Blandford 2003; Zhang & Yan 2011) models.

drops. The first drop occurs at the photosphere radius where a significant amount of thermal energy is released as thermal photons. The μ value drops from η to Γ_{ph}. The second drop occurs at the internal shock radii where significant dissipation of the fireball kinetic energy occurs and additional photon energy (in the form of synchrotron radiation) is released from the fireball. The μ value drops from Γ_{ph} to Γ_0 before entering the deceleration phase.

For a fireball with an isotropic-equivalent total mass M, the initial, total energy of the fireball is

$$E_{tot} = \eta M c^2. \tag{4}$$

The energy emitted in thermal emission from the photosphere is

$$E_{th} = (\eta - \Gamma_{ph}) M c^2; \tag{5}$$

that emitted in nonthermal emission from internal shocks is

$$E_{nth} = (\Gamma_{ph} - \Gamma_0) M c^2; \tag{6}$$

and the total emitted energy is

$$E_\gamma = E_{th} + E_{nth} = (\eta - \Gamma_0) M c^2. \tag{7}$$

The kinetic energy left in the afterglow is

$$E_k = \Gamma_0 M c^2, \tag{8}$$

so the radiative efficiency (1) becomes

$$\eta_\gamma = \frac{\eta - \Gamma_0}{\eta}. \tag{9}$$

2.2. Prompt Emission Constraint

The fireball initially undergoes a rapid acceleration with $\Gamma \propto R$ due to the internal pressure of the fireball (Mészáros et al. 1993; Piran et al. 1993; Kobayashi et al. 1999). It coasts at a radius $R_c = \Gamma_c R_0$ at which acceleration essentially stops, where R_0 is the initial radius of the fireball, and Γ_c is the coasting Lorentz factor. In order to constrain Lorentz factor using the thermal emission information, the photosphere radius R_{ph} needs to be greater than R_c. In previous treatments (e.g., Mészáros & Rees 2000; Pe'er et al. 2007), Γ_c is approximated as η (for the regime we are interested in, i.e., $R_{ph} > R_c$). We note that the fireball Lorentz factor never fully achieves η, as the fireball contains a significant amount of internal energy, especially below R_{ph}. Numerical simulations (Kobayashi et al. 1999) showed that acceleration does not stop abruptly, but undergoes a smooth transition around R_c (see also Figure 1). As a result, a more reasonable approximation would be that the Lorentz factor of the fireball only reaches Γ_{ph} at R_{ph}, when the fireball becomes transparent. After discharging photons at R_{ph}, the internal energy becomes negligibly small, so μ becomes close to the bulk Lorentz factor $\Gamma = \Gamma_{ph}$, which coasts with this value afterwards. As a result, one may approximately treat the fireball dynamics as having an effective coasting Lorentz factor $\Gamma_c \sim \Gamma_{ph}$ and an effective coasting radius at $R_c \sim \Gamma_{ph} R_0$.

For $R_{ph} > R_c$ (i.e., $\Gamma_{ph} < \Gamma_{ph,*}$), the observer-frame (without the $(1 + z)$ correction from cosmological expansion) luminosity and temperature of the photosphere emission can be estimated as (Mészáros & Rees 2000, but with η replaced by Γ_{ph} and $L_{w,0}$ replaced by $L_{w,ph}$)

$$\frac{L_{ph}}{L_{w,ph}} \simeq \left(\frac{\Gamma_{ph}}{\Gamma_{ph,*}}\right)^{8/3} = \left(\frac{R_{ph}}{R_c}\right)^{-2/3} = \left(\frac{r_{ph}}{R_0}\right)^{-2/3}, \tag{10}$$

$$\frac{T_{ph}}{T_0} \simeq \left(\frac{\Gamma_{ph}}{\Gamma_{ph,*}}\right)^{8/3} = \left(\frac{R_{ph}}{R_c}\right)^{-2/3} = \left(\frac{r_{ph}}{R_0}\right)^{-2/3}, \tag{11}$$

where L_{ph} is the photosphere emission luminosity (i.e., the luminosity of the thermal spectral component), $L_{w,ph}$ is the kinetic luminosity of the wind at the photosphere, which is related to the total wind luminosity through $L_{w,ph} = L_{w,0}(\Gamma_{ph}/\eta)$,

$$r_{ph} = \frac{R_{ph}}{\Gamma_{ph}} \tag{12}$$

is the radius of the projected photosphere area for a relativistically moving fireball,

$$\Gamma_{ph,*} = \left(\frac{L_{w,ph}\mathcal{Y}\sigma_T}{8\pi m_p c^3 R_0}\right)^{1/4} \simeq 870 \left(\frac{L_{w,ph,52}\mathcal{Y}}{R_{0,7}}\right)^{1/4} \tag{13}$$

is the critical Γ_{ph} above which R_{ph} becomes smaller than R_c so that the method discussed here no longer applies, and

$$T_0 \simeq \left(\frac{L_{w,0}}{4\pi R_0^2 \sigma_B}\right)^{1/4} \simeq 1.9 \times 10^{10} \, \text{K} \left(\frac{L_{w,0,52}}{R_{0,7}}\right)^{1/4} \tag{14}$$

is the initial temperature at the central engine. Here m_p is the proton mass, c is the speed of light, σ_T is the Thomson cross section, σ_B is the Stefan–Boltzmann constant, $\mathcal{Y}$ is the lepton-to-baryon number ratio, which equals unity for a pure hydrogen fireball but could be greater (for a pair-loaded fireball) or slightly smaller (for a neutron-rich fireball without pair loading) than unity. Both $L_{w,ph}$ and $L_{w,0}$ are normalized to 10^{52} erg s^{-1} (hereafter the convention $Q = 10^n Q_n$ is adopted in cgs units). Notice that in Equation (14) we have neglected a coefficient of order unity, which depends on the composition of the outflow at the jet base (Kumar & Zhang 2015). Other coefficients of the order unity are also neglected in our derivations below.

The observed flux of the photosphere blackbody[7] component is $F_{bb}^{ob} = (4\pi r_{ph}^2 \sigma_B T_{ph}^4)/(4\pi D_L^2)$. Using Equation (11) and noticing $L_{w,0} = 4\pi D_L^2 F_\gamma^{ob} \eta_\gamma^{-1}$ (F_γ^{ob} is the observed total gamma-ray flux), one can derive (Pe'er et al. 2007)

$$R_0 \simeq \frac{D_L}{(1 + z)^2} \eta_{th}^{3/2} \mathcal{R}, \tag{15}$$

where

$$\mathcal{R} \equiv \left(\frac{F_{bb}^{ob}}{\sigma_B T_{ob}^4}\right)^{1/2} \simeq \frac{r_{ph}}{D_L}(1 + z)^2, \tag{16}$$

$$\eta_{th} \equiv \frac{\eta_\gamma F_{bb}^{ob}}{F_\gamma^{ob}} = \frac{E_{th}}{E_{tot}}, \tag{17}$$

---

[7] The photosphere spectrum is not exactly a blackbody, but does not significantly deviate from it (Pe'er 2012; Deng & Zhang 2014).

and $T_{\rm ob} = T_{\rm ph}/(1+z)$ is the effective temperature of the observed thermal spectrum.

Making use of Equation (10) and noticing $L_{\rm w,ph} = 4\pi D_{\rm L}^2 F_\gamma^{\rm ob} f_\gamma^{-1}$, where

$$f_\gamma = \frac{L_\gamma}{L_{\rm w,ph}} = \frac{\eta - \Gamma_0}{\Gamma_{\rm ph}}, \tag{18}$$

one can further derive

$$\Gamma_{\rm ph} \simeq \left[(1+z)^2 D_{\rm L} \frac{\mathcal{Y}\sigma_{\rm T} F_\gamma^{\rm ob}}{2m_p c^3 \mathcal{R}} \frac{f_\gamma^{1/2}}{\eta_\gamma^{3/2}} \right]^{1/4}$$

$$= \left[(1+z)^2 D_{\rm L} \frac{\mathcal{Y}\sigma_{\rm T} F_\gamma^{\rm ob}}{2m_p c^3 \mathcal{R}} \frac{\eta^{3/2}}{(\eta - \Gamma_0)\Gamma_{\rm ph}^{1/2}} \right]^{1/4}. \tag{19}$$

One can see that the parameters η and Y in Equation (4) of Pe'er et al. (2007) are replaced by $\Gamma_{\rm ph}$ and $f_\gamma^{1/2}/\eta_\gamma^{3/2}$, respectively. In the second equation, Equation (18) has been used. Solving for $\Gamma_{\rm ph}$, one can further derive

$$\Gamma_{\rm ph} = \left[(1+z)^2 D_{\rm L} \frac{\mathcal{Y}\sigma_{\rm T} F_\gamma^{\rm ob}}{2m_p c^3 \mathcal{R}} \frac{\eta^{3/2}}{\eta - \Gamma_0} \right]^{2/9}. \tag{20}$$

2.3. Afterglow Constraint

For a constant density interstellar medium,[8] one can estimate Γ_0 using the observed deceleration time $t_{\rm dec}$. The deceleration radius can be estimated with $(4\pi/3)R_{\rm dec}^3 n m_p c^2 = E_k/(\hat\gamma \Gamma_0 \Gamma_{\rm dec})$, where $\Gamma_{\rm dec} = \Gamma_0/2$. This gives the deceleration radius $R_{\rm dec} = (3E_k/2\pi\hat\gamma\Gamma_0^2 n m_p c^2)^{1/3} \simeq (6.2 \times 10^{16}\,{\rm cm}) E_{k,52}^{1/3} \Gamma_{0,2}^{-2/3} n^{-1/3}$. The deceleration time in the observer frame can be calculated as $t_{\rm dec} = \int_0^{R_{\rm dec}} (1+z)/(2\Gamma(r)^2 c) dr \simeq 0.9(1+z) R_{\rm dec}/\Gamma_0^2 c$. Reversely solving it, one finally gets (Zhang 2018)

$$\Gamma_0 \simeq 0.9^{3/8} \left(\frac{3E_k(1+z)^3}{2\pi\hat\gamma n m_p c^5 t_{\rm dec}^3} \right)^{1/8}$$

$$\simeq 170 t_{\rm dec,2}^{-3/8} \left(\frac{1+z}{2} \right)^{3/8} \left(\frac{E_{k,52}}{n} \right)^{1/8}$$

$$= 170 t_{\rm dec,2}^{-3/8} \left(\frac{1+z}{2} \right)^{3/8} \left(\frac{E_{\gamma,52}}{n} \right)^{1/8} \left(\frac{\Gamma_0}{\eta - \Gamma_0} \right)^{1/8}. \tag{21}$$

2.4. Dissecting Fireball Energy Budget

The five unknown parameters that characterize a GRB fireball, i.e., η, $\Gamma_{\rm ph}$, Γ_0, η_γ, and M can be in principle solved with Equations (5), (6), (9), (20), and (21), using the observed quantities $E_{\rm th}$, $E_{\rm nth}$, E_γ, $F_\gamma^{\rm ob}$, $F_{\rm bb}^{\rm ob}$, $T_{\rm ob}$, $t_{\rm dec}$, and z. There are only two free parameters. One is $\mathcal{Y}$, which depends on the composition of the fireball (pairs, protons, and neutrons), but a reasonable

estimate is $\mathcal{Y} \sim 1$. The second parameter is the density parameter n, which may be further constrained via afterglow modeling (e.g., Panaitescu & Kumar 2001, 2002). Even if it is not constrained, the solutions only weakly depend on it. One may take a standard value $n = 1\,{\rm cm}^{-3}$ when solving the problem.

There is no analytical solution to the problem. One can numerically solve the problem using a root-finding algorithm. From Equations (5) or (6), one can solve

$$M = \frac{E_\gamma}{(\eta - \Gamma_0)c^2}, \tag{22}$$

$$\Gamma_{\rm ph} = \frac{\eta E_{\rm nth} + \Gamma_0 E_{\rm th}}{E_\gamma}. \tag{23}$$

From Equation (21), one can derive

$$\eta = 3.19 \left(\frac{\Gamma_0}{300} \right)^{-7} t_{\rm dec,2}^{-3} \left(\frac{1+z}{2} \right)^3 \left(\frac{E_{\gamma,52}}{n} \right) + \Gamma_0. \tag{24}$$

Inserting Equations (23) and (24) into Equation (20), Γ_0 can be then solved by assigning typical values for $\mathcal{Y}$ and n. Once Γ_0 is solved, η can be solved from Equation (24); $\Gamma_{\rm ph}$ and M can be solved from Equations (23) and (22), respectively, and η_γ can be solved from Equation (9).

3. Examples

In order to perform the diagnosis proposed in this paper, a GRB needs to satisfy the following three requirements:

1. The burst needs to have a matter-dominated composition with a distinct thermal spectral component. One may use the contrast between the thermal and nonthermal components to estimate the magnetization parameter σ_0 at the central engine based on the hybrid-jet diagnostic method proposed by Gao & Zhang (2015; see Li 2020 for a systematic analysis of the GRB data using the method). If σ_0 is close to 0, the burst would be a fireball.
2. The burst needs to have early afterglow data that show a distinct bump that is consistent with deceleration of a fireball in a constant density medium (e.g., Molinari et al. 2007; Liang et al. 2010).
3. The burst needs to have a measured redshift.

Few GRBs satisfy these constraints in the current database. We have gone over the currently detected GRBs from the archives, but could not find an ideal case with all three criteria satisfied. One GRB to which this method may be applied is GRB 190114C, which is studied elsewhere (Li et al. 2021).

Instead of performing case studies, in the following we perform calculations for some example cases and explore the dependence of the results on various parameters. For example, we consider a GRB at $z = 1$ with the following observed quantities: $E_{\rm th} = 10^{53}$ erg, $E_{\rm nth} = 5 \times 10^{52}$ erg, $F_\gamma^{\rm ob} = 10^{-5}$ erg s^{-1} cm^{-2}, $F_{\rm bb}^{\rm ob} = 6 \times 10^{-6}$ erg s^{-1}cm^{-2}, $T = 100$ keV, and $t_{\rm dec} = 20$ s. According to the formalism discussed in Section 2, the following fireball parameters can be derived: $\eta \simeq 695$, $\Gamma_{\rm ph} \simeq 554$, $\Gamma_0 \simeq 408$, $\eta_\gamma \simeq 30.4\%$, and $M \simeq 3.91 \times 10^{-4} M_\odot$.

In general, the results are mainly defined by three energy values (only two are independent), i.e., $E_{\rm th}$, $E_{\rm nth}$, and $E_\gamma = E_{\rm th} + E_{\rm nth}$. This is because given a GRB duration T_{90} and a redshift, the energy parameters ($E_{\rm th}$ and E_γ) can be

---

[8] We do not discuss the case of a wind medium (Dai & Lu 1998; Mészáros et al. 1998; Chevalier & Li 1999) in this paper. Afterglow observations suggest that the majority of GRBs, especially those with the clear deceleration signature, are consistent with having a constant density medium (Zhang et al. 2007; Liang et al. 2010).
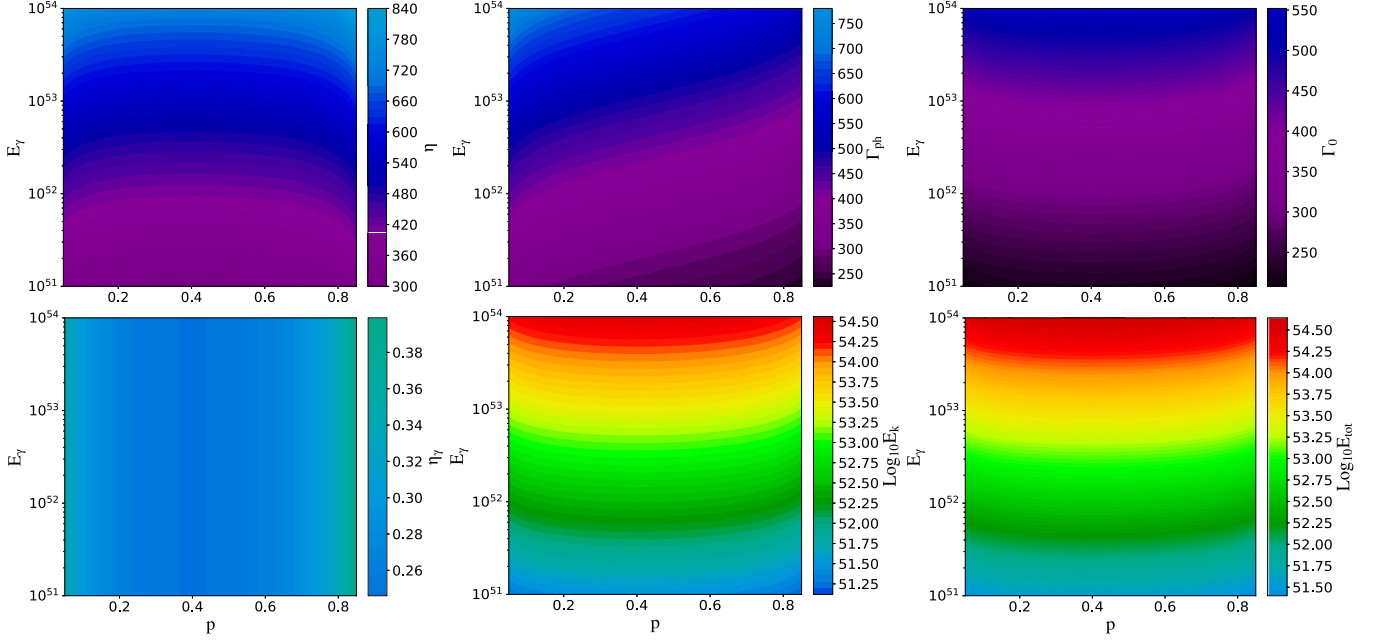
Figure 2. Contour plots of η, Γ_{ph}, Γ_0, η_γ, E_k, and E_{tot} in the E_γ–p plane.

Figure 3. Contour plots of η, Γ_{ph}, Γ_0, η_γ, E_k, and E_{tot} in the T_{ob}–p plane.

approximately translated to the flux parameters (F_{bb}^{ob} and F_γ^{ob}).[9] The observed temperature T_{ob} is also related to F_{bb}^{ob} through r_{ph}. Figure 2 shows the contours of η, Γ_{ph}, Γ_0, η_γ, E_k, and E_{tot} in the $E_\gamma - p$ plane, where $p \equiv E_{th}/E_\gamma$ is the thermal emission fraction. The following parameters, i.e., $z = 1$, $n = 1\,\mathrm{cm}^{-3}$,

$\mathcal{Y} = 1$, $T_{90} = 15\,\mathrm{s}$, $t_{dec} = 30\,\mathrm{s}$, and $T_{ob} = 60\,\mathrm{keV}$, are adopted in the calculations. One can see that the efficiency η_γ is reasonably high, between $\sim(25\%–40\%)$ for the parameter space explored. The derived parameters η, Γ_0, E_k, and E_{tot} are all insensitive to the thermal emission fraction p but positively scale with E_γ. Only the Γ_{ph} contour positively scales with both E_γ and p. Fixing E_γ, Γ_{ph} decreases as p increases. This is fully consistent with intuition.

Figure 3 shows the contours of η, Γ_{ph}, Γ_0, η_γ, E_k, and E_{tot} in the $T_{ob} - p$ plane. The following parameters, i.e., $z = 1$, $n = 1\,\mathrm{cm}^{-3}$, $\mathcal{Y} = 1$, $T_{90} = 15\,\mathrm{s}$, $t_{dec} = 30\,\mathrm{s}$, and $E_\gamma = 10^{52}\,\mathrm{erg}$, are adopted for the calculations. The patterns are more

---

[9] E_{th}, E_{nth}, and E_γ include the energies during the entire T_{90} of GRB prompt emission, whereas F_γ and F_{bb} are measured during the time intervals when the thermal emission presents. For typical GRBs, the prompt emission lightcurves show a rough fast-rise-exponential-decay behavior and the thermal emission usually appears at the most luminous peak region. For a theoretical estimation, we may calculate the flux at the peak region as $\sim$3 times the average flux during T_{90}, e.g., $F_\gamma^{ob} \sim 3(1 + z)E_\gamma/4\pi D_L^2 T_{90}$.

complicated, which is a result of the complicated relationship between $r_{\rm ph}$ and various energy budget parameters. The bottom-left panel again shows that usually the fireball radiative efficiency η_γ is high, i.e., $\sim(20\%–60\%)$ for reasonable values of the measured blackbody temperatures and a typical observed value for $T_{\rm ob}$. Given a measured $T_{\rm ob}$, η_γ increases as the thermal fraction p increases to high values. This is due to the significant increase of η in these cases.

4. Conclusions and Discussion

We have proposed a method to dissect the energy budget of a GRB fireball making use of the constraints derived from the thermal and nonthermal emission components in the prompt emission spectrum and the deceleration bump feature in the early afterglow lightcurve of a GRB. The key point is that the blackbody spectral component observed in the prompt emission phase and the early afterglow bump are measuring the bulk Lorentz factor of the fireball at two different stages, i.e., $\Gamma_{\rm ph}$ and Γ_0, respectively. Both are lower than the initial dimensionless specific enthalpy density of the fireball η. With observational quantities such as $E_{\rm th}$, $E_{\rm nth}$, E_γ, $F_\gamma^{\rm ob}$, $F_{\rm bb}^{\rm ob}$, $T_{\rm ob}$, $t_{\rm dec}$, and z, one can directly measure several crucial fireball parameters, including η, $\Gamma_{\rm ph}$, Γ_0, η_γ, and M.

In order to apply the method, the three criteria discussed in Section 3 are needed. The lack of GRBs satisfying all three criteria is the combination of the rareness of fireballs and some observational selection effects. For example, the GRBs with well-studied prompt emission spectra were usually detected by Fermi, whereas those with early afterglow and redshift measurements were usually detected by Swift. On the other hand, bursts that can satisfy all three constraints may be regularly discovered by the upcoming Chinese-French GRB detector SVOM (Wei et al. 2016), which has the capability of obtaining both broadband prompt emission spectra (using ECLAIRS and GRM) and early optical afterglow lightcurves (using VT). Many of these bursts will have redshift measurements with the detection of early afterglows. The diagnosis proposed in this paper can be routinely applied to those bursts.

There are some caveats when applying the method proposed here. First, we have applied the standard fireball photosphere-internal-shock model (Rees & Mészáros 1994; Mészáros & Rees 2000; Daigne & Mochkovitch 2002) that invokes two distinct emission sites. Some models interpret both thermal and nonthermal emissions as arising from the photosphere region (e.g., Vurm et al. 2011; Veres et al. 2012). Our method does not apply to those models. Second, if the central engine carries significant magnetization ($\sigma_0 \gg 1$), which seems to be the case for most GRBs (Zhang 2018), the simple method proposed here does not apply. More work is needed to extend this analysis to the case of hybrid jets following the approach of Gao & Zhang (2015). Finally, there is another channel to leak energy from the fireball, which is neutrino emission due to hadronic interactions of high-energy protons accelerated from shocks. This channel may be important for hadronic GRB models under extreme conditions (e.g., Asano & Mészáros 2011), but would not be important for the standard fireball model. The nondetection of neutrinos from GRBs (Aartsen et al. 2017) suggests that the nonthermal GRB emission region is likely far from the central engine (He et al. 2012; Zhang & Kumar 2013), where the hadronic interaction optical depth is low. This is also consistent with the assumption that neutrino energy loss channel is unimportant.

ORCID iDs

Bing Zhang ⓘ https://orcid.org/0000-0002-9725-2524
Liang Li ⓘ https://orcid.org/0000-0002-1343-3089

References

Aartsen, M., Ackermann, M., Adams, J., et al. 2017, ApJ, 843, 112
Abdo, A. A., Ackermann, M., Ajello, M., et al. 2009a, ApJL, 706, L138
Abdo, A. A., Ackermann, M., Arimoto, M., et al. 2009b, Sci, 323, 1688
Asano, K., & Mészáros, P. 2011, ApJ, 739, 103
Axelsson, M., Baldini, L., Barbiellini, G., et al. 2012, ApJL, 757, L31
Baring, M. G., & Harding, A. K. 1997, ApJ, 491, 663
Beniamini, P., & Giannios, D. 2017, MNRAS, 468, 3202
Beniamini, P., Nava, L., Duran, R. B., & Piran, T. 2015, MNRAS, 454, 1073
Burgess, J. M., Bégué, D., Greiner, J., et al. 2020, NatAs, 4, 174
Chevalier, R. A., & Li, Z.-Y. 1999, ApJL, 520, L29
Dai, Z. G., & Lu, T. 1998, MNRAS, 298, 87
Daigne, F., & Mochkovitch, R. 2002, MNRAS, 336, 1271
Deng, W., & Zhang, B. 2014, ApJ, 785, 112
Freedman, D. L., & Waxman, E. 2001, ApJ, 547, 922
Gao, H., & Zhang, B. 2015, ApJ, 801, 103
Ghirlanda, G., Nappo, F., Ghisellini, G., et al. 2018, A&A, 609, A112
Guiriec, S., Connaughton, V., Briggs, M. S., et al. 2011, ApJL, 727, L33
Guiriec, S., Kouveliotou, C., Daigne, F., et al. 2015, ApJ, 807, 148
Gupta, N., & Zhang, B. 2008, MNRAS, 384, L11
He, H.-N., Liu, R.-Y., Wang, X.-Y., et al. 2012, ApJ, 752, 29
Kobayashi, S., Piran, T., & Sari, R. 1999, ApJ, 513, 669
Kumar, P., & Zhang, B. 2015, PhR, 561, 1
Li, L. 2019a, ApJS, 242, 16
Li, L. 2019b, ApJS, 245, 7
Li, L. 2020, ApJ, 894, 100
Li, L., Wang, Y., & Ryde, F. 2021, NatAs, submitted
Li, L., Wu, X.-F., Lei, W.-H., et al. 2018, ApJS, 236, 26
Liang, E.-W., Yi, S.-X., Zhang, J., et al. 2010, ApJ, 725, 2209
Lithwick, Y., & Sari, R. 2001, ApJ, 555, 540
Lloyd-Ronning, N. M., & Zhang, B. 2004, ApJ, 613, 477
Lü, J., Zou, Y.-C., Lei, W.-H., et al. 2012, ApJ, 751, 49
Lyutikov, M., & Blandford, R. 2003, arXiv:astro-ph/0312347
Mészáros, P., Laguna, P., & Rees, M. J. 1993, ApJ, 415, 181
Mészáros, P., & Rees, M. J. 1993, ApJ, 405, 278
Mészáros, P., & Rees, M. J. 1997, ApJL, 482, L29
Mészáros, P., & Rees, M. J. 2000, ApJ, 530, 292
Mészáros, P., Rees, M. J., & Wijers, R. A. M. J. 1998, ApJ, 499, 301
Metzger, B. D., Giannios, D., Thompson, T. A., Bucciantini, N., & Quataert, E. 2011, MNRAS, 413, 2031
Molinari, E., Vergani, S. D., Malesani, D., et al. 2007, A&A, 469, L13
Oganesyan, G., Nava, L., Ghirlanda, G., & Celotti, A. 2017, ApJ, 846, 137
Panaitescu, A., & Kumar, P. 2001, ApJL, 560, L49
Panaitescu, A., & Kumar, P. 2002, ApJ, 571, 779
Pe'er, A. 2012, ApJL, 752, L8
Pe'er, A. 2015, AdAst, 2015, 907321
Pe'er, A., Barlow, H., O'Mahony, S., et al. 2015, ApJ, 813, 127
Pe'er, A., Ryde, F., Wijers, R. A. M. J., Mészáros, P., & Rees, M. J. 2007, ApJL, 664, L1
Pe'er, A., Zhang, B.-B., Ryde, F., et al. 2012, MNRAS, 420, 468
Piran, T., Shemi, A., & Narayan, R. 1993, MNRAS, 263, 861
Racusin, J. L., Liang, E. W., Burrows, D. N., et al. 2009, ApJ, 698, 43
Ravasio, M. E., Ghirlanda, G., Nava, L., & Ghisellini, G. 2019, A&A, 625, A60
Rees, M. J., & Mészáros, P. 1992, MNRAS, 258, 41P
Rees, M. J., & Mészáros, P. 1994, ApJL, 430, L93
Rees, M. J., & Mészáros, P. 2005, ApJ, 628, 847
Ryde, F. 2005, ApJL, 625, L95
Ryde, F., Axelsson, M., Zhang, B. B., et al. 2010, ApJL, 709, L172
Ryde, F., & Pe'er, A. 2009, ApJ, 702, 1211
Sari, R., & Piran, T. 1999, ApJL, 517, L109
Veres, P., Zhang, B.-B., & Mészáros, P. 2012, ApJL, 761, L18
Vurm, I., Beloborodov, A. M., & Poutanen, J. 2011, ApJ, 738, 77
Wang, X.-G., Zhang, B., Liang, E.-W., et al. 2015, ApJS, 219, 9
Wei, J., Cordier, B., Antier, S., et al. 2016, arXiv:1610.06892

Zhang, B. 2018, The Physics of Gamma-Ray Bursts (Cambridge: Cambridge Univ. Press)
Zhang, B., & Kumar, P. 2013, PhRvL, 110, 121101
Zhang, B., Liang, E., Page, K. L., et al. 2007, ApJ, 655, 989
Zhang, B., & Pe'er, A. 2009, ApJL, 700, L65
Zhang, B., & Yan, H. 2011, ApJ, 726, 90
Zhang, B.-B., Uhm, Z. L., Connaughton, V., Briggs, M. S., & Zhang, B. 2016, ApJ, 816, 72
Zhang, B.-B., Zhang, B., Castro-Tirado, A. J., et al. 2018, NatAs, 2, 69
Zhang, B.-B., Zhang, B., Liang, E.-W., et al. 2011, ApJ, 730, 141

Testing the High-latitude Curvature Effect of Gamma-Ray Bursts with Fermi Data: Evidence of Bulk Acceleration in Prompt Emission

Liang Li[1,2,3] and Bing Zhang[4]

[1] ICRANet, Piazza della Repubblica 10, I-65122 Pescara, Italy; liang.li@icranet.org
[2] INAF—Osservatorio Astronomico d'Abruzzo, Via M. Maggini snc, I-64100, Teramo, Italy
[3] Dip. di Fisica and ICRA, Sapienza Universita di Roma, Piazzale Aldo Moro 5, I-00185 Rome, Italy
[4] Department of Physics and Astronomy, University of Nevada, Las Vegas, NV 89154, USA; zhang@physics.unlv.edu

Abstract

When a gamma-ray burst (GRB) emitter stops emission abruptly, the observer receives rapidly fading emission from high latitudes with respect to the line of sight, known as the "curvature effect." Identifying such emission from GRB prompt-emission lightcurves would constrain the radius of prompt emission from the central engine and the composition of GRB jets. We perform a dedicated search of high-latitude emission (HLE) through spectral and temporal analyses of a sample of single-pulse bursts detected by the Gamma-ray Burst Monitor on board the Fermi satellite. We identify HLE from a subsample of bursts and constrain the emission radius to be $R_{\mathrm{GRB}} \sim (10^{15}$–$10^{16})$ cm from the central engine. Some bursts have the HLE decay faster than predicted by a constant Lorentz factor jet, suggesting that the emission region is undergoing acceleration during prompt emission. This supports the Poynting-flux-dominated jet composition for these bursts. The conclusion is consistent with previous results drawn from spectral-lag modeling of prompt emission and HLE analysis of X-ray flares.

Unified Astronomy Thesaurus concepts: Gamma-ray bursts (629); Relativistic jets (1390); Astronomy data analysis (1858)

1. Introduction

Gamma-ray bursts (GRBs) are the most luminous explosions in the universe. While it is well established that the γ-ray emission originates from an internal site in a relativistic jet beaming toward Earth, the composition of the jet as well as the origin of γ-rays (energy-dissipation mechanism and radiation mechanism) are subject to intense debate (Zhang 2018). The simplest model is the "fireball" model, which invokes a thermally accelerated, matter-dominated ejecta (Goodman 1986; Paczynski 1986). Within this framework, the outflow initially undergoes a rapid acceleration phase as the thermal energy of the fireball is quickly converted into the kinetic energy of the baryons at the coasting radius $\sim \Gamma$ $(ct_{\mathrm{pulse}}) = 3 \times 10^{12} \, \mathrm{cm} \Gamma_2 t_{\mathrm{pulse}}$ (Shemi & Piran 1990; Meszaros et al. 1993; Piran et al. 1993; Kobayashi et al. 1999), where Γ is the Lorentz factor, and t_{pulse} is the duration of the GRB pulse in the source frame (the observed duration divided by the $(1 + z)$ time dilation factor, where z is the source redshift), and the convention $Q = 10^n Q_n$ is adopted in cgs units throughout the text. Within this model, the γ-ray emission is released at the internal shock radius (Rees & Meszaros 1994) and the photospheric radius (Mészáros & Rees 2000); both are typically smaller than $\sim 10^{14}$ cm from the central engine. The fireball is decelerated at $\sim 10^{17}$ cm by a pair of external shocks (Rees & Meszaros 1992; Meszaros & Rees 1993).

An alternative scenario involves a Poynting-flux-dominated outflow to interpret GRBs. Within this model, the outflow initially has a magnetization parameter $\sigma_0 \gg 1$ (defined as the ratio between the Poynting flux and the plasma matter flux). The jet is accelerated gradually as the Poynting flux energy is converted to kinetic energy (e.g., Granot et al. 2011). Since the majority of energy is not in the thermal form initially, the photosphere emission is suppressed (Daigne & Mochkovitch 2002; Zhang & Pe'er 2009).[5] If the jet composition is still Poynting-flux dominated ($\sigma > 1$) at the traditional internal shock radius, the eventual energy-dissipation site would be at the location for internal collision-induced magnetic reconnection and turbulence (ICMART), which is typically beyond 10^{15} cm from the central engine (Zhang & Yan 2011). In reality, the jet composition may differ among different GRBs. Most likely the jet composition could be hybrid (Gao & Zhang 2015; Li 2020), characterized by a relativistic outflow with a hot fireball component (defined by the dimensionless enthalpy η) and a cold Poynting-flux component (defined by magnetization σ_0 at the central engine). Indeed, observations show that GRB composition seems diverse. Whereas some GRBs indeed show the signature properties of a fireball with a dominant photospheric thermal spectral component (Abdo et al. 2009; Ryde et al. 2010; Pe'Er et al. 2012; Li 2019a), some others show evidence of a Poynting-flux-dominated flow (Abdo et al. 2009; Zhang & Pe'er 2009; Zhang et al. 2016, 2018). The nondetection of high-energy neutrinos from GRBs disfavors the possibility that the majority of GRBs are matter dominated and is consistent with the hypothesis that most GRBs are Poynting-flux dominated (Zhang & Kumar 2013; Aartsen et al. 2017).

For a relativistic jet, the observed emission does not stop immediately, even if the emission ceases abruptly. This is because the emission from higher latitudes with respect to the line of sight arrives at the observer later because of the extra path that photons travel. This high-latitude emission (HLE) "curvature effect" (e.g., Fenimore et al. 1996;

---

[5] If subphotosphere magnetic dissipation is significant such that σ already drops to around unity at the photosphere, then the photosphere emission could be bright (e.g., Rees & Mészáros 2005; Giannios 2006; Pe'er et al. 2006; Beloborodov 2010; Levinson 2012; Vurm et al. 2013; Bégué & Pe'er 2015).

Ryde & Svensson 1999; Kumar & Panaitescu 2000; Zhang et al. 2006; Li et al. 2019, and references therein) has some testable predictions. In particular, if the emitter Lorentz factor remains constant during the decaying wing of a pulse, the temporal index $\hat{\alpha}$ and the spectral index $\hat{\beta}$ should satisfy a simple closure relation (Kumar & Panaitescu 2000):

$$\hat{\alpha} = 2 + \hat{\beta}, \qquad (1)$$

where the convention $F_{\nu,t} \propto t^{-\hat{\alpha}} \nu^{-\hat{\beta}}$ is adopted, and the zero time to define the power-law temporal decay index is set to the beginning of the pulse (Zhang et al. 2006). If the emission region is accelerating or decelerating, the decay slope $\hat{\alpha}$ is steeper or shallower than this predicted relation (Uhm & Zhang 2015).

Testing the curvature effect using the data can bring clues to the unknown jet composition and GRB mechanism from two aspects. First, if a temporal segment during the decay phase of a GRB pulse is identified as HLE, one can immediately place a constraint on the GRB emission radius at

$$R_{\rm GRB} \gtrsim \Gamma^2 ct_{\rm HLE} = (3 \times 10^{14}\ {\rm cm})\Gamma_2^2\left(\frac{t_{\rm HLE}}{1\ {\rm s}}\right), \qquad (2)$$

where $t_{\rm HLE}$ is the duration of the HLE in the source frame (again the observed HLE duration divided by $(1 + z)$). For seconds-duration pulses, a positive detection of HLE would immediately derive a GRB radius $R_{\rm GRB}$ much greater than the photosphere radius and the standard internal shock radius, lending support to Poynting-flux-dissipation models such as the ICMART model. Second, if GRB prompt emission is powered by dissipation of a Poynting flux, one would expect that about half of the dissipated magnetic energy goes to accelerate the ejecta while the other half powers the radiation. As a result, one would expect bulk acceleration in the emission region. An HLE curvature-effect test may help to find evidence of bulk acceleration and, hence, evidence of Poynting-flux dissipation in the GRB jet.

Some attempts have been made to test the curvature effect using the GRB prompt-emission data (e.g., Fenimore et al. 1996; Ryde & Svensson 1999), but no firm conclusion has been drawn. This is because the prompt emission often has overlapping pulses that smear the curvature effect (if any). Uhm & Zhang (2016a) tested the HLE curvature effect in two X-ray flares with clean and extended decay tails and found convincing evidence of bulk acceleration in these two GRBs. Jia et al. (2016) extended the analysis to a large sample of GRB X-ray flares and found that bulk acceleration seems ubiquitous. Modeling of prompt-emission spectral lags by Uhm & Zhang (2016b) also provided independent evidence of bulk acceleration in the GRB prompt-emission region. In all these analyses, the inferred GRB emission radius is $\sim(10^{15}–10^{16})$ cm from the central engine, again consistent with the physical picture of magnetic energy dissipation in a Poynting-flux-dominated flow.

Since its launch in 2008, Fermi-GBM has triggered more than 2000 GRBs and collected a large trove of prompt-emission data. Usually GRB prompt-emission lightcurves show a complicated and irregular temporal profile with overlapping pulses, suggesting an erratic central engine at work. Observationally, a small fraction of bursts only have one single pulse. Some other bursts may exhibit multiple pulses that are well

separated. These bursts form a unique sample for testing the HLE curvature effect from the prompt-emission data.

In this paper, we collect a sample of GRBs with single pulses and use the sample to test the curvature effect in the prompt-emission phase. The paper is organized as follows. In Section 2, we present our sample selection criteria and data reduction procedure. In Section 3, we present the detailed data analysis methods. Our results are presented in Section 4, and conclusions and discussions are summarized in Section 5.

2. Sample Selection and Data Reduction

Since our primary interest concerns individual emission episodes, we pay special attention to single pulses. Our sample selection allows many smaller spikes on top of the main pulse structures. This is because for the specific large-radius magnetic-dissipation models (e.g., the ICMART) we are testing, rapid variability is expected to be superposed on the broad pulses, due to the existence of minijets from locally dissipated regions (Zhang & Yan 2011; Zhang & Zhang 2014). We first visually inspected all of the time-tagged event (TTE) lightcurves to search for single-pulse bursts from the bursts detected by the Gamma-ray Burst Monitor (GBM; Meegan et al. 2009) on board the Fermi Gamma-ray Space Telescope during its first 10 years of mission. During this time period, GBM has triggered at least 2000 bursts. After our initial checking, about 300 well-defined single-pulse bursts are selected as our initial sample.

Our next step is to use the Bayesian blocks (BBlocks; Scargle et al. 2013) method to rebin the TTE lightcurve of each individual burst from our initial sample. The significance (S; Li & Ma 1983; Vianello 2018) for each individual time bin is calculated. In order to make the physical inferences trustworthy, high-quality data are required. In particular, the decay phase is our main interest. We therefore require at least five time bins with $S > 15$ measured during the decay phase. Our final sample is reduced to 24 bursts that satisfy this criterion. The sample is listed in Table 1, including 24 individual pulses from 23 long GRBs and one short GRB. Note that our sample selection is similar to that of Yu et al. (2019). However, compared with the sample in Yu et al. (2019), our sample is obtained with a higher selection criterion.

The prompt-emission properties of our sample are reported in Table 1. We collect duration (t_{90}, Column 1) and 10–1000 keV fluence (Column 2) from the online Fermi-GBM GRB repository.[6] We also list the detectors used, the source and background intervals used in the analysis, the number of time bins using the BBlocks method across the source interval, and the number of time bins with statistical significance $S > 15$ selected from the decay wing of the pulses. The detector in brackets is the brightest one, which is used for background and BBlock fits.

3. Methodology

3.1. Pulse Properties

To delineate the characteristics of the pulses, several functional forms have been proposed (e.g., Kocevski et al. 2003; Norris et al. 2005). In order to adequately characterize a pulse shape, our next step is to employ an asymmetric fast-rising and exponential-decay function, the so-called FRED

---

[6] https://heasarc.gsfc.nasa.gov/W3Browse/fermi/fermigbrst.html

Table 1
Properties of Prompt Emission of Our Sample

GRB	t_{90} (s)	Fluence (erg cm^{-2})	Detectors	ΔT_{src} (s)	$[\Delta T_{(\mathrm{bkg},1)}, \Delta T_{(\mathrm{bkg},2)}]$ (s)	N_{tot} (Number)	$N_{(S \geqslant 15)}$ (Number)
(1)	(2)	(3)	(4)	(5)	(6)	(7)	(8)
081224887	16.448 ± 1.159	$(3.76 \pm 0.02) \times 10^{-5}$	(n6)n7n9b1	$-1 \sim 20$	$[-20 \sim -10, 40 \sim 60]$	9	5
090620400	13.568 ± 0.724	$(1.33 \pm 0.01) \times 10^{-5}$	n6(n7)nab1	$-1 \sim 30$	$[-20 \sim -10, 40 \sim 60]$	11	5
090719063	11.392 ± 0.896	$(4.68 \pm 0.02) \times 10^{-5}$	n7(n8)b1	$-1 \sim 20$	$[-20 \sim -10, 40 \sim 60]$	13	7
090804940	5.568 ± 0.362	$(1.42 \pm 0.02) \times 10^{-5}$	n3n4(n5)b0	$-1 \sim 15$	$[-25 \sim -10, 40 \sim 60]$	11	6
100707032	81.793 ± 1.218	$(8.77 \pm 0.02) \times 10^{-5}$	n7(n8)b1	$-1 \sim 20$	$[-50 \sim -10, 80 \sim 100]$	16	10
110721200	21.822 ± 0.572	$(3.70 \pm 0.01) \times 10^{-5}$	(n6)n7n9b1	$-1 \sim 25$	$[-20 \sim 10, 40 \sim 60]$	10	8
110920546	160.771 ± 5.221	$(1.72 \pm 0.01) \times 10^{-4}$	(n0)n1n3b0	$-1 \sim 160$	$[-20 \sim -10, 180 \sim 190]$	11	8
120323507	0.384 ± 0.036	$(1.04 \pm 0.01) \times 10^{-5}$	n0(n3)b0	$-1 \sim 5$	$[-20 \sim -10, 10 \sim 20]$	12	7
120426090	2.688 ± 0.091	$(2.10 \pm 0.01) \times 10^{-5}$	(n2)nab1	$-1 \sim 10$	$[-20 \sim -10, 40 \sim 60]$	15	7
130305486	25.600 ± 1.557	$(4.65 \pm 0.01) \times 10^{-5}$	n6(n9)nab1	$-1 \sim 35$	$[50–70]$	11	6
130614997	9.280 ± 1.972	$(6.72 \pm 0.10) \times 10^{-6}$	(n0)n1n3b0	$-1 \sim 10$	$[-25 \sim -10, 20 \sim 45]$	8	5
131231198	31.232 ± 0.572	$(1.52 \pm 0.01) \times 10^{-4}$	n0(n3)n4b0	$0.064 \sim 60$	$[-50 \sim -10, 80 \sim 100]$	31	17
141028455	31.489 ± 2.429	$(3.48 \pm 0.01) \times 10^{-5}$	(n6)n7n9b1	$-1 \sim 40$	$[-30 \sim -10, 50 \sim 100]$	15	8
150213001	4.096 ± 0.091	$(2.88 \pm 0.01) \times 10^{-5}$	n6n7(n8)b1	$-1 \sim 10$	$[-25 \sim -10, 20–40]$	23	11
150314205	10.688 ± 0.143	$(8.16 \pm 0.01) \times 10^{-5}$	n1(n9)b1	$-1 \sim 15$	$[-25 \sim -10, 30 \sim 50]$	16	11
150510139	51.904 ± 0.384	$(9.86 \pm 0.01) \times 10^{-5}$	n0(n1)n5b0	$-1 \sim 50$	$[-25 \sim -10, 100 \sim 130]$	22	16
150902733	13.568 ± 0.362	$(8.32 \pm 0.01) \times 10^{-5}$	(n0)n1n3b0	$-1 \sim 25$	$[-25 \sim -10, 30 \sim 60]$	17	9
151021791	7.229 ± 0.602	$(1.23 \pm 0.01) \times 10^{-5}$	n9(na)b1	$-1 \sim 10$	$[-25 \sim -10, 30 \sim 50]$	9	5
160216801	7.677 ± 0.571	$(9.90 \pm 0.02) \times 10^{-6}$	(n9)nanbb1	$-1 \sim 15$	$[-20 \sim -10, 40 \sim 60]$	13	6
160530667	9.024 ± 3.584	$(9.19 \pm 0.01) \times 10^{-5}$	n1(n2)n5b0	$-1 \sim 25$	$[-40 \sim -10, 40 \sim 100]$	21	12
170114917	12.032 ± 1.305	$(1.82 \pm 0.01) \times 10^{-5}$	n1(n2)nab0	$-1 \sim 15$	$[-20 \sim 10, 80 \sim 100]$	11	7
170921168	39.361 ± 4.481	$(6.56 \pm 0.03) \times 10^{-5}$	(n1)n2n5b0	$-1 \sim 40$	$[-20 \sim -10, 40 \sim 60]$	8	6
171210493	143.107 ± 2.573	$(8.08 \pm 0.01) \times 10^{-5}$	n0(n1)n2b0	$-1 \sim 100$	$[-30 \sim -10, 210 \sim 240]$	13	9
180305393	13.056 ± 0.810	$(5.80 \pm 0.01) \times 10^{-5}$	n1(n2)nab0	$-1 \sim 20$	$[-20 \sim -10, 40 \sim 60]$	12	5

Note. A sample of 23 long GRBs and one short GRB including 24 individual pulses used in this study. Column (1) lists GRB name, Column (2) lists the corresponding duration, Column (3) lists the fluence at 10–1000 keV, Column (4) lists the detectors used, and Columns (5) and (6) list the source and background intervals used in the analysis. Columns (7) and (8) list the number of time bins using the BBlocks method across the source interval, and the number of time bins with statistical significance $S > 15$ selected from the decay wing of the pulses. The detector in brackets is the brightest one, used for background and BBlock fits.

model (Kocevski et al. 2003), to fit the entire lightcurve of that pulse (Figure A1). The peak time of the pulse can be then determined. The function reads as

$$I(t) = I_p \left(\frac{t + t_0}{t_p + t_0} \right)^r \left[\frac{d}{r + d} + \frac{r}{r + d} \left(\frac{t + t_0}{t_p + t_0} \right)^{r+1} \right]^{-\frac{r+d}{r+1}}, \quad (3)$$

where I_{p} is the amplitude, t_0 and t_p are the zero time and the peak time of the pulse, and r and d are the rise and decay timescale parameters, respectively. The model invokes five parameters (I_{p}, t_0, t_p, r, and d). We also considered a broken power-law (BKPL) fit to the pulse (Appendix). In Figure A2 we present a comparison of the fitting results between the FRED model and the BKPL model.

In Table 2, we list the best-fit parameters by adopting the FRED model for our sample. We list the time resolution of the count rate (counts/sec) lightcurve used for each burst (Column 2), the start and stop times of the selected pulses (Column 3), and the corresponding significance S (Column 4), as well as the best-fit parameters for the FRED model (Columns 5–9) including the normalization I_{p}; the zero time t_0, which we fixed to zero for each case; the peak time t_p of the pulse; and the rise r and decay d timescale parameters. The reduced chi-squared χ^2/dof (Column 10), the Akaike information criterion (AIC) statistic (Column 11), and the Bayesian information criterion (BIC) statistic (Column 12) are also presented. Note

that the goodness of fit (GOF) can be evaluated by calculating the reduced chi-squared statistic when the uncertainties in the data have been obtained. For a set of N data points $\{x_i, y_i\}$ with the estimated uncertainties $\{\sigma_i\}$ in the y_i values, one has $\chi^2 = \Sigma_{i=1}^{N} \frac{(y_i - \hat{y}_i)^2}{\sigma_i^2}$ and reduced $\chi_\nu^2 = \chi^2/\mathrm{dof}$, where dof $= (N - N_{\mathrm{varys}})$ is the degrees of freedom, N is the number of data points, and N_{varys} is the number of variables in the fit. The bad fits (large χ_ν^2 values) indicate that these pulses cannot be well delineated by the FRED model. In Table 2, AIC is calculated by $N \ln(\chi^2/N) + 2N_{\mathrm{varys}}$, and BIC by $N \ln(\chi^2/N) + \ln(N)N_{\mathrm{varys}}$.

3.2. Method to Measure Temporal Indices with a Simple Power-law Model

We use the energy flux lightcurves to measure the temporal indices. This is because the indices thus defined can be better compared with model predictions.

Our procedure to obtain the temporal indices includes the following steps:

1. Calculate the energy flux in each selected time bin. In order to obtain the energy flux, one needs to perform the spectral fits. For a given burst in our final sample, we therefore use the typical spectral model, called the Band function model (Band et al. 1993), to fit the spectral data of each time bin ($S > 15$) selected by the BBlocks method, and the best-fit parameters are evaluated by

Table 2
Results of Lightcurve (Pulses) Fitting of Our Sample with FRED Model

GRB (1)	Time Res (2)	$t_{start} \sim t_{stop}$ (3)	S (4)	I_p (5)	t_0 (6)	t_p (7)	r (8)	d (9)	χ^2/dof (10)	AIC (11)	BIC (12)
081224887	0.128-s	$0 \sim 10$	100.96	4413 ± 59	0	1.04 ± 0.06	0.18 ± 0.03	1.10 ± 0.24	33/73	−1241	−1232
090620400	0.128-s	$0 \sim 20$	46.40	2216 ± 45	0	3.19 ± 0.20	0.38 ± 0.05	1.45 ± 0.38	324/151	−2144	−2132
090719063	0.128-s	$0 \sim 25$	117.04	4629 ± 99	0	3.79 ± 0.16	0.56 ± 0.06	2.25 ± 0.43	774/190	−3137	−3124
090804940	0.128-s	$0 \sim 10$	97.93	4245 ± 84	0	1.88 ± 0.08	0.56 ± 0.06	2.27 ± 0.51	117/73	−1270	−1260
100707032	0.256-s	$0 \sim 30$	138.83	6407 ± 83	0	1.68 ± 0.05	0.86 ± 0.06	0.70 ± 0.02	66/112	−2118	−2107
110721200	0.128-s	$0 \sim 10$	112.92	3865 ± 68	0	1.28 ± 0.07	0.28 ± 0.03	2.62 ± 0.86	77/73	−1269	−1260
110920546	1.024-s	$0 \sim 150$	54.53	3172 ± 16	0	9.95 ± 0.32	0.28 ± 0.02	0.28 ± 0.01	80/141	−2242	−2230
120323507	0.032-s	$0 \sim 1$	177.24	63949 ± 2469	0	0.04 ± 0.002	0.52 ± 0.07	2.40 ± 0.42	191/26	−710	−704
120426090	0.064-s	$0 \sim 6$	145.48	8927 ± 182	0	1.04 ± 0.03	0.87 ± 0.07	3.65 ± 0.61	726/89	−1759	−1749
130305486	0.128-s	$0 \sim 20$	54.24	2901 ± 72	0	4.63 ± 0.23	0.81 ± 0.10	1.78 ± 0.41	684/151	−2233	−2221
130614997	0.128-s	$0 \sim 10$	59.80	3158 ± 57	0	0.22 ± 0.09	0.04 ± 0.02	1.89 ± 0.73	49/73	−1260	−1251
131231198	0.512-s	$0 \sim 60$	324.86	5324 ± 169	0	24.76 ± 0.57	3.34 ± 0.37	3.17 ± 0.50	1875/112	−1878	−1867
141028455	0.256-s	$0 \sim 50$	68.31	2085 ± 45	0	11.57 ± 0.57	0.77 ± 0.09	1.46 ± 0.30	784/190	−2613	−2600
150213001	0.064-s	$0 \sim 6$	295.19	17545 ± 570	0	2.08 ± 0.05	1.93 ± 0.19	10.00 ± 3.76	1692/89	−1805	−1795
150314205	0.128-s	$0 \sim 20$	177.73	7426 ± 133	0	1.85 ± 0.06	0.72 ± 0.06	1.41 ± 0.10	386/151	−2813	−2801
150510139	0.256-s	$0 \sim 50$	96.98	5796 ± 242	0	0.08 ± 0.01	0.57 ± 0.15	0.26 ± 0.01	296/190	−2904	−2891
150902733	0.128-s	$0 \sim 25$	137.63	4538 ± 121	0	8.44 ± 0.23	1.67 ± 0.16	3.72 ± 0.80	1794/190	−3069	−3056
151021791	0.128-s	$0 \sim 10$	63.15	3672 ± 83	0	0.80 ± 0.05	0.51 ± 0.07	0.82 ± 0.07	96/73	−1242	−1233
160216801	0.128-s	$0 \sim 15$	98.56	4676 ± 139	0	3.97 ± 0.14	1.37 ± 0.15	3.05 ± 0.63	1064/112	−1865	−1854
160530667	0.128-s	$0 \sim 20$	228.04	12390 ± 148	0	5.93 ± 0.04	3.83 ± 0.15	3.01 ± 0.12	1671/151	−3119	−3107
170114917	0.128-s	$0 \sim 10$	76.96	3269 ± 100	0	2.05 ± 0.14	0.75 ± 0.13	1.33 ± 0.33	261/73	−1131	−1122
170921168	0.256-s	$0 \sim 50$	68.47	2975 ± 41	0	4.35 ± 0.25	0.21 ± 0.03	1.11 ± 0.17	241/190	−2929	−2916
171210493	0.512-s	$0 \sim 100$	93.34	2798 ± 24	0	5.24 ± 0.17	0.61 ± 0.04	0.36 ± 0.01	58/190	−2973	−2960
180305393	0.128-s	$0 \sim 20$	95.60	3941 ± 82	0	4.65 ± 0.18	0.84 ± 0.09	2.04 ± 0.39	647/151	−2395	−2383

Note. Column (1) lists GRB name; Column (2) lists the time resolution used (Time Res) of the count-rate lightcurve of each burst; Column (3) lists the start and stop times of the pulses, in units of s; Column (4) lists the significance S of the entire pulse; Columns (5)–(9) list the best-fit parameters for the FRED model: normalization I_p, the zero time t_0, the peak time t_p of pulses, and the rise r and decay d timescale parameters; Column (10) lists the reduced χ^2/dof; Column (11) lists the AIC statistic; Column (12) lists the BIC statistic.

adopting the maximum-likelihood estimation (MLE) technique. The energy flux in such narrow time bins thus can be also calculated from the best fits, with a k-correction (1–10^4 keV) applied.[7]

2. Determine the entire time interval of the decay wing of the pulses. In order to determine the entire time interval of the decay wing of the pulses, one needs to determine the peak times of the pulses. The peak times of the pulses can be roughly obtained by using the FRED model to fit their pulse lightcurves as we discussed in Section 3.1. We find that the peak time determined by the FRED model for a good fraction of our sample can exactly match the true peaks of pulses (e.g., GRB 110920546). However, there are still some bursts whose peak times determined by the FRED model do not exactly describe the true peaks of the pulses.[8] Therefore, we use two selection criteria. First, for the cases where the peak times determined by the FRED model can exactly match the true peaks of pulses, we use these values (see the vertical yellow dashed lines in Figure 1). That is, as long as the peak time (t_p) of a certain pulse is obtained from the

FRED model fits, the time window of the decaying wing of the pulse can be determined as $t_p - t_{stop}$, where t_{stop} is the end time of a pulse. The stop time of the decay wing of a certain pulse can be precisely determined by the stop time of the last time bin that satisfies $S > 15$. Second, for the cases whose peak times determined by the FRED model do not exactly describe the true peaks of the pulses, we inspect the peak times from their lightcurves by eye (see the vertical black dashed lines in Figure 1). We define this phase as "Phase I" throughout the paper.

3. Determine the late-time interval of the decay wing of the pulses. Physically, the decay for prompt emission may not be fully controlled by the curvature effect. As shown in the theoretical modeling in Uhm & Zhang (2016b) and Uhm et al. (2018), the spectral lags are not caused by the curvature effect, and the temporal peaks of the pulses are often related to the time when the characteristic energy crosses the gamma-ray band as it decays with time. One possible test for this is to see whether the temporal peaks of the lightcurves for different GBM detectors that have different energy ranges occur at different times. We therefore compare the Na I (8 keV–1 MeV) and BGO (200 keV–40 MeV) lightcurves for each individual burst, as shown in Figure A3. We find that in many cases in our sample the peak times are clearly shifted between two different detectors (GRB 081224887, GRB 110721200, GRB 120426090, GRB 160216801, GRB 170921168, and GRB 171210493), indicating that the peaks of the pulses are

---

[7] Note that the energy flux obtained from different spectral models (Band and cutoff power law (CPL)) for the same time bin is very similar (Li 2019a; Li et al. 2020).

[8] This is because some pulse lightcurves do not show an "ideal" asymmetric fast-rising and exponential-decay shape (e.g., GRB 090719063). In these cases, usually the true peak time of the pulse is apparently later than that derived from the FRED model.
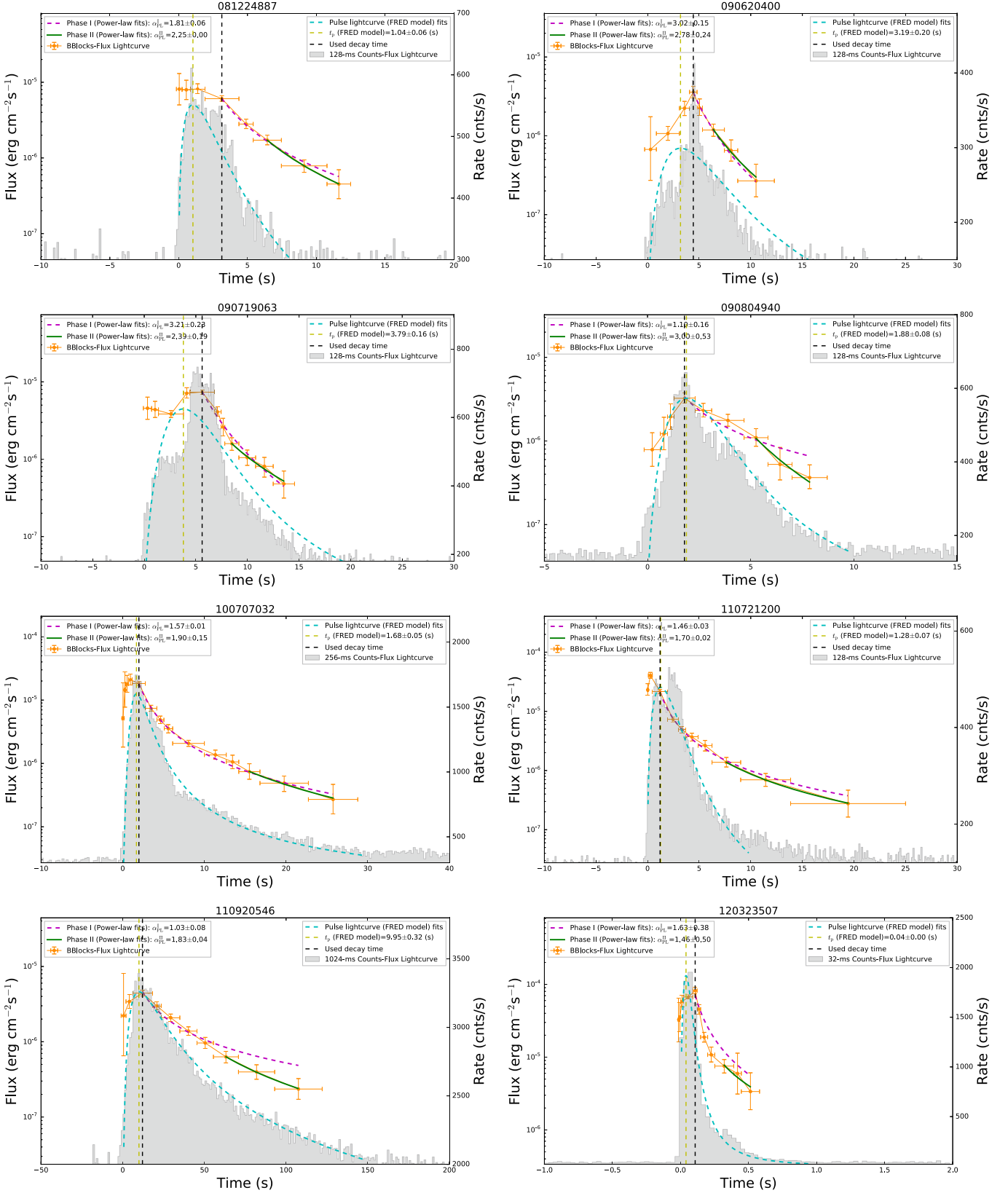
Figure 1. Lightcurves of the pulses in our sample. For each panel, the left axis marks the energy flux. Its evolution is marked in orange. The best fits for Phase I are indicated with the purple dashed lines, while those for Phase II are indicated with green solid lines. The right axis displays the count flux. The count lightcurves are in gray, overlaid with the best FRED model fits (cyan). The vertical yellow dashed line is the peak of the FRED fitting curve. The vertical black dashed line is the peak time identified by eye by inspecting the BBlock energy flux.
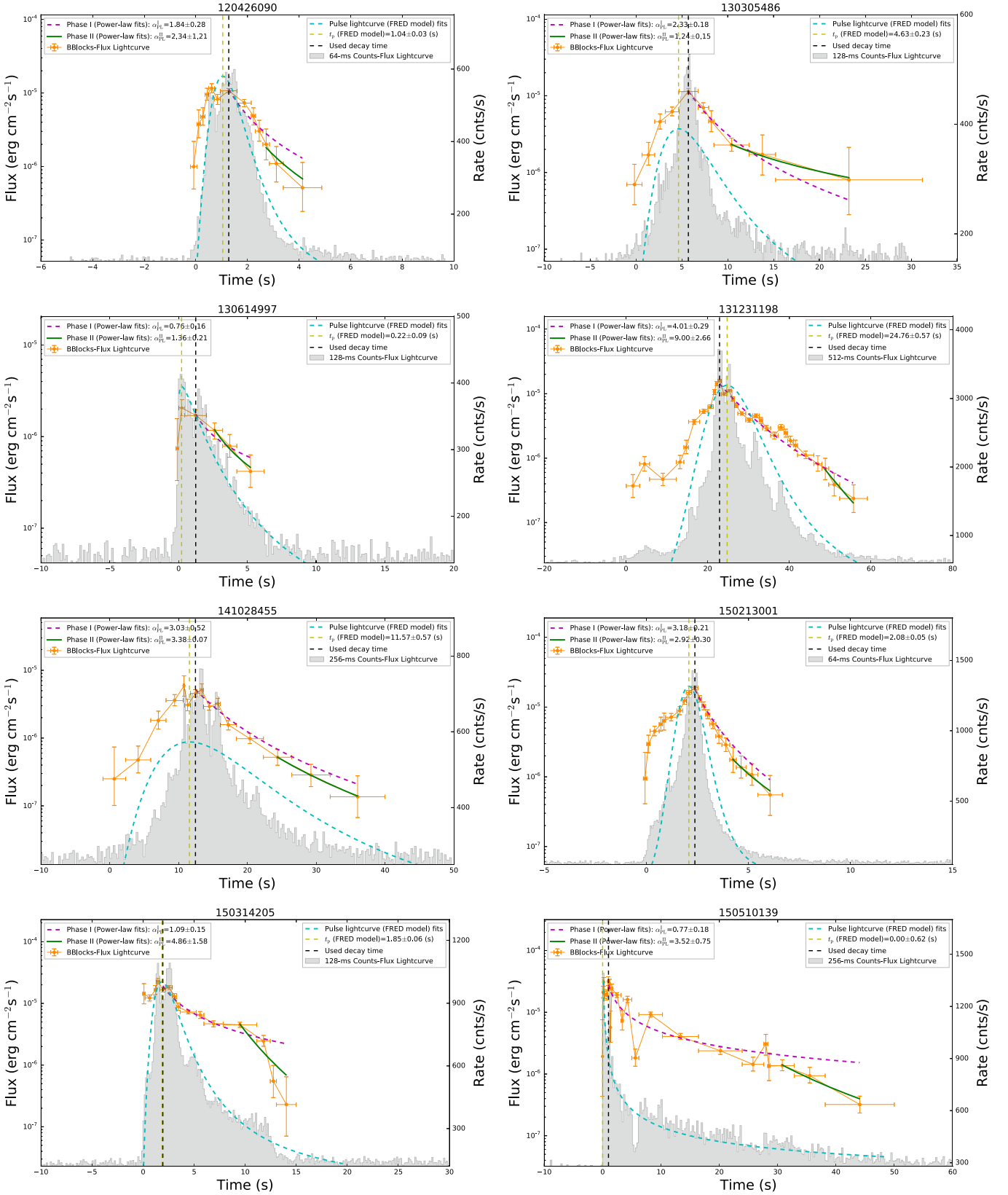
Figure 1. (Continued.)
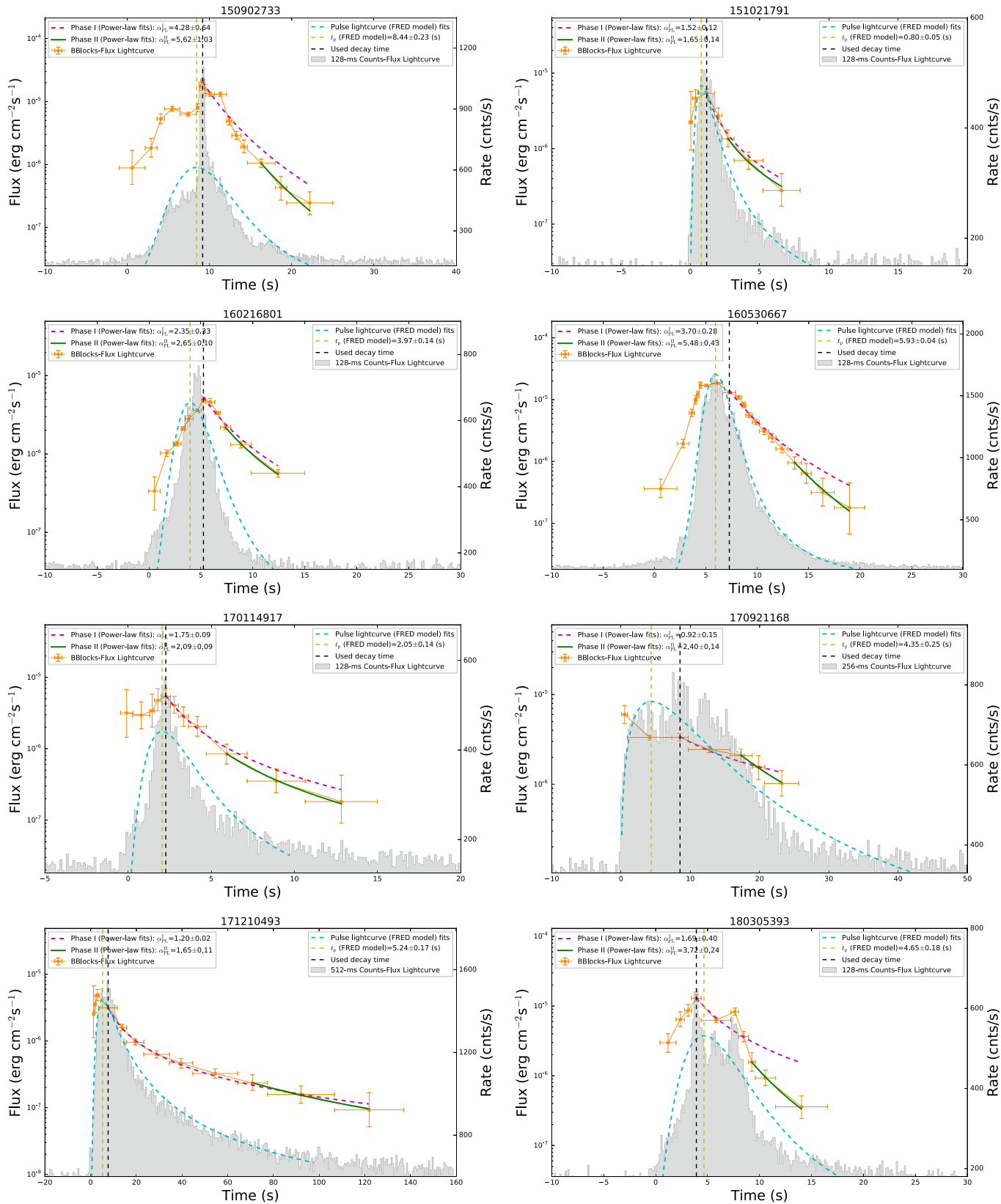
Figure 1. (Continued.)

indeed related to crossing of a spectral break.[9] For these bursts, the curvature effect does not kick in right after the peak. It may show up later in some bursts or would not show up at all in some others. When they show up, they may be related to the later part of the decay, usually not related to the decay right after the peak time. This brings an additional difficulty (other than the fact that the decay phase is usually short for prompt-emission pulses) in studying the curvature effect with the prompt-emission data. Besides testing the entire decay phase, we also adopt a more conservative approach by only testing the late-part time interval of the decay phase. Quantitatively, we only consider the last three time bins with $S > 15$. In practice, when a certain model is used to fit the data, the number of data points N should be greater than the number of variables N_{varys} of the model in order to get a good fitting result. The power-law model we use has two variables: amplitude and power-law index. This is why we include at least three data points in the fits. We define this phase as "Phase II" throughout the paper.

4. After the time intervals are clearly defined in the aforementioned two cases, we then perform two fits[10] (see Figure 1): one uses a power-law model to fit the entire decay phase and obtain a temporal decay index defined as $\hat{\alpha}_{\mathrm{PL}}^{\mathrm{I}}$; the other uses a power-law model to fit the later part of the decay to obtain a temporal decay index defined as $\hat{\alpha}_{\mathrm{PL}}^{\mathrm{II}}$. The power-law function we use to fit the lightcurves in order to obtain the $\hat{\alpha}$ indices is given by

$$F_t = F_{t,0} \, (t + t_0)^{-\hat{\alpha}}, \qquad (4)$$

where $F_{t,0}$ is the amplitude and $\hat{\alpha}$ is the temporal slope. The t_0 parameter is fixed in the beginning of the pulse ($t_0 = 0$) for all cases in this task because this is physically more relevant (Zhang et al. 2006; Uhm & Zhang 2015). Note that the peak time t_p does not enter the problem of defining $\hat{\alpha}$, so the inaccurate determination of t_p in the pulse lightcurve fitting does not noticeably affect our results. All these lightcurve fits are performed using a pure Python package called *lmfit* (Newville et al. 2016) by applying a nonlinear least-squares method using the Levenberg–Marquardt algorithm to fit a function to the data. Within *lmfit* fits, we can set parameters with a varied or fixed value in the fit, or place an upper or lower bound on the value. The weight of parameter error is also easily taken into account in the fits. In Figure A2, we also use GRB 131231198 as an example case to compare the fitting results obtained from different Python packages (*lmfit* and *scipy. optimize. curve_fit*).

The start and stop times of each selected time interval (Column 2), the corresponding S value (Column 3), the adopted zero time t_0 (Column 4), the best-fit parameters, include the normalization (Column 5), the power-law index (Column 6), and the AIC and BIC statistics (Column 7) are listed in Table 3.

For each burst, the entire decay phase is marked with (1) and the late-part decay phase is marked with (2).

3.3. Method to Measure Spectral Indices with a Simple Power-law Model

The GRB prompt-emission spectra are likely curved. However, since the simplest curvature-effect model (Equation (1)) applies to single power-law spectral models, we first apply a simple power-law fit to the time bins where the curvature effect is tested:

$$F_\nu = F_{\nu,0} \, \nu^{-\hat{\beta}}, \qquad (5)$$

where $F_{\nu,0}$ is the amplitude and $\hat{\beta}$ is the spectral index. The spectral analysis is performed using a pure Python package called the Multi-Mission Maximum Likelihood Framework (3ML; Vianello et al. 2015). The best model parameters can be evaluated using a given model to fit the data by applying either the MLE technique or the full Bayesian approach. Usually the best-fit results obtained from both methods are the same.[11]

We attempt two fits using the simple power-law model. One is to select the entire decay phase as the time interval to perform the spectral fit. The spectral index obtained this way is defined as $\hat{\beta}_{\mathrm{PL}}^{\mathrm{I}}$. The other is to select the later part of the decay as the time interval. The spectral index thus obtained is defined as $\hat{\beta}_{\mathrm{PL}}^{\mathrm{II}}$.

For each spectral fit, we employ a fully Bayesian approach to explore the best parameter space and to obtain the best-fit parameters. The best-fit parameters, including the normalization (Column 8) and the power-law index (Column 9), as well as the deviance information criterion (DIC; Moreno et al. 2013; Column 10) and p_{DIC} (Gelman et al. 2014; Column 10), are tabulated in Table 3.

3.4. Method to Measure Spectral Indices with a General Non-power-law Spectral Model

The aforementioned discussion invokes the simplest curvature-effect model, which assumes that the instantaneous spectrum of the prompt-emission tail is a simple power law. In this case, the predicted temporal decay and the spectral indices satisfy the simplest closure relation (Equation (1)). However, the instantaneous spectrum upon the cessation of prompt emission is likely not a simple power law, but it may follow a non-power-law model such as the Band function (e.g., Band et al. 1993). The characteristic frequency ν_c may not be far outside the GBM spectral window. In this case, testing the curvature effect would become more complicated.

We also test the curvature effect using the more complicated model as described in Zhang et al. (2009). We consider that for each time bin the photon flux can be described by a power-law spectrum with an exponential cutoff. This spectrum has one parameter less than the Band function and is found to be

---

[9] Several other bursts, for example, GRBs 090620400, 090804940, 110920546, 130614997, 150510139, and 170114917, are consistent with having the same peak times in different bands. The HLE may come into play right after the peak time.

[10] Note that we present the [log (Flux), time] plots in Figure 1 since the count lightcurve before the GBM trigger relates to negative time. However, the power-law fits invoke the [log (Flux), log(time)] plots, so we give an example to show the [log (Flux), log(time)] plots (see Figure A4).

[11] There are some unexpected cases. For example, the prior range for the Bayesian inference is not included in the real solution; namely, the prior settings are not very informative, or the analyzed time bin has a low significance (e.g., $S < 15$) or low peak energy (e.g., $E_p < 20$ keV). We refer to Li (2019a, 2019b, 2020) and Li et al. (2020) for the details of the data reduction procedure.

Table 3
Results of Lightcurve and Spectral Fitting of the Decaying Wing of the Pulses

GRB (1)	$t_{start} \sim t_{stop}$ (2)	S (3)	t_0 (4)	Lightcurve Power-law Fitting $F_{t,0}$ (5)	$\hat{\alpha}$ (6)	AIC/BIC (7)	Spectral Power-law Fitting $F_{\nu,0}$ (8)	$\hat{\beta}$ (9)	DIC/p_{DIC} (10)	Spectral Cutoff Power-law Fitting $N_{0,p}$ (11)	t_p (12)	$\hat{\Gamma}$ (13)	E_c (14)	DIC/p_{DIC} (15)
081224887(1)	1.896 ~ 12.502	88.10	0	$(2.62 \pm 0.06) \times 10^{-6}$	1.81 ± 0.06	$-159/-160$	$(1.62^{+0.04}_{-0.04}) \times 10^{1}$	$0.43^{+0.00}_{-0.00}$	8255/1.98	...	...	...	...	...
081224887(2)	5.424 ~ 12.502	47.56	0	$(8.16 \pm 0.01) \times 10^{-7}$	2.25 ± 0.00	$-121/-123$	$(1.43^{+0.06}_{-0.06}) \times 10^{1}$	$0.52^{+0.01}_{-0.01}$	5533/2.00	...	...	...	...	...
090620400(1)	4.076 ~ 12.289	47.80	0	$(2.46 \pm 0.05) \times 10^{-6}$	3.02 ± 0.15	$-161/-162$	$(1.27^{+0.05}_{-0.05}) \times 10^{1}$	$0.48^{+0.01}_{-0.01}$	6135/2.02	...	...	...	...	5116/2.83
090620400(2)	5.319 ~ 12.289	35.56	0	$(4.91 \pm 0.34) \times 10^{-7}$	2.78 ± 0.24	$-101/-103$	$(1.34^{+0.07}_{-0.07}) \times 10^{1}$	$0.55^{+0.01}_{-0.01}$	5301/1.99	$(5.43 \pm 0.34) \times 10^{-2}$	4.076	0.51 ± 0.04	117.3 ± 6.8	4827/2.57
090719063(1)	4.443 ~ 14.562	128.19	0	$(3.68 \pm 0.17) \times 10^{-6}$	3.21 ± 0.23	$-207/-207$	$(3.73^{+0.08}_{-0.08}) \times 10^{1}$	$0.53^{+0.00}_{-0.00}$	6860/1.98	$(5.25 \pm 0.53) \times 10^{-2}$	5.319	0.55 ± 0.06	87.9 ± 6.8	4292/2.95
090719063(2)	7.810 ~ 14.562	66.34	0	$(8.21 \pm 0.34) \times 10^{-7}$	2.39 ± 0.19	$-132/-133$	$(5.05^{+0.24}_{-0.24}) \times 10^{1}$	$0.77^{+0.01}_{-0.01}$	4085/1.98	$(8.73 \pm 0.25) \times 10^{-2}$	4.443	0.79 ± 0.02	182.8 ± 6.9	...
090804940(1)	1.279 ~ 8.705	98.14	0	$(1.09 \pm 0.14) \times 10^{-6}$	1.10 ± 0.16	$-179/-179$	$(7.29^{+0.19}_{-0.20}) \times 10^{1}$	$0.73^{+0.01}_{-0.01}$	7458/1.99	...	...	...	...	...
090804940(2)	4.678 ~ 8.705	40.50	0	$(5.12 \pm 0.58) \times 10^{-7}$	3.09 ± 0.53	$-97/-99$	$(7.21^{+0.48}_{-0.48}) \times 10^{1}$	$0.92^{+0.02}_{-0.02}$	4486/1.98	$(54.40 \pm 2.66) \times 10^{-2}$	4.678	0.72 ± 0.09	49.4 ± 4.0	4167/2.73
100707032(1)	1.631 ~ 28.780	131.02	0	$(4.27 \pm 0.05) \times 10^{-6}$	1.57 ± 0.01	$-320/-319$	$(2.42^{+0.04}_{-0.04}) \times 10^{1}$	$0.49^{+0.01}_{-0.01}$	9384/1.98	...	...	...	...	...
100707032(2)	14.210 ~ 28.78	47.30	0	$(4.01 \pm 0.17) \times 10^{-7}$	1.90 ± 0.15	$-105/-107$	$(3.23^{+0.23}_{-0.23}) \times 10^{1}$	$0.82^{+0.02}_{-0.02}$	4646/1.97	...	...	...	...	...
110721200(1)	0.470 ~ 25.000	76.49	0	$(2.72 \pm 0.09) \times 10^{-6}$	1.46 ± 0.03	$-243/-242$	$(1.06^{+0.02}_{-0.02}) \times 10^{1}$	$0.44^{+0.00}_{-0.00}$	7613/1.99	...	...	...	...	...
110721200(2)	6.252 ~ 25.000	28.610	0	$(4.07 \pm 0.05) \times 10^{-7}$	1.70 ± 0.02	$-112/-114$	$5.51^{+0.34}_{-0.34}$	$0.51^{+0.01}_{-0.01}$	6119/1.99	...	...	...	...	...
110920546(1)	9.966 ~ 122.091	59.68	0	$(2.75 \pm 0.12) \times 10^{-6}$	1.03 ± 0.08	$-241/-241$	$8.71^{+0.20}_{-0.20}$	$0.42^{+0.00}_{-0.00}$	12386/2.00	...	...	...	...	...
110920546(2)	55.534 ~ 122.091	34.09	0	$(3.39 \pm 0.04) \times 10^{-7}$	1.83 ± 0.04	$-113/-115$	$8.00^{+0.37}_{-0.37}$	$0.53^{+0.01}_{-0.01}$	9532/1.99	...	...	...	...	...
120323507(1)	0.094 ~ 0.581	130.70	0	$(15.32 \pm 1.63) \times 10^{-6}$	2.72 ± 0.19	$-176/-177$	$(8.57^{+0.33}_{-0.33}) \times 10^{2}$	$0.90^{+0.01}_{-0.01}$	1643/1.00	...	...	...	...	...
120323507(2)	0.252 ~ 0.581	66.33	0	$(5.31 \pm 0.57) \times 10^{-6}$	1.46 ± 0.50	$-83/-85$	$(6.13^{+0.13}_{-0.13}) \times 10^{2}$	$1.00^{+0.00}_{-0.00}$	1161/1.00	...	...	...	...	...
120426090(1)	1.044 ~ 4.882	125.87	0	$(4.94 \pm 0.53) \times 10^{-6}$	1.84 ± 0.28	$-190/-190$	$(1.41^{+0.04}_{-0.04}) \times 10^{2}$	$0.70^{+0.01}_{-0.01}$	5338/2.04	...	...	...	...	...
120426090(2)	2.600 ~ 4.882	35.11	0	$(6.14 \pm 1.14) \times 10^{-7}$	3.67 ± 0.66	$-94/-96$	$(1.25^{+0.05}_{-0.05}) \times 10^{2}$	$0.99^{+0.01}_{-0.01}$	2529/1.14	$(9.19 \pm 2.13) \times 10^{-2}$	2.600	1.06 ± 0.12	52.9 ± 7.4	2408/−0.66
130305486(1)	4.632 ~ 32.212	36.88	0	$(3.12 \pm 0.26) \times 10^{-6}$	2.33 ± 0.18	$-173/-173$	$4.02^{+0.12}_{-0.12}$	$0.30^{+0.01}_{-0.01}$	8462/1.99	$(1.53 \pm 0.04) \times 10^{-2}$	4.632	0.67 ± 0.03	545.7 ± 44.0	7110/2.92
130305486(2)	8.849 ~ 32.212	16.99	0	$(9.97 \pm 0.87) \times 10^{-7}$	1.24 ± 0.15	$-96/-98$	$2.20^{+0.15}_{-0.15}$	$0.33^{+0.01}_{-0.01}$	6953/2.00	...	...	...	...	...
130614997(1)	0.457 ~ 6.210	64.91	0	$(0.90 \pm 0.10) \times 10^{-6}$	0.76 ± 0.16	$-123/-124$	$(7.23^{+0.32}_{-0.32}) \times 10^{1}$	$0.85^{+0.01}_{-0.01}$	4828/2.00	...	...	...	...	...
130614997(2)	2.030 ~ 6.210	44.82	0	$(6.37 \pm 0.51) \times 10^{-7}$	1.36 ± 0.21	$-98/-100$	$(6.41^{+0.40}_{-0.40}) \times 10^{1}$	$0.89^{+0.02}_{-0.02}$	4217/1.97	...	...	...	...	...
131231198(1)	22.406 ~ 59.114	298.10	0	$(1.43 \pm 0.20) \times 10^{-6}$	4.01 ± 0.29	$-555/-553$	$(1.22^{+0.01}_{-0.01}) \times 10^{2}$	$0.75^{+0.00}_{-0.00}$	12654/2.01	$(7.56 \pm 0.11) \times 10^{-2}$	22.406	1.34 ± 0.01	239.8 ± 6.1	8716/2.97
131231198(2)	47.97 ~ 59.114	31.39	0	$(2.87 \pm 0.60) \times 10^{-7}$	9.00 ± 2.64	$-98/-100$	$(4.10^{+0.13}_{-0.13}) \times 10^{1}$	$0.99^{+0.01}_{-0.01}$	5371/1.08	$(0.98 \pm 0.18) \times 10^{-2}$	47.970	1.62 ± 0.09	132.7 ± 30.7	5314/0.75
141028455(1)	11.565 ~ 40.000	69.79	0	$(2.96 \pm 0.24) \times 10^{-6}$	3.03 ± 0.52	$-258/-257$	$8.35^{+0.23}_{-0.23}$	$0.46^{+0.01}_{-0.01}$	7260/2.02	$(1.73 \pm 0.05) \times 10^{-2}$	11.565	1.00 ± 0.02	364.8 ± 25.8	6401/2.92
141028455(2)	22.335 ~ 40.000	21.28	0	$(2.27 \pm 0.04) \times 10^{-7}$	3.38 ± 0.07	$-114/-116$	$4.17^{+0.37}_{-0.38}$	$0.54^{+0.02}_{-0.02}$	5685/1.96	$(0.68 \pm 0.08) \times 10^{-2}$	22.335	1.08 ± 0.08	269.6 ± 60.7	5620/1.80
150213001(1)	2.227 ~ 6.661	198.47	0	$(2.56 \pm 0.05) \times 10^{-6}$	3.86 ± 0.05	$-342/-341$	$(4.17^{+0.08}_{-0.08}) \times 10^{2}$	$0.93^{+0.01}_{-0.01}$	6143/2.04	$(17.50 \pm 0.59) \times 10^{-2}$	2.227	1.33 ± 0.02	114.0 ± 4.0	4426/2.94
150213001(2)	4.085 ~ 6.661	49.81	0	$(8.86 \pm 0.50) \times 10^{-7}$	2.95 ± 0.30	$-130/-131$	$(1.29^{+0.03}_{-0.03}) \times 10^{2}$	$1.00^{+0.00}_{-0.00}$	3350/1.03	...	...	...	...	...
150314205(1)	1.846 ~ 14.999	176.97	0	$(8.70 \pm 0.73) \times 10^{-6}$	1.09 ± 0.15	$-287/-287$	$(3.93^{+0.06}_{-0.06}) \times 10^{1}$	$0.46^{+0.00}_{-0.00}$	11811/2.01	...	...	...	...	...
150314205(2)	7.847 ~ 14.999	71.42	0	$(1.86 \pm 0.51) \times 10^{-6}$	4.86 ± 1.58	$-111/-112$	$(1.95^{+0.07}_{-0.07}) \times 10^{1}$	$0.48^{+0.01}_{-0.01}$	4482/1.98	$(3.44 \pm 0.11) \times 10^{-2}$	7.847	1.03 ± 0.02	499.7 ± 44.1	3734/2.94
150510139(1)	0.889 ~ 49.997	90.65	0	$(8.14 \pm 1.96) \times 10^{-6}$	0.77 ± 0.18	$-390/-389$	$9.19^{+0.17}_{-0.17}$	$0.40^{+0.00}_{-0.00}$	10870/1.99	...	...	...	...	...
150510139(2)	28.736 ~ 49.997	34.51	0	$(5.90 \pm 0.94) \times 10^{-7}$	3.52 ± 0.75	$-95/-97$	$7.31^{+0.43}_{-0.43}$	$0.54^{+0.01}_{-0.01}$	6605/1.99	$(0.90 \pm 0.06) \times 10^{-2}$	28.736	1.21 ± 0.04	575.0 ± 122.1	6447/2.29
150902733(1)	8.934 ~ 25.000	112.07	0	$(2.51 \pm 0.71) \times 10^{-6}$	4.28 ± 0.64	$-260/-260$	$(1.65^{+0.03}_{-0.03}) \times 10^{1}$	$0.40^{+0.00}_{-0.00}$	11345/2.01	$(4.68 \pm 0.07) \times 10^{-2}$	8.934	0.77 ± 0.01	375.8 ± 13.5	6656/2.97
150902733(2)	14.609 ~ 25.000	32.82	0	$(3.49 \pm 0.64) \times 10^{-7}$	5.62 ± 1.03	$-97/-99$	$9.79^{+0.61}_{-0.61}$	$0.56^{+0.01}_{-0.01}$	5601/2.01	$(2.05 \pm 0.20) \times 10^{-2}$	14.609	0.87 ± 0.07	161.8 ± 19.8	5366/2.51
151021791(1)	0.797 ~ 7.923	62.48	0	$(8.56 \pm 1.15) \times 10^{-7}$	1.52 ± 0.12	$-151/-152$	$(1.62^{+0.06}_{-0.06}) \times 10^{1}$	$0.50^{+0.01}_{-0.01}$	4361/1.99	...	...	...	...	...
151021791(2)	2.286 ~ 7.923	36.55	0	$(4.81 \pm 0.39) \times 10^{-7}$	1.65 ± 0.14	$-100/-102$	$(1.47^{+0.10}_{-0.10}) \times 10^{1}$	$0.60^{+0.02}_{-0.02}$	3488/2.00	...	...	...	...	...
160216801(1)	5.031 ~ 14.999	53.76	0	$(1.18 \pm 0.21) \times 10^{-6}$	2.35 ± 0.33	$-175/-175$	$(8.11^{+0.12}_{-0.12}) \times 10^{1}$	$1.00^{+0.00}_{-0.00}$	6954/1.00	...	...	...	...	...
160216801(2)	6.876 ~ 14.999	21.46	0	$(7.69 \pm 0.27) \times 10^{-7}$	2.65 ± 0.10	$-103/-104$	$(3.40^{+0.12}_{-0.12}) \times 10^{1}$	$1.00^{+0.00}_{-0.00}$	5288/1.02	...	...	...	...	...
160530667(1)	6.661 ~ 20.442	168.89	0	$(4.36 \pm 0.31) \times 10^{-6}$	3.70 ± 0.28	$-336/-335$	$(6.19^{+0.09}_{-0.09}) \times 10^{1}$	$0.58^{+0.00}_{-0.00}$	13223/2.00	$(14.30 \pm 0.33) \times 10^{-2}$	6.661	0.77 ± 0.01	130.3 ± 3.1	6883/2.99
160530667(2)	12.961 ~ 20.442	37.55	0	$(3.15 \pm 0.24) \times 10^{-7}$	5.48 ± 0.43	$-136/-137$	$(3.03^{+0.22}_{-0.21}) \times 10^{1}$	$0.81^{+0.02}_{-0.02}$	5215/2.00	$(4.44 \pm 0.68) \times 10^{-2}$	12.961	0.86 ± 0.08	66.6 ± 6.9	5001/1.85
170114917(1)	2.047 ~ 14.999	57.52	0	$(1.01 \pm 0.08) \times 10^{-6}$	1.75 ± 0.09	$-217/-217$	$(1.28^{+0.05}_{-0.05}) \times 10^{1}$	$0.52^{+0.01}_{-0.01}$	6211/2.02	...	...	...	...	...
170114917(2)	4.702 ~ 14.999	30.73	0	$(2.94 \pm 0.12) \times 10^{-7}$	2.09 ± 0.09	$-107/-109$	$(1.01^{+0.09}_{-0.09}) \times 10^{1}$	$0.63^{+0.02}_{-0.02}$	5404/2.01	...	...	...	...	...
170921168(1)	4.353 ~ 25.654	92.75	0	$(2.03 \pm 0.13) \times 10^{-6}$	0.92 ± 0.15	$-150/-150$	$(2.57^{+0.06}_{-0.06}) \times 10^{-2}$	$0.97^{+0.00}_{-0.01}$	8470/1.97	...	...	...	...	...

Table 3
(Continued)

GRB	$t_{start} \sim t_{stop}$	S	t_0	Lightcurve Power-law Fitting			Spectral Power-law Fitting			Spectral Cutoff Power-law Fitting					
				$F_{t,0}$	$\hat{\alpha}$	AIC/BIC	$F_{\nu,0}$	$\hat{\beta}$	DIC/p_{DIC}	$N_{0,p}$	t_p	$\hat{\Gamma}$	E_c	DIC/p_{DIC}
(1)	(2)	(3)	(4)	(5)	(6)	(7)	(8)	(9)	(10)	(11)	(12)	(13)	(14)	(15)
170921168(2)	$15.707 \sim 25.654$	43.76	0	$(1.38 \pm 0.03) \times 10^{-6}$	2.40 ± 0.14	$-101/-103$	$(1.75^{+0.02}_{-0.02}) \times 10^{-2}$	$1.00^{+0.00}_{-0.00}$	6527/0.99	$(3.81 \pm 0.43) \times 10^{-2}$	15.707	1.73 ± 0.05	105.0 ± 13.1	6147/2.05
171210493(1)	$5.237 \sim 137.109$	74.10	0	$(2.28 \pm 0.02) \times 10^{-6}$	1.20 ± 0.02	$-310/-309$	$(1.11^{+0.03}_{-0.03}) \times 10^{1}$	$0.59^{+0.01}_{-0.01}$	10380/2.03	⋯	⋯	⋯	⋯	⋯
171210493(2)	$64.334 \sim 137.109$	27.51	0	$(1.32 \pm 0.04) \times 10^{-7}$	1.65 ± 0.11	$-113/-114$	$9.59^{+0.73}_{-0.72}$	$0.78^{+0.02}_{-0.02}$	8145/2.02	⋯	⋯	⋯	⋯	⋯
180305393(1)	$3.449 \sim 16.537$	101.51	0	$(2.72 \pm 0.86) \times 10^{-6}$	1.69 ± 0.40	$-181/-181$	$(1.60^{+0.03}_{-0.03}) \times 10^{1}$	$0.36^{+0.00}_{-0.00}$	11378/1.98	⋯	⋯	⋯	⋯	⋯
180305393(2)	$8.933 \sim 16.537$	35.63	0	$(4.78 \pm 0.33) \times 10^{-7}$	3.72 ± 0.24	$-101/-103$	$(1.27^{+0.07}_{-0.07}) \times 10^{1}$	$0.53^{+0.01}_{-0.01}$	5710/2.00	$(6.05 \pm 0.73) \times 10^{-2}$	8.933	0.47 ± 0.07	80.5 ± 7.0	5312/2.31

Note. Column (1) lists the GRB name; Column (2) lists the start and stop times of the decay phases (in units of s); Column (3) lists the statistical significance S; Column (4) lists the model parameter t_0 as described in Equations (4), (7), and (8), which we fixed to zero; Columns (5)–(7) list the best-fit parameters for the power-law model in Equation (4): the normalization $F_{t,0}$ (in units of erg cm^{-2} s^{-1}), the power-law index $\hat{\alpha}$, and the AIC and BIC statistics; Columns (8)–(10) list the best-fit parameters for the power-law model as shown in Equation (5): normalization $F_{\nu,0}$ (in units of phs cm^{-2} s^{-1} keV^{-1}), the power-law index $\hat{\beta}$, and the DIC and p_{DIC} statistics; Columns (11)–(15) list the best-fit parameters for the cutoff power-law model as presented in Equations (6)–(8): normalization $N_{0,p}$ (in units of phs cm^{-2} s^{-1} keV^{-1}), parameter t_p, which we fixed at the beginning of the decay phases, the cutoff power-law index Γ, the $\hat{\beta}$ index derived from Γ, and the AIC and BIC statistics. Note that (1) marks the entire decay phase of the pulses and (2) marks the late-part decay phase of the pulses. Note that we did not apply the chi-squared test for our sample, because the sample size in our selected bursts is not large enough; the chi-squared test usually requires a relatively large sample size.

adequate to describe the GRB spectra during the decay phase[12]:

$$N(E, t) = N_0(t) \left(\frac{E}{E_{\text{piv}}} \right)^{-\hat{\Gamma}} \exp \left\{ -\left[\frac{E}{E_c(t)} \right] \right\}, \qquad (6)$$

where $\hat{\Gamma} = \hat{\beta} + 1$ is the power-law photon index, E_{piv} is the pivot energy fixed at 100 keV, and $N_0(t) = N_{0,\text{p}}[(t - t_0)/(t_\text{p} - t_0)]^{-(1+\hat{\Gamma})}$ is the time-dependent photon flux (in units of photons keV^{-1} cm^{-2} s^{-1}) at 100 keV (see also Equation (7) in Zhang et al. 2009). For such a spectrum, the standard curvature effect predicts

$$E_c(t) = E_{c,\text{p}} \left(\frac{t - t_0}{t_\text{p} - t_0} \right)^{-1} \qquad (7)$$

where $E_{c,\text{p}} = E_c(t_\text{p})$, t_0 is fixed to zero, and t_p is the beginning of the decay of the pulses; and

$$F_{\nu,c}(t) = F_{\nu,c,p} \left(\frac{t - t_0}{t_\text{p} - t_0} \right)^{-2} \qquad (8)$$

where $F_{\nu,c}(t) = E_c(t) N_c(t)$ and $F_{\nu,c,p} = E_{c,\text{p}} N_{c,\text{p}}$, where $N_c(t) = N(E_c, t) = N_0(t)(E_c/E_{\text{piv}})^{-\hat{\Gamma}} \exp(-1)$, which is calculated using Equation (6) when E is at cutoff energy E_c, and $N_{c,\text{p}} = N(E_c, t_\text{p}) = N_0(t_\text{p})(E_c/E_{\text{piv}})^{-\hat{\Gamma}} \exp(-1)$, which is calculated at time t_p and cutoff energy E_c.

With Equations (7) and (8), one can also get a direct relation between $F_{\nu,c}(t)$ and $E_c(t)$:

$$F_{\nu,c}(t) = \frac{N_{c,\text{p}}}{E_{c,\text{p}}} E_c^2(t). \qquad (9)$$

From the data, the time-dependent parameters $E_c(t)$ and $F_{\nu,c}(t)$ can be directly measured. One can then directly compare the data against the model predictions in Equations (7)–(9).

4. Results

4.1. The Case of Power-law Spectra

For the case of power-law spectra, as discussed above, we measure the temporal indices for two phases (Phase I and II) and their corresponding spectral indices (using a time-integrated spectrum throughout the decay phase). The results are as follows:

1. Entire decay phase (Phase I): The parameter set $(\hat{\alpha}_{\text{PL}}^{\text{I}} - \hat{\beta}_{\text{PL}}^{\text{I}})$ is presented as orange dots in Figure 2. Eight out of 24 cases satisfy the inequality $\hat{\alpha} \geqslant 2 + \hat{\beta}$. These bursts are GRB 090620400, GRB 090719063, GRB 130305486, GRB 131231198, GRB 141028455, GRB 150213001, GRB 150902733, and GRB 160530667. Other bursts are below the line, suggesting that not the entire decay segment can be attributed to the curvature effect for these bursts, which is quite reasonable

---

[12] Previous studies show that the CPL model is a sufficient model for the majority of GRB spectra (e.g., Yu et al. 2019; Li et al. 2020). On the other hand, GRBs usually exhibit strong spectral evolution. In order to best characterize the spectral shape, one needs to introduce an evolving spectral model within a burst or even within a pulse (Li et al. 2020). For simplicity, we perform the HLE test only considering the CPL model. We also notice that there are clear predictions for α evolution for HLE if the emergent spectrum is indeed described by the Band function, which has been studied by some authors (e.g., Genet & Granot 2009).
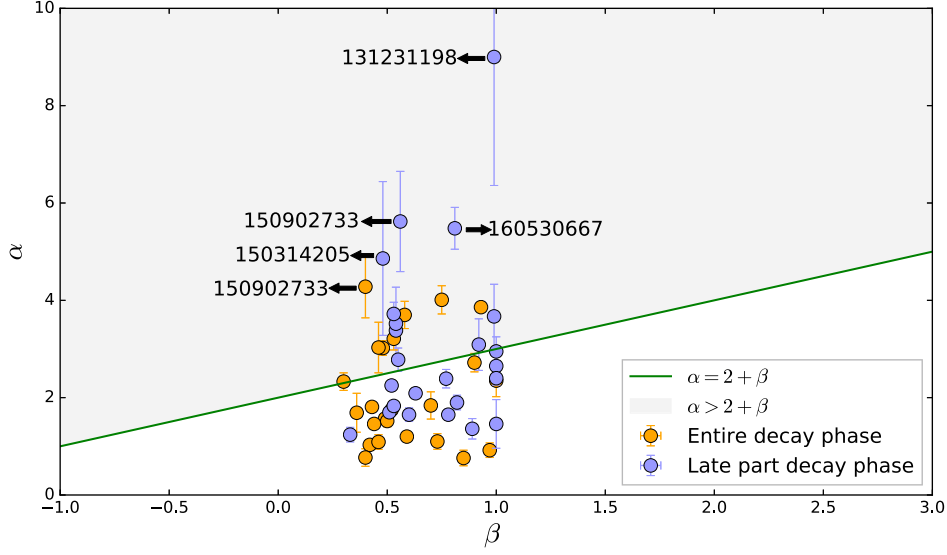
in view of the modeling presented in Uhm & Zhang (2016b) and Uhm et al. (2018).

2. Late-part decay phase (Phase II): The parameter set $(\hat{\alpha}_{\text{PL}}^{\text{II}} - \hat{\beta}_{\text{PL}}^{\text{II}})$ is presented as blue dots in Figure 2. Upward of 11 out of 24 cases now satisfy the inequality $\hat{\alpha} \geqslant 2 + \hat{\beta}$. These bursts include GRB 090620400, GRB 090804940, GRB 120426090, GRB 131231198, GRB 141028455, GRB 150314205, GRB 150510139, GRB 150902733, GRB 160530667, GRB 170921168, and GRB 180305393. This suggests that three additional bursts have the curvature effect showing up during the last three data points, while the remaining 13 bursts still do not have the HLE turned on by the end of the observed pulse.

One immediate observation is that a good fraction of our sample has entered the $\hat{\alpha} > 2 + \hat{\beta}$ regime. Since the HLE curvature effect defines the steepest decay index allowed in a GRB pulse, the results strongly suggest that the emission region is undergoing bulk acceleration in the region where prompt emission is released. We calculated the distance of this region from the central engine, R_{GRB}, using Equation (2) and found that they are typically $\sim 10^{15}$–10^{16} cm for a typical Lorentz factor $\Gamma \sim 100$ (Table 4). In this region, it is impossible to have thermally driven bulk acceleration. The only possibility is that the jet is Poynting-flux dominated in the region, and the GRB emission is powered by the dissipation of a Poynting flux (Zhang & Yan 2011). About one-half of the dissipated energy is released as GRB emission, while the other one-half is used to accelerate the ejecta. This conclusion is consistent with previous results from prompt-emission spectral-lag analysis (Uhm & Zhang 2016b) and the curvature-effect test of X-ray flares (Jia et al. 2016; Uhm & Zhang 2016a).

A few bursts (GRB 081224887, GRB 090719063, GRB 100707032, GRB 110721200, and GRB 110920546) have been reported in some previous studies (Iyyani et al. 2013, 2015, 2016; Li 2019b) to require an additional thermal component in order to produce acceptable spectral fits. The thermal component is also included in our analysis for these bursts. For a self-consistency test, it is worth noting that these GRBs do not qualify for our Phase II sample and only one burst (GRB 090719063) is included in our Phase I sample. The results imply that the emission in these bursts may be dominated by other mechanisms (e.g., photosphere emission). The existence of a thermal component is consistent with a lower magnetization in the jet (Gao & Zhang 2015).

We notice that six cases (GRB 090804940, GRB 120426090, GRB 150314205, GRB 150510139, GRB 170921168, and GRB 180305393) are not included in the Phase I sample but are included in the Phase II sample, indicating that the curvature effect may only dominate the later part of emission for these bursts. It is also interesting to note that three cases (GRB 090719063, GRB 130305486, and GRB 150213001) are included in the Phase I sample but not in the Phase II sample. These may be spurious cases, which may have contamination from another emission episode. Our analysis below confirms this speculation.

4.2. The Case of Cutoff Power-law Spectra

In total, 14 bursts (including eight cases in the Phase I sample and 11 cases in the Phase II sample, noticing that some cases appear in both samples) meet the HLE-dominated

Figure 2. Testing the closure relation of the curvature effect in the decaying wing using prompt-emission data. The closure relation between the temporal index $\hat{\alpha}$ and the spectral index $\hat{\beta}$ (Kumar & Panaitescu 2000), that is, $\hat{\alpha} \geqslant 2 + \hat{\beta}$, is marked as the solid green line, with the convention $F_{\nu_{obs}}^{obs} \propto t_{obs}^{-\hat{\alpha}} \nu_{obs}^{-\hat{\beta}}$. The orange and blue colors indicate different decay phases, Phase I and Phase II, respectively, as defined in the text. The shaded area stands for $\hat{\alpha} > 2 + \hat{\beta}$, which requires bulk acceleration in the emission region.

Table 4
Estimation of GRB Emission Radius Using High-latitude Emission

GRB	Γ_2 (used)	z (used)	t_{HLE}^{I} (s)	R_{GRB}^{I} (cm)	t_{HLE}^{II} (s)	R_{GRB}^{II} (cm)
(1)	(2)	(3)	(4)	(5)	(6)	(7)
090620400	1.0	1.0	4.11	1.2×10^{15}	3.48	1.0×10^{15}
090719063	1.0	1.0	5.06	1.5×10^{15}	...	...
090804940	1.0	1.0	...	...	2.01	0.6×10^{15}
120426090	1.0	1.0	...	...	1.14	0.3×10^{15}
130305486	1.0	1.0	13.79	4.1×10^{15}	...	...
131231198	1.0	0.642	22.36	6.7×10^{15}	6.79	2.0×10^{15}
141028455	1.0	2.33	8.54	2.6×10^{15}	5.30	1.6×10^{15}
150213001	1.0	1.0	2.22	0.7×10^{15}	...	...
150314205	1.0	1.758	...	...	2.59	0.8×10^{15}
150510139	1.0	1.0	...	...	10.63	3.2×10^{15}
150902733	1.0	1.0	8.03	2.4×10^{15}	5.20	1.6×10^{15}
160530667	1.0	1.0	6.89	2.1×10^{15}	3.74	1.1×10^{15}
170921168	1.0	1.0	...	...	4.97	1.5×10^{15}
180305393	1.0	1.0	...	...	3.80	1.1×10^{15}

Note. Column (1) lists the GRB name. Column (2) lists the Γ values used, where we adopted a typical value ($\Gamma_2 = 1$) for all cases. Column (3) lists the redshift used; a majority of bursts in our sample have no redshift observations, so we adopt a typical value ($z = 1$) instead. Column (4) lists the duration of the HLE in the source frame for "Phase I," which is calculated using the observed HLE duration divided by $(1+z)$. Column (5) lists the GRB emission radius R_{GRB} for Phase I, derived using Equation (2). Again, Column (6) lists the duration of the HLE in the source frame for Phase II, and Column (5) lists the GRB emission radius R_{GRB} for Phase II.

criterion based on the power-law spectral analysis. These bursts are our primary interest. Our next step is to study these bursts in detail by investigating their compliance with the curvature-effect predictions in the more complicated cutoff power-law model using a time-dependent analysis.

To test whether the CPL can account for the observed data as well, we adopt the following procedures:

1. We first apply the CPL model to fit the spectral data for these cases using the same episodes as the PL model to check whether the CPL model can improve the spectral fit results compared with the PL model. We find that the CPL fits are much better than the PL fits for all these cases by comparing the DIC statistic. We report our results in Table 3. For each individual fit, we fix t_0 to zero and t_p to the starting time of Phase I or Phase II. The best-fit parameters, including t_0 (fixed, Column 4), $N_{0,p}$ (Column 11), t_p (fixed, Column 12), Γ index (Column 13), and cutoff energy E_c (Column 14), as well as the DIC (Column 15) and p_{DIC} statistics (Column 15), are listed in Table 3.

2. Theoretically, we consider the evolution of E_c and $F_{\nu,c}$ according to Equations (7) and (8) as predicted by the HLE curvature-effect theory (for a constant Γ). The predicted parameter evolution curves for both $F_{\nu,c}(t)$ and $E_c(t)$ are plotted in the left panel of Figure 3 for each case to be directly compared with the data. In the right panel of Figure 3, we plot the theoretically predicted $E_c - F_{\nu,c}$ relation for each case to be directly compared with the observations.

3. The observed parameters for each time slice, including $N_0(t)$, Γ, and $E_c(t)$, have been obtained by applying Step (1) in Section 3.2. Since we consider the case at the characteristic energy E_c, one needs to obtain $F_{\nu,c}(t)$ and $E_c(t)$. The characteristic energy E_c is straightforwardly obtained, and $F_{\nu,c}(t)$ is derived using Equation (8). For this step, $N_{c,p}$ is calculated at peak time t_p with characteristic energy E_c using Equation (6).

4. Test the model with observed data. Through Step (3), the observed data points are available in the forms of $[F_{\nu,c}(t), t]$, $[E_c(t), t]$, and $[F_{\nu,c}(t), E_c(t)]$. The $[F_{\nu,c}(t), t]$, $[E_c(t), t]$ data points are plotted in the left panel of Figure 3, and the $[F_{\nu,c}(t), E_c(t)]$ data points are plotted in the right panel of Figure 3 for each burst. They are directly compared with the model predictions.
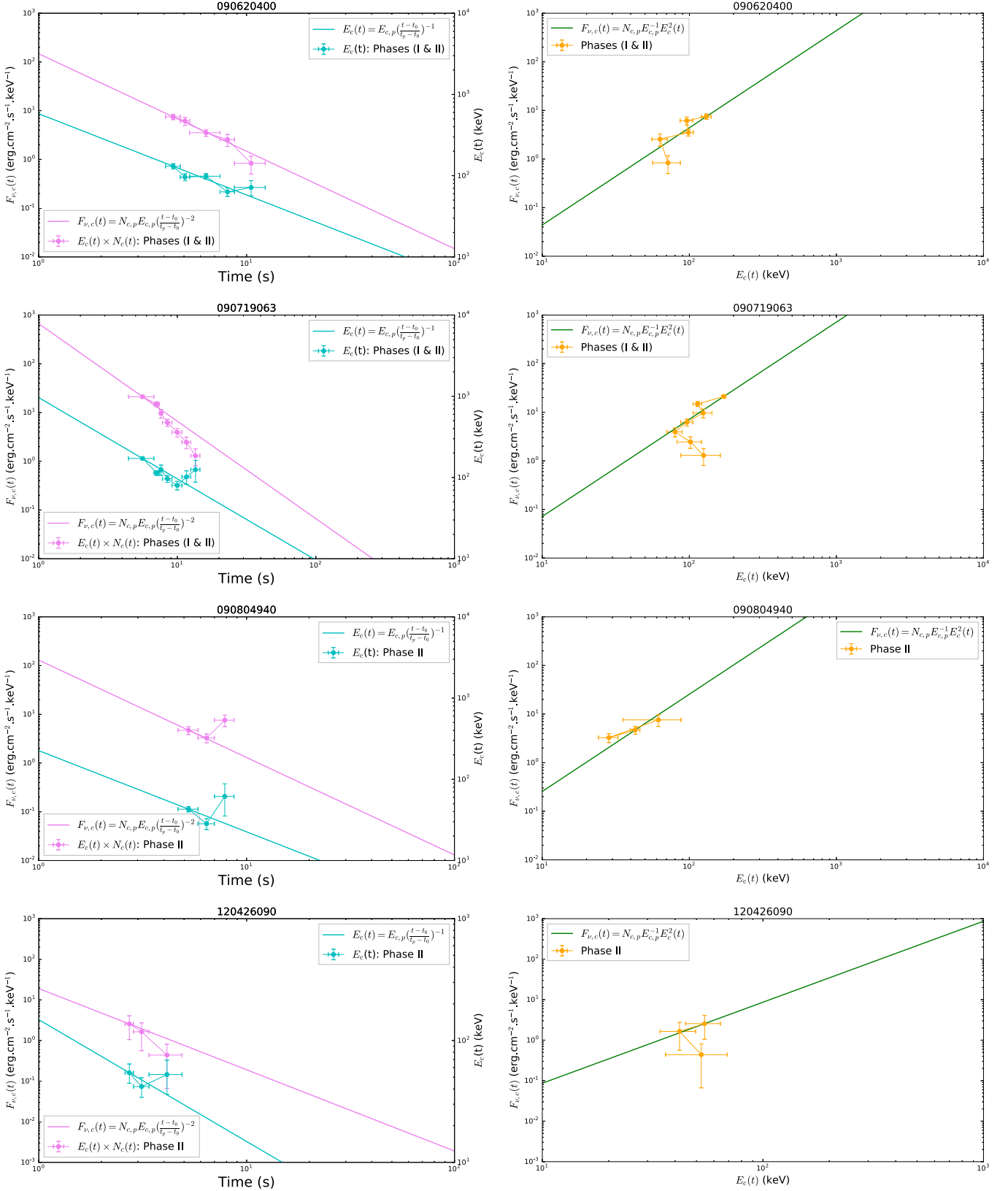
Figure 3. Testing the non-power-law curvature-effect model developed in Zhang et al. (2009) with observed data. The two panels in each row represent one individual pulse. Left panels: the cyan data points indicate the temporal evolution of the flux density $F_{\nu,c}(t)$ at the characteristic energy $E_c(t)$, while the pink data points indicate the evolution of the characteristic energy $E_c(t)$. The cyan and pink solid lines represent the relevant theoretical predictions. Right panels: the orange data points indicate the data observed in the $[F_{\nu,c}(t), E_c(t)]$ plane, while the green line represents the theoretical prediction between the two parameters.
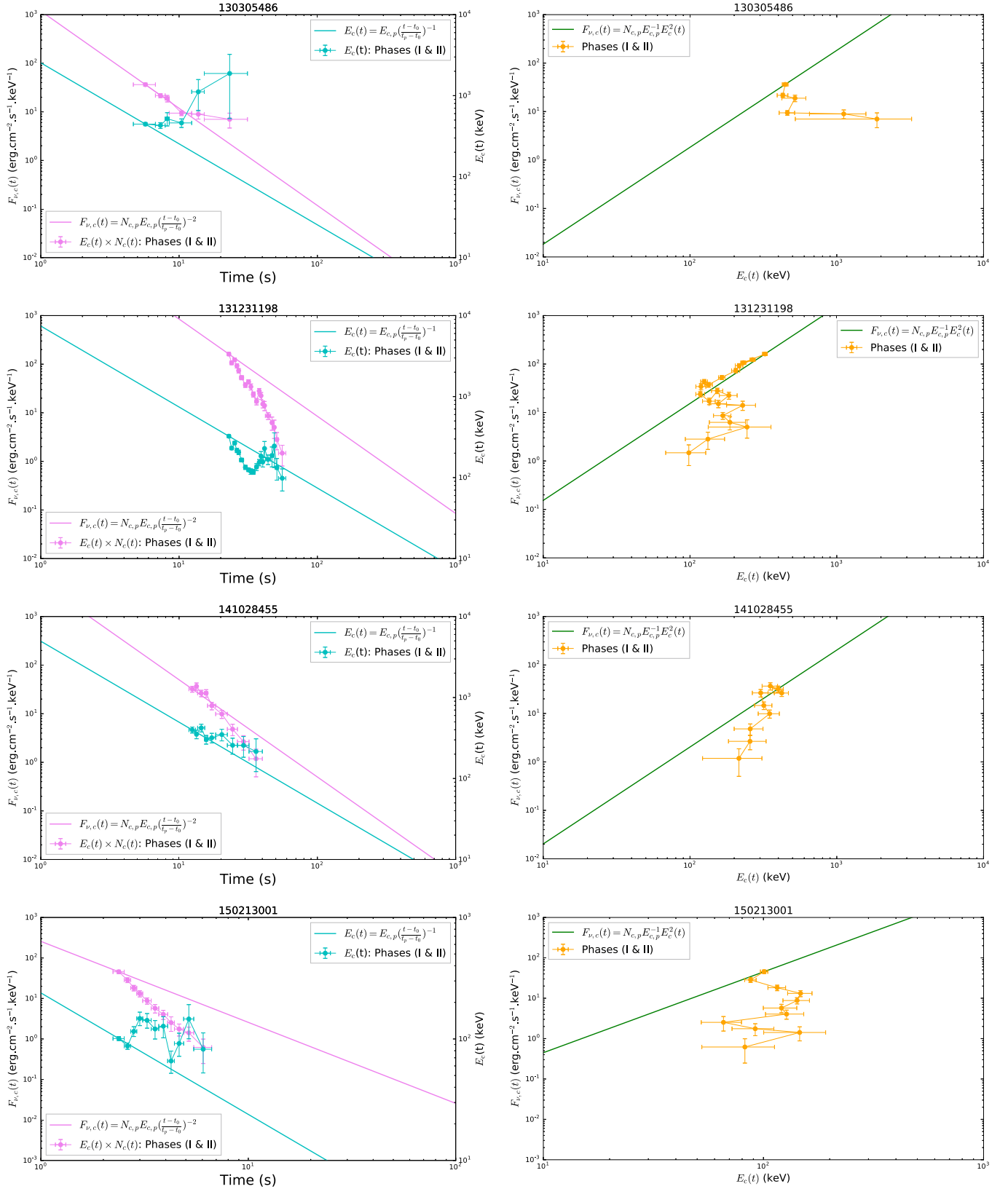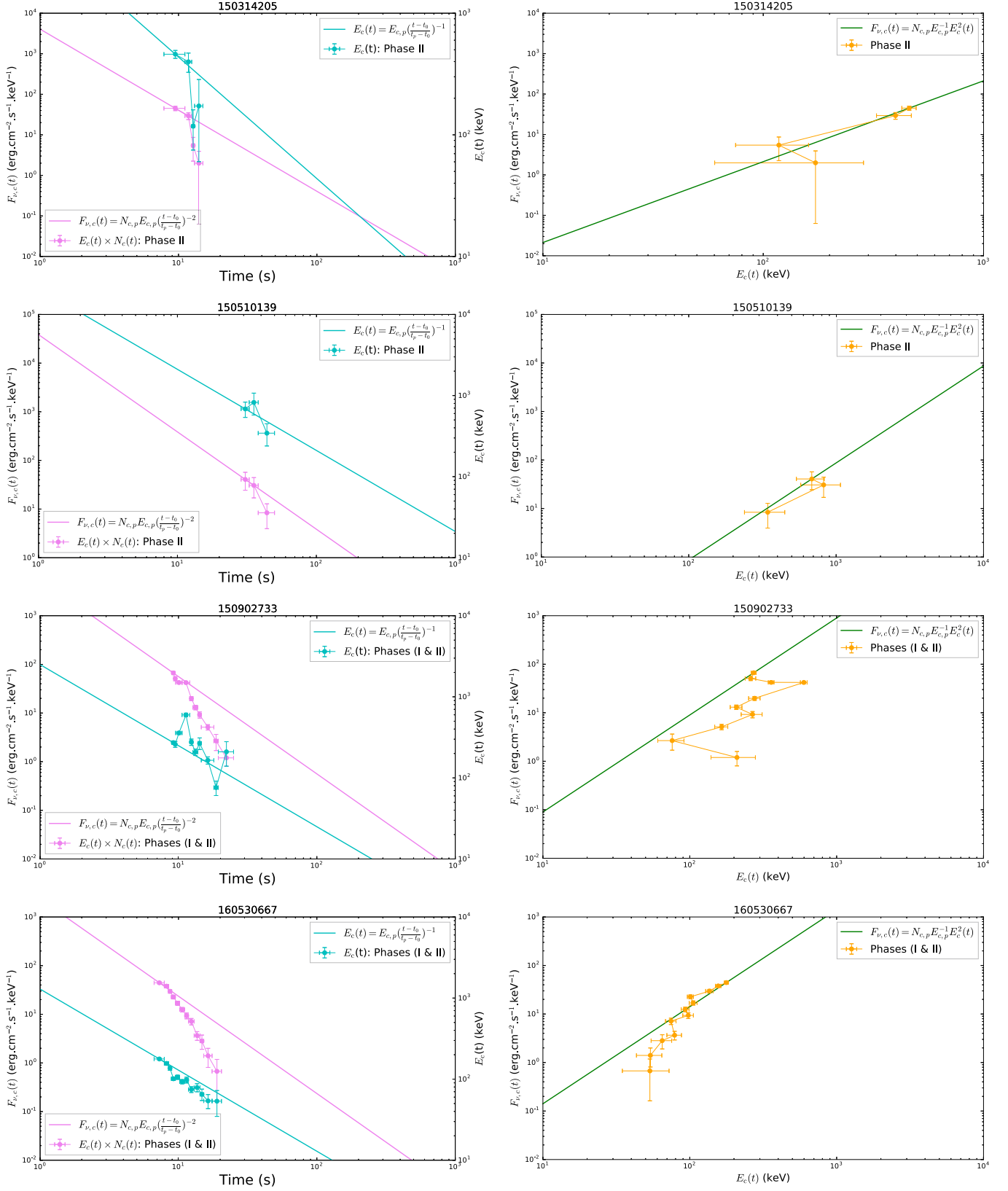
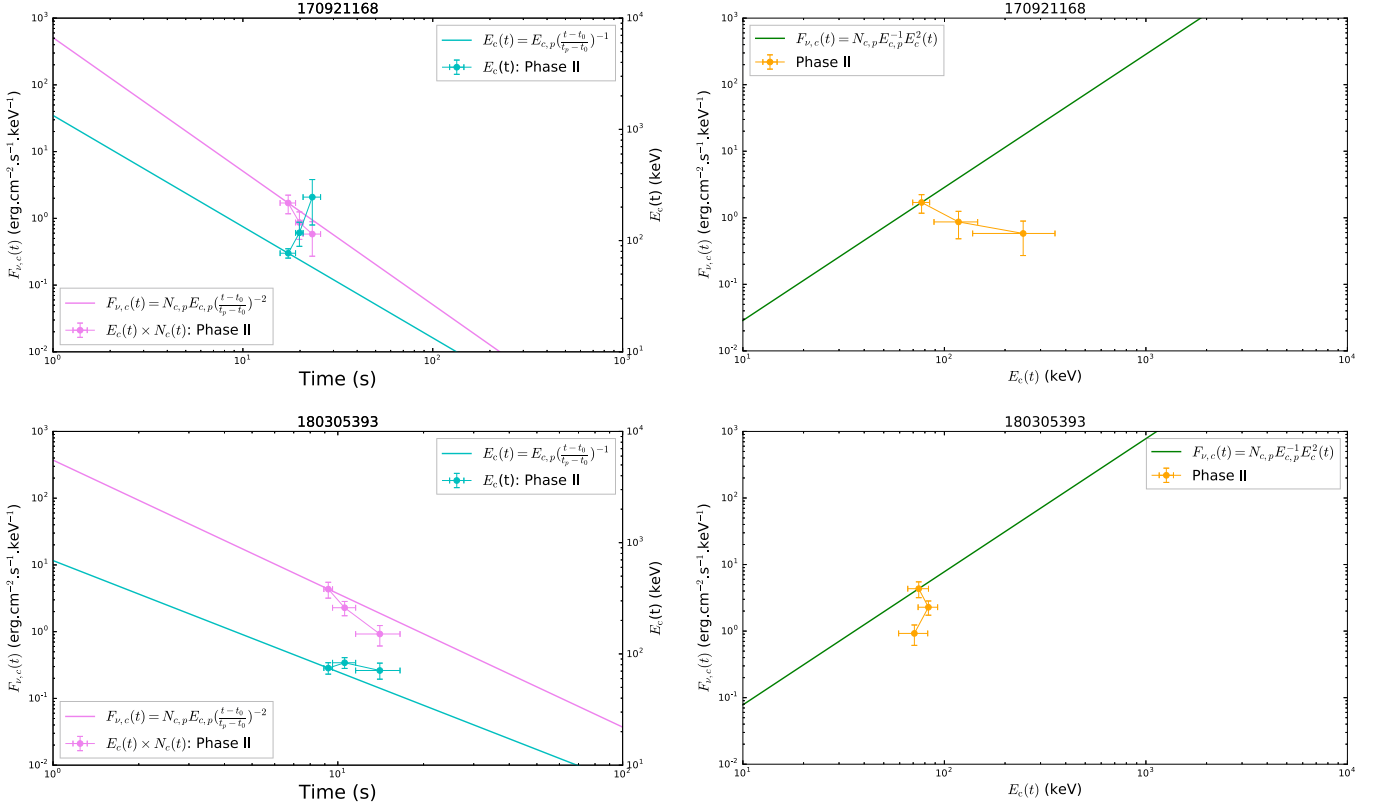**Figure 3.** (Continued.)

Figure 3. (Continued.)

Figure 3. (Continued.)

From the left panel in Figure 3, we can see that, except for several apparent cases that violate the predictions (090719063, 090804940, 130305486, 150213001, 150902733, 170921168), all other data points are generally consistent with the model predictions. The data of some bursts (090620400, 120426090, 150510139) match the constant Γ predictions well, suggesting that they are consistent with HLE emission with no significant acceleration. Some other cases (131231198, 141028455, 150314205, 160530667, 180305393) have either $E_c(t)$ or $F_{\nu,c}(t)$ below the model prediction lines, consistent with the bulk acceleration in the emission region. For both cases, the $[F_{\nu,c}(t), E_c(t)]$ test generally satisfies the model prediction (Equation (9)) within error. This is consistent with Z. Uhm & B. Zhang (2018, unpublished) and D. Tak et al. (2020, in preparation), who first performed such a test and showed that Equation (9) is generally valid regardless of bulk Lorentz factor evolution in the emission region.

It is interesting to note that the three cases (GRB 090719063, GRB 130305486, and GRB 150213001) that are in the Phase I sample but not in the Phase II sample indeed do not satisfy the simple model predictions in the $[F_{\nu,c}(t), E_c(t)]$ test, supporting that the cases are spurious.

5. Conclusions and Discussions

In this paper, we have tested the HLE curvature effect using the prompt-emission data. We selected 24 single-pulse GRBs detected by Fermi that are ideal for performing such a test. In order to avoid the t_0 effect and the overlapping effect, we focused on the single-pulse cases. In order to make the physical inferences trustworthy, we only selected the bursts with high

statistical significance. In order to determine the temporal peaks (t_p) of the pulses so that the starting time of the decay phase can be estimated, we employed the FRED model to fit the count-rate lightcurves for our sample. The time window of the entire decay phase is thus determined. Since the curvature effect is more likely to dominate the late-part emission of the decay phase, we are also concerned with such late-time segments. For the most conservative approach, we only selected the time intervals of the last three time bins with $S > 15$ to conduct the HLE test.

We then used two methods to measure the temporal indices and corresponding spectral indices: $\hat{\alpha}_{PL}^{I}$ and $\hat{\beta}_{PL}^{I}$ as derived from the entire decay phase, and $\hat{\alpha}_{PL}^{II}$ and $\hat{\beta}_{PL}^{II}$ as derived from the late-time decay phase. We perform the HLE curvature effect during these two phases. Using the simple power-law spectral analysis, we tested the $\hat{\alpha}_{PL}-\hat{\beta}_{PL}$ relation. We found that five out of 24 pulses for Phase I (except for three spurious cases as we discussed in Section 4) and 11 out of 24 pulses for Phase II are consistent with the curvature effect. Some fall into the regime that requires bulk acceleration in the emission region.

We further test these candidate HLE-dominated pulses using a more complicated HLE model (Zhang et al. 2009), invoking cutoff power-law fits to the time-dependent spectra. We confirm that the HLE effect is still valid for most of the cases, and that some of them indeed showed evidence of bulk acceleration in the emission region.

Based on the duration of the HLE-dominated emission, we estimated the radius of the emission region from the central engine. For a typical bulk Lorentz factor, the radius R_{GRB} is

typically of the order of 10^{15}–10^{16} cm, which is much greater than the photosphere radius and the standard internal shock radius.

The evidence of bulk acceleration and a large emission radius in these bursts is fully consistent with the GRB prompt-emission models invoking direct dissipation of a Poynting flux to power γ-ray emission (e.g., Zhang & Yan 2011). This suggests that at least for some GRBs, the jet composition is Poynting-flux dominated at the central engine and even in the emission region. This conclusion is consistent with previous independent modeling of GRB spectral lags (Uhm & Zhang 2016b) and E_p evolution patterns (Uhm et al. 2018), the HLE test for a sample of X-ray flares (Jia et al. 2016; Uhm & Zhang 2016a), and the nondetection of high-energy neutrinos from GRBs (Zhang & Kumar 2013; Aartsen et al. 2017). Our analysis is also consistent with the recent investigations of Z. Uhm & B. Zhang (2018, unpublished) and D. Tak et al. (2020, in preparation).

Appendix

In this appendix, we provide additional figures. Figure A1 shows count-rate lightcurves with the best-fit results using the FRED model.

In addition to the FRED model with a given t_0, another five-parameter (F_0, t_b, α_1, α_2, ω) model, the smoothly broken power law (BKPL), may also be used to characterize the pulse shape:

$$F(t) = F_0 \left[\left(\frac{t + t_0}{t_b + t_0} \right)^{\alpha_1 \omega} + \left(\frac{t + t_0}{t_b + t_0} \right)^{\alpha_2 \omega} \right]^{-1/\omega}, \qquad \text{(A1)}$$

where α_1, and α_2 are the temporal slopes, t_b is the break time, $F_b = F_0 \, 2^{-1/\omega}$ is the flux of the break time, and ω describes the sharpness of the break. Note that the smaller the ω parameter, the smoother the break, and it is often fixed as 3. On the other hand, several other similar Python packages (e.g., *scipy.optimize.curve_fit* and *kmpfit*) may also be competent to carry out the current task. Figure A2 shows the fit results of the lightcurve of GRB 131231198, compared with the different models (FRED and BKPL) or packages (*lmfit* and *scipy.optimize.curve_fit*), or the same model (BKPL) set up with different ω values ($\omega = 1$, $\omega = 3$, and $\omega = 10$).

Figure A3 displays the comparison of the count lightcurves for different GBM detectors. Figure A4 gives an example to show the [log (Flux), log(time)] plots, as compared with the [log (Flux), time] plots in Figure 1.
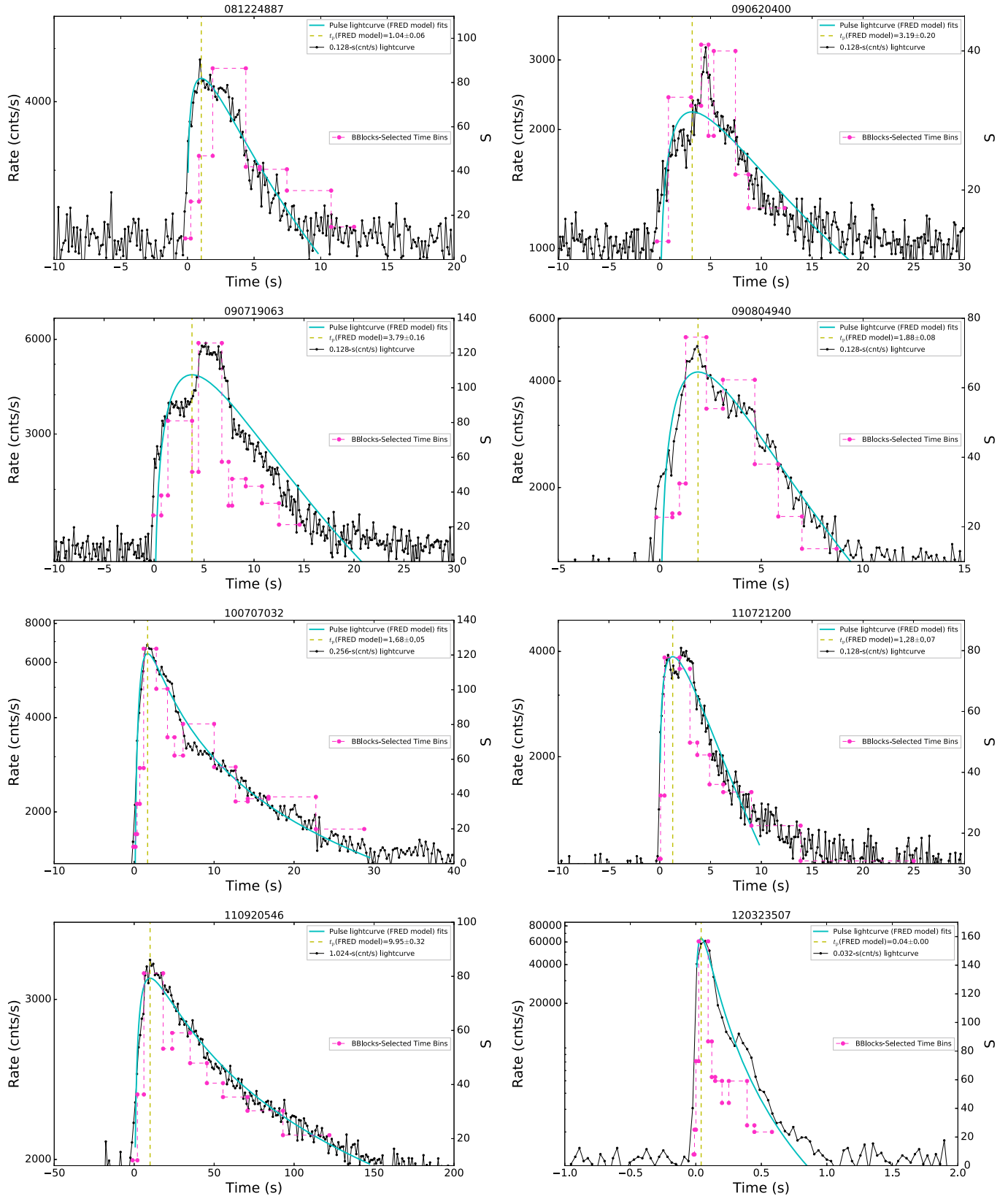
Figure A1. Count-rate lightcurves, as well as their best-fit results using the FRED model. Solid points connected by the black solid line represent the lightcurve, while the cyan solid lines are the best FRED model fits. The peak times obtained from the best-fit FRED model are indicated by the yellow vertical dashed line. Solid points connected by the pink dashed line represent the time bins selected using the BBlocks method.
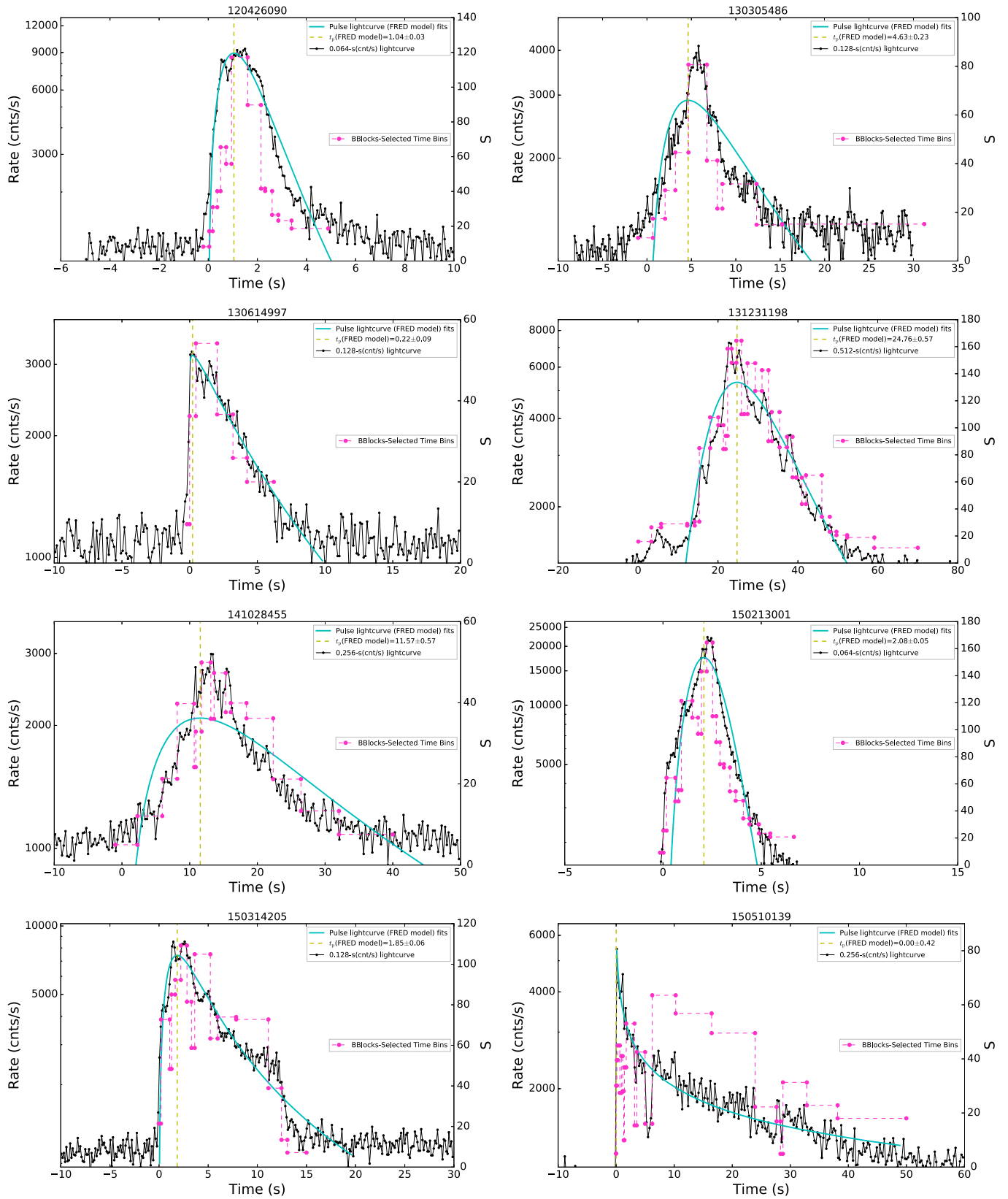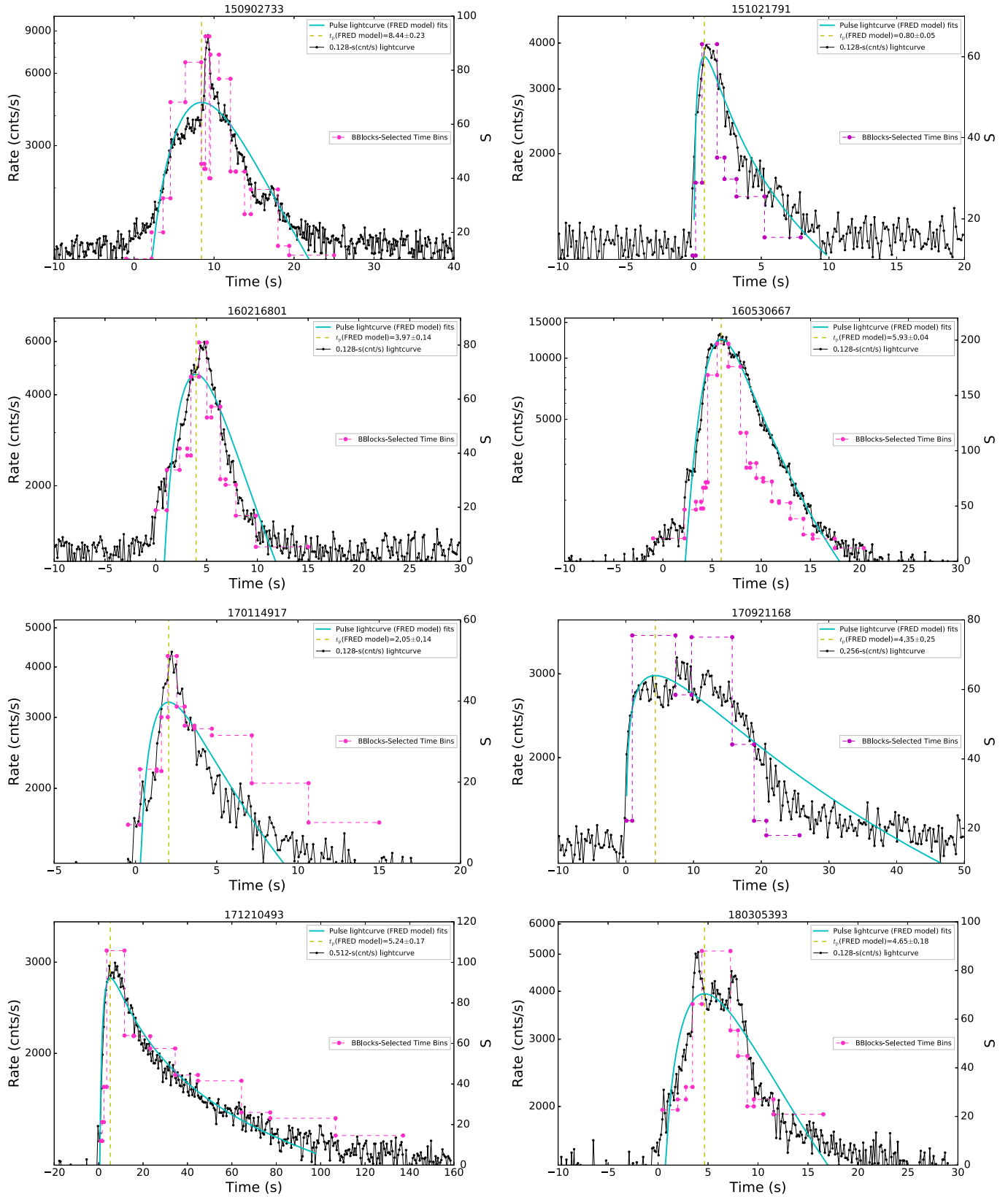
Figure A1. (Continued.)
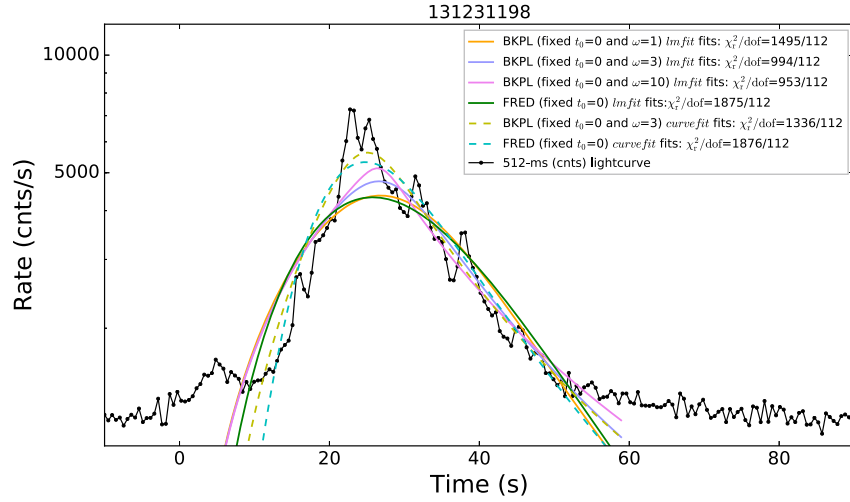
Figure A1. (Continued.)

Figure A2. Example of the best fits of the count-rate lightcurve for GRB 131231198 with different models (comparing FRED with BKPL) or packages used (comparing *lmfit* with *scipy. optimize. curve_fit*) or the same BKPL model with different ω values (comparing $\omega = 1$, $\omega = 3$, and $\omega = 10$). The points connected by the black solid line represent its 512 ms count-rate lightcurve. Solid curves with different colors indicate the *lmfit* cases (orange: BKPL model with fixed $\omega = 1$; violet: BKPL model with fixed $\omega = 3$; pink: BKPL model with fixed $\omega = 10$; green: FRED model), while dashed lines indicate the *scipy. optimize. curve_fit* cases (yellow: BKPL model with fixed $\omega = 3$; cyan: FRED model). The reduced chi-squared is calculated by assuming its uncertainties with a typical value: 10% of the values of its data points.
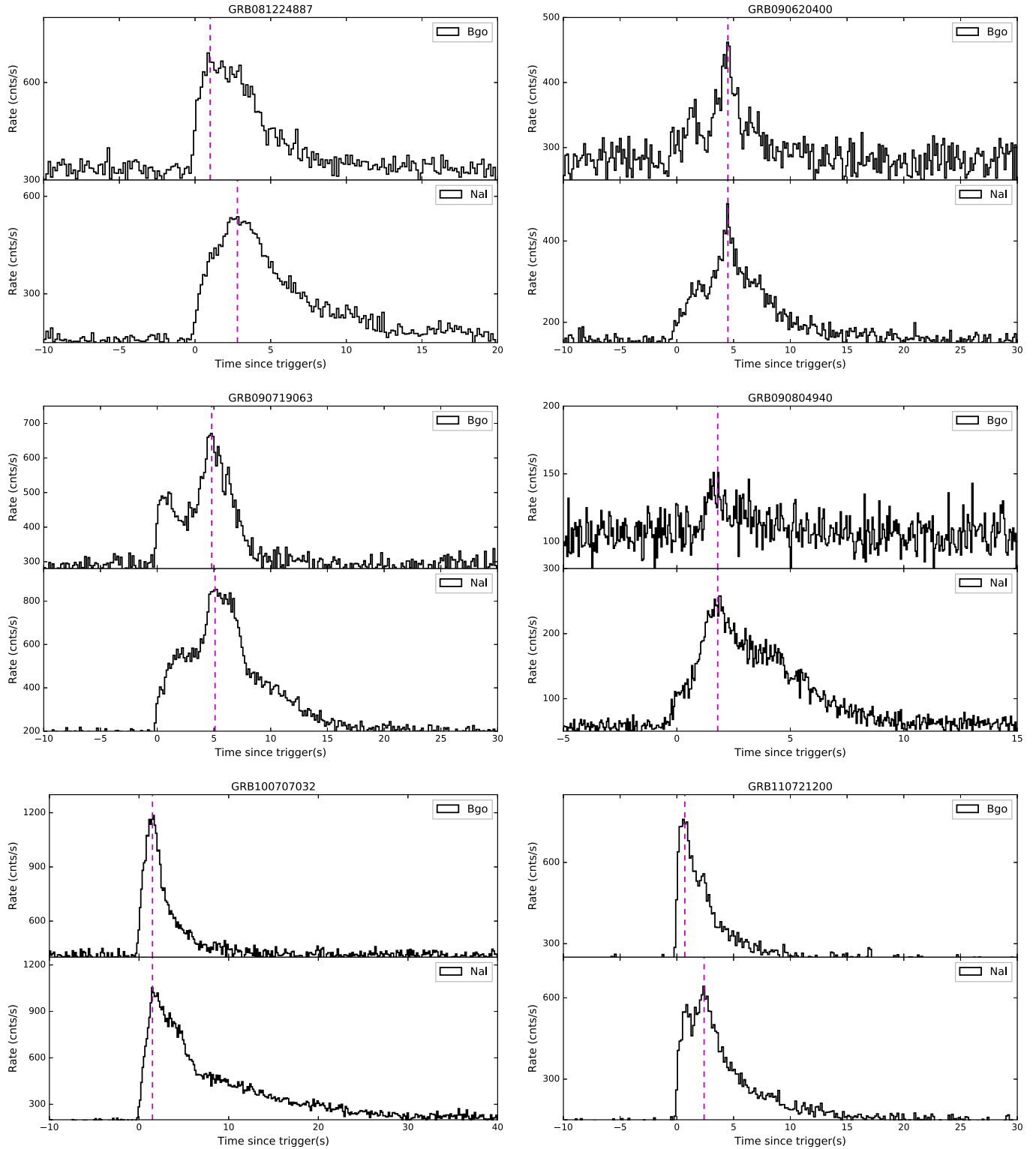
Figure A3. Comparison of the count lightcurves for different GBM detectors (Na I and BGO). For each individual burst, the vertical magenta dashed lines are the peak times of two detectors identified by eye by inspecting the flux.
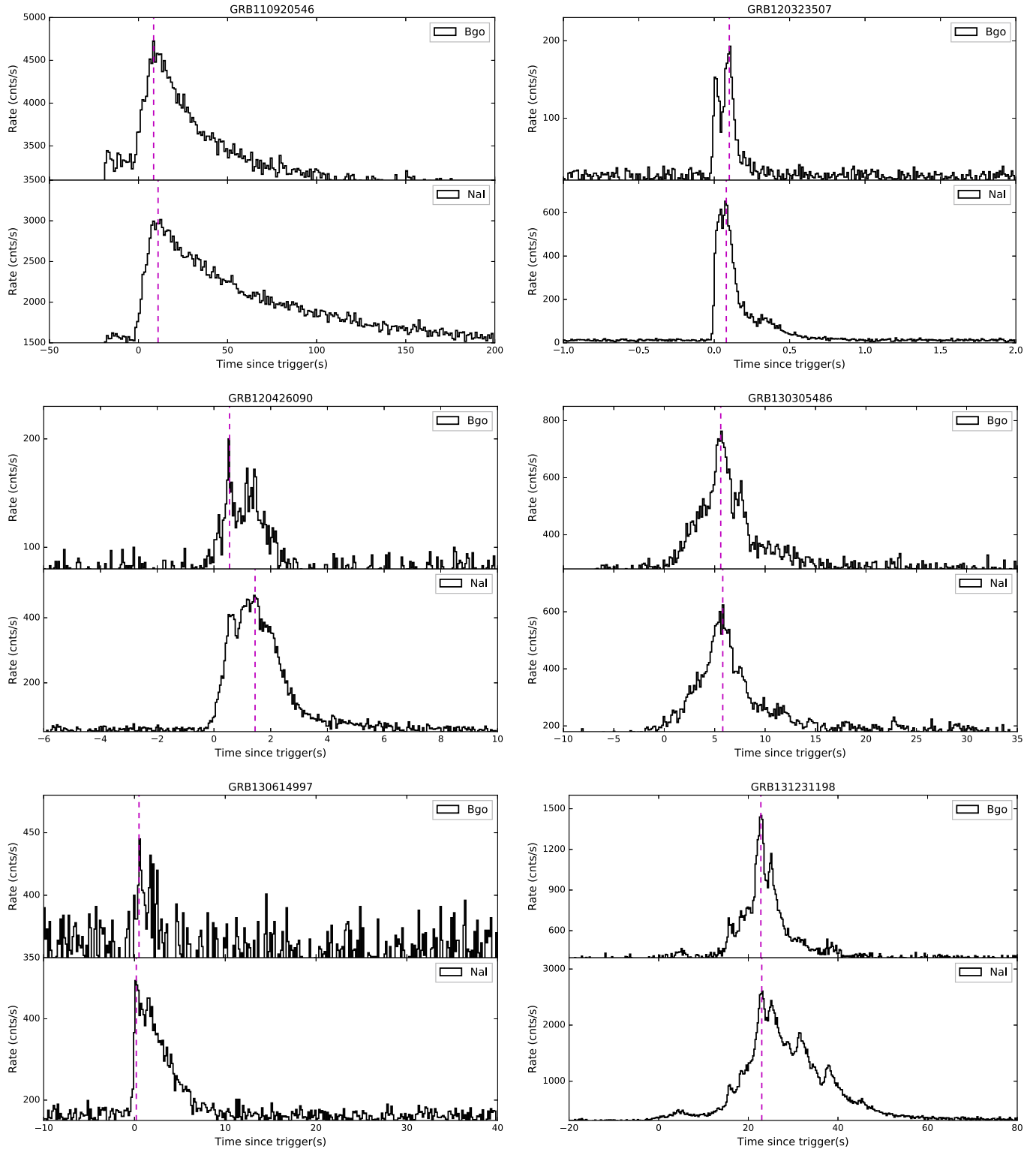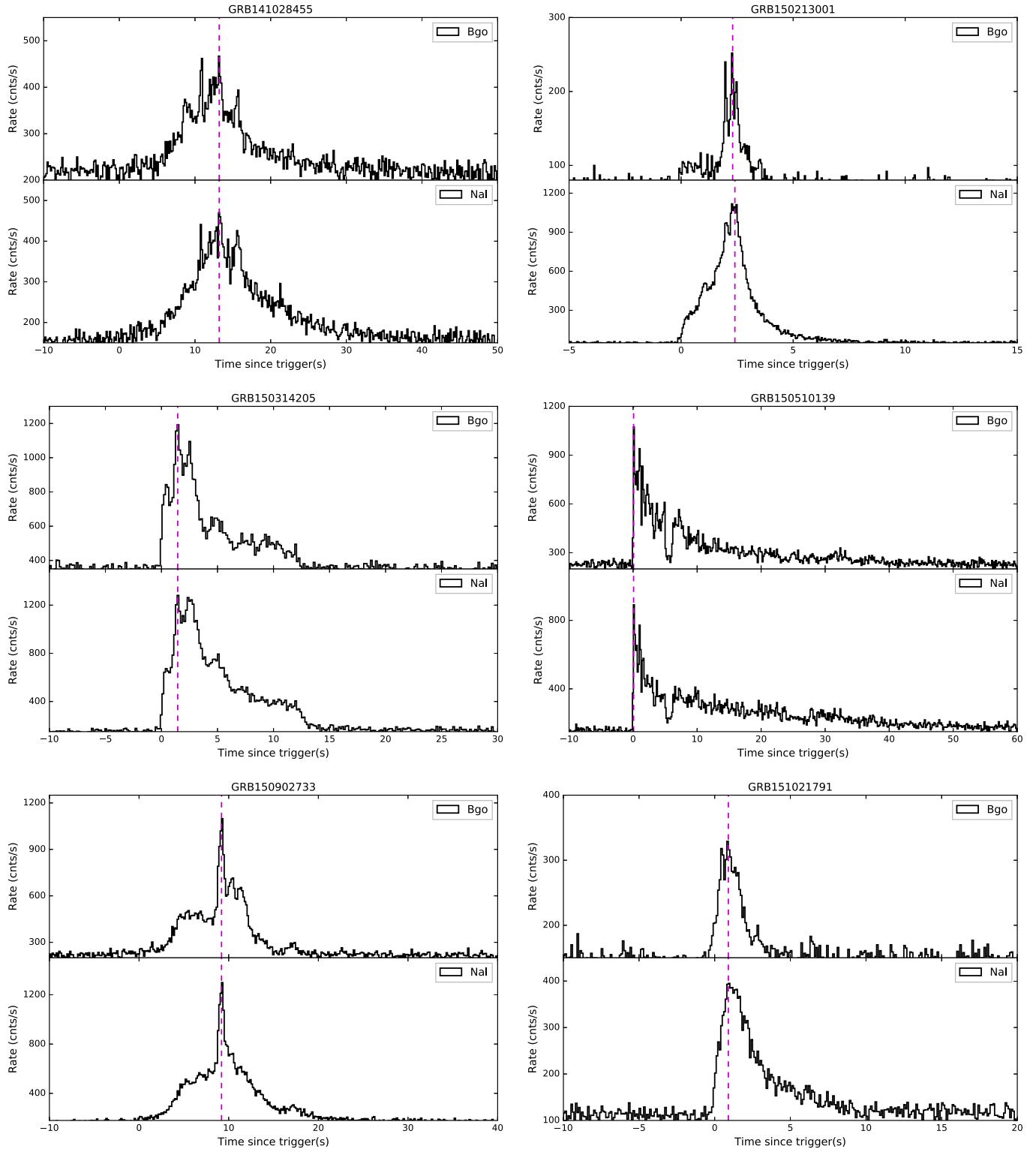
Figure A3. (Continued.)
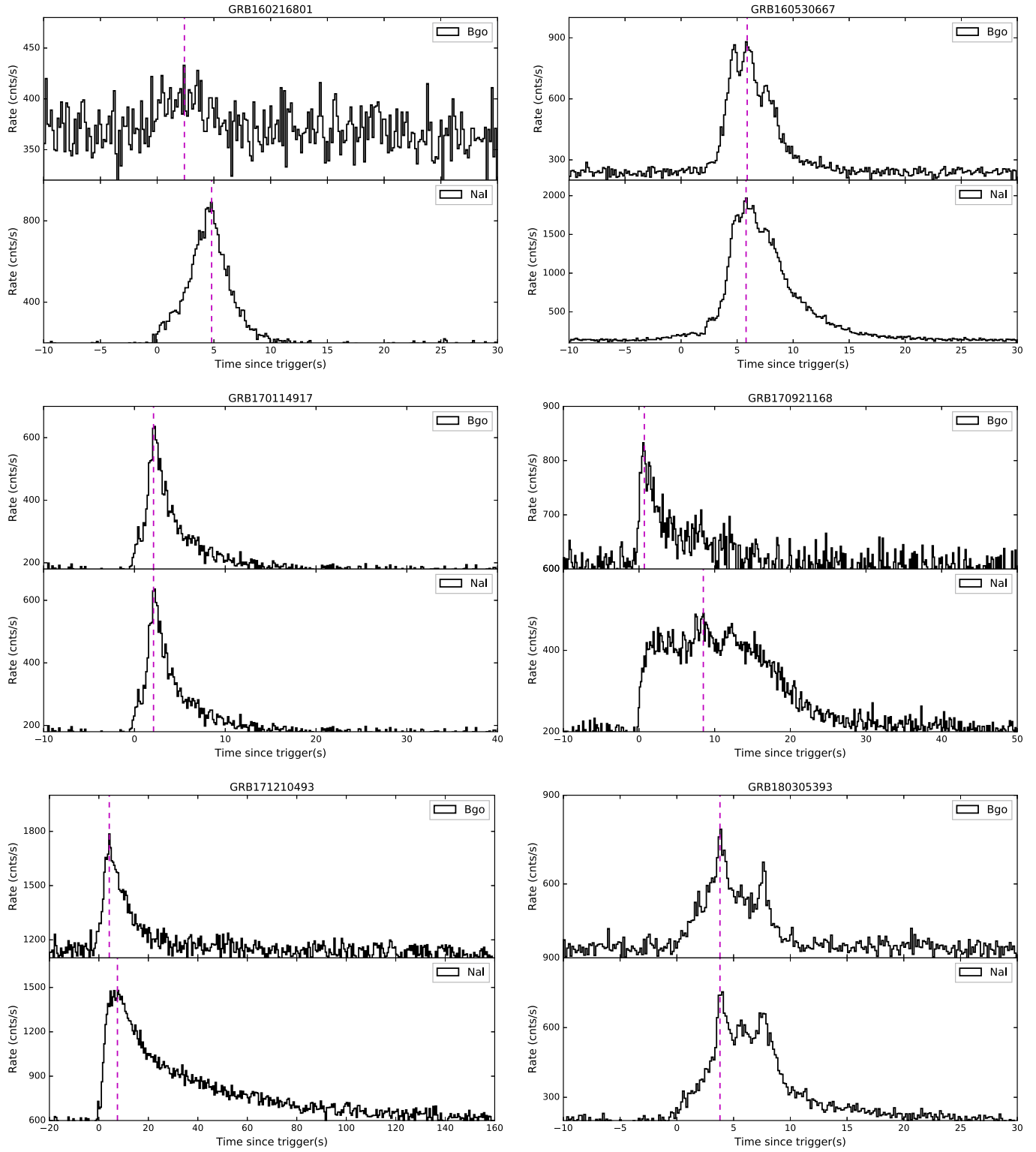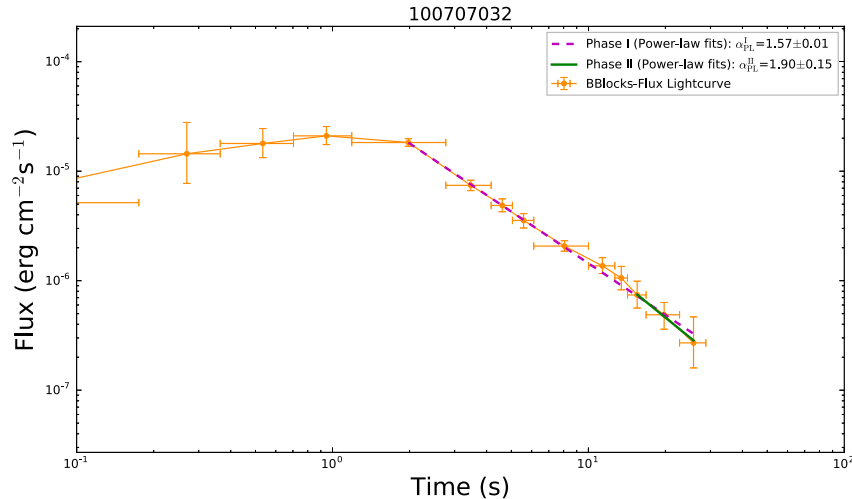
Figure A3. (Continued.)

Figure A3. (Continued.)

Figure A4. Same as Figure 1 but for the [log(Flux),log(time)] lightcurve. GRB 100707032 is taken as an example.

ORCID iDs

Liang Li ● https://orcid.org/0000-0002-1343-3089
Bing Zhang ● https://orcid.org/0000-0002-9725-2524

References

Aartsen, M. G., Ackermann, M., Adams, J., et al. 2017, ApJ, 843, 112
Abdo, A. A., Ackermann, M., Ajello, M., et al. 2009, ApJL, 706, L138
Abdo, A. A., Ackermann, M., Arimoto, M., et al. 2009, Sci, 323, 1688
Band, D., Matteson, J., Ford, L., et al. 1993, ApJ, 413, 281
Bégué, D., & Pe'er, A. 2015, ApJ, 802, 134
Beloborodov, A. M. 2010, MNRAS, 407, 1033
Daigne, F., & Mochkovitch, R. 2002, MNRAS, 336, 1271
Fenimore, E. E., Madras, C. D., & Nayakshin, S. 1996, ApJ, 473, 998
Gao, H., & Zhang, B. 2015, ApJ, 801, 103
Gelman, A., Hwang, J., & Vehtari, A. 2014, Stat. Comput., 24, 997
Genet, F., & Granot, J. 2009, MNRAS, 399, 1328
Giannios, D. 2006, A&A, 457, 763
Goodman, J. 1986, ApJ, 308, L47
Granot, J., Komissarov, S. S., & Spitkovsky, A. 2011, MNRAS, 411, 1323
Hunter, J. D. 2007, CSE, 9, 90
Iyyani, S., Ryde, F., Ahlgren, B., et al. 2015, MNRAS, 450, 1651
Iyyani, S., Ryde, F., Axelsson, M., et al. 2013, MNRAS, 433, 2739
Iyyani, S., Ryde, F., Burgess, J. M., Pe'er, A., & Bégué, D. 2016, MNRAS,
    456, 2157
Jia, L.-W., Uhm, Z. L., & Zhang, B. 2016, ApJS, 225, 17
Kobayashi, S., Piran, T., & Sari, R. 1999, ApJ, 513, 669
Kocevski, D., Ryde, F., & Liang, E. 2003, ApJ, 596, 389
Kumar, P., & Panaitescu, A. 2000, ApJL, 541, L51
Levinson, A. 2012, ApJ, 756, 174
Li, L. 2019a, ApJS, 242, 16
Li, L. 2019b, ApJS, 245, 7
Li, L. 2020, ApJ, 894, 100
Li, L., Geng, J.-J., Meng, Y.-Z., et al. 2019, ApJ, 884, 109
Li, L., Ryde, F., Pe'er, A., Yu, H.-F., & Acuner, Z. 2020, arXiv:2012.03038
Li, T.-P., & Ma, Y.-Q. 1983, ApJ, 272, 317
Meegan, C., Lichti, G., Bhat, P. N., et al. 2009, ApJ, 702, 791
Meszaros, P., Laguna, P., & Rees, M. J. 1993, ApJ, 415, 181
Meszaros, P., & Rees, M. J. 1993, ApJ, 405, 278
Mészáros, P., & Rees, M. J. 2000, ApJ, 530, 292
Moreno, E., Vazquez-Polo, F. J., & Robert, C. P. 2013, arXiv:1310.2905
Newville, M., Stensitzki, T., Allen, D. B., et al. 2016, Lmfit: Non-Linear Least-
    Square Minimization and Curve-Fitting for Python, Astrophysics Source
    Code Library, ascl:1606.014
Norris, J. P., Bonnell, J. T., Kazanas, D., et al. 2005, ApJ, 627, 324
Paczynski, B. 1986, ApJL, 308, L43
Pe'er, A., Mészáros, P., & Rees, M. J. 2006, ApJ, 642, 995
Pe'Er, A., Zhang, B.-B., Ryde, F., et al. 2012, MNRAS, 420, 468
Piran, T., Shemi, A., & Narayan, R. 1993, MNRAS, 263, 861
Rees, M. J., & Meszaros, P. 1992, MNRAS, 258, 41P
Rees, M. J., & Meszaros, P. 1994, ApJL, 430, L93
Rees, M. J., & Mészáros, P. 2005, ApJ, 628, 847
Ryde, F., Axelsson, M., Zhang, B. B., et al. 2010, ApJL, 709, L172
Ryde, F., & Svensson, R. 1999, ApJ, 512, 693
Scargle, J. D., Norris, J. P., Jackson, B., & Chiang, J. 2013, ApJ, 764, 167
Shemi, A., & Piran, T. 1990, ApJL, 365, L55
Uhm, Z. L., & Zhang, B. 2015, ApJ, 808, 33
Uhm, Z. L., & Zhang, B. 2016a, ApJL, 824, L16
Uhm, Z. L., & Zhang, B. 2016b, ApJ, 825, 97
Uhm, Z. L., Zhang, B., & Racusin, J. 2018, ApJ, 869, 100
Vianello, G. 2018, ApJS, 236, 17
Vianello, G., Lauer, R. J., Younk, P., et al. 2015, arXiv:1507.08343
Vurm, I., Lyubarsky, Y., & Piran, T. 2013, ApJ, 764, 143
Yu, H.-F., Dereli-Bégué, H., & Ryde, F. 2019, ApJ, 886, 20
Zhang, B. 2018, The Physics of Gamma-Ray Bursts (Cambridge: Cambridge
    Univ. Press)
Zhang, B., Fan, Y. Z., Dyks, J., et al. 2006, ApJ, 642, 354
Zhang, B., & Kumar, P. 2013, PhRvL, 110, 121101
Zhang, B., & Pe'er, A. 2009, ApJL, 700, L65
Zhang, B., & Yan, H. 2011, ApJ, 726, 90
Zhang, B., & Zhang, B. 2014, ApJ, 782, 92
Zhang, B.-B., Uhm, Z. L., Connaughton, V., Briggs, M. S., & Zhang, B. 2016,
    ApJ, 816, 72
Zhang, B.-B., Zhang, B., Castro-Tirado, A. J., et al. 2018, NatAs, 2, 69
Zhang, B.-B., Zhang, B., Liang, E.-W., & Wang, X.-Y. 2009, ApJL, 690,
    L10

Bayesian Time-resolved Spectroscopy of Multipulse GRBs: Variations of Emission Properties among Pulses

Liang Li[1,2,3,4,5] , Felix Ryde[4] , Asaf Pe'er[6] , Hoi-Fung Yu[7] , and Zeynep Acuner[4]
[1] ICRANet, Piazza della Repubblica 10, I-65122 Pescara, Italy; liang.li@icranet.org
[2] INAF–Osservatorio Astronomico d'Abruzzo, Via M. Maggini snc, I-64100, Teramo, Italy
[3] ICRA, Dipartimento di Fisica, Sapienza Università di Roma, P.le Aldo Moro 5, I-00185 Rome, Italy
[4] Department of Physics, KTH Royal Institute of Technology, and the Oskar Klein Centre for Cosmoparticle Physics, SE-10691 Stockholm, Sweden
[5] Department of Physics, Stockholm University, AlbaNova, SE-10691 Stockholm, Sweden
[6] Department of Physics, Bar-Ilan University, Ramat-Gan 52900, Israel
[7] Faculty of Science, The University of Hong Kong, Pokfulam, Hong Kong
Received 2020 December 4; revised 2021 February 18; accepted 2021 February 19; published 2021 June 7

Abstract

Gamma-ray bursts (GRBs) are highly variable and exhibit strong spectral evolution. In particular, the emission properties vary from pulse to pulse in multipulse bursts. Here we present a time-resolved Bayesian spectral analysis of a compilation of GRB pulses observed by the Fermi/Gamma-ray Burst Monitor. The pulses are selected to have at least four time bins with a high statistical significance, which ensures that the spectral fits are well determined and spectral correlations can be established. The sample consists of 39 bursts, 117 pulses, and 1228 spectra. We confirm the general trend that pulses become softer over time, with mainly the low-energy power-law index α becoming smaller. A few exceptions to this trend exist, with the hardest pulse occurring at late times. The first pulse in a burst is clearly different from the later pulses; three-fourths of them violate the synchrotron line of death, while around half of them significantly prefer photospheric emission. These fractions decrease for subsequent pulses. We also find that in two-thirds of the pulses, the spectral parameters (α and peak energy) track the light-curve variations. This is a larger fraction compared to what is found in previous samples. In conclusion, emission compatible with the GRB photosphere is typically found close to the trigger time, while the chance of detecting synchrotron emission is greatest at late times. This allows for the coexistence of emission mechanisms at late times.

Unified Astronomy Thesaurus concepts: Gamma-ray bursts (629); Astronomy data analysis (1858)

Supporting material: machine-readable table

1. Introduction

Gamma-ray burst (GRB) emission exhibits significant variability and spectral evolution. The prompt emission light curves typically have irregular, multipulse temporal profiles, in some cases having a complex structure (e.g., Norris et al. 1996, 2005). The emission spectrum typically changes from having both large spectral peak energies and hard spectral slopes below the peak (so-called hard spectra) to having lower peak energies and softer spectral slopes (soft spectra). Such variations occur both within individual pulse structures and as an overall trend during the burst (Mazets et al. 1982; Ford et al. 1995; Crider et al. 1997).

Within the fireball model of GRBs, there are two main emission sources for the prompt gamma rays. The first is radiation from where the jet becomes transparent, namely, the photosphere region (e.g., Goodman 1986; Rees & Mészáros 2005; Pe'er et al. 2006a). The second is radiation from a region at a larger distance from the progenitor, where the kinetic energy of the jet is dissipated and radiated away in the form of synchrotron emission (e.g., Piran et al. 1993; Sari et al. 1998; Lloyd & Petrosian 2000). The timescale for the gamma-ray emission, relative to the launching of the jet, depends on the distances to the different emission sites, r_γ, and the Lorentz factor of the jet, Γ, according to $t_\gamma = r_\gamma/(c\Gamma^2)$, where c is the speed of light. For the typical outflow parameters, the photosphere is expected to occur at $r_\gamma^{\rm ph} \sim 3 \times 10^{12}$ cm, while the synchrotron emission is expected at larger radii, for instance, $r_\gamma^{\rm IS} \sim 10^{13}$ cm for internal shocks and $r_\gamma^{\rm ES} \sim 10^{17}$ cm for external shocks (e.g., Rees & Mészáros 1998).

Therefore, a central engine activity will first be observed by its thermal emission and followed by synchrotron emission, with a delay of a few or even hundreds of seconds (Rees & Meszaros 1994). In such a case, one should expect to observe an initial photospheric emission episode followed by synchrotron emission activity.

Alternatively, variations of the jet property, such as the entropy and magnetization (e.g., Rees & Meszaros 1994; Beloborodov 2013; Uhm & Zhang 2014; Zhang 2018; Li 2019a, 2020; Li & Zhang 2021), can cause the variations in the observed emission. For instance, the interaction between the jet and the surrounding material as the jet passes though the progenitor star will cause variable mixing and thereby a change in the entropy of the flow (Lazzati et al. 2009; López-Cámara et al. 2014; Ito et al. 2015). This directly affects the properties of the observed emission, since the entropy determines the position of the photosphere, $r_{\rm ph}$, relative to the saturation radius, $r_{\rm s}$ (e.g., Mészáros & Rees 2000). If $r_{\rm ph}/r_{\rm s} \lesssim 1$, a photosphere will dominate the emission,[8] while in the opposite cases, $r_{\rm ph}/r_{\rm s} \gg 1$, the photosphere will be very weak, and only nonthermal emission, such as synchrotron, will be expected. Furthermore, in the case of photospheric emission, the entropy

---

[8] A typical result from an analysis of the photospheric spectra is that the initial radius of the jet is $r_0 \sim$ few $\times\ 10^9$ cm (e.g., Pe'er et al. 2007; Ryde & Pe'er 2009; Iyyani et al. 2015). This is also expected theoretically due to interaction between the jet and the progenitor surrounding it, which prevents the jet from accelerating while it is within the star (e.g., Thompson 2006; Gottlieb et al. 2019). A consequence of this fact is that the saturation radius of the jet $r_{\rm s} = \Gamma r_0 \sim r_{\rm ph}$.

variation will allow for a varying amount of broadening of the spectral shape due to subphotospheric dissipation. The reason is that strong dissipation is not expected below the saturation radius. Therefore, significant spectral broadening of the photospheric spectrum is only expected when $r_{\rm ph}/r_{\rm s} \gtrsim 1$. In this alternative scenario, the evolution of the spectral properties of consecutive pulses is interpreted as variations of properties in the jet.

The two main emission sources can also coexist, giving rise to multicomponent emission spectra (e.g., Ryde 2005; Ryde & Pe'er 2009; Guiriec et al. 2011; Ajello et al. 2020). The observed evolution in spectral shape might then be driven by the relative change in the contribution of the two emission sources in superposition.

In all cases, observed trends and variations among pulses carry important clues to the physics of GRBs. The multipulse nature indicates a continuous ejection from the progenitor, implying that (i) it is not destroyed immediately, (ii) the variation in flux between pulses represents the variation of the available energy, and (iii) the time difference between the pulses represents some characteristic internal time, possibly the fallback time of the material or accretion into the surface of the newly formed neutron star until it reaches a critical mass and reexplodes. In this paper, we therefore analyze a sample of multipulse bursts in order to investigate whether there is any variation in spectral characteristics depending on the sequel position among pulses within a burst. In particular, we examine the spectral shape, correlations between spectral parameters, and compatibility with photospheric emission. Our sample is obtained from the first 11 yr of the Fermi Gamma-ray Burst Monitor (GBM) operation, consisting of 117 well-separated pulses and 1228 spectra from 39 bursts.

The paper is organized as follows. The methods are presented in Section 2. The detailed observational properties are summarized in Section 3. In Section 4, we present an assessment of the compatibility with emission models. The discussion and summary are presented in Sections 5 and 6, respectively. Throughout the paper, the standard ΛCDM cosmology with the parameters $H_0 = 67.4\,{\rm km\,s^{-1}\,Mpc^{-1}}$, $\Omega_M = 0.315$, and $\Omega_\Lambda = 0.685$ are adopted (Planck Collaboration et al. 2020).

2. Methodology

2.1. Initial Burst Selection

We use data obtained by the Fermi Gamma-ray Space Telescope, which was launched in 2008, and carries two instruments: the GBM (Meegan et al. 2009) and the Large Area Telescope (LAT; Atwood et al. 2009). Together, they cover an energy range from a few keV to a few hundred GeV. The GBM harbors 14 detectors, of which 12 are sodium iodide (NaI; 8 keV–1 MeV) and two are bismuth germanate (BGO; 200 keV–40 MeV) scintillators. By 2019 June, Fermi had completed 11 yr of operation, and at least 2388 GRBs had been observed.

Among these bursts, we want to identify the ones that have at least two individual emission episodes, which can be assumed to be independent from each other. Since there is no theoretical prediction of the shape and form of individual emission episodes, we choose to make a general definition for our selection, which does not limit the sample to smooth pulses only. Indeed, numerical simulations of jet emission propagating through the progenitor star show that not only smooth pulses

are expected but also more complex morphologies (Lazzati et al. 2009; López-Cámara et al. 2014). This choice also avoids omitting too many bursts. Following Yu et al. (2019), we thus allow subdominant variations on top of the main pulse structures. In addition, we also include emission activities with many smaller spikes but whose heights are limited by an approximate pulse-shaped envelope. The pulse-shaped envelope indicates that such emission could be connected, in spite of its large variability. Examples of the light curves that are selected for the sample are shown in Section 3.2 and the Appendix.

We first visually inspected the time-tagged event (TTE) light curves from each of the 2388 GRBs obtained from NASA/HEASARC.[9] We identified more than 120 bursts that had at least two clear emission episodes. The light curves exhibit diverse temporal properties. Some have a precursor-like pulse followed by a main pulse, while others exhibit a main pulse followed by a small pulse, and yet others consist of several pulses with similar strength. Many of the pulses are well separated by quiescent intervals, while others have a slight temporal overlap.

2.2. Detector, Source, and Background Selections

We use the standard selection criteria adopted in GBM catalogs (Goldstein et al. 2012; Gruber et al. 2014; Yu et al. 2016). Following the common practice, we choose the triggered detectors that have a viewing angle of less than 60° (Goldstein et al. 2012). Typically, one to three NaI and one BGO detector are selected. The period of GRB emission that is considered is in most cases somewhat longer than the T_{90} reported in the HEASARC database. This is done so that all relevant features in the light curve can be incorporated. In order to determine the background emission, we select one interval located tens of seconds before the triggered time and one interval located tens of seconds after the emission has ended. We fit the background photon count level with a polynomial function, which typically has an order lower than 4. The optimal order is determined through a likelihood ratio test. The polynomial is applied to fit all 128 energy channels and then interpolated into the pulse interval to yield the background photon count estimate. In a few bursts, there are several pulses that are separated by long quiescent intervals. In these cases, we select three background intervals to better constrain the background levels (e.g., GRB 140810782). The spectral energy range is set from 10 to 900 keV for the NaI detectors and 300 keV to 30 MeV for the BGO detectors. In order to avoid the K-edge at 33.17 keV, we ignore the range 30–40 keV.

2.3. Light-curve Binning

In order to follow and study spectral evolution in individual bursts, detailed time-resolved spectroscopy is needed (see, e.g., Crider et al. 1997; Kaneko et al. 2006; Goldstein et al. 2012). The question is then how to divide the light curve into time bins, since this choice might affect the results. Foremost, it is important to minimize the amount of variation of the emission during a time bin, since such variations will obscure the intrinsic spectral shape. A method to account for this is to identify Bayesian blocks (BBlocks) in the light curve (Scargle et al. 2013). Therefore, we apply the BBlock method with a false-alarm probability $p_0 = 0.01$ to the TTE light curve of the

---

[9] https://heasarc.gsfc.nasa.gov/W3Browse/fermi/fermigbrst.html

brightest NaI detector (see Li 2019a; Yu et al. 2019, for further details). This binning is then used for the other detectors as well.

The BBlock method will create time bins that have varied signal-to-noise ratios. Therefore, some time bins will not have enough signal for a fit to be reliable. A suitable measure of the signal-to-noise ratio is the statistical significance S.[10] Dereli-Bégué et al. (2020) demonstrated that to fully determine the spectral shape, a value of $S = 15$–20 is needed. In particular, this ensures that the model parameters converge properly (see also, e.g., Vianello et al. 2018; Li 2019a, 2019b; Ryde et al. 2019). We therefore follow this recommendation and only select the BBlock time bins that have $S \geqslant 20$.

This specific selection thus provides time bins during which (i) there is no significant spectral evolution and (ii) there is highly significant data. Such spectra are Required in order to make firm inferences on the intrinsic emission spectrum. However, a consequence of this selection is that intervals with rapid variations will be dismissed. This is often the case for the rise phase of pulses, which could carry particular information about the emission process (see further discussion in Section 5.2). A possibility of incorporating these dismissed intervals would be to perform joint fits of many intervals at the same time by assuming a prescription of the spectral evolution. This would increase the statistical significance while maintaining the temporal resolution. However, since further assumptions need to be made on the spectral evolution (e.g., Ryde & Svensson 1999), such studies are deferred to other publications.

2.4. Sample (Pulse) Definition

The purpose of this study is to relate the emission properties between pulses within a burst. We therefore only consider bursts that have multiple distinguishable pulses. One of the properties that we will relate is the spectral evolution during the individual pulses. Hence, in order to include a pulse in the study, it needs to have at least four time bins with $S \geqslant 20$ ($N_{(S \geqslant 20)} \geqslant 4$). This allows one to determine the spectral evolution and the correlation between spectral parameters. Our final selection criterion is, therefore, that the burst should have at least two such pulses. This criterion strongly reduces the sample size. However, the pulses that pass the criterion will provide well-determined spectra and evolution characteristics. This final selection yields a sample of 39 bursts. From these, we obtain 117 pulses and 1228 time-resolved spectra, of which 103 pulses have $N_{(S \geqslant 20)} \geqslant 4$, consisting of 944 spectra.

The properties of our sample are summarized in Table 1 and include the Fermi/GBM ID (column 1), redshift (column 2), and observed duration t_{90} (column 3), together with the used detectors (column 4), the selected source and background intervals (columns 5 and 6), the number of total (column 7) and used ($S \geqslant 20$; parentheses in column 7) BBlock time bins, and the

number of total (column 8) and used (parentheses in column 8) pulses for each burst. The detector in parentheses is the brightest one, used for the BBlocks and background determinations.

Inevitably, there will be some overlap between many of the pulses. During such periods, emission from both pulses will be present, and the observed spectrum will be a superposition of two spectra. Depending on their mutual strengths, a fit with a single spectral component might give misleading results. We therefore group the pulses in the 39 bursts into three subsamples.

1. *Gold.* No overlap, and the pulses are completely independent. There are 13 such pulses, which are listed in Table 2 (column 5).
2. *Silver.* Slight overlap. There are 90 such pulses (column 5 in Table 2).
3. *Bronze.* Pulses that have less than four time bins $S \geqslant 20$. There are 14 such pulses (column 5 in Table 2). Note that these pulses are not used in our final statistical analysis.

2.5. Spectral Fitting

The physical model of the GRB spectra is not yet firmly established. Likewise, the possible regimes of the suggested emission models are not clarified. Therefore, empirical models are typically used in the analysis. This offers the flexibility to explore many different models and, at the same time, to explore the models without limiting certain spectral regimes. The typically used functions are the Band function, which is a broken power-law function, and the cutoff power-law (CPL) function (Band et al. 1993; Gruber et al. 2014). Another advantage of these empirical models is that they are used in all catalogs mapping the behavior and characteristics of observed bursts.

However, the empirical models do not necessarily correspond to the underlying physical model (e.g., Lloyd-Ronning & Petrosian 2002; Burgess 2014; Acuner et al. 2019). Therefore, the empirical parameter values that are inferred from the data cannot be directly translated into physical model parameters. However, the way the physical model parameters map onto the Band parameters has been established for a few emission models (e.g., Lloyd & Petrosian 2000; Acuner et al. 2019; see also Section 4). Moreover, Acuner et al. (2020) showed that the values of, e.g., α can be used to decisively distinguish between various types of emission models, as long as the data have a high signal strength (as is the case in the present study).

We will therefore make use of these empirical functions. The Band function is defined by the low-energy power-law index (α) and the high-energy index (β), which are connected smoothly around the break energy (E_0).

The photon number spectrum is defined as

$$f_{\text{Band}}(E) = A \begin{cases} \left(\dfrac{E}{E_{\text{piv}}}\right)^{\alpha} \exp\left(-\dfrac{E}{E_0}\right), & E \leqslant (\alpha - \beta)E_0 \\[2em] \left[\dfrac{(\alpha - \beta)E_0}{E_{\text{piv}}}\right]^{(\alpha - \beta)} \exp(\beta - \alpha)\left(\dfrac{E}{E_{\text{piv}}}\right)^{\beta}, & E \geqslant (\alpha - \beta)E_0 \end{cases} . \tag{1}$$

The energy of the spectral peak of the νF_{ν} spectrum (assuming $\beta < -2$) is in units of keV,

$$E_{\text{p}} = (2 + \alpha)E_0, \tag{2}$$

---

[10] The statistical significance, S, is suitable for data with Poisson sources with Gaussian backgrounds, which is the case for GBM data (Vianello et al. 2018).

Table 1
Global Properties of the Sample

GRB	z	T_{90} (s)	Detectors	$\Delta T_{\rm src}$ (s)	$[\Delta T_{\rm (bkg,1)}, \Delta T_{\rm (bkg,2)}]$ (s)	Spectra ($N_{S \geqslant 20}$) (Number)	Pulse ($N_{(S \geqslant 20)} \geqslant 4$) (Number)
(1)	(2)	(3)	(4)	(5)	(6)	(7)	(8)
081009140	⋯	41.345 ± 0.264	(n3)b1	−1.0 to 52.0	[−20 to 10, 80 to 100]	23(21)	2(2)
081215784	⋯	5.568 ± 0.143	n9(na)nbb1	−1.0 to 10.0	[−30 to 10, 40 to 60]	27(22)	3(3)
090131090	⋯	35.073 ± 1.056	(n9)nab1	−1.0 to 40.0	[−20 to 10, 60 to 80]	30(16)	3(2)
090618353	0.54	112.386 ± 1.086	(n4)b0	−1.0 to 150.0	[−20 to 10, 200 to 220]	28(25)	3(2)
091127976	0.49	8.701 ± 0.571	(n6)n9ab1	−1.0 to 10.0	[−20 to 10, 50 to 100]	21(17)	3(3)
100719989	⋯	21.824 ± 1.305	(n4)n5b0	−1.0 to 25.0	[−30 to 20, 60 to 100]	18(12)	3(3)
100826957	⋯	84.993 ± 0.724	n7n8b1	−1.0 to 120.0	[−20 to 10, 200 to 250]	31(26)	3(3)
101014175	⋯	449.415 ± 1.409	n6(n7)b1	−1.0 to 230.0	[−30 to 10, 300 to 320]	110(81)	6(5)
110301214	⋯	5.693 ± 0.362	n7(n8)nbb1	−1.0 to 10.0	[−20 to 10, 40 to 60]	16(14)	2(2)
110625881	⋯	26.881 ± 0.572	n7n8(nb)b1	−1.0 to 32.0	[−20 to 10, 80 to 100]	37(28)	4(3)
120129580	⋯	3.072 ± 0.362	(n8)b1	−1.0 to 4.0	[−20 to 10, 80 to 100]	17(17)	2(2)
120328268	⋯	29.697 ± 1.056	n7n9(nb)b1	−1.0 to 40.0	[−20 to 10, 60 to 80]	23(20)	3(3)
120711115	1.405	44.033 ± 0.724	(n2)nab0	−1.0 to 120.0	[−20 to 10, 150 to 160]	30(25)	2(2)
120728434	⋯	100.481 ± 6.623	n1(n2)b0	−1.0 to 100.0	[−20 to 10, 200 to 220]	42(36)	2(2)
121225417	⋯	58.497 ± 0.820	(n1)n3n5b0	−1.0 to 75.0	[−30 to 10, 100 to 120]	26(19)	2(2)
130504978	⋯	73.217 ± 2.111	n2(n9)nab1	−1.0 to 84.0	[−50 to 10, 200 to 220]	51(43)	6(4)
130606497	⋯	52.225 ± 0.724	n7(n8)b1	−1.0 to 63.0	[−40 to 20, 100 to 120]	43(40)	4(4)
131014215	⋯	3.200 ± 0.091	n9na(nb)b1	−1.0 to 6.0	[−50 to 10, 50 to 80]	29(29)	2(2)
131127592	⋯	18.176 ± 0.724	n1n2(n5)b0	−1.0 to 22.0	[−20 to 10, 40 to 60]	30(22)	5(4)
140206275	2.73	146.690 ± 4.419	n0(n1)n3b0	−1.0 to 50.0	[−40 to 20, 70 to 90]	23(17)	2(2)
140213807	1.2076	18.624 ± 0.716	n0(n1)n2b0	−1.0 to 15.0	[−20 to 10, 40 to 60]	15(11)	2(2)
140416060	⋯	31.744 ± 1.280	(n2)b0	−1.0 to 30.0	[−20 to 10, 60 to 80]	31(26)	4(4)
140508128	1.027	44.288 ± 0.231	(na)b1	−1.0 to 52.0	[−20 to 10, 70 to 80]	40(17)	3(2)
140523129	⋯	19.200 ± 0.362	(n3)n4n5b0	−1.0 to 25.0	[−20 to 10, 40 to 60]	41(26)	5(4)
140810782	⋯	81.665 ± 0.572	n2(n5)b0	−1.0 to 102.0	[−110 to 90, 150 to 170, 250 to 270]	33(16)	4(3)
141222691	⋯	34.049 ± 0.724	n9na(nb)b1	−1.0 to 40.0	[−20 to 10, 60 to 80]	18(12)	3(3)
150118409	⋯	40.193 ± 0.572	n1(n2)n5b0	−1.0 to 55.0	[−50 to 30, 80 to 100]	43(29)	3(3)
150201574	⋯	15.616 ± 0.362	(n3)n4n7b0	−1.0 to 20.0	[−20 to 10, 40 to 60]	25(24)	2(2)
150330828	⋯	153.859 ± 0.810	n1(n2)n5b0	−1.0 to 180.0	[−50 to 20, 50 to 60, 220 to 240]	40(34)	3(3)
151231443	⋯	71.425 ± 0.724	(n8)nbb1	−1.0 to 80.0	[−20 to 10, 40 to 50]	23(9)	2(2)
160422499	⋯	12.288 ± 0.362	n0(n1)n5b0	−1.0 to 15.0	[−20 to 10, 40 to 60]	22(22)	3(3)
160802259	⋯	16.384 ± 0.362	(n2)b0	−1.0 to 20.0	[−20 to 10, 60 to 80]	27(22)	3(3)
170207906	⋯	38.913 ± 0.572	n1(n2)n5b0	−1.0 to 42.0	[−20 to 10, 60 to 80]	33(17)	4(4)
171120556	⋯	44.062 ± 0.383	n0n1(n3)b0	−1.0 to 48.0	[−20 to 10, 60 to 80]	21(9)	2(2)
171227000	⋯	37.633 ± 0.572	(n5)b0	−1.0 to 60.0	[−50 to 10, 60 to 100]	43(40)	3(3)
180113418	⋯	24.576 ± 0.362	n1(n2)n9b0	−1.0 to 40.0	[−20 to 10, 60 to 80]	25(22)	2(2)
180120207	⋯	28.928 ± 0.724	n9na(nb)b1	−1.0 to 50.0	[−20 to 10, 60 to 80]	24(20)	2(2)
180722993	⋯	86.530 ± 1.056	n1(n2)b0	−1.0 to 110.0	[−20 to 10, 120 to 140]	18(10)	2(2)
190114873	0.425	116.354 ± 2.563	n3(n4)n7b0	−1.0 to 110.0	[−20 to 10, 180 to 200]	51(48)	3(3)

Note. Fermi burst ID (column 1), redshift (column 2), and t_{90} (column 3), together with the detectors (column 4), source (column 5) and background (column 6) intervals, total (column 7) and effective ($S \geqslant 20$; parentheses in column 7) time bins using the BBlocks across the source intervals, and the number of total (column 8) and used (parentheses in column 8) pulses for each burst. Note that the detector in parentheses is the brightest one, used for BBlocks and background fitting.

A is the normalization factor at 100 keV in units of ph cm^{-2} keV^{-1} s^{-1}, $E_{\rm piv}$ is the pivot energy fixed at 100 keV, and α and β are the low- and high-energy power-law photon spectral indices, respectively.

The CPL function is given by

$$f_{\rm CPL}(E) = A \left(\frac{E}{E_{\rm piv}}\right)^{\alpha} \exp\left(-\frac{E}{E_c}\right). \quad (3)$$

Note that the CPL model approaches the Band model as β tends to $-\infty$. The peak energy $E_{\rm p}$ of the νF_{ν} spectrum is related to E_c through $E_{\rm p} = (2+\alpha)E_c$.

The analysis in this work is performed with the Multi-Mission Maximum Likelihood Framework (3ML; Vianello et al. 2015), and we use a Bayesian approach, using the Markov Chain Monte Carlo (MCMC) method (e.g., Foreman-Mackey et al. 2013). We use the typical spectral parameters obtained from the previous Fermi/GBM catalog as the prior information of the Bayesian inference.

For the Band model,

$$\begin{cases} A \sim \log\mathcal{N}(\mu = 0, \sigma = 2) & {\rm cm}^{-2}\ {\rm keV}^{-1}\ {\rm s}^{-1} \\ \alpha \sim \mathcal{N}(\mu = -1, \sigma = 0.5) \\ \beta \sim \mathcal{N}(\mu = -2, \sigma = 0.5) \\ E_{\rm p} \sim \log\mathcal{N}(\mu = 2, \sigma = 1) & {\rm keV} \end{cases}, \quad (4)$$

and for CPL model,

$$\begin{cases} A \sim \log\mathcal{N}(\mu = 0, \sigma = 2) & {\rm cm}^{-2}\ {\rm keV}^{-1}\ {\rm s}^{-1} \\ \alpha \sim \mathcal{N}(\mu = -1, \sigma = 0.5) \\ E_{\rm c} \sim \log\mathcal{N}(\mu = 2, \sigma = 1) & {\rm keV}. \end{cases} \quad (5)$$

Table 2
Pulsewise Properties of the Sample

GRB (1)	Pulse (2)	ΔT_{src} (s) (3)	$N_{tot}(N_{S\geq20})$ (Number) (4)	Pulse (Grade) (5)	Spectral Model (Preferred) (6)	Physical Model (Preferred) (7)	E_p (Evolution) (8)	α (Evolution) (9)	$F - \alpha$ Type (r) (10)	$F - E_p$ Type (r) (11)	$\alpha - E_p$ Type (r) (12)
081009140	P_1	0.0 to 10.0	18(15)	Gold	Band	Above SCS line	f.-t.	f.-t.	2p(0.11)	1p(0.41)	3(−0.55)
081009140	P_2	35.0 to 52.0	10(6)	Gold	CPL	Above SCS line	f.-t.	h.-t.-s.	1n(−0.83)	3(0.20)	1p(−0.03)
081215784	P_1	−1.0 to 2.9	10(8)	Silver	Band	Ph	h.-t.-s.	f.-t.	1p(0.69)	2p(0.50)	2p(−0.12)
081215784	P_2	2.9 to 4.4	5(5)	Silver	CPL	Above SCS line	f.-t.	f.-t.	1p(0.70)	1p(0.70)	3(0.20)
081215784	P_3	4.4 to 10.0	12(9)	Silver	Band	Ph	f.-t.	f.-t.	1p(0.90)	1p(1.00)	1p(0.90)
090131090	P_1	0 to 5.5	7(2)	Bronze	CPL	Above SCS line	...	...	...	...	...
090131090	P_2	5.5 to 10	10(6)	Silver	Band	*	h.-t.-s.	f.-t.	1p(0.83)	1p(0.77)	1p(0.37)
090131090	P_3	22.0 to 40	13(8)	Silver	Band	*	h.-t.-s.	f.-t.	1p(0.75)	1n(−0.14)	1n(−0.29)
090618353	P_1	−1.0 to 48.0	5(2)	Bronze	Band	Above SCS line	...	...	...	...	...
090618353	P_2	48.0 to 75.5	11(11)	Silver	Band	*	f.-t.	f.-t.	3(0.03)	1p(0.79)	1n(−0.17)
090618353	P_3	75.5 to 102	12(12)	Silver	Band	*	f.-t.	f.-t.	3(−0.21)	1p(0.85)	1n(−0.55)
091127976	P_1	−1 to 1.1	7(6)	Silver	Band	Ph	h.-t.-s.+f.-t.	f.-t.	1p(0.77)	3(−0.31)	1n(−0.43)
091127976	P_2	1.1 to 5.0	7(7)	Silver	CPL	*	f.-t.	f.-t.	3(0.28)	1p(0.54)	1n(−0.43)
091127976	P_3	5.0 to 10.0	7(4)	Silver	Band	*	f.-t.	f.-t.	1p(−0.40)	1p(0.80)	1p(0.20)
100719989	P_1	0.0 to 3.2	6(4)	Silver	CPL	Ph	f.-t.	h.-t.-s.	2p(−0.80)	1p(0.80)	1n(−0.40)
100719989	P_2	3.2 to 8.0	8(7)	Silver	Band	Ph	f.-t.	f.-t.	1n(0.82)	1p(0.75)	2p(0.54)
100719989	P_3	20 to 25	4(1)	Bronze	CPL	*	...	...	...	...	...
100826957	P_1	−1.0 to 58.0	20(16)	Silver	Band	Ph	f.-t.	h.-t.-s.	2p(0.19)	2n(0.77)	1n(−0.31)
100826957	P_2	58.0 to 71.0	5(4)	Silver	Band	*	h.-t.-s.	h.-t.-s.	1p(−0.20)	1p(1.00)	1n(−0.20)
100826957	P_3	71 to 120	6(6)	Silver	CPL	*	h.-t.-s.	h.-t.-s.	1p(0.29)	1p(0.77)	1n(0.55)
101014175	P_1	0.0 to 16.0	35(31)	Silver	Band	Ph	h.-t.-s.	h.-t.-s.	1p(0.82)	1p(0.48)	1p(0.16)
101014175	P_2	16.0 to 31.2	25(17)	Silver	CPL	*	f.-t.	f.-t.	1p(0.64)	1p(0.73)	1p(0.12)
101014175	P_3	31.2 to 40.0	9(7)	Silver	CPL	*	f.-t.	f.-t.	1p(0.96)	1p(0.39)	1p(0.43)
101014175	P_4	99.2 to 120.0	10(8)	Gold	CPL	*	h.-t. to s.-t.-h.	h.-t. to s.-t.-h.	3(0.18)	3(−0.62)	1p(0.22)
101014175	P_5	155.0 to 168.0	9(3)	Bronze	CPL	*	...	...	...	...	...
101014175	P_6	197.9 to 220.1	22(15)	Silver	Band	*	f.-t.	f.-t.	1p(0.82)	1p(0.36)	1n(0.24)
110301214	P_1	−1.0 to 3.5	7(6)	Silver	Band	Above SCS line	f.-t.	f.-t.	1p(−0.71)	3(0.49)	1n(−0.26)
110301214	P_2	3.5 to 10.0	9(8)	Silver	CPL	*	h.-t.-s.	h.-t.-s.	1n(0.86)	1p(0.95)	1p(0.81)
110625881	P_1	−1.0 to 9.7	8(3)	Bronze	CPL	Ph	...	...	...	...	...
110625881	P_2	9.7 to 20.0	11(8)	Silver	Band	Ph	h.-t.-s.	f.-t.	1p(0.95)	2p(0.48)	2p(0.41)
110625881	P_3	20.0 to 26.0	8(8)	Silver	Band	Above SCS line	f.-t.	f.-t.	1p(0.57)	1p(0.81)	1p(0.29)
110625881	P_4	26 to 32.0	10(9)	Silver	Band	Above SCS line	f.-t.	f.-t.	1p(0.56)	1p(0.90)	1p(0.24)
120129580	P_1	0.0 to 2.5	10(10)	Silver	Band	Above SCS line	f.-t.	Flat	3(0.07)	1p(0.96)	2n(−0.10)
120129580	P_2	2.5 to 4.0	7(7)	Silver	CPL	Above SCS line	f.-t.	f.-t.	1p(0.95)	1p(0.04)	1p(−0.09)
120328268	P_1	−1.0 to 16.5	9(7)	Silver	Band	Above SCS line	h.-t.-s.	f.-t.	1p(0.56)	3(0.32)	1n(−0.02)
120328268	P_2	16.5 to 25.0	7(7)	Silver	Band	Above SCS line	f.-t.	f.-t.	1p(0.89)	3(0)	1n(−0.39)
120328268	P_3	25.0 to 40.0	7(6)	Silver	Band	*	h.-t.-s.	f.-t.	3(−0.03)	3(0.77)	1n(−0.60)
120711115	P_1	60.0 to 85.0	9(8)	Silver	CPL	*	h.-t.-s.+f.-t.	h.-t.-s.	1p(0.86)	3(0.24)	2n(0.17)

Table 2
(Continued)

GRB (1)	Pulse (2)	ΔT_{src} (s) (3)	$N_{tot}(N_{S\geq20})$ (Number) (4)	Pulse (Grade) (5)	Spectral Model (Preferred) (6)	Physical Model (Preferred) (7)	E_p (Evolution) (8)	α (Evolution) (9)	$F-\alpha$ Type (r) (10)	$F-E_p$ Type (r) (11)	$\alpha-E_p$ Type (r) (12)
120711115	P_2	85.0 to 120.0	21(17)	Silver	Band	*	f-t.	f-t.	1p(0.44)	1p(0.81)	2p(0)
120728434	P_1	−1.0 to 65.0	26(23)	Silver	Band	Ph	f-t.	Chaotic	1n(−0.66)	2p(0.83)	1n(−0.90)
120728434	P_2	65.0 to 100.0	16(13)	Silver	Band	Ph	h-t-s.	Chaotic	1n(−0.31)	1p(0.65)	1n(−0.88)
121225417	P_1	−1.0 to 40.0	13(6)	Silver	Band	*	f-t.	h-t-s.	1p(0.26)	1p(0.77)	2p(0.14)
121225417	P_2	40.0 to 75.0	13(13)	Silver	Band	Ph	h-t-s.	h-t-s.	1p(0.54)	1p(0.62)	1p(0.01)
130504978	P_1	−1.0 to 22.0	11(9)	Silver	Band	*	h-t-s.	f-t.	1p(0.62)	1p(−0.27)	1p(−0.02)
130504978	P_2	22.0 to 45.0	15(15)	Silver	Band	*	f-t.	f-t.	1p(0.64)	1p(0.60)	1p(0.06)
130504978	P_3	45.0 to 59.0	5(3)	Bronze	CPL	*	...	...	...	...	...
130504978	P_4	59.0 to 65.3	5(5)	Silver	CPL	*	f-t.	f-t.	1p(0.74)	3(−0.19)	3(−0.74)
130504978	P_5	65.3 to 74.0	10(9)	Silver	CPL	Above SCS line	f-t.	f-t.	1p(0.95)	1p(0.37)	1p(0.25)
130504978	P_6	74.0 to 84.0	5(2)	Bronze	CPL	*	...	...	...	...	...
130606497	P_1	−1.0 to 12.0	13(11)	Silver	Band	Above SCS line	f-t.	f-t.	1n(−0.59)	1p(0.80)	1n(−0.84)
130606497	P_2	12.0 to 24.0	12(12)	Silver	Band	*	f-t.	h-t-s.	1p(0.64)	1p(0.88)	2n(0.46)
130606497	P_3	24.0 to 43.0	10(10)	Silver	Band	Above SCS line	f-t.	f-t.	1p(0.43)	1p(0.36)	1n(−0.57)
130606497	P_4	43.0 to 63.0	8(7)	Silver	CPL	Above SCS line	h-t-s.	f-t.	1p(0.96)	1p(0.93)	1p(0.82)
131014215	P_1	−1.0 to 2.45	15(15)	Silver	Band	Ph	f-t.	f-t.	1n(−0.30)	1p(0.66)	1f(−0.09)
131014215	P_2	2.45 to 6.0	14(14)	Silver	Band	Ph	f-t.	h-t-s.	1p(0.74)	1p(0.94)	1p(0.71)
131127592	P_1	0.0 to 5.0	5(4)	Silver	CPL	*	f-t.	f-t.	3(0.40)	1p(1.00)	1f(0.40)
131127592	P_2	5.0 to 8.5	7(7)	Silver	Band	*	f-t.	f-t.	1p(0.64)	1p(0.93)	1p(0.54)
131127592	P_3	8.5 to 11.0	4(4)	Silver	CPL	*	h-t-s.	h-t-s.	1p(1.00)	3(1.00)	2p(1.00)
131127592	P_4	11.0 to 15.5	5(2)	Bronze	CPL		...	...	...	...	...
131127592	P_5	15.5 to 22.0	9(5)	Silver	Band	Above SCS line	f-t.	f-t.	1p(0.70)	3(0.60)	1n(−0.10)
140206275	P_1	−1.0 to 26.0	15(11)	Silver	Band	Ph	h-t-s.	f-t.	1p(0.62)	2p(0.35)	2p(−0.10)
140206275	P_2	26.0 to 50.0	8(6)	Silver	CPL	*	h-t-s.	f-t.	1p(0.89)	1p(0.89)	1p(0.83)
140213807	P_1	−1.0 to 5.0	6(4)	Silver	Band	Above SCS line	f-t.	f-t.	1p(−0.30)	2p(0.90)	2p(−0.60)
140213807	P_2	5.0 to 15.0	9(7)	Silver	Band	Above SCS line	f-t.	f-t.	1p(0.90)	1p(0.94)	1p(0.81)
140416060	P_1	−1.0 to 6.0	6(4)	Silver	Band	Ph	f-t.	h-t-s.	1p(0.80)	3(0.20)	1n(−0.40)
140416060	P_2	6.0 to 12.0	12(11)	Silver	Band	Above SCS line	h-t-s.	f-t.	1p(0.22)	1p(0.38)	2p(−0.71)
140416060	P_3	12.0 to 21.0	5(4)	Silver	Band	*	f-t.	h-t-s.	3(0.60)	1p(0.80)	1p(0)
140416060	P_4	21.0 to 30.0	10(8)	Gold	Band	*	f-t.	f-t.	1n(−0.36)	1p(0.86)	1n(0)
140508128	P_1	−1 to 12	16(10)	Gold	Band	Ph	f-t.	f-t.	1p(0.89)	1p(0.42)	2p(0.09)
140508128	P_2	23 to 29	12(4)	Gold	CPL	Ph	h-t-s.	h-t-s.	1p(1.00)	1p(0.60)	1p(0.60)
140508128	P_3	36 to 42	12(3)	Bronze	CPL	*	...	...	...	...	...
140523129	P_1	−1.0 to 2.5	4(4)	Silver	Band	Ph	f-t.	f-t.	3(0.60)	1p(0.80)	2p(0)
140523129	P_2	2.5 to 6.8	11(6)	Silver	CPL	Ph	f-t.	f-t.	1p(0.71)	3(−0.43)	1n(−0.60)
140523129	P_3	6.8 to 12.0	10(6)	Silver	Band	Ph	h-t-s.	h-t-s.	1p(0.49)	1p(0.71)	2n(−0.26)
140523129	P_4	12.0 to 15.0	4(1)	Bronze	CPL	*	...	...	...	...	...
140523129	P_5	15.0 to 25.0	16(10)	Silver	Band	Ph	h-t-s.	f-t.	1p(0.82)	1p(0.53)	1p(0.28)

Table 2
(Continued)

GRB (1)	Pulse (2)	ΔT_{src} (s) (3)	$N_{tot}(N_{S\geq20})$ (Number) (4)	Pulse (Grade) (5)	Spectral Model (Preferred) (6)	Physical Model (Preferred) (7)	E_p (Evolution) (8)	α (Evolution) (9)	$F - \alpha$ Type (r) (10)	$F - E_p$ Type (r) (11)	$\alpha - E_p$ Type (r) (12)
140810782	P_1	−1.0 to 20.0	11(1)	Silver	CPL	*	...	...	...	...	...
140810782	P_2	20.0 to 29.0	7(4)	Silver	CPL	Above SCS line	f.-t.	h-t.-s.	3(0.52)	1p(0.94)	1n(0.44)
140810782	P_3	29 to 41.0	6(6)	Silver	Band	Above SCS line	f.-t.	f.-t.	1p(0.37)	1p(1.00)	1p(0.37)
140810782	P_4	41.0 to 55.0	9(5)	Silver	Band	Ph	f.-t.	f.-t.	1p(0.20)	1p(0.70)	1n(−0.50)
141222691	P_1	−1.0 to 12.0	7(5)	Silver	Band	Ph	h-t.-s.	f.-t.	1p(0.30)	2p(0.20)	1n(−0.70)
141222691	P_2	12.0 to 30.0	7(6)	Silver	Band	*	f.-t.	h-t.-s.	1p(0.71)	1p(0.26)	1p(−0.20)
141222691	P_3	30 to 40	4(1)	Bronze	CPL	*	...	...	...	...	...
150118409	P_1	−1.0 to 19.8	19(14)	Silver	Band	Above SCS line	f.-t.	f.-t.	1p(0.62)	1p(0.84)	1n(0.20)
150118409	P_2	19.8 to 40.0	12(9)	Silver	Band	Above SCS line	f.-t.	f.-t.	1p(0.75)	1p(0.97)	1p(0.65)
150118409	P_3	40.0 to 55.0	13(6)	Gold	Band	Above SCS line	f.-t.	h-t.-s.	1p(0.71)	1p(0.20)	1p(−0.09)
150201574	P_1	−1.0 to 4.0	9(8)	Silver	Band	Ph	f.-t.	f.-t.	1p(0.79)	3(0.38)	3(0.02)
150201574	P_2	4.0 to 20.0	16(16)	Silver	Band	Ph	f.-t.	f.-t.	1p(0.89)	1p(0.97)	1p(0.82)
150330828	P_1	−1.0 to 10.0	6(4)	Gold	Band	Ph	h-t.-s.	s.-t.-h.	1n(−0.40)	3(0.40)	1n(−1.00)
150330828	P_2	100.0 to 143.0	23(22)	Silver	Band	Above SCS line	f.-t.	f.-t.	1p(0.62)	3(0.43)	1n(−0.02)
150330828	P_3	143.0 to 180.0	11(8)	Silver	Band	*	h-t.-s.	f.-t.	1p(0.71)	3(0.50)	3(0.02)
151231443	P_1	−1.0 to 20.0	12(5)	Gold	Band	Above SCS line	f.-t.	f.-t.	1p(0.50)	1p(1.00)	2p(0.50)
151231443	P_2	60.0 to 80.0	11(4)	Gold	CPL	*	f.-t.	s.-t.-h.	1p(0.74)	1p(0.40)	1n(−0.32)
160422499	P_1	−1.0 to 3.8	6(6)	Silver	Band	Ph	f.-t.	h-t.-s.	1f(−0.78)	1p(0.94)	1n(−0.70)
160422499	P_2	3.8 to 7.0	4(4)	Silver	Band	Above SCS line	f.-t.	h-t.-s.	1n(−0.80)	1p(1.00)	1n(−0.80)
160422499	P_3	7.0 to 15.0	12(12)	Silver	Band	*	f.-t.	h-t.-s.	1p(0.83)	1p(0.97)	1p(0.81)
160802259	P_1	−1.0 to 3.5	9(8)	Gold	Band	Ph	h-t.-s.	f.-t.	1p(0.48)	2p(0.92)	2p(0.24)
160802259	P_2	3.5 to 10.0	8(7)	Silver	Band	Ph	h-t.-s.	f.-t.	1p(0.71)	1p(0.89)	1p(0.29)
160802259	P_3	10.0 to 20.0	10(7)	Gold	Band	Ph	h-t.-s.	f.-t.	1p(0.67)	2p(0.93)	2p(0.45)
170207906	P_1	−1.0 to 12.0	13(8)	Silver	Band	Ph	s.-t.-h.	h-t.-s.	1n(−0.06)	1p(0.95)	2p(0.02)
170207906	P_2	12.0 to 20.0	7(3)	Bronze	CPL	Above SCS line	f.-t.	...	...	...	...
170207906	P_3	20.0 to 30.0	13(4)	Silver	CPL	Ph	f.-t.	h-t.-s.	1f(0.40)	3(−0.40)	3(−1.00)
170207906	P_4	30.0 to 42.0	5(2)	Bronze	CPL	*	...	...	...	...	...
171120556	P_1	−1.0 to 2.0	14(5)	Gold	Band	Ph	h-t.-s.	f.-t.	1n(−0.90)	1p(0.90)	1n(−1.00)
171120556	P_2	37.0 to 48	7(4)	Gold	Band	Above SCS line	h-t.-s.	h-t.-s.	1p(0.80)	1p(0.40)	3(0)
171227000	P_1	−1.0 to 24.0	17(17)	Silver	Band	Ph	f.-t.	h-t.-s.	1n(0.06)	1p(0.82)	1n(0.09)
171227000	P_2	24.0 to 35.0	15(15)	Silver	CPL	*	f.-t.	f.-t.	1p(0.45)	1p(0.72)	1p(−0.05)
171227000	P_3	35.0 to 60.0	11(8)	Silver	Band	*	f.-t.	h-t.-s.	1n(0.38)	1p(0.52)	1n(−0.40)
180113418	P_1	−1.0 to 19.6	12(10)	Silver	Band	Above SCS line	h-t.-s.	Flat	1n(−0.19)	1p(0.27)	1n(−0.91)
180113418	P_2	19.6 to 40.0	13(12)	Silver	Band	Ph	f.-t.	s.-t.-h.	1n(−0.89)	1p(0.90)	1n(−0.95)
180120207	P_1	−1.0 to 13.0	10(9)	Silver	CPL	Ph	h-t.-s.	h-t.-s.	1p(0.20)	1p(0.72)	2n(0.53)
180120207	P_2	13.0 to 50.0	14(11)	Silver	Band	Ph	f.-t.	f.-t.	1p(0.32)	1p(0.92)	2n(0.04)
180722993	P_1	−1.0 to 30.0	8(5)	Silver	CPL	Ph	h-t.-s.	f.-t.	3(−0.50)	1p(0.50)	1f(−0.50)

Table 2
(Continued)

GRB (1)	Pulse (2)	ΔT_{src} (s) (3)	$N_{tot}(N_{S \geqslant 20})$ (Number) (4)	Pulse (Grade) (5)	Spectral Model (Preferred) (6)	Physical Model (Preferred) (7)	E_p (Evolution) (8)	α (Evolution) (9)	$F - \alpha$ Type (r) (10)	$F - E_p$ Type (r) (11)	$\alpha - E_p$ Type (r) (12)
180722993	P_2	30.0 to 100.0	10(5)	Silver	CPL	Ph	h.-t.-s.	f.-t.	3(0.10)	1p(0.70)	1f(−0.40)
190114873	P_1	−1.0 to 2.3	12(11)	Silver	Band	Ph	f.-t.	f.-t.	1p(0.96)	3(0.12)	3(−0.05)
190114873	P_2	2.3 to 15.0	24(24)	Silver	Band	Ph	h.-t.-s.	f.-t.	1p(0.93)	1p(−0.04)	1p(−0.22)
190114873	P_3	15.0 to 110.0	15(13)	Silver	Band	*	h.-t.-s.+f.-t.	h.-t.-s.	3(0.76)	1p(−0.36)	1n(−0.21)

Note. Fermi burst ID (column 1), pulse group name (column 2), source interval of each pulse (column 3), total and effective ($S \geqslant 20$) time bins using the BBlocks across the source intervals (column 4), identified grade of pulse (column 5), preferred spectral model indicated by ΔDIC (column 6), preferred physical model (column 7), pulsewise E_p (column 8) and α (column 9) evolution, and type of parameter relation with Spearman's rank coefficient r in parentheses for the gold and silver samples: α–E_p relation (column 10), F–E_p relation (column 11), and F–α relation (column 12). In column 7, we use an asterisk for spectra that have α_{max} above the SCS line and Ph for spectra that are classified as being from the photosphere. Note that Ph implies that the pulse has at least one time bin that is compatible with the photosphere.

A posterior distribution is obtained from the prior distribution and the likelihood that combines the model and the observed data. The best model parameters are estimated from the posterior probability distribution obtained by MCMC sampling. When using MCMC sampling, in order to obtain the steady-state chains of the parameter distributions, the sampling needs to reach a certain number of times; therefore, the first part of the sample that has not reached the steady-state distribution is discarded. Therefore, for each parameter estimation, we take 10,000 MCMC samples and discard the initial 20%. The fitted parameters are estimated by the maximum a posteriori probability (MAP) with uncertainties at the 1σ (68%) Bayesian credible level and based the last 80% of the MCMC samples. We also provide all of the analysis results of each time-resolved spectrum, which includes the best parameter value estimates, covariance matrices, and the statistical information criteria. They can be retrieved at doi:10.5281/zenodo.4746267.

2.6. High-energy Power Law, β, and the Preferred Model Selection

For a majority of time-resolved burst spectra, the CPL model is a sufficient model (e.g., Kaneko et al. 2006; Goldstein et al. 2012; Burgess et al. 2019; Yu et al. 2019). However, in some cases, a high-energy power law significantly improves the fit, indicating a significant flux contribution beyond the spectral peak. In the case of synchrotron emission, the high-energy power law provides information about the particle acceleration and the nature of the shocks, while in the case of photospheric emission, it provides information about the energy dissipation in the emitting region.

In order to determine whether a high-energy power law gives significant improvement in our analysis, we compare the information criteria of the Band and CPL fits. Acuner et al. (2020) showed that the information criteria capture everything important in the fits and that the difference in information criteria can be used in the model comparison. In particular, they showed that a significance of 99% of preferring one model over the other is found for a difference in log evidence greater than 5 (their Equation (6)) and that this corresponds approximately to a difference in information criteria of 10 (further discussion can be found in Acuner 2019). In this work, we therefore adopt the information criterion to compare models, and, following the literature in the field (e.g., Greiner et al. 2016; Yu et al. 2019), we particularly use the deviance information criterion (DIC; Spiegelhalter et al. 2002; Moreno et al. 2013), which is defined as $\text{DIC} = -2\log[p(\text{data}\,|\,\hat{\theta})] + 2p_{\text{DIC}}$, where $\hat{\theta}$ is the posterior mean of the parameters, and p_{DIC} is a term to penalize the more complex model for overfitting (Gelman et al. 2014). We consequently accept the Band function as the preferred model if the difference between the Band's DIC and the CPL's DIC $\Delta\text{DIC} = \text{DIC}_{\text{Band}} - \text{DIC}_{\text{CPL}} > -10$.

For consistency, one needs to use the same empirical model throughout the whole pulse in order to avoid artificial fluctuation due to a change of spectral model (see Yu et al. 2019). Consequently, if one time bin has $\Delta\text{DIC} < -10$, then we use the Band function throughout the pulse. Otherwise, we use the simpler CPL model. Therefore, the pulses that are fitted by a Band function have at least one time bin in which a high-energy power law is significantly detected. The model used for each pulse is listed in column 6 in Table 2.

Among all of the individual time bins, we find that in only 29% (274/944) is $\Delta\text{DIC} < -10$; i.e., the Band function is preferred. For these time bins, a high-energy power law is required by the data (see also Gruber et al. 2014; Yu et al. 2019). For the sequence of pulses, we find the corresponding fractions to be 36% (122/338) for the first pulse P_1, 28% (101/361) for P_2, 22% (34/156) for P_3, 15% (7/46) for P_4, 15% (4/26) for P_5, and 29% (5/17) for P_6. There is only a weak trend, with the first pulse P_1 having the largest fraction.

Turning over to the pulses, we find that 66% (77/117) of them have at least one time bin with $\Delta\text{DIC} < -10$; therefore, the Band function is used for the entire pulse. For the sequence of pulses, we find that the corresponding fractions are 77% (30/39) for P_1, 69% (27/39) for P_2, 63% (15/24) for P_3, 22% (2/9) for P_4, 50% (2/4) for P_5, and 50% (1/2) for P_6. Again, there is only a weak trend, with the first pulse P_1 having a larger fraction.

In addition to the ΔDIC criterion, we also examined the p_{DIC} values following Yu et al. (2019). In some instances, the values were found to be anomalously large (hundreds of thousands), which typically indicates that a local rather than a global minimum of the likelihood function is found. In these cases, we reran the Bayesian fits with new initial values to ensure proper convergence to the global minimum.

3. Observational Properties among Pulses

We now investigate how the emission properties vary among the pulses within bursts. We compare the group consisting of the first pulse in every burst (P_1) with the group containing the second pulse in each burst (P_2), and so on. The number of spectra in each pulse group decreases, with the first three groups having above 100 spectra each (338, 361, and 156) and the last three only having a few tens (46, 26, and 17).

The identification and binning of the analyzed pulses, as well as their spectral properties, are listed in Table 2. The table includes the Fermi/GBM ID (column 1), the time-series pulse (column 2), the pulsewise source intervals (column 3), the total and used ($S \geqslant 20$) time bins (column 4) by using the BBlocks across the source intervals for each pulse, the identified grade of the pulse (column 5), the best spectral model (column 6), the preferred physical model (column 7), the pulsewise evolution of the spectral parameters (column 8 for E_p and column 9 for α), and the type of parameter relations with the Spearman's rank coefficient, r, in parentheses: F–α (column 10), F–E_p (column 11), and α–E_p (column 12). Figure 1 shows the histograms of the number of pulses in each pulse group (left side) and the corresponding number of spectra (right side). In the following section, we only consider the best-fit model for each pulse according to Section 2.6.

3.1. Parameter Distributions

Figure 2 shows the parameter distributions for every group of pulses, including α, E_p, and the K-corrected energy flux F (erg cm^{-2} s^{-1}), over the range 1–10^4 keV, as well as the duration, Δt, of the pulses. In the following figures, the data points are orange (P_1), blue–magenta (P_2), violet (P_3), yellow (P_4 or P_{4+5+6}),[11] cyan (P_5), and green (P_6). The best Gaussian fit for each distribution is presented, and the corresponding

---

[11] Note that, in some cases, we combine the data for the three last pulse groups (P_{4+5+6}), since the parameter distributions are typically similar and an increased sample size improves the fits.
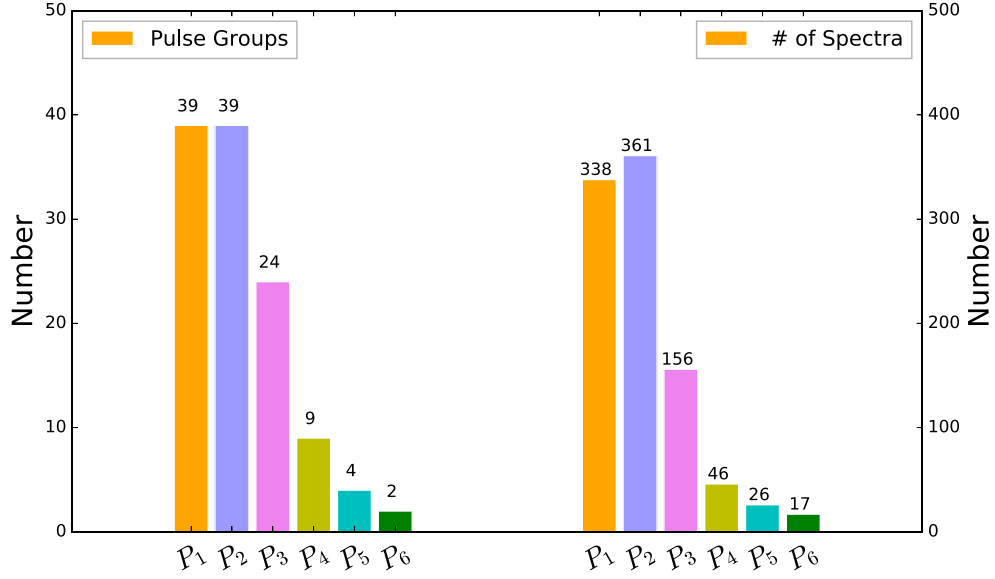
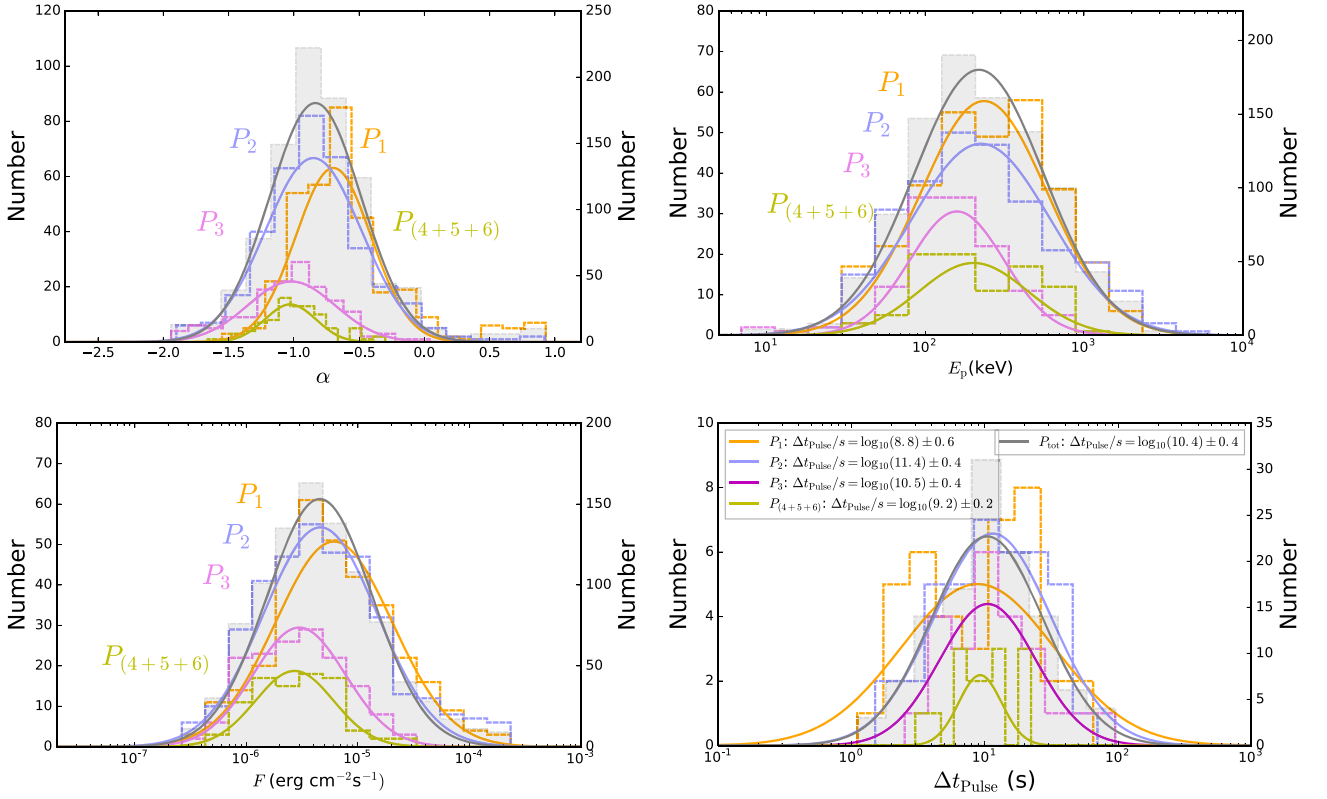**Figure 1.** Histograms of the numbers of pulses (left) and spectra (right) in each pulse grouping.

Figure 2. Distributions of α, E_p, and energy flux, as well as the duration (t_{90}) for each pulse group. The distributions correspond to P_1 (orange), P_2 (blue–magenta), P_3 (violet), P_4 or $P_{(4+5+6)}$ (yellow), P_5 (cyan), and P_6 (green). The black line is for the full sample. The y-axes on the left are for the pulse groups, while the ones on the right are for the full sample.

average values and standard deviations are presented in Table 3. The average value of the full sample, including all pulses, is $\alpha = -0.84 \pm 0.35$ and $E_p = \log_{10}(214) \pm 0.42$. These values are in agreement with previous catalogs (e.g., Kaneko et al. 2006).

In order to assess whether the distributions change between the different pulse groups, we use the Kolmogorov–Smirnov

(K-S) test. This test determines the chance probability, P, that two distributions are sampled from populations with identical distributions. For our purposes, we use $P < 10^{-2}$ to ensure that the distributions are truly different. In Table 4, we present the P-values for all of the α and E_p distributions for the pulse groups.

These results indicate that the groups of pulses could be divided into two categories with two different behaviors. The

Table 3
Results of the Average and Deviation Values of the Parameter Distribution

Pulse (Group) (1)	Model (Selected) (2)	Spectra (Number) (3)	α (4)	E_p (keV) (5)	F (erg s^{-1} cm^{-2}) (6)	β (Well Converged) (7)	β (Unconverged) (8)
P_1	Best	338	-0.70 ± 0.29	$\log_{10}(234) \pm 0.40$	$\log_{10}(6.17e{-}6) \pm 0.51$	$\cdots$	$\cdots$
P_2	Best	361	-0.85 ± 0.37	$\log_{10}(224) \pm 0.44$	$\log_{10}(4.57e{-}6) \pm 0.51$	$\cdots$	$\cdots$
P_3	Best	156	-1.02 ± 0.33	$\log_{10}(158) \pm 0.30$	$\log_{10}(2.95e{-}6) \pm 0.39$	$\cdots$	$\cdots$
$P_{(4+5+6)}$	Best	89	-1.03 ± 0.19	$\log_{10}(202) \pm 0.34$	$\log_{10}(2.92e{-}5) \pm 0.39$	$\cdots$	$\cdots$
Overall	Best	944	-0.84 ± 0.35	$\log_{10}(214) \pm 0.42$	$\log_{10}(4.57e{-}6) \pm 0.47$	$\cdots$	$\cdots$

Note. Column 1 lists the pulse name, column 2 lists the used model, column 3 lists the number of spectra for each pulse, and columns 4–8 list the average and its deviation (1σ) for the spectral parameters and energy flux.

Table 4
Probability of the K-S Test for the Spectral Parameter Distributions

	$\alpha(P_1)$	$\alpha(P_2)$	$\alpha(P_3)$	$\alpha[P_{(4+5+6)}]$		$E_p(P_1)$	$E_p(P_2)$	$E_p(P_3)$	$E_p[P_{(4+5+6)}]$
$\alpha(P_1)$	1.0	$<10^{-2}$	$<10^{-2}$	$<10^{-2}$	$E_p(P_1)$	1.0	0.11	$<10^{-2}$	0.37
$\alpha(P_2)$	$<10^{-2}$	1.0	$<10^{-2}$	$<10^{-2}$	$E_p(P_2)$	0.11	1.0	$<10^{-2}$	0.43
$\alpha(P_3)$	$<10^{-2}$	$<10^{-2}$	1.0	0.12	$E_p(P_3)$	$<10^{-2}$	$<10^{-2}$	1.0	0.03
$\alpha[P_{(4+5+6)}]$	$<10^{-2}$	$<10^{-2}$	0.12	1.0	$E_p[P_{(4+5+6)}]$	0.37	0.43	0.03	1.0

Note. The probability of the K-S statistic on two samples. The left part is for α distributions, and the right part is for E_p distributions.

first category, with P_1 and P_2, is different from the rest of the pulse groups. In the first group of two pulses (P_1 and P_2), the peak energy E_p does not change, while the spectral slope α exhibits a clear softening. Compared to the second category, with the later pulse groups (P_3–P_6), there is a change, with both α and E_p decreasing. However, within this second category, the distributions are not significantly different. Based on this analysis alone, it can, therefore, be argued that these two categories represent different types of spectral characteristics and, therefore, possibly different emissions.

The comparison between the fluxes and pulse durations is shown in the bottom panels of Figure 2. The fluxes have a similar pattern as α. There is a steady decrease, except for the last two groups, which have a similar distribution. Finally, the pulse duration distributions are comparable, and the first three groups have increasing average values.

Another way to compare the variation of emission properties in between pulses is to study the maximal value of the parameters of α and E_p in each pulse and how they vary. Note that α_{max} and $E_{p, max}$ do not necessarily need to be at the same time bin. In the upper panels in Figure 3, we present $\alpha_{max} = \alpha_{max}(t)$ and $E_{p, max} = E_{p, max}(t)$ versus time. Here the trend of softening is again revealed for α_{max}. Later pulses typically have smaller α_{max}. There is also a trend that α_{max} for the first pulse is softer the further it is delayed from the trigger. For $E_{p, max}$, however, there is no trend, and the distinction between the two categories from the K-S tests is not as apparent. This means that, when it comes to $E_{p, max}$ and α_{max}, it is mainly the spectral shape that changes and not the location of the peak energy when we compare the six pulse groups.

In the lower panels in Figure 3, the dependency of α_{max} and $E_{p, max}$ on pulse duration Δt is shown. The colored stars correspond to the average values. For the first three groups, the increase in average pulse duration is correlated with the decrease in the average values of α_{max} and $E_{p, max}$ (see Figure 2). Again, the last group with $P_{(4+5+6)}$ differs from the trend by having a shorter (average) pulse duration. However, instrumental effects might play a role here. The fluxes of later

pulses are lower; hence, the full duration of the pulses might not be apparent above the background noise level.

3.2. Spectral Evolution

Early investigations of GRB emission identified a significant correlation between spectral properties, such as a relation between the intensity and the shape of the spectrum (Wheaton et al. 1973), and a correlation between the intensity and the spectral peak (Golenetskii et al. 1983). In this section, we classify the evolution of α and E_p relative to the count light curves, as commonly done in the literature (e.g., Kargatis et al. 1994; Ford et al. 1995). In Section 3.3, we will quantify this further by investigating the actual correlations between the parameters.

Examples of the evolution of the spectral parameters E_p and α and the νF_ν flux are provided in the upper panels of Figure 4. Here the parameter evolutions are overlaid on the count light curve. In the Appendix, we further provide the corresponding figures for all bursts (Figures A1–A3) as well as the figures for all bursts for the evolution of the spectral parameter β. Following the traditional classification, we use the notation that the parameter value is denoted as "hard" when referring to large values of both α and E_p, as opposed to soft values (low values of α and E_p). We categorize the evolution in the two main groups: those with a hard-to-soft (h.-t.-s.) pattern, that is, the parameters decrease independent of the rise and decay of the pulse, and those with a flux-tracking (f.-t.) pattern, that is, the parameters are correlated with the rise and decay of the flux with or without a time lag. In a handful of cases, other patterns are also identified. The classification of the pulses is given in Table 2 (columns 8–9).

For the E_p evolution (see Figure A1 and column 8 in Table 2), we find that the hard-to-soft and flux-tracking patterns are the two dominant patterns in our multipulse sample. We find that about two-thirds $(63/103 = 61\%)$ of the pulses show a flux-tracking pattern and about one-third $(32/103 = 31\%)$ of the pulses exhibit a hard-to-soft
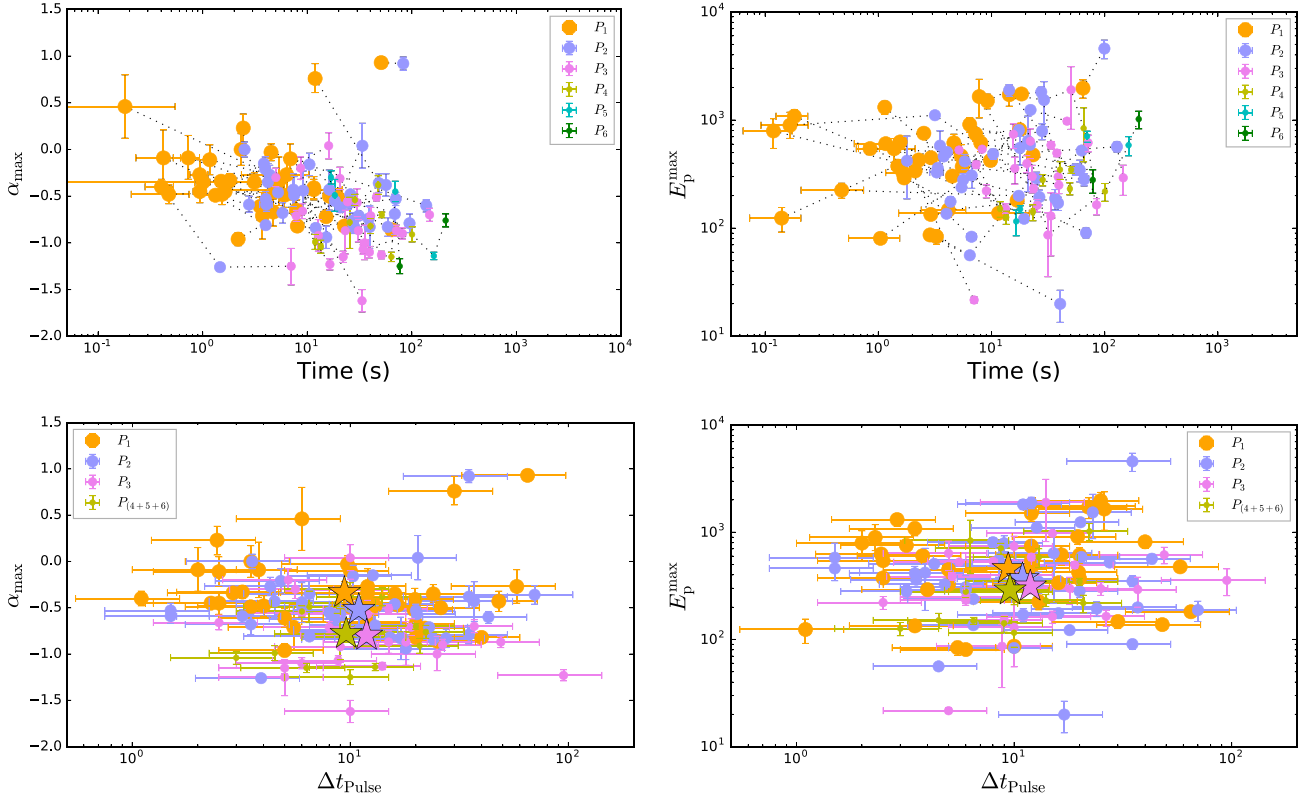
Figure 3. Upper panels: evolution of α_{max} (left panel) and $E_{p, max}$ (right panel). Pulses from each individual burst are connected by dashed lines. Color notation is the same as in Figure 2. lower panels: α_{max} (left panel) and $E_{p, max}$ (right panel) vs. pulse duration. The corresponding mean value of each individual pulse group is indicated by colored stars.
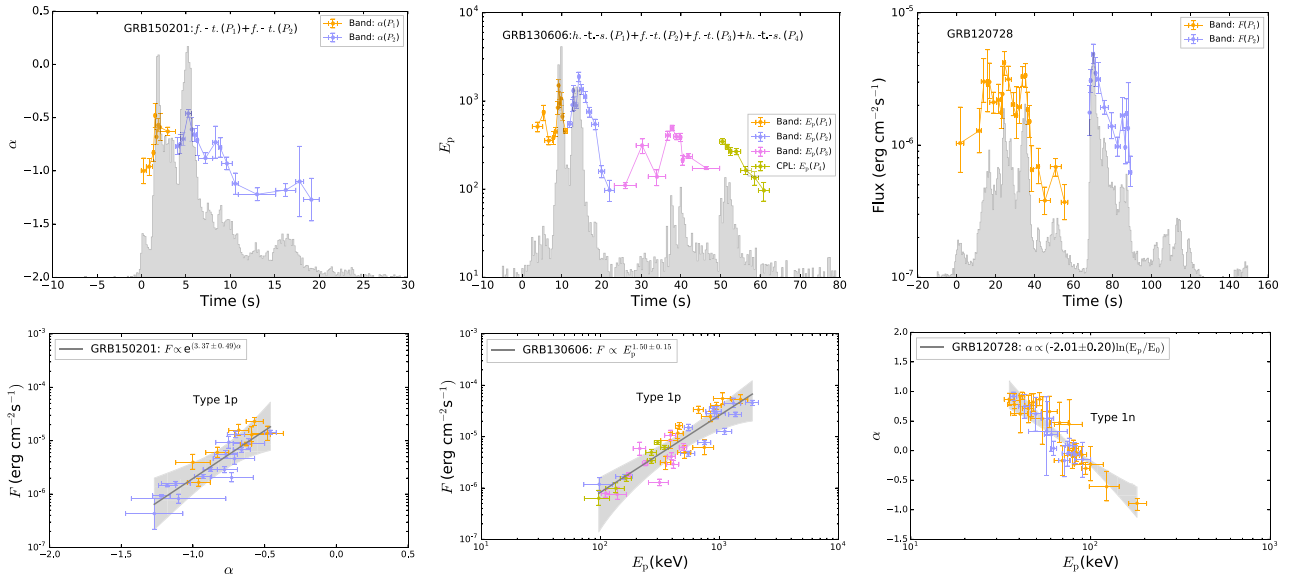

Figure 4. Upper panels: examples of the parameter evolution of the E_p, α, and νF_ν flux. The count light curves are shown (in arbitrary units) by the gray histograms. Lower panels: examples of the parameter relations of $F - \alpha$, $F - E_p$, and $\alpha - E_p$, as well as the best-fit relations with the 2σ error region.

pattern. Other evolution patterns are rarely observed. For instance, we only identify two cases showing the hard-to-soft-to-hard pattern (e.g., P_4 in GRB 101014175), one case displaying the soft-to-hard evolution (P_1 in GRB 170207906), and three cases exhibiting a hard-to-soft followed by a flux-tracking evolution within a pulse (e.g., P_1 in GRB

091127976). Here we note that previous investigations found that about two-thirds of cases have hard-to-soft behavior, while a smaller fraction has flux-tracking behavior (e.g., Ford et al. 1995; Crider et al. 1997; Lu et al. 2012; Yu et al. 2019). This fact is at odds with the observation in our sample. This is further discussed in Section 5.2.

Table 5
Statistical Results of the Pulsewise Spectral Evolution

Pulse (Group) (1)	Full Sample (Number) (2)	Used Sample (Number) (3)	Hard-to-soft (Number) (4)	Hard-to-soft (Percentage) (5)	Flux-tracking (Number) (6)	Flux-tracking (Percentage) (7)	Others (Number) (8)	Others (Percentage) (9)
$E_{\rm p}$ Evolution								
P_1	39	35	12	34%	20	57%	3	9%
P_2	39	38	13	34%	25	66%	0	0%
P_3	24	20	7	35%	12	60%	1	5%
P_4	9	6	1	17%	4	67%	1	16%
P_5	4	3	1	33%	2	67%	0	0%
P_6	2	1	0	0%	1	100%	0	0%
Overall	117	103	34	26%	64	63%	5	3%
α Evolution								
P_1	39	35	10	29%	21	60%	4	11%
P_2	39	38	10	26%	25	66%	3	8%
P_3	24	20	8	40%	12	60%	0	0%
P_4	9	6	0	0%	5	83%	1	17%
P_5	4	3	0	0%	3	100%	0	0%
P_6	2	1	0	0%	1	100%	0	0%
Overall	117	103	28	27%	67	65%	8	8%

Note. Column 1 lists the pulse groups, columns 2 and 3 list the number of the full (gold+silver+bronze) and used (gold+silver) samples for each pulse group, and columns 4–9 list the number and percentage of the hard-to-soft, flux-tracking, and other patterns, respectively.

For the α evolution (see Figure A2 and column 9 in Table 2), we find, similarly, that the hard-to-soft and flux-tracking patterns dominate. The flux-tracking pattern accounts for 65% (67/103) of the pulses, while the hard-to-soft pattern accounts for 25% (26/103) of the pulses. These two patterns thus account for 90% of the pulses. Among the rest of the pulses, we find that three cases have a soft-to-hard evolution (e.g., P_1 in GRB 110625881), and one case has a hard-to-soft-to-hard evolution (P_4 in GRB 101014175). Moreover, we also identify two cases showing a "flat" (or weak rise) behavior throughout the pulse (e.g., P_1 in GRB 120129580), and two cases have no clear trend at all (e.g., P_1 in GRB 120728434), which is not found in the $E_{\rm p}$ evolution.

We note that the $E_{\rm p}$ and α evolutionary patterns during a single pulse are not necessarily the same. In roughly half of the pulses (51% = 53/103), the $E_{\rm p}$ and α evolution are classified to have the same pattern, while 49% (50/103) of the pulses do not have the same pattern.

Finally, the patterns of the spectral evolution for $E_{\rm p}(t)$ and $\alpha(t)$ can vary from pulse to pulse within a burst. We find that in only about half of the pulses, the patterns of the $E_{\rm p}(t)$ evolution between two adjacent pulses are the same (55% = 35/64), and the rest 45% (29/64) are the inconsistent cases. Similarly, for $\alpha(t)$, we also find that for about half of the pulses, the spectral evolution among different pulses shares a similar pattern, accounting for 58% (37/64) of the pulses, while the inconsistent cases account for 42% (23/64) of the pulses. However, there is no significant variation in the fraction of pulses that are classified as having tracking behavior between the six pulse groups, which all have around a two-thirds fraction (Table 5 and Figure 5).

3.3. Parameter Correlations

We now turn to investigating the correlation between the following parameter pairs: ($\log F$, α), ($\log F$, $\log E_{\rm p}$), and (α, $\log E_{\rm p}$). Examples of these relations are provided in the lower panels of Figure 4, where functional fits are made. The leftmost panel shows the fit of $F = F_0 e^{k\alpha}$, where $k \sim 3.37 \pm 0.49$ (a typical value; Ryde et al. 2019), the middle panel shows the power law between F and $E_{\rm p}$ with index 1.50 ± 0.15 (a typical value; Borgonovo & Ryde 2001), and the rightmost panel shows a fit to $\alpha = k_2 \ln(E_{\rm p}/E_0) + \alpha_0$, where $k_2 = -2.01 \pm 0.20$. In the Appendix, we further provide the corresponding figures of these correlations for the full sample (Figures A5–A7).

We visually inspect the correlations and classify them according to the scheme in Yu et al. (2019), who classified them into three behaviors. The first behavior is a monotonic relation, defining type 1. It can be divided into three categories: type 1p, monotonic positive correlation; type 1n, monotonic negative correlation; and type 1f, flat relation. The second behavior has two piecewise monotonic relations combined at a break point. This behavior is defined as type 2 and is divided into two subcategories, either a concave (type 2p) or a convex (type 2n) function. No clear trend is classified as type 3. The classification is given in Table 2.

The strengths of the correlations are given by the Spearman's rank r. Strong correlations have $r > 0.7$, and weak correlations have $r < 0.4$. For both the F–α and F–$E_{\rm p}$ relations, around half of the pulses have strong correlations (47/103 and 54/103), and a quarter have weak correlations (27/103 and 26/103). In contrast, the α–$E_{\rm p}$ relations have the reverse properties: strong correlations in 21/103 and weak correlations in 57/103.

Among the pulses with strong correlations, we find that for the F–α relation, the vast majority has a positive monotonic relation (1p; 38/47), only a few have a negative relation (1n; 6/47). Similarly, for the F–$E_{\rm p}$ relation, a vast majority have a positive power law (1p; 45/51). Finally, for the α–$E_{\rm p}$ relation, negative and positive relations are equally common (1n; 9/21) and (1p; 8/21).

The three relations F–α, F–$E_{\rm p}$, and $E_{\rm p}$–α typically do not have strong correlations at the same time. However, in a few
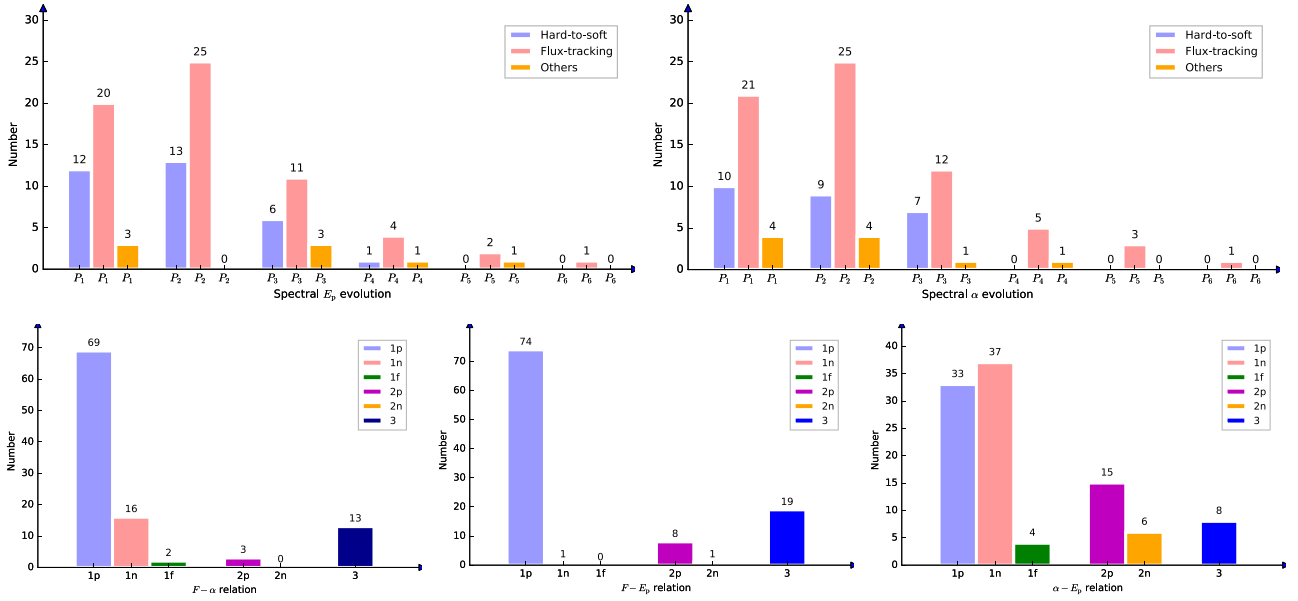
Figure 5. Histograms of the spectral evolution and parameter relations. Upper left panel: E_p evolution. Upper right panel: α evolution. For each pulse, the histograms show the number of hard-to-soft and flux-tracking patterns, as well as some particular cases, denoted as "others." Lower panels: classification of parameter relations in the entire sample. The histograms display the number pulses in the three main categories, as well as the subcategories for categories 1 and 2, as defined in the text. Lower left panel: F–α relation. Lower middle panel: F–E_p relation. Lower right panel: α–E_p relation.

cases, they do: 13 out of the 103 pulses have $r > 0.7$ or $r < -0.7$ for all correlations at the same time. An example of a spectral evolution with simultaneous strong correlations is the single-pulse burst GRB 131231A, where all three relations have monotonic positive correlations (Li et al. 2019). In the following discussions, we summarize the correlations of all of the pulses independent of their r values.

3.3.1. Individual F–α Relation

For each individual burst, the F–α plot is shown in Figure A5, and the identified type, as well as its Spearman's coefficient r, is summarized in column 10 in Table 2. The statistical results are presented in the lower left panel in Figure 5.

We find that the dominant F–α relation is a monotonic correlation in the log-linear plots (type 1) accounting for 87 pulses (84%). Of these, 69 are of type 1p, accounting for 67%, and 16 are of type 1n, accounting for 15%. Among the rest, 13% (13/103) are of type 3.

To identify any change in spectral properties among the pulses, we compare the frequency of the dominating types 1p and 1n in each pulse group. The proportion of the frequencies of these types are all high. For P_1, the proportion of type 1p versus type 1n is 19/8, and for the following pulses, it is 28/6 (P_2), 14/1 (P_3), 4/1 (P_4), 3/0 (P_5), and 1/0 (P_6). No apparent variation in the relative frequency is identified, apart from the tendency that the negative F–α relations are proportionally more common in P_1. An example is given by GRB 150330, which has three well-separated pulses; the first pulse is a clear type 1n, while the following two pulses have positive relations (type 1p), also studied in detail by Li (2019a). The change in correlation pattern corresponds to a change in the range of α values for the pulses. Li (2019a) therefore suggested that a change in jet properties should account for both of these properties.

We also note that there are only three pulses that are classified as type 2 (relation with a break), and all of these are type 2p and identified in the first pulse (GRB 081009, GRB 100719, and GRB 100826). Finally, we find that in 25% (14/57) of cases, the types change between adjacent pulses.

3.3.2. Individual F–Ep Relation

The classification of the F–E_p relation in Figure A6 is shown in column 11 of Table 2 and the lower middle panel of Figure 5. We find that a monotonic correlation in the log–log plots is again the most common type in the F–E_p relation, accounting for 75 (72%) of the pulses, of which 74 (71%) are type 1p (similar to the fraction for the F–α relation), only one case (P_3 in GRB 090131) is identified as type 1n (a much lower fraction compared to the F–α relation), and no type 1f pulse is found. Among the rest, 18% (19/103) of the pulses have no clear trend (type 3), and 8% (8/103) have a broken power-law behavior (type 2p).

We again compare the frequency of the dominating types, which in this case are type 1p versus type 2p. The proportions are all very high, without any significant variation among the groups: 20/6 (P_1), 33/1 (P_2), 14/1 (P_3), 4/0 (P_4), 2/0 (P_5), and 1/0 (P_6). There is a slight tendency, though, for type 2p to be proportionally more prevalent in P_1. We note that the F–E_p relation does not change between two adjacent pulses for a majority of cases.

3.3.3. Individual α–Ep Relation

For the α–E_p relation (see Figure A7 and column 12 in Table 2), we find that pulses with a monotonic relation (type 1) dominate (72% = 74/103). However, compared to the F–α and F–E_p relations, the number of type 1p and type 1n are more even: 32% = 33/103 and 36% = 37/103, respectively. Type 2 pulses account for 20% (21/103) of cases, of which 15 are type 2p and six are type 2n. Type 3 has 8% (8/103).

The proportion between the frequencies of the two dominating types, type 1p and type 1n, for the six pulse groups are 2/15 (P_1), 18/11 (P_2), 8/7 (P_3), 3/2 (P_4), 2/1 (P_5), and 0/1 (P_6). Apart from P_1, there is no apparent variation between the pulse groups. However, for P_1, there is a disparity; only 44% (17/39) are of type 1, compared to 72% for all pulses. Out of these 17, type 1n clearly dominates, in contrast to all other pulses, where type 1p is slightly dominant instead. We note that, in contrast to the other correlations, most of the α–E_p correlations are weak (Section 3.3). To confirm this tendency, we therefore particularly investigate only the strong correlations (21 pulses with $r > 0.7$). Of these, there are seven P_1, and they all are of type 1n. Ten cases are P_2, and of these, three are of type 1n and five of type 1p. We therefore conclude that for the α–E_p relation, the first pulses have (i) a smaller fraction of type 1, and (ii) of these, type 1n have a higher fraction compared to the later pulses. Finally, we find that 46% (26/57) of the α–E_p relations change between two adjacent pulses.

4. Assessment of the Compatibility with Emission Models

In both synchrotron and photosphere models, there are many different types of spectra that can be produced, mainly depending on the location of the emission site and the flow properties. The spectral shape from a synchrotron emitting source depends on the relation between the radiative cooling time and other timescales related to heating and adiabatic expansion (Lloyd & Petrosian 2000; Tavani et al. 2000). The steepest low-energy power law that is allowed (for isotropically distributed pitch angles) is $\alpha = -2/3$ for slow-cooled emission, while steeper slopes down to $\alpha = -3/2$ are expected for (marginally) fast-cooling emission. Similarly, the properties of the emission from the photosphere depend on the emission site and the amount of dissipation that occurs in the vicinity of the photosphere. If there is no energy dissipation, the spectrum is expected to be slightly broader than a Planck function, namely the nondissipative photosphere (NDP; Beloborodov 2011; Acuner & Ryde 2018; Meng et al. 2019). Typically, though, dissipation is expected around the photosphere, which thus causes the spectral shape to broaden further (Giannios & Spruit 2005; Rees & Mészáros 2005; Pe'er et al. 2006b; Vurm et al. 2013).

A few attempts have been made to fit particular cases of these models to the data directly (e.g., Lloyd-Ronning & Petrosian 2002; Ryde 2004, 2005; Ahlgren et al. 2015; Ryde et al. 2017; Oganesyan et al. 2019; Acuner et al. 2020; Burgess et al. 2020). However, such studies are limited by the range of models that are used and the limited samples that can be studied due to the computationally costly procedures. Alternatively, synthetic data from a certain physical model can be produced by using the detector response. The synthetic data can then be fitted with empirical models, accounting for the limitations of the typically adopted analysis methods. Such a procedure identifies the parameter space of the empirical model that corresponds to that particular physical model.

The relation between α and E_p that such investigations yield for slow-cooled synchrotron (SCS) and the NDP are shown by the yellow–green and pink lines in the upper panel of Figure 6. These lines are reproduced from Figure 4 of Burgess et al. (2015) and Figure 3 of Acuner et al. (2019). Using these lines, general assessments of the emission process can be made. For instance, if we assume that the same
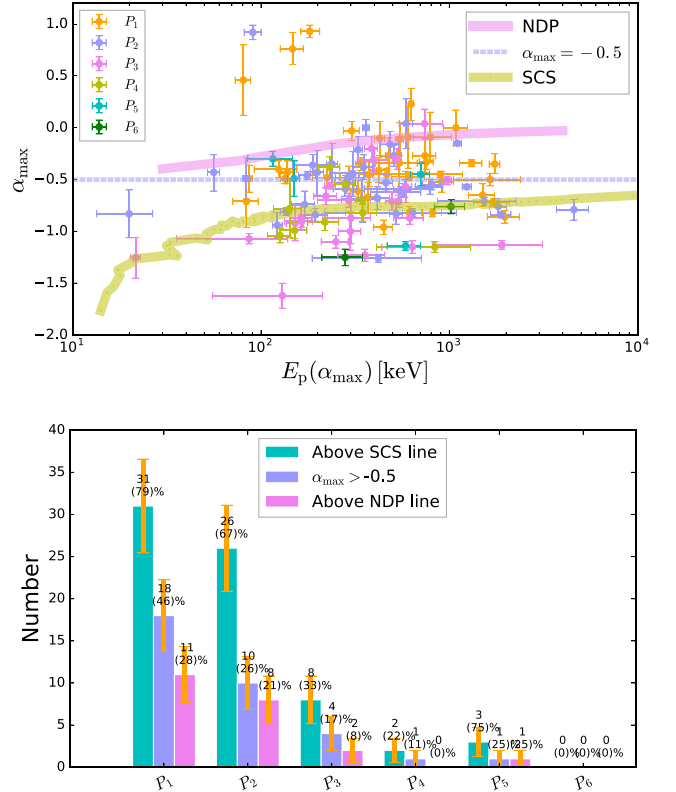

Figure 6. Compatibility with photospheric emission models. Upper panel: α_{max} vs. the corresponding E_p with the same color notation as in Figure 2. The pink line is the limiting line for the NDP and the yellow–green line is the limiting line for SCS. Lower panel: number and fraction of α_{max} bins that lie above the SCS line (green), with $\alpha_{max} > -0.5$ (blue), and that lie above the NDP line (pink).

emission mechanisms operate throughout the pulse, a single data point above the SCS line indicates that the pulse has a higher probability of being of a photospheric origin (Acuner et al. 2019; Dereli-Bégué et al. 2020).

4.1. Spectral Shape

In the upper panel of Figure 6, we plot the values of α_{max} and the corresponding value of E_p, with one data point from every pulse. Comparing with the limiting lines for SCS and the NDP, we find that 67% (79/103) of all pulses have at least one data point above the SCS line and 21% (22/103) of all pulses have a data point above the NDP line.

The number of pulses that are above the NDP and SCS lines for the sequence of pulses is shown in the lower panel of Figure 6, together with the corresponding fractions. The first two pulses in a burst have a larger fraction above the SCS line. There is a clear decrease in later pulses. There are, however, a couple of bursts in which the hardest spectrum occurs at late times. This fact is reflected in the large fraction for P_5 in Figure 6. Examples of these bursts are GRB 121225 and GRB 140810, where the largest α occurs around 50 s after the trigger.

As mentioned above, the spectra with (E_p, α_{max}) values lying above the SCS line can be expected to have a higher probability of having a photospheric origin. However, how big this probability is can only be answered by a model comparison of the physical models, for instance, through Bayesian

evidence. In any case, for spectra close to the SCS line, a model comparison will be inconclusive, since both models can produce similar spectra (over the observed energy range). Acuner et al. (2020) investigated this point quantitatively and found that a photospheric preference can be claimed, with great confidence, only for spectra with $\alpha \gtrsim -0.5$, as long as the data have a high significance. To illustrate this point, we perform the Bayesian model comparison for two example time bins in GRB 150330 (at 1.4 and 137.0 s). We calculate the Bayesian evidence for the NDP spectrum, Z_{NDP}, and the evidence for the the slow-cooled synchrotron spectrum, Z_{SCS}. As shown in Acuner et al. (2020), a log-evidence difference of $\ln Z_{NDP} / \ln Z_{SCS} \gtrsim 2$ indicates that the NDP spectrum is preferred, while if the ratio is less than -2, the SCS spectrum is the preferred model. For the 1.4 s time bin, $\alpha = -0.24$, and we find that $\ln Z_{NDP} / \ln Z_{SCS} = 33.6$, strongly favoring a photospheric origin. Correspondingly, for the 137.0 s time bin, which has $\alpha = -0.9$, we find that $\ln Z_{NDP} / \ln Z_{SCS} < -78.9$, strongly favoring an SCS origin (in the comparison between these two specific models). This shows again that the α value can be used to make an approximate model comparison in order to identify the preferred model, which is sufficient for the present study. A full model comparison investigation based on Bayesian evidence is beyond the scope of this paper.

We therefore identify spectra that have $\alpha_{max} > -0.5$ according to the Acuner et al. (2020) criterion. These spectra are denoted by Ph in Table 2 and shown by the blue bars in the lower panel of Figure 6. The fraction of these spectra steadily decreases for subsequent pulses. For the first pulse in a burst, nearly half of all pulses (18/39) pass this very stringent criterion. The fraction decreases by approximately half for every following pulse.

4.2. Spectral Evolution and Correlations

We now examine the spectral evolution and correlations for the pulses that are compatible with photospheric emission (Ph in Table 2). The purpose is to assess whether they have different characteristics of their spectral properties.

For the photospheric pulses, the majority are classified as flux-tracking or hard-to-soft for both E_p and α. For the E_p evolution, the tracking pattern is found in about half, or 47% (20/43), which is only somewhat lower than in the full sample. However, for the α evolution, flux tracking is still dominant with 63% (27/43), similar to the full sample.

Turning to the parameter correlations, we find that 47% (20/43), 51% (22/43), and 26% (11/43) have a strong correlation ($r > 0.7$) for the F–α, F–E_p, and α–E_p relations, respectively. These fractions are similar to the ones for the full sample, which indicates that the strength of the correlation does not depend on whether the pulses are photospheric or not.

We again consider the two main types of correlations for each pair of parameters. For the F–α relation, the two main types in the full sample were positive (1p) and negative (1n) monotonic correlations. For the photospheric pulses, these fractions are 60% (26/43) type 1p and 21% (9/43) type 1n. For the F–E_p relation, the two main patterns are type 1p and the convex relation (type 2p), and the photospheric pulses have 60% (26/43) type 1p and 16% (7/43) type 2p. Finally, the α–E_p relation has 21% (9/43) type 1p and 35% (15/43) type 1n. Compared to the full sample (Section 3), these fractions are not significantly different.

5. Discussion

5.1. Comparison with a Single-pulse Sample

The bursts in our sample were specifically selected, since they have multiple pulses. Here we address the question of whether or not the spectral properties of the pulses in our sample are similar to those of the single-pulse bursts. To do this, we compare the results in Yu et al. (2019), who studied a sample of 37 single-pulse bursts.

In Figure 7, we compare the distributions of duration T_{90}, peak flux, fluence, and the time-integrated spectral shape (E_p, α, and β from the Band function fit). Our sample is shown by magenta lines, and the Yu et al. (2019) sample is shown by the green lines. All of these parameters are collected from the Fermi/GBM catalog. Both the peak flux (1024 ms timescale) and the fluence are taken over the 10–1000 keV range. The average values and standard deviations (1σ error) are presented in Table 6. Both the peak flux and the fluence are approximately double for the multipulse bursts. Also, the α distribution is shifted to softer values for the multipulse bursts. On the other hand, the E_p and β values are similar between the samples. The corresponding probabilities from K-S tests are 0.02, $<10^{-2}$, $<10^{-2}$, 0.86, $<10^{-2}$, and 0.19 for t_{90}, peak flux, fluence, E_p, α, and β, respectively.

In Figure 8, we compare the distributions of the time-resolved spectral parameters. In order to make a consistent comparison, we compare the results from using the CPL function throughout for both samples. This choice is based on the fact that in the Yu et al. (2019) sample, the CPL model is the best model. Likewise, we find that in only 29% of the time-resolved bins is the Band function a better choice (Section 2.6). We find that the average distribution of α is softer and the flux is larger for the multipulse sample. However, the E_p distributions are similar. These results are similar to the time-integrated spectra comparison. If we instead particularly identify the distribution of P_1, we find that α distributions have similar peak values. On the other hand, the flux of P_1 is double the corresponding flux for the single-pulse bursts.

We also compare the frequency of the parameter relations between the samples. Most proportions between the patterns are similar. However, for the α–E_p relation, there is a notable difference. In our sample, the proportions are (72%) 74/103 for type 1 and (20%) 21/103 for type 2, while for the single-pulse sample, the proportions are (32%) 12/38 for type 1 and (45%) 17/38 for type 2. There is still a similarity in that the two pattern types are frequent in both samples; there is no strong dominance. However, in the multipulse sample, the type 1 pattern is relatively more frequent.

5.2. On the Dominance of the Flux-tracking Pattern

We find that the largest fraction of pulses in our sample follow a tracking pattern, which is at odds with earlier investigations that instead found that the hard-to-soft evolution accounts for about two-thirds and the flux-tracking evolution only accounts for one-third of the observations (e.g., Ford et al. 1995; Lu et al. 2012; Basak & Rao 2013; Yu et al. 2019).

Lu et al. (2012) argued that if there is a significant overlap between pulses, the classified pattern might be affected. For instance, an apparently flux-tracking pulse might be a consequence of two overlapping hard-to-soft pulses. In our sample, many pulses are slightly overlapping, which means that in the transition period between the pulses, there are
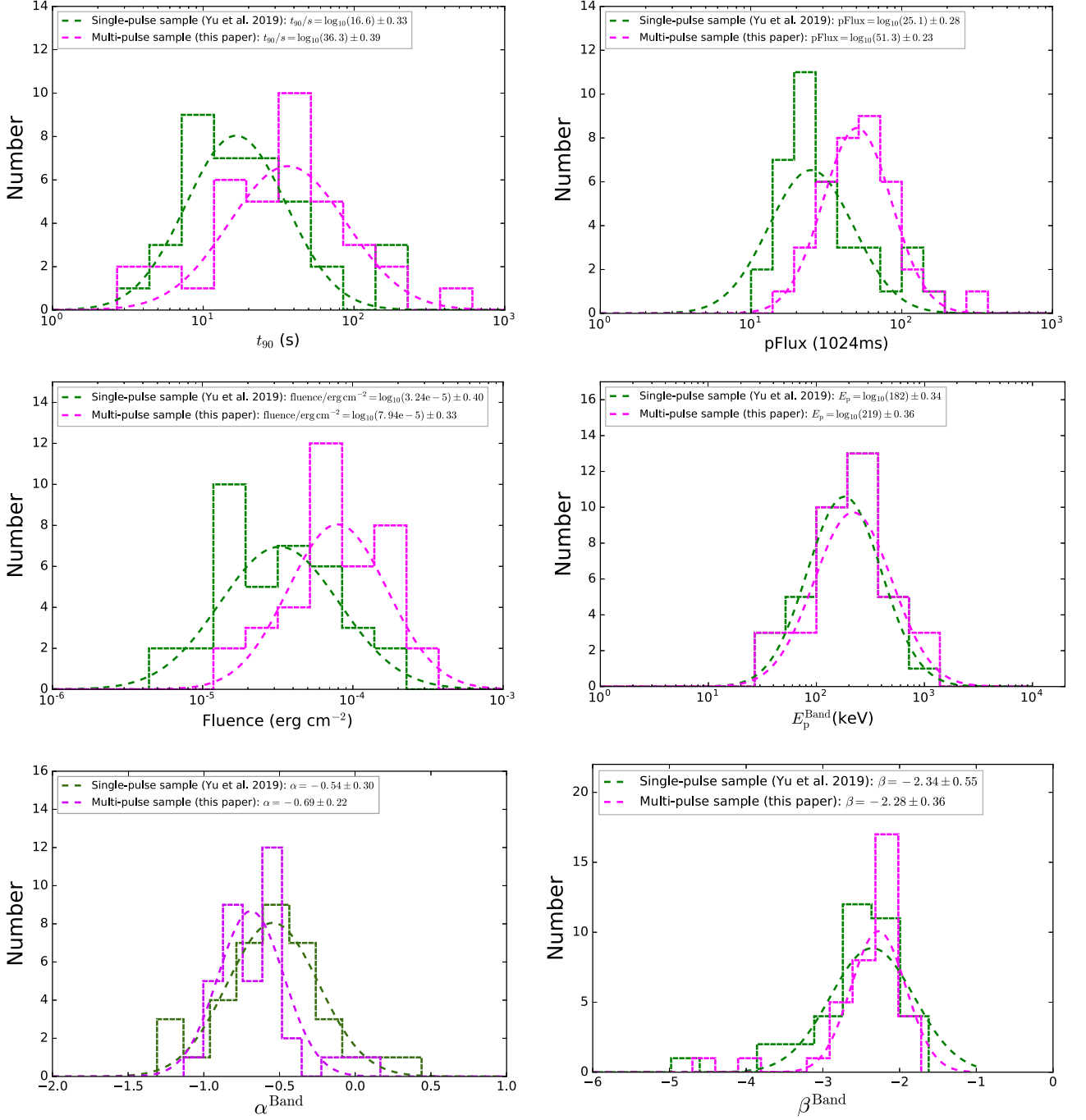
Figure 7. Parameter distributions of the duration T_{90}, peak flux, fluence, E_p, α, and β from time-integrated spectra. The sample in this paper is shown by the magenta curves, while the single-pulse sample in Yu et al. (2019) is shown by the green curves.

contributions from both pulses. Therefore, this might affect our results. To investigate this point, we particularly study the "gold" sample (see column 5 in Table 2). These nine bursts[12] have 22 pulses that are clearly separated by periods of no emission. Among these, the flux-tracking pattern accounts for 59% (13/22) of the pulses, while the hard-to-soft pattern only accounts for 36% (8/22) of the pulses. These fractions are

similar to the ones from the full sample (see Section 3.2). We conclude, therefore, that our sample is not greatly affected by the overlap between pulses.

Another possible reason for the difference is the binning methods used. We use a combination of BBlocks and significance and only consider the most significant time bins. The advantage of our method is that the substantial variations in the light curve are captured and the spectral fits are reliable. On the other hand, we might miss some of the rising phases of the pulses. Including a larger fraction of the pulse duration by

---

[12] GRB 081009, GRB 101014, GRB 140416, GRB 140508, GRB 150118, GRB 150330, GRB 151231, GRB 160802, and GRB 171120.

Table 6
Comparison between the Multipulse Sample in This Paper and the Single-pulse Sample in Yu et al. (2019)

Sample	Sample Source	Sample Size (Number)	$\log_{10}(t_{90})$ (s)	$\log_{10}$(Fluence) (erg cm^{-2})	$\log_{10}$(Peak flux)	$\log_{10}(E_p)$ (keV)	α	β
(1)	(2)	(3)	(4)	(5)	(6)	(7)	(8)	(9)
Single-pulse sample	Yu et al. (2019)	37 bursts	$\log_{10}(16.6) \pm 0.33$	$\log_{10}(3.24e{-}5) \pm 0.40$	$\log_{10}(25.1) \pm 0.28$	$\log_{10}(182) \pm 0.34$	-0.54 ± 0.30	-2.34 ± 0.55
Multipulse sample	This paper	39 bursts	$\log_{10}(36.3) \pm 0.39$	$\log_{10}(7.94e{-}5) \pm 0.33$	$\log_{10}(51.3) \pm 0.23$	$\log_{10}(219) \pm 0.36$	-0.69 ± 0.22	-2.28 ± 0.36

Note. Column 1 lists the samples, column 2 lists the sample source, column 3 lists the sample size, and columns 4–9 list the average and its deviation (1σ) value of the distributions, including the duration, fluence, peak flux, E_p, α, and β.
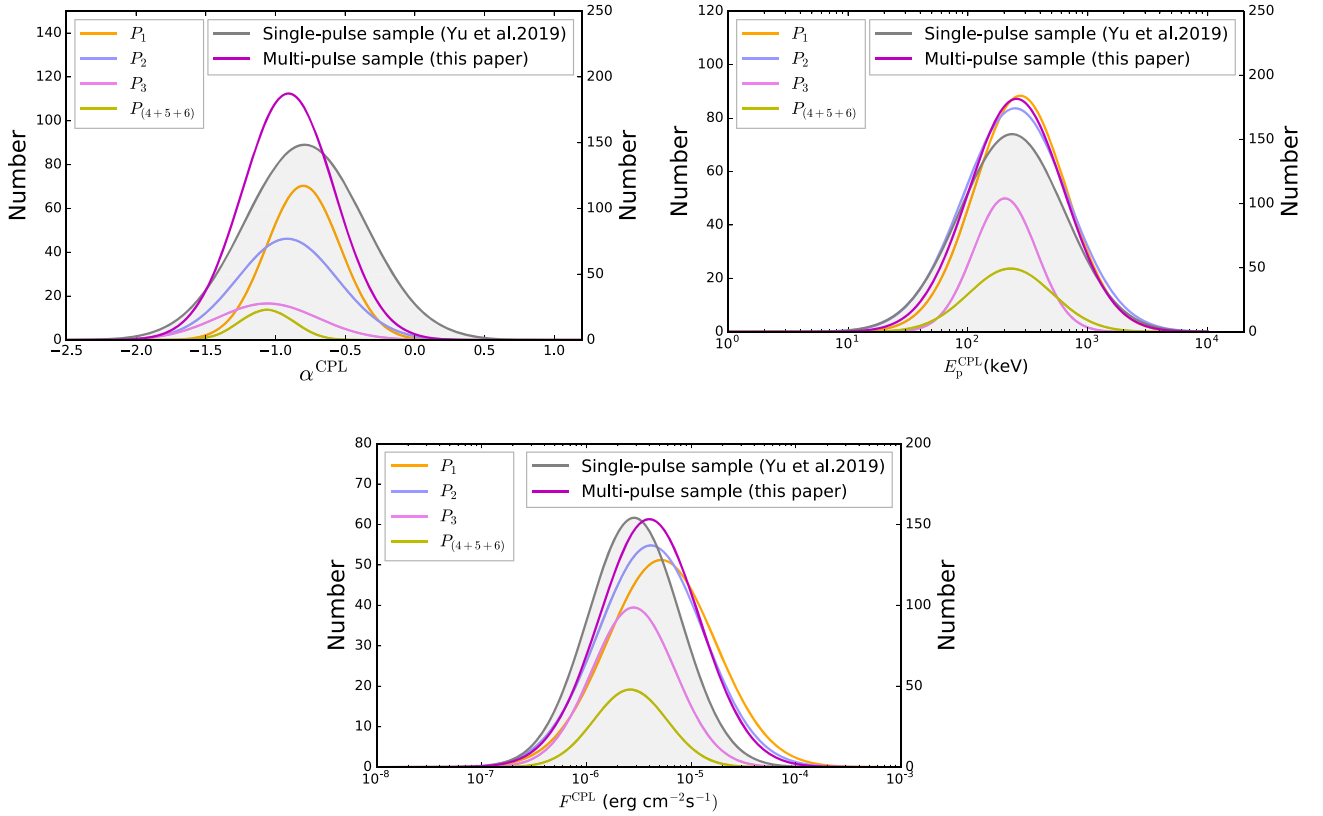
Figure 8. Same as Figure 7, but the analysis is based on the time-resolved spectral results. The y-axes on the left are for the pulse groups, while the ones on the right are for the full samples. The color notation is the same as in Figure 2 for the pulse group samples. The black line is for the full sample in Yu et al. (2019), while the purple line is for the full sample in this paper.

using less significant data ($S < 20$) could change the apparent pattern of evolution. The spectral evolution of the added periods might indeed be different, but more seriously, the spectral fits are less reliable and could therefore give misleading results.

A further uncertainty is the inherent problem in this type of classification. A subjective decision needs to be made on where a pulse starts and ends. This can affect the classification. Another point is the fact that the tracking behavior, in many cases, involves a time lag, both positive and negative. If this lag is large compared to the pulse size, the pulse could be classified as a hard-to-soft (or soft-to-hard) pulse instead. An example is the E_p pattern for GRB 120328, where the tracking pattern depends on one data point during the rise phase. The same issue happens for α in other cases.[13] These uncertainties can affect the classification of different samples. However, these cases are not sufficient to explain the whole discrepancy.

Our results thus indicate that the flux-tracking pattern is the prevalent pattern for α and E_p, at least around the peak of the pulse, where the significance is the largest. This is also consistent with the global F–E_p relation in the middle panels in Figure A9.

5.3. Implication for the Radiation Process

Based on the analysis of the change in α and E_p (Section 3.1 and Figure 2) alone, it was suggested that there are two categories of pulse groups. The first one, consisting of P_1 and

P_2, has a constant E_p, while α softens. Within the second category, there is not much change, but they are all different from the first two pulses. Moreover, we found that the initial pulses had different spectral properties (frequency of different parameter correlation) as a group (Section 3.3). These distinctions lead to the possibility that they are due to different emission mechanisms.

In the simplest internal shock model, the late pulses (P_i with $i > 1$) occur above the photosphere and hence must have a synchrotron origin. We do not see such a clear distinction, indicating that at least the simplest version of the internal shock model does not represent what we see.

For the photospheric scenario, the α value reflects the energy dissipation and photon production below the photosphere (e.g., Pe'er et al. 2006b; Vurm & Beloborodov 2016). The E_p instead is mainly set by properties at high optical depths. Therefore, if the first two pulses are photospheric, the fact that E_p is similar while α varies could be due to similar properties close to the central engine but a varying amount of turbulence in the flow causing the dissipation. The variability and pulse structures of the photospheric emission have been reproduced by numerical simulations of a jet passing through the progenitor surrounding. For instance, López-Cámara et al. (2014) showed that even with a steady central engine, a light curve with a pulse structure and large variability arises. The main cause is the Rayleigh–Taylor instabilities that arise in the contact between the layers of jet and the surrounding progenitor material. This leads to a variable amount of mixing between the layers and thereby a variable baryon load of the jet, which has a direct influence on

---

[13] GRB 110301, GRB 130606, GRB 131014, GRB 140213, GRB 141222, GRB 160422, and GRB 160802.

the radiative efficiency and spectral shape (see, e.g., Rees & Mészáros 2005; Gottlieb et al. 2019).

On the other hand, the pulse groups, P_3–P_6, all have $\alpha \sim -1$ (Figure 2). This could be explained by synchrotron emission from electrons that are marginally fast-cooled (Daigne et al. 2011; Yu et al. 2015; Geng et al. 2018). It can thus be argued that the first two pulses are typically photospheric, while the rest are due to synchrotron emission. If this interpretation is correct, one would expect that the two categories would have distinct and different spectral properties. There are several points in the analysis above that, therefore, do not support this interpretation. First, the values of $E_{p, max}$ are similar for all of the pulse groups (Figure 3); there is no clear distinction between the pulse groups. Second, there is no clear distinction between pulse groups when it comes to the spectral evolution (Section 3.2) and types of correlations (apart from the initial pulses; Section 3.3). Third, the average pulse durations are also similar in all pulse groups. All of these points indicate that there is no drastic change in emission pattern between the pulses (apart from α).

On the contrary, the properties of the last four pulse groups can also be interpreted as photospheric emission. Previous studies have shown that pulses that, beyond any doubt, are photospheric all have significant spectral evolution (e.g., Ryde et al. 2019). In particular, at the end of such pulses, α values down to -1 and below are common, which is interpreted as the result of subphotospheric dissipation with varying jet properties (e.g., Ryde et al. 2010, 2011). Consequently, pulses with $\alpha \sim -1$ could be the result of dissipative photospheres throughout the pulse. Indeed, the observation that the last four pulse groups all peak at around $\alpha \sim -1$ is in line with the theoretical expectations of fully dissipative photospheres, i.e., flows where there is no strong limitation, not on the soft photon production deep in the flow or the amount of dissipation in the parts of the flow where the spectrum is formed (Beloborodov 2010; Vurm et al. 2013).

Even though this line of argument makes the subphotospheric dissipation model appealing for most of the pulses, some admixture of synchrotron pulses is expected. The most prominent example of this is GRB 190114C, which, apart from a very hard spectral component, showed a clear afterglow emission component already during the prompt phase (Ajello et al. 2020). This proved that a synchrotron component was present during the prompt phase (see also Axelsson et al. 2012; Iyyani et al. 2013). Further early examples of such a suggestion are given in Ryde (2005), Ryde & Pe'er (2009), and Guiriec et al. (2011) and more recently in Burgess et al. (2019 and Wang et al. (2019a, 2019b)).

Many of these synchrotron components are observed at late times. Combined with the fact that the fraction of (certain) photospheric pulses decreases with pulse number (Figure 6), emission compatible with synchrotron appears to prevail mainly at the end of the prompt phases. Different possibilities exist for synchrotron emission to arise toward the end of the prompt phase. One example is GRB 150330, for which Li (2019a) suggested that the jet composition changes from a baryon-dominated flow during the first pulse to a Poynting flux–dominated flow during the rest of the burst, producing synchrotron emission (see also Zhang et al. 2018). Alternatively, during the early phases of the afterglow, shocks due to interaction between the jet and slower-moving material ahead

of the jet will also produce efficient synchrotron emission (e.g., Duffell & MacFadyen 2015).

However, from the GBM data alone, it is not possible to make a firm conclusion as to whether a soft pulse is due to synchrotron or photospheric emission subject to dissipation below the photosphere, since they are indistinguishable in many cases (e.g., Acuner et al. 2020). Simultaneous data from other wavelengths can be useful in some cases (e.g., Ravasio et al. 2018; Ahlgren et al. 2019; Ajello et al. 2020) or polarization measurements (e.g., Sharma et al. 2019).

6. Summary

In this paper, we performed time-resolved spectroscopy on a sample of multipulse GRBs observed by Fermi/GBM during the first 11 yr of its mission. We investigated the variation in emission properties between the pulses in light of the prediction of emission models. Our sample consists of 39 bursts, which have 117 distinct pulse structures, entailing 1228 time-resolved spectra. All of the spectra have a very high statistical significance of $S \geqslant 20$. This ensures that the spectral fits are well determined and that the low-energy power-law index α can be used to discriminate between spectra that are compatible with the photosphere or synchrotron emission. The emission properties we studied include the spectral shape and the correlations between spectral shape parameters.

For the sample as a whole, we found that flux-tracking evolution is more common than hard-to-soft evolution, independent of the E_p or α evolution, differing from previous findings. We also found that a positive correlation is most common for the F–α and F–E_p relations. In contrast, for the α–E_p relation, both the positive and negative correlations are equally common. In addition, we compared our sample to that of the single-pulse sample of Yu et al. (2019). We found that the peak flux is significantly larger and the average α value is softer in our sample, while peak energies are similar. On the other hand, we found that the average α value of the initial pulse of our multipulse sample is similar to that of the single-pulse sample.

Specifically, we searched for signatures of any characteristic variation in the emission properties between pulses that might reveal different underlying emission processes. We find that the characteristics of the pulses remain astonishingly similar. It is mainly the low-energy power-law index α that has a significant softening (gets smaller). In addition, we find that, on average, the first pulse in each burst behaves slightly differently than consecutive pulses when it comes to correlations between spectral shape parameters.

We further assessed the compatibility of the data with emission models for each individual pulse. Assuming that the same emission mechanism operates during a pulse, any single time bin that violates the synchrotron limit indicates that a photospheric origin is more probable (Figure 6). We also used the criterion that $\alpha_{max} > -0.5$, which identifies pulses that significantly prefer photospheric emission (Acuner et al. 2020). The first pulse in a burst is clearly different from the later pulses; three-fourths of them violate the synchrotron emission, and half of them prefer photospheric emission. These fractions decrease rapidly for subsequent pulses.

We argue that in many cases, synchrotron emission in later pulses might contribute to these trends. However, the similarity between pulses, averaging over the whole sample, points to a

photospheric origin of most pulses, albeit with greatly varying dissipation properties

We conclude that photospheric emission can be found at any time during the burst duration; however, it is more common in the early phase. In order to make a general statement of the emission mechanism in a GRB, the spectral softening of α between pulses is a property that needs to be considered. In particular, the analysis of individual pulses will be influenced by their occurrence relative to the trigger time. The chance to detect the photosphere is largest among the first few pulses, while synchrotron emission is mainly found at late times. This also allows for the coexistence of emissions at late times.

Appendix A

In this appendix, we provide additional figures and tables and present the definition of the fitting models, as well as the discarded sample.

A.1. Best Model-based Parameter Evolution in Different Pulses Text

In Figures A1–A4, we provide the evolution of the spectral parameters E_p, α, νF_ν flux, and β for all the bursts based on the best models defined in Section 2.6.
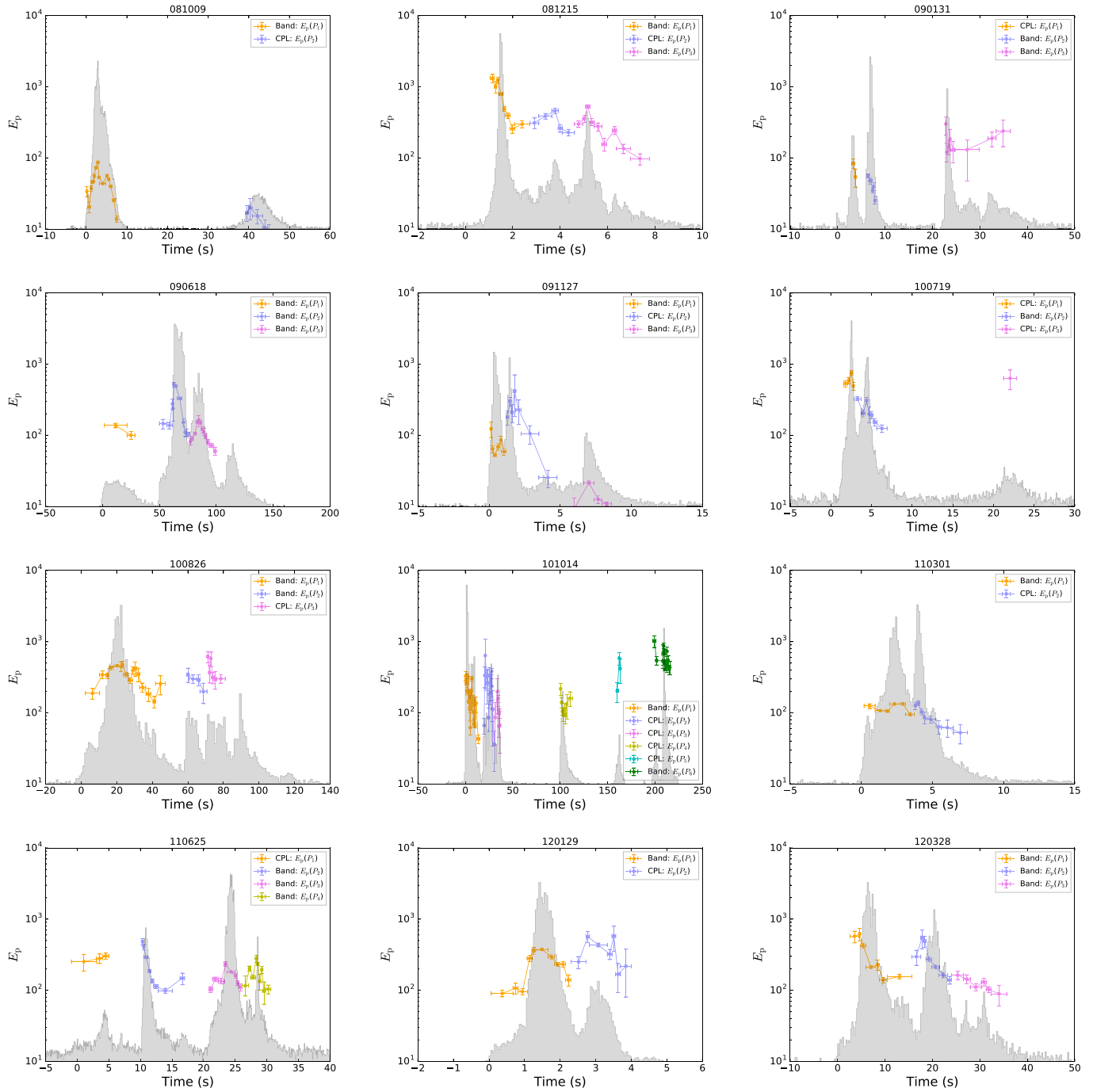
Figure A1. Temporal evolution of E_p. Data points with solid orange, blue–magenta, violet, yellow, cyan, and green colors indicate time-series pulses of P_1, P_2, P_3, P_4, P_5, and P_6, respectively. Count-rate light curves are overlaid in gray. All data points correspond to a statistical significance $S \geqslant 20$.
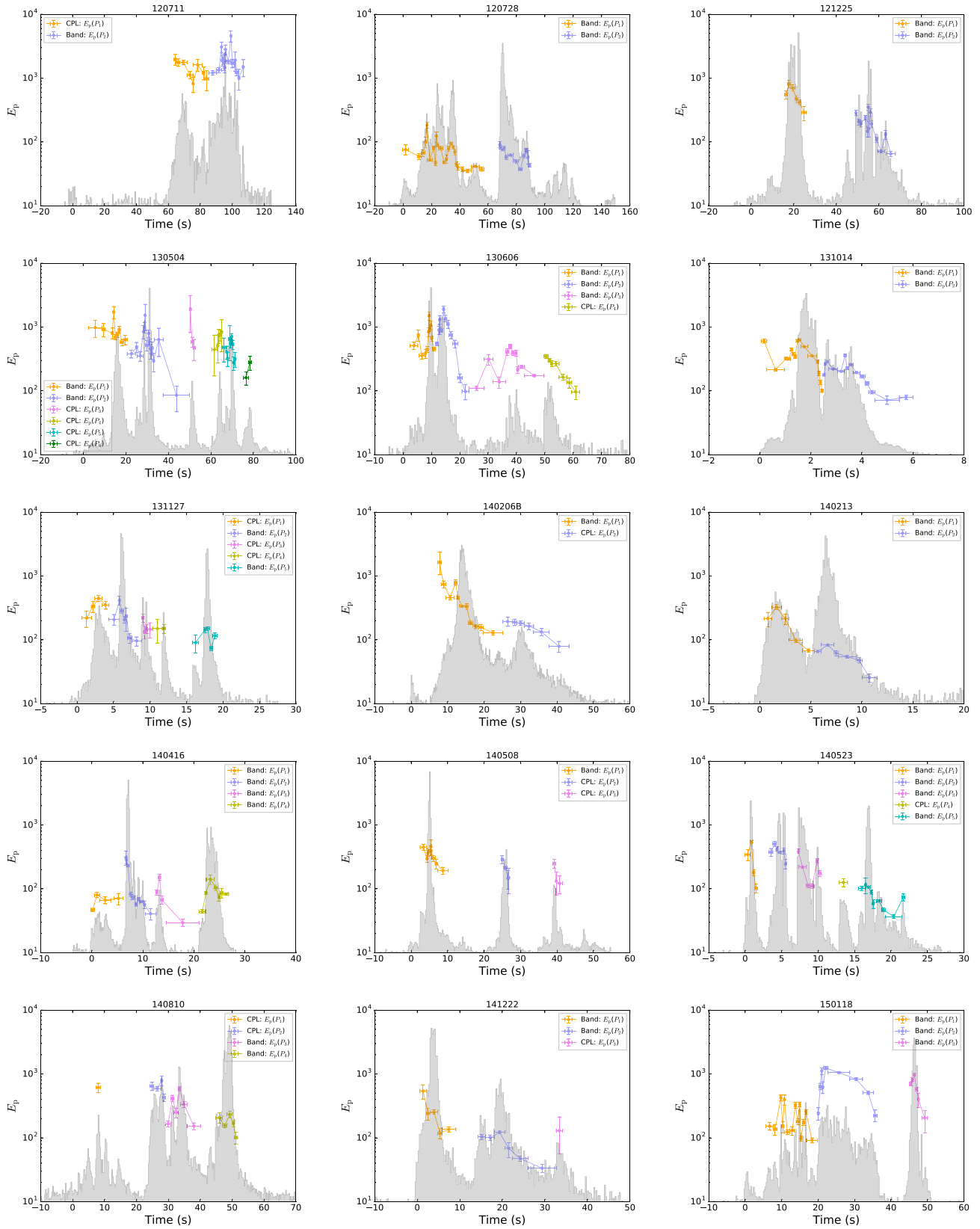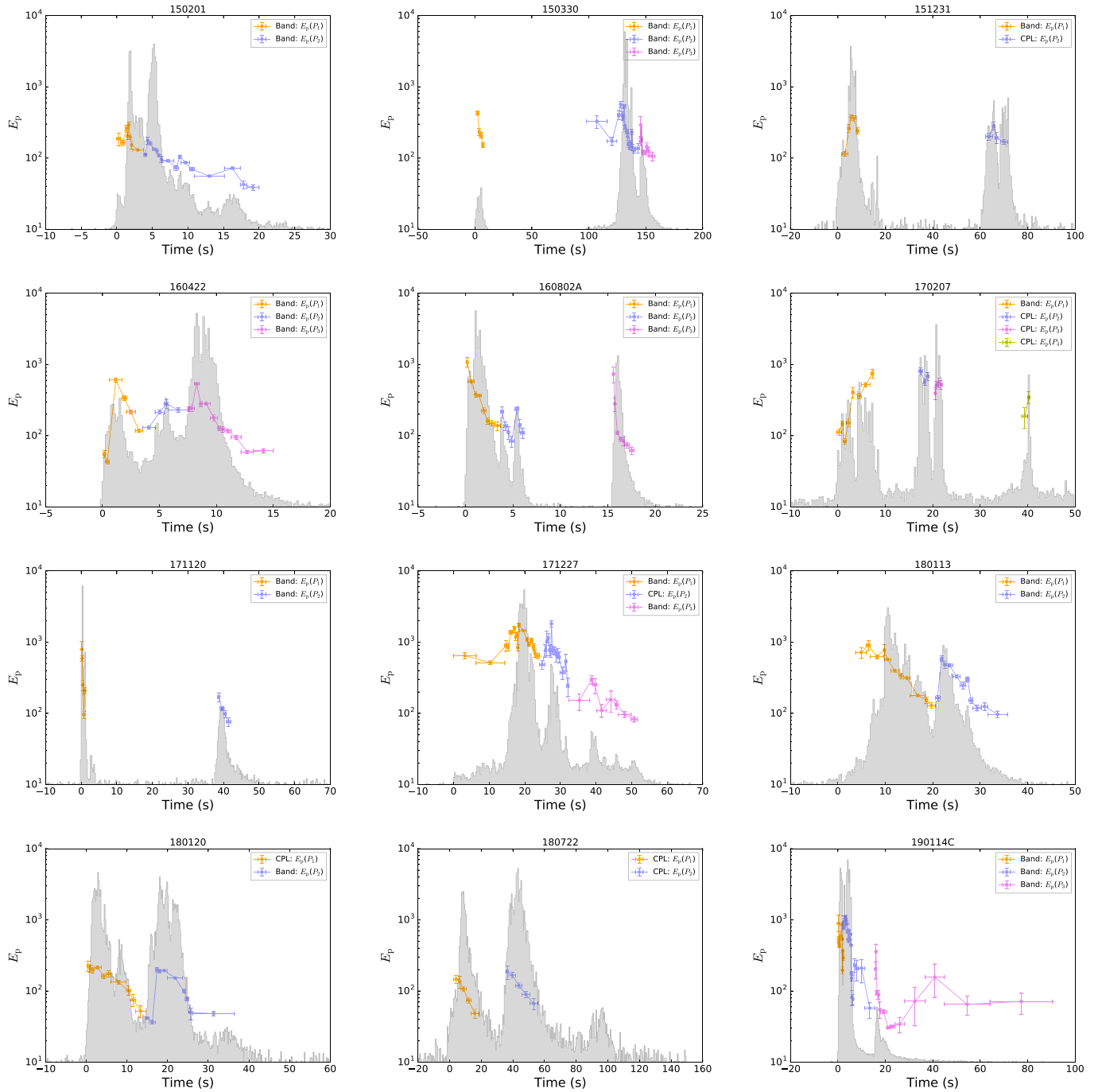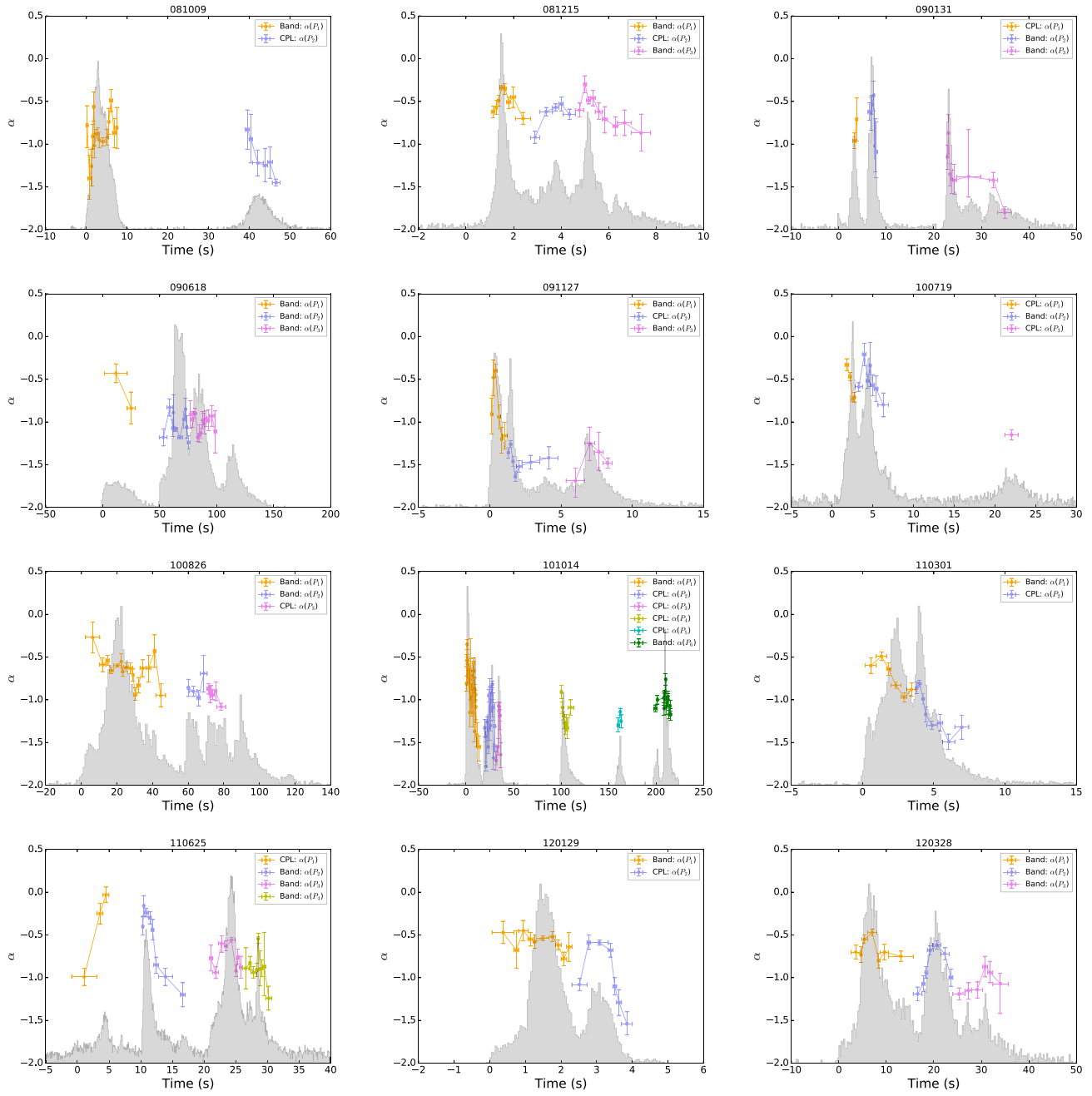
Figure A1. (Continued.)

Figure A1. (Continued.)

Figure A2. Temporal evolution of the α index. The symbols and colors are the same as in Figure A1.
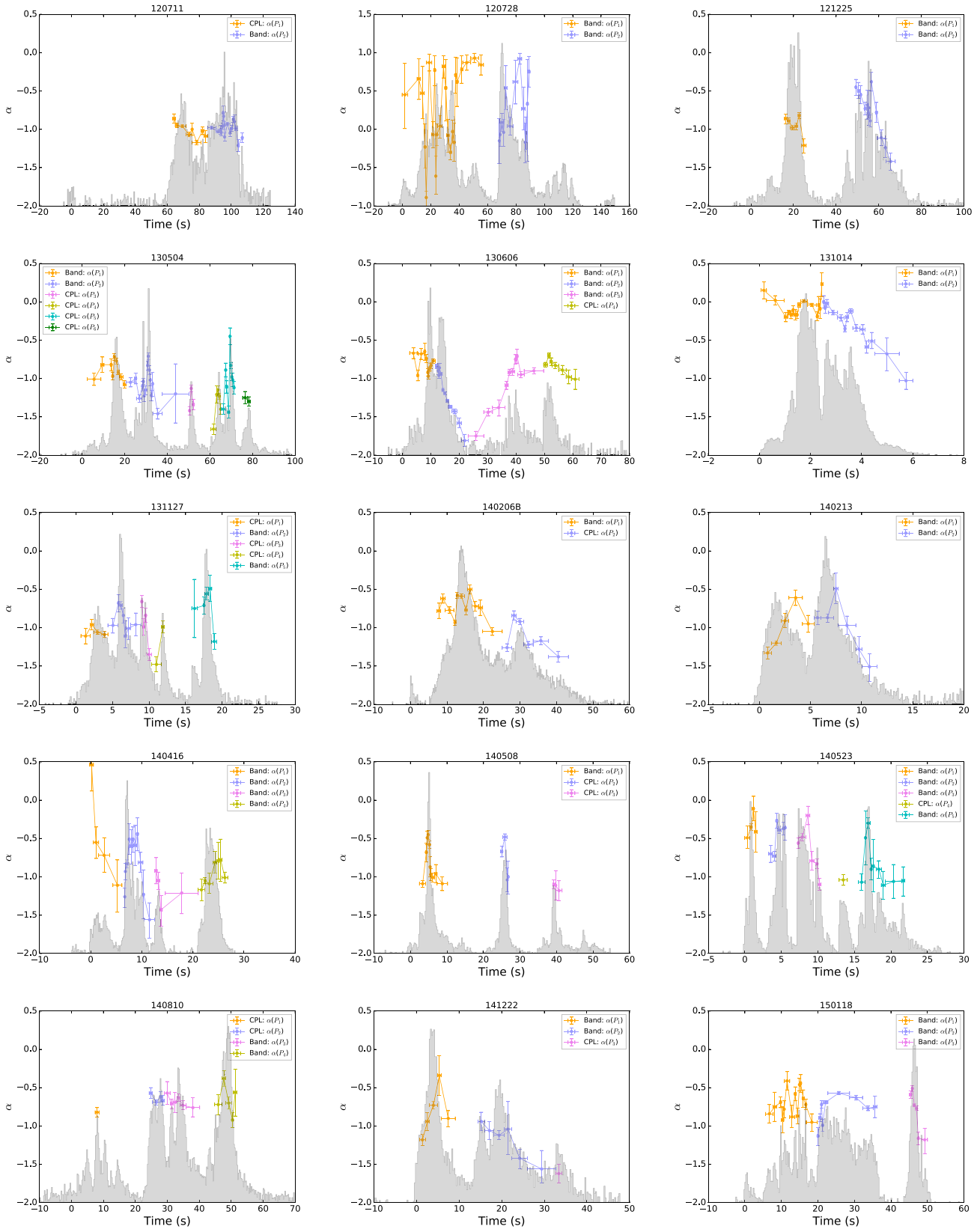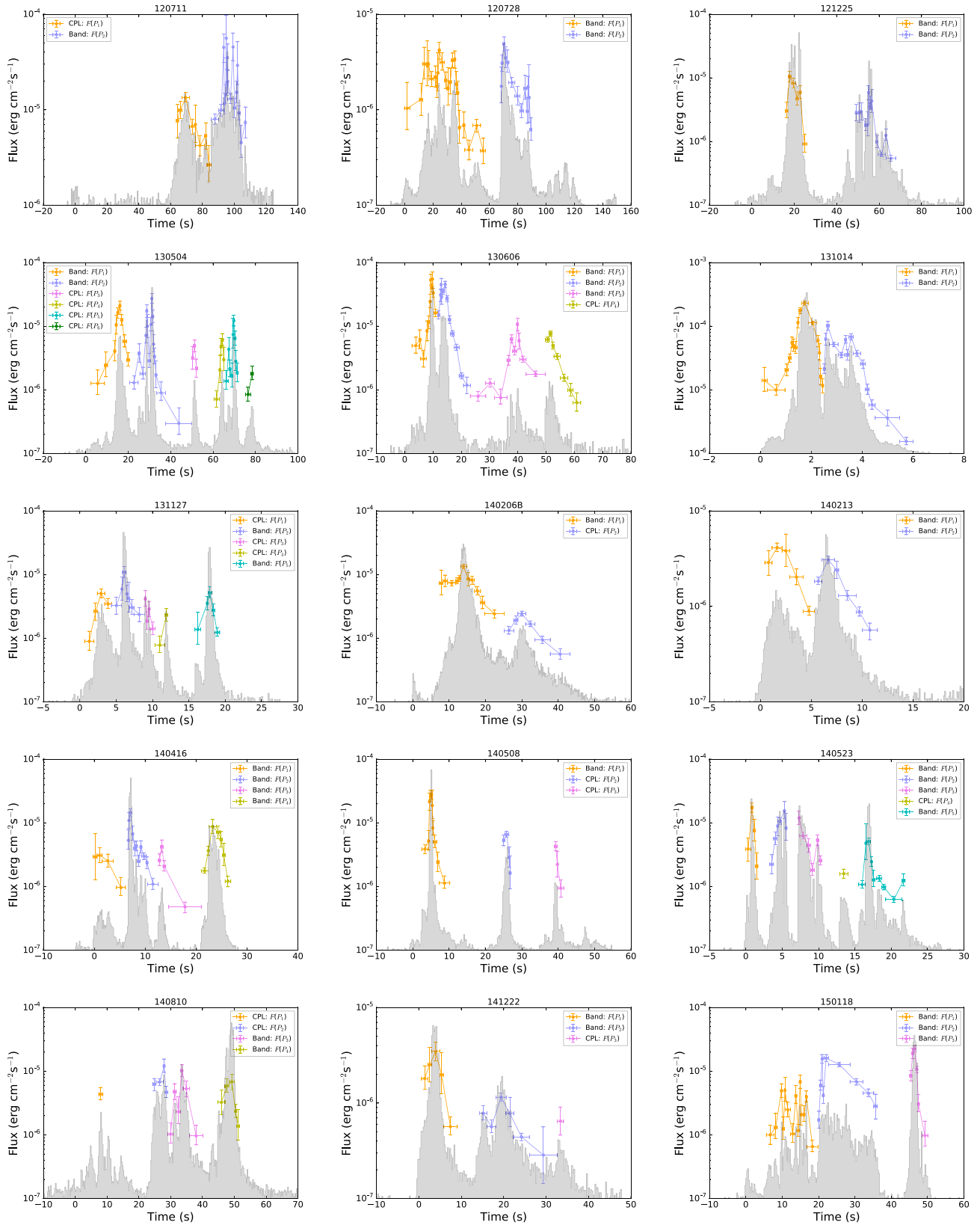
Figure A2. (Continued.)
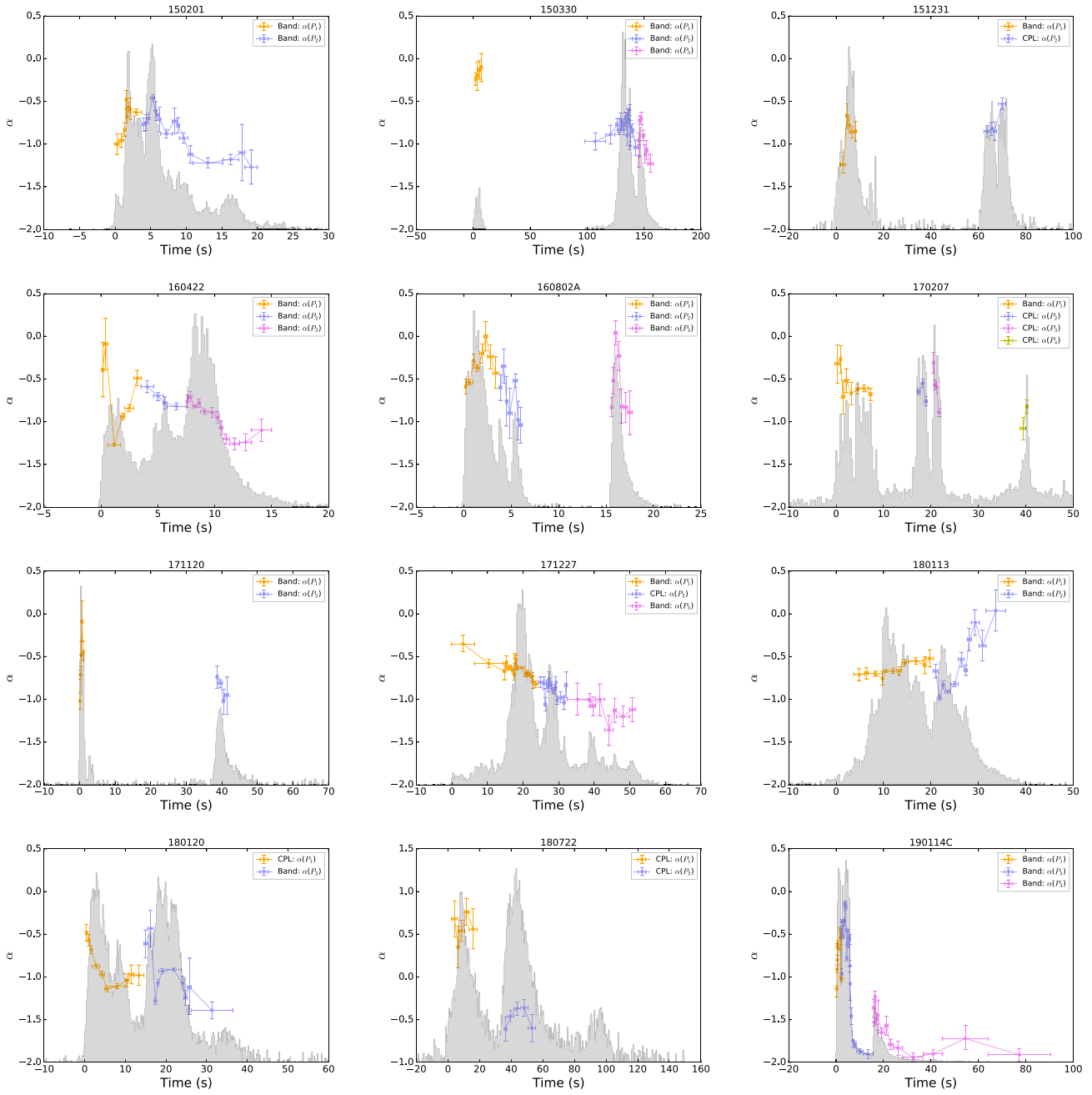
Figure A2. (Continued.)
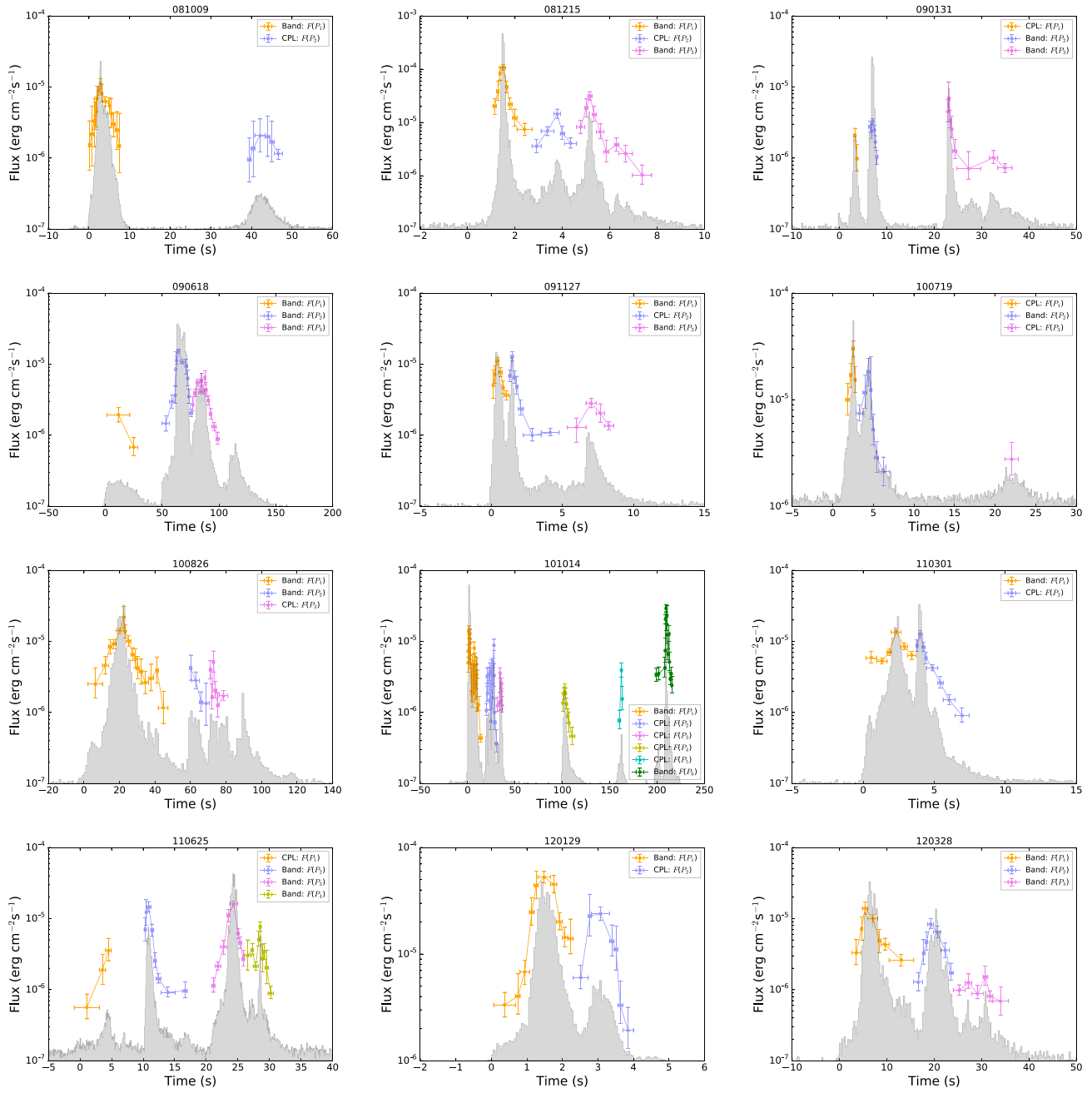
Figure A3. Temporal evolution of energy flux *F*. The symbols and colors are the same as in Figure A1.

Figure A3. (Continued.)
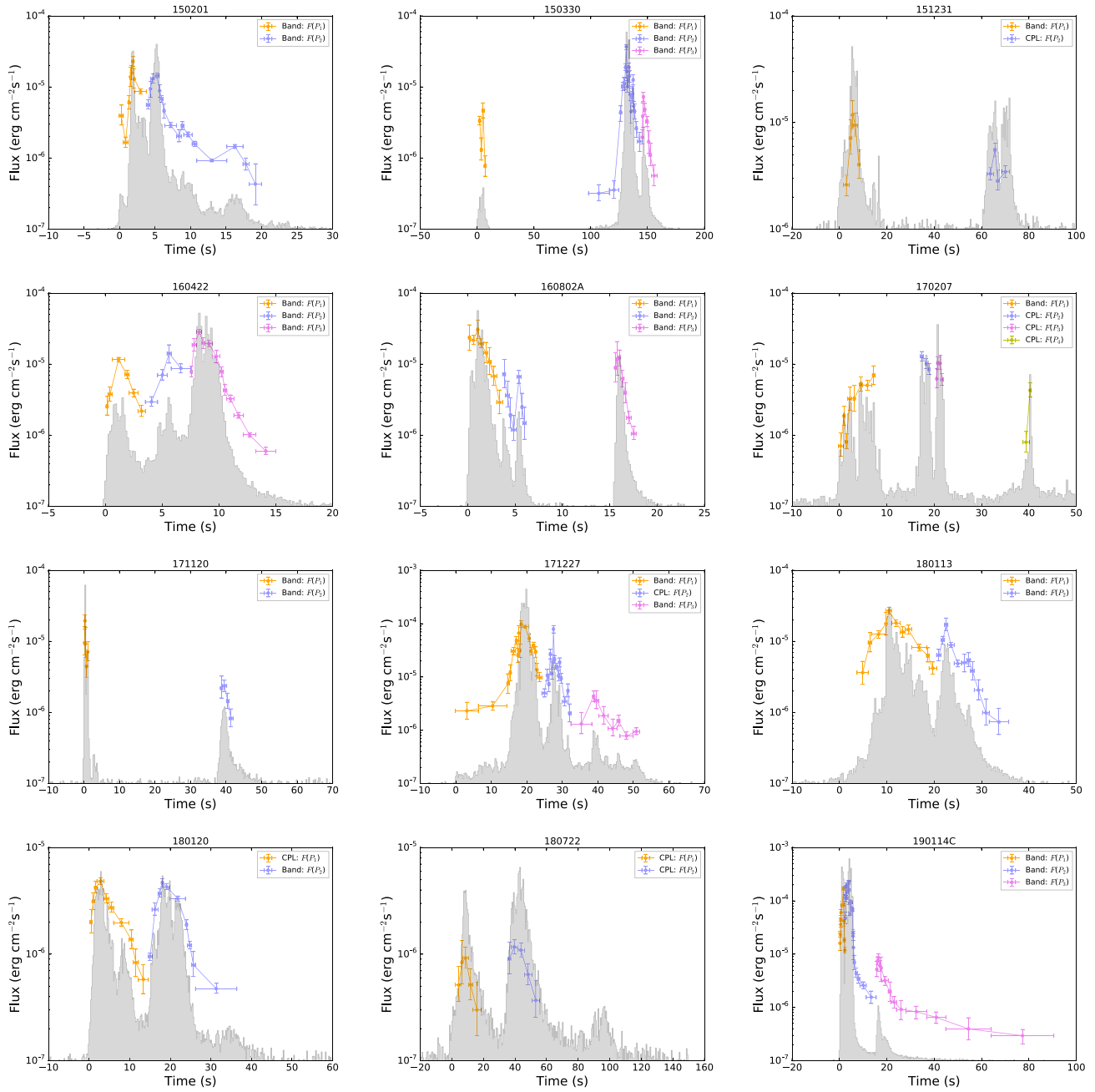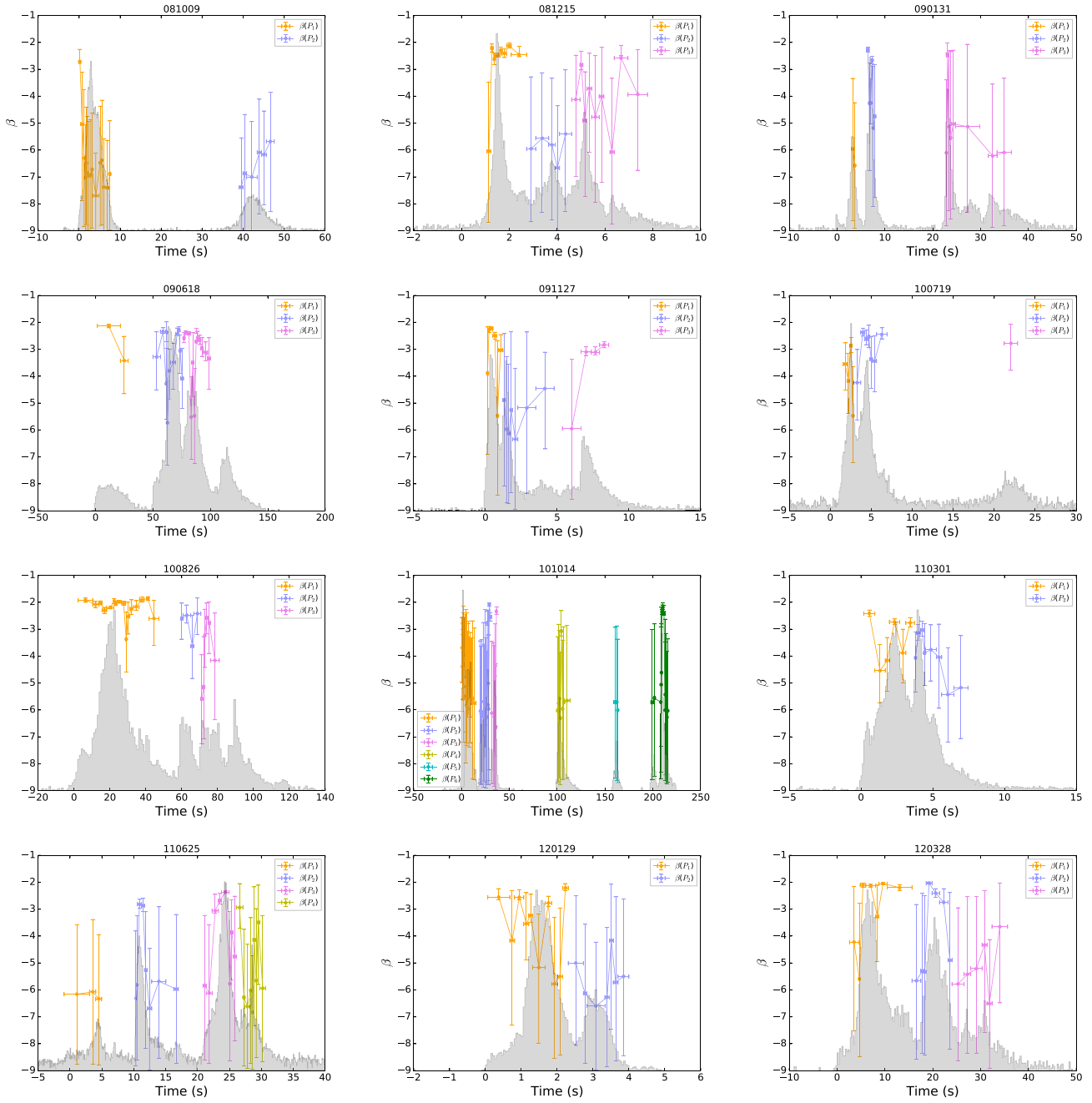
Figure A3. (Continued.)

Figure A4. Temporal evolution of the β index of the Band model. The symbols and colors are the same as in Figure A2.
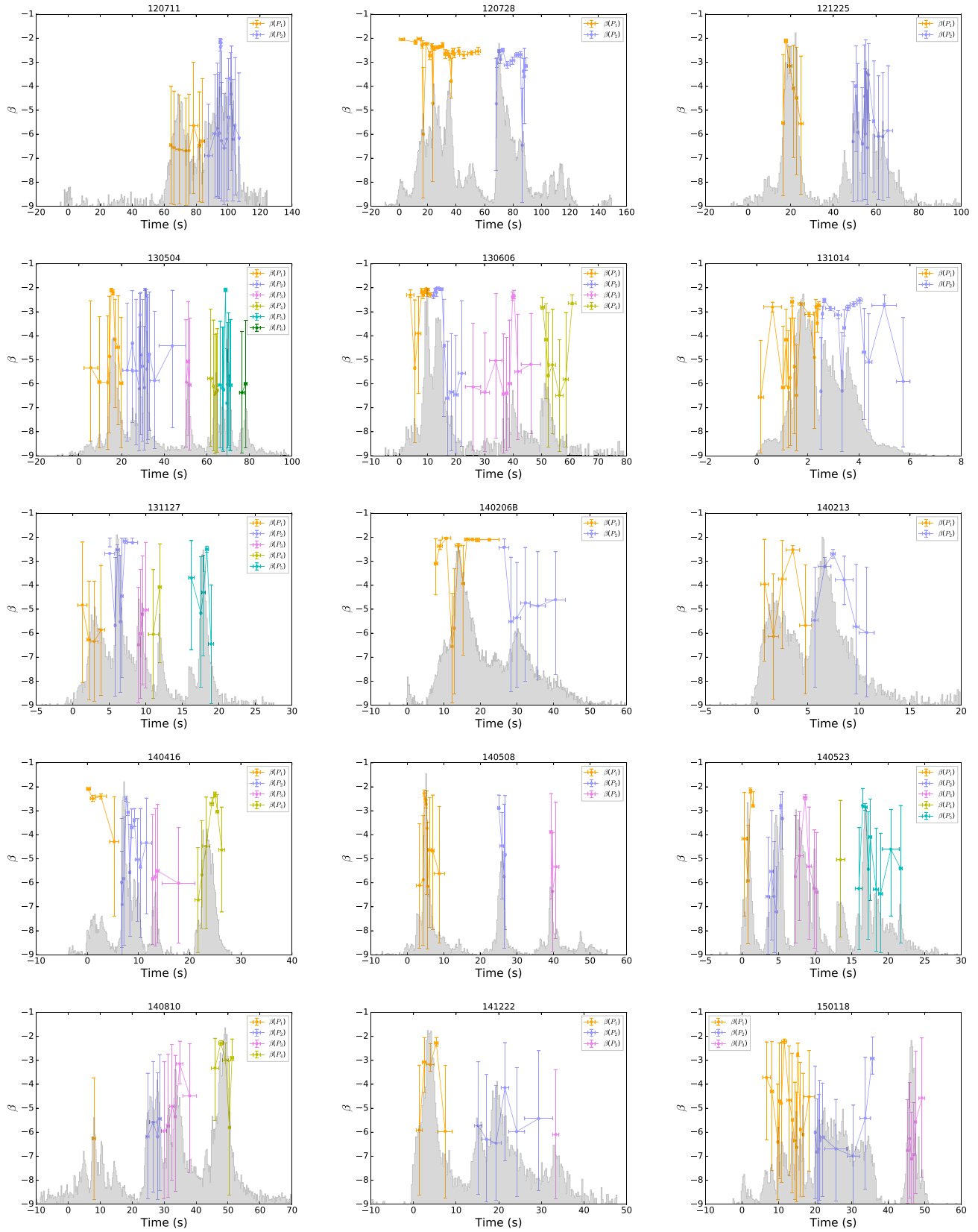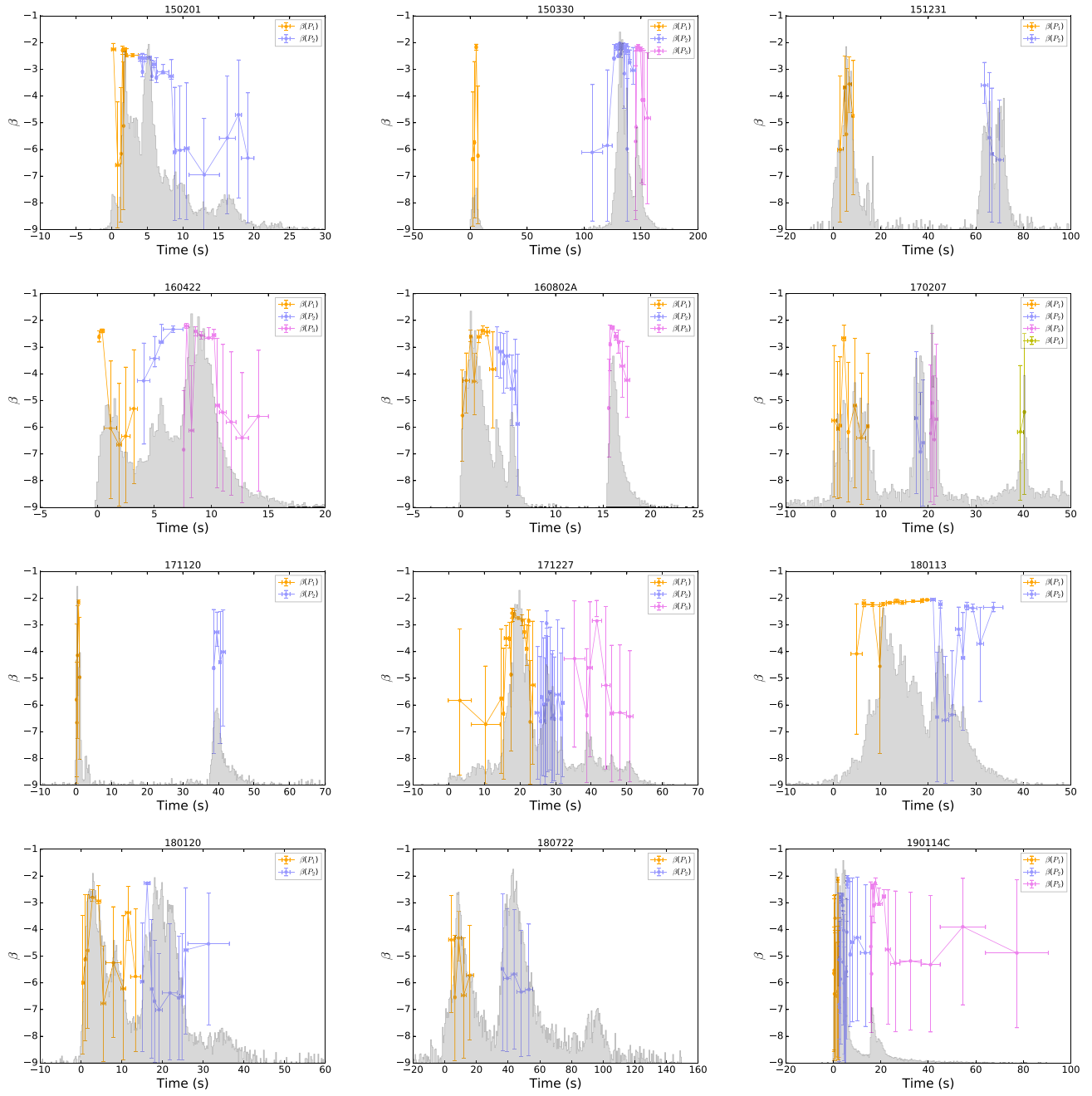
Figure A4. (Continued.)

Figure A4. (Continued.)

A.2. Best Model-based Parameter Relations in Different Pulses Text

In Figures A5–A7, we provide the F–α, F–E_p, and α–E_p relations for all the bursts based on the best models defined in Section 2.6.
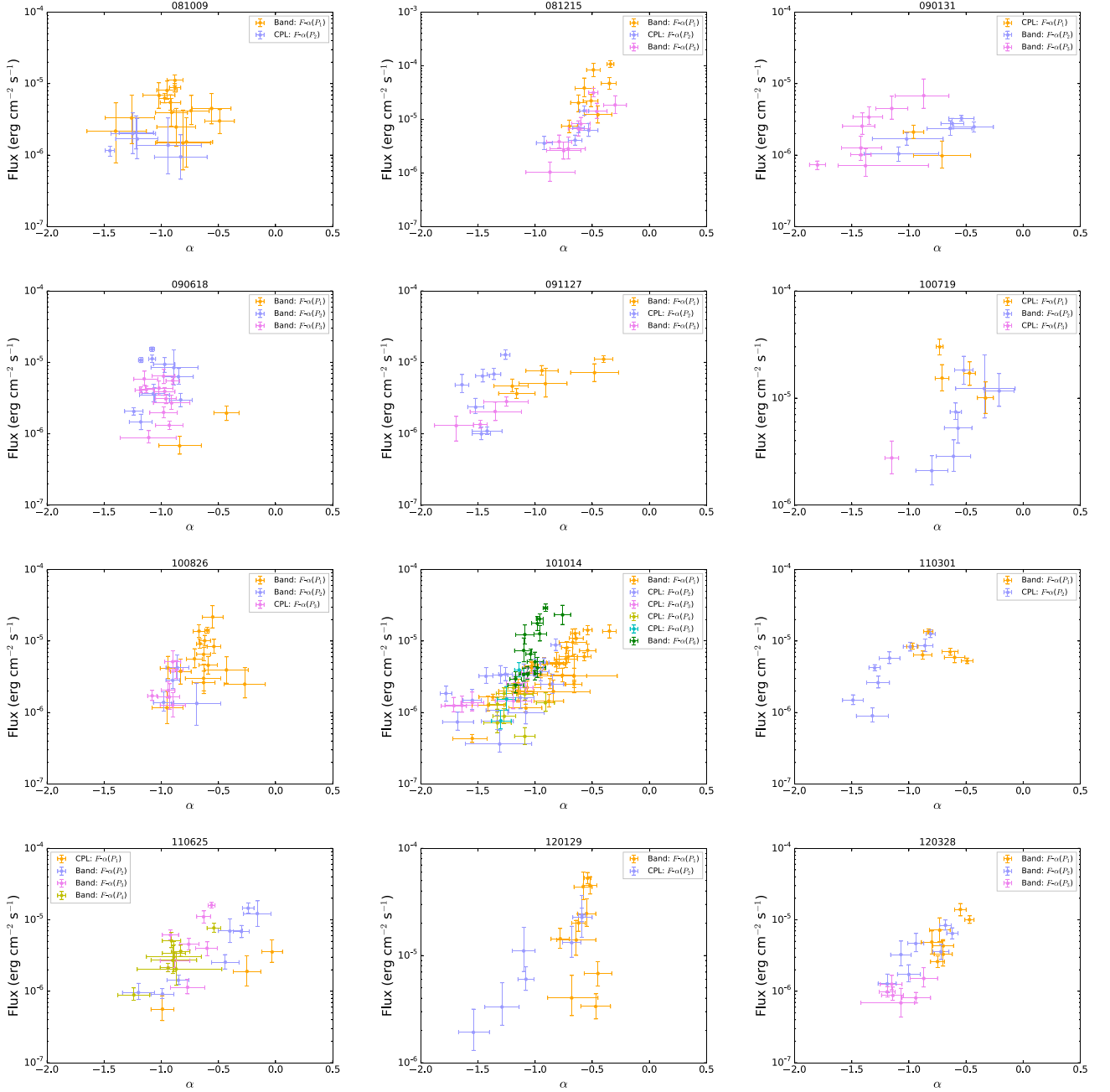

Figure A5. The F–α relation. Data points with solid orange, blue–magenta, violet, yellow, cyan, and green colors indicate time-series pulses of P_1, P_2, P_3, P_4, P_5, and P_6, respectively. All data points correspond to a statistical significance $S \geqslant 20$.
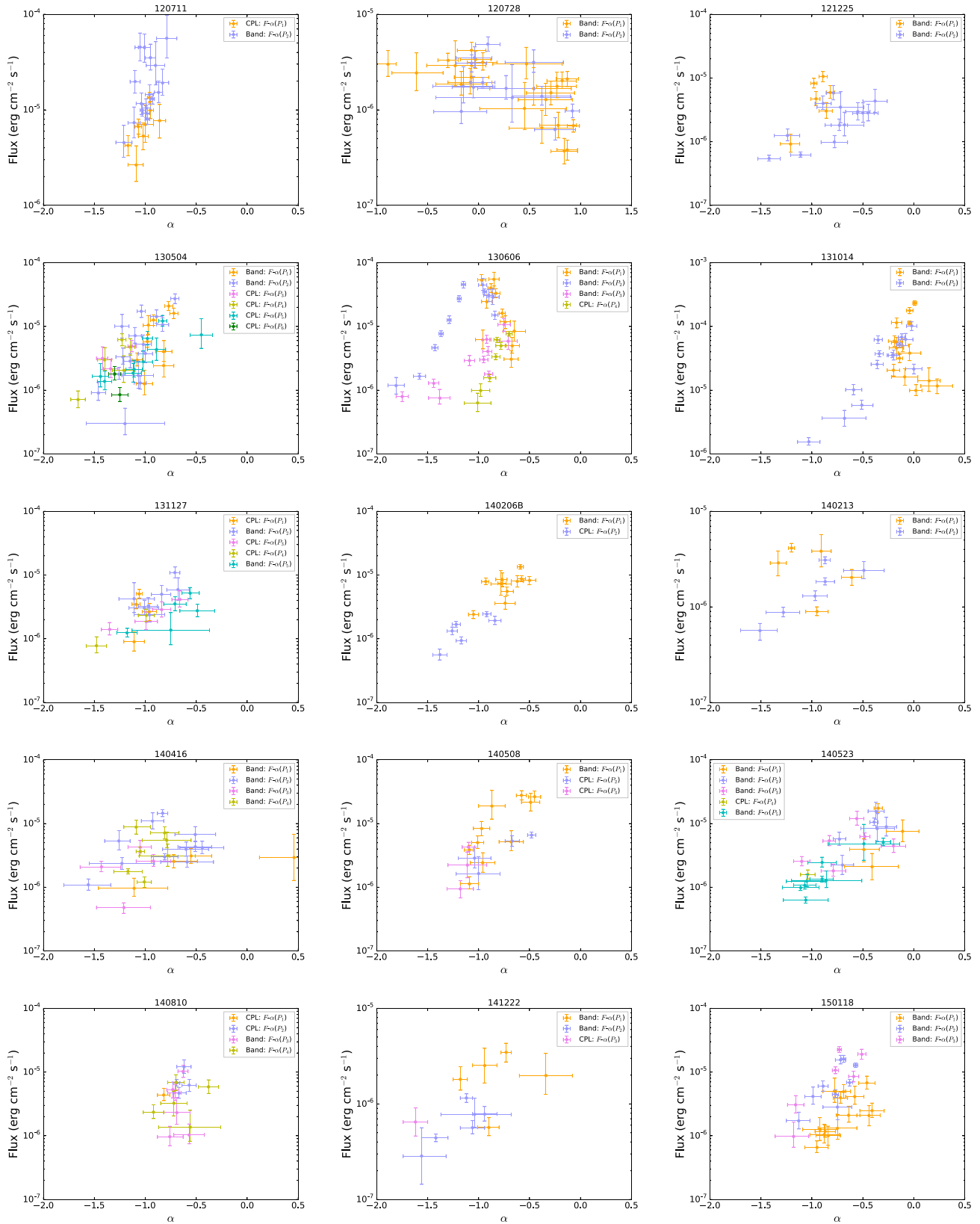
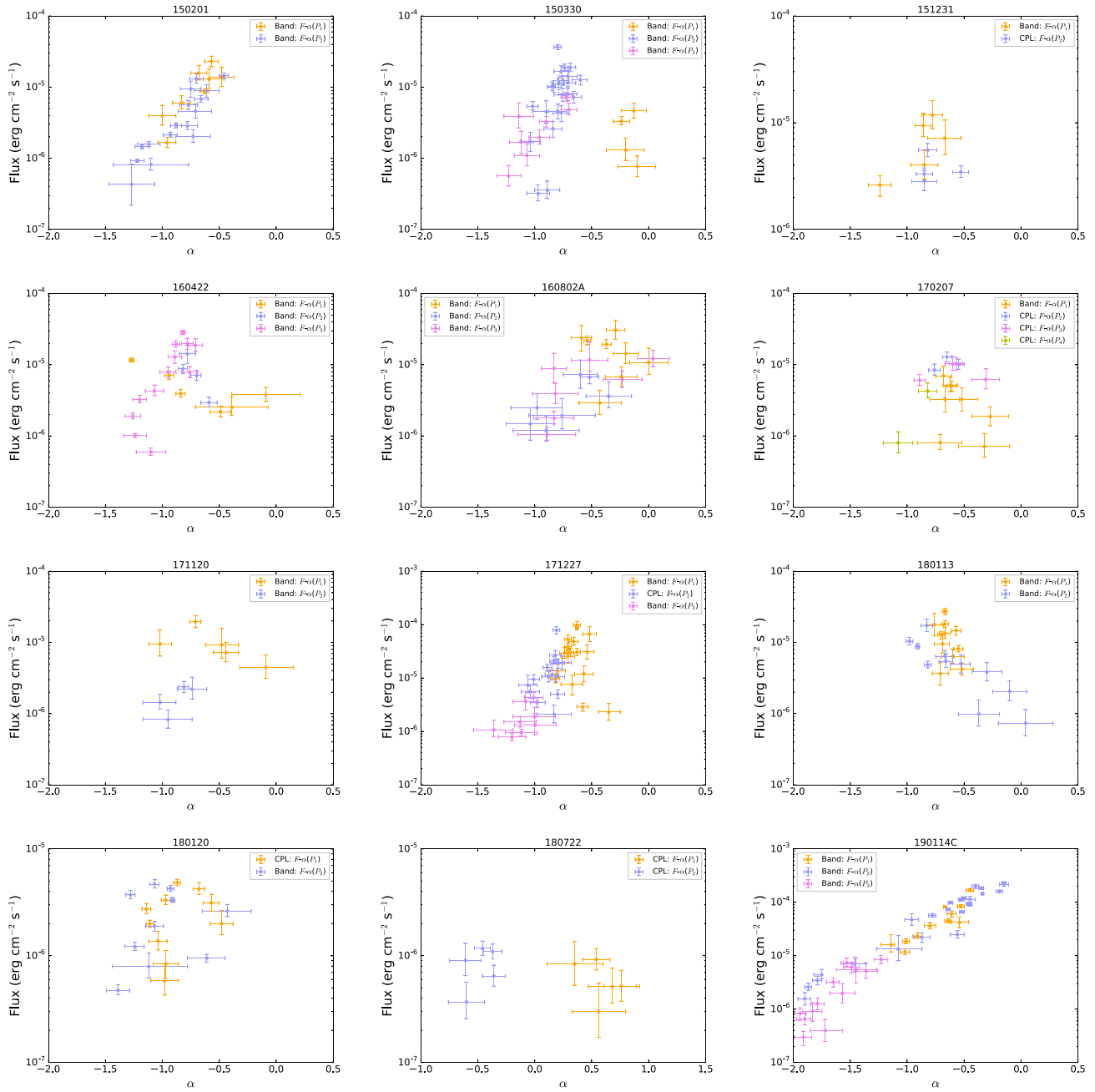34

Figure A5. (Continued.)
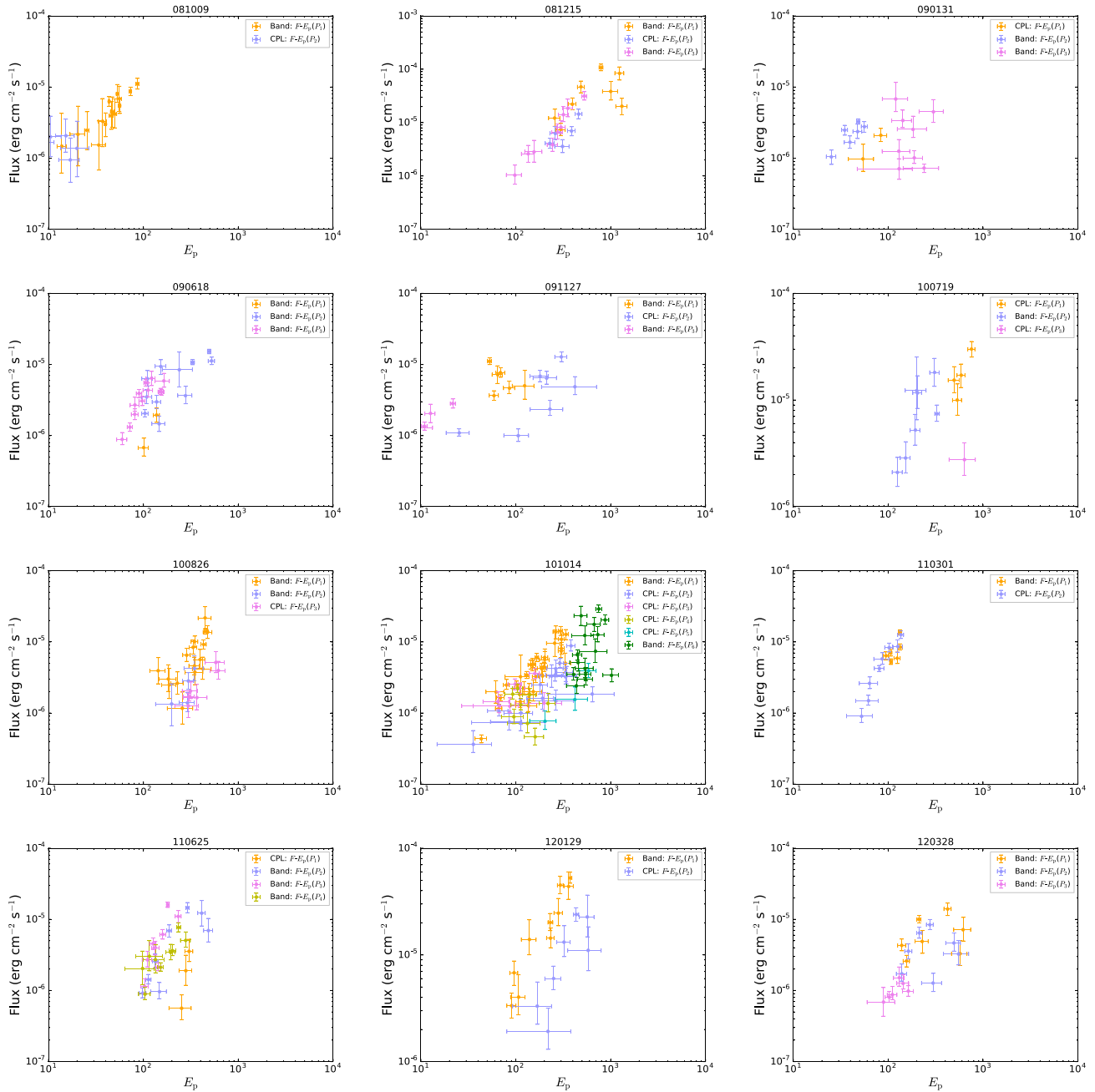
Figure A5. (Continued.)

Figure A6. The F–E_p relation. The symbols and colors are the same as in Figure A5.
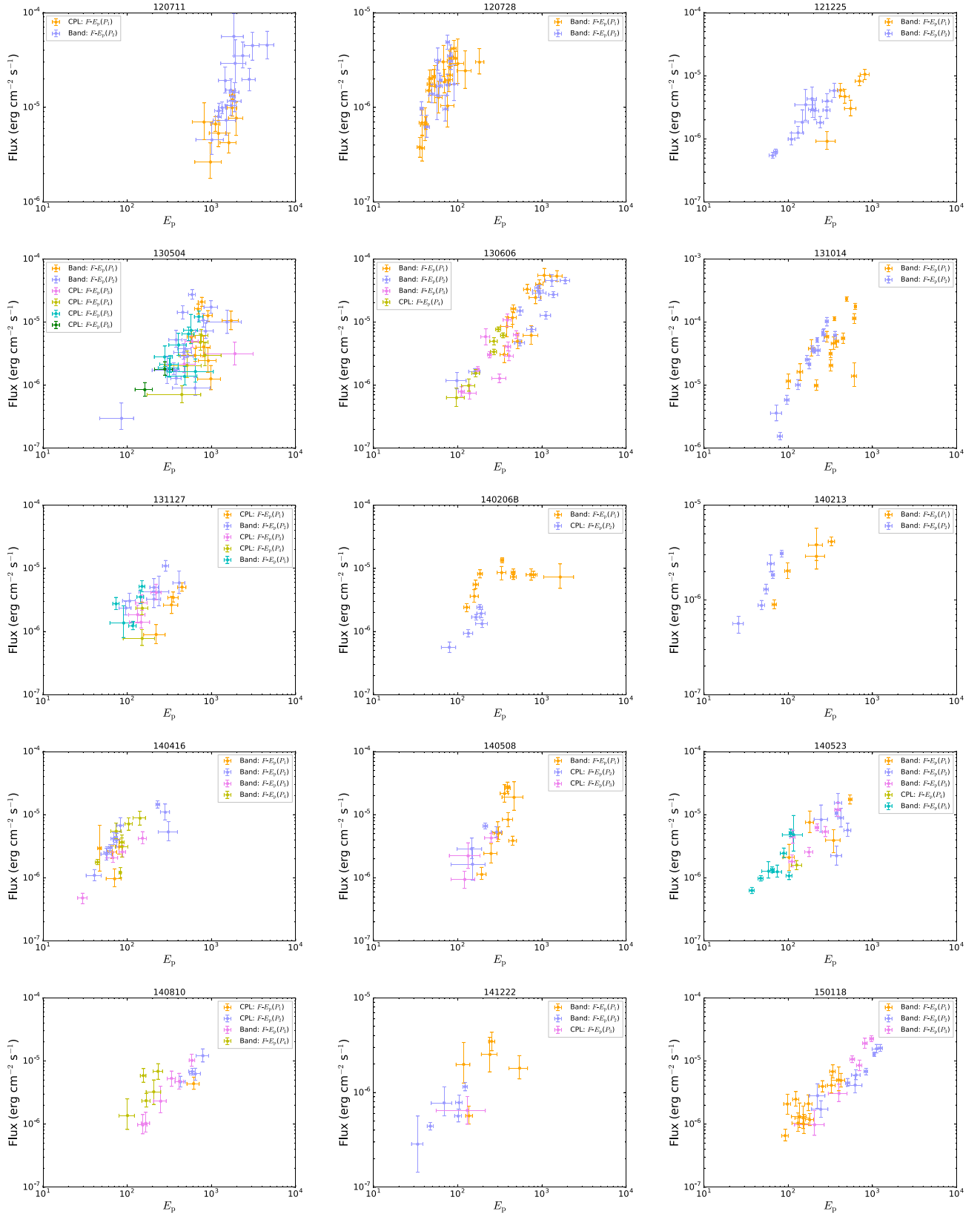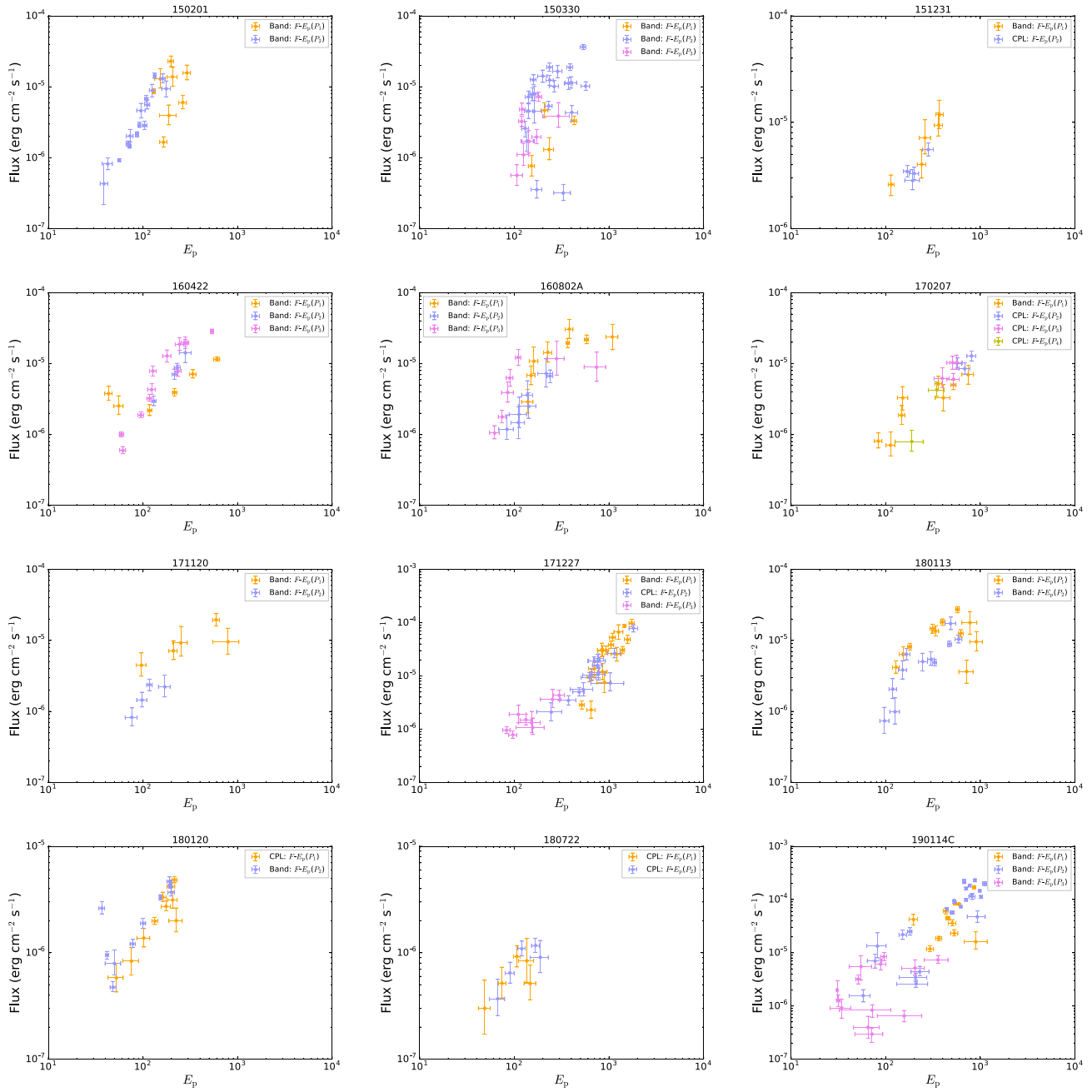
Figure A6. (Continued.)
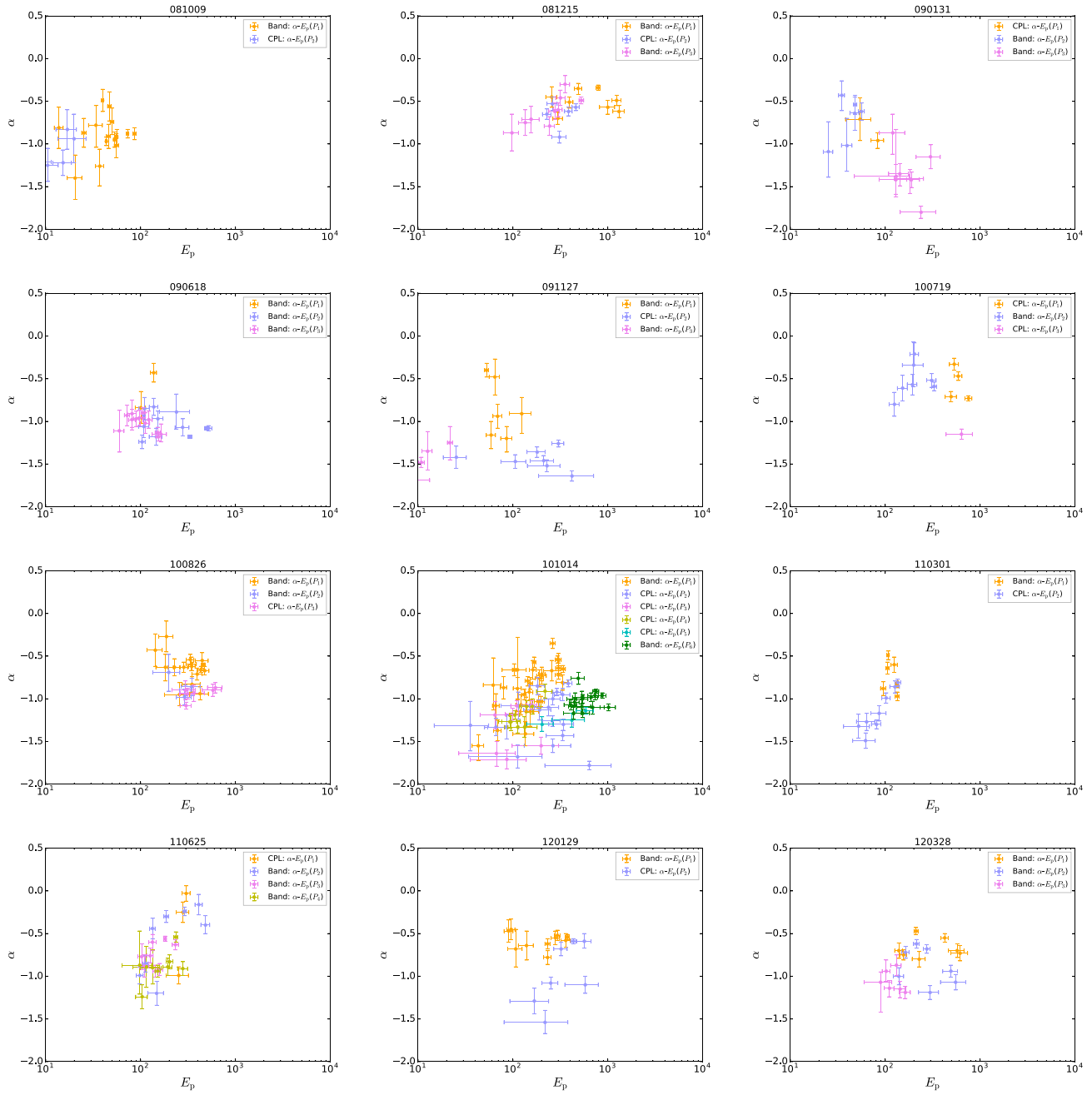
Figure A6. (Continued.)

Figure A7. The α–E_p relation. The symbols and colors are the same as in Figure A7.
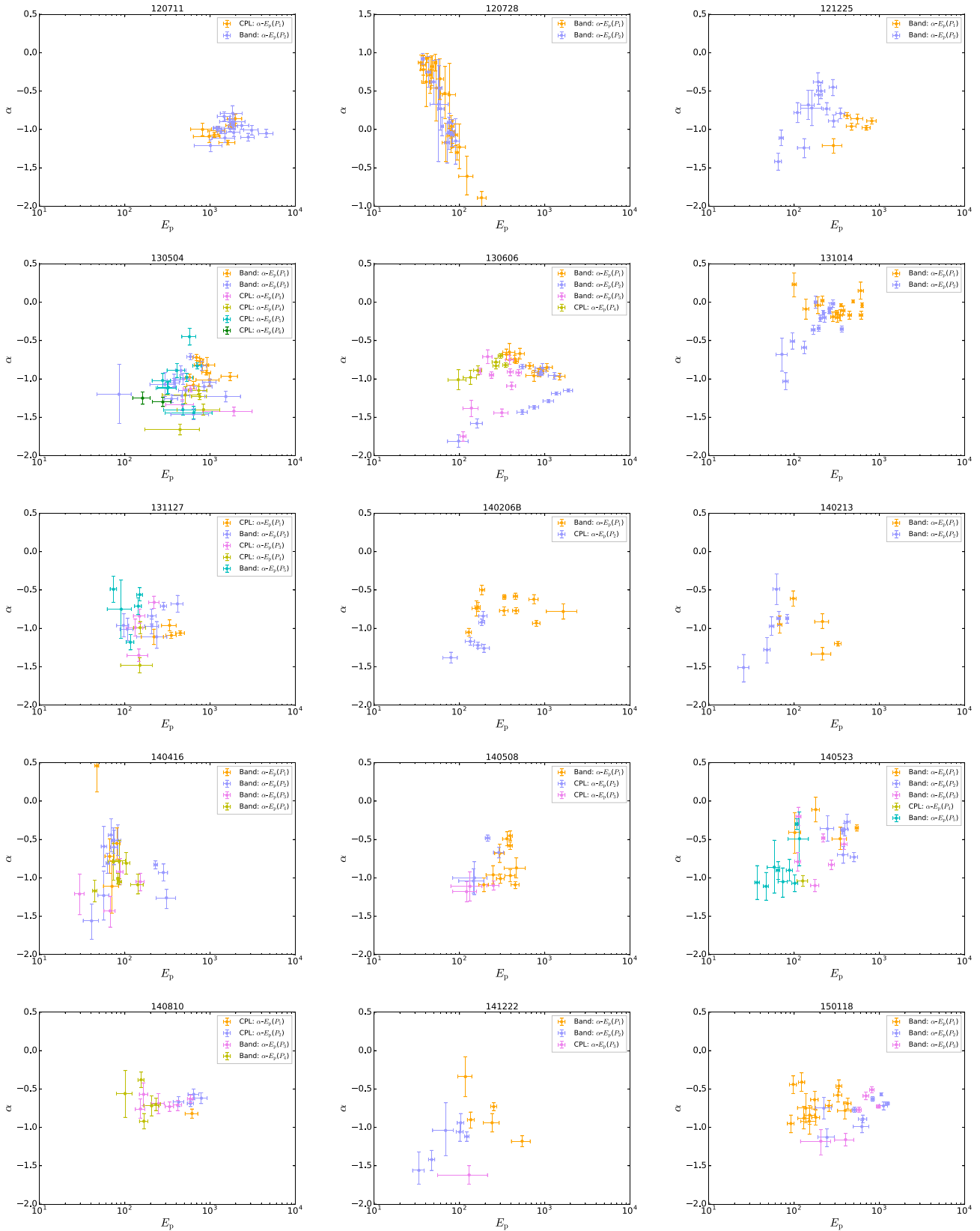
Figure A7. (Continued.)
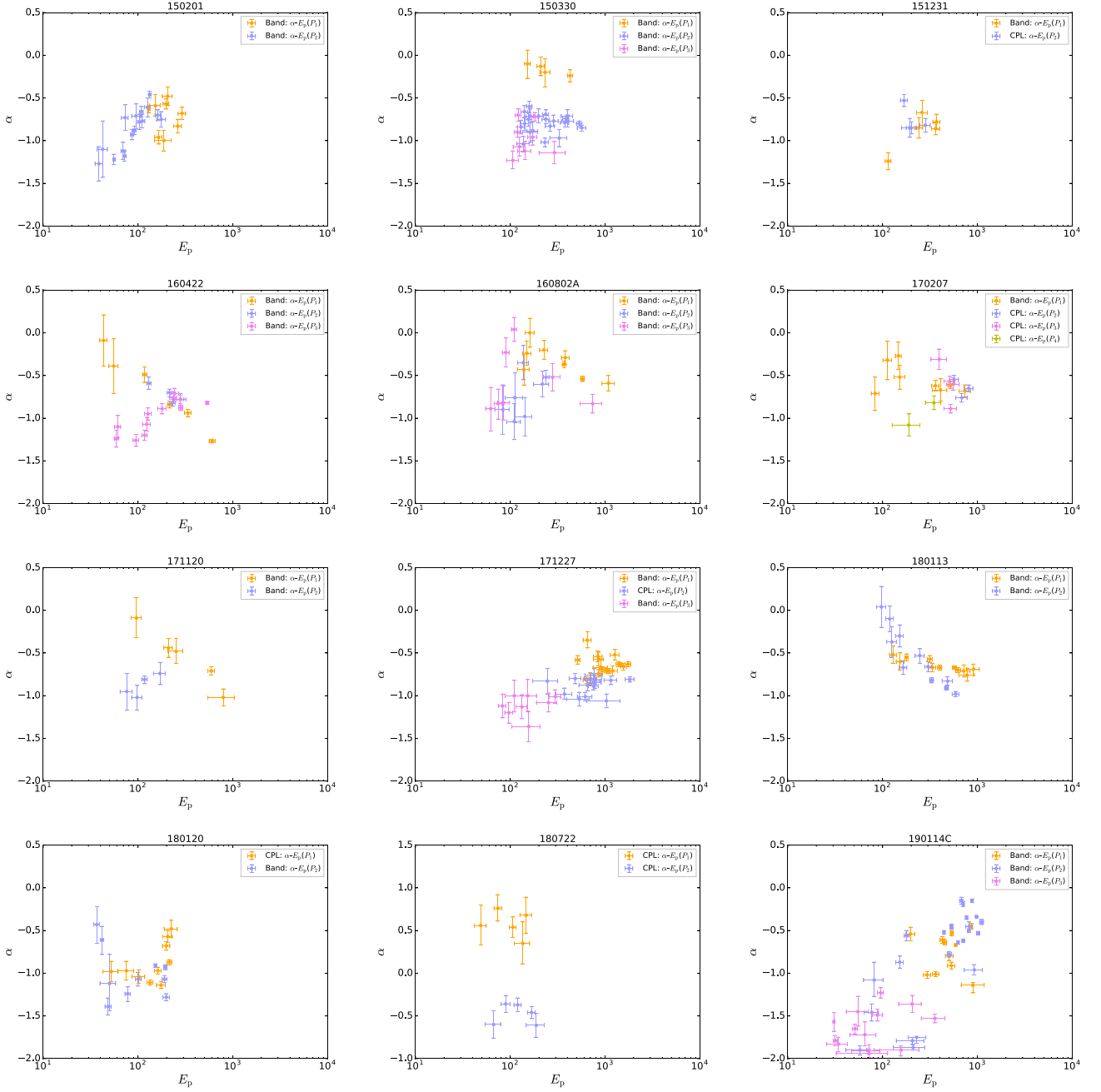
Figure A7. (Continued.)

A.3. Single Model-based Parameter Distributions in Different Pulses

In Figure A8, we provide the results of the parameter distributions, separated by two empirical photon models (Band and CPL). The overall parameter distributions we studied include four parameters (α, β, E_p, and F) in the Band model and three parameters (α, E_p, and F) in the CPL model. The corresponding average values and standard deviations from the best Gaussian fit for each distribution are presented in Table A1.

The main results of parameter distributions (α, E_p, and F) among pulses obtained from a single model (Figure A8), either

the Band or the CPL model, are consistent with the finding in the best model (Figure 2), as we discussed in the main text. For the β distribution, we find a bimodal distribution for each time-series pulse sample, as well as the global sample, where the harder peak is at ~ -2.3 and the softer peak is at ~ -6.1. The two peaks are basically the same for all different time-series pulses. We also find that the β indices are typically softer (about half of the Band spectra; the obtained β indices cannot be well converged) than some previous catalogs, whose analysis is based on the frequency analysis method, but consistent with the results found in Yu et al. (2019), who also adopted a fully Bayesian method but for a single-pulse sample.

Figure A8. Same as Figure 2, but the analysis is based on the spectral parameters derived from a single model (Band or CPL). Colors are the same as in Figure 2. Left panels are for the Band model, and right panels are for the CPL model. The lower panel shows the distribution of β for the Band model.
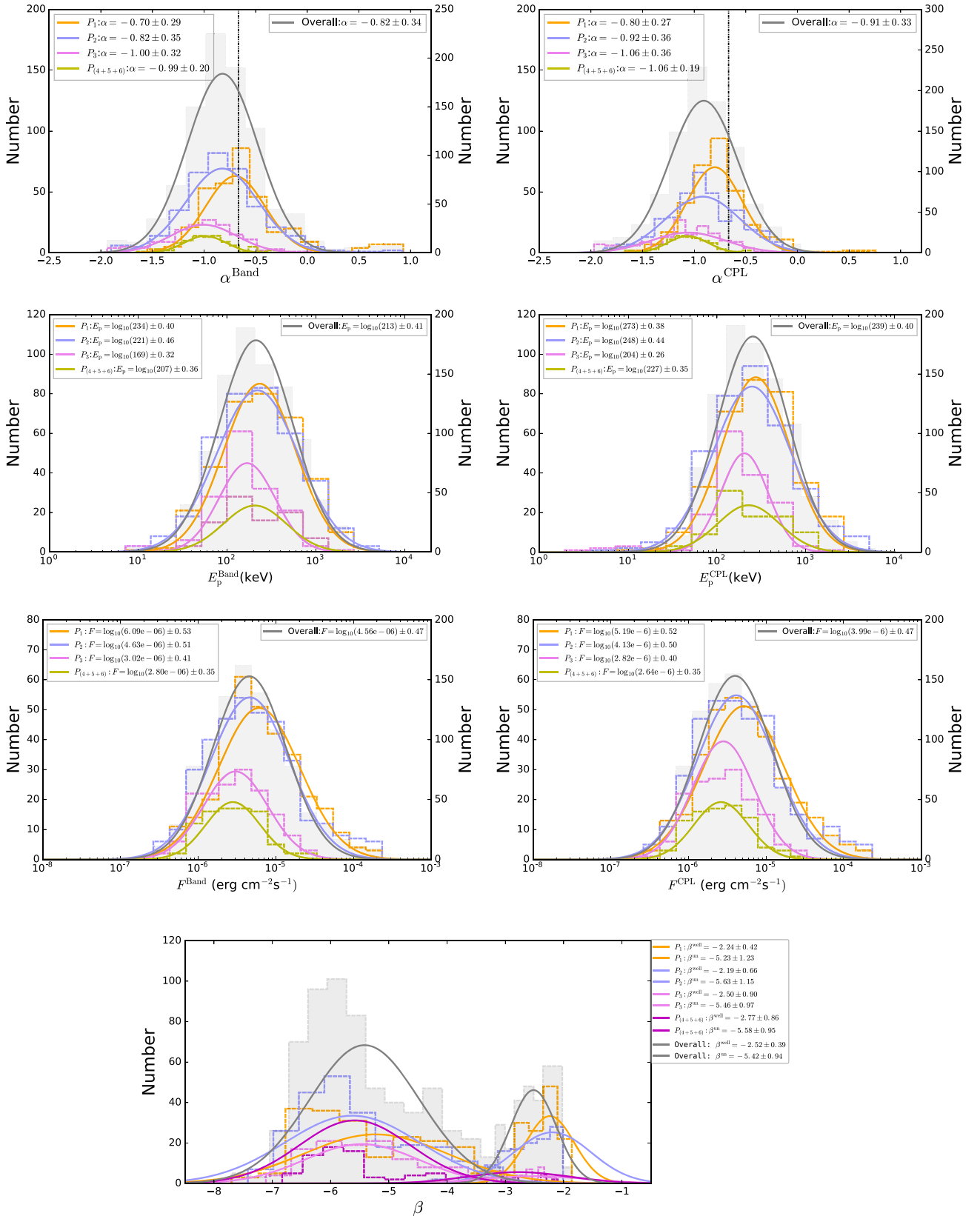
Table A1
Results of the Average and Deviation Values of the Parameter Distribution

Pulse (Group) (1)	Model (Selected) (2)	Spectra (Number) (3)	α (4)	E_p (keV) (5)	F (erg s^{-1} cm^{-2}) (6)	β (Well Converged) (7)	β (Unconverged) (8)
P_1	CPL	338	-0.80 ± 0.27	$\log_{10}(273) \pm 0.38$	$\log_{10}(5.19e{-}6) \pm 0.52$	$\cdots$	$\cdots$
P_2	CPL	361	-0.92 ± 0.36	$\log_{10}(248) \pm 0.44$	$\log_{10}(4.13e{-}6) \pm 0.50$	$\cdots$	$\cdots$
P_3	CPL	156	-1.06 ± 0.36	$\log_{10}(204) \pm 0.26$	$\log_{10}(2.82e{-}6) \pm 0.40$	$\cdots$	$\cdots$
$P_{(4+5+6)}$	CPL	89	-1.06 ± 0.19	$\log_{10}(218) \pm 0.31$	$\log_{10}(2.98e{-}6) \pm 0.38$	$\cdots$	$\cdots$
Overall	CPL	944	-0.91 ± 0.33	$\log_{10}(239) \pm 0.40$	$\log_{10}(3.99e{-}6) \pm 0.47$	$\cdots$	$\cdots$
P_1	Band	338	-0.70 ± 0.29	$\log_{10}(234) \pm 0.40$	$\log_{10}(6.09e{-}6) \pm 0.53$	-2.24 ± 0.42	-5.23 ± 1.23
P_2	Band	361	-0.82 ± 0.35	$\log_{10}(221) \pm 0.46$	$\log_{10}(4.63e{-}6) \pm 0.51$	-2.19 ± 0.66	-5.63 ± 1.15
P_3	Band	156	-1.00 ± 0.32	$\log_{10}(169) \pm 0.32$	$\log_{10}(3.02e{-}6) \pm 0.41$	-2.50 ± 0.90	-5.46 ± 0.97
$P_{(4+5+6)}$	Band	89	-0.99 ± 0.20	$\log_{10}(207) \pm 0.36$	$\log_{10}(2.98e{-}6) \pm 0.39$	-2.77 ± 0.86	-5.58 ± 0.95
Overall	Band	944	-0.82 ± 0.34	$\log_{10}(213) \pm 0.41$	$\log_{10}(4.56e{-}6) \pm 0.47$	-2.52 ± 0.39	-5.42 ± 0.94

Note. Same as Table 3, but the results are based on a single empirical photon model.

A.4. Single Model-based Parameter Relations in Different Pulses

We show global pulsewise parameter relations for our full sample in Figure A9. We present each parameter relation based on the two different photon models (the Band and CPL): F–α relation based on the Band model (first left panel), F–α relation based on the CPL model (first right panel), F–E_p relation based on the Band model (second left panel), F–E_p relation based on the CPL model (second right panel), α–E_p relation based on the Band model (third left panel), α–E_p relation based on the CPL model (third right panel), and α–β relation based on the Band model (bottom panel).

We find that there is no significant difference in the global parameter relations between the Band and CPL models. In addition, the F–E_p Golenetskii relation based on the Band model shows a stronger monotonic positive correlation than the CPL model. For the F–α relation, a cluster of data points that significantly deviate from the peak of the distribution (probably mainly contributed by type 2 in the individual parameter relations) mainly come from the early (P_1) pulse. In short, the global F–α relation shows a monotone positive correlation following a break behavior. Such a break may be originated from thermal emission. The global F–E_p relation displays type 1p behavior, while the global α–E_p shows an anticorrelation type 1n behavior. Finally, we do not find a clear trend in the global α–β relation.
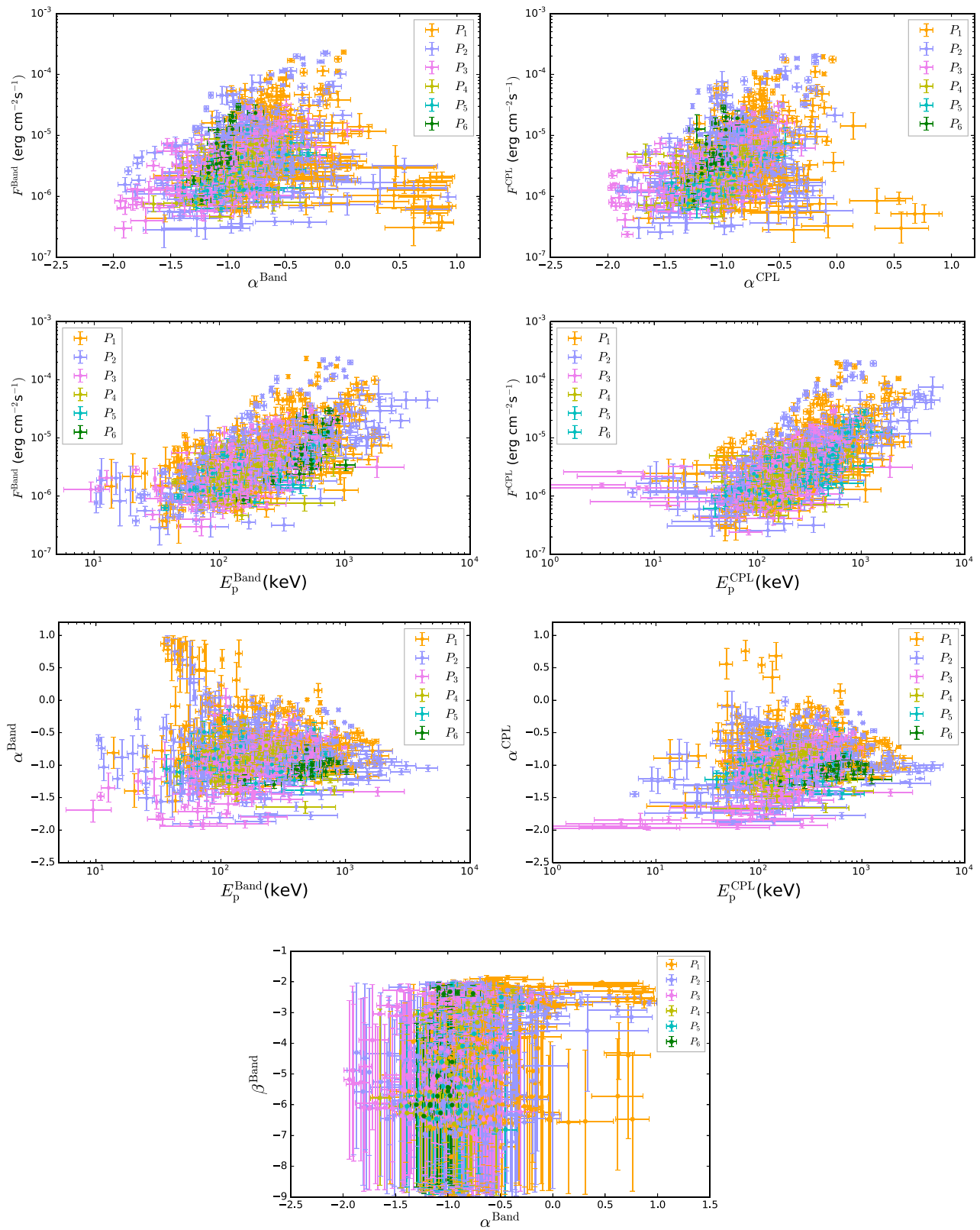
Figure A9. Pulsewise global relations of the fitted parameters of the Band and CPL models with statistical significance $S \geqslant 20$. The colors are the same as in Figure 2. Left panels are for the Band model, right panels are for the CPL model, and the bottom panel is only for the Band model.

Appendix B
Additional Table

The spectral parameters for each time bin are obtained by applying both the Band and CPL models to fit all 944 spectra. The results of the time-resolved spectral fits for each burst in our global sample, which include the start and stop times of the BBlocks (column 1); the statistical significance S (column 2); the best-fit parameters of the CPL model (columns 3–7), including the normalization K, low-energy power-law photon spectral index α, break energy E_c, peak energy[14] E_p, and νF_ν flux F; the best-fit parameters of the Band model (columns 8–12), containing the normalization, low-energy power-law photon spectral index α, high-energy power-law photon spectral index β, peak energy E_p, and νF_ν flux F; the ΔDIC (column 13); the $p_{\rm DIC}^{\rm CPL}$ based on the CPL model fitting (column 14); and the $p_{\rm DIC}^{\rm Band}$ based on the Band model fitting (column 15) are listed in Table B1. For the definition of ΔDIC, as well as the discussion for $p_{\rm DIC}$, please see Section 2.6 for details.

---

[14] We note that in a few cases, the value of E_p is close to the lower limit of the detector range. Since the effective area decreases rapidly at the edges of the detector energy range and the determination of α suffers from the lack of dynamical range below the peak, the time bins with $E_p < 20$ keV should be largely ignored (see, e.g., Ravasio et al. 2019).

Table B1
Time-resolved Spectral Fit Results of GRB 081009140

$t_{start} \sim t_{stop}$ (1)	S (2)	CPL Fitting K (3)	α (4)	E_c (5)	E_p (6)	F (7)	Band Fitting K (8)	α (9)	β (10)	E_p (11)	F (12)	Difference ΔDIC (13)	p_{DIC}^{CPL} (14)	p_{DIC}^{Band} (15)
Pulse 1														
0.000~0.368	21.46	$0.08^{+0.03}_{-0.02}$	$-1.36^{+0.17}_{-0.15}$	75^{+17}_{-18}	48^{+17}_{-16}	$1.31^{+0.71}_{-0.41}\times10^{-6}$	$0.38^{+0.19}_{-0.21}$	$-0.78^{+0.23}_{-0.26}$	$-2.72^{+0.46}_{-0.02}$	34^{+6}_{-6}	$1.53^{+1.81}_{-0.85}\times10^{-6}$	-13.5	0.8	-5.4
0.368~1.114	47.31	$0.12^{+0.05}_{-0.05}$	$-1.63^{+0.20}_{-0.20}$	52^{+14}_{-14}	19^{+12}_{-11}	$2.46^{+1.87}_{-1.04}\times10^{-6}$	$0.23^{+0.14}_{-0.12}$	$-1.40^{+0.27}_{-0.25}$	$-5.04^{+1.93}_{-2.83}$	20^{+4}_{-4}	$2.17^{+3.21}_{-1.39}\times10^{-6}$	-11.9	-16.9	-28.5
1.114~1.358	39.81	$0.24^{+0.09}_{-0.09}$	$-1.36^{+0.20}_{-0.20}$	62^{+16}_{-16}	40^{+16}_{-11}	$3.45^{+2.55}_{-1.42}\times10^{-6}$	$0.32^{+0.10}_{-0.15}$	$-1.26^{+0.20}_{-0.23}$	$-6.30^{+2.53}_{-2.55}$	37^{+4}_{-4}	$3.31^{+3.59}_{-1.86}\times10^{-6}$	-7.4	-7.0	-15.0
1.358~1.662	57.46	$0.66^{+0.17}_{-0.18}$	$-0.94^{+0.14}_{-0.14}$	44^{+6}_{-6}	47^{+9}_{-9}	$4.06^{+1.59}_{-1.21}\times10^{-6}$	$0.70^{+0.19}_{-0.20}$	$-0.91^{+0.14}_{-0.14}$	$-7.03^{+1.96}_{-1.99}$	46^{+2}_{-2}	$3.95^{+2.24}_{-1.41}\times10^{-6}$	1.8	-0.5	0.9
1.662~1.895	58.56	$1.53^{+0.46}_{-0.52}$	$-0.62^{+0.16}_{-0.17}$	35^{+4}_{-4}	48^{+8}_{-8}	$4.71^{+2.35}_{-1.65}\times10^{-6}$	$1.71^{+0.56}_{-0.59}$	$-0.56^{+0.17}_{-0.17}$	$-6.48^{+2.07}_{-2.29}$	47^{+2}_{-2}	$4.49^{+2.77}_{-1.76}\times10^{-6}$	3.7	-6.1	-2.4
1.895~2.042	58.16	$0.74^{+0.20}_{-0.20}$	$-1.04^{+0.14}_{-0.14}$	60^{+10}_{-9}	57^{+12}_{-12}	$6.84^{+3.00}_{-1.98}\times10^{-6}$	$0.77^{+0.20}_{-0.20}$	$-1.02^{+0.14}_{-0.14}$	$-6.84^{+2.10}_{-2.14}$	56^{+3}_{-3}	$6.85^{+3.40}_{-2.31}\times10^{-6}$	2.0	-0.3	1.6
2.042~2.724	139.74	$0.95^{+0.09}_{-0.09}$	$-0.88^{+0.05}_{-0.05}$	65^{+4}_{-4}	73^{+5}_{-5}	$8.68^{+1.21}_{-1.08}\times10^{-6}$	$0.95^{+0.09}_{-0.09}$	$-0.88^{+0.05}_{-0.05}$	$-6.96^{+2.02}_{-2.08}$	73^{+2}_{-2}	$8.74^{+1.22}_{-1.14}\times10^{-6}$	-0.1	2.7	2.8
2.724~3.004	102.13	$0.98^{+0.12}_{-0.12}$	$-0.89^{+0.07}_{-0.07}$	78^{+7}_{-7}	87^{+9}_{-9}	$11.29^{+1.92}_{-1.78}\times10^{-6}$	$0.99^{+0.12}_{-0.12}$	$-0.88^{+0.07}_{-0.07}$	$-6.91^{+2.05}_{-2.08}$	87^{+3}_{-3}	$11.11^{+2.14}_{-1.74}\times10^{-6}$	0.7	2.6	3.0
3.004~3.291	91.74	$1.04^{+0.19}_{-0.19}$	$-0.96^{+0.09}_{-0.09}$	52^{+5}_{-5}	54^{+7}_{-7}	$8.09^{+2.16}_{-1.61}\times10^{-6}$	$1.07^{+0.19}_{-0.20}$	$-0.95^{+0.09}_{-0.09}$	$-6.72^{+2.09}_{-2.17}$	53^{+2}_{-2}	$8.03^{+2.81}_{-1.94}\times10^{-6}$	0.8	1.6	2.4
3.291~4.845	178.12	$0.98^{+0.10}_{-0.10}$	$-0.98^{+0.05}_{-0.05}$	43^{+2}_{-2}	44^{+3}_{-3}	$6.28^{+0.79}_{-0.78}\times10^{-6}$	$0.98^{+0.10}_{-0.10}$	$-0.97^{+0.05}_{-0.05}$	$-7.70^{+1.59}_{-1.60}$	44^{+1}_{-1}	$6.26^{+1.03}_{-0.89}\times10^{-6}$	0.8	2.5	3.0
4.845~5.379	92.71	$0.73^{+0.12}_{-0.12}$	$-0.93^{+0.09}_{-0.09}$	53^{+5}_{-5}	57^{+7}_{-7}	$5.54^{+1.30}_{-1.09}\times10^{-6}$	$0.75^{+0.13}_{-0.13}$	$-0.92^{+0.09}_{-0.09}$	$-6.47^{+2.10}_{-2.33}$	56^{+2}_{-2}	$5.46^{+1.54}_{-1.21}\times10^{-6}$	0.4	1.6	2.2
5.379~5.654	58.38	$0.90^{+0.27}_{-0.27}$	$-0.78^{+0.16}_{-0.15}$	42^{+6}_{-6}	51^{+10}_{-10}	$4.59^{+2.18}_{-1.48}\times10^{-6}$	$1.00^{+0.30}_{-0.30}$	$-0.74^{+0.16}_{-0.15}$	$-6.38^{+2.23}_{-2.41}$	50^{+2}_{-2}	$4.18^{+2.65}_{-1.51}\times10^{-6}$	2.1	-2.2	-0.1
5.654~6.403	77.43	$1.63^{+0.43}_{-0.43}$	$-0.48^{+0.13}_{-0.13}$	26^{+2}_{-2}	40^{+5}_{-5}	$3.02^{+1.26}_{-0.87}\times10^{-6}$	$1.62^{+0.44}_{-0.43}$	$-0.49^{+0.13}_{-0.13}$	$-7.38^{+1.80}_{-1.82}$	40^{+1}_{-1}	$3.01^{+1.32}_{-1.00}\times10^{-6}$	2.3	-1.8	0.4
6.403~7.223	66.04	$0.99^{+0.40}_{-0.38}$	$-0.86^{+0.18}_{-0.18}$	23^{+3}_{-3}	26^{+5}_{-5}	$2.40^{+1.69}_{-0.97}\times10^{-6}$	$0.95^{+0.35}_{-0.34}$	$-0.87^{+0.17}_{-0.17}$	$-7.40^{+1.76}_{-1.78}$	25^{+1}_{-1}	$2.47^{+2.03}_{-1.15}\times10^{-6}$	11.4	-15.5	-4.1
7.223~7.710	31.68	$1.44^{+0.96}_{-0.89}$	$-0.89^{+0.28}_{-0.30}$	12^{+2}_{-2}	14^{+4}_{-4}	$1.84^{+2.49}_{-1.17}\times10^{-6}$	$1.68^{+0.95}_{-0.92}$	$-0.81^{+0.24}_{-0.24}$	$-6.89^{+1.98}_{-2.06}$	14^{+1}_{-1}	$1.48^{+2.79}_{-0.86}\times10^{-6}$	21.7	-32.1	-10.5
Pulse 2														
39.073~39.961	26.55	$0.70^{+0.41}_{-0.35}$	$-0.83^{+0.23}_{-0.23}$	14^{+2}_{-2}	17^{+4}_{-4}	$0.95^{+0.98}_{-0.49}\times10^{-6}$	$0.65^{+0.41}_{-0.38}$	$-0.88^{+0.27}_{-0.28}$	$-7.38^{+1.83}_{-1.80}$	16^{+2}_{-2}	$0.82^{+1.71}_{-0.51}\times10^{-6}$	-1.5	-11.0	-12.7
39.961~40.823	37.34	$0.65^{+0.41}_{-0.38}$	$-0.94^{+0.29}_{-0.28}$	19^{+4}_{-4}	20^{+7}_{-7}	$1.37^{+1.94}_{-0.83}\times10^{-6}$	$0.90^{+0.45}_{-0.54}$	$-0.82^{+0.27}_{-0.28}$	$-6.87^{+2.14}_{-2.14}$	20^{+2}_{-2}	$1.27^{+2.19}_{-0.81}\times10^{-6}$	17.1	-57.0	-40.3
40.823~43.426	81.42	$0.45^{+0.16}_{-0.16}$	$-1.22^{+0.15}_{-0.15}$	20^{+2}_{-2}	15^{+3}_{-3}	$2.07^{+1.48}_{-0.85}\times10^{-6}$	$0.47^{+0.17}_{-0.16}$	$-1.21^{+0.16}_{-0.15}$	$-7.00^{+2.06}_{-2.08}$	15^{+1}_{-1}	$2.04^{+1.73}_{-0.97}\times10^{-6}$	10.4	-20.1	-9.7
43.426~44.500	46.19	$0.60^{+0.28}_{-0.27}$	$-1.25^{+0.20}_{-0.19}$	14^{+2}_{-2}	10^{+3}_{-3}	$2.00^{+1.90}_{-0.95}\times10^{-6}$	$1.10^{+0.54}_{-0.57}$	$-1.03^{+0.21}_{-0.21}$	$-6.09^{+1.98}_{-2.30}$	12^{+1}_{-1}	$1.89^{+2.54}_{-1.16}\times10^{-6}$	2.0	-25.4	-24.9
44.500~45.653	37.00	$0.62^{+0.28}_{-0.27}$	$-1.21^{+0.18}_{-0.18}$	12^{+1}_{-1}	9^{+2}_{-2}	$1.68^{+1.60}_{-0.79}\times10^{-6}$	$2.28^{+1.08}_{-1.05}$	$-0.74^{+0.17}_{-0.17}$	$-6.17^{+1.62}_{-1.87}$	11^{+1}_{-1}	$1.33^{+1.48}_{-0.79}\times10^{-6}$	1.3	-7.7	-7.7
45.653~47.578	28.55	$0.21^{+0.02}_{-0.02}$	$-1.45^{+0.04}_{-0.04}$	11^{+1}_{-1}	6^{+1}_{-1}	$1.15^{+0.18}_{-0.19}\times10^{-6}$	$2.14^{+0.60}_{-0.64}$	$-0.61^{+0.08}_{-0.09}$	$-5.68^{+1.83}_{-2.61}$	$10.4^{+0.3}_{-0.3}$	$0.77^{+0.37}_{-0.26}\times10^{-6}$	1.4	1.6	-0.7

Note. Column 1 lists the start and stop times of the BBlock time bins; column 2 lists the significance S of the time bin; columns 3–6 list the best-fit parameters for the CPL model: normalization K, low-energy power-law index α, cutoff energy E_c, and peak energy $E_p = (2+\alpha)E_c$ in the $N^2 N(E)$ or νF_ν spectrum; column 7 lists the derived CPL (νF_ν) energy flux F; columns 8–11 list the best-fit parameters for the Band model: normalization K, low-energy power-law index α, high-energy power-law index β, and peak energy E_p; column 12 lists the Band (νF_ν) energy flux F; column 13 lists the difference between the DIC for the CPL and the Band model, ΔDIC $=$ DIC$_{Band}$$-DIC_{CPL}$; and columns 14 and 15 list the effective number of parameters (p_{DIC}) for the CPL and Band model, respectively. The complete set of spectral fit results for all pulses for all GRBs is available in machine-readable format in the online journal. Fits for GRB 081009140 pulses 1 and 2 are shown here for guidance regarding the form and content.

(This table is available in its entirety in machine-readable form.)

ORCID iDs

Liang Li ⬤ https://orcid.org/0000-0002-1343-3089
Felix Ryde ⬤ https://orcid.org/0000-0002-9769-8016
Asaf Pe'er ⬤ https://orcid.org/0000-0001-8667-0889
Hoi-Fung Yu ⬤ https://orcid.org/0000-0001-5643-7445
Zeynep Acuner ⬤ https://orcid.org/0000-0002-4604-280X

References

Acuner, Z. 2019, PhD thesis, KTH Royal Institute of Technology, Stockholm, http://urn.kb.se/resolve?urn=urn:nbn:se:kth:diva-265527
Acuner, Z., & Ryde, F. 2018, MNRAS, 475, 1708
Acuner, Z., Ryde, F., Pe'er, A., Mortlock, D., & Ahlgren, B. 2020, ApJ, 893, 128
Acuner, Z., Ryde, F., & Yu, H.-F. 2019, MNRAS, 487, 5508
Ahlgren, B., Larsson, J., Nymark, T., Ryde, F., & Pe'er, A. 2015, MNRAS, 454, L31
Ahlgren, B., Larsson, J., Valan, V., et al. 2019, ApJ, 880, 76
Ajello, M., Arimoto, M., Axelsson, M., et al. 2020, ApJ, 890, 9
Atwood, W. B., Abdo, A. A., Ackermann, M., et al. 2009, ApJ, 697, 1071
Axelsson, M., Baldini, L., Barbiellini, G., et al. 2012, ApJL, 757, L31
Band, D., Matteson, J., Ford, L., et al. 1993, ApJ, 413, 281
Basak, R., & Rao, A. R. 2013, ApJ, 768, 187
Beloborodov, A. M. 2010, MNRAS, 407, 1033
Beloborodov, A. M. 2011, ApJ, 737, 68
Beloborodov, A. M. 2013, ApJ, 764, 157
Borgonovo, L., & Ryde, F. 2001, ApJ, 548, 770
Burgess, J. M. 2014, MNRAS, 445, 2589
Burgess, J. M., Bégué, D., Greiner, J., et al. 2020, NatAs, 4, 174
Burgess, J. M., Greiner, J., Bégué, D., & Berlato, F. 2019, MNRAS, 490, 927
Burgess, J. M., Ryde, F., & Yu, H.-F. 2015, MNRAS, 451, 1511
Crider, A., Liang, E. P., Smith, I. A., et al. 1997, ApJL, 479, L39
Daigne, F., & Bošnjak, Ž., & Dubus, G. 2011, A&A, 526, A110
Dereli-Bégué, H., Pe'er, A., & Ryde, F. 2020, ApJ, 897, 145
Duffell, P. C., & MacFadyen, A. I. 2015, ApJ, 806, 205
Ford, L. A., Band, D. L., Matteson, J. L., et al. 1995, ApJ, 439, 307
Foreman-Mackey, D., Hogg, D. W., Lang, D., & Goodman, J. 2013, PASP, 125, 306
Gelman, A., Hwang, J., & Vehtari, A. 2014, Stat. Comput., 24, 997
Geng, J.-J., Huang, Y.-F., Wu, X.-F., Zhang, B., & Zong, H.-S. 2018, ApJS, 234, 3
Giannios, D., & Spruit, H. C. 2005, A&A, 430, 1
Goldstein, A., Burgess, J. M., Preece, R. D., et al. 2012, ApJS, 199, 19
Golenetskii, S. V., Mazets, E. P., Aptekar, R. L., & Ilinskii, V. N. 1983, Natur, 306, 451
Goodman, J. 1986, ApJL, 308, L47
Gottlieb, O., Levinson, A., & Nakar, E. 2019, MNRAS, 488, 1416
Greiner, J., Burgess, J. M., Savchenko, V., & Yu, H.-F. 2016, ApJL, 827, L38
Gruber, D., Goldstein, A., Weller von Ahlefeld, V., et al. 2014, ApJS, 211, 12
Guiriec, S., Connaughton, V., Briggs, M. S., et al. 2011, ApJL, 727, L33
Ito, H., Matsumoto, J., Nagataki, S., Warren, D. C., & Barkov, M. V. 2015, ApJL, 814, L29
Iyyani, S., Ryde, F., Ahlgren, B., et al. 2015, MNRAS, 450, 1651
Iyyani, S., Ryde, F., Axelsson, M., et al. 2013, MNRAS, 433, 2739
Kaneko, Y., Preece, R. D., Briggs, M. S., et al. 2006, ApJS, 166, 298
Kargatis, V. E., Liang, E. P., Hurley, K. C., et al. 1994, ApJ, 422, 260
Lazzati, D., Morsony, B. J., & Begelman, M. C. 2009, ApJL, 700, L47
Li, L. 2019a, ApJS, 242, 16
Li, L. 2019b, ApJS, 245, 7

Li, L. 2020, ApJ, 894, 100
Li, L., Geng, J.-J., Meng, Y.-Z., et al. 2019, ApJ, 884, 109
Li, L., & Zhang, B. 2021, ApJS, 253, 43
Lloyd, N. M., & Petrosian, V. 2000, ApJ, 543, 722
Lloyd-Ronning, N. M., & Petrosian, V. 2002, ApJ, 565, 182
López-Cámara, D., Morsony, B. J., & Lazzati, D. 2014, MNRAS, 442, 2202
Lu, R.-J., Wei, J.-J., Liang, E.-W., et al. 2012, ApJ, 756, 112
Mazets, E. P., Golenetskii, S. V., Ilinskii, V. N., et al. 1982, Ap&SS, 82, 261
Meegan, C., Lichti, G., Bhat, P. N., et al. 2009, ApJ, 702, 791
Meng, Y.-Z., Liu, L.-D., Wei, J.-J., Wu, X.-F., & Zhang, B.-B. 2019, ApJ, 882, 26
Mészáros, P., & Rees, M. J. 2000, ApJ, 530, 292
Moreno, E., Vazquez-Polo, F. J., & Robert, C. P. 2013, arXiv:1310.2905
Norris, J. P., Bonnell, J. T., Kazanas, D., et al. 2005, ApJ, 627, 324
Norris, J. P., Nemiroff, R. J., Bonnell, J. T., et al. 1996, ApJ, 459, 393
Oganesyan, G., Nava, L., Ghirlanda, G., Melandri, A., & Celotti, A. 2019, A&A, 628, A59
Pe'er, A., Mészáros, P., & Rees, M. J. 2006a, ApJ, 642, 995
Pe'er, A., Mészáros, P., & Rees, M. J. 2006b, ApJ, 652, 482
Pe'er, A., Ryde, F., Wijers, R. A. M. J., Mészáros, P., & Rees, M. J. 2007, ApJL, 664, L1
Piran, T., Shemi, A., & Narayan, R. 1993, MNRAS, 263, 861
Planck Collaboration, Aghanim, N., Akrami, Y., et al. 2020, A&A, 641, A6
Ravasio, M. E., Ghirlanda, G., Nava, L., & Ghisellini, G. 2019, A&A, 625, A60
Ravasio, M. E., Oganesyan, G., Ghirlanda, G., et al. 2018, A&A, 613, A16
Rees, M. J., & Meszaros, P. 1994, ApJL, 430, L93
Rees, M. J., & Mészáros, P. 1998, ApJL, 496, L1
Rees, M. J., & Mészáros, P. 2005, ApJ, 628, 847
Ryde, F. 2004, ApJ, 614, 827
Ryde, F. 2005, ApJL, 625, L95
Ryde, F., Axelsson, M., Zhang, B. B., et al. 2010, ApJL, 709, L172
Ryde, F., Lundman, C., & Acuner, Z. 2017, MNRAS, 472, 1897
Ryde, F., & Pe'er, A. 2009, ApJ, 702, 1211
Ryde, F., Pe'er, A., Nymark, T., et al. 2011, MNRAS, 415, 3693
Ryde, F., & Svensson, R. 1999, ApJ, 512, 693
Ryde, F., Yu, H.-F., Dereli-Bégué, H., et al. 2019, MNRAS, 484, 1912
Sari, R., Piran, T., & Narayan, R. 1998, ApJL, 497, L17
Scargle, J. D., Norris, J. P., Jackson, B., & Chiang, J. 2013, ApJ, 764, 167
Sharma, V., Iyyani, S., Bhattacharya, D., et al. 2019, ApJL, 882, L10
Spiegelhalter, D. J., Best, N. G., Carlin, B. P., & Van Der Linde, A. 2002, J. R. Stat. Soc. B, 64, 583
Tavani, M., Band, D., & Ghirlanda, G. 2000, in AIP Conf. Ser. 526, Gamma-ray Bursts, 5th Huntsville Symp., ed. R. M. Kippen, R. S. Mallozzi, & G. J. Fishman (Melville, NY: AIP), 185
Thompson, C. 2006, ApJ, 651, 333
Uhm, Z. L., & Zhang, B. 2014, NatPh, 10, 351
Vianello, G., Gill, R., Granot, J., et al. 2018, ApJ, 864, 163
Vianello, G., Lauer, R. J., Younk, P., et al. 2015, arXiv:1507.08343
Vurm, I., & Beloborodov, A. M. 2016, ApJ, 831, 175
Vurm, I., Lyubarsky, Y., & Piran, T. 2013, ApJ, 764, 143
Wang, X.-Y., Liu, R.-Y., Zhang, H.-M., Xi, S.-Q., & Zhang, B. 2019a, ApJ, 884, 117
Wang, Y., Li, L., Moradi, R., & Ruffini, R. 2019b, arXiv:1901.07505
Wheaton, W. A., Ulmer, M. P., Baity, W. A., et al. 1973, ApJL, 185, L57
Yu, H.-F., Dereli-Bégué, H., & Ryde, F. 2019, ApJ, 886, 20
Yu, H.-F., Greiner, J., van Eerten, H., et al. 2015, A&A, 573, A81
Yu, H.-F., Preece, R. D., Greiner, J., et al. 2016, A&A, 588, A135
Zhang, B. 2018, The Physics of Gamma-Ray Bursts (Cambridge: Cambridge Univ. Press)
Zhang, B.-B., Zhang, B., Castro-Tirado, A. J., et al. 2018, NatAs, 2, 69

Do All Long-duration Gamma-Ray Bursts Emit GeV Photons?

Yu Wang[1,2,3]

[1] ICRANet, P.zza della Repubblica 10, I-65122 Pescara, Italy; yu.wang@uniroma1.it
[2] INAF—Osservatorio Astronomico d'Abruzzo,Via M. Maggini snc, I-64100 Teramo, Italy
[3] ICRA, Dipartimento di Fisica, Sapienza Università di Roma, P.le Aldo Moro 5, I-00185 Rome, Italy

Abstract

GRB 190114C extends the focus of gamma-ray burst (GRB) research to the high-energy regime, in which a prime question is "Do all long-duration GRBs emit GeV photons?" Based on the Fermi Large Area Telescope (LAT) 10 yr observations, 54 GRBs initially within the Fermi-LAT field of view and with known redshift are sampled. Within 26 of these GRBs at least one GeV photon has been detected with a probability of >95%, while the other 28 GRBs have no confident GeV photon detection. We hypothesize that all the samples intrinsically emit GeV photons, and the lack of detection is due to the limited capacity of the satellite. We estimate the theoretical number of photons that LAT receives by considering the GRB energy, the distance, and the LAT effective area. Results show, within the uncertainty, that all 26 GRBs with GeV photon detection have a theoretical photon number of >1, and 27 out of 28 GRBs without GeV photon detection have a theoretical photon number of <1. This agreement tends to support our hypothesis and give an answer of "yes" to our initial question.

1. Introduction

The hitherto most comprehensively studied gamma-ray burst—GRB 190114C—spotlights the high-energy emission (Wang et al. 2019a). It has prominent GeV radiation that was observed by the Fermi Large Area Telescope (LAT) (Kocevski et al. 2019) allowed TeV photons to be detected by the MAGIC telescope for the first time; (Mirzoyan et al. 2019). The confirmation of the existence of TeV emission extends the boundary of GRB high-energy emission by orders of magnitude; therefore, the energy deposited in the high-energy photons (>10 MeV) is probably greater than the traditional isotropic energy $E_{\rm iso}$ (1 keV to 10 MeV) in some GRBs (Wang et al. 2019a). The elevation of high-energy emission to the dominant band urges one to revisit current GRB models, and one prime question that the modeling must address is the universality of the high-energy emission, as the title of this article suggests.

To have a reliable answer, it is preferable to implement the logic in a model-independent approach, and to avoid many assumptions. In this article, we attempt to offer a reply based entirely on observations. Fermi-LAT has been the leading telescope observing the high-energy sky since 2008; it has published two GRB catalogs (Ackermann et al. 2013; Ajello et al. 2019) and spawned several works on the large sample analysis (see, e.g., Zhang et al. 2011; Ackermann et al. 2012; Panaitescu 2017; Nava 2018).

Our analysis surveys the Fermi-LAT GRBs up to the end of 2018. We limit our discussion to the long-duration GRBs, since there is only one short-duration burst, GRB 090510, which has measured redshift and GeV photons (Ackermann et al. 2010). We propose a hypothesis that all the long-duration GRBs emit GeV photons, but not all can be detected by Fermi-LAT. The detection or the absence of GeV photons emitted from a given burst is practically determined by whether there are photons reaching the effective area of Fermi-LAT. In this article, we define the criteria of detection as Fermi-LAT, within its energy band of 0.1–100 GeV, detecting at least one photon with

probability >95% coming from a given source in the first 200 s of its rest-frame time after the trigger.

Following the above logic, in Section 2, we give an analytical approximation of the Fermi-LAT effective area. In Section 3, we formulate the expected number of photons detected by Fermi-LAT from a burst of given energy and distance. In Section 4, we compare, for 54 GRBs, the theoretical expectation of GeV photon detection that stemmed from our hypothesis with the real Fermi-LAT observations; the result shows that observations support our hypothesis. In Section 5, a discussion and summary are presented.

2. Effective Area of Fermi-LAT

The Fermi-LAT capacity for detecting gamma-ray photons is described by the satellite's response functions, which are generalized by the effective area ($A_{\rm eff}$). It represents the effective size of the detector responding to incident photons with different energy and different directions (Atwood et al. 2009).

The effective area can be expressed as $A_{\rm eff}(\theta, \epsilon)$, where θ is the bore-sight angle (the bore-sight of the satellite with respect to the direction of the observing object), and ϵ is the photon energy. We here ignore the azimuthal angle, which has a weak influence (∼5% variation of effective area) and we take the initial bore-sight angle at the time of the Fermi-GBM trigger and/or when the GRB enters the Fermi-LAT field of view in case of repointing. We ignore the time variation of the bore-sight angle since it changes nonobviously during the prompt emission.[4] The exact effective area has a complicated form consisting of numerical matrices,[5] so here we fit the numerical

---

[4] For the majority of GRBs, the bore-sight angle changes less than 10° in the first 100 s after the trigger.
[5] More information on the Fermi-LAT effective area: http://www.slac.stanford.edu/exp/glast/groups/canda/lat_Performance.htm and https://fermi.gsfc.nasa.gov/ssc/data/analysis/documentation/Cicerone/Cicerone_LAT_IRFs/IRF_EA.html.
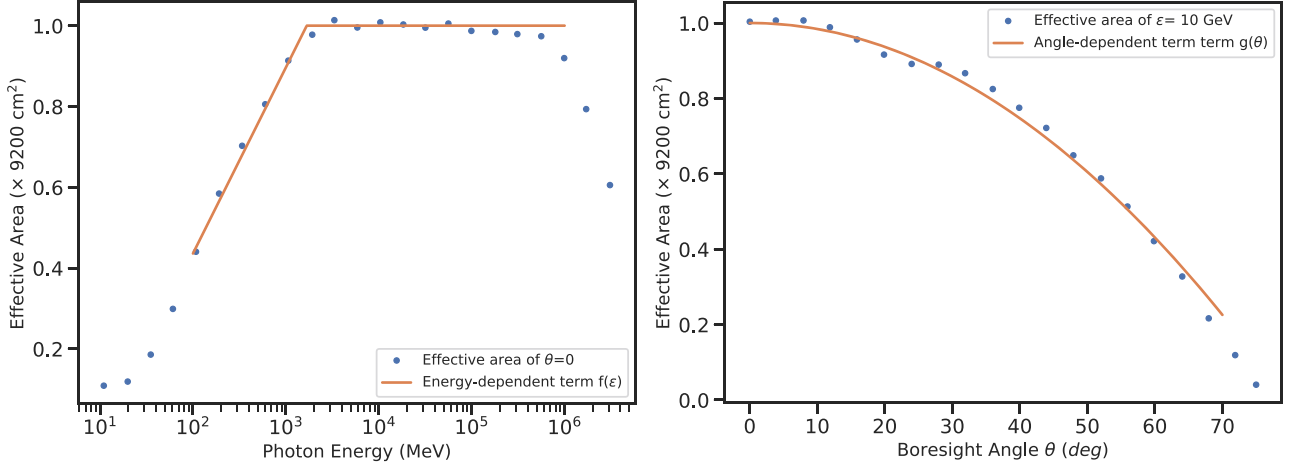
Figure 1. Effective area of Fermi-LAT. Left: the energy-dependent effective area at a constant bore-sight angle $\theta = 0$. Right: the angle-dependent effective area at a constant energy $\epsilon = 10$ GeV. The solid blue dots are the experimental measured effective area, and the dashed orange lines are the fittings of $f(\epsilon)$ and $g(\theta)$.

form to present approximately in a simple analytical way:

$$A_{\text{eff}}(\theta, \epsilon) \simeq A_0 f(\epsilon) g(\theta) \qquad (1)$$

where $A_{\text{eff}}(\theta, \epsilon)$ is separated into the energy-dependent term, $f(\epsilon)$, and the angle-dependent term, $g(\theta)$, and A_0 is a constant.

The suggested band of Fermi-LAT covers from 100 MeV to 100 GeV. In Figure 1, from the effective area at a constant bore-sight angle $\theta = 0$, the analytical fitting infers the constant $A_0 = 9200 \text{ cm}^2$ and the energy-dependent term

$$f(\epsilon) \simeq \begin{cases} 0.2\ln(\epsilon) - 0.489 & \text{for } 100 \text{ MeV} \leqslant \epsilon < 1678 \text{ MeV}, \\ 1 & \text{for } 1678 \text{ MeV} \leqslant \epsilon < 100 \text{ GeV}. \end{cases} \qquad (2)$$

Conversely, by setting a constant energy at 10 GeV, we obtain the angle-dependent term

$$g(\theta) \simeq 1 - 1.58 \times 10^{-4}\theta^2 \text{ for } 0° \leqslant \theta < 70°. \qquad (3)$$

A smaller bore-sight angle corresponds to a larger effective area. At $\theta > 70°$, the effective area becomes tiny, which is considered to be beyond the threshold. As we will show, the accuracy of the above approximation of effective area is adequate for the discussions within this article.

3. Detectability of GeV Photon

Fermi-LAT is able to recognize a single photon and assign the probability of this photon belonging to a given source. For reporting the observation of GeV emission in a specific GRB, this article takes the criteria that at least one photon from the GRB shall reach the detecting area of Fermi-LAT. This suggests the possibility that some GRBs do not emit powerful GeV radiation or/and they locate at a very large distance, so there may not even be one photon that can be received by the satellite, since the effective area is limited.

Following this, we estimate the theoretical number of photons received by Fermi-LAT for a GRB occurring at redshift z with the isotropic GeV energy E_{LAT} defined in the Fermi-LAT energy band (100 MeV to 100 GeV). In the GRB's cosmological rest frame, the photon number density at energy ϵ

is

$$n(\epsilon) = \frac{dN}{d\epsilon} = C\epsilon^{-2}. \qquad (4)$$

The power-law index -2 is a typical value from the Fermi-LAT spectral fitting (Ajello et al. 2019) and C is the normalization, which can be obtained by solving

$$E_{\text{LAT}} = \int_{100 \text{ MeV}}^{100 \text{ GeV}} \epsilon\, n(\epsilon)d\epsilon = \int_{100 \text{ MeV}}^{100 \text{ GeV}} C\epsilon\epsilon^{-2}d\epsilon = \frac{C}{0.145}. \qquad (5)$$

Therefore, we obtain

$$C = 0.145E_{\text{LAT}}, \qquad (6)$$

where the energy is in units of MeV. The observed photon number density depends on the distance of the source, and the effective area of the satellite,

$$n_{\text{obs}}(\epsilon) = n((1 + z)\epsilon)\frac{A_{\text{eff}}(\theta, \epsilon)}{4\pi D_l^2(z)}, \qquad (7)$$

where z is the redshift, D_l is the luminosity distance,[6] and $(1 + z)\epsilon$ is due to the cosmological expansion. The analytical effective area $A_{\text{eff}}(\theta, \epsilon)$ has been presented in Equations (1), (2), and (3). Finally the total photon number observed by the satellite from a burst at bore-sight angle θ is

$$n_{\text{obs}}(\theta) = \int_{100 \text{ MeV}}^{100 \text{ GeV}} n_{\text{obs}}(\epsilon)d\epsilon$$
$$= \frac{0.145E_{\text{LAT}}}{4\pi(1 + z)^2 D_l^2(z)} \int_{100 \text{ MeV}}^{100 \text{ GeV}} \frac{A_{\text{eff}}(\theta, \epsilon)}{\epsilon^2}d\epsilon, \qquad (8)$$

where the bore-sight angle $\theta = 0°$ and $\theta = 70°$ give the upper and the lower limits.

4. Do All Long-duration GRBs Emit GeV Photons?

Do all long-duration GRBs emit GeV photons? We are unable to affirm a direct answer from the current observation,

---

[6] Distance is computed by the FLRW metric adopting the cosmological parameters from the Planck mission (Planck Collaboration et al. 2020): Hubble constant $H0 = (67.4 \pm 0.5)$ km s^{-1} Mpc^{-1}, and matter density parameter $\Omega_M = 0.315 \pm 0.007$.

since GRB is a very complicated system at cosmological distances. It initially undergoes an optically thick period when the photon–photon and photon–lepton collisions may occur (see, e.g., Razzaque et al. 2004; Bosnjak & Kumar 2012; Bégué & Iyyani 2014; Gill & Granot 2018), and we receive only a tiny fraction of the GRB emission; this fraction is even affected by the circumburst medium and the interactions along its billions of light-year transportation (see, e.g., Shao & Dai 2007; Li et al. 2008; Desai et al. 2017; Ajello et al. 2018; Li et al. 2018a). Instead, we restrict the question to "Does Fermi-LAT observe all the GRBs that it shall observe, and miss all the GRBs that it shall miss?"; here "shall observe" and "shall miss" correspond to $n_{obs} > 1$ and $n_{obs} < 1$, respectively. In other words, we expect, if $n_{obs} > 1$, Fermi-LAT probably detects at least one GeV photon; if $n_{obs} < 1$, Fermi-LAT probably misses the detection even though the GRB has GeV emission.

Estimating n_{obs} using Equation (8) requires the redshift z, the bore-sight angle θ, and the GeV isotropic energy E_{LAT}. For the first two requirements, we select our sample of GRBs with known redshift, and within the threshold of bore-sight angle ($\theta < 70°$) at the trigger time. The GeV isotropic energy E_{LAT} is integrated from the spectrum fitted by the unbinned likelihood analysis (Abdo et al. 2009) in the energy band of 100 MeV to 100 GeV and for a duration of 200 s in the cosmological rest frame since the Fermi-LAT trigger and k-correlation is applied[7]; for the GRBs without any GeV photons observed, we postulate the existence of GeV emission from the source, and infer the E_{LAT} from the $E_{LAT} - E_{iso}$ correlation, which is to be fitted and confirmed from the Fermi GRBs.

Our sample is composed of 54 GRBs that initially locate within the threshold of bore-sight angle ($\theta < 70°$) and have measured redshift. It includes two groups: 26 GRBs with GeV photon detection and 28 GRBs without GeV photon detection.[8] We apply the Markov Chain Monte Carlo (MCMC) iteration to verify the correlation between E_{iso} and E_{LAT}[9], a correlation coefficient 0.867 ± 0.047 is obtained from the group of 26 GRBs having detected GeV emission, and a simple power-law dependence is given:

$$E_{LAT} = 1.12^{+0.95}_{-0.68} \times 10^{52} \left(\frac{E_{iso}}{10^{53}\ \text{erg}} \right)^{1.18^{+0.16}_{-0.12}}\ \text{erg}. \qquad (9)$$

As shown in Figure 2, the error corresponds to the 95% confidence region. Such a high correlation coefficient indicates that E_{iso} and E_{LAT} are strongly correlated. Therefore, we are safe to infer the postulated E_{LAT} from the measured E_{iso} for the group of 28 GRBs.

In practice, we solve Equation (8) by replacing E_{LAT} with E_{iso} via Equation (9) and setting $n_{obs} = 1$. As a result, we have E_{iso} as a function of z and θ. In Figure 3, $E_{iso}(z)$ is shown as the solid blue curve and the dashed orange curve, corresponding to the conditions of $\theta = 0°$ and $\theta = 70°$, respectively. These two curves give two limits: the region below the solid blue curve represents the scenario where less than one GeV photon will arrive at Fermi-LAT even though the source is along the line of sight $\theta = 0°$ ("shall miss," $n_{obs} < 1$), and the region above the dashed orange curve represents the scenario where more than

---

Figure 2. $E_{LAT} - E_{iso}$ correlation: the fitting of 26 Fermi-LAT GRBs gives $E_{LAT} \propto E_{iso}^{1.18}$. The correlation coefficient reaches 0.867 ± 0.047. The shadow corresponds to the 95% confidence region.

Figure 3. $z - E_{iso}$ map: the solid blue/dashed orange curve presents the theoretical estimation that one photon from the GRB with energy E_{iso}, redshift z, and bore-sight angle $\theta = 0°/70°$ can reach the detecting area of Fermi-LAT. The shadow presents the uncertainty brought by the $E_{LAT} - E_{iso}$ fitting. The points are the observed GRBs, the black ones are the GRBs that Fermi-LAT has observed GeV photons from, while the gray ones have not had any observed GeV photons.

one photon will arrive at Fermi-LAT even though the source is on the edge $\theta = 70°$ ("shall observe," $n_{obs} > 1$). We expect that for our sample, the GRBs below the solid blue curve shall all belong to the group of red sources that have no GeV photon detection, and the GRBs above the dashed orange curve shall all belong to the group of 26 sources that have observed GeV photons; the GRBs between the two curves can belong to either group. The result shows, within the 95% confidence region, nearly all GRBs meet our expectation. It tends to support that all long-duration GRBs emit GeV photons.

5. Discussion and Summary

The only outsider GRB 180728A is weak and nearby ($E_{iso} = 2.81 \times 10^{51}$ erg and $z = 0.117$). Statistically, one exception from a sample of 54 GRBs does not affect the conclusion. But as a single event, it brings two major possibilities: (1) Weak GRBs have GeV emission, but the power-law correlation of $E_{iso} - E_{LAT}$ deviates at the low E_{iso}

tail. Currently, the lowest energy GRB from which GeV photons have been detected is GRB 091127, of which $E_{\rm iso} = 7.8 \times 10^{51}$ erg, below this energy we have no knowledge to confidently infer the $E_{\rm iso} - E_{\rm LAT}$ correlation. (2) Weak GRBs have no GeV emission, as predicted by some models (Ruffini et al. 2018a; Rueda et al. 2019). This possibility aligns with all five GRBs of $E_{\rm iso} < 5 \times 10^{51}$ having no detection of GeV emission.

The energies of $E_{\rm iso}$ and $E_{\rm LAT}$ are both considered in an isotropic form, but this is not equivalent to having intrinsically isotropic MeV and GeV emissions. Our method relies on the existence of a correlation between the MeV and GeV emissions, adopting the isotropic form keeps the correctness of the conclusion and makes the expression simple. We realize different opening angles in each energy band of each GRB influence the fitting, but apparently the influence does not propagate significantly to the final assessment. On the other hand, the Fermi satellite is triggered mainly by MeV emission (Ajello et al. 2019), and from the fact that Fermi-LAT has observed all the GRBs that it shall observe; it infers the opening angles of MeV and GeV emissions are comparable in the early phase at least.

The fitting of the $E_{\rm iso} - E_{\rm LAT}$ correlation gives a wide confidence region in Figure 2 because the data points are scattered, which is expected since many nonintrinsic factors may enlarge the data dispersion, for example, different absorption from different galaxy environments. This large uncertainty propagates to the $z - E_{\rm iso}$ map in Figure 3, bringing corresponding large confidence regions at high energy. If we assess in a more deterministic way that ignoring those GRBs located in these uncertain regions, the remaining ones, except GRB 180728A, still conform to our expectation.

To summarize, the methodology throughout this article is to have a simple and clear logic. We ask one question (Do all long-duration gamma-ray bursts emit GeV photons?), do the plain estimation (number of GeV photons received by Fermi-LAT), and involve the smallest number of GRB parameters (energy and redshift). We avoid complexity since the current knowledge of GRBs and their environment, as well as the capacity of current satellites, cannot afford a decimal-level precision of analysis. We expect our result based on the concise analysis at least shows the possible direction of the answer. In reality, nearly the entire sample complies with our theoretical expectation. The goodness of the result confirms that the energy and the redshift are the leading factors affecting the GeV detection by Fermi-LAT, and it tends to support the answer of "yes" to the question in the title of this article.

Appendix A
GRB Sample

Our sample is composed of Fermi long-duration GRBs with an initial bore-sight angle of $\theta < 70°$ and with measured redshift until the end of 2018. It contains two subsamples that have or have not detected GeV photons. For the GRBs with detected GeV photons, by applying our criteria that at least one photon with the probability $>95\%$ was detected in the first 200 s of rest-frame time, our complete survey finds, after excluding GRB 150403A, which is influenced by the Earth limb emission for its initial zenith angle $\zeta > 100°$, 26 GRBs, as the first subsample. For the GRBs that have no detection of GeV photons, excluding the ultra-long GRB 130925A because its long duration brings inconsistency in computing isotropic energy, we eventually have 28 GRBs in the second subsample. All GRBs are listed in Table 1. Our sample mostly coincides with the sample in Ajello et al. (2019), in which different selection criteria are applied, e.g., they require at least three photons with probability $>90\%$.

The above survey requires the data analysis of assigning the probability of each photon belonging to a given burst, we perform the unbinned likelihood analysis following Abdo et al. (2009) and the corresponding tutorial[10] by utilizing the likelihood functions provided by Fermitools.[11] Pass 8 data are retrieved from the Fermi Science Support Center[12], background models of Galactic diffuse emission, extragalactic isotropic diffuse emission, and point-like source models are included in the Fermitools distribution, and we adopt the response function for the transient sources.

---

[10] https://fermi.gsfc.nasa.gov/ssc/data/analysis/scitools/likelihood_tutorial.html
[11] https://github.com/fermi-lat/Fermitools-conda/wiki
[12] https://fermi.gsfc.nasa.gov/ssc/

Table 1
List of Fermi Long-duration GRBs Initially within the Threshold of Bore-sight Angle ($\theta < 70$) and with the Redshift Measured

GRB	z	θ (degree)	TS	E_{iso} (10^{52} erg)	E_{LAT} (10^{52} erg)	Reference
080916C	4.35	49.0	1537	647.2 ± 12.50	276.12 ± 44.20	Ackermann et al. (2013); Ajello et al. (2019)
090323	3.57	56.5	213	411.7 ± 11.70	54.16 ± 18.38	Ackermann et al. (2013); Ajello et al. (2019)
090328	0.74	65.7	148	11.7 ± 0.50	1.08 ± 0.29	Ackermann et al. (2013); Ajello et al. (2019)
090902B	1.82	50.3	3179	343.6 ± 2.60	77.73 ± 9.59	Ackermann et al. (2013); Ajello et al. (2019)
090926A	2.11	48.0	2867	242.0 ± 5.10	184.62 ± 25.01	Ackermann et al. (2013); Ajello et al. (2019)
091003	0.90	12.2	187	9.9 ± 0.30	1.39 ± 0.61	Ackermann et al. (2013); Ajello et al. (2019)
091127	0.49	25.8	34	0.78 ± 0.08	0.10 ± 0.09	Troja et al. (2012); Ajello et al. (2019)
100414A	1.37	69.6	209	52.5 ± 1.10	7.82 ± 3.51	Ackermann et al. (2013); Ajello et al. (2019)
100728A	1.57	60.5	44	95.0 ± 0.71	2.02 ± 1.52	Atteia et al. (2017); Ajello et al. (2019)
110731A	2.83	2.9	196	71.7 ± 2.80	18.43 ± 6.17	Ackermann et al. (2013); Ajello et al. (2019)
120624B	2.20	68.2	434	320.9 ± 0.55	20.12 ± 4.75	Atteia et al. (2017); Ajello et al. (2019)
130427A	0.34	46.4	3913	105.0 ± 15.00	3.69 ± 0.44	Amati et al. (2013); Wang et al. (2019b); Ajello et al. (2019)
130518A	2.49	40.3	133	150.0 ± 15.98	20.14 ± 7.56	Atteia et al. (2017); Ajello et al. (2019)
131108A	2.40	20.4	686	51.2 ± 3.82	38.62 ± 6.84	Atteia et al. (2017); Ajello et al. (2019)
131231A	0.64	37.2	204	39.0 ± 2.00	1.22 ± 0.55	Liu et al. (2014); Li et al. (2019); Ajello et al. (2019)
141028A	2.33	36.4	166	63.2 ± 0.27	12.82 ± 4.89	Atteia et al. (2017); Ajello et al. (2019)
141220A	1.3195	47	16	5.73 ± 0.16	0.36 ± 0.30	Yu (2014); Atteia et al. (2017)
150314A	1.76	45.1	33	70.1 ± 3.25	2.13 ± 1.23	Atteia et al. (2017); Ajello et al. (2019)
150514A	0.81	39.2	10	1.26 ± 0.05	0.16 ± 0.14	Roberts et al. (2015); Dirirsa et al. (2017); Ajello et al. (2019)
151027A	0.81	10	12	3.94 ± 1.33	0.38 ± 0.34	Wang et al. (2018)
160509A	1.17	33.1	485	92.9 ± 14.02	6.88 ± 44.20	Atteia et al. (2017); Ajello et al. (2019)
160625B	1.41	41.2	1551	421.5 ± 8.49	19.32 ± 18.38	Atteia et al. (2017); Ajello et al. (2019)
170214A	2.53	33.2	1144	549.0 ± 0.61	58.38 ± 0.29	Mailyan & Meegan (2017); Tang et al. (2017); Ajello et al. (2019)
170405A	3.51	52.0	75	411.5 ± 3.66	276.12 ± 9.59	Hui & Meegan (2017); Ajello et al. (2019)
180703A	0.6678	48	43	3.38 ± 0.06	54.16 ± 25.01	Poolakkil & Meegan (2018)
180720B	0.65	49.1	750	68.2 ± 2.30	1.08 ± 0.61	Cherry et al. (2018); Fraija et al. (2019); Ajello et al. (2019)
081222	2.77	50	⋯	16.9 ± 1.92	⋯	Atteia et al. (2017)
090516A	4.109	20	⋯	69.02 ± 7.54	⋯	Li et al. (2018b)
091208B	1.063	55.6	⋯	3.0 ± 0.40	⋯	Ackermann et al. (2013)
100615A	1.398	64	⋯	5.82 ± 0.24	⋯	Li et al. (2018b)
100728B	2.106	57.1	⋯	3.8 ± 0.12	⋯	Atteia et al. (2017)
101219B	0.55	59	⋯	4.2 ± 0.3	⋯	Lü et al. (2018)
110128A	2.339	45	⋯	1.58 ± 0.21	⋯	Ruffini et al. (2018b)
111228A	0.716	70	⋯	4.17 ± 0.45	⋯	Li et al. (2018b)
120119A	1.728	31.4	⋯	35.2 ± 4.15	⋯	Atteia et al. (2017)
120712A	4.175	42	⋯	18.57 ± 0.27	⋯	Li et al. (2018b)
120716A	2.486	63	⋯	29.1 ± 0.14	⋯	Atteia et al. (2017)
120909A	3.93	66	⋯	69.0 ± 5.0	⋯	Golenetskii et al. (2012)
130528A	1.25	60	⋯	18.0 ± 2.3	⋯	Ruffini et al. (2018b)
131105A	1.686	37	⋯	34.31 ± 2.63	⋯	Li et al. (2018b)
140206A	2.73	46	⋯	35.8 ± 7.90	⋯	Wang et al. (2018)
140213A	1.2076	48.5	⋯	8.4 ± 0.29	⋯	Atteia et al. (2017)
140423A	3.26	44	⋯	55.98 ± 3.04	⋯	Ghirlanda et al. (2018)
140606B	0.384	66	⋯	0.25 ± 0.2	⋯	Golenetskii et al. (2014)
140623A	1.92	32	⋯	7.50 ± 0.95	⋯	Ghirlanda et al. (2018)
140703A	4.13	16	⋯	1.95 ± 0.11	⋯	Li et al. (2018b)
140907A	1.21	16	⋯	2.6 ± 0.04	⋯	Atteia et al. (2017)
150301B	1.5169	39	⋯	1.9 ± 0.03	⋯	Atteia et al. (2017)
150727A	0.313	46	⋯	0.21 ± 0.08	⋯	Younes (2015)
151111A	3.5	50	⋯	3.43 ± 1.19	⋯	Ruffini et al. (2018b)
161014A	2.823	69	⋯	10.1 ± 1.7	⋯	Ruffini et al. (2018b)
171222A	2.409	43	⋯	3.21 ± 0.18	⋯	Stanbro et al. (2017)
180728A	0.117	35	⋯	0.281 ± 0.01	⋯	Wang et al. (2019b)
181010A	1.39	48.1	⋯	0.32 ± 0.05	⋯	von Kienlin (2018)

Note. Including 26/28 GRBs with/without the GeV photon detection: the redshift (z), the bore-sight angle (θ), the test statistics (TS), and the gamma-ray isotropic E_{iso} (1 keV to 10 MeV) are from the quoted references. The GeV isotropic energy E_{LAT} (100 MeV to 100 GeV, first 200 s of rest-frame time) and TS value are computed by the unbinned likelihood analysis.
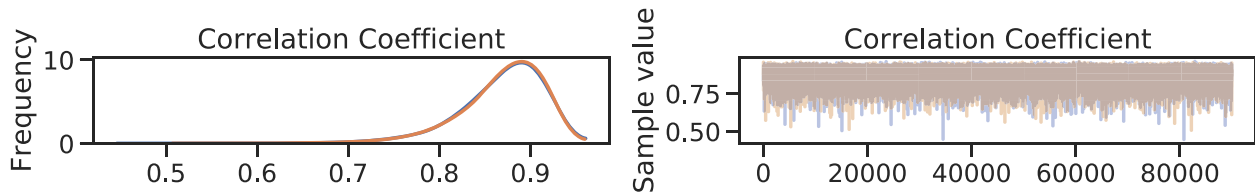
Figure 4. MCMC iteration for the correlation coefficient, including the value of 10^5 iterations (right) and their distribution (left).

Appendix B
Correlation Coefficient

The reliability of the correlation between the gamma-ray isotropic energy (E_{iso}) and the GeV isotropic energy (E_{LAT}) is tested by the correlation coefficient. Here we apply the Markov Chain Monte Carlo (MCMC) algorithm to obtain the covariance matrix of the multivariate normal distribution, and consequently the correlation coefficient (Chib & Winkelmann 2001). By implementing the Python package *PyMC3* (Salvatier et al. 2016), we iterate 10^5 times and burn the first 10^4 times. The correlation coefficient and its uncertainty is obtained as 0.867 ± 0.047, which indicates a strong correlation. Figure 4 shows the value of iterations and the corresponding distribution. If only considering GRBs of $E_{iso} > 3 \times 10^{53}$ erg, for which scattering occurs as shown in Figure 2, the correlation coefficient is 0.830 ± 0.076, indicating a strong correlation as well.

References

Abdo, A. A., Ackermann, M., Ajello, M., et al. 2009, ApJS, 183, 46
Ackermann, M., Ajello, M., Asano, K., et al. 2013, ApJS, 209, 11
Ackermann, M., Ajello, M., Baldini, L., et al. 2012, ApJ, 754, 121
Ackermann, M., Asano, K., Atwood, W. B., et al. 2010, ApJ, 716, 1178
Ajello, M., Arimoto, M., Axelsson, M., et al. 2019, ApJ, 878, 52
Ajello, M., Baldini, L., Barbiellini, G., et al. 2018, ApJ, 863, 138
Amati, L., Dichiara, S., Frontera, F., & Guidorzi, C. 2013, GCN, 14503, 1
Atteia, J.-L., Heussaff, V., Dezalay, J.-P., et al. 2017, ApJ, 837, 119
Atwood, W. B., Abdo, A. A., Ackermann, M., et al. 2009, ApJ, 697, 1071
Bégué, D., & Iyyani, S. 2014, ApJ, 792, 42
Bosnjak, Z., & Kumar, P. 2012, MNRAS, 421, L39
Cherry, M. L., Yoshida, A., Sakamoto, T., et al. 2018, GCN, 23042, 1
Chib, S., & Winkelmann, R. 2001, J. Bus. Econ. Stat., 19, 428
Desai, A., Ajello, M., Omodei, N., et al. 2017, ApJ, 850, 73
Dirirsa, F. F., Razzaque, S., & Piron, F. 2017, in The Proceedings of SAIP2017 (Pretoria: The South African Institute of Physics), 234
Fraija, N., Dichiara, S., Pedreira, A. C. C. d. E. S., et al. 2019, ApJ, 885, 29
Ghirlanda, G., Nappo, F., Ghisellini, G., et al. 2018, A&A, 609, A112
Gill, R., & Granot, J. 2018, MNRAS, 475, L1
Golenetskii, S., Aptekar, R., Frederiks, D., et al. 2014, GCN, 16374, 1
Golenetskii, S., Aptekar, R., Mazets, E., et al. 2012, GCN, 13736, 1
Hui, C. M., & Meegan, C. 2017, GCN, 20986, 1
Kocevski, D., Omodei, N., Axelsson, M., et al. 2019, GCN, 23709, 1
Li, A., Liang, S. L., Kann, D. A., et al. 2008, ApJ, 685, 1046
Li, L., Geng, J.-J., Meng, Y.-Z., et al. 2019, ApJ, 884, 109
Li, L., Wang, Y., Shao, L., et al. 2018a, ApJS, 234, 26
Li, L., Wu, X.-F., Lei, W.-H., et al. 2018b, ApJS, 236, 26
Liu, B., Chen, W., Liang, Y.-F., et al. 2014, ApJL, 787, L6
Lü, H.-J., Lan, L., Zhang, B., et al. 2018, ApJ, 862, 130
Mailyan, B., & Meegan, C. 2017, GCN, 20675, 1
Mirzoyan, R., Noda, K., Moretti, E., et al. 2019, GCN, 23701, 1
Nava, L. 2018, IJMPD, 27, 1842003
Panaitescu, A. 2017, ApJ, 837, 13
Planck Collaboration, Aghanim, Akrami, N. Y., et al. 2020, A&A, 641, A6
Poolakkil, S., & Meegan, C. 2018, GCN, 22896, 1
Razzaque, S., Mészáros, P., & Zhang, B. 2004, ApJ, 613, 1072
Roberts, O. J., Zhang, B.-B., & Meegan, C. 2015, GCN, 17819, 1
Rueda, J. A., Ruffini, R., & Wang, Y. 2019, Univ, 5, 110
Ruffini, R., Moradi, R., Rueda, J. A., et al. 2018a, arXiv:1803.05476
Ruffini, R., Wang, Y., Aimuratov, Y., et al. 2018b, ApJ, 852, 53
Salvatier, J., Wiecki, T. V., & Fonnesbeck, C. 2016, PeerJ Comput. Sci., 2, e55
Shao, L., & Dai, Z. G. 2007, ApJ, 660, 1319
Stanbro, M., Hui, C. M., & Meegan, C. 2017, GCN, 22277, 1
Tang, Q.-W., Wang, X.-Y., & Liu, R.-Y. 2017, ApJ, 844, 56
Troja, E., Sakamoto, T., Guidorzi, C., et al. 2012, ApJ, 761, 50
von Kienlin, A. 2018, GCN, 23320, 1
Wang, Y., Aimuratov, Y., Moradi, R., et al. 2018, MmSAI, 89, 293
Wang, Y., Li, L., Moradi, R., & Ruffini, R. 2019a, arXiv:1901.07505
Wang, Y., Rueda, J. A., Ruffini, R., et al. 2019b, ApJ, 874, 39
Younes, G. 2015, GCN, 18081, 1
Yu, H. F. 2014, GCN, 17205, 1
Zhang, B.-B., Zhang, B., Liang, E.-W., et al. 2011, ApJ, 730, 141

The morphology of the X-ray afterglows and of the jetted GeV emission in long GRBs

R. Ruffini,[1,2,3,4,5]⋆ R. Moradi,[1,2,6]⋆ J. A. Rueda [1,2,7,8,9]⋆ L. Li,[1,2,6] N. Sahakyan,[10,1] Y.-C. Chen [1,2]
Y. Wang,[1,2,6] Y. Aimuratov,[1,2,11,18] L. Becerra,[1,2,12] C. L. Bianco,[1,2,9] C. Cherubini,[1,13,14] S. Filippi,[1,13,15]
M. Karlica,[1,2] G. J. Mathews,[1,16] M. Muccino,[17] G. B. Pisani[1,2] and S. S. Xue[1,2]

[1]*ICRANet, Piazza della Repubblica 10, I-65122 Pescara, Italy*
[2]*ICRA, Dipartimento di Fisica, Università di Roma 'La Sapienza', Piazzale Aldo Moro 5, I-00185 Roma, Italy*
[3]*ICRANet-Rio, Centro Brasileiro de Pesquisas Físicas, Rua Dr. Xavier Sigaud 150, 22290-180 Rio de Janeiro, Brazil*
[4]*Université de Nice Sophia-Antipolis, Grand Château Parc Valrose, 06103 Nice, CEDEX 2, France*
[5]*INAF, Viale del Parco Mellini 84, I-00136 Rome, Italy*
[6]*INAF – Osservatorio Astronomico d'Abruzzo, Via M. Maggini snc, I-64100 Teramo, Italy*
[7]*ICRANet-Ferrara, Dipartimento di Fisica e Scienze della Terra, Università degli Studi di Ferrara, Via Saragat 1, I-44122 Ferrara, Italy*
[8]*Dipartimento di Fisica e Scienze della Terra, Università degli Studi di Ferrara, Via Saragat 1, I-44122 Ferrara, Italy*
[9]*INAF, Istituto di Astrofisica e Planetologia Spaziali, Via Fosso del Cavaliere 100, I-00133 Rome, Italy*
[10]*ICRANet-Armenia, Marshall Baghramian Avenue 24a, Yerevan 0019, Republic of Armenia*
[11]*Fesenkov Astrophysical Institute, Observatory 23, 050020 Almaty, Kazakhstan*
[12]*Instituto de Astrofísica, Facultad de Física, Pontificia Universidad Católica de Chile, Av. Vicuña Mackenna 4860, Macul, 8970117 Santiago, Chile*
[13]*ICRA, University Campus Bio-Medico of Rome, Via Alvaro del Portillo 21, I-00128 Rome, Italy*
[14]*Department of Science and Technology for Humans and the Environment and Nonlinear Physics and Mathematical Modeling Lab, University Campus Bio-Medico of Rome, Via Alvaro del Portillo 21, I-00128 Rome, Italy*
[15]*Department of Engineering, University Campus Bio-Medico of Rome, Nonlinear Physics and Mathematical Modeling Lab, Via Alvaro del Portillo 21, I-00128 Rome, Italy*
[16]*Center for Astrophysics, Department of Physics, University of Notre Dame, Notre Dame, IN 46556, USA*
[17]*Istituto Nazionale di Fisica Nucleare, Laboratori Nazionali di Frascati, I-00044 Frascati, Italy*
[18]*Al-Farabi Kazakh National University, al-Farabi avenue 71, 050040 Almaty, Kazakhstan*

ABSTRACT

We recall evidence that long gamma-ray bursts (GRBs) have binary progenitors and give new examples. Binary-driven hypernovae (BdHNe) consist of a carbon–oxygen core (CO_{core}) and a neutron star (NS) companion. For binary periods ~ 5 min, the CO_{core} collapse originates the subclass BdHN I characterized by (1) an outstanding supernova (SN; the '*SN-rise*'); (2) a black hole (BH), born from the NS collapse by SN matter accretion, leading to a GeV emission with luminosity $L_{GeV} = A_{GeV} t^{-\alpha_{GeV}}$, observed only in some cases; and (3) a new NS (νNS), born from the SN, originating from the X-ray afterglow with $L_X = A_X t^{-\alpha_X}$, observed in all BdHN I. We record 378 sources and present for four prototype GRBs 130427A, 160509A, 180720B, and 190114C: (1) spectra, luminosities, SN-rise duration; (2) A_X, $\alpha_X = 1.48 \pm 0.32$, and (3) the νNS spin time evolution. We infer (i) A_{GeV}, $\alpha_{GeV} = 1.19 \pm 0.04$ and (ii) the BdHN I morphology from time-resolved spectral analysis, three-dimensional simulations, and the GeV emission presence/absence in 54 sources within the *Fermi*-Large Area Telescope boresight angle. For 25 sources, we give the integrated and time-varying GeV emission, 29 sources have no GeV emission detected and show X/gamma-ray flares previously inferred as observed along the binary plane. The 25/54 ratio implies the GeV radiation is emitted within a cone of half-opening angle $\approx 60°$ from the normal to the orbital plane. We deduce BH masses of 2.3–8.9 $M_\odot$ and spin of 0.27–0.87 by explaining the GeV emission from the BH rotational energy extraction, while their time evolution validates the BH mass–energy formula.

Key words: black hole physics – binaries: general – gamma-ray bursts – transients: supernovae.

1 INTRODUCTION

The year 2021 marks the 50th anniversary of the paper 'Introducing the black hole' (Ruffini & Wheeler 1971) and of the black hole (BH)

mass–energy formula (Christodoulou 1970; Christodoulou & Ruffini 1971; Hawking 1971; Hawking 1972). Since those days, interest in BHs has spread worldwide and their study represents one of the most innovative fields of fundamental physics and astrophysics. There has also been an exponential growth of observational and theoretical developments that are finally reaching the momentous result of unveiling the process of rotational energy extraction from a rotating Kerr BH. We indicate the path of this discovery in

this paper. This realization has allowed for the identification of the code of gamma-ray bursts (GRBs): one of the most complex sequences of a very large number of non-repetitive classical and quantum events, each of which are characterized by specific spectral and temporal properties. In parallel, a new arena for fundamental physics has been revealed by the dubbed '*blackholic quantum*' (Rueda & Ruffini 2020). This enormous conceptual progress has not been reached straightforwardly: it has come from an intense dedicated process with continuous feedback between theoretical understanding, unprecedented panchromatic observational progress, and modification of basic interpretation paradigms: they have all been truly essential. We first summarize in this introduction some of the contributions which have initiated this most complex inquiry into the the most powerful energy source in the Universe and identify the rotational energy of a Kerr BH as their energy source.

1.1 The initial 'golden age' of relativistic astrophysics

The first breakthrough in relativistic astrophysics was the discovery of pulsars in 1967 (Hewish et al. 1968), and the discovery of a pulsar in the core of the Crab Nebula (Staelin & Reifenstein 1968; Reifenstein, Brundage & Staelin 1969). The identification of the energy source of the pulsar with a fast rotating newly born neutron star (NS); the new NS (νNS), coincident with the supernova (SN) explosion led to a new paradigm in SN understanding (Shklovskij 1969). As we show in this paper, we are gaining a deeper understanding of both of SNe and of the role of the νNS in the binary-driven hypernova (BdHN) systems.

The second breakthrough came from the launch in 1970 of the first X-ray telescope, observing in the 2–20 keV energy band: the *Uhuru* satellite (see e.g. Giacconi & Ruffini 1978; Giacconi 2003). *Uhuru* paved the way for a crucial working method in developing a multiwavelength collaboration with optical and radio observatories. Thanks to the theoretical understanding, this led to the discovery, inside our own galaxy, of a large number of binary X-ray sources composed of a main-sequence star and a companion NS (like Hercules X-1 and Centaurus X-3) and a binary system composed of a main-sequence star and a BH, which gave the first evidence for the discovery of a BH in our Galaxy (see Ruffini 1974; Giacconi & Ruffini 1978, for details). It was soon realized that these binary X-ray sources would themselves further evolve as the companion main-sequence star would undergo an SN explosion on time-scales of 10^8 yr (Ruffini 1974). In view of the limited number of such binary X-ray sources in our Galaxy, the expected observational rate of the final evolution of such binary systems would be of the order of 10^{-8} events per yr in our Galaxy. The point that was missed at the time was the existence of the process of '*induced gravitational collapse*', which was identified years later (Ruffini et al. 2001; Rueda & Ruffini 2012). This implies an unprecedented energy emission of $\sim 10^{54}$ erg, making them observable from all galaxies in the entire Universe: if the number of galaxies in our past light-cone is taken into account, the expected observational rate of the final evolution of such binary X-ray sources in the entire Universe is of the order of 10–100 events per yr. *The third breakthrough* was the introduction in 1971 of the BH mass–energy formula by Christodoulou, Hawking, Ruffini (Christodoulou 1970; Christodoulou & Ruffini 1971; Hawking 1971, 1972), and the BH extractable energy by reversible and irreversible transformation (in geometric $c = G = 1$ units):

$$M^2 = \frac{J^2}{4M_{\rm irr}^2} + M_{\rm irr}^2, \tag{1a}$$

$$S = 16\pi M_{\rm irr}^2 \tag{1b}$$

$$\delta S = 32\pi M_{\rm irr}\delta M_{\rm irr} \geq 0, \tag{1c}$$

where J, M, $M_{\rm irr}$, and S are the angular momentum, mass, irreducible mass, and horizon surface area of the BH, respectively.

Again in this article, we indicate the path to observe for the first time the BH extractable energy process, which can be as high as 29% of the BH mass for an extreme Kerr BH. We measure as well the BH mass and spin in selected BdHN.

Just at the end of this 'initial golden age of relativistic astrophysics', the discovery of GRBs was publicly announced in 1974 February at the annual meeting of the American Association for the Advancement of Science, in San Francisco (see details in Gursky & Ruffini 1975). In that meeting, observations by the Vela 5 and Vela 6 satellites were presented. These satellites operated in the 3–12 keV X-ray energy band and, for the first time, in the 150–750 keV (Vela 5) and 300–1500 keV (Vela 6) gamma-ray energy bands. Tens of gamma-ray events per year of unknown origin, lasting for a few seconds, and originating outside the Solar system, were named 'gamma-ray bursts' (details in Klebesadel, Strong & Olson 1973; Strong 1975).

What has became clear only recently, and further clarified in this article, is that precisely the late catastrophic evolution of the binary X-ray sources leads to the BdHNe: the progenitors of a class of long GRBs. Indeed, these highest luminosity energy sources in the Universe are observed to occur at a rate of 10–100 events per yr, consistent with the order of magnitude estimate given above.

We proceed to focus on the most recent developments, selecting crucial observational milestones, theoretical developments, and define the interpretation paradigms that have recently led to a unified understanding of the GRBs.

1.2 The largest ever multiwavelength observational efforts

The earliest evidence for high-energy radiation above 100 MeV from GRBs was the observations by the Energetic Gamma-Ray Experiment Telescope (*EGRET*), operating in the energy range $\sim$ 20 MeV–30 GeV, onboard of the Compton Gamma-Ray Observatory (*CGRO*, 1991–2000). The detection was triggered by the Burst And Transient Source Experiment (*BATSE*), operating in energy range of $\sim$20–2000 keV. *EGRET* has detected five GRBs that, from our understanding today, were long-duration bursts: GRB 910503, GRB 910601, GRB 930131, GRB 940217, and GRB 940301 (see e.g. Kanbach 1996, and references therein). Unfortunately, no redshift was known at the time.

A new epoch started with the launch of the *Beppo-Sax* satellite in 1996, joining the expertise of the X-ray and gamma-ray communities. Its gamma-ray burst monitor (GRBM) operating in the 40–700 keV energy band determined the trigger of the GRB, and two wide-field cameras operating in the 2–30 keV X-ray energy band allowed the localization of the source to within arcminutes resolution. This enabled a follow-up with the narrow-field instruments (NFI) in the 2–10 keV energy band.

Beppo-SAX achieved three major results:

(i) The discovery of the X-ray afterglow (GRB 970228; Costa et al. 1997), characterized by an X-ray luminosity decreasing with a power law with index of $\alpha_X = -1.48 \pm 0.32$ (see de Pasquale et al. 2006, as well as Li et al. 2015, 2018b; Pisani et al. 2016). In this article, we specifically address the astrophysical origin of the afterglow.

(ii) The determination of the accurate positions by the NFI, transmitted to the optical (van Paradijs et al. 1997) and radio telescopes (Frail et al. 1997), allowed the determination of the GRB cosmological redshifts. The first redshift was measured for GRB 970508 (Metzger et al. 1997), using the LRIS instrument of the Keck II telescope (Oke et al. 1995). The derived distances of ≈5–10 Gpc confirmed their cosmological origin and their unprecedented energetics, ≈10^{50}–10^{54} erg, thus validating our hypothesis derived from first principles (Damour & Ruffini 1975; Ruffini 1998).

(iii) The discovery of the temporal and spatial coincidence of GRB 980425 with SN 1998bw (Galama et al. 1998), which suggested the connection between GRBs and SNe, was soon supported by many additional events (see e.g. Woosley & Bloom 2006; Della Valle 2011; Hjorth & Bloom 2012; Li et al. 2012, 2018a). The astrophysical origin of this coincidence is addressed in this article within the BdHN approach.

The Neil Gehrels *Swift* Observatory (hereafter indicated as *Swift*) followed in 2004. It was conceived as a panchromatic space observatory dedicated to the observations of GRBs. The GRB trigger is detected by the large field of view of its Burst Alert Telescope (BAT; Barthelmy et al. 2005), operating in the hard X-ray band. This is followed up by the fast and automatic observations of the onboard narrow fields instruments XRT (Burrows et al. 2005) and UVOT (Roming et al. 2005) operating in the soft/medium X-ray and in the optical/UV bands, respectively. The BAT telescope operates in the 15–150 keV energy band and can detect the GRB prompt emission while accurately determining its position in the sky within 3 arcmin. Within 90 s, *Swift* can repoint the XRT telescope, operating in the 0.3–10 keV energy range, and relay promptly the burst position to the ground. Unfortunately, this does not allow the establishment of the initial *Swift*-XRT detection prior to the *Swift*-BAT trigger, as later explained in this article.

Thanks to the *Swift* satellite, the number of detected GRBs increased rapidly to 1300 sources with known redshifts (see e.g. Giommi et al. 2020). By analysing the light curve of some long GRBs, Nousek et al. (2006) and Zhang et al. (2006) discovered three power-law segments in the XRT flux light curves prior to the afterglow emission (see also Li et al. 2015, 2018a). We refer in this article to these segments as the 'Nousek–Zhang power laws'. All the X-ray afterglow observations considered in this article refer to *Swift*-XRT observation.

The high-energy astrophysics era of GRB observations started with the launch of *AGILE* in 2007 (Tavani et al. 2009) with the onboard Gamma-Ray Imaging Detector (*GRID*) operating in the 30 MeV–50 GeV energy range. *AGILE* was soon followed by the launch in 2008 June of the *Fermi* satellite, having onboard the gamma-ray burst monitor (GBM) operating in the 8 keV–40 MeV energy range (Meegan et al. 2009) and the Large Area Telescope (LAT) operating in the 20 MeV–300 GeV energy range (Atwood et al. 2009).

AGILE-GRID detected the first long GRB with emission above 100 MeV and with a photometric redshift of $z = 1.8$, GRB 080514B (Giuliani et al. 2008). It was followed four months later by the detection of GRB 080916C (Greiner et al. 2009) by *Fermi* with one of the largest isotropic energies ever detected, $E_{iso} = (4.07 \pm 0.86) \times 10^{54}$ erg, and a photometric redshift of $z = 4.35$. These were followed by a large number of long GRBs observed by LAT with both GeV emission and with a well-defined z. All the high-energy long GRBs considered in this article are based on the first and second

Fermi-LAT GRB catalogues (Ackermann et al. 2013; Ajello et al. 2019).

The leading observations from space observatories were followed by a multitude of equally essential observations from ground-based observatories spanning the globe. The leading role was taken by the largest optical telescopes, e.g. the VLT from ESO with its X-shooter instrument (Vernet et al. 2011) and radio telescopes. This vastest ever multiwavelength observational campaign has been recently further extended to the very-high-energy (VHE) domain with the GRB detection by observatories on the ground. This is the case of the observations of GRB 190114C by the Imaging Atmospheric Cherenkov Telescopes MAGIC (see Fig. 1 and MAGIC Collaboration 2019a), designed to detect VHE gamma-rays from 30 GeV to more than 50 TeV (see e.g. Aleksić et al. 2016a, b), the observations of GRB 180720B by H.E.S.S (see Fig. 2 and Abdalla et al. 2019), operating in the energy range from tens of GeV to tens of TeV (see e.g. Aharonian et al. 2006), as well as GRB 190829A (Chand et al. 2020), which we also address in this article.

1.3 The short GRBs with binary NS progenitors

One of the main results of the observations of the *CGRO* satellite (Murdin 2000) was the isotropic distribution of the GRBs when expressed in galactic coordinates (Meegan et al. 1992). This result gave the first preliminary indication of the cosmological nature of GRBs. This was later confirmed by irrefutable evidence from the observations of *Beppo-Sax*, as mentioned above. An additional result was the clear indication of the existence of two different classes of GRBs: the short and the long GRBs (Kouveliotou et al. 1993). This classification has been confirmed and further extended as we recall in Section 2, now duly expressing all quantities, after *Beppo-Sax*, in the rest frame of the source.

The first proposal of successfully relating a GRB to an astrophysical cosmological source came from the vision of Bohdan Paczynski and collaborators, who identified the progenitors of short GRBs (S-GRBs) with merging NS binaries (see e.g. Paczynski 1986; Eichler et al. 1989; Narayan, Piran & Shemi 1991; Mao & Paczynski 1992; Narayan et al. 1992; Narayan, Paczynski & Piran 1992). This result was later confirmed by *Beppo-Sax* (Li & Paczyński 1998, 2000, 2006; Berger 2014). Complementary information came from the localization of S-GRBs at large off-sets from their host galaxies and with no star formation evidence (see e.g. Fox et al. 2005; Gehrels et al. 2005; Berger 2014). The following fundamental discovery came from the identification of the first S-GRB in the GeV band by *AGILE*. The first observation of an S-GRB was done by *AGILE* who detected GRB 090510A at a spectroscopic redshift of $z = 0.903$, with $E_{iso} = (3.95 \pm 0.21) \times 10^{52}$ erg, and a significant GeV emission $E_{LAT} = (5.78 \pm 0.60) \times 10^{52}$ erg. On the basis of the observed energetics of this source, and its spectral properties, we proposed that in this S-GRB we witness the birth of a BH, which we associate with the onset of the GeV emission: the signature of this event (Ruffini et al. 2016a).

This identification further evolved with the introduction of the two subclasses of short bursts (Ruffini et al. 2015b, 2016a, b; Aimuratov et al. 2017). The first subclass corresponds to short bursts with isotropic energies $E_{iso} < 10^{52}$ erg (in the rest-frame 1–10^4 keV energy band) and rest-frame spectral peak energies $E_{p,i} < 2$ MeV. These are expected to originate when the NS–NS merger leads to a single massive NS (M-NS) with a mass below the NS critical mass. We have called these sources short gamma-ray flashes (S-GRFs).
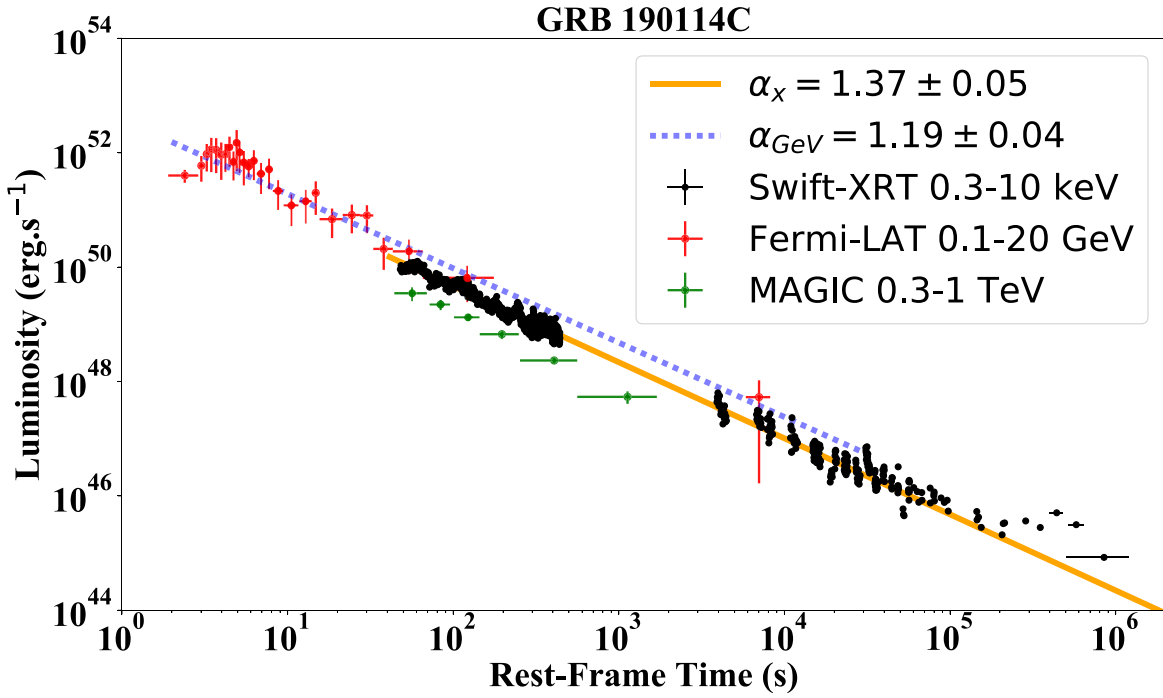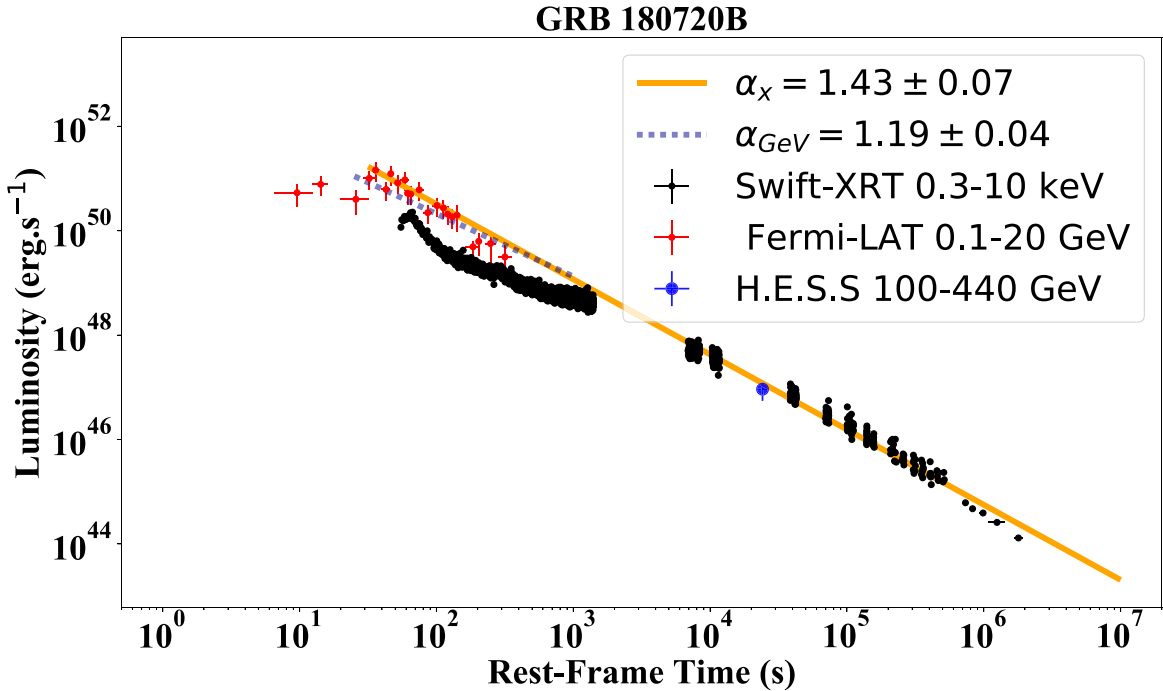
Figure 1. Luminosity of BdHN I 190114C: the black data points represent the rest-frame 0.3–10 keV luminosity obtained from *Swift*-XRT. It follows a decaying power law with index $\alpha_X = 1.37 \pm 0.05$. The red data points show the rest-frame 0.1–20 GeV luminosity observed by *Fermi*-LAT. It follows a decaying power law with amplitude $(4.6 \pm 0.6) \times 10^{52}$ erg s^{-1} and index $\alpha_{GeV} = 1.19 \pm 0.04$. The green data points show the rest-frame 0.3–1 TeV luminosity obtained from MAGIC. Details are given in Sections 4, 5, and 8.

Figure 2. Luminosity of BdHN I 180720B: the black data points represent the rest-frame 0.3–10 keV luminosity obtained from *Swift*-XRT. It follows a decaying power law with index $\alpha_X = 1.43 \pm 0.07$. The blue data point shows the rest-frame 100–440 GeV luminosity observed by H.E.S.S. The red data points show the rest-frame 0.1–20 GeV luminosity observed by *Fermi*-LAT. It follows a decaying power law with amplitude $(5.4 \pm 0.6) \times 10^{52}$ erg s^{-1} and index $\alpha_{GeV} = 1.19 \pm 0.04$. Details are given in Sections 4, 5, and 8.
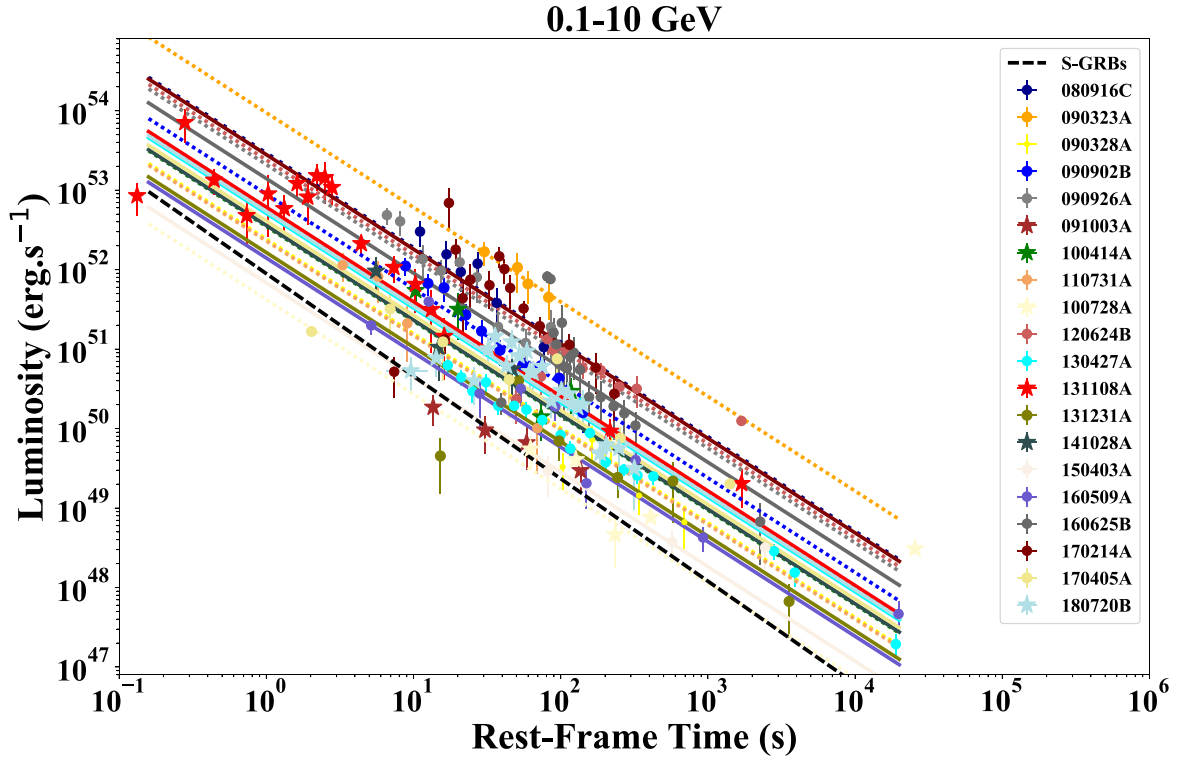
0.1–10 GeV

Figure 3. The rest-frame 0.1–10 GeV isotropic luminosity of 20 selected BdHNe with LAT emission. The solid red line marks the common power-law behaviour of the GeV emission for BdHNe with slope $\alpha_{\rm GeV} = 1.19 \pm 0.04$; the shaded grey area encloses all the luminosity light curves of the selected BdHNe. The dashed black line marks the common power-law behaviour of the GeV emission in S-GRBs with a slope of $\gamma = 1.29 \pm 0.06$.

The second subclass corresponds to short bursts with $E_{\rm iso} \gtrsim 10^{52}$ erg and $E_{\rm p,i} \gtrsim 2$ MeV. It was assumed that these sources, in analogy with the prototype GRB 090510, originate from an NS–NS merger in which the merged core overcomes the NS critical mass and gravitationally collapses to form a BH. We have called these sources genuine S-GRBs (see Ruffini et al. 2016a, 2019c); six of such S-GRBs have been identified, all emitting GeV emission with a decaying luminosity of index $\alpha_{\rm GeV,short} = -1.29 \pm 0.06$ (Ruffini et al. 2019c); see Fig. 3 in Section 8.

We show how, by following these pathfinding works on S-GRBs, we have progressed in formulating the theory of the BdHNe: the theory of long GRBS based on binary progenitors. Before this, however, we summarize the traditional long GRB models based upon a single progenitor.

1.4 Long GRBs in the traditional model

A review of the traditional long GRB model is facilitated by the extensive book by Bing Zhang and many references therein (Zhang 2018). As recounted there, the papers by Rees & Meszaros (1992), Mészáros & Rees (1997), and Woosley (1993) have characterized this traditional model. Rees & Meszaros (1992) proposed a single BH as the origin of GRBs emitting an ultrarelativistic blast wave, whose expansion follows the Blandford–McKee self-similar solution (Blandford & McKee 1976). Woosley (1993) linked the GRB origin to a Kerr BH emitting an ultrarelativistic jet originating from the accretion of toroidal material on to the BH. The BH was assumed to be produced from the direct collapse of a massive star, a 'failed' SN leading to a large BH of approximately 5 M$_\odot$, possibly as high as 10

M$_\odot$, a '*collapsar*'. We will address this interesting idea within our BdHN model in Section 9.

In these ultrarelativistic blast wave models, the afterglow is explained by the synchrotron/synchrotron self-Compton (SSC) emission from accelerated electrons when the blast wave of $\Gamma \sim 1000$ is slowed down by the circumburst medium (Waxman & Piran 1994; Sari & Piran 1995; Sari 1997; Wijers, Rees & Meszaros 1997; Sari, Piran & Narayan 1998).

As pointed out by Zhang (2018), these ultrarelativistic blast wave models have been applied to explain a vast number of observations:

(i) The X-ray afterglow as well as the steep and shallow decay in the 'Nousek–Zhang' phase, the X-ray, and the gamma-ray flares.
(ii) The optical and radio emissions.
(iii) The high-energy emission in the GeV band observed in some long GRBs by *Fermi*-LAT.

An example of this method is the recent case of GRB 190114C, in which the traditional approach has been applied:

(i) To jointly explain the emissions in the TeV observed recently by MAGIC (MAGIC Collaboration 2019a, b; Mirzoyan et al. 2019); see Fig. 1.
(ii) To explain the emission in the MeV and GeV bands observed by the *Fermi* GBM and LAT satellites in the jetted emission.
(iii) To explain the emission in the MeV and keV bands observed by *Swift* including the emission in the optical and radio emissions.

In the traditional model, all of these emissions occur jointly using the kinetic energy of an ultrarelativistic blast wave with Lorentz

Table 1. Alphabetic ordered list of the acronyms used in this work.

Extended wording	Acronym
Binary-driven hypernova	BdHN
Black hole	BH
Carbon–oxygen star	CO-star
Fallback-powered kilonova	FB-KN
Gamma-ray burst	GRB
Gamma-ray flash	GRF
Gamma-ray flash kilonovae	GR-K
Massive neutron star	M-NS
Neutron star	NS
New neutron star	νNS
Short gamma-ray burst	S-GRB
Short gamma-ray flash	S-GRF
Supernova	SN
Supernova rise	SN-rise
Ultrashort gamma-ray burst	U-GRB
White dwarf	WD
X-ray flash	XRF

factor Gamma $\sim 10^3$, emitting at distances of $\sim 10^{16}$–10^{18} cm, implying total energies reaching 10^{55} erg.

This approach, however, encounters some contradictions with model-independent constraints. Moreover, there is no requirement that these different emission processes be explained by a single origin, i.e. the kinetic energy of a blast wave. As we are going to show in this article, each one of the above mentioned emissions finds its reason for existence in different specific processes originating in different specific episodes during the BdHN evolution. Each episode implies a different process and less demanding energy requirements.

1.5 The role of binary systems as progenitors of long GRBs

The role of binary systems as progenitors of long GRBs in our approach involves three assumptions:

(i) That all long GRBs, not only the S-GRBs, originate from binary systems. These binaries are composed of different combinations of CO_{core}, NS, white dwarfs (WDs), BH, and νNS; see Table 1. We classify all GRBs in nine different subclasses on the basis of their energetics, their spectra, and their duration expressed in the rest frame of the source. Only in *some* of these subclasses the presence of a BH occurs (see e.g. Ruffini et al. 2016b, 2018c; Wang et al. 2019); see in detail in Section 2.

(ii) We focus on BdHNe with a binary progenitor composed of a CO-star and a companion binary NS. As the CO_{core} gravitationally collapses, it gives origin to an SN and its iron core collapses to form a νNS. The hypercritical accretion of the SN ejecta on the companion NS leads, for binary periods $\lesssim 5$ min, to the formation of a BH. This happens when the NS critical mass is reached and overcome (Becerra et al. 2016). We denote these systems as BdHNe I in which a BH is formed. The BdHNe I are characterized by an isotropic energy, estimated by the *Fermi*-GBM, in the range $10^{52} < E_{iso} < 10^{54}$ erg. In the opposite case, i.e. for longer binary periods, a more M-NS originates from the SN hypercritical accretion process (Wang et al. 2019). These BdHNe II are characterized by $10^{50} < E_{iso} < 10^{52}$ erg (Ruffini et al. 2016b). The BdHNe III are characterized by binaries with even longer periods, so with more widely separated components, leading to an even weaker energy emission with $10^{48} < E_{iso} < 10^{50}$ erg.

(iii) We make use of recent theoretical results in the study of the hypercritical accretion of the SN ejecta both on the companion NS

and the νNS (see e.g. Becerra et al. 2016, 2019; Ruffini et al. 2016b, 2018a; Rueda et al. 2020). We rely on the three-dimensional (3D) simulations performed with a new smoothed particle hydrodynamics (SPH) code developed in collaboration with Los Alamos National laboratory (see e.g. Becerra et al. 2019, and reference therein). We here give special attention to this procedure in order to reconstruct the morphology of the BdHNe, which has a strong dependence on the viewing angle as a result of the binary nature of the progenitor. We use the observations of the GeV emission observed by *Fermi*-LAT present only in *some* BdHN to infer their morphology and visualize its nature by SPH simulations (see Sections 6 and 7 and Fig. 4).

1.6 The role of the binary progenitor in the SN associated with long GRBs

Contrary to the case of S-GRBs, the necessity of a binary progenitor in long GRBs did not arise from the very beginning, and possibly the most important observational piece of evidence of this need can be identified in the temporal and spatial coincidence of GRB 980425 (Pian et al. 2000) and SN 1998bw (Galama et al. 1998), and the subsequent systematic spectroscopic analysis of additional GRB-SN associations (see Cano et al. 2017, for a review).

There are two key observational aspects of the SNe associated with GRBs pointing to a relevant role of binary interactions: (1) they are of type Ic, namely both hydrogen and helium lack in their spectra, and (2) the spectral lines are broad-lined implying their ejecta expand at very high expansion velocities of the order of 10^4 km s^{-1}, implying kinetic energies of up to 10^{52} erg, the reason for which they have been dubbed HN (Cano et al. 2017).

The first feature, namely that these SNe are of type IC implies that they possibly originate from helium stars, CO_{core}, or Wolf–Raye stars that have rid of their outermost layers (see e.g. Smith et al. 2011). Indeed, it has been recognized that a binary companion would most efficiently help in stripping off the pre-SN star outermost layers by tidal effects, multiple mass-transfer, and common-envelope episodes (see e.g. Nomoto & Hashimoto 1988; Iwamoto et al. 1994; Fryer et al. 2007; Yoon, Woosley & Langer 2010; Smith et al. 2011).

The second feature, namely the observed high-expansion velocities of the SN ejecta, is more delicate and less straightforward to account for in theoretical models. In the BdHN model, numerical simulations in Ruffini et al. (2018a) have shown that the explosion of the GRB within the SN might transfer to it sufficient energy and momentum to convert an initial ordinary SN into an HN. Therefore, broad-lined SNe or HNe in the BdHN model does not necessarily need to be born as such, instead they can be the outcome of the GRB feedback into the SN (see also Becerra et al. 2019). Evidence of such a transition from an SN into an HN in a BdHN has been observationally identified in GRB 151027A (see Ruffini et al. 2018c, for details).

In addition, binary interactions may enforce corotation of the pre-SN star (i.e. the CO_{core}) thereby spinning it up to high rotation rates. For BdHN I, this implies a rotation period of the CO_{core} of the order of minutes, so a rotational energy $\sim 10^{50}$ erg (Wang et al. 2019). Of course, this cannot explain directly an observed kinetic energy of 10^{52} erg. The core collapse of the iron core of this rotating CO_{core}, by angular momentum conservation, implies the birth of a millisecond period νNS, which may well power the SN by injecting into it energies of the order of 10^{52} erg (see Wang et al. 2019; Rueda et al. 2020, for more details). It may also happen that binary interactions spin-up the CO_{core} beyond corotation bringing it to even to higher rotation rates ~ 1 rad s^{-1} (see e.g. Nakamura et al. 2014;
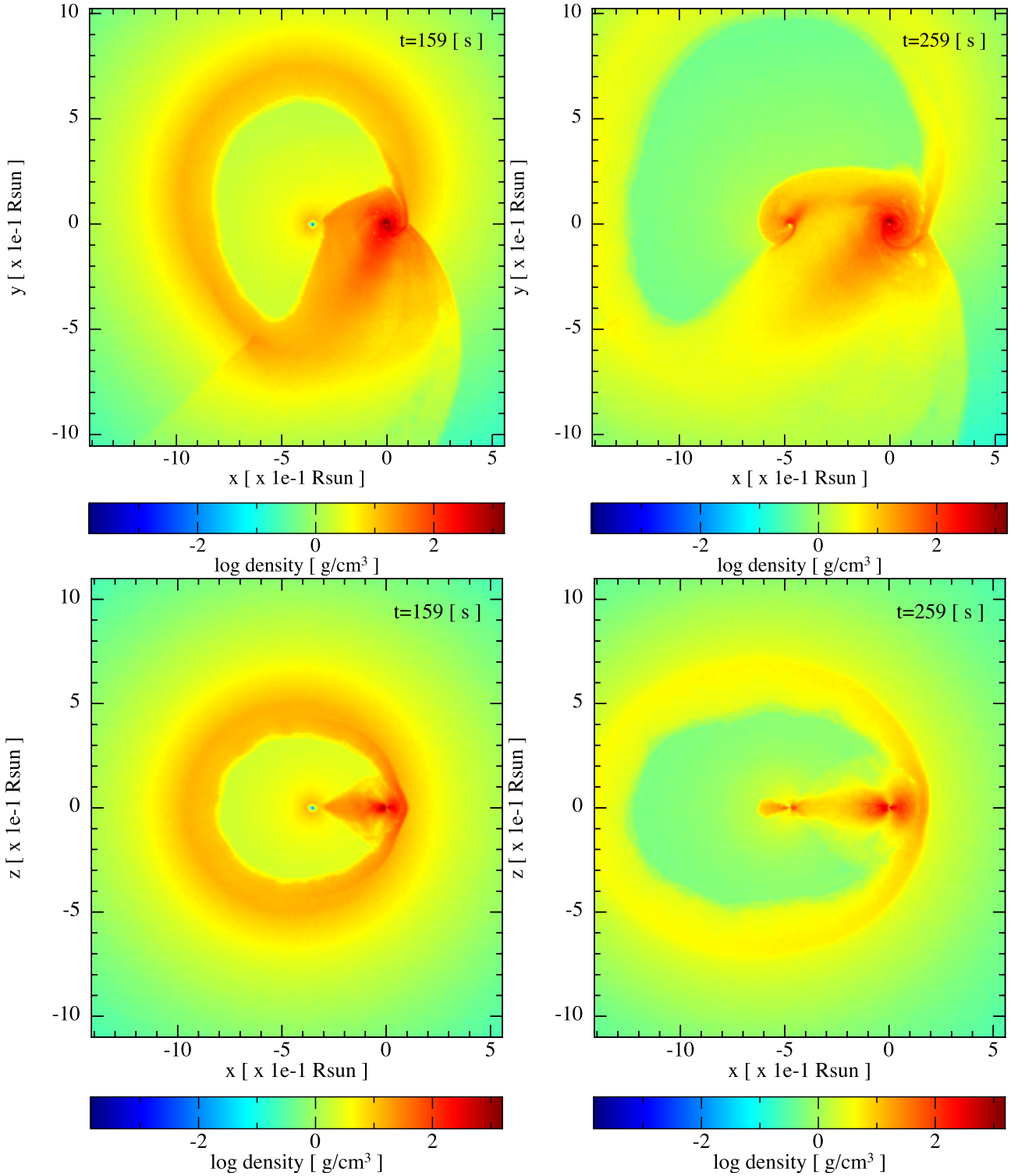
Figure 4. An SPH simulation from Becerra et al. (2019) of the exploding CO-star as the SN in the presence of a companion NS: Model '25m1p08E' (see table 2 therein). The CO-star is obtained from the evolution of a 25 $M_\odot$ zero-age main-sequence (ZAMS) progenitor that leads to a pre-SN CO-star mass $M_{CO} = 6.85\ M_\odot$. The initial mass of the νNS (formed at the centre of the SN) is 1.85 $M_\odot$ and the one of the NS companion is $M_{NS} = 2\ M_\odot$. The initial orbital period is 4.8 min. The upper panels show the mass density on the binary equatorial plane and the lower ones correspond to the plane orthogonal to it, at two selected times from the SN explosion ($t = 0$ of the simulation), 159 and 259 s. The reference system is rotated and translated so that the x-axis is along the line that joins the νNS and the NS, and the axis origin $(0, 0)$ is located at the NS position. For this simulation, the NS collapses reaching the secular axisymmetric instability point with a mass 2.26 $M_\odot$ and angular momentum $1.24 GM_\odot^2/c$, while the νNS is stable with mass and angular momentum, respectively, 2.04 $M_\odot$ and $1.24 GM_\odot^2/c$. Up to the final simulation time, the binary system kept bound although the binary orbit widens, reaching an orbital period of 16.5 min and an eccentricity of $\epsilon = 0.6$. The collapse of the NS to the newly formed BH, characteristic of a BdHN I, occurs at $t = 21.6$ min.

Gilkis 2018; Fujisawa et al. 2019), which would imply a much larger rotational energy of a few 10^{52} erg, ready to be used in the SN event.

There is increasing observational evidence on the high energetics of up to 10^{52} erg and the complex nature of the SN from the X- and gamma-ray precursors to the prompt radiation in long GRBs (see e.g. Wang et al. 2019). In order to account for such a complexity, we have dubbed these early phases of the BdHN as 'SN-rise' (Li et al. 2019). The *SN-rise* triggers the entire BdHN, so it includes the SN explosion as well as the feedback of the hypercritical accretion on to the νNS and on to the binary companion NS. We dedicate Section 3 to their analysis giving examples in the case of BdHN I and II.

We can conclude that the binary progenitor of the BdHN model provides a natural explanation of the observational features of the SN associated with long GRBs. Having said this, it is now appropriate to discuss the formation of the CO$_{core}$–NS binary progenitors of the BdHN from the stellar evolution viewpoint.

It is well known from the stellar evolution theory and observations that massive binaries might evolve to form binaries composed of compact objects, e.g. WD–WD, NS–WD, NS–NS and NS–BH. Leaving aside specific technical details, traditional evolutionary paths lead the compact remnant of the more massive star, after undergoing SN, to common-envelope phase with the companion, and after the collapse of the companion star leading to the second SN, the system forms a compact-object binary provided it keeps bound (Fryer, Woosley & Hartmann 1999; Dominik et al. 2012; Postnov & Yungelson 2014). It is very interesting that alternative evolutionary scenarios have been recently proposed in the X-ray binary and SN community leading to the so-called *ultrastripped* binaries used to explain NS–NS and low-luminosity SNe (see e.g. Tauris et al. 2013; Tauris, Langer & Podsiadlowski 2015, for details). The binary in these cases, after first SN, experiences multiple mass-transfer phases leading to the expulsion of the hydrogen and helium shells of the secondary. As proposed in Becerra et al. (2015) and Fryer et al. (2015), these evolutionary scenarios are a plausible path to form CO$_{core}$–NS binary progenitors of BdHN.

From the above descends the question of whether such a population of binaries might or not include the progenitors of the BdHN. The orbital periods of the binary at the end of the evolution in these population synthesis codes are 50–5000 h (Tauris et al. 2013). They have been used as a main channel to form NS–NS, but the formation of NS–BH binaries, which are the final outcome left by BdHN I, have not been up to now considered in population synthesis numerical codes. One of the main reasons for this is that the physical processes involved in a BdHN I, occurring when shorter orbital periods of the order of minutes are allowed, lead to BH formation and they have not accounted for yet in these numerical codes. This is certainly a major research that deserves to be pursued in the near future.

We refer to Fryer et al. (2015) for additional details on the following estimation of the BdHN progenitor population. Ultrastripped binaries are expected to be 0.1–1 per cent of the total SN (Tauris et al. 2013), which is estimated to be 2×10^4 Gpc^{-3} yr^{-1} (see e.g. Guetta & Della Valle 2007). The population densities of BdHN II/III and BdHN I have been estimated to be ~100 and ~1 Gpc^{-3} yr^{-1}, respectively (Ruffini et al. 2016b). The above numbers imply, for instance, that BdHN I would comprise of only the 0.5 per cent of the ultrastripped binaries. These estimates confirm, in passing, the rareness of the GRB phenomenon.

Since 2018, our research on BdHN has acquired a different status by promoting technical progress in the visualization and in the data analysis, as well as in the introduction of new theoretical paradigms and identification of new astrophysical regimes that we further extend in this article. We start with a specific example of BdHN simulation.

1.7 A specific BdHN I SPH simulation

In Fig. 4, we show the results of a specific SPH simulation of a BdHN I from Becerra et al. (2019). It represents the implosion of a CO$_{core}$ of 6.85 M$_\odot$ giving origin to the explosion of an SN in presence of a binary companion NS of $M_{NS} = 2$ M$_\odot$. An additional NS of 1.85 M$_\odot$ originates from the collapse of the Fe-core within the CO$_{core}$ (the green dot at the centre of the SN in the two left figures). We indicate as νNS this newborn neutron star, in order to differentiate it from the binary companion NS. The two upper panels correspond to the mass density in the binary equatorial plane of the binary progenitor, which we label for short as 'seen in the orbital plane'. The lower panels correspond to viewing in a plane orthogonal to the equatorial plane of the binary progenitor, indicated for short as 'seen from the top'. This figure well summarizes the central role of the SN in triggering the BDHN1 phenomenon: by first creating the νNS and the accreting SN ejecta both on the νNS and the binary NS companion. The sequence of the accretion process is followed in these Figs 159 s and 259 s. Following the hypercritical accretion process, the νNS reaches a mass and angular momentum, 2.04 M$_\odot$ and $1.24GM_\odot^2/c$, respectively. Up to the final simulation time. Similarly, the binary NS companion collapses reaching the secular axisymmetric instability point with a mass of 2.26 M$_\odot$ and angular momentum $1.24GM_\odot^2/c$ at $t = 21.6$ min. In this model, the initial binary period of the circular orbit is 4.8 min. The binary orbit then widens, reaching an orbital period of 16.5 min and an eccentricity of $\epsilon = 0.6$. We are going to give specific examples in selected GRBs of this process in Section 10 with the determination of the mass and spin of the newborn BH. This figure is also essential in emphasizing the implications of the different viewing angles implied by the binary nature of the progenitors, which have been also neglected in the traditional approach.

We further exemplify, in the next two sections, the large amount of results inferred on the BdHN nature utilizing the two above viewing angles.

1.8 The upper limits on the Lorentz Γ factor and nature of the afterglow

The observations of BdHN I 'seen in the orbital plane' have been addressed in a series of articles based essentially on the X-ray observations made with the XRT detector in *Swift* (see e.g. Ruffini et al. 2018a, and references therein). They have been essential in identifying model-independent upper limits on the Lorenz Γ factors of the emission regions during the gamma-ray flare, the X-ray flares phase, the flare-plateau, and the early afterglow phases (the Nousek–Zhang phase), following the initial ultrarelativistic prompt radiation phase.

The traditional approach had shown that gamma-ray spikes in the prompt emission occur at $\sim10^{15}$–10^{17} cm with Lorentz gamma factor $\Gamma \sim 10^2$–10^3 (e.g. Li 2020). Using a novel data analysis, we have shown that the time of occurrence, duration, luminosity, and total energy of the X-ray flares correlate with E_{iso}. A crucial feature has been identified in the observation of thermal emission in the X-ray flares that we have shown occurs at radii $\sim10^{12}$ cm with $\Gamma \lesssim 4$. The upper limit of Lorentz factor, $\Gamma \lesssim 2$, has been there established in the analysis of the X-ray flares. Equally, an upper limit $\Gamma \lesssim 3$ has been set in the transition from a SN to an HN in GRB 151027A (Ruffini et al. 2018c). Finally, the limit $\Gamma \lesssim 2$ has been established in the thermal emission in the early part of the afterglow phase of GRB 130427A (Ruffini et al. 2018b).

The enormous kinetic energy of an ultrarelativistic blast wave needed in the traditional approach to explain the energy source of

the afterglow has been therefore superseded: the above mentioned stringent upper limits on the Γ factors exclude any ultrarelativistic motion.

The origin of the afterglow of long GRBs and these mildly relativistic processes have been successfully identified in the synchrotron emission produced by relativistic electrons in the SN ejecta, powered by the hypercritical accretion of the SN into the spinning νNS of 1.5 $M_\odot$ and its pulsar-like emission (Ruffini et al. 2018b; Wang et al. 2019; Rueda et al. 2020). From the amplitude of their decaying X-ray luminosities observed by *Swift*-XRT (Pisani et al. 2016), the spin of the νNS and the strength and structure of its magnetic field in specific BdHN I and II have recently been obtained (Rueda et al. 2020).

It is important that the synchrotron process occurring in the interaction of the SN ejecta with the νNS requires a much smaller energy to explain the nature of the afterglow in our present approach based on the hypercritical accretion from the SN on to the νNS (Wang et al. 2019; Rueda et al. 2020) than the ones purported in the ultrarelativistic blast waves.

1.9 The '*inner engine*' of BdHN I

The observations of the BdHN I 'seen from the top' are the main topic of this article. They lead to an identification of the morphology of BdHN I, to the origin of the MeV, GeV, and TeV emissions observed by the GBM and LAT instruments onboard the *Fermi* satellite, the *MAGIC* and the H.E.S.S telescopes, as well as a contribution to ultrahigh-energy cosmic rays (UHECRs) from GRBs (see e.g. Rueda & Ruffini 2020). Particularly important has been the recent identification of the physical process occurring in the '*inner engine*' originating from the GeV emission as 'seen from the top' in GRB 130427A, also confirmed in three additional BdHN I GRB 160509A, GRB 160625B, and GRB 190114C (Li et al. 2019; Ruffini et al. 2019c).

In these works:

(i) We have proposed that the *inner engine* of a BdHN I is composed of a Kerr BH in a non-stationary state, embedded in a uniform magnetic field B_0 aligned with the BH rotation axis, as modelled by the Papapetrou–Wald solution of the Einstein–Maxwell equations (Papapetrou 1966; Wald 1974), and surrounded by an extremely low density ionized plasma of 10^{-14} g cm^{-3}. Using GRB 130427A as a prototype, we have shown that this *inner engine* acts in a sequence of *elementary impulses* emitting '*blackholic quanta*' (Rueda & Ruffini 2020). The repetition time of the emission of each '*blackholic quantum*' of energy $\mathcal{E} \sim 10^{37}$ erg is $\sim 10^{-14}$ s at the beginning of the process. Then, it slowly increases with the time evolution. Electrons are accelerated to ultrarelativistic energy near the BH horizon and propagate along the polar axis, $\theta = 0$. They can reach energies of $\sim 10^{18}$ eV, and partially contribute to UHECRs. When propagating along $\theta \neq 0$ through the magnetic field B_0 they give rise to the synchrotron emission of GeV and TeV photons. The *inner engine* operates within a 'cavity' formed during the hypercritical accretion of the SN ejecta on to the NS binary companion, and during the BH formation (Ruffini, Melon Fuksman & Vereshchagin 2019b). This result is the first step towards identifying the BdHN I morphology, presented in this article.

(ii) It has been shown that the multiwavelength emissions corresponding to the above acceleration process leading to synchrotron radiation occur in a jet with a half-opening angle of 60° from the normal to the binary plane. The jetted emission occurs in selected energy bands in the MeV, GeV, TeV, and UHECR.

(iii) This result has been applied to GRB 130427A, and we here show that it applies generally to all BdHN I as a consequence of the novel morphology identified in this article.

(iv) We have evaluated the total GeV emission in GRB 130427A and identified its decaying luminosity in the GeV range with a power-law index of $\alpha_{\mathrm{GeV}} = -1.19 \pm 0.04$, using the first and the second *Fermi*-GRB catalogues (Ackermann et al. 2013; Ajello et al. 2019). In this article, we generalize this result to all BdHN I emitting GeV radiation.

1.10 On the measure of the BH mass and spin in BdHN I

For the first time, in Ruffini et al. (2019c) it was shown how to extract the rotational energy of a Kerr BH in an astrophysical system, using GRB 130427A as a prototype. This was made possible making use of the the mass–energy formula of the Kerr BH (Christodoulou 1970; Christodoulou & Ruffini 1971; Hawking 1971, 1972), given in equation (1a). There, it was shown how through the '*inner engine*' activity the energetics of the GeV emission could originate near the BH horizon and be explained using the extractable energy of the BH, keeping constant the BH *irreducible mass*. In turn, this has led to the first measure of the initial mass and spin of the BH at its moment of formation: $M = 2.3$ $M_\odot$, its spin, $\alpha = a/M = 0.47$. This article is dedicated to extend this classic result to all BdHN I, where sufficient GeV emission data are available. This same procedure will be soon extended to active galactic nuclei with BH masses up to 10^{10} $M_\odot$.

1.11 Structure of the article

We first give in Section 2 an outline of the nine GRB subclasses presented in Ruffini et al. (2016b), with a brief summary of their initial states (*in-state*), their final state (out-state), their energetics, and spectral properties in the gamma-rays both in the MeV and in the GeV emissions. We also recall the binary mergers that include the NS–NS binaries leading to the two classes of S-GRBs.

In Section 3, we summarize the previous results (Li et al. 2019) on the analysis of the SN-rise of BdHNe I and II obtained from *Fermi*-GBM, and present their relation with the X-ray afterglow observed by *Swift*-XRT.

In Section 4, following our previous works (Ruffini et al. 2018b; Wang et al. 2019; Rueda et al. 2020), we study properties of the X-ray afterglow of BdHNe and we determine the spin of the νNS in two BdHNe I, two BdHNe II, and one BdHN III system.

In Section 5, we analyse the properties of the GeV emission in BdHNe I updated following the second GRB catalogue presented by *Fermi*-LAT, which covers the first 10 yr of its operations, from 2008 August 4 to 2018 August 4 (Ajello et al. 2019). We address the 378 BdHNe I with known cosmological redshift; see the list of BdHNe I in Pisani et al. (2016), Ruffini et al. (2018a), and also the updated list in Appendix A. We then consider only the 54 BdHN I with the boresight angle of *Fermi*-LAT smaller than 75° at the trigger time. We give the details of the 25 BdHNe I with observed GeV radiation, out of the 54. For each of them, we list in Table 5 the cosmological redshift, the $E_{\mathrm{p,i}}$ of the spectrum, the $E_{\gamma,\mathrm{iso}}$ of the source, the *Fermi* GCN, the boresight angle, the E_{LAT}, the likelihood test statistic (TS), and some additional distinguishing properties. In Table 6 for the 29 BdHNe I, we then give the cosmological redshift, the $E_{\mathrm{p,i}}$ of the spectrum, the $E_{\gamma,\mathrm{iso}}$ of the source, the *Fermi* GCN, the boresight angle, and some distinguishing properties of the associated X-ray emissions.

In Section 6, we explain the nature of the these BdHNe in terms of a novel morphology of the binary system. The BdHN I have a conical

structure normal to the equatorial plane of the binary progenitor. When the observations are made with a viewing angle lying in the orbital plane of the binary progenitor then the GeV emission is not observable. In this case, only the gamma-ray flare, the X-ray flares, and the X-ray plateau remain observable. From the ratio $N_{LAT}/N_{tot} = 25/54$, we infer the presence in the BdHN I of a conical structure of approximately $60°$ around the normal to the plane of the binary progenitors. Within this cone all emissions are observable, namely the X-ray, the gamma-ray, the GeV and TEV emission, and UHECRs. For larger inclination angle as confirmed theoretically in Ruffini et al. (2018c, 2019c), the GeV radiation is not observable and only flaring activities are observed following the prompt radiation phase.

In Section 7, we show that this novel geometry is indeed present in the recent 3D SPH numerical simulations at the moment of BH formation in a BdHN (Becerra et al. 2019).

In Section 8, for each of the 25 BdHNe I, we provide the 0.1–10 GeV luminosity light curves as a function of the time in the rest frame of the source. We obtain a power-law fit $L_n = A_n t^{-1.19 \pm 0.04}$ erg s^{-1} and report the amplitude A_n and the luminosity at 10 s from the beginning of the prompt radiation, L_{10s}, with their associated uncertainties. We also provide a correlation between L_{10s} and $E_{\gamma,iso}$.

In Section 9, we determine the values of the mass and spin of the BH and the strength of the magnetic field surrounding the BH in the '*inner engine*' of the selected BdHNe I. We also show the process of hypercritical accretion of the SN on a companion NS gives in all cases origin to the newborn BH.

In Section 10, we confirm (1) the central role of the SN in giving rise to its hypercritical accretion on the νNS and the newly born BH, to the afterglow observed by SWIFT and to the high-energy GeV and TeV emission observed by Fermi-LAT, (2) that the MeV–GeV energetic range is explainable by extractable rotational energy of a Kerr BH operating n the '*inner engine*' and this result allows the determination of the initial mass and spin of the BH, and (3) the power-law evolution of the 0.1–100 GeV luminosity after the prompt phase arises from the slowing down rate of the BH spin, keeping constant the irreducible mass M_{irr} of the BH.

We finally proceed to the general conclusions in Section 11. Before proceeding, we indicate in Table 1 the alphabetic ordered list of acronyms used in this work.

2 SUBCLASSES OF GRBS AND DEFINITIONS OF BDHN

We address the specific role of the X-ray emission observed by the *Swift* satellite as well as the MeV–GeV radiation observed by the *Fermi* satellite in order to further characterize the nine subclasses of GRBs presented in Ruffini et al. (2016b) and updated in Ruffini et al. (2018a), Wang et al. (2019), and here further updated in Section 4 and Appendix A. In Table 2, we summarize for each GRB subclass their name, the number of observed sources with cosmological redshift, and their progenitors characterizing their 'in-state'.

In all cases, the GRB progenitors are binary systems composed of various combinations of CO_{core}, of NSs, of WDs, and of BHs. The 'out-state' of the corresponding mergers or accretion processes have been represented in fig. 7 in Ruffini et al. (2016b) where we also presented the interesting possibility that 'out-states' of the GRB subclasses can become the 'in-states' of new GRB subclasses. In particular, we indicate an example in which the 'out-state' of a BdHN I can become the 'in-state' of an S-GRB.

In this article, we focus only on long GRBs with BdHN progenitors (Ruffini et al. 2016b): binary systems composed of a CO_{core},

exploding as SN Ic, and an NS binary companion. The presence of such an NS binary companion in close orbit can explain the removing of the outer layers of hydrogen and helium of the massive star leading to the CO_{core} (see e.g. Ruffini et al. 2001; Rueda & Ruffini 2012; Fryer, Rueda & Ruffini 2014).

As noted in the introduction, when the CO_{core} gravitationally collapses, it gives origin to an SN and its Fe core collapses to form a νNS. The entire dynamics and evolution of the BdHN is essentially based on these three different components and their interplay: the SN explosion (SN-rise), the νNS undergoing an overcritical accretion process of the SN ejecta, and the binary companion NS also undergoes an overcritical accretion process of the SN ejecta that monotonically increases the binary NS companion mass. In compact binary systems, this accretion causes the NS to reach its critical mass leading to the formation of a newborn BH (Becerra et al. 2015, 2016); see also Fig. 4.

We first address the SN hypercritical accretion on to the binary NS companion: the outcome is a strong function of the compactness of the binary system and its binary orbital period.

When the orbital period is as short as 5 min, the hypercritical accretion proceeds at higher rates and the companion NS reaches its critical mass leading to:

(i) the formation of a BH and consequently a formation of a new binary system composed of a BH and a νNS (Fryer et al. 2014);

(ii) the emission of a very energetic GRB in the range of $10^{52} \lesssim E_{iso} \lesssim 10^{54}$ erg and, peak energy in the range of 0.2 MeV $< E_{p,i} <$ 2 MeV lasting a few seconds known as the ultrarelativistic prompt emission phase (UPE);

(iii) the onset of the prolonged power-law GeV emission, triggered by the formation of the newborn BH, with a luminosity described in the rest frame of the source

$$L_{GeV} = A_{GeV} \left(\frac{t}{1\,s} \right)^{-\alpha_{GeV}} , \qquad (2)$$

with $\alpha_{GeV} = 1.19 \pm 0.04$. One of the main results in this paper is to show that this radiation is present only in a subset of BdHN and the explanation of this result will lead to the determination of the conical BdHN morphology, see Section 8.

These systems have been indicated as BdHN I (Becerra et al. 2015, 2016; Ruffini et al. 2015b, 2016b, 2019c; Wang et al. 2019).

The first list of the BdHNe I was composed of 161 sources spanning 12 yr of *Swift*/XRT observation activity till 2015 presented in Pisani et al. (2016) which was further extended to 173 sources in Ruffini et al. (2018a) up through the end of 2016 which led to a total of 345 BdHNe I within 1997–2016 observed by other satellites like *Fermi* and *Konus*-WIND in addition to *Swift*. This list is further extended here to 378 BdHN I till 2018 December (see Appendix A and Table 2).

When the orbital period of the binary system is $\gtrsim$5 min, the hypercritical accretion is not sufficient to trigger the collapse of the NS companion into a BH: therefore, no GeV emission can be produced nor be observed. Therefore, an M-NS is formed. In these systems, the observed peak energy is in the range 4 keV $< E_{p,i} <$ 300 keV and the isotropic energy is the range of $10^{48} \lesssim E_{iso} \lesssim 10^{52}$ erg, as observed by the *Fermi*-GBM. They have been indicated as X-ray flashes (XRF) in contrast with the more energetic BdHN I (Becerra et al. 2015, 2016; Ruffini et al. 2015b, 2016b). We here use for the XRFs the name BdHN II, according to Wang et al. (2019). A canonical example has been given in Wang et al. (2019); see Table 2.

BdHNe III have the same composition as BdHNe II, but the binary is further detached. No BH is formed and no GeV radiation

Table 2. Summary of the GRB subclasses. In addition to the subclass name, we report the number of GRBs for each subclass. We recall as well the 'in-state' representing the progenitors and the 'out-state' and the $E_{p,i}$ and $E_{\gamma,iso}$ for each subclass. The GeV emission is indicated in the last column: for long GRBs it appears only in BdHN I and BdHN IV (BH-SN) while, for short bursts, it appears only for S-GRBs. In all sources with GeV emission, it is $\gtrsim 10^{52}$ erg.

Class	Type	Number	In-state	Out-state	$E_{p,i}$ (MeV)	$E_{\gamma,iso}$ (erg)	$E_{iso,Gev}$ (erg)
Binary driven	I	378	CO star–NS	νNS–BH	$\sim$0.2–2	$\sim 10^{52}$–10^{54}	$\gtrsim 10^{52}$
hypernova	II	(49)	CO star–NS	νNS–NS	$\sim$0.01–0.2	$\sim 10^{50}$–10^{52}	–
(BdHN)	III	(19)	CO star–NS	νNS–NS	$\sim$0.01	$\sim 10^{48}$–10^{50}	–
	IV	0	CO star–NS	BH	–	$>10^{54}$	$\gtrsim 10^{53}$
	I	18	NS–NS	MNS	$\sim$0.2–2	$\sim 10^{49}$–10^{52}	–
Binary	II	6	NS–NS	BH	$\sim$2–8	$\sim 10^{52}$–10^{53}	$\gtrsim 10^{52}$
merger	III	(1)	NS–WD	MNS	$\sim$0.2–2	$\sim 10^{49}$–10^{52}	–
(BM)	IV	(1)	WD–WD	NS/MWD	$<$0.2	$<10^{51}$	–
	V	(0)	NS–BH	Direct BH	$\gtrsim$2	$>10^{52}$	–

is produced nor observed. This subclass is characterized by binary systems widely separated and weaker energy emission with E_{iso} in the range of 10^{48}–10^{50} erg.

As we will see in Section 10, the most energetic BdHN I originate from extremely tight binary systems with the companion NS grazing the radius of the CO$_{core}$. It is therefore conceivable that in some systems the NS companion merges with the CO$_{core}$ just prior to the SN explosion leading to the possible direct formation of a BH, a concept envisaged by Woosley (1993) in the failed SN scenario. We have left such a possibility opened in an additional BdHN IV family; see Table 2.

The hypercritical accretion of the SN ejecta on to the νNS leads to the pulsar-like emission that gives rise to the X-ray afterglow emission observed by *Swift* (Rueda et al. 2020). This is a property intrinsic to the nature of the model and shared by all BdHN subclasses. It is therefore natural to expect, as has been verified, that the luminosity of the X-ray afterglows of *all* long GRBs, in all BdHN subclasses, follow a common decaying power law of

$$L_X = A_X \left(\frac{t}{1\,s} \right)^{-\alpha_X}, \qquad (3)$$

with $\alpha_X = 1.48 \pm 0.32$, including the SN-rise, when averaged over all BdHN I up to 10^6 s (Pisani et al. 2016). The different amplitudes, A_X, and power-law indices, α_X, of the X-ray afterglow luminosity can be used to determine the spin and magnetic field of the νNS (Wang et al. 2019; Rueda et al. 2020).

Before leaving this topic, we mention a few cases of X-ray afterglows in BdHN II and BdHN III. Each BdHN II and BdHN III must be also characterized by an X-ray afterglow originating from the accretion of the SN ejecta into the νNS. Their power-law index α_X coincides with the one of BdHN I, although the difference in the total angular momentum of the binary progenitors and its conservation leads necessarily to a smaller value of the amplitude A_X in equation (3), to a corresponding lower value of the νNS spin, and to a smaller value of the SN-rise; see Fig. 5.

In the rest of this article, we mainly examine the properties of BdHN I with special attention to:

(i) their SN-rise emission;
(ii) the power-law decay of the X-ray emission of the afterglow observed by *Swift*, measured in the cosmological rest frame of the source;
(iii) the corresponding GeV emission observed by *Fermi*-LAT, centring on the identification of the BdHN morphology to explain the absence of this emission in a subclass of BdHN I.

3 THE SN-RISE IN BDHN I AND BDHN II: FERMI OBSERVATION

The trigger of all BdHNe is represented by the gravitational collapse of the CO$_{core}$ that gives origin to an SN and its Fe-core collapses to form a νNS. We have indicated the first appearance of the SN as the SN-rise. In BdHN I, the SN-rise is characterized by the presence of the thermal component in the *Fermi*-GBM data with isotropic energy of $\sim 10^{52}$ erg (see Fryer et al. 2014; Li et al. 2019; Ruffini et al. 2019a). In BdHN II, the SN-rise is weaker and has no thermal component in the *Fermi*-GBM data with energy of $\sim 10^{50}$ erg (see Li et al. 2019; Ruffini et al. 2019a; Wang et al. 2019; Fig. 6 and Table 3). In this article, we just recall the observation of the SN-rise in four BdHNe I: GRB 130427A, GRB 160509A, GRB 180720B, and GRB 190114C, as well as in two BdHNe II: GRB 180728A and GRB 190829A. In Fig. 6, we show the spectra of the SN-rise in the aforementioned sources and in Fig. 7 we show their corresponding luminosity.

4 THE AFTERGLOWS OF BDHN I, BDHN II, AND BDHN III: THE SWIFT OBSERVATIONS

Following the CO$_{core}$ gravitational collapse and the appearance of the SN-rise, which characterizes all BdHN subclasses, the hypercritical accretion of the SN ejecta on to the νNS and the magnetic field of the νNS leads to the pulsar-like emission powering the X-ray afterglow observed by the *Swift* satellite (Rueda et al. 2020).

We present four afterglows of BdHN I (Fig. 7), two afterglows of BdHNe II, and one afterglow of BdHNe III (Fig. 5). In each case, we also reproduce the SN-rise presented in the previous section (see Figs 5 and 7).

The BdHN I in GRB 130427A, GRB 190114C, GRB 180720B, and GRB 160509A follow a decaying luminosity consistent with equation (3) (see Fig. 7):

(i) GRB 130427A with amplitude $(3.65 \pm 0.63) \times 10^{52}$ erg s^{-1} and power-law index $\alpha_X = 1.24 \pm 0.02$.
(ii) GRB 160509A with amplitude $(22.68 \pm 24.00) \times 10^{52}$ erg s^{-1} and power-law index $\alpha_X = 1.22 \pm 0.09$.
(iii) GRB 180720B with amplitude $(112.67 \pm 93.89) \times 10^{52}$ erg s^{-1} and power-law index $\alpha_X = 1.43 \pm 0.07$.
(iv) GRB 190114C with amplitude $(5.14 \pm 2.03) \times 10^{52}$ erg s^{-1} and power-law index $\alpha_X = 1.37 \pm 0.05$.

The BdHNe II in GRB 180728A and GRB 190829A follow a decaying luminosity consistent with equation (3) (see Wang et al. 2019; Figs 5a and b):
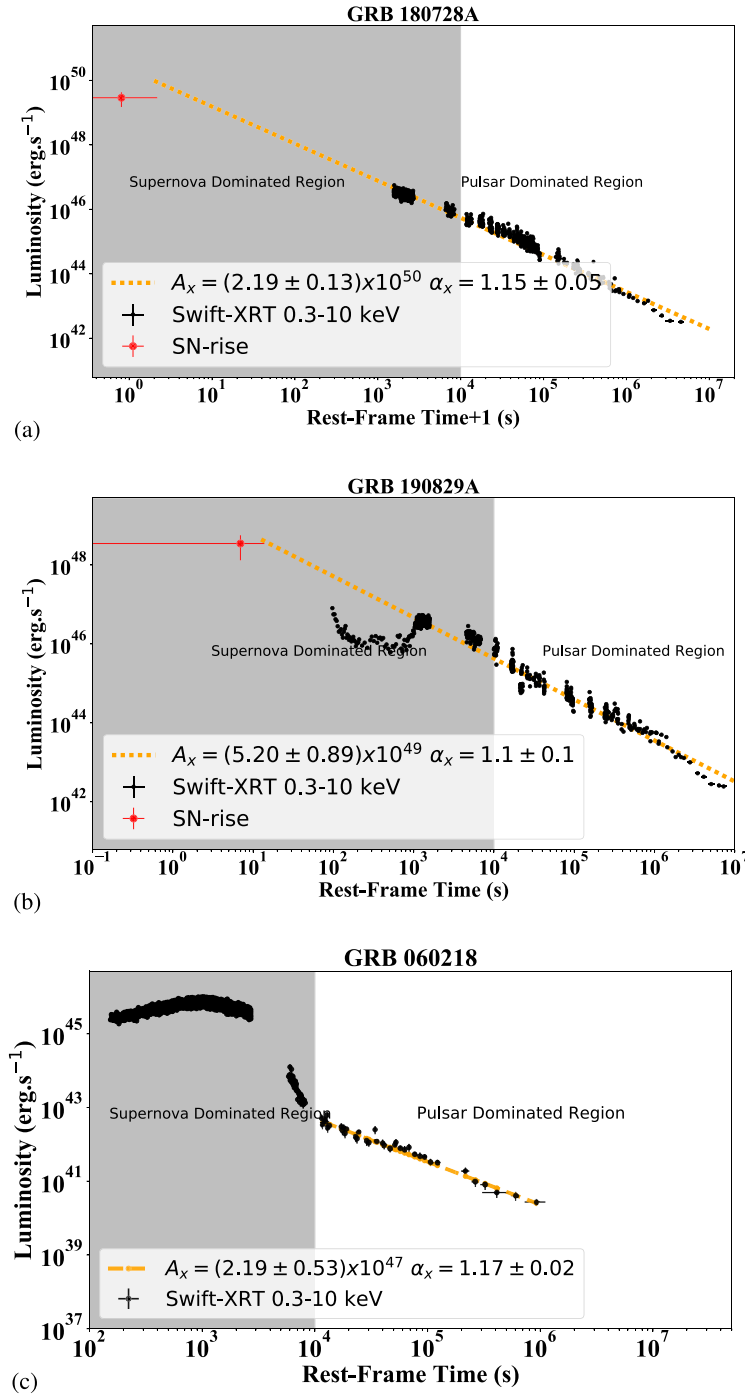
Figure 5. The X-ray afterglow luminosity observed by *Swift*-XRT that follow a decaying power law: (a) GRB 180728A (BdHN II) with amplitude $(2.19 \pm 0.13) \times 10^{50}$ erg s^{-1} and power-law index $\alpha_X = 1.15 \pm 0.05$. (b) GRB 190829A (BdHN II) with amplitude $(5.20 \pm 0.89) \times 10^{49}$ erg s^{-1} and power-law index $\alpha_X = 1.1 \pm 0.1$. (c) GRB 060218 (BdHN III) with amplitude $(2.19 \pm 0.53) \times 10^{47}$ erg s^{-1} and power-law index $\alpha_X = 1.17 \pm 0.02$. The fallback material of the SN on the νNS produce this X-ray afterglow emission (Rueda et al. 2020). In Section 4.1, we report the result of the simultaneous fit of the X-ray afterglow of all types of BdHN in order to find the universal power-law index. As shown in Ruffini et al. (2018a, c), until $\sim 10^4$ s the gamma/X-ray afterglow is mainly produced by the SN kinetic energy (*SN dominated region*) and its interaction with the magnetic field of the νNS. After 10^4 s, as shown by Ruffini et al. (2018b), the role of νNS becomes prominent (*pulsar dominated region*).

(i) GRB 180728A with amplitude $(2.19 \pm 0.13) \times 10^{50}$ erg s^{-1} and power-law index $\alpha_X = 1.15 \pm 0.05$.

(ii) GRB 190829A with amplitude $(5.20 \pm 0.89) \times 10^{49}$ erg s^{-1} and power-law index $\alpha_X = 1.1 \pm 0.1$.

As an example of the X-ray afterglow luminosity of a BdHN III, we indicate the case of GRB 060218 where the X-ray luminosity, as in the case of BdHNe I and II, follows a decaying power-law consistent with equation (3), with an amplitude $(2.19 \pm 0.53) \times 10^{47}$ erg s^{-1}
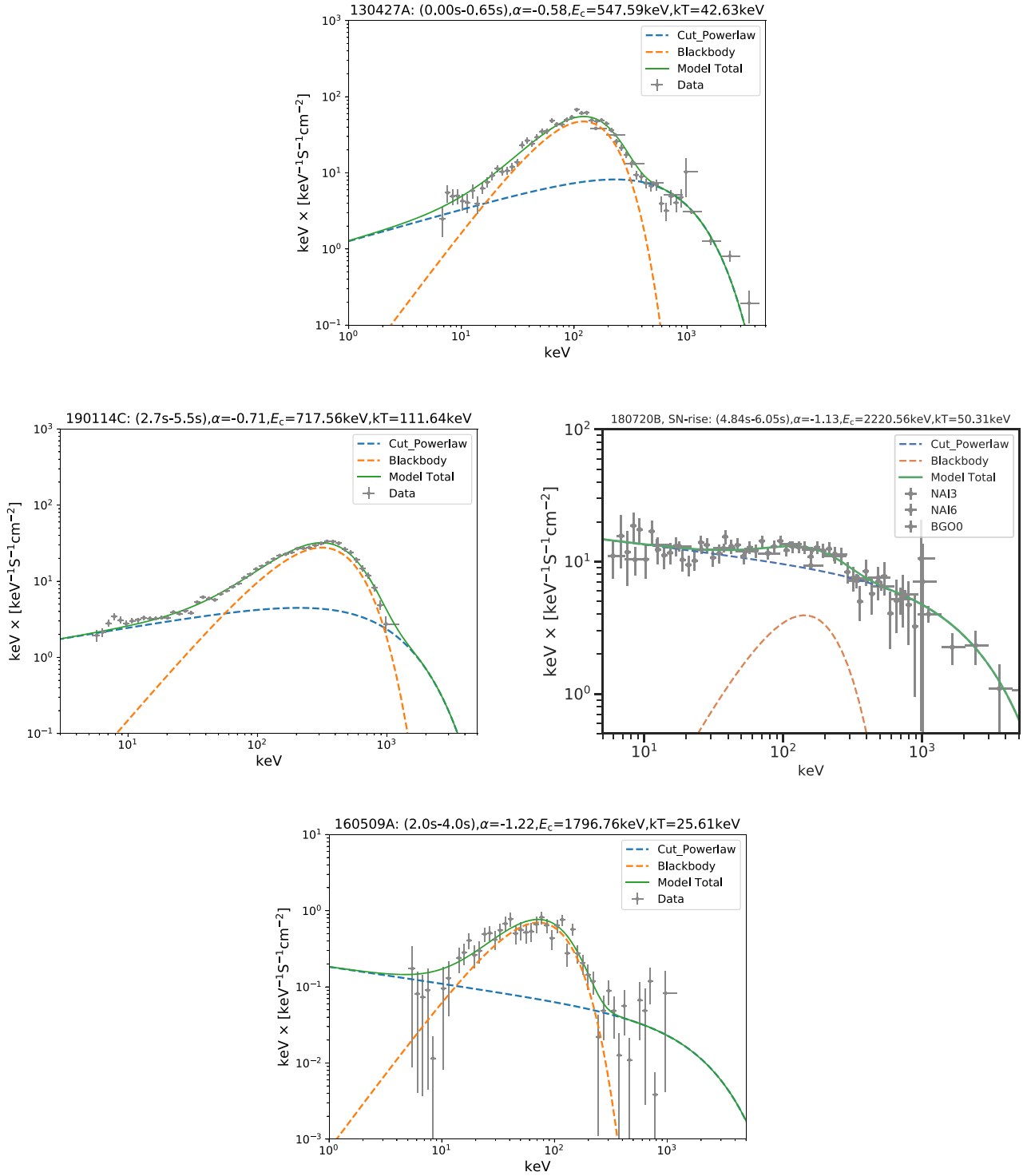
Figure 6. The spectrum of the SN-rise of GRB 160509A as observed by *Fermi*-GBM in the energy range of 8–900 keV. Upper left: SN-rise spectrum of BdHN I 130427A, well fitted by a CPL + BB model, from 0 to 0.65s ($t_{rf} \simeq 0.49s$); the spectral index α is -0.58, cut-off energy E_c is 547.59 keV, and the BB temperature is 42.63 keV in the observer's frame. Upper right: The spectra of SN-rise of BdHN I 190114C corresponding to $t = 1.12$ s ($t_{rf} = 0.79s$) to $t = 1.68$ s ($t_{rf} = 1.18s$), which is best fit by a CPL + BB model, with a low-energy photon index α of -0.71, and a peak energy E_c of 524.7 keV, and a BB temperature 18.42 keV. Time is reported in both the observer's frame and the rest frame. Spectral parameters of the best fit are presented in the observer's frame. Lower left: SN-rise spectrum of BdHN I 180720B, well fitted by a CPL + BB model, from 4.84 to 6.05 s ($t_{rf} \simeq 0.s$); the spectral index α is -1.13, cut-off energy E_c is 2220.569 keV, and the BB temperature is 50.31 keV in the observer's frame. Lower right: SN-rise spectrum of BdHN I 160509A, well fitted by a CPL + BB model, from 2.0 to 4.0 s ($t_{rf} \simeq 0.s$); the spectral index α is $-1.22.$, cutoff energy E_c is 1796.76 keV, and the BB temperature is 25.66 keV in the observer's frame.

Table 3. The properties of the SN-rise in BdHN I: GRB 190114C, GRB 130427A, GRB 160509A, and GRB 160625B; and the properties of the SN-rise in BdHN II: GRB 180728A.

GRB	t_1–t_2 (s) (Observation)	Duration (s) (Rest)	Flux (erg cm^{-2} s^{-1})	E_{sh} (10^{52} erg) (SN-rise)	E_{iso} (erg) (Total)	Temperature (keV) (Rest)	Redshift	Reference (For SN-rise)
190114C	1.12–1.68	0.39	$1.06^{+0.20}_{-0.20}(10^{-4})$	$2.82^{+0.13}_{-0.13}$	$(2.48 \pm 0.20) \times 10^{53}$	$27.4^{+45.4}_{-25.6}$	0.424	Melandri et al. (2019)
130427A	0.0–0.65	0.49	$2.14^{+0.28}_{-0.26}(10^{-5})$	$0.65^{+0.17}_{-0.17}$	$\sim 1.40 \times 10^{54}$	$44.9^{+1.5}_{-1.5}$	0.3399	Xu et al. (2013)
160509A	2.0–4.0	0.92	$1.82^{+1.23}_{-0.76}(10^{-6})$	$1.47^{+0.6}_{-0.6}$	$\sim 1.06 \times 10^{54}$	$25.6^{+4.8}_{-4.7}$	1.17	Tam et al. (2017)
160625B	0–2.0	0.83	$6.8^{+1.6}_{-1.6}(10^{-7})$	$1.09^{+0.2}_{-0.2}$	$\sim 3.00 \times 10^{54}$	$36.8^{+1.9}_{-1.9}$	1.406	This paper
180728A	−1.57 to 1.18	0.83	$4.82^{+1.16}_{-0.82}(10^{-8})$	$7.98^{+1.92}_{-1.34} \times 10^{49}$	$2.76^{+0.11}_{-0.10} \times 10^{51}$	-	0.117	Izzo et al. (2018)
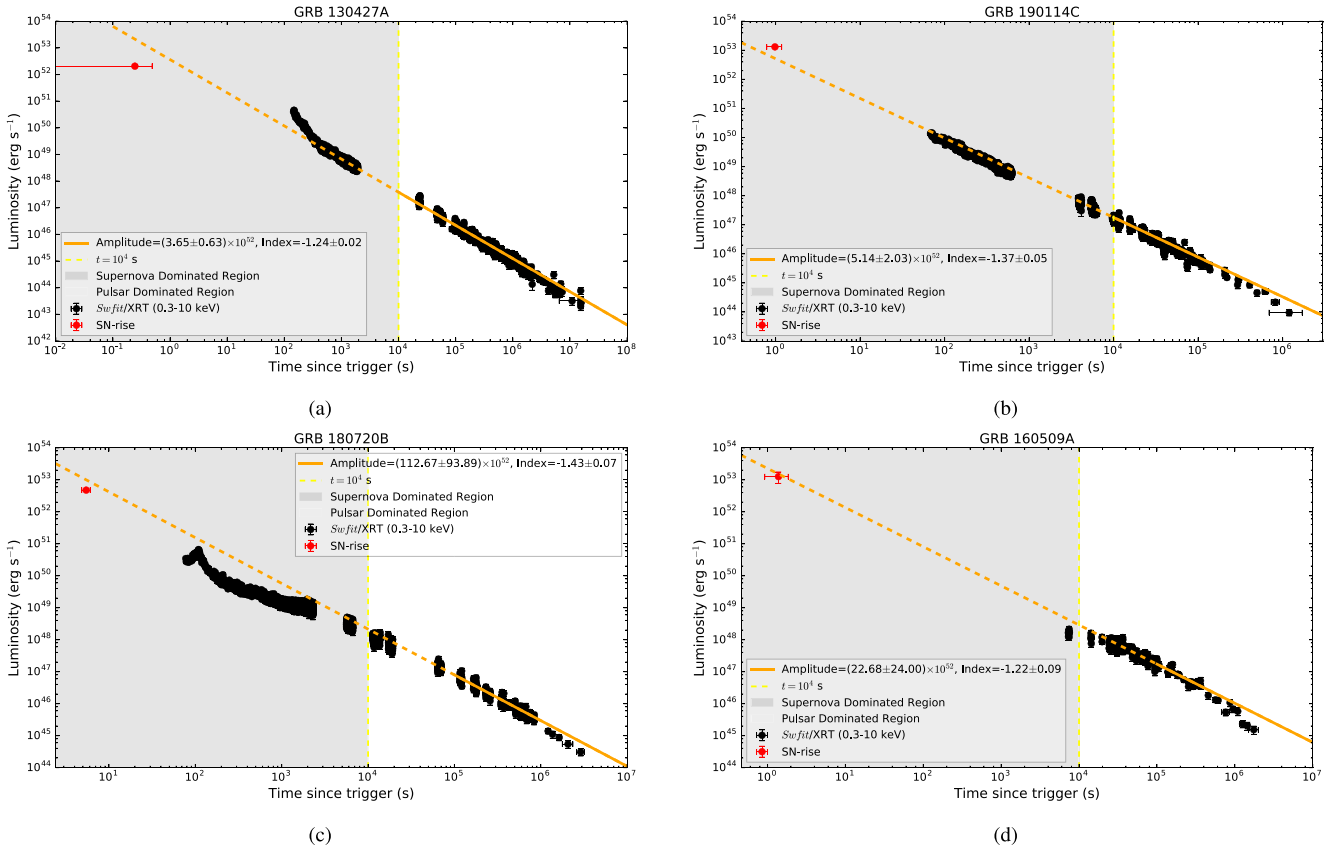
Figure 7. X-ray afterglow luminosities of four BdHNe I observed by *Swift*-XRT that follow a decaying power law: (a) GRB 130427A (BdHNe I) with amplitude $(3.65 \pm 0.63) \times 10^{52}$ erg s^{-1} and power-law index $\alpha_X = 1.24 \pm 0.02$. (b) GRB 190114C with amplitude $(5.14 \pm 2.03) \times 10^{52}$ erg s^{-1} and power-law index $\alpha_X = 1.37 \pm 0.05$. (c) GRB 180720B with amplitude $(112.67 \pm 93.89) \times 10^{52}$ erg s^{-1} and power-law index $\alpha_X = 1.43 \pm 0.07$. (d) GRB 160509A with amplitude $(22.68 \pm 24.00) \times 10^{52}$ erg s^{-1} and power-law index $\alpha_X = 1.22 \pm 0.09$. The red points show the luminosity of SN-rise in each BdHN. The fallback of material from the SN on to the νNS produces this X-ray afterglow emission (Rueda et al. 2020). As shown in Ruffini et al. (2018a, c), till $\sim 10^4$ s the gamma/X-ray afterglow is mainly produced by the SN kinetic energy (*SN dominated region*) and its interaction with the magnetic field of the νNS. After 10^4 s, as shown by Ruffini et al. (2018b), the role of νNS becomes prominent (*pulsar dominated region*).

and power-law index $\alpha_X = 1.17 \pm 0.02$. This is consistent with $\alpha_X = 1.2 \pm 0.1$ obtained by Campana et al. (2006; see Fig. 5c).

We can then reach the following general conclusions:

(i) The X-ray afterglow is present in all three BdHN subclasses: BdHN I, BdHN II, and BdHN III.

(ii) The X-ray afterglow is always present in *all* of the 378 BdHNe I (see Appendix A).

(iii) This result clearly indicates the spherical symmetry, or a very wide-angle emission of the X-ray afterglow.

4.1 The spin of the νNS

In Ruffini et al. (2018b), Rueda et al. (2020), and Wang et al. (2019), the bolometric luminosity contributing to the optical and X-ray bands by the νNS rotational energy loss by magnetic braking has been modelled for the emission at late times $t \gtrsim 10^4$ s of the 'Nousek–Zhang' (flare-plateau-afterglow, FPA phase). This allows the inference of the initial rotation period of the νNS as well as its magnetic field structure. The origin of the long GRB afterglows at this phase is the interaction between the SN ejecta and the spinning magnetized νNS and their synchrotron emission (Ruffini et al. 2018b).

Since the νNS is just born, it must be rapidly rotating and contains abundant rotational energy:

$$E_{\rm rot} = \frac{1}{2} I \Omega^2, \tag{4}$$

where I is the moment of inertia and $\Omega = 2\pi/P_{\nu\rm NS}$ is the angular velocity. For a νNS with a period of $P_{\nu\rm NS} = 1$ ms, $M = 1.4$ M$_\odot$, $R = 10$ km, the moment of inertia is $I \sim 10^{45}$ g cm^2. This leads to a total rotational energy of $E \sim 2 \times 10^{52}$ erg.

We assume that the rotational energy of the νNS provides the energy budget of the X-ray radiation via synchrotron emission of the electrons (Ruffini et al. 2018b):

$$E_{\rm rot} = E_{\rm X}. \tag{5}$$

This is reminiscent of the extraction of the BH rotational energy via synchrotron radiation of electrons radiating in the GeV energy band (Ruffini et al. 2019c).

Therefore, using the equation (4) and substituting the equation (3)

$$\frac{{\rm d}E_X}{{\rm d}t} = L_{\rm X}(t) = A_{\rm X} \left(\frac{t}{1 \rm s}\right)^{-\alpha_{\rm x}} = -I\Omega\dot{\Omega}. \tag{6}$$

The best fit to the X-ray luminosity of equation (3), together with equation (6), allow an estimate of the spin of the νNS in *all* BdHNe, as well as their spin evolution (see Table 4 and Fig. 8).

In Table 4, we report the physical quantities of three BdHNe I, GRB 130427A, GRB 180720B, and GRB 190114C, together with two BdHNe II, GRB 180728A and GRB 190829A, as well as one BdHN III, GRB 060218; assuming a νNS of mass and radius, respectively, 1.4 M$_\odot$ and 10^6 cm. The νNS emission is not able to explain the emission of the 'Nousek–Zhang' phase at early times 10^2–10^4 s. As it is shown in Ruffini et al. (2018b, c), that emission is mainly powered by the mildly relativistic SN kinetic energy that we refer to as the *SN dominated region*. After 10^4 s, as shown by Ruffini et al. (2018b), the role of νNS becomes prominent, referred to as *pulsar dominated region*.

The first main results of this paper are: (1) the first identification of the SN-rise, (2) the agreement of the extrapolated luminosity of the X-ray afterglow with the luminosity of the SN-rise, and (3) the measurement of the νNS period, leading to the power-law emission of the afterglow (see Fig. 7). The two process of the SN-rise energetics and the νNS dynamics appear to be strongly correlated.

5 BDHN I: THE FERMI-LAT OBSERVATIONS

5.1 BdHNe I observed by Fermi-LAT

We now address the 378 BdHNe I with known redshifts (see Pisani et al. 2016; Ruffini et al. 2018a; Appendix A): out of them, we are first interested in the 25 BdHNe I emitting GeV radiation and within the boresight angle of *Fermi*-LAT, i.e. $\theta < 75°$, at the time of the trigger, since exposure drops quickly for larger angles (Ajello et al. 2019). They have as well a TS value >25, which means the GeV photons are excluded at the 5σ level from background sources. We follow the first and second *Fermi* catalogues (Ackermann et al. 2013; Ajello et al. 2019) for the time-resolved likelihood spectral analysis. Therefore, we divide the data into logarithmic spaced bins and, if the TS value of each bin is smaller than 16, we merge the time bin with the next one and repeat the likelihood analysis. In Table 5, we indicate in the first column the name of the BdHNe I, in the second their measured redshift, we report in the third column the $E_{\rm p,i}$ obtained from the *Fermi* data, we estimate in the fourth column the

$E_{\gamma,\rm iso}$, which is itself larger than the 10^{52} erg. In the fifth column, the *Fermi* GCN numbers are shown. In the sixth column, the values of $E_{\rm LAT}$ are provided and finally we add the boresight angle of the LAT $\theta < 75°$ and the TS values of these GRBs observed by LAT.

5.2 BdHNe I without GeV emission and geometry of the BdHNe I

We now turn to an additional unexpected result obtained in the analysis of the BdHNe I subtended within the $75°$ of the *Fermi*-LAT boresight angle: the existence of 29 BdHNe I without observed GeV emission (see Table 6). Although the distribution of the boresight angle and redshift is analogous to the one of the 25 sources considered in Section 5, no GeV emission is observed.

Some BdHNe I of this group have been observed previously by *Swift* and have been identified as sources of (i) gamma and hard X-ray flares, (ii) soft X-ray flares, and of (iii) the extended thermal emission (see Ruffini et al. 2018a, for details). A particular example has been given by GRB 151027A in Nappo et al. (2017) and Ruffini et al. (2018c). There, we assumed that the viewing angle of these sources lies in the equatorial plane of the progenitor system (see Section 1 and Fig. 4). As we will show in this article, in none of these sources GeV radiation can be observed due to the new morphology discovered in the BdHNe I (see next section).

6 MORPHOLOGY OF BDHN I

We here assume that the 25 sources considered in Table 5, all emitting in the GeV have a viewing angle close to the normal of the plane. This assumption is confirmed in Ruffini et al. (2019c) where indeed the high-energy GeV–TeV radiations are emitted in direction close to the BH rotation axis.

The remaining 29 sources in Table 6 have a viewing angle in the equatorial plane of the binary progenitor and in that case only flaring activities in gamma and X-ray are observable, i.e. no GeV–TeV emission, as explicitly shown in Ruffini et al. (2018c, 2019c). This allows us to introduce a new morphology for the BdHNe I and predict specific observational properties.

We now look at the ratio between the number of GRBs with an observed GeV radiation, $N_{\rm LAT}$, and the total number of GRBs, $N_{\rm tot}$, both within the LAT $75°$ boresight angle. We assume that: (1) BdHNe I follow the same cosmological isotropic distribution of all GRBs first observed by the BATSE instrument onboard the CGRO satellite (see e.g. Meegan et al. 1992; Paciesas et al. 1999); (2) all orientations of the BdHNe I with respect to the LAT detector are equally probable; (3) the GeV emitting region is a two-side cone whose opening angle is the same for all sources. Under these assumptions, we can then estimate the half-opening angle of a single cone ϑ as

$$1 - \cos\vartheta = \frac{N_{\rm LAT}}{N_{\rm tot}}. \tag{7}$$

Our search in the LAT data[1] gives $N_{\rm LAT} = 25$ and $N_{\rm tot} = 54$, leading to $\vartheta \approx 60°$. Therefore, in BdHN I the GeV emission comes from a wide-angle emission, as it is schematically shown in Fig. 9. This is in agreement with theory of synchrotron radiation produced around the Kerr BH along the rotation axis (see details in Ruffini et al. 2019c).

Therefore, we have identified a *new* morphology of the BdHN I (see Figs 9 and 10). The identification of this morphology has been possible thanks to the analysis of the GeV emission in this paper, by

---

[1] https://fermi.gsfc.nasa.gov/ssc/observations/types/grbs/lat_grbs/table.php

Table 4. Observational properties of three BdHN I, GRB 130427A, GRB 180720B, and GRB 190114C together with two BdHNe II 180728A and 190829A as well as one BdHN III, GRB 060218 and inferred physical quantities of the νNS of the corresponding BdHN model that fits the GRB data. Column 1: GRB name; column 2: identified BdHN type; column 3: cosmological redshift (z); column 4: the isotropic energy released ($E_{\rm iso}$) in gamma-rays; column 5: νNS rotation period ($P_{\nu \rm NS}$) at 10^4 s, column 6: The isotropic energy of the X-ray afterglow ($E_{\rm X}$). We assume the NS mass of 1.4 M$_\odot$ and the NS radius of 10^6 cm for all these cases.

GRB	Type	Redshift	$E_{\rm iso}$ (erg)	$P_{\nu \rm NS}$ @10^4 s (ms)	$E_{\rm X}$(after10^4 s) (erg)	$A_{\rm X}$ (erg s^{-1})	$\alpha_{\rm X}$
130427A	BdHN I	0.34	9.2×10^{53}	1.15	1.67×10^{52}	$(3.65 \pm 0.63) \times 10^{52}$	1.24 ± 0.02
180720B	BdHN I	0.654	6.8×10^{53}	0.66	4.99×10^{52}	$(112.67 \pm 93.89) \times 10^{52}$	1.43 ± 0.07
190114C	BdHN I	0.42	1.5×10^{53}	2.19	4.60×10^{51}	$(5.14 \pm 2.03) \times 10^{52}$	1.37 ± 0.05
180728A	BdHN II	0.117	2.3×10^{51}	7.74	3.68×10^{50}	$(2.19 \pm 0.13) \times 10^{50}$	1.15 ± 0.05
190829A	BdHN II	0.0785	2.2×10^{50}	10.31	2.07×10^{50}	$(5.20 \pm 0.89) \times 10^{49}$	1.10 ± 0.06
060218	BdHN III	0.033	5.4×10^{49}	285.81	2.69×10^{47}	$(2.19 \pm 0.53) \times 10^{47}$	1.17 ± 0.02
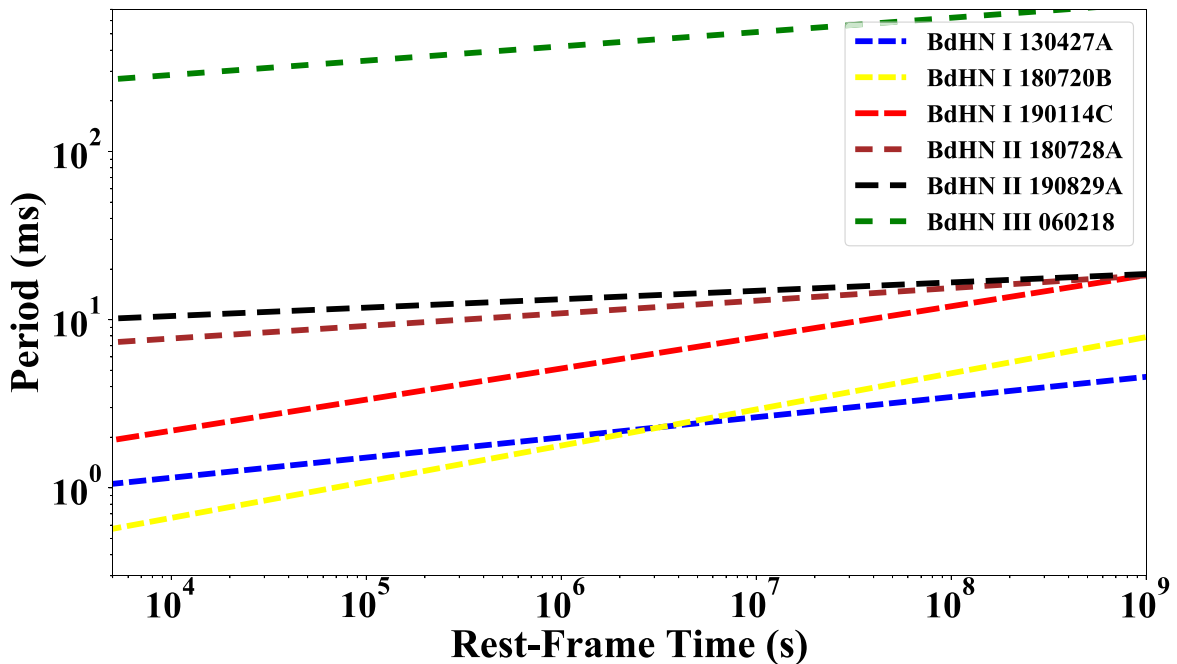
Figure 8. The evolution of the νNS period of six BdHNe, as a function of rest-frame time. The values of the νNS period at 10^4 s, namely in the pulsar dominated region of the afterglow are tabulated in Table 4. The trend of the νNS period indicates that the rotational energy is being released due to the radiation losses in the keV band revealing itself as the X-ray afterglow luminosity.

the soft and hard X-ray flares in Ruffini et al. (2018a), the extended thermal emission in Nappo et al. (2017), and Ruffini et al. (2018a) in GRB 151027A. In this identification, we have been guided by the large number of numerical simulations describing the accretion of the SN ejected material around the NS companion (see Figs 4 and 10, and its idealized representation in Fig. 9; see Becerra et al. 2016, 2019, for additional details).

What can be concluded from the above results is that in BdHNe I, the GeV emission is only detectable when the viewing angle is less than $\approx 60°$ from the normal to the plane and the BdHN I is 'seen from the top' (see the left-hand plot in Fig. 9). Whenever the viewing angle is within $60°$ from the orbital plane, no GeV emission is observed, though X-ray and gamma-ray flares are observed (see right-hand plot in Fig. 9).

Therefore, the second main result of this paper is the identification of the BdHN I morphology and its explanation within the BdHN I model.

7 SPH SIMULATION OF BDHNE I

The numerical simulations at the moment of BH formation in a BdHN I is presented in Becerra et al. (2016, 2019). 3D views of the density distribution at the moment of the BH formation in a BdHN I are shown Fig. 10. These plots correspond to the simulation of the SN ejecta expansion in the presence of the NS companion. The simulation is performed using an SPH code in which the SN ejecta material is evolved with N point-like particles, in the present case 16 million, with different masses and their motion is followed under the NS gravitational field. The orbital motion of the NS around the SN explosion centre is also taken into account as the NS star gravitational mass changes via the hypercritical accretion process. The latter was modelled independently estimating the accretion rate on to the NS via the Bondi–Hoyle formalism. For the initial conditions of the simulation, an homologous velocity distribution in free expansion was adopted and a power-law initial density profile of the SN matter was modelled by populating the inner layers with more particles (see

Table 5. Prompt and GeV emission of the 25 long GRBs inside the *Fermi*-LAT boresight angle and with GeV photons detected. The columns list: the source name, z, $E_{p,i}$, $E_{\gamma,iso}$, E_{LAT} in 0.1–10 GeV, the position of the source from the LAT boresight θ, the likelihood TS. The E_{LAT} includes only the energy in the observed time duration, which does not cover the whole GeV emission period, and is different for each GRB, so we put a symbol '$\gtrsim$' to indicate that the value is the lower limit.

GRB	z	$E_{p,i}$ (MeV)	$E_{\gamma,iso}$ (10^{52} erg)	Fermi GCN	E_{LAT} (10^{52} erg)	θ (deg)	TS
080916C	4.35	2.27 ± 0.13	407 ± 86	8246	230 ± 10	48.8	1450
090323A	3.57	2.9 ± 0.7	438 ± 53	9021	120 ± 20	57.2	150
090328A	0.736	1.13 ± 0.08	14.2 ± 1.4	9044	2.7 ± 0.4	64.6	107
090902B	1.822	2.19 ± 0.03	292.0 ± 29.2	9867	47 ± 2	50.8	1832
090926A	2.106	0.98 ± 0.01	228 ± 23	9934	149 ± 8	48.1	1983
091003A	0.897	0.92 ± 0.04	10.7 ± 1.8	9985	0.8 ± 0.3	12.3	108
091127	0.49	0.05 ± 0.01	0.81 ± 0.18	10204	0.03 ± 0.02	25.8	34
091208B	1.063	0.25 ± 0.04	2.10 ± 0.11	10266	$\gtrsim 0.41 \pm 0$	55.6	20
100414A	1.368	1.61 ± 0.07	55.0 ± 0.5	10594	7 ± 1	69	81
100728A	1.567	1.00 ± 0.45	72.5 ± 2.9	11006	0.9 ± 0.3	59.9	32
110731A	2.83	1.21 ± 0.04	49.5 ± 4.9	12221	15 ± 2	3.4	460
120624B	2.197	1.39 ± 0.35	347 ± 16	13377	22 ± 2	70.8	312
130427A	0.334	1.11 ± 0.01	92 ± 13	14473	8.6 ± 0.4	47.3	163
130518A	2.488	1.43 ± 0.38	193 ± 1	14675	15 ± 5	41.5	50
131108A	2.40	1.27 ± 0.05	51.20 ± 3.83	15464	37 ± 4	23.78	870
131231A	0.642	0.27 ± 0.01	21.50 ± 0.02	15640	1.6 ± 0.3	38	110
141028A	2.33	0.77 ± 0.05	76.2 ± 0.6	16969	9 ± 2	27.5	104.5
150314A	1.758	0.86 ± 0.01	70.10 ± 3.25	17576	1.8 ± 0.7	47.13	27.1
150403A	2.06	0.95 ± 0.04	87.30 ± 7.74	17667	1.1 ± 0.4	55.2	37
150514A	0.807	0.13 ± 0.01	1.14 ± 0.03	17816	0.06 ± 0.05	38.5	33.9
160509A	1.17	0.80 ± 0.02	84.5 ± 2.3	19403	10 ± 1	32	234
160625B	1.406	1.3 ± 0.1	337 ± 1	19581, 19604	17 ± 1	41.46	961.33
170214A	2.53	0.89 ± 0.04	392 ± 3	20675, 20686	53 ± 4	33.2	1571
170405A	3.51	1.20 ± 0.42	241.01 ± 52.02	20990, 20986	16 ± 7	52.0	56
180720B	0.654	1.06 ± 0.24	68.2 ± 2.2	22996, 23042	2.2 ± 0.2	49.1	975

Fryer et al. 2014; Becerra et al. 2016, 2019, for additional details). Figs 4 and 10 correspond to an initial binary system formed by a $2\,M_\odot$ NS and the CO_{core} obtained from a progenitor with $M_{ZAMS} = 30\,M_\odot$. When the CO_{core} collapses and explodes, it ejects $7.94\,M_\odot$ and leads a νNS of $1.5\,M_\odot$ at its centre. The initial binary period is about 5 min, corresponding to a binary separation of $\approx 1.5 \times 10^{10}$ cm.

The new morphology of the BdHNe I presented here and in the previous section leads to a difference in the observed energy spectra and time variability for sources with viewing angle in the plane, or normal to the orbital plane of the binary progenitor. We infer that our 25 BdHNe I, with viewing angles less than $\approx 60°$ from the normal to the orbital plane of the binary progenitor, 'seen from the top', have larger $E_{\gamma,iso}$ than the ones with a viewing angle lying in the plane of the binary system (see Tables 5 and 6). This explains the association/non-association of the GeV emission with bright GRBs often mentioned in the current literature (see Cenko et al. 2011; Racusin et al. 2011, and fig. 4 in Nava 2018).

An additional issue in the traditional approach (see e.g. Racusin et al. 2011; Beniamini et al. 2015, and sections 3 and 4 in Nava 2018) is also solvable: the sources that are seen with a viewing angle lying in the orbital plane have stronger flaring activities in the X-ray afterglow when compared to the 25 emitting in the GeV range. Therefore, the ratio between E_{iso} and the luminosity in the X-ray afterglow is systematically smaller than in the 25 with GeV emission. This offers a different explanation than the one presented in the traditional approach. However, all of these matters that have already been mentioned in Ruffini et al. (2018c) need a new operational definition of $E_{\gamma,iso}$, taking into due account the hard and soft X-ray flares and the extended thermal emission (see also Ruffini et al. 2019b).

Another important specific feature of the new morphology of BdHN I is the presence of the νNS formed at the centre of the exploding SN (see Fig. 4 and Becerra et al. 2016, 2019). We have shown that the νNS manifests itself through the synchrotron emission by relativistic electrons injected from it into the expanding magnetized SN ejecta, as well as through its pulsar emission that explain the early and late optical and X-ray afterglow, respectively, allowing the inference of the νNS rotation period (see Ruffini et al. 2018b). A smoking gun of this picture, namely the verification of the νNS activity following the above mechanism, both in XRFs (BdHNe II) and in BdHNe I, and the connection of the inferred rotation period of the νNS to the one of the CO-star and to the orbital period, from angular momentum conservation, has been explicitly shown in the GRB 180728A (BdHN II) and GRB 130427A (BdHN I) and GRB 190114C (BdHN I) (see Wang et al. 2019 for details).

8 THE LUMINOSITY POWER-LAW BEHAVIOUR IN BDHNE MEASURED IN THE REST FRAME

In the following, we fit simultaneously the luminosity light curves of all the 25 BdHNe with GeV emission expressed in their rest frame. We assume the same power-law decay index for all of them, but allow different amplitude values. This assumption is consistent with our model, moreover, it is a benefit for those GRBs with limited data that cannot be fitted solely.

Table 6. List of 29 BdHNe I inside the *Fermi*-LAT boresight angle and with no GeV photons detected: 29 BdHNe I with redshift taken from (Ruffini et al. 2016b) from 2008, when *Fermi* started to operate, till the end of 2016. All of them are within the boresight of *Fermi*-LAT, but no detected GeV photons. For each source the columns list: z, $E_{\gamma,\mathrm{iso}}$, E_p, GCN number, position of the source from LAT boresight θ, whether there was a detection by LAT, and additional information.

GRB	z	E_p (MeV)	$E_{\gamma,\mathrm{iso}}$ ($\times 10^{52}$ erg)	*Fermi* GCN	θ (deg)	GeV observed	Comments
081222	2.77	0.51 ± 0.03	27.4 ± 2.7	8715	50.0	No	
090424A	0.544	0.27 ± 0.04	4.07 ± 0.41	9230	71.0	No	
090516A	4.109	0.14 ± 0.03	99.6 ± 16.7	9415	20.0	No	Clear X-ray flare
100615A	1.398	0.21 ± 0.02	5.81 ± 0.11	10851	64.0	No	
100728B	2.106	0.32 ± 0.04	3.55 ± 0.36	11015	57.1	No	
110128A	2.339	0.46 ± 0.01	1.58 ± 0.21	11628	45.0	No	
111228A	0.716	0.060 ± 0.007	2.75 ± 0.28	12744	70.0	No	
120119A	1.728	0.52 ± 0.02	27.2 ± 3.6	12874	31.4	No	
120712A	4.175	0.64 ± 0.13	21.2 ± 2.1	13469	42.0	No	
120716A	2.486	0.4 ± 0.04	30.2 ± 3.0	13498	63.0	No	
120909A	3.93	0.87 ± 0.01	87 ± 10	13737	66.0	No	
130528A	1.250	0.27 ± 0.18	18.01 ± 2.28	14729	60.0	No	X-ray flare
130925A	0.347	0.14 ± 0.04	3.23 ± 0.37	15261	22.0	No	X-ray flare
131105A	1.686	0.55 ± 0.08	34.7 ± 1.2	15455	37.0	No	
140206A	2.73	1.1 ± 0.03	144.24 ± 19.20	15790	46.0	No	Clear X-ray flare
140213A	1.2076	0.176 ± 0.004	9.93 ± 0.15	15833	48.5	No	
140423A	3.26	0.53 ± 0.04	65.3 ± 3.3	16152	44.0	No	
140623A	1.92	1.02 ± 0.64	7.69 ± 0.68	16450	32.0	No	
140703A	4.13	0.91 ± 0.07	1.72 ± 0.09	16512	16.0	No	
140907A	1.21	0.25 ± 0.02	2.29 ± 0.08	16798	16.0	No	X-ray flare
141220A	1.3195	0.42 ± 0.02	2.44 ± 0.07	17205	47.0	No	
150301B	1.5169	0.45 ± 0.10	2.87 ± 0.42	17525	39.0	No	
150821A	0.755	0.57 ± 0.03	14.7 ± 1.1	18190	57.0	No	
151027A	0.81	0.62 ± 0.11	3.94 ± 1.33	18492	10.0	No	Clear X-ray flare
151111A	3.5	0.25 ± 0.04	3.43 ± 1.19	18582	50.0	No	X-ray flare observed
161014A	2.823	0.64 ± 0.06	10.1 ± 1.7	20051	69.0	No	
171222A	2.409	0.1 ± 0.01	20.73 ± 1.7	22272, 22277	43	No	
180703A	0.67	0.58 ± 0.05	3.15 ± 0.7	23889, 22896	44	No	
180728A	0.117	0.1 ± 0.02	3.15 ± 0.7	23055, 23067	35	No	
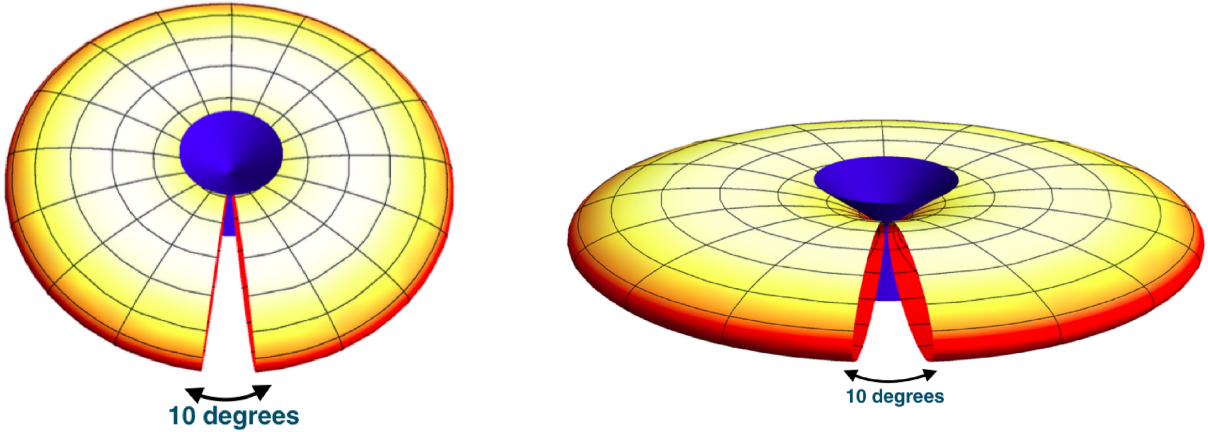
Figure 9. Schematic plot for showing the morphology of the BdHNe I. The GeV emission is detectable when the viewing angle is less than the 60° from the normal to the orbital plane. Left-hand panel is the situation in which the detectors can observe GeV and prompt emissions and the right-hand panel is the one for which GeV emission is not detectable and only gamma-ray and X-ray flares are detectable. The 10° cuts in both figures indicate the low-density region in Fig 10 through which the prompt radiation phase can be 'seen in the orbital plane'. The existence of such a 10° cut was first identified by the SPH simulation quoted in Becerra et al. (2016, 2019) and further confirmed in GRB 151027A (Ruffini et al. 2018c).

We limit our analysis of the light curves after the BdHN I prompt emission, when the GeV luminosity is already in the asymptotic power-law regime. We assume the power-law

$$L_n(t) = A_n t^{\alpha_{\mathrm{GeV}}}, \tag{8}$$

describing the rest-frame 0.1–100 GeV isotropic luminosity light curve of nth BdHN I. In the simultaneous fitting, we perform the Levenberg–Marquardt method to perform the minimization (Gill & Wright 1981). The basic idea of fitting is to minimize the χ^2; when fitting one curve to one equation, the χ^2 is minimized. To fit N curves
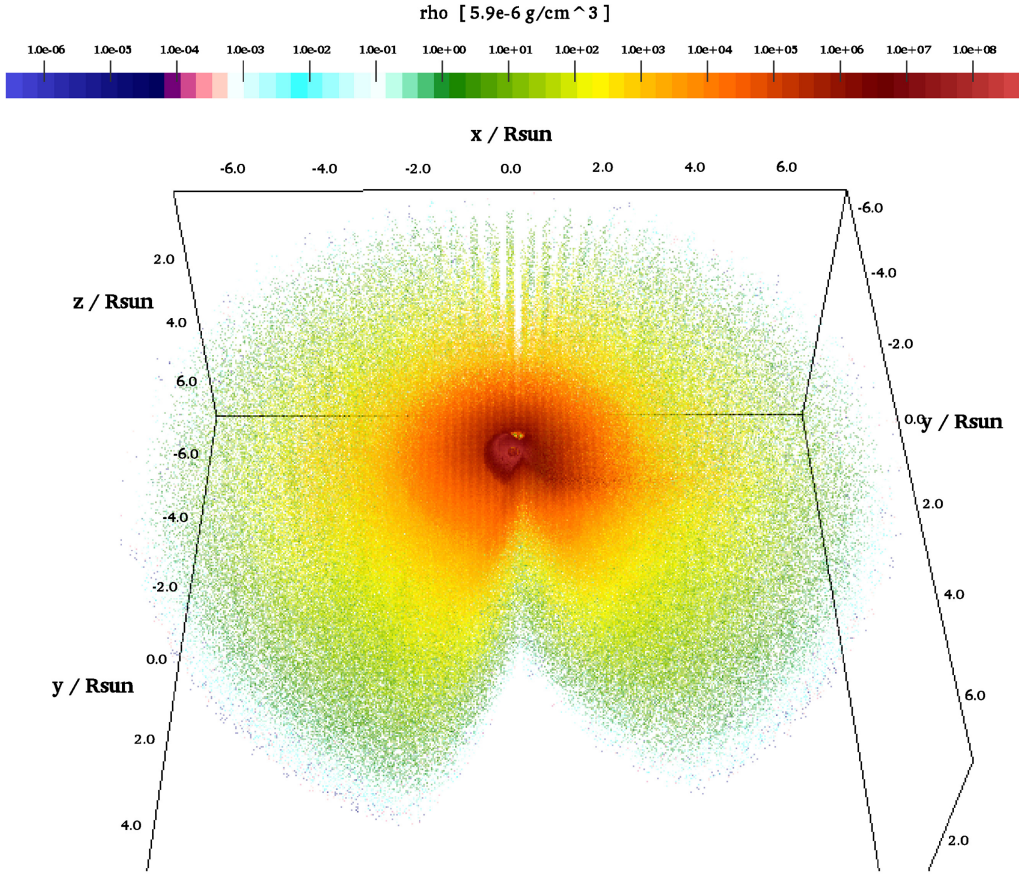
Figure 10. 3D, half-hemisphere views of the density distribution of the SN ejecta at the moment of BH formation in a BdHN I. The simulation is performed with an SPH code that follows the SN ejecta expansion under the influence of the NS companion gravitational field including the effects of the orbital motion and the changes in the NS gravitational mass by the hypercritical accretion process. The initial conditions of the SN ejecta are set as a homologous velocity distribution in free expansion and the mass distribution is modelled with 16 millions point-like particles (see Becerra et al. 2016, 2019, for additional details). The binary parameters of this simulation are: the NS companion has an initial mass of 2.0 M$_\odot$; the CO-star, obtained from a progenitor with ZAMS mass $M_{\mathrm{ZAMS}} = 30$ M$_\odot$, leads to a total ejecta mass of 7.94 M$_\odot$ and to a 1.5 M$_\odot$ νNS, the orbital period is $P \approx 5$ min (binary separation $a \approx 1.5 \times 10^{10}$ cm). The distribution of the ejecta is not axially symmetric; it is strongly influenced by the rotation of the system and accretion occurring in the binary component (see Fig. 4). Particularly relevant for the observations is the low-density region of $\approx 10°$ which allows the sources with viewing angle in the equatorial plane to detect the prompt radiation phase. This has been qualitatively indicated in Fig. 9. In these sources, only a fraction of approximately 10 per cent of the prompt radiation can be detectable, they are the only ones able to trigger the *Fermi*-GBM and the remaining 90 per cent will not have detectable prompt radiation (see Ruffini et al. 2018c). Figure is taken from Ruffini et al. (2018c) with the kind permission of the authors.

to N equations simultaneously, the sum of the χ^2 values should be minimized. The related equations are

$$\chi^2 = \sum_{n=1}^{N} \chi_n^2, \tag{9}$$

$$\chi_n^2 = \sum_{i=1}^{M} \frac{1}{\sigma_{ni}^2} (L_{ni} - L_n(t_{ni}, A_n, \alpha_{\mathrm{GeV}}))^2, \tag{10}$$

where n represents each BdHN I, i represents each data point in a given BdHN I, A_n is the amplitude of a power-law function for the nth BdHN I, and α_{GeV} is the common power-law index shared for all the BdHNe I. Thus, for the nth BdHN I, at time t_{ni}, the observed luminosity is L_{ni}, and the predicted luminosity is $L_n(t_{ni}, A_n, \alpha)$. The value of χ^2 represents the difference between the best power-law fitting and all the observed data; it is a summation of individual χ_n^2, which represents the difference between the power-law fitting and the observed value of each GRB.

Out of 25 BdHNe I presented in Table 5, we perform the fitting for only 20 GRBs that have more than two data points in their luminosity light curves. Therefore, for the fitting of BdHNe I, there are 20 bursts and each one has its power-law function. Consequently, there are in

total 17 parameters, including 20 amplitudes, and 1 power-law index. The fitting gives a power-law index of $\alpha_{\mathrm{GeV}} = 1.19 \pm 0.04$, i.e.:

$$L_n = A_n \, t^{-1.19 \pm 0.04}, \tag{11}$$

which is plotted in Fig. 3 and the amplitudes of each GRB, A_n, with the uncertainty are shown in Table 7. This inferred power-law index is similar to the one obtained from fitting the GeV flux, $f_\nu(t)$ (see e.g. Kumar & Barniol Duran 2009; Panaitescu 2017), in which the power-law index is $\alpha_{\mathrm{GeV}} = 1.2 \pm 0.2$ and $\alpha_{\mathrm{GeV}} = 1.2 \pm 0.4$, respectively.

In our approach, we adopt an alternative interpretation of these power laws: instead of using the flux expressed in arrival time, we use the luminosity expressed in the rest frame of the source. Since the luminosity is proportional to the flux, i.e. $L = 4\pi d_L^2 (1+z)^{\alpha_{\mathrm{GeV}}-2} f_\nu$, where d_L is the luminosity distance, this similarity of the power-law index is not surprising. The advantage of using luminosity expressed in the rest frame of the source, instead of flux in arrival time, is that one can determine the intrinsic energy loss of the system that produces the GeV radiation, regardless of differences in the redshift

Table 7. Fitting parameters of the 0.1–10 GeV power-law luminosity when measured in the rest frame of 20 BdHNe with GeV emission: amplitude of the 0.1–10 GeV luminosity, A_n, and its uncertainty, the inferred 0.1–10 GeV luminosity at 10 s from the fitting and its uncertainty. The common power-law index is $\alpha_{\rm GeV} = 1.19 \pm 0.04$. Out of 25 BdHNe emitting GeV emission, we performed the fitting for 20 GRBs that have more than two data points in their luminosity light curves. GRBs 091127, 091208B, 130518A, 150314A, 150514A have only two data points in their GeV luminosity light curves.

BdHN	A_n (Amplitude)	Uncertainty of A_n	$L_{10\rm s}$	Uncertainty of L_{10s}
080916C	2.9×10^{53}	$^{+9.1}_{-7.4} \times 10^{52}$	1.88×10^{52}	$^{+1.1}_{-1.0} \times 10^{52}$
090323A	9.4×10^{53}	$^{+3.5}_{-2.9} \times 10^{53}$	6.04×10^{52}	$^{+3.8}_{-1.4} \times 10^{52}$
090328A	2.4×10^{52}	$^{+1.1}_{-0.7} \times 10^{52}$	1.5×10^{51}	$^{+1.0}_{-0.9} \times 10^{51}$
090902B	8.9×10^{52}	$^{+2.5}_{-2.0} \times 10^{52}$	5.7×10^{51}	$^{+3.3}_{-3.0} \times 10^{51}$
090926A	2.1×10^{53}	$^{+5.9}_{-4.8} \times 10^{52}$	1.4×10^{52}	$^{+7.9}_{-7.3} \times 10^{51}$
091003A	5.7×10^{51}	$^{+1.7}_{-1.5} \times 10^{51}$	3.7×10^{50}	$^{+2.1}_{-2.0} \times 10^{50}$
100414A	3.5×10^{52}	$^{+1.4}_{-1.1} \times 10^{52}$	2.3×10^{51}	$^{+1.4}_{-1.3} \times 10^{51}$
100728A	4.2×10^{51}	$^{+1.9}_{-1.5} \times 10^{51}$	2.7×10^{50}	$^{+1.9}_{-1.6} \times 10^{50}$
110731A	2.3×10^{52}	$^{+0.8}_{-0.5} \times 10^{52}$	1.8×10^{51}	$^{+0.9}_{-0.8} \times 10^{51}$
120624B	2.4×10^{53}	$^{+8.2}_{-6.2} \times 10^{52}$	1.6×10^{52}	$^{+9.6}_{-8.5} \times 10^{51}$
130427A	5.1×10^{52}	$^{+2.1}_{-2.0} \times 10^{51}$	3.3×10^{51}	$^{+1.3}_{-1.3} \times 10^{51}$
131108A	6.1×10^{52}	$^{+9.1}_{-8.9} \times 10^{51}$	3.9×10^{51}	$^{+2.0}_{-1.9} \times 10^{51}$
131231A	1.64×10^{52}	$^{+7.9}_{-5.4} \times 10^{51}$	1.1×10^{51}	$^{+7.3}_{-6.1} \times 10^{50}$
141028A	3.6×10^{52}	$^{+1.2}_{-1.1} \times 10^{52}$	2.3×10^{51}	$^{+1.4}_{-1.3} \times 10^{51}$
150403A	6.8×10^{51}	$^{+3.0}_{-2.3} \times 10^{51}$	4.3×10^{50}	$^{+2.9}_{-3.0} \times 10^{50}$
160509A	1.4×10^{52}	$^{+4.9}_{-3.8} \times 10^{51}$	8.9×10^{50}	$^{+5.4}_{-4.1} \times 10^{50}$
160625B	1.4×10^{53}	$^{+4.6}_{-3.4} \times 10^{52}$	8.7×10^{51}	$^{+5.2}_{-4.6} \times 10^{51}$
170214A	2.8×10^{53}	$^{+7.4}_{-5.9} \times 10^{52}$	1.8×10^{52}	$^{+1.0}_{-0.9} \times 10^{52}$
170405A	4.1×10^{52}	$^{+1.1}_{-1.0} \times 10^{52}$	2.5×10^{51}	$^{+1.5}_{-1.4} \times 10^{51}$
180720B	5.4×10^{52}	$^{+6.6}_{-6.1} \times 10^{51}$	3.5×10^{51}	$^{+2.2}_{-2.1} \times 10^{50}$

of the sources. This allows us following our recent understanding of the BdHN I 130427A (see Ruffini et al. 2019c, and references therein), to relate the GeV radiation to the slowing down of the BH spin (see Section 10).

After obtaining the best power-law parameters for the luminosity light curve for each BdHNe I, we check the correlation between the GeV luminosity at 10 s from equation (11) using the fitted parameters and the isotropic energy $E_{\gamma,\rm iso}$. The power-law fitting gives (see Fig. 11)

$$L_{10\rm s} = (4.7 \pm 1.2) \times 10^{48} \, (E_{\rm iso}/10^{52})^{\,1.3\pm0.3}, \tag{12}$$

and the fitting parameters for each GRB including their uncertainties are shown in Table 7. Furthermore, we estimate the energy released in the GeV band by each GRB in the 0.1–10^4 s time interval, i.e.:

$$E_{0.1-10^4\rm s} = A_{\rm GRB} \int_{0.1}^{10000} t^{-1.19} \, {\rm d}t \ , \tag{13}$$

and the derived $E_{0.1-10^4\rm s}$ are shown in Table 8. The parameters $E_{0.1-10^4\rm s}$ and $E_{\gamma,\rm iso}$ (isotropic energy of the prompt emission in γ band) are also correlated by a power-law relation (see Fig. 11):

$$E_{0.1-10^4\rm s} = (4.4 \pm 1.5) \times 10^{50} \, (E_{\rm iso}/10^{52})^{1.4\pm0.3}. \tag{14}$$

This positive correlation indicates that the BdHNe I with higher isotropic energy are also more luminous and more energetic in the GeV emission.

9 THE DETERMINATION OF THE MASS AND SPIN OF THE BH IN BDHNE I

The theoretical progress introduced in Ruffini et al. (2019c) has identified the GeV radiation as originating in the *inner engine* of BdHN I. There, for the first time, it has been shown that indeed the rotational energy of a Kerr BH can be extracted for powering an astrophysical system. The *inner engine* is composed of (i) a non-stationary Kerr BH, (ii) a uniform magnetic field of $\sim 10^{10}$ G aligned with the rotation axis, and (iii) the presence of a very tenuous fully ionized electron–nuclei plasma. The fundamental new conceptual breakthrough introduced by the physics of the *inner engine* is developed in parallel papers (see e.g. Rueda & Ruffini 2020). The main goal here is to show, using our recently published results, that the rotational energy of the Kerr BH is indeed sufficient to explain the energetics of the GeV emission. In turn, this allows us to determine here the mass and spin of the Kerr BH in each BdHN I.

We here apply the self-consistent solution already well tested in the case of GRB 130427A (Ruffini et al. 2019c) and GRB 190114C (Moradi et al. 2019) for determining the three parameters of the *inner engine*, namely the mass and spin of the BH as well as the strength of the surrounding magnetic field B_0. The values are obtained satisfying three conditions:

(i) The energy budget for the observed GeV luminosity is provided by the extractable rotational energy of a Kerr BH (see equation (1a); see equation 34 in Ruffini et al. 2019c).

(ii) The magnetic field B_0 fulfills the transparency condition for the propagation of the GeV radiation imposed by the e^+e^- pair
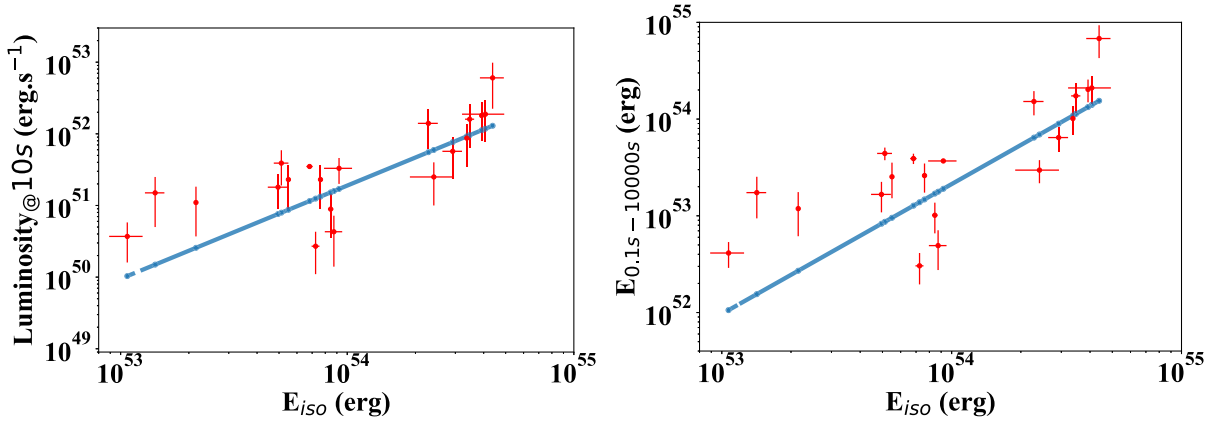
Figure 11. Left: The *Fermi*-LAT luminosity at 10 s in the energy range 0.1–10 GeV versus the isotropic gamma-ray energy from 1 keV to 10 MeV. The BdHNe are listed in Table 7. Right: The *Fermi*-LAT energy from 0.1 to 10^4 s versus isotropic gamma-ray energy from 1 keV to 10 MeV. See the corresponding values in Table 8.

Table 8. Results of $E_{0.1-10^4 s}$ and related error of 20 BdHNe. $E_{0.1-10^4 s}$ is the total GeV energy (in erg) emitted from 0.1 to 10^4 s. GRBs 091127, 091208B, 130518A, 150314A, 150514A are excluded since they have only two data points in their GeV luminosity light curves.

BdHN	$E_{0.1-10^4 s}$	Uncertainty of $E_{0.1-10^4 s}$
080916C	2.1×10^{54}	6.6×10^{53}
090323A	6.8×10^{54}	2.5×10^{54}
090328A	1.73×10^{53}	7.9×10^{52}
090902B	6.4×10^{53}	1.8×10^{53}
090926A	1.54×10^{54}	5.60×10^{53}
091003A	4.12×10^{52}	1.58×10^{52}
100414A	2.53×10^{53}	1.18×10^{53}
100728A	3.0×10^{52}	1.6×10^{52}
110731A	1.6×10^{53}	5.8×10^{52}
120624B	1.7×10^{54}	7.2×10^{53}
130427A	3.6×10^{53}	1.8×10^{52}
131108A	4.4×10^{53}	1.2×10^{53}
131231A	1.2×10^{53}	6.3×10^{52}
141028A	2.6×10^{53}	1.1×10^{53}
150403A	4.9×10^{52}	1.7×10^{52}
160509A	1.1×10^{53}	3.5×10^{52}
160625B	1.1×10^{54}	3.3×10^{53}
170214A	2.1×10^{54}	5.3×10^{53}
170405A	3.0×10^{53}	7.9×10^{52}
180720B	3.8×10^{53}	4.7×10^{52}

Table 9. The mass, M, the spin parameter, $\alpha = J/M^2$, and surrounding magnetic field, B_0 in 11 BdHNe I, out of the 25 long GRBs in Table 5. The high-quality GeV data of this sample allows for a measurement of the lower limit of their 'inner engine' parameters; see equation (1a).

Source	α	$M(\alpha)$ $(M_\odot)$	M_{irr} $(M_\odot)$	B_0 10^{10} G
BdHN I 080916C	0.87	8.9	7.6	1.9
BdHN I 090902B	0.59	5.3	5	2.8
BdHN I 090926A	0.76	8.4	7.7	2.1
BdHN I 110713A	0.37	4.7	4.6	4.5
BdHN I 130427A	0.40	2.3	2.24	4.1
BdHN I 130518A	0.50	2.5	2.4	3.3
BdHN I 131108A	0.56	4.7	4.4	2.9
BdHN I 160509A	0.41	2.4	2.3	4
BdHN I 170214A	0.80	2.8	2.5	2.1
BdHN I 170405A	0.45	3.4	3.3	3.7
BdHN I 180720B	0.27	2.3	2.29	6

with the upper limit of the critical mass of the NS in Rhoades & Ruffini (1974) and the mass and spin of rotating NSs computed in Cipolletta et al. (2015); see Fig. 12.

This has indeed been addressed in recent works (Ruffini et al. 2019c), where we have developed a complementary theory and its related analysis to identify the physical conditions that have to be enforced in order to extract the rotational energy of a Kerr BH. We have there addressed an approach of considering a Kerr BH placed in a uniform magnetic field of 10^{10} G aligned along the BH symmetry axis, fulfilling the Einstein–Maxwell equations via the Papapetrou–Wald solution (Papapetrou 1966; Wald 1974) modelling the *inner engine* that produces the MeV, GeV, and TeV radiation and UHECRs as well (Rueda & Ruffini 2020).

production process in the *inner engine* (see equation 35 in Ruffini et al. 2019c).

(iii) The 'quantized' emission of the GeV radiation is determined by the density of the plasma and by the synchrotron radiation time-scale (Ruffini et al. 2019c) (see equation 36 in Ruffini et al. 2019c).

The high-quality GeV data in 11 BdHNe I out of the 25 long GRBs in Table 5 allow us to determine the starting point of the decreasing luminosity, by identifying the transition of the power-law dependence of the GeV luminosity from a positive to a negative slope (see Ruffini et al. 2019c, for more information). This enables us to calculate the lower limit of the mass, M, spin parameter of the BH, α, the corresponding irreducible mass of the BH, M_{irr}, which remains constant during the energy extraction process, and finally the surrounding magnetic field strength, B_0, as reported in Table 9. The values of the masses $M > 2.21$ M$_\odot$ and spin parameters of $\alpha < 0.71$ of the BH for BdHNe I presented in Table 9 show the consistency

10 SPIN-DOWN OF THE BH IN BDHNE I

Following our previous work (Ruffini et al. 2019c), we can turn now from the luminosity expressed in the rest frame of the sources, see equation (11), and from the initial values of the spin and mass of the BH expressed in Section 9, to derive the slowing down of the BH due to the energy loss in the GeV emission.
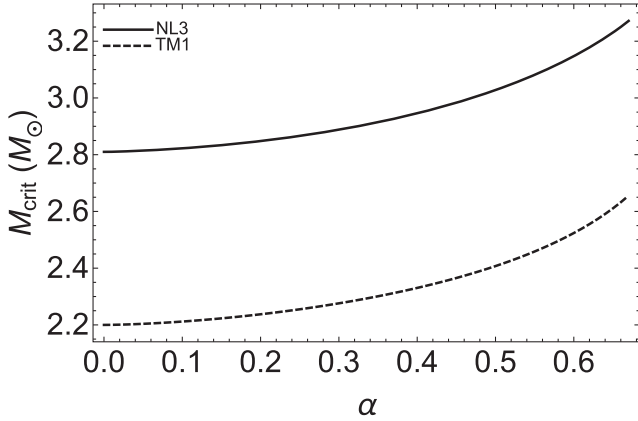
Figure 12. NS critical mass as a function of the spin parameter α for the NL3 and TM1 EOS. We recall that the maximum spin parameter of a uniformly rotating NS is $\alpha_{max} \approx 0.71$, independently of the NS EOS (see e.g. Cipolletta et al. 2015).

The relation of the luminosity and the extractable rotational energy is (see equation 39 in Ruffini et al. 2019c)

$$L = -\frac{dE_{extr}}{dt} = -\frac{dM}{dt}. \tag{15}$$

For each BH during the GeV emission process the M_{irr} is constant. Utilizing the best fit obtained for the GeV luminosity $L_{GeV} = A_{GeV} \, t^{-1.2} \, \mathrm{erg \, s^{-1}}$, we obtain a relation for the loss of mass energy of the BH by integrating equation (15):

$$M = M_0 + 5At^{-0.2} - 5At_0^{-0.2}, \tag{16}$$

where M_0 is the initial mass of the newborn BH tabulated in Table 9. From the mass–energy formula of the BH, we have (Ruffini et al. 2019c)

$$a = \frac{J}{M} = 2M_{irr}\sqrt{1 - \frac{M_{irr}^2}{(M_0 + 5At^{-0.2} - 5At_0^{-0.2})^2}}, \tag{17}$$

where M_0 is the initial mass of the BH presented in Table 9 as M α at time t_0 at which the decaying part of GeV luminosity begins.

As indicative examples, we show in Fig. 13 the decrease of the BH spin, $\alpha = a/M = J/M^2$, as a function of time in GRBs 090902B, 131108A, and 170405A.

The third main results of this paper are: the identification of the rotational energy extraction from a Kerr BH and the consequent measure of the BH mass and spin.

11 CONCLUSIONS

The unprecedented observations of GRBs, pioneered by the *Beppo-Sax* satellite, have developed into the largest ever observational multiwavelength effort in astrophysics: starting with the *Swift*, BAT, and XRT instruments in the X-ray band; see Fig. 14, progressing with the *AGILE* and with *Fermi*-GBM in the MeV–GeV bands. These have worked in synergy with hundreds of optical, radio, and VHE telescopes worldwide including MAGIC (see Fig. 1) and H.E.S.S. (see Fig. 2).

This unprecedented observational effort assisted by parallel theoretical developments has allowed in this article the achievement of a new understanding of three new basic properties of the BdHNe: the first appearance of the SN triggering the entire BdHN process, the SN-rise; the presence of a mildly relativistic afterglow in the

X-ray in *all* BdHN; the identification in *all* BdHN of the origin of the high-energy emission in an *inner engine* driven by a newborn BH; the description of their morphology. We show, for the first time, the extractable energy of a Kerr BH as an astrophysical energy source, which has allowed the inference of the BH mass and spin.

In Section 2, we first recall that binary systems have an important role in understanding both short and long GRBs and we report the progress in the classification of GRBs in nine different subclasses (see e.g. Wang et al. 2019, and references therein). We then focus on the BdHNe: long GRB model with progenitors composed of CO_{core} and the binary NS companion. The CO_{core} undergoes gravitational collapses that gives origin to an SN and the collapse of its Fe-core produces a νNS.

We also there recall the fundamental role of the hypercritical accretion of the SN into the companion binary NS and into the νNS determine the BdHNe further evolution (see Fig. 4 and Pisani et al. 2016; Ruffini et al. 2016b, 2018c; Wang et al. 2019 for further details). The SN accretion on to the νNS gives origin to the X-ray afterglow emission, while the SN accretion on to the companion NS leads to different outcomes as a function of the binary period. For periods shorter than 5 min, the hypercritical accretion on to the companion NS is sufficient for the NS to overcome its critical mass and gravitationally collapse to a BH. The BH formation characterizes a BdHN I with an isotropic energy in the range of $10^{52} \, \mathrm{erg} \lesssim E_{is} \lesssim 10^{54}$ erg. We here show that it gives origin, *only in some* of them, to the GeV emission observed by *Fermi*-LAT. For larger binary periods, no BH is formed and consequently no GeV radiation is observed, the hypercritical SN accretion leads to an M-NS with an isotropic energy in the range of $10^{50} \, \mathrm{erg} \lesssim E_{is} \lesssim 10^{52}$ erg. We refer to these binaries as BdHN II paradigm. The same occurs for more detached binary systems leading to a BdHN III, where the isotropic energy is in the range of $10^{48} \, \mathrm{erg} \lesssim E_{iso} \lesssim 10^{50}$ erg.

In Section 3, we have given the spectral properties of the first appearance of the SN-rise in BdHN I and in BdHN II and also differentiate their energetics.

In Section 4, we have related the SN-rise luminosity to the X-ray luminosity of the afterglow in all three BdHNe types. It is a fortunate coincidence that we have recently understood the origin of the afterglow as a consequence of the SN hypercritical accretion on to the νNS. This process is dominated by a mildly relativistic synchrotron pulsar-like emission with Lorentz factor $\Gamma \sim 2$ that gives rise to the X-ray afterglow (Ruffini et al. 2018b; Wang et al. 2019; Rueda et al. 2020), and we have also related their X-ray luminosity to the NS spin. This has allowed us to represent in Fig. 8 the afterglows for two BdHNe I, for two BdHNe II, and one BdHN III and estimate in Table 4 the initial spin value of the νNS. What is most remarkable is that the X-ray afterglow is present in *all* BdHN types which implies that, unlike the GeV emission, which as we show in this article to be necessarily beamed, the X-ray afterglow emission is necessarily isotropic. What is equally relevant is that independently of the differences among these four subclasses of BdHN, the X-ray afterglow luminosity emission is consistent with a power-law index of -1.48 ± 0.32 as measured from the *Swift* observations (Pisani et al. 2016), and a common energy source well explained by the rotational energy of the νNS.

The *first main result of this paper* identification of the SN-rise and the measurement of the νNS spin originating the power-law emission of the afterglow (see Figs 7 and 8). The two process of the SN-rise energetics and the νNS dynamics appear to be strongly correlated.

We then turn in Section 5 to consider only the case of BdHN I and their *Fermi*-GBM and LAT observations. In Appendix A, we update
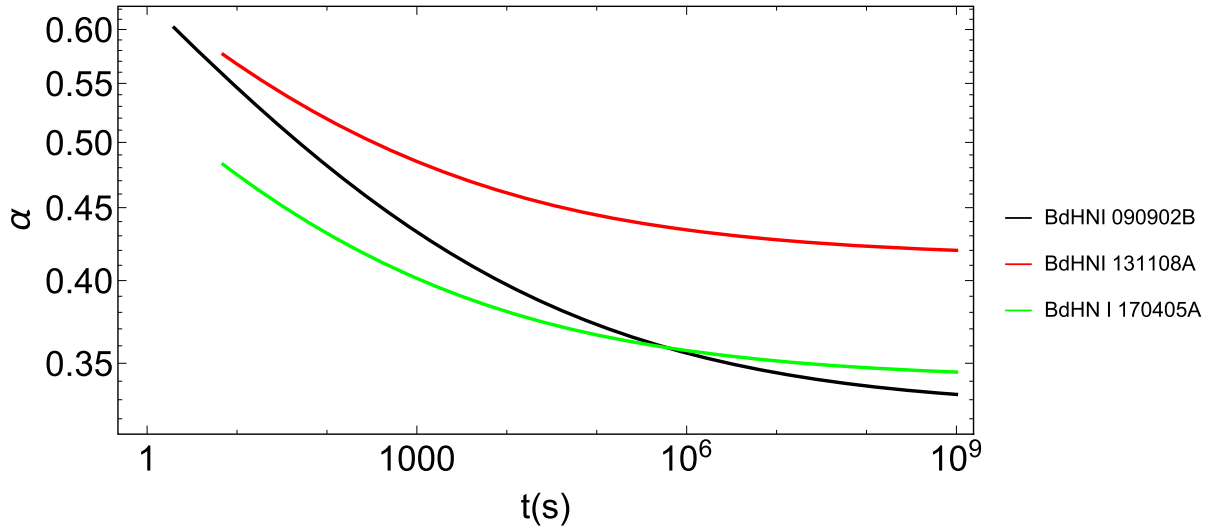
Figure 13. The BH spin as a function of rest-frame time. The initial values of the spin and mass of the BH for GRB 090902B are $\alpha = 0.59$ and $M(\alpha) = 5.3$ $M_\odot$; for 131108A: $\alpha = 0.56$ and $M(\alpha) = 4.7$ $M_\odot$; and for 170405A: $\alpha = 0.45$ and $M(\alpha) = 3.4$ $M_\odot$. This behaviour of the spin parameter indicates that the rotational energy of the BH is decreasing due to the radiation losses in the GeV energy band.
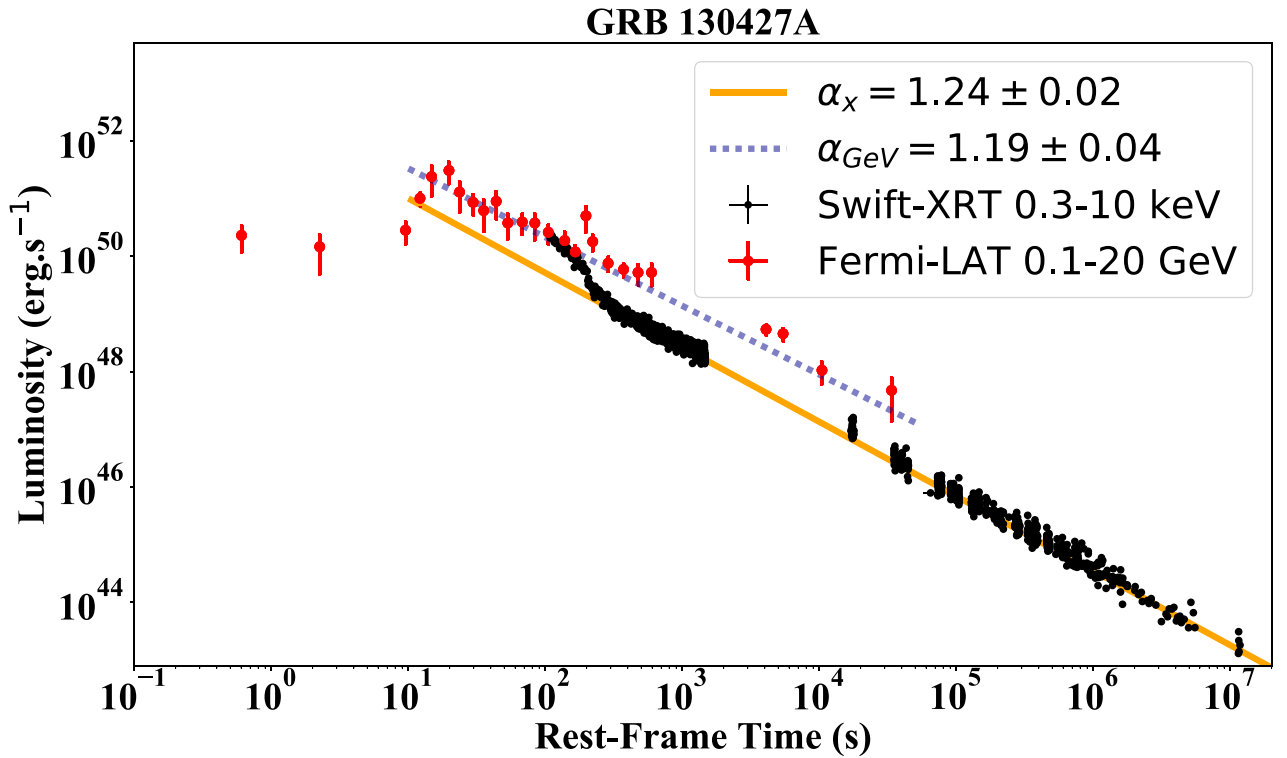

Figure 14. Luminosity of BdHN I 130427A: the black data points represent the rest-frame 0.3–10 keV luminosity obtained from *Swift*-XRT. It follows a decaying power law with amplitude $(3.65 \pm 0.63) \times 10^{52}$ erg s^{-1} and index $\alpha_X = 1.24 \pm 0.02$. The red data points show the rest frame in 0.1–20 GeV luminosity observed by *Fermi*-LAT. It follows a decaying power law with an amplitude of $(5.1 \pm 0.2) \times 10^{52}$ erg s^{-1} and index $\alpha_{GeV} = 1.19 \pm 0.04$. Details are given in Sections 4, 5, and 8.

our previous classification of BdHN I following Pisani et al. (2016), Ruffini et al. (2016b, 2018c) reaching the total number of 378 BdHN I, *all* of them are characterized by

(i) a measured cosmological redshift;

(ii) a prompt emission of $T_{90} > 2$ s, measured by *Fermi*-GBM, with isotropic energy larger than 10^{52} erg;

(iii) a decaying X-ray afterglow, measured by *Swift*-XRT, characterized by a luminosity decreasing with a mean power law with index of $\alpha_X = -1.48 \pm 0.32$.

Contrary to the case of the X-ray afterglow, universally present in *all* BdHN types, the GeV radiation is present *only in some* BdHN I. No GeV emission occurs in BdHN II and BdHN III. We first explore the possibility that the non-detection of GeV radiation in

some of BdHNe I could be due to the observational limitation of the LAT field of view, i.e. because of the boresight angle smaller than 75°. Indeed, we find that only $N_{\rm tot} = 54$ out of the 378 BdHNe I are inside the boresight angle of *Fermi*-LAT. What is unexpected is that only $N_{\rm LAT} = 25$ out of these 54 BdHNe I exhibit the GeV emission observed by *Fermi*-LAT. For each of these 25 sources, we have given the basic parameters in Table 5. The corresponding data of the remaining 29 BdHN I, without observed GeV radiation, are given in Table 6.

In Section 6, we have assumed that *all* BdHNe I, like all GRBs are homogeneously distributed in space (see e.g. Meegan et al. 1992; Paciesas et al. 1999), we have inferred that the emission of the GeV radiation occurs in two opposite cones each of half-opening angle of ∼60° from the normal to the binary plane.

We duly recall as well that the visualization of the morphology has been made possible thanks to a close collaboration with LANL (see Becerra et al. 2016, 2019, for additional details), leading to the results well illustrated in the simulation presented in Figs 4 and 10. We then conclude from this simulation that all of the 25 LAT sources are actually 'seen from the top' that allows us to fully observe the conical emission of 60° half-opening angle. For the remaining 29 BdHN I without an observed GeV emission, we provide evidence that when the *Swift* data are available, gamma-ray flares and hard and soft X-ray flares as well as extended thermal emissions are observed in these systems (Ruffini et al. 2018a, c), and that these sources have a viewing angle laying in the 'orbital plane' of the binary progenitor system.

We conclude that we are faced with a new morphology of the BdHN I that depends significantly on the viewing angle, 'seen from the top', normal to the binary orbital plane when the GeV emission is observed, or seen 'in the plane' of the binary when the observation of the GeV radiation is impeded by the accreting binary material (see Figs 4, 9, and 10). This is reminiscent of the morphology encountered in some AGNs (see e.g. the AGN IC 310 in Aleksić et al. 2014).

The second main result of this paper is the identification of the BdHN I conical morphology and its explanation within the BdHN I model.

We then recall some theoretical progresses in understanding the origin of the GeV emission:

(i) The identification of the three components of the GRB *inner engine* in GRB 130427A (Ruffini et al. 2019c), composed of a Kerr BH with a magnetic field B_0 aligned with the BH rotation axis, both embedded in a tenuous ionized plasma composed of electrons and ions, has represented a turning point in the study of BdHN I. The electrodynamics of this *inner engine*, based on the Papapetrou–Wald solution (Papapetrou 1966; Wald 1974; Ruffini et al. 2019c), leads to a high-energy emission in two opposite lobes in the MeV, GeV, and TeV radiation as well as narrowly beamed UHECR along the BH polar axis (Moradi et al. 2019).

(ii) This high-energy emission, unlike the traditional models, that implies ultrarelativistic baryonic motion with $\Gamma \sim 10^3$ at 10^{16}–10^{18} cm occurs very close to the BH horizon.

(iii) The energy source is the extractable energy of the BH (Christodoulou 1970; Christodoulou & Ruffini 1971; Hawking 1971, 1972; see equation 1a), and is emitted in a sequence of impulsive process, the '*blackholic quanta*', occurring on a time-scale of 10^{-14} s (Rueda & Ruffini 2020).

On the basis of these results, we have examined the physical origin of the GeV emission observed by *Fermi*-LAT both in BdHN I. We find that the luminosity of the GeV emission as a function of time in the rest frame of the source fulfils a universal decaying power-law

dependence with index of -1.19 ± 0.04; see Fig 3. This has allowed: (1) to verify that indeed the entire GeV radiation observed by *Fermi*-LAT can be energetically expressed in terms of the rotational energy of the Kerr BH; (2) following the procedures in Ruffini et al. (2019c) to evaluate the mass and spin of the BH (see Table 9); and (3) to explicitly compute the slowing down rate of the BH spin due to the GeV emission (see Fig. 13).

It has been possible for some of the 25 sources with the best data:

(i) To compute the lower limit of the initial value of the BH masses, *M*, and show their consistency with the absolute upper limit of the NS critical mass (Rhoades & Ruffini 1974), and the upper limit of the NS mass of $M = 2.21$ M$_\odot$ and spin parameter of $\alpha < 0.71$ computed in Cipolletta et al. (2015).

(ii) To evaluate the value of the spin, *a*, and show the consistency with the canonical upper limit $\alpha = a/M \leq 1$.

(iii) By combining the value of the spin of the νNS observed from the afterglow (see Table 4), the time intervening between the SN-rise and the UPE phase, the mass estimate of the BH in GRB 190114C and in GRB 090926A and in GRB 180720B, we infer that necessarily in these system we are observing the presence of a BdHN precursor with a companion NS grazing the surface of the CO$_{\rm core}$.

The third main results of this paper is the identification of the rotational energy extraction from a Kerr BH as the origin of the GeV emission and allowing the consequent measure of the BH mass and spin.

All the above three main results are important: the underlying proof that indeed we can use the extractable rotational energy of a Kerr BH for explaining the high-energy jetted emissions of GRBs and AGNs stands alone. Even more subtle is the fact that the jetted emission does not originate from massive ultrarelativistic jetted emissions, but from very special energy-saving ultrarelativistic quantum and classical electrodynamical processes originating in the high-energy jetted emission. We were waiting for this result for 49 yr, since the writing of equation (1a).

Far from completing an era, GRBs are a fertile ground to discover new physical laws. In front of us: the identification of the nature of the SN-rise, the constituent of the UPE emission, the further application of the *blackholic* energy (Rueda & Ruffini 2020), and the identification of their timescales ranging from 10^{-15} s to 10^{17} s.

Division at NASA/GSFC and the High Energy Astrophysics Division of the Smithsonian Astrophysical Observatory.

DATA AVAILABILITY

The data underlying this article are available in Appendix A of the article.

REFERENCES

Abdalla H. et al., 2019, Nature, 575, 464
Ackermann M. et al., 2013, ApJS, 209, 11
Aharonian F. et al., 2006, A&A, 457, 899
Aimuratov Y. et al., 2017, ApJ, 844, 83
Ajello M. et al., 2019, ApJ, 878, 52
Aleksić J. et al., 2014, Science, 346, 1080
Aleksić J. et al., 2016a, Astropart. Phys., 72, 61
Aleksić J. et al., 2016b, Astropart. Phys., 72, 76
Amati L. et al., 2000, Science, 290, 953
Atwood W. B. et al., 2009, ApJ, 697, 1071
Barraud C. et al., 2003, A&A, 400, 1021
Barthelmy S. D. et al., 2005, Space Sci. Rev., 120, 143
Becerra L., Cipolletta F., Fryer C. L., Rueda J. A., Ruffini R., 2015, ApJ, 812, 100
Becerra L., Bianco C. L., Fryer C. L., Rueda J. A., Ruffini R., 2016, ApJ, 833, 107
Becerra L., Ellinger C. L., Fryer C. L., Rueda J. A., Ruffini R., 2019, ApJ, 871, 14
Beniamini P., Nava L., Duran R. B., Piran T., 2015, MNRAS, 454, 1073
Berger E., 2014, ARA&A, 52, 43
Blandford R. D., McKee C. F., 1976, Phys. Fluids, 19, 1130
Burrows D. N. et al., 2005, Space Sci. Rev., 120, 165
Campana S. et al., 2006, Nature, 442, 1008
Cano Z., Wang S.-Q., Dai Z.-G., Wu X.-F., 2017, Adv. Astron., 2017, 8929054
Cenko S. B. et al., 2006, ApJ, 652, 490
Cenko S. B. et al., 2011, ApJ, 732, 29
Chand V. et al., 2020, ApJ, 898, 42
Christodoulou D., 1970, Phys. Rev. Lett., 25, 1596
Christodoulou D., Ruffini R., 1971, Phys. Rev. D, 4, 3552
Cipolletta F., Cherubini C., Filippi S., Rueda J. A., Ruffini R., 2015, Phys. Rev. D, 92, 023007
Costa E. et al., 1997, Nature, 387, 783
de Pasquale M. et al., 2006, A&A, 455, 813
Damour T., Ruffini R., 1975, Phys. Rev. Lett., 35, 463
Della Valle M., 2011, Int. J. Mod. Phys. D, 20, 1745
Dominik M., Belczynski K., Fryer C., Holz D. E., Berti E., Bulik T., Mandel I., O'Shaughnessy R., 2012, ApJ, 759, 52
Eichler D., Livio M., Piran T., Schramm D. N., 1989, Nature, 340, 126
Fox D. B. et al., 2005, Nature, 437, 845
Frail D. A., Kulkarni S. R., Nicastro L., Feroci M., Taylor G. B., 1997, Nature, 389, 261
Frontera F. et al., 1998, ApJ, 493, L67
Fryer C. L., Woosley S. E., Hartmann D. H., 1999, ApJ, 526, 152
Fryer C. L. et al., 2007, PASP, 119, 1211
Fryer C. L., Rueda J. A., Ruffini R., 2014, ApJ, 793, L36
Fryer C. L., Oliveira F. G., Rueda J. A., Ruffini R., 2015, Phys. Rev. Lett., 115, 231102
Fujisawa K., Okawa H., Yamamoto Y., Yamada S., 2019, ApJ, 872, 155
Galama T. J. et al., 1998, Nature, 395, 670
Gehrels N. et al., 2005, Nature, 437, 851
Giacconi R., 2003, Rev. Mod. Phys., 75, 995
Giacconi R., Ruffini R., eds, 1978, Physics and Astrophysics of Neutron Stars and Black Holes. North Holland Publishing Co., Amsterdam
Gilkis A., 2018, MNRAS, 474, 2419
Gill P. R., Murray W., Wright M. H., 1981, 500, 136
Giommi P. et al., 2020, A&A, 642, A141
Giuliani A. et al., 2008, A&A, 491, L25

Greiner J. et al., 2009, A&A, 498, 89
Guetta D., Della Valle M., 2007, ApJ, 657, L73
Gursky H., Ruffini R., eds, 1975, Astrophysics and Space Science Library Neutron Stars, Black Holes and Binary X-ray Sources . Springer-Verlag, Berlin
Hawking S. W., 1971, Phys. Rev. Lett., 26, 1344
Hawking S. W., 1972, Commun. Math. Phys., 25, 152
Hewish A., Bell S. J., Pilkington J. D. H., Scott P. F., Collins R. A., 1968, Nature, 217, 709
Hjorth J., Bloom J. S., 2012, The Gamma-Ray Burst - Supernova Connection. Cambridge Univ. Press, Cambridge, p. 169
Hurley K. et al., 2000, ApJ, 534, L23
in 't Zand J. J. M. et al., 1998, ApJ, 505, L119
in't Zand J. J. M. et al., 2001, ApJ, 559, 710
Iwamoto K., Nomoto K., Höflich P., Yamaoka H., Kumagai S., Shigeyama T., 1994, ApJ, 437, L115
Izzo L. et al., 2018, GCN Circ., 23142, 1
Kanbach G., 1996, Mem. Soc. Astron. Ital., 67, 161
Klebesadel R. W., Strong I. B., Olson R. A., 1973, ApJ, 182, L85
Kouveliotou C., Meegan C. A., Fishman G. J., Bhat N. P., Briggs M. S., Koshut T. M., Paciesas W. S., Pendleton G. N., 1993, ApJ, 413, L101
Kumar P., Barniol Duran R., 2009, MNRAS, 400, L75
Li L., 2020, ApJ, 894, 100
Li L.-X., Paczyński B., 1998, ApJ, 507, L59
Li L.-X., Paczyński B., 2000, ApJ, 534, L197
Li L.-X., Paczyński B., 2006, MNRAS, 366, 219
Li L. et al., 2012, ApJ, 758, 27
Li L. et al., 2015, ApJ, 805, 13
Li L., Wang Y., Shao L., Wu X.-F., Huang Y.-F., Zhang B., Ryde F., Yu H.-F., 2018a, ApJS, 234, 26
Li L., Wu X.-F., Lei W.-H., Dai Z.-G., Liang E.-W., Ryde F., 2018b, ApJS, 236, 26
Li L., Ruffini R., Rueda J. A., Moradi R., Wang Y., Xue S. S., 2019, preprint (arXiv:1910.12615)
MAGIC Collaboration, 2019a, Nature, 575, 455
MAGIC Collaboration, 2019b, Nature, 575, 459
Mao S., Paczynski B., 1992, ApJ, 388, L45
Meegan C. A., Fishman G. J., Wilson R. B., Paciesas W. S., Pendleton G. N., Horack J. M., Brock M. N., Kouveliotou C., 1992, Nature, 355, 143
Meegan C. A. et al., 2008, GCN Circ., 8100, 1
Meegan C. et al., 2009, ApJ, 702, 791
Melandri A. et al., 2019, GCN Circ.
Mészáros P., Rees M. J., 1997, ApJ, 482, L29
Metzger M. R., Djorgovski S. G., Kulkarni S. R., Steidel C. C., Adelberger K. L., Frail D. A., Costa E., Frontera F., 1997, Nature, 387, 878
Mirzoyan R., et al., 2019, GCN Circ.
Moradi R., Rueda J. A., Ruffini R., Wang Y., 2019, A&A, preprint (arXiv:1911.07552)
Murdin P., ed., 2000, Compton Gamma Ray Observatory (CGRO). Institute of Physics Publishing, Bristol, p. 4537
Nakamura K., Kuroda T., Takiwaki T., Kotake K., 2014, ApJ, 793, 45
Nappo F. et al., 2017, A&A, 598, A23
Narayan R., Piran T., Shemi A., 1991, ApJ, 379, L17
Narayan R., Paczynski B., Piran T., 1992, ApJ, 395, L83
Nava L., 2018, Int. J. Mod. Phys. D, 27, 1842003
Nomoto K., Hashimoto M., 1988, Phys. Rep., 163, 13
Nousek J. A. et al., 2006, ApJ, 642, 389
Oke J. B. et al., 1995, PASP, 107, 375
Paciesas W. S. et al., 1999, ApJS, 122, 465
Paczynski B., 1986, ApJ, 308, L43
Panaitescu A., 2017, ApJ, 837, 13
Papapetrou A., 1966, Annales de L'Institut Henri Poincare Section (A) Physique Theorique, 4, 83
Pian E. et al., 2000, ApJ, 536, 778
Pisani G. B. et al., 2016, ApJ, 833, 159
Pisani G. B. et al., 2018, in EPJ Web Conf., 168, 04002
Postnov K. A., Yungelson L. R., 2014, Living Rev. Relativ., 17, 3
Racusin J. L. et al., 2011, ApJ, 738, 138

Rees M. J., Meszaros P., 1992, MNRAS, 258, 41

Reifenstein E. C., Brundage W. D., Staelin D. H., 1969, Phys. Rev. Lett., 22, 311

Rhoades C. E., Ruffini R., 1974, Phys. Rev. Lett., 32, 324

Roming P. W. A. et al., 2005, Space Sci. Rev., 120, 95

Rueda J. A., Ruffini R., 2012, ApJ, 758, L7

Rueda J. A., Ruffini R., 2020, Eur. Phys. J. C, 80, 300

Rueda J. A., Ruffini R., Karlica M., Moradi R., Wang Y., 2020, ApJ, 893, 148

Ruffini R., 1974, in Astrophysics and Gravitation: Proceedings of the Sixteenth Solvay Conference on Physics. Editions de l'Universite de Bruxelles, Brussels, p. 349

Ruffini R., 1998, in Sato H., Sugiyama N., eds, Frontiers Science Series 23: Black Holes and High Energy Astrophysics. Universal Academic Press Inc., Tokyo, Japan, p. 167

Ruffini R., Wheeler J. A., 1971, Phys. Today, 24, 30

Ruffini R., Bianco C. L., Fraschetti F., Xue S.-S., Chardonnet P., 2001, ApJ, 555, L117

Ruffini R. et al., 2015a, Astron. Rep., 59, 626

Ruffini R. et al., 2015b, ApJ, 798, 10

Ruffini R. et al., 2016a, ApJ, 831, 178

Ruffini R. et al., 2016b, ApJ, 832, 136

Ruffini R. et al., 2018a, ApJ, 852, 53

Ruffini R., Karlica M., Sahakyan N., Rueda J. A., Wang Y., Mathews G. J., Bianco C. L., Muccino M., 2018b, ApJ, 869, 101

Ruffini R. et al., 2018c, ApJ, 869, 151

Ruffini R. et al., 2019a, preprint (arXiv:e-prints)

Ruffini R., Melon Fuksman J. D., Vereshchagin G. V., 2019b, ApJ, 883, 191

Ruffini R. et al., 2019c, ApJ, 886, 82

Ruffini R., Bianco C. L., Fraschetti F., Xue S.-S., Chardonnet P., 2001, ApJ, 555, L117

Sari R., 1997, ApJ, 489, L37

Sari R., Piran T., 1995, ApJ, 455, L143

Sari R., Piran T., Narayan R., 1998, ApJ, 497, L17

Shirasaki Y. et al., 2008, PASJ, 60, 919

Shklovskij I. S., 1969, Supernovae. Interscience Publishers, New York, NY (USA)

Smith N., Li W., Silverman J. M., Ganeshalingam M., Filippenko A. V., 2011, MNRAS, 415, 773

Staelin D. H., Reifenstein Edward C. I., 1968, Science, 162, 1481

Strong I. B., 1975, Cosmic Gamma-Ray Bursts. D. Reidel Publishing Co., Dordrecht, Holland, p. 47

Tam P.-H. T., He X.-B., Tang Q.-W., Wang X.-Y., 2017, ApJ, 844, L7

Tauris T. M., Langer N., Moriya T. J., Podsiadlowski P., Yoon S.-C., Blinnikov S. I., 2013, ApJ, 778, L23

Tauris T. M., Langer N., Podsiadlowski P., 2015, MNRAS, 451, 2123

Tavani M. et al., 2009, A&A, 502, 995

van Paradijs J. et al., 1997, Nature, 386, 686

Vernet J. et al., 2011, A&A, 536, A105

Wald R. M., 1974, Phys. Rev. D, 10, 1680

Wang Y., Rueda J. A., Ruffini R., Becerra L., Bianco C., Becerra L., Li L., Karlica M., 2019, ApJ, 874, 39

Waxman E., Piran T., 1994, ApJ, 433, L85

Wijers R. A. M. J., Rees M. J., Meszaros P., 1997, MNRAS, 288, L51

Woosley S. E., 1993, ApJ, 405, 273

Woosley S. E., Bloom J. S., 2006, ARA&A, 44, 507

Xu D. et al., 2013, ApJ, 776, 98

Yoon S.-C., Woosley S. E., Langer N., 2010, ApJ, 725, 940

Zhang B., 2018, The Physics of Gamma-Ray Bursts. Cambridge Univeristy Press, Cambridge, UK

Zhang B., Fan Y. Z., Dyks J., Kobayashi S., Mészáros P., Burrows D. N., Nousek J. A., Gehrels N., 2006, ApJ, 642, 354

SUPPORTING INFORMATION

Supplementary data are available at *MNRAS* online.

stab724.pdf

Please note: Oxford University Press is not responsible for the content or functionality of any supporting materials supplied by the authors. Any queries (other than missing material) should be directed to the corresponding author for the article.

This paper has been typeset from a TEX/LATEX file prepared by the author.

Nature of the ultrarelativistic prompt emission phase of GRB 190114C

R. Moradi,[1,2,3,*] J. A. Rueda,[1,2,4,5,6,†] R. Ruffini,[1,2,7,‡] Liang Li,[1,2,7,§] C. L. Bianco,[1,2,6] S. Campion,[1,2]
C. Cherubini,[2,8,9] S. Filippi,[2,8,10] Y. Wang,[1,2,11,‖] and S. S. Xue[1,2]

[1]*ICRA and Dipartimento di Fisica, Università di Roma "La Sapienza",*
Piazzale Aldo Moro 5, I-00185 Roma, Italy
[2]*International Center for Relativistic Astrophysics Network, Piazza della Repubblica 10,*
I-65122 Pescara, Italy
[3]*INAF—Osservatorio Astronomico d'Abruzzo, Via M. Maggini snc, I-64100 Teramo, Italy*
[4]*ICRANet-Ferrara, Dipartimento di Fisica e Scienze della Terra, Università degli Studi di Ferrara,*
Via Saragat 1, I–44122 Ferrara, Italy
[5]*Dipartimento di Fisica e Scienze della Terra, Università degli Studi di Ferrara,*
Via Saragat 1, I–44122 Ferrara, Italy
[6]*INAF, Istituto di Astrofisica e Planetologia Spaziali, Via Fosso del Cavaliere 100, 00133 Rome, Italy*
[7]*INAF, Viale del Parco Mellini 84, 00136 Rome, Italy*
[8]*ICRA, University Campus Bio-Medico of Rome, Via Alvaro del Portillo 21, I-00128 Rome, Italy*
[9]*Department of Science and Technology for Humans and the Environment and Nonlinear Physics*
and Mathematical Modeling Lab, University Campus Bio-Medico of Rome,
Via Alvaro del Portillo 21, 00128 Rome, Italy
[10]*Department of Engineering, University Campus Bio-Medico of Rome, Nonlinear Physics*
and Mathematical Modeling Lab, Via Alvaro del Portillo 21, 00128 Rome, Italy
[11]*INAF—Osservatorio Astronomico d'Abruzzo, Via M. Maggini snc, I-64100, Teramo, Italy*

We address the physical origin of the ultrarelativistic prompt emission (UPE) phase of GRB 190114C observed in the interval $t_{\rm rf} = 1.9$–3.99 s, by the *Fermi*-GBM in 10 keV–10 MeV energy band. Thanks to the high signal-to-noise ratio of *Fermi*-GBM data, a time-resolved spectral analysis has evidenced a sequence of similar blackbody plus cutoff power-law spectra (BB + CPL), on ever decreasing time intervals during the entire UPE phase. We assume that during the UPE phase, the "*inner engine*" of the GRB, composed of a Kerr black hole (BH) and a uniform test magnetic field B_0, aligned with the BH rotation axis, operates in an overcritical field $|\mathbf{E}| \geq E_c$, where $E_c = m_e^2 c^3/(e\hbar)$, being m_e and $-e$ the mass and charge of the electron. We infer an e^+e^- pair electromagnetic plasma in presence of a baryon load, *a PEMB pulse*, originating from a vacuum polarization quantum process in the *inner engine*. This initially optically thick plasma self-accelerates, giving rise at the transparency radius to the MeV radiation observed by *Fermi*-GBM. At times $t_{\rm rf} > 3.99$ s, the electric field becomes undercritical, $|\mathbf{E}| < E_c$, and the *inner engine*, as previously demonstrated, operates in the classical electrodynamics regime and generate the GeV emission. During both the "quantum" and the "classical" electrodynamics processes, we determine the time varying mass and spin of the Kerr BH in the *inner engine*, fulfilling the Christodoulou-Hawking-Ruffini mass-energy formula of a Kerr BH. For the first time, we quantitatively show how the *inner engine*, by extracting the rotational energy of the Kerr BH, produces a series of PEMB pulses. We follow the quantum vacuum polarization process in sequences with decreasing time bins. We compute the Lorentz factors, the baryon loads and the radii at transparency, as well as the value of the magnetic field, B_0, assumed to be constant in each sequence. The fundamental hierarchical structure, linking the quantum electrodynamics regime to the classical electrodynamics regime, is characterized by the emission of "*blackholic quanta*" with a timescale $\tau \sim 10^{-9}$ s, and energy $\mathcal{E} \sim 10^{45}$ erg.

*rahim.moradi@inaf.it
†jorge.rueda@icra.it
‡ruffini@icra.it
§liang.li@icranet.org
‖yu.wang@uniroma1.it

I. INTRODUCTION

It is by now clear that gamma-ray bursts (GRBs), far from being a short single elementary process lasting less than 10^2 s, are possibly the most complex astrophysical systems in the Universe, an authentic fundamental physics

laboratory. A series of Episodes, corresponding to new different physical laws, take place on vastly different characteristic timescales ranging from quantum electrodynamics (QED) timescales of 10^{-21} s, to classical electrodynamics processes of 10^{-14} s, as well as to gravitational processes of 10^{-6} s, and to hydrodynamics timescales of 1 s and of 10^{7} s, and the GRB source lifetime can indeed be as long as 10^{17} s, i.e., the Universe lifetime (see [1], and references therein).

One of the most intriguing phenomena occurring in the most energetic long GRBs is the ultrarelativistic prompt emission (UPE) phase. In the case of GRB 190114C: (1) it takes place on a 2 s rest-frame time ($t_{\rm rf}$) interval, (2) it encompasses 40% of the GRB isotropic energy, and (3) it occurs in an originally optically thick domain reaching transparency in the keV-MeV energy range.

We address in this article the challenge of inferring, from spectral properties, on an ever-decreasing timescales, the nature of this new and yet unexplained process. We use: (A) The concepts previously developed for a self-accelerating optically thick $e^{+}e^{-}$ pair-electromagnetic-baryon plasma (PEMB pulse) originated from vacuum polarization produced by a overcritically charged Kerr-Newman black hole (BH) [2–7]. (B) A specific property of the PEMB pulse: the reaching of the transparency radius with $\Gamma \sim 100$ [3], which is essential to overcome the compactness problem of the UPE phase; see e.g., [8,9] (C) The Papapetrou-Wald solution [10,11] as an alternative to the charged Kerr-Newman BH as the source of vacuum polarization process. (D) The concept of an "effective charge", $Q_{\rm eff}$, which overcomes the difficulty of adopting the unexplained origin of a charged BH. This concept allows to explain in an "effective way" the electric field which arises from the gravitomagnetic interaction of a Kerr BH with a surrounding magnetic field, B_0. The effective charge has been used in the study of the "*inner engine*" of GRB 130427A [12] and GRB 190114C [13].

We address the UPE phase of GRB 190114C that, owing to its morphology, can be identified as a canonical binary driven hypernova (BdHN) of type I (see details below), observed with a viewing angle orthogonal to the orbital plane of the GRB binary progenitor. Indeed, a variety of episodes of GRB 190114C have been already identified and duly explained [1], including the x-ray afterglow [14] and the GeV emission [13].

It has been possible since the beginning of 2018 [1,14–17] to obtain specific new results thanks to a variety of factors, including the identification of new GRB paradigms, a novel time-resolved spectral analysis fulfilling stringent criteria of statistical significance [18–23], and three-dimensional, numerical smoothed-particle-hydrodynamic (SPH) simulations of BdHNe presented in Becerra *et al.* [24]. From these results, it has been concluded:

(A) There is clear evidence that the progenitors of long GRBs are binary systems composed of a carbon-oxygen (CO) star and a neutron star (NS) companion: the BdHN. The gravitational collapse of the iron core of the CO star leads to the SN and forms the newborn NS (νNS). When the binary period is short i.e., ~ 5 min, the SN ejecta hypercritically accretes onto the companion NS, leading to the formation of a BH [1]. These systems are known as BdHN of type I (BdHN I). This approach was successfully adopted in explaining the physical origin of the x-ray flares [25], further confirmed in Ruffni *et al.* [26].

(B) The accretion of the SN ejecta onto the νNS in BdHNe has given the opportunity to explain the underlying physical nature of the x-ray afterglow in GRB 130427A, GRB 160509A, GRB 160625B, GRB 180720A and GRB 190114C; see [14] and [15].

(C) The observations of a mildly relativistic phase in the GRB plateau and in the afterglow [25,26], have motivated the use of BdHNe model in order to explain the energetic of the GeV emission as originating from the extraction of rotational energy of a Kerr BH very close to the BH horizon, described by the *inner engine*, addressed in Ruffni *et al.* [12], Rueda and Ruffni [17].

The *inner engine* is composed of: (1) a Kerr BH with mass of M and angular momentum of J, (2) an asymptotically uniform magnetic field, B_0 aligned with the BH rotation axis, the Papapetrou-Wald solution [11], and (3) a very low density plasma composed of ions and electrons with density of 10^{-14} g cm^{-3}; see Ruffni *et al.* [12]. The effective charge, $Q_{\rm eff}$, of this system:

$$Q_{\rm eff} = 2B_0 JG/c^3, \tag{1}$$

originates from the gravitomagnetic interaction of the Kerr BH with the surrounding magnetic field, B_0, being c and G the speed of light in vacuum and the gravitational constant, respectively; see Ruffni *et al.* [12], Rueda and Ruffni [17], and Moradi *et al.* [13].

In order to explain the GeV emission the *inner engine* operates in an undercritical electric field regime, i.e., $|\mathbf{E}| < E_c$, where $E_c = m_e^2 c^3/(e\hbar)$, being m_e and $-e$ the electron mass and charge, respectively, in presence of a magnetic field of $B_0 \sim 10^{10}$ G, assumed to be constant in the entire process of emission. During this process:

(1) electrons are injected close to the horizon with an initial Lorentz factor of $\gamma = 1$;

(2) electrons are accelerated by the electromagnetic fields of the *inner engine* and radiate synchrotron photons of GeV energies;

(3) the radiation does not occur continuously but is emitted in elementary events (quanta) of $\sim 10^{37}$ erg on a timescale of $\sim 10^{-14}$ s. This energy is paid by the rotational energy of the Kerr BH implying a corresponding decrease of the angular momentum J of the Kerr BH [12,13,17].

The emission of the quanta is repetitive. After the emission of each quanta, a new process occurs starting

from a new value $J^* = J - \Delta J$ of the angular momentum, with $\Delta J/J \sim 10^{-16}$, being ΔJ the angular momentum extracted to the Kerr BH by the event in each repetitive step [12,13].

In this article, we address the study of the UPE phase utilizing our previous background and being guided by: (1) the hierarchical structure of the UPE in GRB 190114C with characteristic spectral signature of a cutoff power-law and a blackbody component (CPL + BB); see Ruffni *et al.* [27]; (2) the *inner engine* model which has been already well tested for the GeV radiation in GRB 130427A [12] and GRB 190114C [13].

We recall that the electric field in the Papapetrou-Wald solution in the slow-rotation approximation is given by [12]:

$$E_r \approx -\frac{1}{2}\alpha B_0 \frac{r_+^2}{r^2},\tag{2}$$

where r_+ is the outer event horizon and $\alpha \equiv cJ/(GM^2)$ is the dimensionless BH spin parameter.

The profound novelty characterizing the UPE phase is the assumption of an overcritical field, i.e., $|\mathbf{E}| \geq E_c$ around the Kerr BH in the *inner engine*. This overcritical field generates, via vacuum polarization, an optically thick PEMB pulse which owing to its high density (here $\sim 10^8$ g cm^{-3}) and high interior pressure, self-accelerates to an ultrarelativistic regime and finally reaching the transparency point [7].

The hydrodynamic equations of the relativistic expanding PEMB pulses are integrated until the point of transparency when the MeV radiation becomes observable. The radius of transparency and Lorentz factor are explicitly evaluated. This solution was first addressed in Ruffni [3], Ruffni *et al.* [5–7]. This is the fundamental physical process which is assumed to be at the very ground of the description of the UPE phase and its spectral properties. Again, the energy in the overcritical field originates from the rotational energy of the Kerr BH in the Papapetrou-Wald solution.

An additional necessary step is how to carry out the matching of the overcritical regime, characterizing the UPE phase, its MeV radiation, and its intrinsic quantum nature, with the already analyzed undercritical regime following the UPE phase. This undercritical regime describes the GeV radiation and is dominated in the *inner engine* by a classical electrodynamics nature with very low density surrounding plasma.

For the determination of the parameters of the *inner engine*, we are guided by the time-resolved spectra analysis and existence of the hierarchical structure found in the UPE
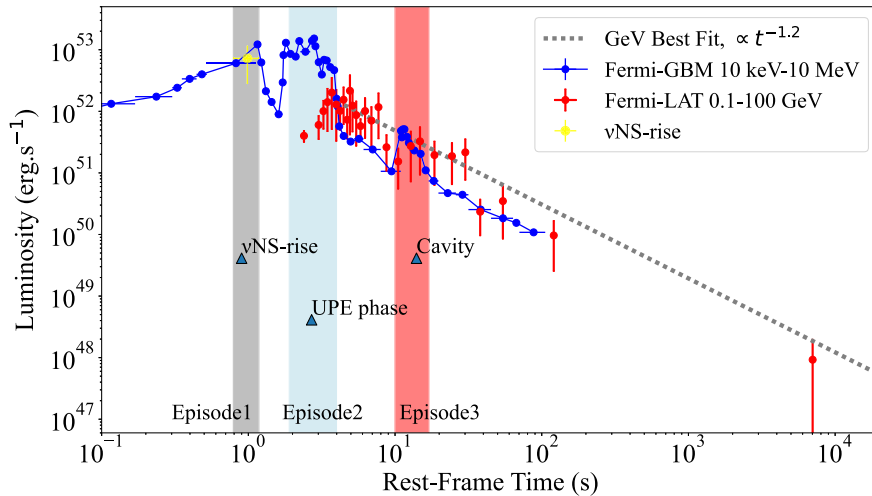
FIG. 1. Luminosity of the *Fermi*-GBM in the 10 keV–10 MeV energy band together with the luminosity of *Fermi*-LAT during and after UPE phase expressed in the rest-frame of the source. The light grey part shows the νNS–rise from $t_{rf} = 0.79$ s to $t_{rf} = 1.18$ s. The light blue part shows the UPE phase which is in the time interval $t_{rf} = 1.9$–3.99 s, whose lower and upper edges correspond, respectively, to the moment of BH formation and to the moment which blackbody component disappears from the GBM data. The corresponding analysis for GRB 130427A, GRB 160509A and GRB 160625B is presented in [28]. The red part shows the Fermi-GBM the *cavity* introduced in Ruffni *et al.* [29]. The rest-frame 0.1–100 GeV luminosity light-curve of GRB 190114C after UPE phase is best fitted by a power-law with slope of 1.2 ± 0.04 and amplitude of 7.75×10^{52} erg s^{-1}
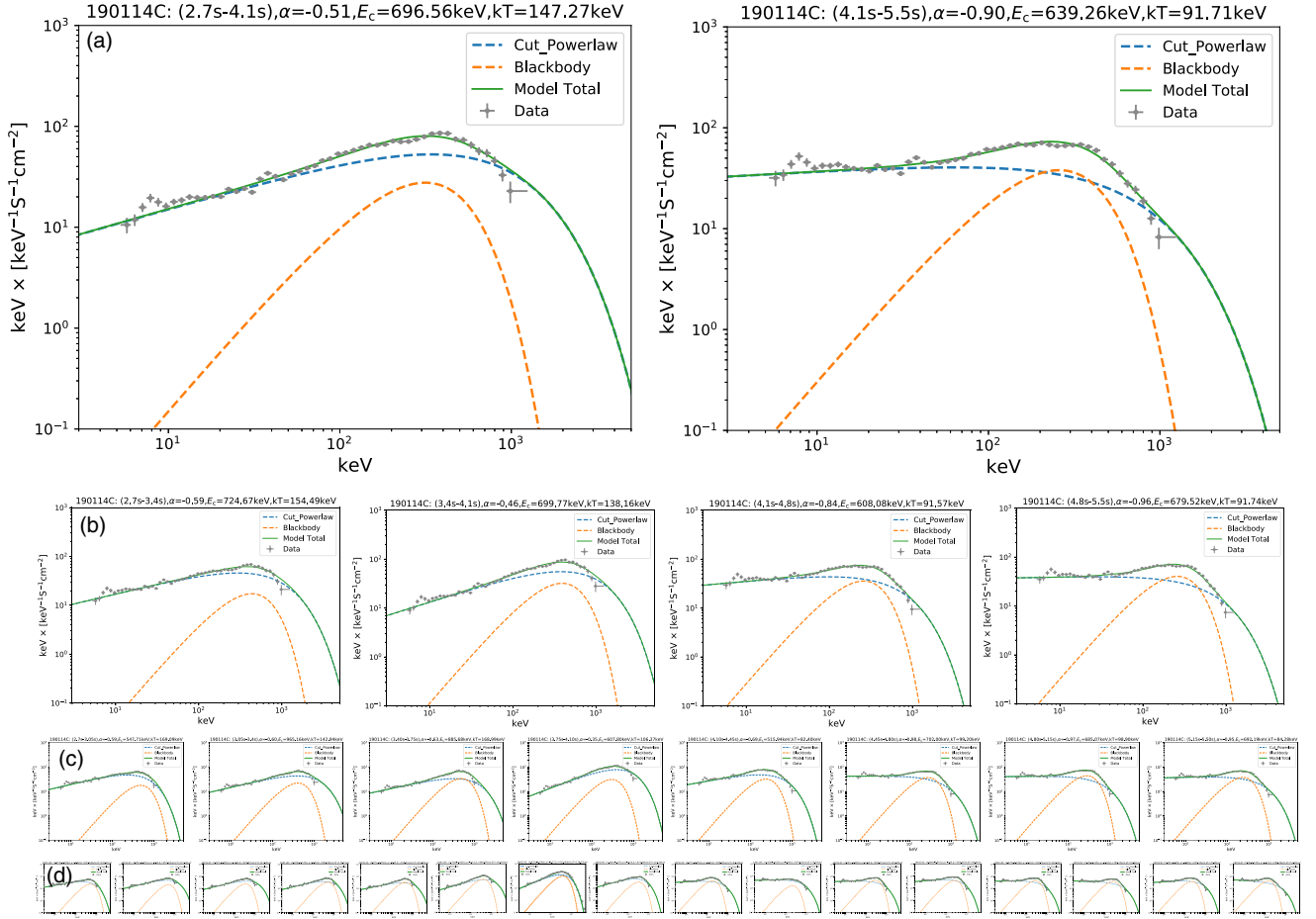
FIG. 2. Time-resolved spectral analysis of UPE phase GRB 190114C: from $t = 2.7$ s ($t_{\rm rf} = 1.9$ s) to $t = 5.5$ s ($t_{\rm rf} = 3.9$ s). For the second iteration: (a) the time interval is divided into two parts, four parts for the third iteration; b, eight parts for the fourth iteration; (c) and sixteen parts for the fifth iteration; (d) respectively. The spectral fitting parameters for each iteration are reported in Table I. Plots are taken from Ruffni *et al.* [27] with permission of authors.
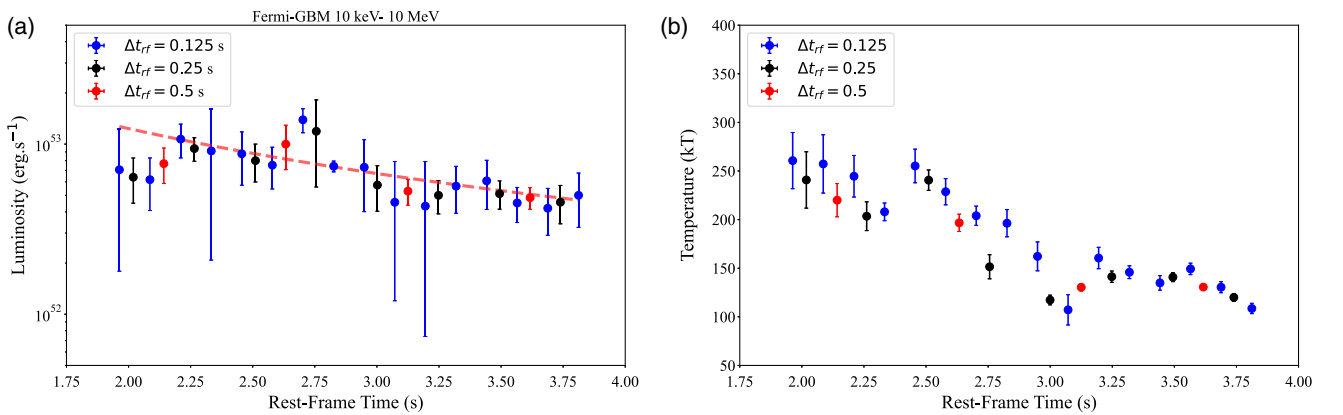

FIG. 3. Luminosity [a] and rest-frame temperature [b] during the UPE observed by *Fermi*-GBM, obtained from analyses with $\Delta t = 0.125$ s (blue circles), $\Delta t = 0.25$ s (black circles) and $\Delta t = 0.5$ s (red circles) time resolutions reported in Table I. The luminosity is best fitted by a power-law of amplitude $(3.5 \pm 1.1) \times 10^{53}$ erg s^{-1} and power-law index -1.50 ± 0.30. The best fit of luminosity, obtained from $\Delta t_{\rm rf} = 0.125$ s time-resolved analysis, is in principle independent of the resolution of data analysis and is fulfilled in all iterative sequences.

phase [27]. Each successive iteration (rebinning) fulfills the total energy requirement and spectral structures in different timescales. We select as the fundamental iterative process the "only" one which allows the electric field to fulfill at the end of the UPE phase the constraint $|\mathbf{E}| = E_c$. This boundary condition determines the value of B_0 and is necessary to join the UPE phase to the classical electro-dynamics regime, originating the GeV radiation.

Similar to the case of the generation of GeV radiation from the *inner engine*, also the emission of the MeV radiation during the UPE phase is not continuous:

1. $e^+e^-\gamma$ plasma, in presence of the baryon load, is generated by the vacuum polarization close to horizon with initial bulk Lorentz factor $\Gamma = 1$ on a characteristic timescale of $\sim \hbar/(m_e c^2) \approx 10^{-21}$ s,
2. these PEMB pulses self-accelerate all the way to the point of transparency at which emit MeV radiation in an ultrarelativistic regime,
3. the process is again repetitive; at the end of each step the process restarts with a value of electric field given by Eq. (2), keeping the magnetic field constant, but with a new value of the BH dimensionless spin parameter $\alpha^* = \alpha - \Delta\alpha$, with $\Delta\alpha/\alpha \sim 10^{-9}$, being $\Delta\alpha$ the amount of dimensionless BH spin extracted to the Kerr BH by the event in each repetitive step.

The UPE phase stops in the sequence which allows the condition $|\mathbf{E}| = E_c$ to be reached at the right time.

In Sec. II, we recall three different Episodes identified in time-resolved spectral analysis of GRB 190114C. We focus on the spectral analysis of the Fermi-GBM (keV-MeV) and the Fermi-LAT (GeV) data during and after the UPE phase; see Fig. 1.

In Sec. III, we present the time-resolved analysis of the UPE phase as well as the appearance of the hierarchical structure of its spectra. These results were announced in Ruffni *et al.* [27] and here presented in an improved numerical analysis, with their theoretical modeling; see Fig. 2.

In Sec. IV, we outline the properties of the *inner engine*. This is composed of a uniform magnetic field aligned with the rotation axis of a Kerr BH, following the exact, mathematical solution of the Einstein-Maxwell equations given by Wald [11]. We here apply this solution to the astrophysical conditions occurring in a BdHN I.

In Sec. V, for $t_{rf} > 3.99$ s, namely after the UPE phase, following Ruffni *et al.* [1,12], Rueda and Ruffni [17] and Moradi *et al.* [13], we proceed to the self-consistent determination of (a) the mass and spin of the BH, (b) the magnetic field B_0. These parameters are determined to fulfill the energetics of GeV radiation and its transparency with respect to the process of pair production by photon-magnetic field interaction. The mass and spin of BH at $t_{rf} = 3.99$ s are, respectively, $M = 4.45\,M_\odot$ and $\alpha = 0.41$, and magnetic field is $B_0 \sim 10^{10}$ G.

In Sec. VI, we determine the mass and spin of BH at $t_{rf} = 1.9$ s, $M = 4.53\,M_\odot$ and $\alpha = 0.54$. This result is consistent with the luminosity obtained from the time-resolved spectral analysis, during the UPE phase, and the above values of the mass and spin for $t_{rf} > 3.99$ s given in Sec. V; see Figs. 3 and 4.
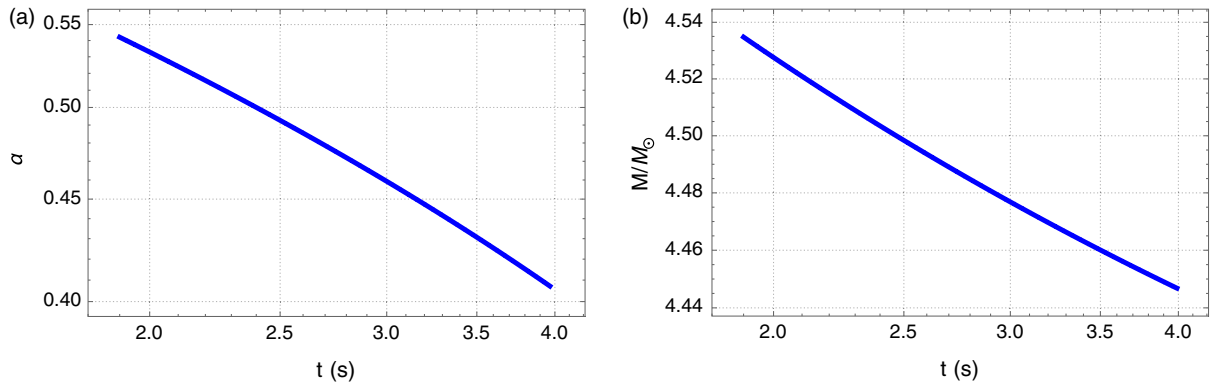

FIG. 4.   The decrease of the BH spin and mass, as a function of rest-frame time for GRB 190114C during the UPE phase, namely in the rest-frame time interval $t_{rf} = 1.9$–3.99 s. The values of spin and mass at the moment when BH formed are, respectively, $M = 4.53\,M_\odot$ and $\alpha = 0.54$. At the moment when the UPE is over, i.e., at $t_{rf} = 3.99$ s, are: $\alpha = 0.41$ and $M = 4.45\,M_\odot$.

In Sec. VII, we address the overcritical regime, $|\mathbf{E}| \geq E_c$, in order to have the vacuum polarization via Schwinger e^+e^- pair production [see discussion in [30]], in the UPE phase; see also Ruffni [3], Ruffni *et al.* [5–7].

In Sec. VIII, we assess the general formulation of the transparency of the MeV photons during the UPE phase.

In Sec. IX, we determine the magnetic field, $B_0 \sim 10^{17}$ G, inferred from the time-resolved spectral analysis with $\Delta t = 0.125$ s resolution, represented in Sec. III, corresponding to the emission at the transparency point of the 16 PEMB pulses with the repetition time of

$\tau = 0.125$ s. This sequence does not fulfill the boundary condition of the UPE phase i.e., $|\mathbf{E}| = E_c$ at $t_{\rm rf} = 3.99$ s; see Fig. 5.

In Sec. X, we obtain the lower limit of magnetic filed around the BH, $B_0 = 2.3 \times 10^{14}$ G, during the UPE phase by imposing $|\mathbf{E}| = E_c$ at $t_{\rm rf} = 3.99$ s, marking the end of UPE phase. We infer that the UPE phase results from emission at the transparency point of the $\sim 10^9$ PEMB pulses, with radiation timescale of $\tau_q \sim 10^{-9}$ s; see Fig. 6.

In Sec. XI, we make a comparison with other approaches In Sec. XII, we outline the conclusions of this article.
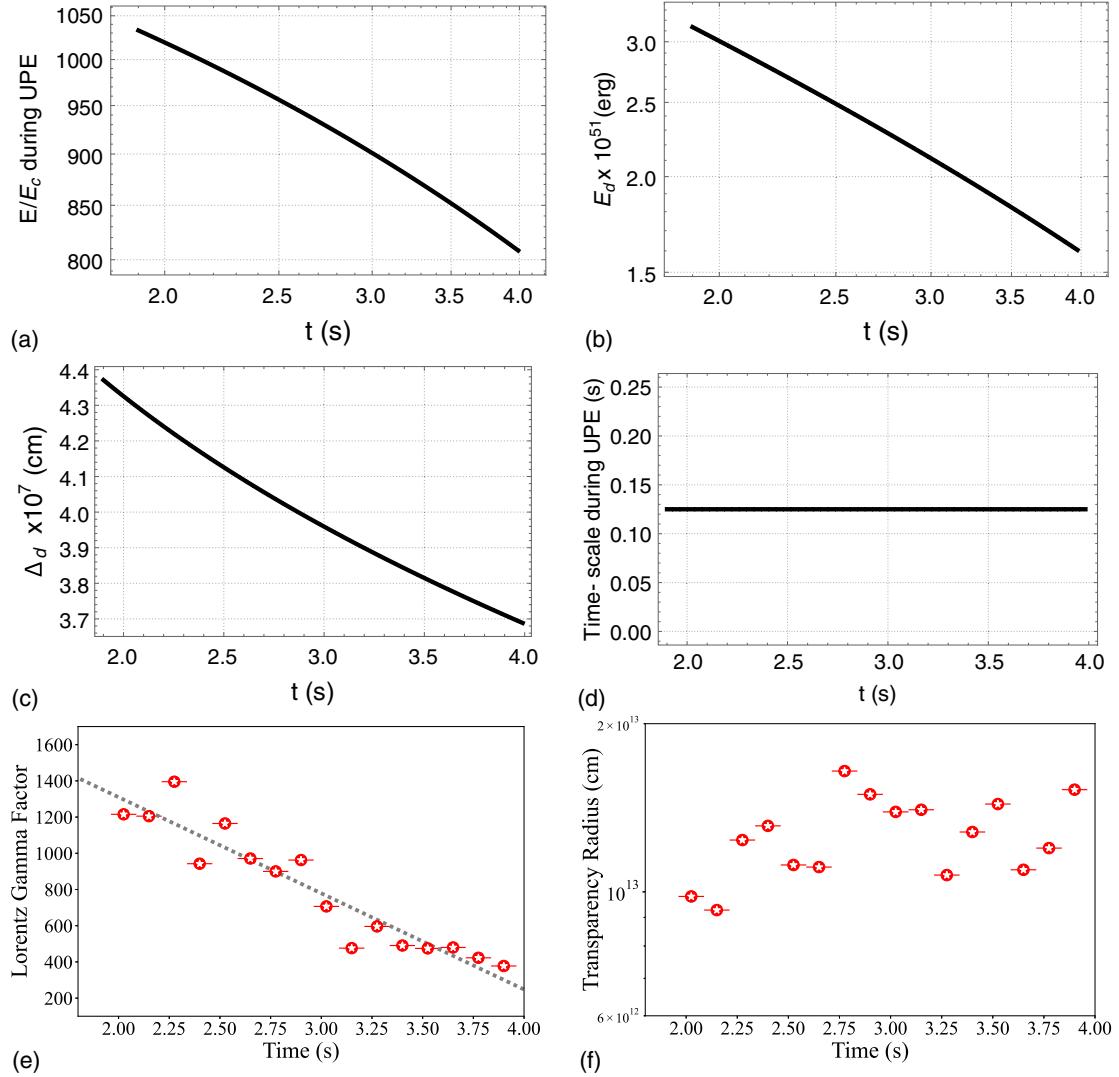
FIG. 5. The parameters of *inner engine* and transparency condition as a function of rest-frame time for GRB 190114C during the UPE phase, namely in the rest-frame time interval $t_{\rm rf} = 1.9$–3.99 s, obtained from a time-resolved analysis down to a $\Delta t = 0.125$ s time resolution reported in Table I. (a): The electric field during UPE phase which is clearly overcritical. (b): The energy of dyadoregion during the UPE phase obtained from Eq. (20). (c): The width of dyadoregion obtained from Eq. (23). (d): Timescale of radiation during the UPE phase. (e): The decrease of the Lorentz gamma factor, Γ, as a function of rest-frame time. (f): The evolution of transparency radius in the UPE phase of GRB 190114C. All values are obtained for magnetic field of, $B_0 = 1.8 \times 10^{17}$ G, calculated in Sec. IX.
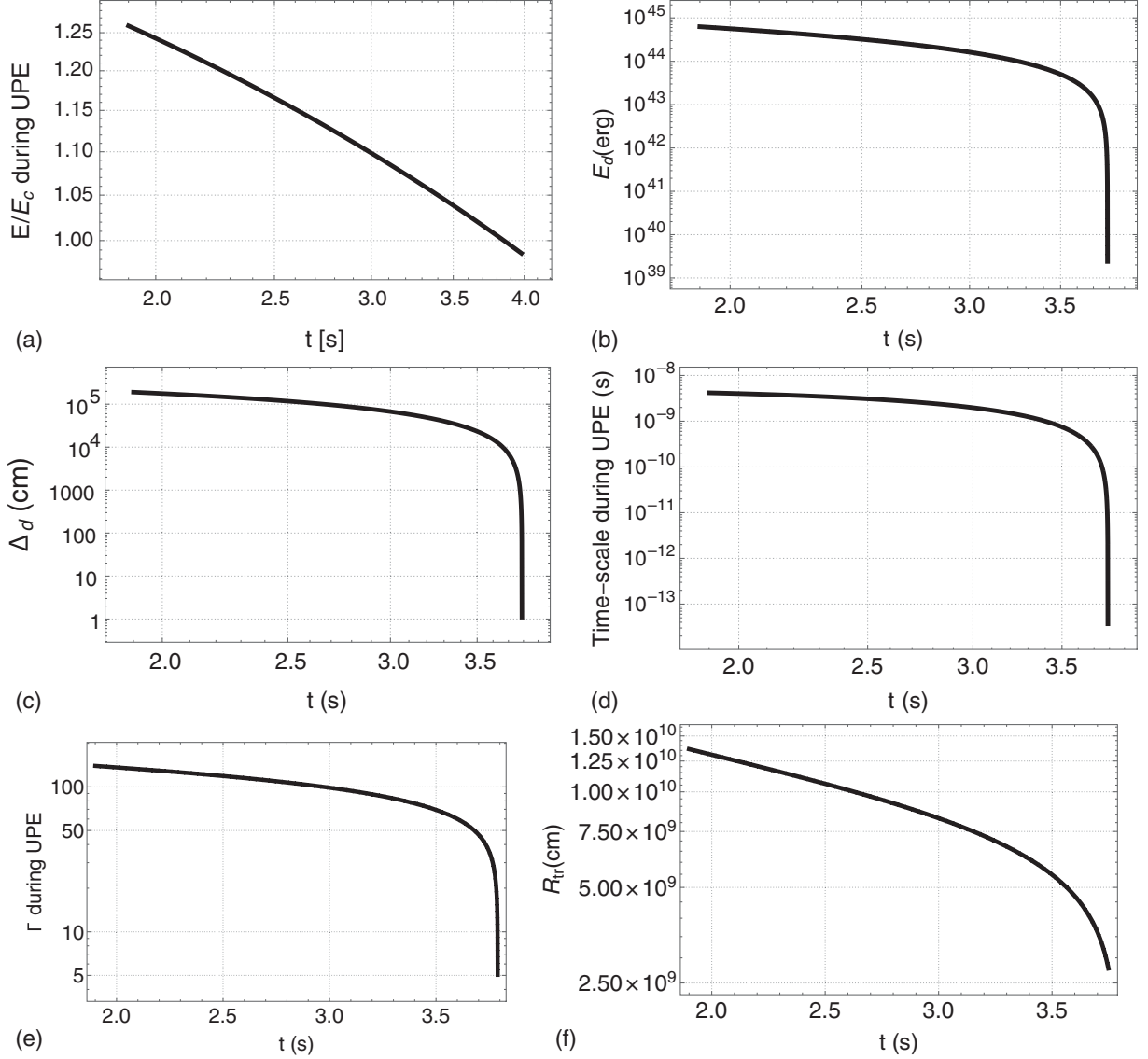
FIG. 6. The parameters of *inner engine* and transparency point, obtained for $B_0 = 2.3 \times 10^{14}$ G, as a function of rest-frame time for GRB 190114C during the UPE phase, namely in the rest-frame time interval $t_{rf} = 1.9$–3.99 s. (a): The electric field during the UPE phase which is clearly overcritical and reaches its critical value at the end of the UPE phase ($t_{rf} = 3.99$ s). (b): The energy of dyadoregion during the UPE phase obtained from Eq. (20). (c): The width of dyadoregion obtained from Eq. (23) which tends to zero at the end of UPE phase, indicating that the number of e^+e^- pairs are suppressed and the UPE phase is over. (d): Repetition timescale of the *inner engine* during the UPE phase obtained from Eq. (44). (e): The decrease of the Lorentz factor, Γ, as a function of rest-frame time. This indicates the fact that Γ tends to unity for the last layers which confirms the end of UPE is reached. (f): The evolution of transparency radius; see Sec. X.

II. *FERMI* DATA OF GRB 190114C

At 20:57:02.63 UT on 14 January 2019, *Fermi*-GBM was triggered by GRB 190114C [31]. The *Fermi*-LAT had a boresight angle of 68 degrees at the trigger time, the GRB remained in the field of view of *Fermi*-LAT for 150 s. With the redshift of $z = 0.424$ [32] the isotropic energy of this burst is $E_{iso} = (2.48 \pm 0.22) \times 10^{53}$ erg. Since BdHNe I are characterized by $E_{iso} \gtrsim 10^{52}$ erg, we have identified GRB 190114C as a BdHN I and predict the occurrence of

an associated SN [33]. This prediction was followed by the successful observation of the SN associated with this burst [34]. The first GeV photon with probability more than 90% belonging to this GRB is a ~0.9 GeV photon observed at $t_{rf} = 1.9$ s after the GBM trigger. The highest-energy photon is a 22.9 GeV event which is observed 15 s after the GBM trigger [35]. GRB 190114C has become since a prototype for identifying the BdHN I episodes.

Three different episodes have been identified in the *Fermi*-GBM data; see Fig. 1:

Episode 1 with an isotropic energy of $E_{\mathrm{iso}} = (1.0 \pm 0.12) \times 10^{53}$ erg, occurs in the rest-frame time interval $t_{\mathrm{rf}} = [0, 1.9]$ s, being $t_{\mathrm{rf}} = 0$ s the *Fermi*-GBM rest-frame trigger time. It reveals a thermal component from $t_{\mathrm{rf}} = 0.79$ s to $t_{\mathrm{rf}} = 1.18$ s, in its spectral analysis, marking the rise of newly born NS (νNS–rise) with a corresponding isotropic energy of $E_{\nu\mathrm{NS}}^{\mathrm{iso}} = (2.82 \pm 0.13) \times 10^{52}$ erg.

Episode 2, with an isotropic energy of $E_{\mathrm{iso}} = (1.47 \pm 0.2) \times 10^{53}$ erg, equivalent to 40% of isotropic energy of the GRB, lasts only 2 s. It occurs in the rest-frame time interval $t_{\mathrm{rf}} = [1.9, 3.99]$ s. It encompasses three major events: (a) The formation of the BH, observation of the first GeV photon at $t_{\mathrm{rf}} = 1.9$ s, see details in Ruffni *et al.* [12]. (b) An increase of the 0.1–100 GeV luminosity following a power-law of $L_{\mathrm{GeV}} = 8.7 \times 10^{50} \, t^{+(1.77\pm0.28)}$ erg s^{-1}. (c) The energetically dominant UPE phase observed by *Fermi*-GBM in the 10 keV–10 MeV band, occurring in the entire interval $t_{\mathrm{rf}} = 1.9$ s–3.99 s fulfilling a hierarchical structure signed by a spectrum composed of a thermal emission and a cutoff power-law component (CPL + BB); see Sec. III.

Episode 3, the "cavity", starts at $t_{\mathrm{rf}} = 11$ s and ends at $t_{\mathrm{rf}} = 20$ s. The presence of a "cavity" in GRB 190114C, carved out in the SN ejecta by the BH formation, has been confirmed in Ruffni *et al.* [29].

The GeV luminosity following the UPE phase is best fitted by the *decreasing* power-law of $L_{\mathrm{GeV}} = (7.75 \pm 0.44) \times 10^{52} \, t^{-(1.2\pm0.04)}$ erg s^{-1}, with an isotropic energy of $E_{\mathrm{GeV}} = (1.8 \pm 1.3) \times 10^{53}$ erg. The spectrum of *Fermi*-LAT in the 0.1–100 GeV energy band, after the UPE phase, is best fitted by a power-law [36]; see Fig. 1 and Moradi *et al.* [13] for more details.

All these results have been presented in Ruffni *et al.* [27], Ruffni *et al.* [29], Ruffni *et al.* [12] and Moradi *et al.* [13].

III. THE TIME-RESOLVED SPECTRAL ANALYSIS, THE HIERARCHICAL STRUCTURE, AND THE MEV LUMINOSITY OF THE UPE PHASE

Following the spectral analysis performed over the UPE phase from $t_{\mathrm{rf}} = 1.9$ s to $t_{\mathrm{rf}} = 3.9$ s (first iteration), we perform the spectral analysis over the 1 second intervals ($\Delta t_{\mathrm{rf}} = 1$ s), namely [1.9s–2.9s] and [2.9s–3.9s](second iteration).

Each half intervals are further divided in half (third iteration), i.e., $\Delta t_{\mathrm{rf}} = 0.5$ s: [1.9s–2.40s], [2.40s–2.9s], [2.9s–3.4s], and [3.4s–3.9s] and the corresponding spectral analysis is performed over each interval.

We further divide the UPE into 8 intervals of $\Delta t_{\mathrm{rf}} = 0.25$ s (fourth iteration): [1.9s–2.15s], [2.15s–2.40s], [2.40s–2.65s], [2.65s–2.9s], [2.9s–3.15s], [3.15s–3.4s], [3.4s–3.65s], and [3.65s–3.9s], and perform the same spectral analysis over each interval.

We continue until the final iteration (fifth iteration), where the adequate signal-to-noise ratio S/N is fulfilled. The UPE is divided into 16 time intervals of $\Delta t_{\mathrm{rf}} = 0.125$ s: [1.896s–2.019s], [2.019s–2.142s], [2.142s–2.265s], [2.265s–2.388s], [2.388s–2.511s], [2.511s–2.633s], [2.633s–2.756s], [2.756s–2.87s], [2.879s–3.002s], [3.002s–3.125s], [3.125s–3.248s], [3.248s–3.371s], [3.371s–3.494s], [3.494s–3.617s], [3.617s–3.739s], and [3.739s–3.862s] and perform the spectral analysis. After dividing into subintervals of 0.125 s one extra time interval of [3.862s–3.985s] has been added.

The spectral fitting of a cutoff power law plus black body (CPL + BB) is confirmed in each time interval and for each iterative process; see Table I, Fig. 2, Ruffni *et al.* [[27] for more details].

From a time-resolved analysis of the UPE phase, performed down to the fifth iteration, a hierarchical structure is obtained. It reveals a common spectral feature for each subinterval characterized by the CPL + BB best-fit model with a rest-frame temperature of $kT = 100$–300 keV and the ratio of blackbody flux (F_{BB}) to the total flux (F_{tot}) of:

$$0.1 \lesssim \frac{F_{\mathrm{BB}}}{F_{\mathrm{tot}}} \lesssim 0.5. \tag{3}$$

see Table I, Fig. 2 and Ruffni *et al.* [[27] for more information]

During the UPE phase the MeV luminosity is best fitted by

$$L_{\mathrm{MeV}} = A_{\mathrm{MeV}} t^{-\alpha_{\mathrm{MeV}}}, \tag{4}$$

with slope $\alpha_{\mathrm{MeV}} = 1.5 \pm 0.3$, and amplitude $A_{\mathrm{MeV}} = (3.5 \pm 1.1) \times 10^{53}$ erg s^{-1}. This best fit is obtained from $\Delta t_{\mathrm{rf}} = 0.125$ s time-resolved analysis and is fulfilled in all iterative sequences; see Table I and Figs. 1 and 3.

The existence of the thermal and the cutoff power-law components in the spectra of the UPE phase have been identified as the characteristic signature of e^+e^- pair creation in presence of baryons (PEMB pulse) originating from the vacuum polarization process [5–7,39]; see Sec. VII.

TABLE I. The parameters of the time-resolved spectral fits of the UPE phase of GRB 190114C, performed from $\Delta t_{\rm rf} = 2$ s down to subintervals of $\Delta t_{\rm rf} = 0.125$ s. The UPE phase extends from $t = 2.7$ s ($t_{\rm rf} = 1.9$ s) to $t = 5.5$ s ($t_{\rm rf} = 3.99$ s). Column 1; represents the time intervals in the observer's frame (Obs), column 2; the time intervals in the rest-frame (rf), column 3; the statistical significance (S) for each time interval, column 4; the power-law index of the cutoff power-law (CPL) component, column 5; the rest-frame cut-off energy, column 6; the rest-frame black body (BB) temperature, column 7; the Akaike Information Criterion/Bayesian Information Criterion (AIC/BIC), column 8; the BB flux ($F_{\rm BB}$), column 9; the CPL + BB or total flux ($F_{\rm tot}$), column 10; the ratio of the BB flux to the total flux, $F_{\rm BB}/F_{\rm tot}$ and, finally column 11; the isotropic energy in each time interval. As it can be seen from column 10, the $F_{\rm BB}/F_{\rm tot}$ remains almost constant in each iteration. The AIC (Akaike [37]) and the BIC (Schwarz *et al.* [38]) methods were used to select non-nested and nested models, respectively [see [18–23], for more information about these methods]. Table is taken from Ruffni *et al.* [27] with permission of authors.

$t_1 \sim t_2$ (s) Obs	$t_{rf,1} \sim t_{rf,2}$ (s) Rest-frame	S	α	E_c (keV)	kT (keV)	ΔDIC	$F_{\rm BB}$ (10^{-6}) (erg cm^{-2} s^{-1})	$F_{\rm tot}$ (10^{-6}) (erg cm^{-2} s^{-1})	$F_{\rm ratio}$	$E_{\rm tot}$ (erg)
$2.700 \sim 5.500$	$1.896 \sim 3.862$	418.62	$-0.71^{+0.02}_{-0.02}$	$717.6^{+25.4}_{-25.4}$	$159.0^{+3.6}_{-3.6}$	$-3344/6697/6719$	$22.49^{+3.21}_{-2.65}$	$111.10^{+11.60}_{-10.40}$	0.20	$1.50e+53$
$2.700 \sim 4.100$	$1.896 \sim 2.879$	296.60	$-0.51^{+0.02}_{-0.02}$	$696.6^{+31.9}_{-32.4}$	$209.7^{+9.3}_{-9.1}$	$-2675/5360/5381$	$24.67^{+6.93}_{-5.35}$	$142.50^{+23.90}_{-21.00}$	0.17	$9.64e+52$
$4.100 \sim 5.500$	$2.879 \sim 3.862$	318.07	$-0.90^{+0.02}_{-0.02}$	$639.3^{+31.9}_{-31.6}$	$130.6^{+2.5}_{-2.5}$	$-2529/5069/5090$	$25.55^{+2.97}_{-2.75}$	$80.98^{+9.68}_{-8.07}$	0.32	$5.48e+52$
$2.700 \sim 3.400$	$1.896 \sim 2.388$	204.30	$-0.59^{+0.03}_{-0.03}$	$724.7^{+44.5}_{-45.5}$	$220.0^{+17.1}_{-17.2}$	$-1882/3774/3796$	$18.55^{+7.09}_{-7.40}$	$123.90^{+29.20}_{-22.30}$	0.15	$4.19e+52$
$3.400 \sim 4.100$	$2.388 \sim 2.879$	225.88	$-0.46^{+0.04}_{-0.04}$	$699.8^{+47.8}_{-48.3}$	$196.7^{+8.9}_{-8.7}$	$-2032/4074/4095$	$31.78^{+9.60}_{-7.31}$	$161.40^{+47.10}_{-32.40}$	0.20	$5.46e+52$
$4.100 \sim 4.800$	$2.879 \sim 3.371$	233.97	$-0.84^{+0.03}_{-0.03}$	$608.1^{+42.1}_{-42.2}$	$130.4^{+3.7}_{-3.9}$	$-1880/3770/3792$	$23.94^{+4.20}_{-4.22}$	$85.37^{+14.83}_{-12.27}$	0.28	$2.89e+52$
$4.800 \sim 5.500$	$3.371 \sim 3.862$	227.90	$-0.96^{+0.03}_{-0.03}$	$679.5^{+49.1}_{-48.7}$	$130.6^{+3.1}_{-3.2}$	$-1809/3628/3649$	$27.18^{+4.01}_{-3.73}$	$78.20^{+11.40}_{-9.66}$	0.35	$2.65e+52$
$2.700 \sim 3.050$	$1.896 \sim 2.142$	148.59	$-0.59^{+0.03}_{-0.03}$	$547.7^{+44.2}_{-44.9}$	$240.8^{+29.2}_{-29.1}$	$-1187/2384/2406$	$19.67^{+17.96}_{-8.88}$	$103.20^{+30.60}_{-20.28}$	0.19	$1.75e+52$
$3.050 \sim 3.400$	$2.142 \sim 2.388$	145.04	$-0.60^{+0.02}_{-0.04}$	$965.2^{+28.5}_{-30.1}$	$203.5^{+14.8}_{-14.8}$	$-1320/2650/2671$	$22.87^{+8.88}_{-7.23}$	$152.00^{+24.00}_{-21.00}$	0.15	$2.57e+52$
$3.400 \sim 3.750$	$2.388 \sim 2.633$	134.60	$-0.63^{+0.04}_{-0.04}$	$885.7^{+70.9}_{-70.1}$	$240.6^{+10.5}_{-10.6}$	$-1224/2458/2480$	$41.02^{+11.09}_{-7.91}$	$129.10^{+32.40}_{-23.40}$	0.32	$2.18e+52$
$3.750 \sim 4.100$	$2.633 \sim 2.879$	187.77	$-0.35^{+0.06}_{-0.05}$	$607.8^{+57.1}_{-60.1}$	$151.5^{+12.4}_{-14.2}$	$-1428/2866/2887$	$23.92^{+12.46}_{-10.40}$	$192.00^{+101.70}_{-60.30}$	0.12	$3.25e+52$
$4.100 \sim 4.450$	$2.879 \sim 3.125$	171.81	$-0.69^{+0.04}_{-0.04}$	$515.9^{+43.6}_{-43.6}$	$117.3^{+5.0}_{-5.0}$	$-1271/2552/2573$	$19.19^{+4.89}_{-4.40}$	$92.71^{+27.69}_{-22.43}$	0.21	$1.57e+52$
$4.450 \sim 4.800$	$3.125 \sim 3.371$	230.14	$-0.98^{+0.04}_{-0.04}$	$702.0^{+78.1}_{-78.2}$	$141.3^{+5.8}_{-5.8}$	$-1254/2518/2539$	$26.76^{+6.41}_{-5.47}$	$80.73^{+17.95}_{-14.95}$	0.33	$1.37e+52$
$4.800 \sim 5.150$	$3.371 \sim 3.617$	166.30	$-0.97^{+0.04}_{-0.04}$	$685.1^{+69.3}_{-68.6}$	$140.8^{+4.6}_{-4.6}$	$-1218/2447/2468$	$31.83^{+6.85}_{-4.98}$	$82.51^{+15.62}_{-12.33}$	0.39	$1.40e+52$
$5.150 \sim 5.500$	$3.617 \sim 3.862$	161.51	$-0.95^{+0.04}_{-0.04}$	$692.2^{+79.1}_{-77.7}$	$120.0^{+4.0}_{-4.0}$	$-1203/2416/2438$	$23.19^{+5.38}_{-3.81}$	$73.57^{+18.69}_{-12.93}$	0.32	$1.24e+52$
$2.700 \sim 2.875$	$1.896 \sim 2.019$	117.09	$-0.58^{+0.05}_{-0.05}$	$470.5^{+74.4}_{-83.7}$	$261.5^{+29.0}_{-27.9}$	$-640/1291/1311$	$33.68^{+20.39}_{-14.33}$	$112.30^{+28.37}_{-25.73}$	0.30	$9.50e+51$
$2.875 \sim 3.050$	$2.019 \sim 2.142$	94.40	$-0.68^{+0.04}_{-0.05}$	$627.6^{+87.0}_{-91.5}$	$258.0^{+30.1}_{-28.7}$	$-664/1337/1359$	$28.45^{+20.42}_{-12.51}$	$98.14^{+35.66}_{-26.44}$	0.29	$8.30e+51$
$3.050 \sim 3.225$	$2.142 \sim 2.265$	106.62	$-0.59^{+0.03}_{-0.03}$	$957.1^{+34.1}_{-34.9}$	$245.3^{+21.5}_{-21.0}$	$-768/1547/1568$	$25.71^{+13.87}_{-9.03}$	$169.30^{+38.20}_{-31.60}$	0.15	$1.43e+52$
$3.225 \sim 3.400$	$2.265 \sim 2.388$	100.40	$-0.73^{+0.06}_{-0.06}$	$1275.9^{+208.9}_{-215.4}$	$208.6^{+9.1}_{-9.2}$	$-669/1349/1369$	$36.78^{+9.54}_{-8.93}$	$144.90^{+33.02}_{-27.63}$	0.25	$1.23e+52$
$3.400 \sim 3.575$	$2.388 \sim 2.511$	98.23	$-0.59^{+0.05}_{-0.05}$	$804.0^{+86.7}_{-82.3}$	$255.9^{+17.4}_{-17.4}$	$-702/1414/1436$	$42.19^{+19.41}_{-13.59}$	$139.30^{+48.30}_{-35.60}$	0.30	$1.18e+52$
$3.575 \sim 3.750$	$2.511 \sim 2.633$	93.84	$-0.65^{+0.04}_{-0.04}$	$916.3^{+64.6}_{-67.7}$	$229.3^{+13.6}_{-13.5}$	$-730/1471/1492$	$39.25^{+11.97}_{-10.71}$	$119.50^{+32.90}_{-25.45}$	0.33	$1.01e+52$
$3.750 \sim 3.925$	$2.633 \sim 2.756$	126.63	$-0.51^{+0.02}_{-0.02}$	$960.9^{+30.9}_{-31.4}$	$204.6^{+9.9}_{-10.0}$	$-808/1627/1648$	$57.70^{+15.81}_{-12.25}$	$221.10^{+35.60}_{-31.50}$	0.26	$1.87e+52$
$3.925 \sim 4.100$	$2.756 \sim 2.879$	141.61	$-0.27^{+0.06}_{-0.06}$	$412.7^{+12.2}_{-11.9}$	$196.8^{+14.0}_{-16.1}$	$-729/1468/1488$	$32.20^{+19.05}_{-18.86}$	$176.50^{+19.05}_{-11.21}$	0.18	$1.49e+52$
$4.100 \sim 4.275$	$2.879 \sim 3.002$	122.91	$-0.54^{+0.06}_{-0.06}$	$474.1^{+45.5}_{-46.2}$	$162.6^{+14.9}_{-14.8}$	$-758/1526/1547$	$24.26^{+17.09}_{-10.09}$	$116.10^{+52.40}_{-35.12}$	0.21	$9.82e+51$
$4.275 \sim 4.450$	$3.002 \sim 3.125$	122.62	$-0.64^{+0.08}_{-0.08}$	$365.0^{+44.9}_{-48.5}$	$107.5^{+15.7}_{-12.6}$	$-675/1360/1380$	$9.04^{+9.47}_{-5.69}$	$72.20^{+19.06}_{-14.95}$	0.13	$6.11e+51$
$4.450 \sim 4.625$	$3.125 \sim 3.248$	111.94	$-1.04^{+0.05}_{-0.05}$	$640.0^{+108.7}_{-106.1}$	$161.0^{+11.1}_{-10.8}$	$-640/1290/1310$	$22.34^{+9.36}_{-6.65}$	$68.54^{+11.70}_{-11.21}$	0.33	$5.80e+51$
$4.625 \sim 4.800$	$3.248 \sim 3.371$	123.33	$-0.95^{+0.05}_{-0.05}$	$694.2^{+96.8}_{-94.2}$	$146.3^{+6.7}_{-6.6}$	$-734/1477/1499$	$35.59^{+9.47}_{-8.00}$	$89.91^{+27.59}_{-18.82}$	0.40	$7.60e+51$
$4.800 \sim 4.975$	$3.371 \sim 3.494$	129.65	$-0.85^{+0.05}_{-0.05}$	$564.5^{+68.9}_{-71.9}$	$135.3^{+7.5}_{-7.6}$	$-744/1498/1519$	$30.78^{+11.12}_{-8.55}$	$96.58^{+31.02}_{-23.68}$	0.32	$8.17e+51$
$4.975 \sim 5.150$	$3.494 \sim 3.617$	107.36	$-1.10^{+0.04}_{-0.04}$	$820.5^{+115.0}_{-111.2}$	$149.7^{+5.9}_{-5.8}$	$-683/1376/1398$	$32.76^{+6.98}_{-5.92}$	$71.57^{+16.74}_{-11.99}$	0.46	$6.05e+51$
$5.150 \sim 5.325$	$3.617 \sim 3.739$	108.96	$-1.04^{+0.05}_{-0.05}$	$765.2^{+119.0}_{-115.8}$	$130.9^{+5.8}_{-5.8}$	$-697/1404/1426$	$26.14^{+7.02}_{-5.96}$	$66.70^{+20.48}_{-14.17}$	0.39	$5.64e+51$
$5.325 \sim 5.500$	$3.739 \sim 3.862$	121.57	$-0.88^{+0.06}_{-0.06}$	$635.3^{+88.7}_{-92.0}$	$108.9^{+5.3}_{-5.4}$	$-736/1483/1504$	$20.90^{+6.51}_{-5.15}$	$79.48^{+28.02}_{-21.03}$	0.26	$6.72e+51$

IV. THE PROPERTIES OF *INNER ENGINE*

The discovery of the *inner engine* obtained by incorporating the Papapetrou-Wald solution [10–13,17], around the newborn Kerr BH in the BdHNe I, in presence of the low density plasma of the cavity, see [29], was operative in the classical electrodynamics with $|\mathbf{E}| < E_c$ process and leading to the generation by synchrotron radiation of the GeV emission in GRB 130427A and GRB190114C. We also apply here this *inner engine* in the $|\mathbf{E}| > E_c$ regime to describe the quantum electrodynamics process.

Wald's work is based on the Papapetrou discovery [10] that Killing vectors are vector potential solutions of

sourceless Maxwell equations in vacuum spacetimes in the test field approximation (i.e., no metric backreaction). A linear combination of these two Killing vector solutions led Wald to the solution for a rotating BH immersed in a uniform magnetic field B_0, aligned with the rotation axis of the Kerr BH at infinity.

The electromagnetic field of the *inner engine* in the Carter's orthonormal tetrad is

$$E_{\hat{r}} = \frac{\hat{a}B_0}{\Sigma}\left[r\sin^2\theta - \frac{\hat{M}(\cos^2\theta+1)(r^2-\hat{a}^2\cos^2\theta)}{\Sigma}\right], \quad (5)$$

$$E_{\hat{\theta}} = \frac{\hat{a}B_0}{\Sigma}\sin\theta\cos\theta\sqrt{\Delta}, \quad (6)$$

$$B_{\hat{r}} = -\frac{B_0\cos\theta}{\Sigma}\left[-\frac{2\hat{a}^2\hat{M}r(\cos^2\theta+1)}{\Sigma} + \hat{a}^2 + r^2\right], \quad (7)$$

$$B_{\hat{\theta}} = \frac{B_0 r}{\Sigma}\sin\theta\sqrt{\Delta}, \quad (8)$$

where $\Sigma = r^2 + \hat{a}^2\cos^2\theta$, $\Delta = r^2 - 2\hat{M}r + \hat{a}^2$, $\hat{M} = GM/c^2$, $\hat{a} = a/c = J/(Mc)$, being M and J the mass and angular momentum of the Kerr BH. The (outer) event horizon is located at $r_+ = (\hat{M} + \sqrt{\hat{M}^2 - \hat{a}^2})$.

The electromagnetic field in the polar direction $\theta = 0$ and at small angles from it is well approximated by [12,17]:

$$E_{\hat{r}} = -\frac{2B_0 JG}{c^3}\frac{(r^2-\hat{a}^2)}{(r^2+\hat{a}^2)^2} \quad (9)$$

$$E_{\hat{\theta}} = 0 \quad (10)$$

$$B_{\hat{r}} = \frac{B_0\left(-\frac{4GJ^2 r}{M(r^2+\hat{a}^2)} + a^2 + r^2\right)}{(r^2+\hat{a}^2)} \quad (11)$$

$$B_{\hat{\theta}} = 0. \quad (12)$$

Equation (9) is the same as the radial electric field of the Kerr-Newman metric in the same tetrad just substituting to the charge Q of the Kerr-Newman solution the effective charge Q_{eff}, given by Eq. (1), see, e.g., [40]. Therefore, up to linear order in θ and in the dimensionless BH spin parameter $\alpha \equiv \hat{a}/(GM/c^2)$, the electric field can be written as

$$E_{\hat{r}} = -\frac{2B_0 JG}{c^3}\frac{(r^2-\hat{a}^2)}{(r^2+\hat{a}^2)^2} \approx -\frac{1}{2}\alpha B_0 \frac{r_+^2}{r^2}, \quad (13)$$

which for spin values $\alpha \lesssim 0.7$, the available electrostatic energy is well approximated by

$$\mathcal{E} \approx \frac{(2B_0 JG/c^3)^2}{2r_+} = \frac{Q_{\text{eff}}^2}{2r_+} = 1.25 \times 10^{43}\frac{\beta^2\alpha^2\mu^3}{1+\sqrt{1-\alpha^2}} \text{ erg}, \quad (14)$$

where we have normalized the mass and magnetic field strength by, respectively, $\mu = M/M_\odot$ and $\beta = B_0/B_c$, being

$$B_c = E_c = \frac{m_e^2 c^3}{e\hbar} \approx 4.41 \times 10^{13} \text{ G}, \quad (15)$$

the critical field for vacuum polarization; see Ruffni *et al.* [12] for more details.

The values μ and β in this general equations will be determined as a function of astrophysical process operative in the *inner engine* in GRB 190114C. The corresponding description of the overcritical and the undercritical fields are represented in the next sections.

We adopt that the magnetic field and BH spin are parallel, therefore along the symmetry axis direction electrons in the surrounding ionized medium are repelled, while protons are pulled into the BH [see [12] for additional details].

V. THE MASS AND SPIN OF THE BH OF GRB 190114C

We here recall the self-consistent solution following the UPE phase, well tested in the case of GRB 130427A [12] and GRB 190114C [13] which fulfills three conditions: (1) The GeV energetics observed by the Fermi-LAT is paid by the extractable energy of the BH, i.e.: $E_{\text{GeV}} = E_{\text{extr}}$. (2) The magnetic e^+e^- pair production (MPP) process does not occur around the BH, therefore the GeV photons fulfill the transparency condition. (3) The timescale of the synchrotron radiation determines the timescale of observed GeV radiation.

Having these conditions, and assuming the minimum energy budget requirement;, the *inner engine* parameters at $t > t_{\text{rf}} = 3.99$ s, i.e., after the UPE phase, are: magnetic field strength $B_0 \approx 3.9 \times 10^{10}$ G, spin and BH mass, respectively, $\alpha = 0.41$ and $M = 4.45\,M_\odot$. The corresponding BH irreducible mass is $M_{\text{irr}} = 4.35\,M_\odot$ see Moradi *et al.* [13] for more details.

VI. DETERMINATION OF THE MASS AND SPIN OF THE BH DURING THE UPE PHASE

We have obtained in the previous section at $t_{\text{rf}} = 3.99$ s the values of mass and spin parameters of the BH and the magnetic field: $M = 4.45\,M_\odot$, $\alpha = 0.41$, and $B_0 = 3.9 \times 10^{10}$ G, respectively. We now turn to the determination of the mass and spin of the BH during the UPE phase. The mass-energy formula of the Kerr BH ([41–43]; see also ch. 33 in [44]) is given by:

$$M^2 = \frac{c^2 J^2}{4G^2 M_{\text{irr}}^2} + M_{\text{irr}}^2. \tag{16}$$

We require that the energetics of the MeV radiation be explained by the extractable rotational energy of the Kerr BH, i.e.,

$$E_{\text{MeV}} = E_{\text{extr}} = (M - M_{\text{irr}})c^2. \tag{17}$$

Therefore, the extractable energy is given by:

$$E_{\text{extr}} = (M - M_{\text{irr}})c^2 = \left(1 - \sqrt{\frac{1 + \sqrt{1 - \alpha^2}}{2}}\right) Mc^2. \tag{18}$$

The time derivative of Eq. (18) gives the luminosity

$$L_{\text{MeV}} = -\frac{dE_{\text{extr}}}{dt} = -\frac{dM}{dt}, \tag{19}$$

in which we assume that M_{irr} is constant for BH during the energy emission process.

From the luminosity of MeV radiation expressed in the rest-frame of the GRB, given by Eq. (4) in the time interval of the UPE phase (see also Fig. 3), and from the values of the spin and of the mass of the BH at $t_{\text{rf}} = 3.99$ s, we can now work backward by integrating Eq. (19) and determine the BH mass and spin at the beginning of the UPE, when the BH is formed, namely at $t_{\text{rf}} = 1.9$ s. We obtain $M = 4.53\ M_\odot$ and $\alpha = 0.54$, respectively.

This assumption demands that all the luminosity of UPE phase originates from the rotational energy of the BH. This point is going to be justified in the next sections.

VII. VACUUM POLARIZATION, DYADOREGION AND THE UPE PHASE

The UPE phase is characterized by an electric field $|\mathbf{E}| > E_c$ [7,26]. The problem of vacuum polarization due to the overcritical field has a vast literature which dates back to the concept of the dyadosphere [3] and dyadotorous in the Kerr-Newman geometry, developed in Cherubini *et al.* [30]. Dyado is from the Greek word "duados" for pair, indicating here the e^+e^- pairs. The dyadotorus is the region where the vacuum polarization processes occur around a rotating charged BH, leading to the production of e^+e^- pairs; see also [7] for details.

In order to evaluate this process in the present case, we adopt a description using the Kerr-Newman geometry for which an analytic formula for the energy contained in the dyadoregion has been derived in Cherubini *et al.* [30]. We have checked numerically that the energy of the dyadoregion in the Kerr-Newman geometry (see Eq. (20) below), setting the BH charge as the effective charge of the Papapetrou-Wald solution, $2B_0 JG/c^3$, is a good approximation of the one estimated numerically with the Papapetrou-Wald solution. We have verified that the quantitative difference is at most 30%, which implies that this approximation does not affect our conclusions.

We can now evaluate the energy of e^+e^- pairs generated in the Papapetrou-Wald solution using the Kerr-Newman analogy. We use the Carter orthonormal frame, in which the flat spacetime Schwinger framework can be locally applied and determine the dyadoregion energy [see discussion in [30]]:

$$E_{(r_+, r_d)} = \frac{(2B_0 JG/c^3)^2}{4r_+}\left(1 - \frac{r_+}{r_d}\right) + \frac{(2B_0 JG/c^3)^2}{4\hat{a}}$$
$$\times \left[\left(1 + \frac{\hat{a}^2}{r_+^2}\right)\arctan\left(\frac{\hat{a}}{r_+}\right)\right.$$
$$\left. - \left(1 + \frac{\hat{a}^2}{r_d^2}\right)\arctan\left(\frac{\hat{a}}{r_d}\right)\right], \tag{20}$$

where r_d is the radius of the dyadoregion

$$\left(\frac{r_d}{\hat{M}}\right)^2 = \frac{1}{2}\frac{\lambda}{\mu\epsilon} - \alpha^2 + \left(\frac{1}{4}\frac{\lambda^2}{\mu^2\epsilon^2} - 2\frac{\lambda}{\mu\epsilon}\alpha^2\right)^{1/2} \tag{21}$$

with $\epsilon = E_c M_\odot G^{3/2}/c^4 \approx 1.873 \times 10^{-6}$, and

$$\lambda = \frac{2B_0 JG/c^3}{\sqrt{GM}} = \frac{Q_{\text{eff}}}{\sqrt{GM}}, \tag{22}$$

is the effective charge-to-mass ratio.

The characteristic width of the *dyadoregion*, i.e., the region around the BH where the electric field overcritical is

$$\Delta_{\text{d}}(t) = r_d(t) - r_+(t). \tag{23}$$

VIII. TRANSPARENCY CONDITION IN THE UPE PHASE

The existence of overcritical fields in the UPE phase and the consequent production of an $e^+e^-\gamma$ plasma, have been addressed in Sec. VII.

In presence of an overcritical electric field around the BH, a sequence of events occur:

(1) An optically thick $e^+e^-\gamma$ plasma of total energy $E_{e^+e^-}^{\text{tot}} = E_{\gamma,\text{iso}}$ endowed with baryon load with a mass of M_B. The self-acceleration and expansion of such *PEMB pulses* has been described in Ruffni *et al.* [5]. The dynamics of the PEMB pulses due to the effect of baryonic matter (the remnant of the collapsed object) has been considered in [6]. The thermalization of the pair plasma is achieved almost instantaneously ($\sim 10^{-13}$ s) and expands due to its self-acceleration up to ultrarelativistic velocities ($\Gamma \sim 100$ in the case of long GRBs; [45,46]).

(2) The transparency of the $e^+e^-\gamma$ plasma. When the PEMB pulses expand with ultrarelativistic velocities, the $e^+e^-\gamma$ plasma becomes optically thin, a thermal radiation that has been called the Proper-GRB (P-GRB) is emitted [5,6]. The P-GRB is characterized by the observed thermal component; see Sec. II and Sec. III. The dynamics of the expanding plasma from the vicinity of the BH up to the transparency point is described by the plasma energy, $E^{\text{tot}}_{e^+e^-}$ and the baryon load parameter, $\mathcal{B} = M_B c^2 / E^{\text{tot}}_{e^+e^-}$ [5,6].

The total P-GRB energy in the comoving frame of each impulsive process is

$$E^{\text{com}}_{\text{P-GRB}} = \int a T^4_{\text{com}} dV_{\text{com}},$$
$$= a T^4_{\text{com}} V_{\text{com}} \qquad (24)$$

where a is radiation constant, T_{com} is the P-GRB temperature in the comoving frame and V_{com} is the volume of the PEMB pulses in the comoving frame.

Dividing Eq. (24) by the Doppler factor $\Gamma(1 - v/c)$ at transparency, i.e., when the P-GRB is emitted, being Γ and v the Lorentz factor and speed of the PEMB pulses, and assuming head-on emission; namely $\cos\vartheta = 1$ one can obtain:

$$\frac{E^{\text{com}}_{\text{P-GRB}}}{\Gamma(1 - v/c)} = \frac{a T^4_{\text{com}}}{\Gamma(1 - v/c)} V_{\text{com}}, \qquad (25)$$

where we have assumed head-on emission and therefore fixed $\cos\vartheta = 1$ in the Doppler factor.

Since:

$$T_{\text{obs}} = \frac{T_{\text{com}}}{\Gamma(1 - v/c)},$$
$$E^{\text{obs}} = \frac{E^{\text{com}}}{\Gamma(1 - v/c)},$$
$$V_{\text{lab}} = \frac{V_{\text{com}}}{\Gamma}, \qquad (26)$$

we have that:

$$E^{\text{obs}}_{\text{P-GRB}} = a T^4_{\text{obs}} \Gamma^3 (1 - v/c)^3 \Gamma V_{\text{lab}}$$
$$= a T^4_{\text{obs}} \Gamma^4 (1 - v/c)^3 4\pi R^2 \Delta_{\text{lab}}, \qquad (27)$$

where we have used the fact that $V_{\text{lab}} = 4\pi R^2 \Delta_{\text{lab}}$, where Δ_{lab} is the thickness of the PEMB pulses, and $a = 4\sigma/c$, being σ the Stefan-Boltzmann constant.

Moreover, we know from the condition of transparency

$$\tau = \sigma_T (n_{e^+e^-} + \bar{Z} n_B) \Delta_{\text{lab}} \approx \sigma_T (\bar{Z} n_B) \Delta_{\text{lab}},$$
$$= \sigma_T \frac{\bar{Z} M_B}{m_N 4\pi R^2 \Delta_{\text{lab}}} \Delta_{\text{lab}} = 1, \qquad (28)$$

where σ_T is the Thomson cross section, $\bar{Z}$ is the average atomic number of baryons ($\bar{Z} = 1$ for Hydrogen atom and $\bar{Z} = 1/2$ for general baryonic matter), m_N is nucleon mass and M_B is the baryon mass. Since the value of number density of e^+e^- can only be obtained numerically, for simplicity we assume here $n_{e^+e^-} \ll n_B$ and we have numerically checked that this assumption is indeed valid for the values of $\mathcal{B}$ considered here; namely $\mathcal{B} = 10^{-3}$–10^{-2}. In addition, we assume the constant slab approximation with a constant width Δ_{lab} in the laboratory frame following Ruffni *et al.* [5,6].

Therefore, the lower bound of the transparency radius is

$$R^{\text{tr}} = \left(\frac{\sigma_T}{8\pi} \frac{M_B}{m_N} \right)^{1/2}. \qquad (29)$$

By substituting Eq. (29) in Eq. (27), and dividing it by E_{iso}, one obtains:

$$\frac{E^{\text{obs}}_{\text{P-GRB}}}{E_{\text{iso}}} = \frac{1}{2} a T^4_{\text{obs}} \Gamma^4 (1 - v/c)^3 \sigma_T \frac{\mathcal{B}}{m_N c^2} \Delta_{\text{lab}}, \qquad (30)$$

where we used the fact that, by definition, $\mathcal{B} \equiv M_B c^2 / E_{\text{iso}}$.

Using the fact that:

$$1 - v/c = \frac{1}{(1 + v/c)\Gamma^2} \simeq \frac{1}{2\Gamma^2}, \qquad (31)$$

where we assumed $v/c \sim 1$, that is certainly accurate at the transparency of the PEMB pulses, we have that:

$$\frac{E^{\text{obs}}_{\text{P-GRB}}}{E_{\text{iso}}} = \frac{a T^4_{\text{obs}}}{16\Gamma^2} \sigma_T \frac{\mathcal{B}}{m_N c^2} \Delta_{\text{lab}}. \qquad (32)$$

From the total energy conservation we have that:

$$E_{\text{iso}} = E^{\text{obs}}_{\text{P-GRB}} + E_{\text{Kinetic}}, \qquad (33)$$

therefore

$$1 = \frac{E^{\text{obs}}_{\text{P-GRB}}}{E_{\text{iso}}} + \frac{E_{\text{Kinetic}}}{E_{\text{iso}}} \qquad (34)$$

where E_{Kinetic} is the kinetic energy of the baryonic PEMB pulses:

$$E_{\text{Kinetic}} = (\Gamma - 1) M_B c^2. \qquad (35)$$

By substituting Eq. (35) in Eq. (34) we have

$$\mathcal{B} = \frac{1}{\Gamma - 1} \left(1 - \frac{E^{\text{obs}}_{\text{P-GRB}}}{E_{\text{iso}}} \right), \qquad (36)$$

or, equivalently:

$$\Gamma = 1 + \mathcal{B}^{-1}\left(1 - \frac{E^{\text{obs}}_{\text{P−GRB}}}{E_{\text{iso}}}\right). \qquad (37)$$

The radius of transparency, R^{tr}, is given by Eq. (29) in this theoretical approach:

$$R^{\text{tr}} = \left(\frac{\sigma_T}{8\pi}\frac{\mathcal{B}E_{\text{iso}}}{m_N c^2}\right)^{1/2}. \qquad (38)$$

In general, from Eqs. (32) and (36), the values of $\mathcal{B}$ and Γ can be estimated by the values of $E^{\text{obs}}_{\text{P−GRB}}/E_{\text{iso}}$, T_{obs} and Δ_{lab}. Also, having E_{iso} and $\mathcal{B}$, we can obtain the transparency radius from Eq. (38).

IX. THE MAGNETIC FIELD INFERRED FROM THE $\Delta t = 0.125$ s TIME RESOLVED SPECTRAL ANALYSIS

As a specific example, we calculate the magnetic field and transparency parameters for the $\Delta t_{\text{rf}} = 0.125$ s time resolved interval, namely the fifth iteration analysis reported in Sec. III. Therefore, the UPE phase is assumed to be composed of 16 expanding PEMB pulses emitting an average isotropic energy of $E_{\text{iso}} \sim 10^{52}$ erg, with radiation timescale of $\tau_q = 0.125$ s, as reported in Table I.

Therefore, from (1) the ratio $E_{\text{P−GRB}}/E_{\text{iso}} = 0.3$, and (2) $E_{\text{P−GRB}} = E_{(r_+, r_d)}$, the electromagnetic energy stored in each expanding PEMB pulse should be $E_{(r_+, r_d)} = 0.3 \times E_{\text{iso}}$. Consequently, from Eq. (20) and the value of mass and spin parameter of the BH, the magnetic field needed to fulfill this energetic is $B_0 = 1.85 \times 10^{17}$ G. The Lorentz factor, $\Gamma \sim 1000$, the baryon load, $\mathcal{B} \sim 2 \times 10^{-3}$, and the radius of transparency, $R^{\text{tr}} \sim 10^{13}$ cm, are obtained using:

(i) the isotropic energy of each time interval, $E_{\text{iso}} \sim 10^{52}$ erg;

(ii) the ratio of black body energy to isotropic energy $E^{\text{obs}}_{\text{P−GRB}}/E_{\text{iso}} \sim 0.3$;

(iii) the value of black body temperature in keV reported in Table I;

(iv) the width of the dyadoregion at decoupling, $\Delta_{\text{lab}} = \Delta_d$ obtained from Eq. (23) for magnetic field of $B_0 = 1.85 \times 10^{17}$ G.

The results are shown in Fig. 5. It is appropriate to notice that the magnetic field of $B_0 = 1.85 \times 10^{17}$ G, obtained from the $\Delta t_{\text{rf}} = 0.125$ s time-resolved analysis, does not fulfill the boundary condition of the UPE phase, $|\mathbf{E}| = E_c$ at $t_{\text{rf}} = 3.99$ s. In the next section, we calculate the lowest limit of magnetic field and the minimum repetition time which fulfill the required boundary condition $|\mathbf{E}| = E_c$ at $t_{\text{rf}} = 3.99$ s.

X. THE LOWER LIMIT OF MAGNETIC FIELD DURING THE UPE PHASE

Having determined the boundary value of the magnetic field at $t_{\text{rf}} = 3.99$ s to be $B_0 = 3.9 \times 10^{10}$ G, we must now require that at $t_{\text{rf}} > 3.99$ s the electric to be undercritical, and overcritical inside the UPE phase. In Sec. VI, we have determined the overall behavior of the mass and spin of BH during the UPE since the moment of the formation of BH; see Fig. 4.

We set the value of B_0 in the UPE phase, i.e., at times $t_{\text{rf}} < 3.99$ s, such that the electric field therein is overcritical. The lower limit of the magnitude of magnetic field is determined in a way that in Eq. (13), $|E_{r_+}| = E_c$ at the end of the UPE phase; at $t_{\text{rf}} = 3.99$ s. For BH mass and spin parameter at the end of UPE, it implies a magnetic field of $\beta = B_0/B_c = 5.1$ or $B_0 = 2.3 \times 10^{14}$ G; see Fig. 6.

For $B_0 = 2.3 \times 10^{14}$ G and at the moment which BH is formed, namely $t_{\text{rf}} = 1.9$ s, $\lambda \approx 4.7 \times 10^{-5}$ [from Eq. (22)], which leads to $r_d = 1.15 r_+$. Having these values, the energy of dyadoregion at $t_{\text{rf}} = 1.9$ s is $E_d \approx 6.27 \times 10^{44}$ erg. The evolution of energy of dyadoregion is shown in Fig. 6(b).

The evolution of characteristic width of the dyadoregion is shown in Fig. 6(c). At $t_{\text{rf}} = 3.99$ s, the extent of the dyadoregion tends to zero confirming that not enough e^+e^- pairs are created and the UPE phase is finished.

A. The transparency condition obtained from the lower limit of magnetic field, $B_0 = 2.3 \times 10^{14}$ G

For $B_0 = 2.3 \times 10^{14}$ G, each expanding PEMB pulse; which are produced via vacuum polarization and self-expanded with different Lorentz factors, has an isotropic energy $\sim 10^{45}$ erg obtained from Eq. (20); see Fig. 6. The total isotropic energy of the UPE phase is $E^{\text{UPE}}_{\text{iso}} = 1.47 \times 10^{53}$ erg, therefore, this phase consists of $\sim 10^8$ impulses in the time interval 1.9–3.99 s. Radiation from each one of these PEMB pulse can be interpreted as a blackholic quantum introduced in Rueda and Ruffni [17].

As expressed in Sec. VIII, the key parameters for calculating the transparency radius of each impulse are: (1) its isotropic energy, E_{iso}, (2) the blackbody to isotropic energy ratio, $E^{\text{obs}}_{\text{P−GRB}}/E_{\text{iso}}$, (3) the blackbody temperature, (T_{obs}), and finally (4) the width $\Delta_{\text{lab}} = \Delta_d$.

From the *inner engine* theory, as presented in the previous subsection, for each impulse we have $E_{\text{iso}} \sim 10^{45}$ erg and the width of the dyadoregion at decoupling is $\Delta_d = 1.9 \times 10^5$ cm. From the hierarchical structure of UPE phase in this GRB presented by Eq. (3), we have $E^{\text{obs}}_{\text{P−GRB}}/E_{\text{iso}} \sim 0.3$ and the temperature $kT_{\text{obs}} \sim 150$ keV.

With these values of $E^{\text{obs}}_{\text{P−GRB}}/E_{\text{iso}}$, Δ_d, T_{obs}, and E_{iso}, we obtain via Eqs. (32), (36) and (38), the transparency radius of

$$R^{\text{tr}} = 9.4 \times 10^9 \text{ cm}, \qquad (39)$$

the baryon load parameter

$$\mathcal{B} = 5.1 \times 10^{-3}, \qquad (40)$$

and finally the Lorentz factor of

$$\Gamma \approx 139. \qquad (41)$$

We have checked that these estimated values are in good agreement with the corresponding ones obtained from the numerical simulation of the PEMB pulses evolution. The corresponding values from the numerical simulation are: $R^{\rm tr} = 9.3 \times 10^9$ cm, temperature $kT = 150$ keV, and Lorentz factor $\Gamma \sim 140$.

The evolution of the Lorentz gamma factor, Γ is shown in Fig. 6(e) indicating the fact that Γ tends to ~ 4 for the last shell which confirms the end of UPE is reached.

The evolution of transparency radius in the UPE of GRB 190114C, using the exact numerical values of energy and width of dyadoregion are also shown in Fig. 6(f).

B. The repetition time of sequence of the blackholic quanta

We now study the timescale of each blackholic quanta in which the system starts over. The new value of the electric field is set by the new values of the BH angular momentum and mass, $J = J_0 - \Delta J$ and $M = M_0 - \Delta M$, keeping the magnetic field value constant B_0 in which at $t_{\rm rf} = 1.9$ s, i.e.,

$$\frac{\Delta J}{J} \approx \frac{\Delta M}{M} = 3.1 \times 10^{-9}. \qquad (42)$$

Regarding the presence of the baryon load obtained from Eq. (36) in the acceleration process, we infer from the MeV luminosity, the evolution of the timescale $\tau_q(t)$ of the blackholic quantum by requiring it to explain the MeV emission, i.e.:

$$L_{\rm MeV} = \frac{[1 - \mathcal{B}(\Gamma - 1)]E_{(r_+(t),r_d(t))}}{\tau_q(t)}. \qquad (43)$$

In fact, the effect of baryon load is $(1 - \mathcal{B}\Gamma) \approx 0.3$. Therefore, we obtain for the timescale

$$\tau_q(t) = \frac{0.3 E_{(r_+(t),r_d(t))}}{L_{\rm MeV}}. \qquad (44)$$

where the $E_{(r_+(t),r_d(t))}$ is the energy of dyadoregion obtained from Eq. (20), determined from the new values of J and M for each blackholic quanta and $L_{\rm MeV}$ is the MeV luminosity obtained from best fit represented by Eq. (4); the evolution of the blackholic timescale is shown in Fig. 6(d).

C. The approach of the $|\mathbf{E}| = E_c$ at the UPE phase boundary

From the above theoretical derivation, we can explicitly see that, for an iteration, such that the duration of each elementary process of the nth iteration is 10^{-9} s, namely

after 10^9 iterations, the physical model can be consistently implemented, deriving the necessary parameters characterizing the process, namely the energy of each PEMB pulse, the baryon load, the Lorentz factor, and the radius at transparency. From Fig. 6, it becomes clear that after $t_{\rm rf} \sim 3.7$ s, the emission of quanta by the QED process becomes not effective and the classical regime is soon approached.

The lowest limit of the magnetic field to reach $|\mathbf{E}| = E_c$ occurs in an *inner engine* composed of a Kerr BH of initial mass of $M = 4.53 \, M_\odot$ and $\alpha = 0.51$, immersed with a uniform magnetic of $B_0 = 2.3 \times 10^{14}$ G with a radiation timescale of $\sim 10^{-9}$ s.

Indeed, the decrease of the magnetic field from $\beta = 5.1$ to $\beta = 8.9 \times 10^{-4}$ at $t_{\rm rf} = 3.99$ s, can be explained as the result of the induced current created by pairs in the inward electric field, which screens the original magnetic field. This is a very interesting process that has consequences in different astrophysical scenarios. Therefore, we here limit ourselves to the above explanation and refer the reader for further details in the dedicated, separated publication [47].

All the above results: (1) are in perfect agreement with observational data; see Fig. 3 and, (2) overcome the compactness problem of the UPE phase. It is appropriate to mention all these results have been obtained guided by the hierarchical structure of the UPE phase.

XI. COMPARISON WITH OTHER APPROACHES

The magnetohydrodynamics of plasma accretion onto the Kerr BH was first addressed in Ruffni and Wilson [48] assuming he infinite conductivity condition, $F_{\mu\nu}U^\nu = 0$ implying $\mathbf{E} \cdot \mathbf{B} = 0$. In view of zero net charge on the surface of the BH, no process of energy extraction, neither by vacuum polarization nor by electromagnetic process was there possible [49].

Blandford and Znajek [50] returned on the same process and in order to overcome the difficulty of extracting energy and they introduced, in analogy with pulsar, the presence "*gaps*" [51,52].

Thorne and MacDonald [53], following Hanni and Ruffni [54], calculated the surface charge induced on the horizon of the Kerr BH immersed in the magnetic field in the Papapetrou-Wald solution [11]. Miniutti and Ruffni [55] explicitly manifested that the Papapetrou-Wald solution [11] implies $\mathbf{E} \cdot \mathbf{B} \neq 0$, and identified that the induced surface charge implies a quadrupolar distribution of electric field around the BH. These results were confirmed in [56]. Applying these works to the case of GRBs, it has been shown that the mathematical Papapetrou-Wald solution can be used in order to describe the *inner engine* of a GRB 130427A [12], which presents mechanism to extract the rotational energy of the Kerr BH. The process which occurs in the undercritical field regime leads to the

emission of synchrotron radiation in the GeV domain as well as ultrahigh energy cosmic rays (UHECRs) [13]. The synchrotron emission of the *inner engine* occurs near the BH horizon and is emitting in blackholic quanta [17].

The extrapolation to overcritical field regime, presented in this paper, leads to the explanation of the MeV radiation during the UPE phase.

In recent years, in parallel to the theoretical progresses in the field, computer simulations were also developed. These simulations point the fact that present plasma in any energy extracting scheme would screen the background electric field of the vacuum solution of Papapetrou-Wald from the magnetosphere; see e.g., Komissarov [57], Parfrey *et al.* [58]. These simulation mainly address the physics of active galactic nuclei (AGNs) and particularly attentive has been the review of their theoretical models indicated in Komissarov [57]. Their choice of parameters and physical processes are quite different from the ones we have used for the GRB analysis. In our GRB approach we have been guided by the theoretical explanation of a vast number of observations obtained from: (1) the unprecedented time-resolved spectral analysis of the UPE phase; (2) the power-law MeV luminosity observed by Fermi-GBM; and (3) the power-law GeV luminosity observed by Fermi-LAT. This allows us to identify the physical processes and parameters which had to be fulfilled in order to obtain the detailed acquired data. Their choice of parameters enforce $\mathbf{E} \cdot \mathbf{B} = 0$ condition so different from $\mathbf{E} \cdot \mathbf{B} \neq 0$ which has allowed us to obtain our results.

In our model, the magnetic field is left over by the collapse of the accreting NS to the BH, rooted in the surrounding material, and the electric field is created by the gravitomagnetic interaction of the spacetime rotation with the present magnetic field; see, e.g., Rueda *et al.* [14]. Following this procedure, and since the electric field is assumed to be overcritical, in a very short timescale $\sim \hbar/(m_e c^2) \approx 10^{-21}$ s, much shorter than any electromagnetic process, a dyadoregion originate dominated by the high density and high pressure of the neutral $e^+ e^- \gamma$ plasma [7].

The optically thick pair electromagnetic-baryon (PEMB) pulse self-accelerates to the ultra-relativistic regime and finally reaches the transparency point at the radius of $\sim 10^{10}$ cm. These classical results were obtained thanks to a collaboration with Wilson at Lawrence Livermore National Laboratory [5,6].

As soon as the BH is formed, the first and the most efficient process in action to produce the $e^+ e^-$ plasma and, consequently decreasing the rotational energy of BH, occurs through the Schwinger critical field pair production. Since an overwhelming amount of pair plasma is created in quantum timescales, the plasma expansion by its internal pressure starts well before any electric field screening.

This process takes a fraction of angular momentum of the Kerr BH. The BH then is left with a slightly smaller angular momentum $J^* = J - \Delta J$, with $\Delta J/J \sim 10^{-9}$, being

ΔJ the angular momentum, and the same magnetic field which leads to a new electric field created by the space-time rotation. As a result, the system starts a new process in presence of the same magnetic field B_0, kept rigorously constant and a new effective charge of $Q^*_{\mathrm{eff}} = Q_{\mathrm{eff}} - \Delta Q_{\mathrm{eff}}$ which $\Delta Q_{\mathrm{eff}} = 2B_0 \Delta J$.

This process continues till the moment that electric field is not overcritical anymore, and after that the sole electromagnetic process is at work. The expanding $e^+ e^- \gamma$ plasma sweeps away the matter in the cavity whose density after this process becomes $\sim 10^{-14}$ g cm^{-3}, and an undercritical electromagnetic field is left; see Ruffni *et al.* [29]. This low-density ionized plasma is needed to fulfill an acceleration of charged particles leading to the electrodynamical process around a newborn BH. In fact, this density is much below the Goldreich-Julian density $\rho_{\mathrm{GJ}} = 8 \times 10^{-12}$ g cm^{-3} obtained for the $B_0 = 3.9 \times 10^{10}$ G and $M = 4.45\ M_\odot$ and $a = 0.41M$. Moreover, the matter energy density inside the cavity is negligible comparing to the electromagnetic energy density, namely $\rho_M/(|B|^2 - |E|^2) \sim 10^{-14}$, while in Komissarov [57] this ratio is 0.05 or higher.

It is interesting that the *inner engine* operates as well in the supermassive BHs in active galactic nuclei in the $|\mathbf{E}| < E_c$ regime. In the case of M87, with a mass of a few $10^9\ M_\odot$, the repetition timescale is 0.68 d in the polar direction, with a quanta of $\mathcal{E} \sim 10^{45}$ erg [13].

XII. CONCLUSIONS

GRB 190114C has offered already the possibility of testing different Episodes of the BdHN I sequence by a time-resolved spectral analysis [1]; the νNS-rise [Becerra *et al.* in preparation], the formation of the BH triggering the UPE phase and the associated GeV emission (see Fig. 1), the formation of the cavity [29], the long-lasting emission in the X-ray afterglow from the spinning νNS [14], and in the GeV emission from the newly-formed BH [13].

The long lasting GeV radiation, with a luminosity following a power-law of $L_{\mathrm{GeV}} = (7.75 \pm 0.44) \times 10^{52}\ t^{-(1.2 \pm 0.04)}$ erg s^{-1}, has been shown to originate from the extraction of the rotational energy of a Kerr BH in a sequence of discrete "blackholic quanta" emission [17]. This process occurs in an *inner engine*, which is composed of an uniform magnetic field aligned with the rotation axis of the Kerr BH described by the Papapetrou-Wald solution [10,11] and immersed in a very low density fully ionized plasma with density as low as 10^{-14} g cm^{-3} [1,13,17,29].

One of the main results has been the concept of effective charge Q_{eff}, given by Eq. (1) driving the acceleration process in the *inner engine*.

The most unexpected result has been the discovery of hierarchical structure in the time-resolved spectral analysis on ever-decreasing timescales of the UPE phase of GRB 190114C by Ruffni *et al.* [27] and here updated in Sec. III. There, we have determined the spectral properties and

luminosities during and after the UPE phase, of the MeV emission observed by *Fermi*-GBM, and of the GeV emission observed by *Fermi*-LAT.

A new arena is open in this article linking the macroscopic hierarchical structure of the UPE phase to a microphysical sequence of discrete elementary events in a QED regime.

For the first time, we have here approached the energy extraction process from a Kerr BH by the general relativistic QED process occurring in the *inner engine*.

We have assumed that the electric field of the *inner engine* operates in an overcritical $|\mathbf{E}| > E_c$ during the UPE phase, and in an undercritical $|\mathbf{E}| < E_c$ just after the end of the UPE phase. A sharp separatix both in the theoretical treatment and in the observational properties of these two domains are evidenced.

The main result of this article is to have compared and contrasted the two different processes for explaining the MeV and GeV emissions of GRBs.

The first process, originating the MeV radiation, is dominated by the vacuum polarization originating from the overcritical field in the UPE phase. The overcritical field generates an initially optically thick $e^+ e^- \gamma$-baryon plasma, which self-accelerates until reaching the point of transparency, a PEMB pulse. Typical values of $\Gamma \sim 100$ guarantee the avoidance of the compactness problem [8,9] in the UPE phase. We have shown that the magnetic field B_0 keeps a constant value during the UPE phase of order of $\sim 10^{14}$ G and reduces to 3.9×10^{10} G after the UPE phase.

The second process, originating the GeV emission, is based on the classical ultrarelativistic electrodynamics generated from the electrons injected in the magnetic field emitting synchrotron radiation close to the BH horizon, in selected energies with specific pitch angle dependence, see Fig. 9 in Ruffni *et al.* [12].

Both these processes originate from the rotational energy of the Kerr BH acting on a uniform magnetic field, aligned with the BH rotation axis, within Papapetrou-Wald solution.

The results presented here were expected since fifty years when the Christodoulou-Hawking-Ruffini mass-energy formula of the BH [41–43], as well as some of the pioneering works, using the vacuum polarization process of a BH, were established [3,59]. They were followed by fundamental contributions on the self-acceleration process of the $e^+ e^- \gamma$ optically thick plasma, PEMB pulses [3,5,6], and by the concepts of *dyadosphere* and *dyadotorus* [see [7], and references therein], which are the fundamental conceptual framework of this article. The revival of these concepts, as we explained in this article, has been made possible by the fundamental introduction of "*the effective charge*" overcoming the concept of a net charged BH and fulfilling, nevertheless, all the necessary electrodynamical process of an electrically charged BH.

The fact that all the properties of GRB 190114C have been confirmed to occur in GRB 130427A, GRB 160509A and GRB 160626B; see [28], allow us to extend and apply the analysis here performed for the *inner engine*, generally to all BdHNe I.

This has introduced a radical change by modifying the traditional energetic arguments based on the gravitational binding energy of massive particles geodesics, following a classical electrodynamics process in the Kerr metric occurring at very high density. Indeed, in [29], it has been shown how this *inner engine* operates most efficiently in a cavity in presence a very tenuous ionized plasma with density of 10^{-14} g cm^{-3} following a classical electrodynamics process. The *inner engine* equally works at high densities of the PEMB pulses in the quantum electrodynamics process. In both processes, the fundamental energetic role is being played by the rotational energy of the Kerr BH, which is converted by associated classical and quantum ultrarelativistic acceleration processes into the observed multiwavelength energy emissions and UHECRs. The application of the classical work of the innermost stable circular orbit (ISCO) of massive particles around Kerr BH, introduced in Ruffni and Wheeler [60], has been superseded in this new approach. The concepts of the dyadosphere and [3,5,6] and dyadotorous [30]s are the fundamental ones in this new electrodynamical scenario.

The most important result in this paper has been the understanding the role of hierarchical structure discovered in the time-resolved spectral analysis of the UPE phase, finally explained by their underlying quantum nature.

This long march was started by the intuitions announced in Ruffni *et al.* [27]. They have been here expanded and approached in their theoretical implication in this article. Although the motivations were clear, their detailed comprehension has needed further work which is here presented. We are ready to look at the implications of these results.

Thanks to the observation of GRB 190114C, which is by far the most complex fundamental physical system ever approached in Science, a new scenario is now open. The most unique complexity of BdHNe, their enormous energy emitted in an observer homogeneous Universe, see e.g., Ruffni *et al.* [61], and the special quantum and classical electrodynamics nature of their radiation make us wonder about the role GRB may play in the appearance of life in the Universe [62]. This new overarching conceptual description appears to be in sight thanks to the observation of GRB 190114C.

[1] R. Ruffini, R. Moradi, J. A. Rueda, L. Li, N. Sahakyan, Y. C. Chen, Y. Wang, Y. Aimuratov, L. Becerra, C. L. Bianco, C. Cherubini, S. Filippi, M. Karlica, G. J. Mathews, M. Muccino, G. B. Pisani, and S. S. Xue, Mon. Not. R. Astron. Soc. **504,** 5301 (2021).

[2] T. Damour and R. Ruffini, Phys. Rev. Lett. **35,** 463 (1975).

[3] R. Ruffini, in *49th Yamada Conference, Kyoto, Japan, 1998* [arXiv:astro-ph/9811232].

[4] T. Damour, R. S. Hanni, R. Ruffini, and J. R. Wilson, Phys. Rev. D **17,** 1518 (1978).

[5] R. Ruffini, J. D. Salmonson, J. R. Wilson, and S.-S. Xue, Astron. Astrophys. **350,** 334 (1999).

[6] R. Ruffini, J. D. Salmonson, J. R. Wilson, and S.-S. Xue, Astron. Astrophys. **359,** 855 (2000).

[7] R. Ruffini, G. Vereshchagin, and S. Xue, Phys. Rep. **487,** 1 (2010).

[8] M. Ruderman, in *Seventh Texas Symposium on Relativistic Astrophysics*, Annals of the New York Academy of Sciences Vol. 262, edited by P. G. Bergman, E. J. Fenyves, and L. Motz (1975), pp. 164–180.

[9] T. Piran, Rev. Mod. Phys. **76,** 1143 (2005).

[10] A. Papapetrou, Ann. L'Institut Henri Poincare Sect. (A) Phys. Theor. **4,** 83 (1966), http://www.numdam.org/item/AIHPA_1966__4_2_83_0/.

[11] R. M. Wald, Phys. Rev. D **10,** 1680 (1974).

[12] R. Ruffini, R. Moradi, J. A. Rueda, L. Becerra, C. L. Bianco, C. Cherubini, S. Filippi, Y. C. Chen, M. Karlica, N. Sahakyan, Y. Wang, and S. S. Xue, Astrophys. J. **886,** 82 (2019).

[13] R. Moradi, J. A. Rueda, R. Ruffini, and Y. Wang, Astron. Astrophys. **649,** A75 (2021).

[14] J. A. Rueda, R. Ruffini, M. Karlica, R. Moradi, and Y. Wang, Astrophys. J. **893,** 148 (2020).

[15] R. Ruffini, M. Karlica, N. Sahakyan, J. A. Rueda, Y. Wang, G. J. Mathews, C. L. Bianco, and M. Muccino, Astrophys. J. **869,** 101 (2018).

[16] Y. Wang, J. A. Rueda, R. Ruffini, L. Becerra, C. Bianco, L. Becerra, L. Li, and M. Karlica, Astrophys. J. **874,** 39 (2019).

[17] J. A. Rueda and R. Ruffini, Eur. Phys. J. C **80,** 300 (2020).

[18] L. Li, J.-J. Geng, Y.-Z. Meng, X.-F. Wu, Y.-F. Huang, Y. Wang, R. Moradi, Z. L. Uhm, and B. Zhang, Astrophys. J. **884,** 109 (2019).

[19] L. Li, Astrophys. J. Suppl. Ser. **242,** 16 (2019).

[20] L. Li, Astrophys. J. Suppl. Ser. **245,** 7 (2019).

[21] L. Li, Astrophys. J. **894,** 100 (2020).

[22] L. Li, F. Ryde, A. Pe'er, H.-F. Yu, and Z. Acuner, Astrophys. J. Suppl. Ser. **254,** 35 (2021).

[23] L. Li and B. Zhang, Astrophys. J. Suppl. Ser. **253,** 43 (2021).

[24] L. Becerra, C. L. Ellinger, C. L. Fryer, J. A. Rueda, and R. Ruffini, Astrophys. J. **871,** 14 (2019).

[25] R. Ruffini, Y. Wang, Y. Aimuratov, U. Barres de Almeida, L. Becerra, C. L. Bianco, Y. C. Chen, M. Karlica, M. Kovacevic, L. Li, J. D. Melon Fuksman, R. Moradi, M. Muccino, A. V. Penacchioni, G. B. Pisani, D. Primorac, J. A. Rueda, S. Shakeri, G. V. Vereshchagin, and S.-S. Xue, Astrophys. J. **852,** 53 (2018).

[26] R. Ruffini, L. Becerra, C. L. Bianco, Y. C. Chen, M. Karlica, M. Kovačević, J. D. Melon Fuksman, R. Moradi, M. Muccino, G. B. Pisani, D. Primorac, J. A. Rueda, G. V. Vereshchagin, Y. Wang, and S. S. Xue, Astrophys. J. 2018) 151 ,**869**).

[27] R. Ruffini, L. Li, R. Moradi, J. A. Rueda, Y. Wang, S. S. Xue, C. L. Bianco, S. Campion, J. D. Melon Fuksman, C. Cherubini, S. Filippi, M. Karlica, and N. Sahakyan, arXiv:1904.04162.

[28] L. Li, R. Ruffini, J. A. Rueda, R. Moradi, Y. Wang, and S. S. Xue, arXiv:1910.12615.

[29] R. Ruffini, J. D. Melon Fuksman, and G. V. Vereshchagin, Astrophys. J. **883,** 191 (2019).

[30] C. Cherubini, A. Geralico, H. J. A. Rueda, and R. Ruffini, Phys. Rev. D **79,** 124002 (2009).

[31] R. Hamburg, P. Veres, C. Meegan, E. Burns, V. Connaughton, A. Goldstein, D. Kocevski, and O. J. Roberts, GRB Coordinates Network **23707,** 1 (2019).

[32] J. Selsing, J. Fynbo, K. Heintz, D. Watson, and S. Dyrbye, GRB Coordinates Network **23695** (2019).

[33] R. Ruffini, R. Moradi, Y. Aimuratov, U. Barres, V. A. Belinski, C. L. Bianco, Y. C. Chen, C. Cherubini, S. Filippi, D. M. Fuksman, M. Karlica, L. Li, D. Primorac, J. A. Rueda, N. Sahakyan, Y. Wang, and S. S. Xue, GRB Coordinates Network **23715,** 1 (2019).

[34] A. Melandri, L. Izzo, P. D'Avanzo, D. Malesani, M. Della Valle, E. Pian, N. R. Tanvir, F. Ragosta, F. Olivares, R. Carini, E. Palazzi, S. Piranomonte, P. Jonker, A. Rossi, D. A. Kann, D. Hartmann, C. Inserra, E. Kankare, K. Maguire, S. J. Smartt *et al.*, GRB Coordinates Network **23983** (2019).

[35] D. Kocevski, N. Omodei, M. Axelsson, and E. Burns, and the Fermi-LAT team, GRB Coordinates Network (2019).

[36] Y. Wang, L. Li, R. Moradi, and R. Ruffini, arXiv:1901.07505.

[37] H. Akaike, IEEE Trans. Autom. Control **19,** 716 (1974).

[38] G. Schwarz *et al.*, Ann. Stat. **6,** 461 (1978).

[39] R. Ruffini, J. D. Salmonson, J. R. Wilson, and S.-S. Xue, Astron. Astrophys. Suppl. Ser. **138,** 511 (1999).

[40] *Physics and Astrophysics of Neutron Stars and Black Holes*, edited by R. Giacconi and R. Ruffini (North-Holland Pub. Co., Amsterdam, New York, 1978).

[41] D. Christodoulou, Phys. Rev. Lett. **25,** 1596 (1970).

[42] D. Christodoulou and R. Ruffini, Phys. Rev. D **4,** 3552 (1971).

[43] S. W. Hawking, Phys. Rev. Lett. **26,** 1344 (1971).

[44] C. W. Misner, K. S. Thorne, and J. A. Wheeler, *Gravitation* (Freeman and Co., San Francisco, 1973).

[45] A. G. Aksenov, R. Ruffini, and G. V. Vereshchagin, Phys. Rev. Lett. **99,** 125003 (2007).

[46] A. G. Aksenov, R. Ruffini, and G. V. Vereshchagin, Phys. Rev. D **79,** 043008 (2009).

[47] S. Campion, J. Rueda, R. Ruffini, and S. Xue, Phys. Lett. B **820,** 136562 (2021).

[48] R. Ruffini and J. R. Wilson, Phys. Rev. D **12,** 2959 (1975).

[49] C. Cherubini, S. Filippi, A. Loppini, R. Moradi, R. Ruffini, Y. Wang, and S.-S. Xue, Phys. Rev. D **97,** 064038 (2018).

[50] R. D. Blandford and R. L. Znajek, Mon. Not. R. Astron. Soc. **179,** 433 (1977).

[51] P. A. Sturrock, Astrophys. J. **164,** 529 (1971).

[52] M. A. Ruderman and P. G. Sutherland, Astrophys. J. **196,** 51 (1975).

[53] K. S. Thorne and D. MacDonald, Mon. Not. R. Astron. Soc. **198,** 339 (1982).

[54] R. S. Hanni and R. Ruffini, Phys. Rev. D **8,** 3259 (1973).

[55] G. Miniutti and R. Ruffini, Nuovo Cimento B Ser. **115**, 751 (2000).

[56] B. Punsly, *Black Hole Gravitohydromagnetics*, Vol. 355 (Springer-Verlag Berlin Heidelberg, 2008).

[57] S. S. Komissarov, Mon. Not. R. Astron. Soc. **359**, 801 (2005).

[58] K. Parfrey, A. Philippov, and B. Cerutti, Phys. Rev. Lett. **122**, 035101 (2019).

[59] T. Damour and R. Ruffini, Phys. Rev. D **14**, 332 (1976).

[60] R. Ruffini and J. A. Wheeler, Phys. Today **24**, No. 1, 30 (1971).

[61] R. Ruffini, D. J. Song, and S. Taraglio, Astron. Astrophys. **190**, 1 (1988).

[62] P. Chen and R. Ruffini, Astronomy Reports **59**, 469 (2015).

Astronomy & Astrophysics

The newborn black hole in GRB 191014C proves that it is alive

R. Moradi[1,2,3], J. A. Rueda[1,2,4,5,6], R. Ruffini[1,2,7], and Y. Wang[1,2,3]

[1] ICRANet, Piazza della Repubblica 10, 65122 Pescara, Italy
e-mail: `rahim.moradi@icranet.org, jorge.rueda@icra.it, ruffini@icra.it`
[2] ICRA, Dipartimento di Fisica, Sapienza Università di Roma, P.le Aldo Moro 5, 00185 Rome, Italy
[3] INAF, Osservatorio Astronomico d'Abruzzo, Via M. Maggini snc, 64100 Teramo, Italy
[4] ICRANet-Ferrara, Dipartimento di Fisica e Scienze della Terra, Università degli Studi di Ferrara, Via Saragat 1, 44122 Ferrara, Italy
[5] Dipartimento di Fisica e Scienze della Terra, Università degli Studi di Ferrara, Via Saragat 1, 44122 Ferrara, Italy
[6] INAF, Istituto de Astrofisica e Planetologia Spaziali, Via Fosso del Cavaliere 100, 00133 Rome, Italy
[7] INAF, Viale del Parco Mellini 84, 00136 Rome, Italy

ABSTRACT

A multi-decade theoretical effort has been devoted to finding an efficient mechanism to use the rotational and electrodynamical extractable energy of a Kerr-Newman black hole (BH), to power the most energetic astrophysical sources such as gamma-ray bursts (GRBs) and active galactic nuclei. We show an efficient general relativistic electrodynamical process which occurs in the "inner engine" of a binary driven hypernova. The inner engine is composed of a rotating Kerr BH of mass M and dimensionless spin parameter α, a magnetic field of strength B_0 aligned and parallel to the rotation axis, and a very low-density ionized plasma. Here, we show that the gravitomagnetic interaction between the BH and the magnetic field induces an electric field that accelerates electrons and protons from the environment to ultrarelativistic energies emitting synchrotron radiation. We show that in GRB 190114C the BH of mass $M = 4.4\,M_\odot$, $\alpha = 0.4$, and $B_0 \approx 4 \times 10^{10}$ G can lead to a high-energy ($\gtrsim$GeV) luminosity of 10^{51} erg s^{-1}. The inner engine parameters are determined by requiring (1) that the BH extractable energy explains the GeV and ultrahigh-energy emission energetics, (2) that the emitted photons are not subjected to magnetic-pair production, and (3) that the synchrotron radiation timescale agrees with the observed high-energy timescale. We find for GRB 190114C a clear jetted emission of GeV energies with a semi-aperture angle of approximately 60° with respect to the BH rotation axis.

Key words. black hole physics – magnetic fields – gamma-ray burst: individual: GRB 190114C – gamma-ray burst: general

1. Introduction

Rotating black holes (BHs) have traditionally been described by the Kerr (Kerr 1963) and the Kerr-Newman metrics (Newman et al. 1965) which assume three conditions: (i) they are in a matter vacuum, (ii) they are embedded in an asymptotically flat spacetime, and (iii) they fulfill global stationarity. Under these conditions, BHs are just a sink of energy, namely "dead BHs". The discovery of the reversible and irreversible transformations in both these spacetimes (Christodoulou 1970; Christodoulou & Ruffini 1971) opened the conceptual possibility of extracting both rotational and electromagnetic energy from a Kerr-Newman BH. These results also led to the asymptotic mass-energy formula relating the mass M of a BH to three independent parameters, the irreducible mass $M_{\rm irr}$, the charge Q, and the angular momentum J, soon confirmed by Hawking (1972). The perspective that up to 50% of the mass-energy of a Kerr-Newman BH could be extracted directed the attention to the alternative view of "alive BHs" whose extractable energy could be used as an astrophysical source (see, e.g., "Introducing the black hole" Ruffini & Wheeler 1971a and "On the energetics of black holes" by R. Ruffini in DeWitt & DeWitt 1973).

Since then an efficient process has been sought that is able to power the most energetic astrophysical sources, gamma-ray bursts (GRBs), and active galactic nuclei (AGNs), using the extractable energy from a BH. The theoretical framework has

been constantly evolving (see, e.g., Tursunov & Dadhich 2019, for a review on this topic). As we show in this paper, the recent discovery of the birth of a BH in GRB 130427A (Ruffini et al. 2019a; Rueda & Ruffini 2020) demonstrates that the Kerr BH harbored in the inner engine of this source is indeed an enormous source of giga-electron volt (GeV) energy. The main topic of this article is to reach a deeper understanding of the process of rotational energy extraction by further identifying the astrophysical setting, the boundary conditions, and the basic new physical laws that allow this process to become observable. Specifically, for the case of GRB 190114C, our goal is to infer the values of the independent physical component, the spectral distribution of the high-energy GeV emission, and the geometrical properties of the GeV and ultrahigh-energy emissions.

Our approach is based on the binary-driven hypernova (BdHN) model of long GRBs (Rueda & Ruffini 2012; Fryer et al. 2014; Becerra et al. 2016; Ruffini et al. 2019a). The BdHN progenitor is a binary system composed of a carbon-oxygen (CO) star and a neutron star (NS) companion. The collapse of the iron core of the evolved CO star forms a newborn NS (νNS) at its center and expels the stellar outermost layers, hence leading to a supernova (SN) explosion. The SN ejecta produces a hypercritical accretion process both onto the νNS and onto the NS companion. For very compact binaries (orbital period on the order of 5 min), the NS companion reaches the critical mass rapidly (a few seconds), undergoes gravitational collapse,

and forms a rotating BH. We have called these long GRBs in which there is BH formation, BdHNe of type I (BdHN I). Their isotropic energy release is in the range $10^{53}-10^{54}$ erg. Numerical simulations of the above process in one, two, and three dimensions have been presented in Fryer et al. (2014), Becerra et al. (2015, 2016, 2019), respectively. Only a fraction of BdHNe form BHs (380 BdHNe I have been identified; see Ruffini et al. 2021). In progenitors with longer binary periods, on the order of hours, no BHs are formed; the outcome is a binary NS with long GRBs in the range $10^{51}-10^{53}$ erg (Wang et al. 2019). For even longer binary periods, on the order of days, even less energetic long GRBs are encountered, the BdHNe III, for example the case of GRB 060218 (Liang et al., in prep.).

We now return to GRB 190114C. It has already been shown that the collapse of the CO star, which triggers the complete GRB process in the presence of a binary NS companion, leads to a SN creating an additional NS (i.e., the νNS). The SN process is observed earlier at X-ray (up to a few keV) and soft gamma-ray (up to a few MeV) wavelengths, and it has been referred to as "SN-rise" (see, e.g., Wang et al. 2019). For GRB 190114C this occurs in the rest-frame interval $t_{\rm rf} \lesssim 1.99\,$s. It carries an energy of $E_{\rm SN-rise} = 2.82 \times 10^{52}$ erg and is characterized by a blackbody plus cutoff power-law spectrum (Liang et al. 2019). The short duration of the SN-rise finds a natural explanation in the BdHN model. In a BdHN I the companion NS is separated at only $10^{10}-10^{11}$ cm (i.e., about 1 light-second) from the CO star, implying that only the first spike becomes observable before the expanding SN ejecta triggers the hypercritical accretion process onto the NS companion (see, e.g., Becerra et al. 2019; Wang et al. 2019).

The newborn BH is embedded in the magnetic field inherited from the NS (Rueda et al. 2020), and sits at the center of a cavity of very low density (see Ruffini et al. 2019b, for numerical simulations) of material from the SN ejecta. For GRB 190114C such a density has been estimated to be on the order of $10^{-14}\,{\rm g\,cm^{-3}}$. The cavity is carved during the accretion and subsequent gravitational collapse of the NS leading to the BH. The magnetic field remains anchored to material that did not participate in the BH formation (see Rueda et al. 2020 for a detailed discussion on the magnetic field around the newborn Kerr BH in a BdHN I).

The Kerr BH in the cavity is therefore not isolated and acts in conjunction with a test magnetic field of strength B_0, aligned with the BH rotation axis. An additional important feature is that there is no vacuum surrounding the BH. As we show in this article, a fully ionized, very low-density plasma is essential to allow the electrodynamical performance of the energy extraction process by the inner engine, which is necessarily non-stationary.

The operation procedure of the inner engine leads the mass and spin of the BH to decrease as functions of time, while the BH irreducible mass ($M_{\rm irr}$) remains constant. The electrons accelerate to ultrahigh energies at the expense of the BH extractable energy[1]

$$E_{\rm extr} \equiv (M - M_{\rm irr})c^2,\tag{1}$$

obtainable from the BH mass-energy formula (Christodoulou 1970; Christodoulou & Ruffini 1971; Hawking 1971)

$$M^2 = \frac{c^2}{G^2}\frac{J^2}{4M_{\rm irr}^2} + M_{\rm irr}^2,\tag{2}$$

where J and M are respectively the angular momentum and the mass of the BH.

As we explain in this article, using the mathematical role of the Papapetrou-Wald solution (Papapetrou 1966; Wald 1974), a profound change of paradigm in relativistic astrophysics has been made possible by the inner engine (Ruffini et al. 2019a), namely the introduction of the effective charge given by the product of J and B_0:

$$Q_{\rm eff} = \frac{G}{c^3}2JB_0.\tag{3}$$

This effective charge originates from the gravitomagnetic interaction of the Kerr BH with the surrounding magnetic field, left over by the collapse of the accreting NS to the BH still rooted in the surrounding material (see, e.g., Rueda et al. 2020). The existence of this effective charge finally explains the success of utilizing the concept of a Kerr-Newman BH as a temporary step to approach the analysis of quantum electrodynamical processes in the field of a rotating BH (see, e.g., Damour & Ruffini 1975).

We are now able to elaborate, with the use of quantum electrodynamics and general relativity, a novel and physically more complete treatment of the GRB high-energy engine in a globally neutral system, therefore satisfying Eq. (2). Starting from these general premises, the main focus of this article is the role of the newborn BH in giving origin to the GeV emission observed by *Fermi*-LAT in the context of the inner engine of a BdHN I. In Sect. 2 we mathematically describe the electromagnetic field surrounding the Kerr BH following the Papapetrou-Wald solution of the Einstein-Maxwell equations (Papapetrou 1966; Wald 1974). Section 3 summarizes the operation of the inner engine, including its energy budget and electric potential energy available for the acceleration of charged particles around the BH. The particle motion along the BH rotation axis and its relation to the inner engine contribution to ultrahigh-energy cosmic rays (UHECRs) is presented in Sect. 4. In Sect. 5 we estimate the energy loss by synchrotron radiation for electrons moving outside the BH rotation axis. We obtain there the typical electron Lorentz factor, the corresponding pitch angles leading to high-energy ($\gtrsim$GeV) photons, and the radiation timescale. Section 6 presents an estimate of the energy and angular momentum extracted to the Kerr BH in the emission process, in the radiation timescale, implied by the BH mass-energy formula. In Sect. 7 we present our method of inferring the inner engine parameters, namely the BH mass and spin, and the magnetic field strength from the three conditions required (the observed high-energy emission covered by the extractable energy of the BH, the observed high-energy luminosity equal to the synchrotron radiation value, the emitted high-energy photons able to freely escape from the system). In Sect. 8 we apply this framework to the case of GRB 190114C obtaining the corresponding inner engine parameters. Section 9 is dedicated to a comparison of our results with previous literature results. Finally, we outline the conclusions in Sect. 10.

2. Electric and magnetic fields around the BH

Following the considerations presented in Ruffini et al. (2015, 2019a) corresponding to GRB 130427A, we turn to a quantitative estimate of the inner engine via a solution of the Einstein-Maxwell equations of a Kerr BH embedded in a test, asymptotically aligned, uniform magnetic field (Papapetrou 1966; Wald 1974), hereafter the Papapetrou-Wald solution.

---

[1] We use cgs-Gaussian units throughout, unless otherwise specified. Careted symbols stand for quantities in geometric units; for example, $\hat{M} \equiv GM/c^2$ denotes geometric mass. See Table 1 for details on the units and conversion factors between the cgs-Gaussian and geometric systems of units.

Table 1. Units of the relevant physical quantities used in this article in the cgs-Gaussian and geometric system of units.

	cgs-Gaussian	Geometric	cgs to geometric
M	g	cm	$G/c^2 = 7.425 \times 10^{-29}$ cm g^{-1}
Q	cm$^{3/2}$ g$^{1/2}$ s^{-1} (statC)	cm	$G^{1/2}/c^2 = 2.874 \times 10^{-25}$ cm$^{-1/2}$ g$^{-1/2}$ s
J	g cm^2 s^{-1}	cm^2	$G/c^3 = 2.477 \times 10^{-39}$ g^{-1} s
Φ	cm^2 g s^{-2} (erg)	cm	$G/c^4 = 8.261 \times 10^{-50}$ cm^{-1} g^{-1} s^2
ϕ	cm$^{1/2}$ g$^{1/2}$ s^{-1} (statV)	cm^0	$G^{1/2}/c^2 = 2.874 \times 10^{-25}$ cm$^{-1/2}$ g$^{-1/2}$ s
E	cm$^{-1/2}$ g$^{1/2}$ s^{-1} (statV cm^{-1})	cm^{-1}	$G^{1/2}/c^2 = 2.874 \times 10^{-25}$ cm$^{-1/2}$ g$^{-1/2}$ s
B	cm$^{-1/2}$ g$^{1/2}$ s^{-1} (gauss, G)	cm^{-1}	$G^{1/2}/c^2 = 2.874 \times 10^{-25}$ cm$^{-1/2}$ g$^{-1/2}$ s

Notes. M mass, Q charge, J angular momentum, Φ electric potential energy, ϕ electric potential, E electric field, B magnetic field. We use length (cm) as the base unit in the geometric system.

The BH rotation and the aligned magnetic field induce an electric field with the following radial and polar components:

$$E_{\hat{r}} = \frac{B_0 \hat{a}\hat{M}}{\Sigma^2 A^{1/2}} \left[2r^2 \sin^2\theta\, \Sigma - (r^2 + \hat{a}^2)(r^2 - \hat{a}^2\cos^2\theta)(1 + \cos^2\theta) \right],$$
(4a)

$$E_{\hat{\theta}} = B_0 \hat{a}\hat{M} \frac{\Delta^{1/2}}{\Sigma^2 A^{1/2}} 2\, r\, \hat{a}^2 \sin\theta\cos\theta\, (1 + \cos^2\theta).$$
(4b)

The magnetic field components are

$$B_{\hat{r}} = \frac{B_0 \cos\theta}{\Sigma^2 A^{1/2}} \left\{ (r^2 + \hat{a}^2)\Sigma^2 - 2\hat{M}r\hat{a}^2[2r^2\cos^2\theta + \hat{a}^2(1 + \cos^4\theta)] \right\},$$
(5a)

$$B_{\hat{\theta}} = -\frac{\Delta^{1/2}}{\Sigma^2 A^{1/2}} B_0 \sin\theta\, [\hat{M}\hat{a}^2(r^2 - \hat{a}^2\cos^2\theta)(1 + \cos^2\theta) + r\Sigma^2],$$
(5b)

where $\Sigma = r^2 + \hat{a}^2\cos^2\theta$, $\Delta = r^2 - 2\hat{M}r + \hat{a}^2$, $A = (r^2 + \hat{a}^2)^2 - \Delta\hat{a}^2\sin^2\theta$, and $\hat{M} = GM/c^2$ and $\hat{a} = \hat{J}/\hat{M} = (GJ/c^3)/(GM/c^2) = J/(Mc)$ are respectively the geometric mass and specific angular momentum of the BH (see Table 1).

We here use the locally non-rotating observer, also known as zero angular momentum observer (ZAMO; see Bardeen 1970; Bardeen et al. 1972). Therefore, the electromagnetic field components ((4a), (4b) and (5a), (5b)) differ from those presented in Ruffini et al. (2019a), where the Carter's observer was used.

For moderate dimensionless spin values, $\alpha \lesssim 0.7$, where $\alpha \equiv \hat{a}/\hat{M} = cJ/(GM^2)$, the electric and magnetic fields are accurately represented by the first-order expansion ($\alpha \ll 1$ or $\hat{a} \ll \hat{M}$):

$$E_{\hat{r}} \approx -\frac{B_0 \hat{a}\hat{M}}{r^2}(3\cos^2\theta - 1), \quad E_{\hat{\theta}} \approx 0,$$
(6a)

$$B_{\hat{r}} \approx B_0 \cos\theta, \quad B_{\hat{\theta}} \approx -B_0 \sqrt{1 - \frac{2\hat{M}}{r}} \sin\theta.$$
(6b)

Thus, the electric field is mainly radial and inwardly directed. The electric field decreases with the square of the distance; therefore, it is maximum at the BH horizon, $r_+ = \hat{M}(1 + \sqrt{1 - \alpha^2})$, and on the rotation axis $\theta = 0$, so $E_{\hat{r},\max} = -2B_0\hat{a}/r_+^2 = -\alpha B_0/2$. The electric field vanishes for $3\cos^2\theta_\pm - 1 = 0$. Therefore, it is inwardly directed in the northern hemisphere for spherical polar angles (measured clockwise) $-\theta_\pm < \theta < \theta_\pm$, where $\theta_\pm = \arccos(\sqrt{3}/3) \approx 55°$ (see Eqs. (6a), (6b) and Fig. 1). Because of the equatorial symmetry it also points inward in the southern hemisphere for $\pi - \theta_\pm < \theta < \pi + \theta_\pm$. In these regions, electrons are outwardly accelerated. In the remaining regions the
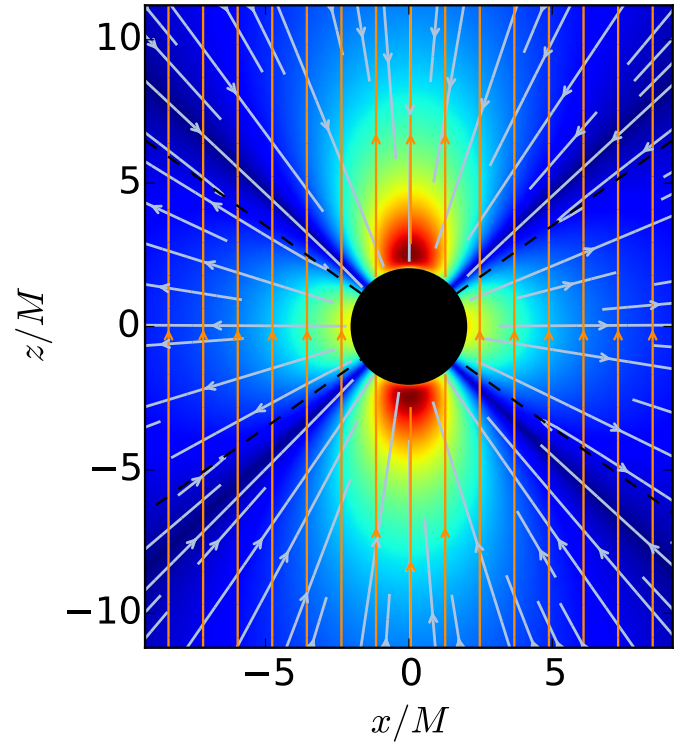

Fig. 1. Electric (blue lines) and magnetic (golden lines) field lines of the Papapetrou-Wald solution in the xz-plane in Cartesian coordinates. The BH spin parameter is set to $a/M = 0.3$ and the magnetic field and the BH spin are aligned and parallel. The background is a density-plot of the electric field energy density which is decreasing from red to blue. The BH horizon is the black disk. Distances are in units of M and the fields in units of B_0. Outward electron acceleration occurs in the region limited by the dashed black lines, i.e., where the electric field is inwardly directed. In the northern hemisphere it covers spherical polar angles (measured clockwise) $-\theta_\pm < \theta < \theta_\pm$, where $\theta_\pm \approx 55°$. By equatorial symmetry, in the southern hemisphere, it covers $\pi - \theta_\pm < \theta < \pi + \theta_\pm$.

electric field reverses sign, becoming outwardly directed (see Fig. 1). The value of $\theta_\pm$ is indeed accurately given by the slow-rotation approximation; for instance, a numerical calculation shows that $\theta_\pm \approx 54.74°-59.76°$ for $\alpha = 0.01-0.99$. We show below in this article that, the electrons located in these northern and southern hemisphere cones of semi-aperture angle of $\approx 60°$, are outwardly accelerated with the appropriate pitch angles leading to GeV photons (see Sect. 5 and Fig. 2 for details). Clearly, being anisotropic, this "jetted" emission is not always visible.

This feature has been crucial for the inference of the morphology of the BdHN I from the high-energy (GeV) data of long GRBs (Ruffini et al. 2021).

It can be also seen that the magnetic field is everywhere nearly aligned with the BH rotation axis; at any distance we have $B_z \gg B_x \sim B_y$, and at distances $r \gg 2\hat{M}$ it is perfectly aligned (i.e., $B_x \to 0$, $B_y \to 0$, and $B_z \to B_0$). All these features can be seen in Fig. 1, which shows the electric and magnetic field lines given by the general expressions given by Eqs. (4a), (4b) and (5a), (5b).

3. Operation of the inner engine

The operation of the inner engine is based on three components naturally present in a BdHN I:

- the Kerr metric that describes the gravitational field produced by the newborn rotating BH;
- an asymptotically uniform magnetic field around the newborn BH fulfilling the Papapetrou-Wald solution (see Sect. 2);
- a very low-density plasma around the newborn BH composed of ions and electrons of $10^{-14}\,\mathrm{g\,cm^{-3}}$ (Ruffini et al. 2019b).

The inner engine operation follows these precise steps:

1. The magnetic field and the BH rotation induce an electric field as given by the Papapetrou-Wald solution (see Sect. 2). For an aligned and parallel magnetic field to the BH spin, the electric field is nearly radial and inwardly directed at, and about, the BH rotation axis within an angle $\theta_\pm$ (see Fig. 1).
2. The induced electric field accelerates electrons outwardly. The number of electrons that can be accelerated is set by the energy stored in the electric field Rueda & Ruffini (2020):

$$\mathcal{E} \approx \frac{1}{2}E_{\hat{r}}^2 r_+^3 = \hbar\,\Omega_{\mathrm{eff}}, \tag{7a}$$

$$\Omega_{\mathrm{eff}} = 4\left(\frac{m_{\mathrm{Pl}}}{m_{\mathrm{n}}}\right)^8 \left(\frac{B_0^2}{\rho_{\mathrm{Pl}}}\right)\alpha\,\Omega_+. \tag{7b}$$

Here $\Omega_+ = c^2 \partial M/\partial J = c\,\alpha/(2\,r_+)$ is the so-called BH angular velocity; m_{n} the neutron mass; and $\rho_{\mathrm{Pl}} \equiv m_{\mathrm{Pl}}c^2/\lambda_{\mathrm{Pl}}^3$, $\lambda_{\mathrm{Pl}} = \hbar/(m_{\mathrm{Pl}}c)$, and $m_{\mathrm{Pl}} = \sqrt{\hbar c/G}$ are respectively the Planck energy-density, length, and mass. These expressions evidence the nature of the underlying physical process generating the electric field and the BH horizon: the electrodynamics of the Papapetrou-Wald solution (Ruffini et al. 2019a), the origin of its magnetic field from the binary NS companion (Rueda et al. 2020), and the smooth formation of the BH from the induced gravitational collapse process (Rueda & Ruffini 2012). Additional details on the above formulation are presented in Rueda & Ruffini (2020).

3. The maximum possible electron acceleration and energy is set by the electric potential energy difference from the horizon to infinity can be written as (Rueda & Ruffini 2020)

$$\Delta\Phi = \frac{1}{c}e\,a\,B_0, = \hbar\,\omega_{\mathrm{eff}}, \tag{8a}$$

$$\omega_{\mathrm{eff}} = \frac{G}{c^4}4\left(\frac{m_{\mathrm{Pl}}}{m_{\mathrm{n}}}\right)^4 e\,B_0\,\Omega_+, \tag{8b}$$

where $a = J/M$.

4. Along the polar axis radiation losses are absent (see below in Sect. 4), while at off-axis latitudes (see below in Sect. 5) the

accelerated electrons emit synchrotron radiation. The radiation timescale τ_{rad} must fulfill

$$\tau_{\mathrm{rad}} = \frac{\mathcal{E}}{L_{\mathrm{GeV}}}, \tag{9}$$

where L_{GeV} is the observed GeV luminosity.

5. After this, the energy $\mathcal{E}$ has been used and emitted. The process restarts with a new angular momentum $J = J_0 - \Delta J$, being ΔJ the angular momentum extracted to the Kerr BH by the event (see below Eqs. (19a)–(19c) in Sect. 6).
6. The above steps are repeated, with the same efficiency, if the density of plasma is sufficient, namely if the number of the particles is enough to cover the new value of the energy $\mathcal{E}$. Therefore, the inner engine evolves in a sequence of elementary processes, each emitting a well-defined, precise amount of energy.

For the sake of example, let us chose fiducial parameters $B_0 = 10^{11}$ G, $M = 3\,M_\odot$, and $\alpha = 0.5$. In this case the available energy is $\mathcal{E} \approx 3.39 \times 10^{37}$ erg, and the maximum energy that an accelerated electron can gain is $\Delta\Phi \approx 1.06 \times 10^7$ erg $= 6.64 \times 10^{18}$ eV.

4. Acceleration on the polar axis: Ultrahigh-energy cosmic rays

Along the polar axis, $\theta = 0$, the electric and magnetic fields only have the z-component and are thus parallel; see Eqs. (4a), (4b) and (5a), (5b), or Eqs. (6a) and (6b). Since the electron is accelerated by the electric field, this implies that the electron pitch angle, which is the angle between the electron's injection velocity (into the magnetic field) and the magnetic field, is zero. Consequently, no radiation losses (by synchrotron emission) occur for motion along the BH rotation axis.

The electrons accelerate outward gaining the total electric potential energy, $\Delta\Phi \sim 10^{18}$ eV. Therefore, the maximum number of electrons that the inner engine can accelerate along the axis is

$$N_{\mathrm{pole}} = \frac{\mathcal{E}}{\Delta\Phi} = \frac{\Omega_{\mathrm{eff}}}{\omega_{\mathrm{eff}}} \sim 10^{31}. \tag{10}$$

These ultrarelativistic electrons contribute to leptonic UHE-CRs. The timescale of this acceleration process along the polar axis is

$$\tau_{\mathrm{pole}} \equiv \frac{\Delta\Phi}{eE_{\hat{r}}\,\mathrm{c}} \approx \frac{r_+}{c} = \frac{\alpha}{2\Omega_+} \approx 10^{-5}\,\mathrm{s}. \tag{11}$$

This implies that the inner engine can accelerate electrons along the BH rotation axis at a rate

$$\dot{N}_{\mathrm{pole}} \equiv \frac{N_{\mathrm{pole}}}{\tau_{\mathrm{pole}}} \sim 10^{36}\,\mathrm{s}^{-1}, \tag{12}$$

leading to a power

$$\dot{\mathcal{E}}_{\mathrm{pole}} = \dot{N}_{\mathrm{pole}}\Delta\Phi = \frac{\mathcal{E}}{\tau_{\mathrm{pole}}} \sim 10^{54}\,\mathrm{eV\,s}^{-1} \approx 10^{42}\,\mathrm{erg\,s}^{-1}. \tag{13}$$

Since the electric and magnetic fields along the rotation axis (and nearly close to it) are parallel (see Fig. 1), the particles in that region are all accelerated (nearly) parallel to the BH rotation axis. Therefore, we do not expect the accelerated particles to have appreciable collisions able to reduce the above estimate of their maximum kinetic energy gain. Therefore, $\dot{\mathcal{E}}_{\mathrm{pole}}$ given by Eq. (13) is the maximum power available for UHECRs.

Table 2. Some astrophysical properties of the inner engine for GRB 190114C and AGN, in the latter adopting as a proxy M 87* (Rueda & Ruffini 2020).

	GRB 190114C	AGN (M 87*-like)
M ($M_\odot$)	4.4	6.0×10^9
α	0.4	0.1
B_0 (G)	4.0×10^{10}	10
τ_{pole}	4.33×10^{-5} s	0.68 d
$\Delta\Phi$ (eV)	3.12×10^{18}	2.66×10^{17}
$\mathcal{E}$ (erg)	7.02×10^{37}	6.96×10^{44}
$\dot{\mathcal{E}}_{\text{pole}}$ (erg s^{-1})	1.62×10^{42}	1.18×10^{40}
χ ($^\circ$)	$0.1805 - 18.05$	$0.0451 - 4.51$
t_{c} (s)	$1.45 \times 10^{-16} - 1.45 \times 10^{-14}$	$0.2939 - 29.39$
L_{GeV} (erg s^{-1})	$4.83 \times 10^{51} - 4.83 \times 10^{53}$	$2.37 \times 10^{43} - 2.37 \times 10^{45}$

Notes. The timescale of particle acceleration along the BH rotation axis τ_{pole} is given by Eq. (11); the maximum energy gained in such acceleration $\Delta\Phi$ is given by Eqs. (8a) and (8b). The energy $\mathcal{E}$ available for acceleration and radiation is given by Eqs. (7a) and (7b). The maximum power available for acceleration (i.e., to power UHECRs) is $\dot{\mathcal{E}}_{\text{pole}}$ and is given by Eq. (13). The pitch angle χ is computed from Eq. (16) adopting the photon energy range $0.1-1$ GeV photons; the corresponding synchrotron radiation timescale t_{c} is given by Eq. (18), and an estimate of the associated GeV luminosity, $L_{\text{GeV}} \sim \mathcal{E}/t_{\text{c}}$, is also shown. In both cases the corresponding inner engine parameters (BH mass M, spin α, and surrounding magnetic field strength B_0) have been fixed to explain the observed high-energy ($\gtrsim$GeV) luminosity (see Sect. 7 for the case of GRB 190114C and Rueda & Ruffini 2020 for M 87*).

The extension of the considerations presented here to very massive BHs and AGN, the role of the accretion disk in these galactic configurations, and the possibility of accelerating protons to produce UHECRs by the BH have started to be addressed (Rueda & Ruffini 2020). We compare and contrast in Table 2 some of the inner engine physical properties applied to the case of GRB 190114C and to M 87*.

5. Acceleration at off-axis latitudes: Synchrotron radiation

For the present electric field, and assuming radial motion, the dynamics of the electrons in the electromagnetic field, for $\gamma \gg 1$, is determined from (de Jager et al. 1996; Ruffini et al. 2019a)

$$m_{\text{e}} c^2 \frac{\text{d}\gamma}{\text{d}t} = e \frac{1}{2} \alpha B_0 \, c - \frac{2}{3} e^4 \frac{B_0^2 \sin^2 \langle \chi \rangle}{m_{\text{e}}^2 c^3} \gamma^2, \qquad (14)$$

where e is the elementary charge, γ is the electron Lorentz factor, $\langle \chi \rangle$ is the injection angle between the direction of electron motion and the magnetic field (the pitch angle), and m_{e} is the electron mass. This equation is integrated assuming the electrons are injected near the horizon (where the electric field strength is $\alpha B_0/2$), for selected values of the injection angle $\langle \chi \rangle$, with an initial Lorentz factor $\gamma = 1$ at $t = 0$.

The synchrotron spectrum peaks roughly at the photon critical energy (see, e.g., Landau & Lifshitz 1975)

$$\epsilon_\gamma = \frac{3e\hbar}{2m_{\text{e}}\,c} B_0 \sin \langle \chi \rangle \gamma^2 = \frac{3}{2} m_{\text{e}} c^2 \beta \sin \langle \chi \rangle \gamma^2, \qquad (15)$$

where in the last expression we introduced $\beta = B_0/B_{\text{c}}$, with $B_{\text{c}} = m_{\text{e}}^2 c^2/(e\hbar) \approx 4.41 \times 10^{13}$ G. Therefore, the synchrotron peak energy shifts from lower to higher energies (soft-to-hard spectral evolution) as the electron accelerates. For example, the photon critical energy ϵ_γ, for $\gamma \gtrsim 10^3$, a magnetic field $B_0 = 10^{11}$ G (so $\beta = 0.0023$), and a pitch angle $\chi = 10°$ falls in the GeV regime.

During the acceleration, the Lorentz factor increases linearly with time up to an asymptotic maximum value (see Ruffini et al.

2019a, for details). This maximum value, set by the balance between the energy gain by acceleration in the electric field and energy loss by synchrotron radiation, is (Ruffini et al. 2019a)

$$\gamma_{\text{max}} = \frac{1}{2} \left[\frac{3}{e^2/(\hbar c)} \frac{\alpha}{\beta \sin^2 \langle \chi \rangle} \right]^{1/2}, \qquad (16)$$

which defines the maximum electron energy $\epsilon_{\text{e}} = \gamma_{\text{max}} m_{\text{e}} c^2$. Associated with γ_{max}, by replacing Eq. (16) into (15) we obtain the maximum peak energy of the spectrum (Ruffini et al. 2019a)

$$\epsilon_{\gamma,\text{max}} = \frac{9}{8} \frac{m_{\text{e}} c^2}{e^2/\hbar c} \frac{\alpha}{\sin \langle \chi \rangle} \approx \frac{78.76}{\sin \langle \chi \rangle} \alpha \, \text{MeV}, \qquad (17)$$

and the synchrotron cooling timescale $t = t_{\text{c}}$ for the above maximum photon critical energy is given by (Ruffini et al. 2019a)

$$t_{\text{c}} = \frac{\hbar}{m_{\text{e}} c^2} \frac{3}{\sin \langle \chi \rangle} \left(\frac{e^2}{\hbar c} \alpha \beta^3 \right)^{-1/2}. \qquad (18)$$

For model parameters $\alpha = 0.5$ and $B_0 = 10^{11}$ G, photons of energy $0.1-10$ GeV (typical photon energy range detected by the *Fermi*-LAT) are emitted by electrons with pitch angles $\chi \approx 0.23-23°$, and electron energy $\epsilon_{\text{e}} = 1.98 \times 10^8 - 1.98 \times 10^{10}$ eV, radiating on a timescale of $t_{\text{c}} = 2.63 \times 10^{-17} - 2.63 \times 10^{-15}$ s. We show in Fig. 2 the pitch angle χ as a function of the maximum photon critical energy (spectrum peak energy) $\epsilon_{\gamma,\text{max}}$, obtained from Eq. (17), in the energy range $0.1-10$ GeV, and for three selected values of α. Figure 3 shows the contours of constant χ for electrons moving in the electromagnetic field of the Papapetrou-Wald solution shown in Fig. 1. In particular, we show pitch angles for which electrons emit photons of GeV energies (see also Fig. 2). It can be seen that this high-energy jetted emission occurs within an effective opening angle $\theta_\pm \approx 60°$. This anisotropic emission is essential to infer the BdHN I morphology from the GeV emission data of long GRBs (Ruffini et al. 2021).
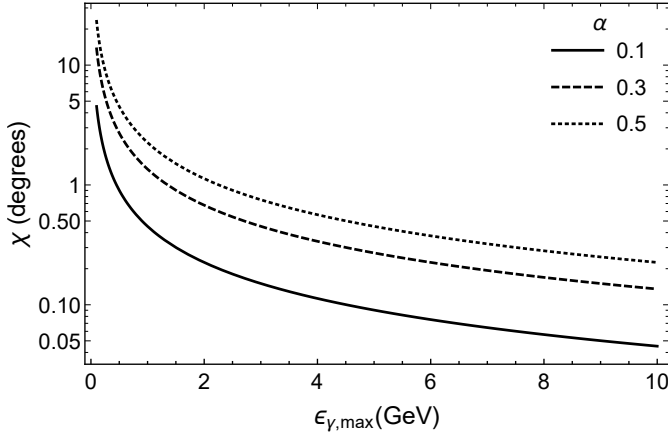
Fig. 2. Pitch angle χ (in units of degrees) as a function of the photon critical energy ϵ_γ (in units of GeV) obtained from Eq. (17). The focus of the plot for photon critical energy is in the range $0.1-10$ GeV. The solid, dashed, and dotted curves correspond to selected values of the BH spin parameter $\alpha = 0.1$, 0.3, and 0.5, respectively.

6. Energy and angular momentum extraction, golden rule, and duration of the inner engine activity

At the end of every elementary process, all the energy $\mathcal{E}$ has been emitted. The inner engine restarts its operation with the same magnetic field of B_0, but with a new slightly smaller angular momentum $J = J_0 - \Delta J$, being ΔJ the angular momentum extracted by the process. From the BH mass-formula (2), keeping the irreducible mass constant (i.e., $\Delta M_{\rm irr} = 0$, and $\Delta M c^2 = \mathcal{E}$), we obtain a change in the BH angular momentum ΔJ in each event:

$$J_{\rm eff} = I_{\rm eff}\Omega_{\rm eff}, \quad I_{\rm eff} = M\left(\frac{2GM_{\rm irr}}{c^2}\right)^2, \tag{19a}$$

$$\Delta J = \frac{J_{\rm eff}}{J}\hbar, \tag{19b}$$

$$\Delta J = \frac{1}{\bar{\Omega}}\Delta E, \quad \bar{\Omega} \equiv \frac{J}{I_{\rm eff}}, \quad \Delta E \equiv \mathcal{E}. \tag{19c}$$

Here the last equation, a truly golden formula, relates the energy radiated ($\Delta E = \mathcal{E}$) to the angular momentum extracted to the rotating BH (ΔJ).

For the fiducial parameters that we used above, $M = 3\,M_\odot$, $\alpha = 0.5$, and $B_0 = 10^{11}$ G, we have $J \approx 3.96 \times 10^{49}$ g cm^2 s^{-1}, $M_{\rm irr} \approx 2.9\,M_\odot$, and $\Delta J \approx 1.0 \times 10^{33}$ g cm^2 s^{-1}, so a fractional change $\Delta J/J \approx 10^{-16}$, implying that the activity can last for thousands of years or more, providing there is ionized plasma to feed the inner engine.

7. Inference of the BH mass, spin, and surrounding magnetic field

We require three physical and astrophysical conditions to obtain the three inner engine parameters, the BH mass and spin, M and α, and the strength of the magnetic field surrounding the BH, B_0. Following Ruffini et al. (2019a), who show that the use of solely the GeV emission data, after the ultrarelativistic prompt emission (UPE) phase (see Liang et al. 2019), is enough to determine the inner engine parameters (see Fig. 4). In particular, we show that this procedure serves to obtain a lower limit to the mass
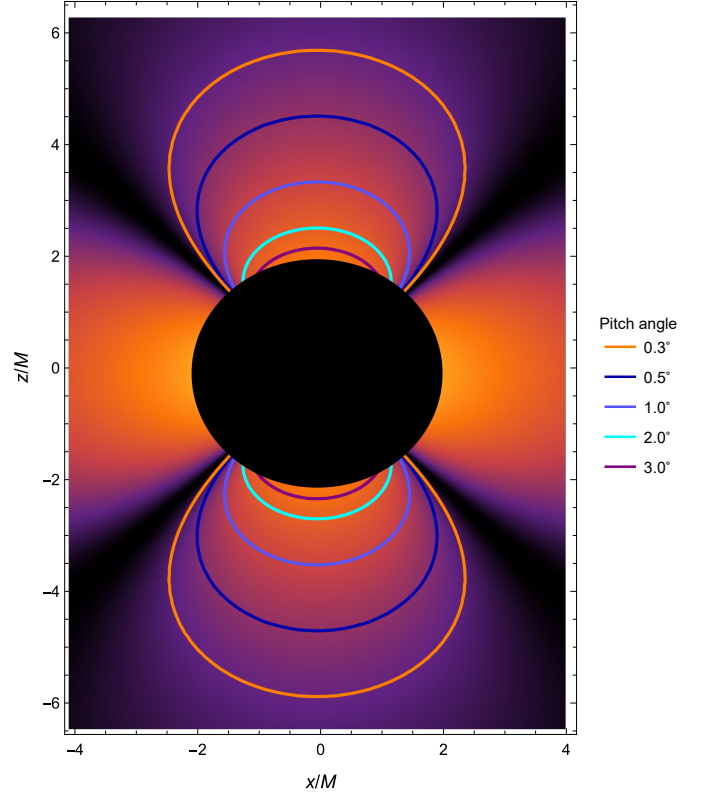
Fig. 3. Contours of constant pitch angle (χ) of electrons moving in the electromagnetic field of the Papapetrou-Wald solution shown in Fig. 1. For the present magnetic dominated case ($|\boldsymbol{E}|/|\boldsymbol{B}| < 1$), charged particles follow the magnetic field lines; therefore, $\sin\chi = |\boldsymbol{B}|^{-1}\sqrt{(\boldsymbol{E}+\boldsymbol{v}\times\boldsymbol{B}/c)^2 - (\boldsymbol{v}\cdot\boldsymbol{E})^2/c^2} \approx \sqrt{|\boldsymbol{E}|^2/|\boldsymbol{B}|^2 - |\boldsymbol{E}_\parallel|^2/|\boldsymbol{B}|^2} \approx |\boldsymbol{E}|/|\boldsymbol{B}|\sin\Psi$ (see, e.g., Kelner et al. 2015), where $\boldsymbol{E}_\parallel$ is the electric field component parallel to the magnetic field, and Ψ is the angle between $\boldsymbol{B}$ and $-\boldsymbol{E}$ (the minus sign is used because we are interested in the pitch angle of electrons). In the slow-rotation regime (see Eqs. (6a) and (6b)), $\sin\Psi \approx \sin\theta/(1-2M\sin^2\theta/r)$, so $\sin\chi \approx |\boldsymbol{E}|/|\boldsymbol{B}|\sin\theta/(1-2M\sin^2\theta/r)$. The BH is indicated by the black disk. The background color map indicates the electric field energy density (lighter colors means more intense).

and spin of the BH. The most important point is that we obtain the value of the irreducible mass of the BH that is kept constant through the energy extraction process. This allows us to determine the time evolution of the BH mass and spin. This can be achieved by fulfilling the three following conditions.

7.1. Condition 1

First, we require that the rotational energy of the BH provides the energy budget for the observed GeV emission energetics,

$$E_{\rm extr} \geq E_{\rm GeV}, \tag{20}$$

which via Eqs. (1) and (2) leads to the following inequality between M, α, and $E_{\rm GeV}$:

$$M \geq \frac{1}{\eta}\frac{E_{\rm GeV}}{c^2}, \quad \eta \equiv 1 - \sqrt{\frac{1+\sqrt{1-\alpha^2}}{2}}. \tag{21}$$

We recall that the maximum value of the efficiency parameter is $\eta_{\rm max} \approx 0.293$, which is attained for a maximally rotating BH, $\alpha_{\rm max} = 1$. It is also important to recall that, by keeping the BH irreducible mass constant in the energy extraction process, we
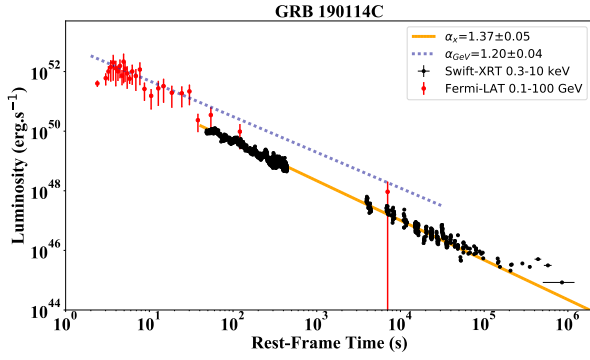
Fig. 4. Red data points: rest-frame $0.1-100$ GeV luminosity light curve of GRB 190114C during and after UPE phase obtained from *Fermi*-LAT. Green dashed line: best fit for power-law behavior of the luminosity following the UPE phase with slope of 1.2 ± 0.04 and amplitude of $7.75 \pm 0.44 \times 10^{52}$ erg s^{-1}. Black data points: rest-frame $0.3-10$ keV luminosity expressed in the rest frame obtained from *Swift*-XRT. It follows a power-law behavior with an amplitude of $A_X = (5.14 \pm 2.03) \times 10^{52}$ erg s^{-1} and a slope of $\alpha_X = 1.37 \pm 0.05$.

are inferring a lower limit to the BH mass. An increasing $M_{\rm irr}$ with time implies a higher BH mass to explain the same GeV energetics.

7.2. Condition 2

We require that the GeV photons must be transparent to the magnetic e^+e^- pair creation process. The attenuation coefficient for this process is (see Daugherty & Harding 1983 and Sect. 5 in Ruffini et al. 2019a)

$$\bar{R} \sim 0.23 \frac{e^2}{\hbar c} \left(\frac{\hbar}{m_e c} \right)^{-1} \beta \sin \langle \chi \rangle \exp \left(-\frac{4/3}{\psi} \right), \qquad (22)$$

where $\psi = \beta \sin \langle \chi \rangle \epsilon_\gamma / (2 m_e c^2)$. Substituting Eq. (17) into Eq. (22), $\bar{R}$ becomes a function of ϵ_γ and the product $\alpha\beta$. For a given ϵ_γ and α, the lower the magnetic field, the larger the mean free path $\bar{R}^{-1}$, as expected. When $\chi \ll 1$, the exponential term dominates, hence $\bar{R}^{-1}$ exponentially increases tending to become infinite. An order-of-magnitude estimate of the magnetic field can be obtained by requiring $\psi \ll 1$,

$$\beta \ll \frac{16}{9} \frac{e^2}{\hbar c} \frac{1}{\alpha} \approx \frac{1.298 \times 10^{-2}}{\alpha}, \quad \text{or} \quad B_0 \ll \frac{5.728 \times 10^{11}}{\alpha} \text{ G}, \qquad (23)$$

which is independent of the photon peak energy. It should be noted that this constraint already restricts the magnetic field to be undercritical ($\beta < 1$), and as we shall see it is sufficient for explaining the GeV emission after the UPE phase. The constraint (23) is analogous to imposing a lower limit on $\bar{R}^{-1}$. For instance, adopting a photon energy of 0.1 GeV, it can be checked that for $\alpha\beta = 1.298 \times 10^{-2}$, the mean free path is $\bar{R}^{-1} = 1.17 \times 10^5$ cm. Lower values of $\alpha\beta$ lead to much larger values of $\bar{R}^{-1}$. It is very interesting that this value is comparable to $GM_\odot/c^2 \approx 1.477 \times 10^5$ cm. Therefore, requesting a value of $\alpha\beta$ lower than the above-mentioned one, implies having a mean free path that is much larger than the BH horizon. Specifically, the high-energy photons are produced in the vicinity of the BH, but they can freely escape from the system. If we adopt as a fiducial value that 0.1 GeV photons have a sufficiently large mean free

path (e.g., $\bar{R}^{-1} \geq 10^{16}$ cm), we obtain (Ruffini et al. 2019a)

$$\beta \leq \frac{3.737 \times 10^{-4}}{\alpha}, \quad \text{or} \quad B_0 \leq \frac{1.649 \times 10^{10}}{\alpha} \text{ G}. \qquad (24)$$

That we are in the exponentially increasing part of the mean free path is evident by the fact that, by requesting a mean free path which is 11 orders of magnitude larger than the one implied by (23), our upper limit to the magnetic field is decreased less than one order of magnitude. Therefore, our estimate of the magnetic field is not sensitive to the choice of the value of $\bar{R}^{-1}$, providing it satisfies $\gtrsim 10^5$ cm. This implies that the magnetic field strength of the inner engine is constrained to have a value, roughly speaking, in the range $10^{10}-10^{11}$ G (see Fig. 5).

7.3. Condition 3

The third condition (i.e., the closure equation) is obtained by requesting that the timescale of the synchrotron radiation, the cooling time t_c given by Eq. (18), be equal to the observed GeV emission timescale (Ruffini et al. 2019a)

$$\tau_{\rm rad,1} = \frac{\mathcal{E}_1}{L_{\rm GeV,1}}, \qquad (25)$$

where $\mathcal{E}$ is the electrostatic energy available for the process (see Eqs. (7a) and (7b)). The subscript "1" refers to quantities evaluated at the beginning of the transparency of the GeV emission (i.e., at the end of the UPE phase) at $t = t_{\rm rf,UPE}$ (see Sect. 8). We refer to this as the first elementary impulsive event. Therefore, the third equation of the system is

$$t_c (\langle \chi \rangle, \alpha, \beta) = \tau_{\rm rad,1} (\mu, \alpha, \beta, L_{\rm GeV,1}), \qquad (26)$$

where $\mu = M/M_\odot$ and $M_\odot$ is the solar mass.

Therefore, having imposed these three conditions, we obtain the three inner engine parameters from the system of Eqs. (21), (24), and (26), as follows:
1. We adopt the equality in Eq. (21), which implies that we will obtain a lower limit to the BH and spin;
2. We replace it into the equality of Eq. (24), which implies that we are adopting the upper limit to the magnetic field strength (for a given α);
3. We obtain the following expression for β as a function of α and of the observables $E_{\rm GeV}$ and $L_{\rm GeV}$ (Ruffini et al. 2019a):

$$\beta = \beta(\epsilon_\gamma, E_{\rm GeV}, L_{\rm GeV,1}, \alpha)$$
$$= \frac{1}{\alpha} \left(\frac{64}{9} \sqrt{3 \frac{e^2}{\hbar c}} \frac{\epsilon_\gamma}{B_c^2 r_+(\mu, \alpha)^3} \frac{L_{\rm GeV,1}}{e B_c c^2} \right)^{2/7}, \qquad (27)$$

where we have substituted Eq. (17) into Eq. (18) to express t_c as a function of the peak photon energy ϵ_γ, instead of the pitch angle χ.

Therefore, the BH horizon r_+ is a function of μ and α, but in view of Eq. (21) it becomes a function of $E_{\rm GeV}$ and α. Given the observational quantities $E_{\rm GeV}$ (integrated after the UPE phase) and the luminosity $L_{\rm GeV,1}$ (at the end of the UPE phase), Eq. (27) gives a family of solutions of β as a function of α. The solution of this equation together with Eq. (24) gives the values of β and α. With the knowledge of α and $E_{\rm GeV}$, we obtain μ from Eq. (21).

8. Application to GRB 190114C

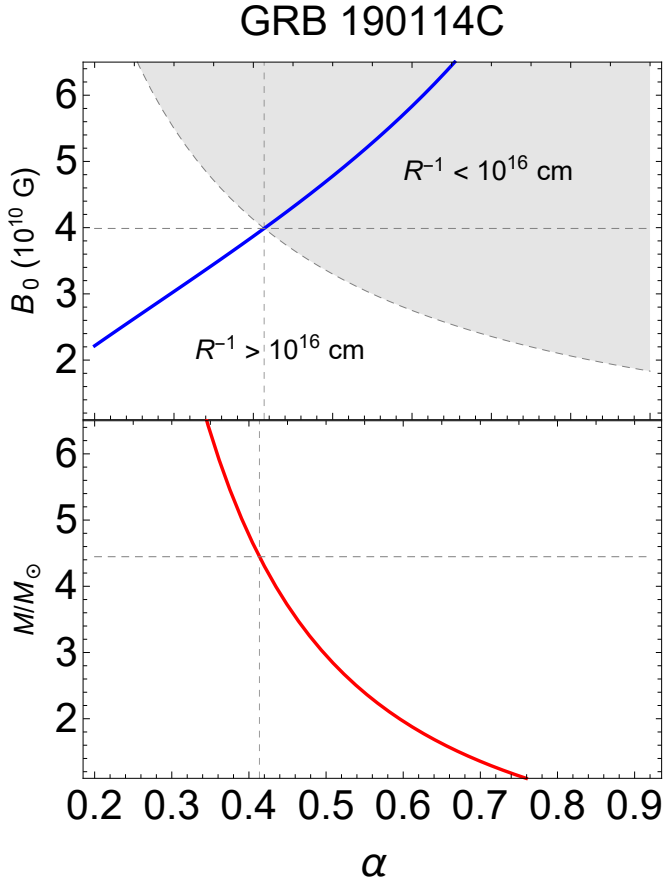We now turn to apply the above procedure to GRB 190114C. For the observational properties of this source we follow the

GRB 190114C

Fig. 5. Parameters of the inner engine of GRB 190114C. For this source we have $L_{\rm GeV,1} = 1.47 \times 10^{52}\,{\rm erg\,s^{-1}}$ and $E_{\rm GeV} = 1.8 \times 10^{53}\,{\rm erg}$. *Upper panel*: family of solutions of B_0 as a function of α (blue curve), given by Eq. (27). We use here a photon energy $\epsilon_\gamma = 0.1\,{\rm GeV}$ (lower edge of the *Fermi*-LAT energy band). In the gray shaded region the mean free path is $\bar{R}^{-1} < 10^{16}\,{\rm cm}$, while in the white shaded region it is $\bar{R}^{-1} \geq 10^{16}\,{\rm cm}$. The curve separating the two regions is therefore given by the equality in (24). *Lower panel*: corresponding family of solutions $M(\alpha)$ (red curve), given by Eq. (21).

results of Liang et al. (2019). The UPE phase has been shown in that paper to end at the rest-frame time $t_{\rm rf,UPE} = 3.99\,{\rm s}$, so we limit our analysis to longer times. Therefore, for GRB 190114C, we have $t_{\rm rad,1} = t_{\rm rf,UPE} = 3.99\,{\rm s}$. The $0.1-100\,{\rm GeV}$ luminosity observed by *Fermi*-LAT, at $t \geq t_{\rm rf,UPE}$, is well fitted by a power-law function analogous to the case of GRB 130427A (Ruffini et al. 2019a) (see our Fig. 4):

$$L_{\rm GeV} = A\,t^{-n} = (7.75 \pm 0.44) \times 10^{52}\,t^{-(1.2\pm0.04)}\,{\rm erg\,s^{-1}}. \tag{28}$$

The associated integrated isotropic energy observed by *Fermi*-LAT, from $t_1 = t_{\rm rf,UPE} = 3.99\,{\rm s}$ to $\sim 10^4\,{\rm s}$, is $E_{\rm GeV} = (1.8 \pm 1.3) \times 10^{53}\,{\rm erg}$, and the luminosity at $t = t_{\rm rad,1}$ is $L_{\rm GeV,1} = 1.47 \times 10^{52}\,{\rm erg\,s^{-1}}$ (see Liang et al. 2019).

For the above numbers, and assuming the minimum energy budget requirement, specifically assuming the equality in Eq. (20), the inner engine parameters are (see Fig. 5) magnetic field $B_0 \approx 3.9 \times 10^{10}\,{\rm G}$, and spin and BH mass $\alpha = 0.41$ and $M = 4.45\,M_\odot$, respectively. The corresponding BH irreducible mass is $M_{\rm irr} = 4.35\,M_\odot$. For the above spin value, Eq. (17) leads to a pitch angle for the emission of $0.1\,{\rm GeV}$ photons, $\theta \approx \pi/9$.

The inequality (20) implies that the above mass and spin values of the BH must be considered as lower limits. As we show in Sect. 6, the inner engine can be long-lasting so it can continue

to emit and so will eventually radiate more than the observed $E_{\rm GeV}$ that we have used limiting ourselves to the first $10^4\,{\rm s}$ of emission. However, in view of the power-law behavior of the GeV luminosity, most of the energy is emitted in this early evolution so the BH parameters do not change significantly if we consider the extrapolation of the energy budget. For example, let us assume that the power-law luminosity (28) extends for 1000 yr. This would increase the total GeV energy radiated by 25%, and recalculating all the parameters we obtain $\alpha = 0.46$, $M = 4.50\,M_\odot$, and $M_{\rm irr} = 4.38\,M_\odot$.

9. Comparison with previous literature

9.1. Long GRBs in the traditional model

We first recall some key features of the traditional model of long GRBs. To this end, we are facilitated by the book by Bing Zhang (Zhang 2018), which includes an extensive number of references. The traditional GRB model roots can be found in the papers by Rees & Meszaros (1992), Mészáros & Rees (1997), and Woosley (1993). The model proposed by Rees & Meszaros (1992) is based on a single system: GRBs are explained by a single BH from which an ultrarelativistic blastwave originates and whose expansion follows the Blandford–McKee self-similar solution (Blandford & McKee 1976). Woosley (1993) connected the GRB origin to a Kerr BH emitting an ultrarelativistic jet that originates from matter accretion onto the BH. The BH was proposed to form from the direct collapse of a massive star, called a failed SN or a "collapsar", leading to a BH in the mass range $5-10\,M_\odot$.

In these models the afterglows are explained via the kinetic energy of the ultrarelativistic blastwave, which can reach very high bulk Lorentz factors, $\Gamma \sim 1000$, to be released when it interacts with the circumburst medium (Waxman & Piran 1994; Sari & Piran 1995; Wijers et al. 1997; Sari 1997; Sari et al. 1998). The observed spectrum is proposed to be produced by synchrotron and synchrotron self-Compton (SSC) emission from accelerated electrons during the deceleration of the ultrarelativistic blastwave radiating at distances $10^{16}-10^{18}\,{\rm cm}$. As pointed out by Zhang (2018), these models based on a ultrarelativistic blastwave radiating at distances $10^{16}-10^{18}\,{\rm cm}$ have been applied to jointly explain in the jetted emission several observations:

1. the X-ray afterglow, the steep and shallow decay of the luminosity in the Nousek-Zhang phase (Nousek et al. 2006; Zhang et al. 2006), the X-ray flares and the gamma-ray flares;
2. the emission in the MeV and in the keV observed by the *Neils Gehrels Swift* Observatory, as well as the emission in the optical and in the radio, as well as the emission in the TeV recently observed by MAGIC (Mirzoyan et al. 2019; MAGIC Collaboration 2019a,b);
3. the high-energy (GeV) emission observed in some long GRBs by *Fermi*-LAT.

Within the traditional model, all the above emissions are explained using solely the kinetic energy of the ultrarelativistic blastwave with $\Gamma \sim 10^3$, and radiating at $10^{16}-10^{18}\,{\rm cm}$. It becomes clear that, requiring to the single kinetic energy of an ultrarelativistic blastwave to account for the entire energetics of all the observed radiation, at all wavelengths, from the prompt to the afterglow, results in an extreme request to the energy reservoir of the GRB engine.

Within the traditional collapsar-fireball model, the presence of a mildly relativistic expanding component has been introduced in Ramirez-Ruiz et al. (2002), called a cocoon, which

moves sideways to the jet. However, as is clearly elucidated in Nakar & Piran (2017; see also references therein), the emission in the X-rays from this cocoon is too low with respect to be observed X-ray afterglow of long GRBs, unless the cocoon Lorentz factor becomes $\Gamma > 10$. The possibility of a mildly relativistic component in the traditional model is interesting for its implications for the nature of the low-energy sources such as GRB 060218 (see, e.g., Nakar 2015). These sources have energies $10^{49}-10^{51}$ erg, which is the range of energies of BdHNe II and III. However, this is beyond the scope of this article, which is dedicated to BdHNe I, which are characterized by the energy range $10^{52}-10^{54}$ erg. In conclusion, an explanation of the X-ray afterglow in the traditional model needs ultrarelativistic values of the Lorentz factor (see also Zhang 2018, for a review on the subject).

9.2. Long GRBs in the BdHN model

As we note in Sect. 1, the BdHNe have a binary progenitor composed of a CO star and a companion NS. The GRB is composed of independent physical process identified by a time-resolved spectral analysis. Some key results are the following:

1. In the analysis of the data of the XRT detector on board the *Neils Gehrels Swift* satellite of the gamma-ray flare, the X-ray flares, the flare-plateau, and the early afterglow phases (the Nousek-Zhang phase), after the ultrarelativistic prompt radiation phase, showed that the emitter in these phases is in mildly relativistic expansion with $\Gamma \lesssim 5$ (see Ruffini et al. 2018a, for details). A similar upper limit $\Gamma \lesssim 3$ was obtained in the case of GRB 151027A (Ruffini et al. 2018b), and for GRB 130427A the corresponding upper limit on the bulk Lorentz factor is $\Gamma \lesssim 2$ (Ruffini et al. 2018c). Therefore, these stringent upper limits on Γ exclude any ultrarelativistic motion following the UPE phase, contrary to the prediction of traditional GRB models based on the ultrarelativistic blastwave.

2. The high-energy GeV emission follows from the action of the inner engine presented in this work, powered by the BH rotational energy extraction process. In the case of GRB 190114C studied in this work, this corresponds to $t_{rf} \gtrsim 3.99$ s (see Fig. 4 and Liang et al. 2019). It is characterized by an afterglow in the GeV radiation which, when expressed in the rest frame, follows a power-law luminosity (see Eq. (28) and Fig. 4), and it carries an energy of $E_{GeV} = (1.8 \pm 1.3) \times 10^{53}$ erg.

3. In parallel, the X-ray afterglow emission observed by the *Swift* satellite originates from the synchrotron radiation produced in the expanding SN ejecta, threaded by the magnetic field of the νNS, and aided by the injection of particles and the pulsar-like radiation from the νNS into the SN ejecta (Ruffini et al. 2018c; Wang et al. 2019; Rueda et al. 2020). These processes are mainly powered by the rotational energy of the νNS and have led to a significant progress in understanding the origin of the X-ray afterglow emission (see, e.g., the case of GRB 130427A in Ruffini et al. 2018c, and GRB 160509A, GRB 160625B, GRB 180728A, and GRB 190114C in Rueda et al. 2020). In these analyses the spin of the νNS and the strength and structure of its magnetic field have been inferred. In the case of GRB 190114C, the luminosity expressed in the rest frame follows a power-law behavior $L_X = A_X t^{-\alpha_X}$, where $A_X = (5.14 \pm 2.03) \times 10^{52}$ erg s^{-1} and $\alpha_X = 1.37 \pm 0.05$ and carries an energy $E_X = 2.11 \times 10^{52}$ erg; see Fig. 4 (Ruffini et al. 2021; see also Liang et al. 2019). This interpretation of the X-ray afterglow

in the BdHN model conforms with the observational upper limits on the Γ factor of the X-ray afterglow emitter summarized in point 1 above (see Ruffini et al. 2018a, for details). In this way, being the total energetics divided into the different components of the system and their associated different physical phenomena, the energetic request to each emission episode in the BdHN becomes affordable.

9.3. Process of BH energy extraction

Having indicated the main differences between the traditional GRB model and the BdHN model regarding the X-ray and the GeV afterglow emissions, we focus now on the mechanism of the high-energy (GeV) emission, which is intimately related to the physics of the GRB central engine.

There is a vast literature devoted to magnetic fields around BHs and how they may act in a mechanism that could extract the rotational energy of a Kerr BH. An early attempt in the absence of a charge by a matter-dominated magnetized plasma accreting in a disk around a pre-existing Kerr BH was presented in Ruffini & Wilson (1975). The effective potential describing the circular orbit of massive particles around a Kerr BH was adopted (see Ruffini & Wheeler 1971b, in problem 2 of Sect. 104 in Landau & Lifshitz 1975). The infinite conductivity condition, $F_{\mu\nu} u^\nu = 0$, where $F_{\mu\nu}$ is the electromagnetic field tensor and u^ν the plasma four-velocity, was used there leading to $E \cdot B = 0$. Under these conditions, the acceleration of particles and processes of energy extraction were not possible.

This work was further developed by Blandford & Znajek (1977); in order to overcome the condition $E \cdot B = 0$ in the magnetosphere, they adopted the concepts of gaps and spontaneous $e^+ e^-$ pair creation, closely following the seminal ideas of pulsar theory by Sturrock (1971) and Ruderman & Sutherland (1975). They imposed a force-free condition, $F_{\mu\nu} J^\nu = 0$, where J^ν is the current density, as well as gaps outside the BH horizon. The aim was to produce an ultrarelativistic matter-dominated plasma whose bulk kinetic energy could be used to explain the energetics of a jet at large distances from the BH.

There is also another direction in the literature following the work of MacDonald & Thorne (1982). It extends the work of Blandford & Znajek (1977) and looks at the problem of matter-dominated accretion in presence of a magnetic field anchored to a rotating surrounding disk. Specifically, they proposed an analogy of a rotating BH immersed in a magnetic field with a rotating conductive sphere and/or with the analogy of such a BH and the surrounding magnetosphere as an electric circuit. Independent of the analogies, the underlying physical system remains the same as that proposed by Blandford & Znajek (1977).

The present model is mainly motivated by fitting the GeV emission of GRBs. There is no matter-dominated disk accretion. There is instead a very low-density ionized plasma fulfilling an acceleration electrodynamical process around a newly born BH. We use the Papapetrou-Wald solution in which the electromagnetic field is naturally characterized by regions where $E \cdot B \neq 0$ (see Sect. 2, Fig. 1, and Wald 1974). This feature naturally allows the acceleration of particles without the need of introducing any gaps. There is no ultrarelativistic matter-dominated plasma outflow. The accelerated charged particles emit synchrotron-radiation photons that carry off energy and angular momentum close to the BH. The BH in our scenario is not pre-existing: it is smoothly formed by the hypercritical accretion onto the binary companion NS. The magnetic field, characterizing the Papapetrou-Wald solution, is amplified during the process of gravitational collapse of the binary companion NS

(Rueda et al. 2020). There is no room in this model for the gravitational stable circular orbits around the Kerr BH. The particles are accelerated by an ultrarelativistic electrodynamical process.

Our description is also different with respect to recent GRB literature. For instance, in Metzger et al. (2011), Beniamini et al. (2017), and references therein, the presence of a magnetized wind, outflow, or jet is powered by a central engine. In these works the engine is represented by a NS endowed with an ultrahigh magnetic field, a magnetar, that loses its rotational energy via magnetic-dipole braking, in complete analogy to pulsars. The magnetar powers the outflows that produce the GRB emission at large radii on the order of 10^{15} cm. These models focus on the explanation of the (MeV) GRB prompt and the (X-ray) afterglow emission using the rotational energy of a magnetar, so they do not look either to the physics of BHs, or to the GeV emission that are the topics of the present article.

The understanding of the complex nature of a BdHN requires the knowledge of different episodes, which in some cases are strictly independent, and their description can occur independently of each other.

For instance, the existence of hyper-energetic SN, the SN-rise, radiates off 10^{52} erg in the case of GRB 190114C (Liang et al. 2019). In parallel, the interaction of the SN ejecta with the magnetic field of the νNS and its pulsar-like emission, explain the observed X-ray afterglow (Ruffini et al. 2018c; Wang et al. 2019; Rueda et al. 2020). This emission is produced at distances $10^{12}-10^{16}$ cm from the binary progenitor.

In the present work we address the most energetic GRB component, the GeV emission originating close to the horizon, at distances of 10^6 cm, starting in the case of GRB 190114C at a rest-frame time of 3.99 s after the trigger.

After the clarification of these concepts, we will be ready to describe the optically thick sub-MeV emission in the time interval $1.99-3.99$ s, which comprises the 55% of the energy of GRB 190114C, overcoming the compactness problem using our classic approach of the fireshell model (see Ruffini et al. 1999, 2000; Bianco et al. 2001; Moradi et al., in prep.).

10. Conclusions

The inner engine theory applied in this work to GRB 190114C represents an authentic full paradigm shift from the traditional model of long GRBs based on the emission of an ultrarelativistic blastwave, somehow powered by a Kerr BH. It seems too expensive for nature to accelerate matter in bulk, against the gravitational pull of the BH, to a large distance of $\sim10^{16}-10^{17}$ cm and with $\Gamma \sim 10^3$ to guarantee the transparency of high-energy radiation. For instance, the explanation of the GRB 190114C high-energy emission needs an ultrarelativistic blastwave with a kinetic energy on the order of 10^{55} erg (see, e.g., MAGIC Collaboration 2019a,b). It is clear that such energy cannot be powered by extracting the rotational energy of a Kerr BH of a few $M_\odot$, which will be a few 10^{53} erg (see Eq. (21)).

We have shown that the inner engine can nicely explain the GeV emission by accelerating electrons in the vicinity of the Kerr BH, which radiate their kinetic energy gain via synchrotron emission. The number of particles needed by the inner engine to explain the observed high-energy emission is relatively low. Let us adopt the derived inner engine parameter for GRB 190114C: $M = 4.4\,M_\odot$, $\alpha = 0.4$, and $B_0 = 4 \times 10^{10}$ G. For instance, from Eq. (17) we obtain that for this α a photon peak energy of 10 GeV is obtained for an electron pitch angle $\chi \approx 0.2°$ (see also Fig. 2). Using Eq. (16), this implies an electron Lorentz factor $\gamma \approx 6.76 \times 10^4$, which corresponds to an

electron energy $\epsilon_e = \gamma m_e c^2 \approx 5.53 \times 10^{-2}$ erg $= 3.45 \times 10^{10}$ eV. Therefore, the number of such electrons needed to power the GeV emission of total energy $E_{GeV} = 1.8 \times 10^{53}$ erg $\approx 0.1\,M_\odot c^2$, is $N_e = E_{GeV}/\epsilon_e = 3.25 \times 10^{54}$, which for ionized matter implies a mass of $m_p N_e \approx 2.73 \times 10^{-3}\,M_\odot$, where m_p is the proton mass.

Therefore, the inner engine uses a more efficient electrodynamical process that produces observable high-energy emission in the vicinity of the BH. In fact the acceleration is not based on a bulk-expanding motion. Every single electron is accelerated from its initial velocity up to an asymptotic value defined by the maximum electric potential energy available for their acceleration, which depends only on the external magnetic field strength and the BH spin parameter; see Eqs. (8a) and (8b). These accelerated electrons radiate mainly at high energies in the GeV domain. The radiation of the inner engine (e.g., at keV to MeV energies) is negligible (with respect to the observed values). The observed radiation in the keV to MeV energy domains is explained by a different mechanism in a BdHN I; see (Rueda et al. 2020). The observed luminosity of GeV allows us to estimate the mass and spin of the BH.

We have determined the parameters of the inner engine of GRB 190114C using only the GeV emission data after the UPE phase. We asked the system to satisfy three physical conditions. First, that the GeV energetics is paid by the extractable energy of the BH (see Eq. (21)); second that the system is transparent to GeV photons produced by the synchrotron radiation of the accelerated electrons (see Eq. (24)); and third that the synchrotron radiation timescale explains the observed GeV emission timescale (see Eq. (26)) with the aid of Eq. (18). In order to be fulfilled, this last constraint implies that the GeV emission is emitted from electrons being accelerated with the appropriate pitch angles (see Figs. 2 and 3). These pitch angles occur within a cone of approximately 60° from the BH rotation axis (see Fig. 3), which is a key result for the interpretation of the morphology of the BdHN I (Ruffini et al. 2021).

From this procedure, we have obtained the inner engine parameters of GRB 190114C: $B_0 \approx 3.9 \times 10^{10}$ G, $\alpha \approx 0.41$, and $M = 4.45\,M_\odot$. The corresponding irreducible mass of the BH is $M_{irr} = 4.35\,M_\odot$. It is worth recalling that both M_{irr} and B_0 are kept constant and this should be all over the evolution. The corresponding BH parameters for GRB 130427A are dimensionless spin $\alpha = 0.47$, mass $M = 2.3\,M_\odot$, and irreducible mass $M_{irr} = 2.2\,M_\odot$ (Ruffini et al. 2019a). The above are the first two BH masses derived directly from the GRB observations, and in both cases they are above the theoretical values of the NS critical mass enforcing the validity of the BdHN I model: the BH are formed by smooth hypercritical accretion of the HN ejecta on the NS binary companion.

Since here we only used the GeV emission data, the BH parameters that we have obtained, namely mass and spin, have to be considered as lower limits. Thus, it is clear that even a slightly higher mass (or spin) of the BH can guarantee even larger and longer emission of the inner engine.

Our analysis paves the way to additional research; the data from the different energy bands (e.g., the higher energy bands; MAGIC Collaboration 2019a,b) might provide additional information on the energy distribution of the electrons injected by the electric field into the magnetic field, and on the pitch angle distribution for the synchrotron emission. Figure 3 shows, for the electromagnetic field configuration of the Papapetrou-Wald solution (see Fig. 1), the contours of constant pitch angle and constant electric energy density.

Before concluding, it is worth recalling some crucial aspects of the inner engine here applied to the case of GRB 190114C.

The nature of the emission results from considering the physical process leading to the electric and magnetic fields and the BH formation (see Sect. 3 and Rueda et al. 2020). This is fundamental to show that the emission process leading to the observed luminosity is not continuous, but discrete. The timescale of the emission in GRBs is too short to be probed directly by current observational facilities. Direct evidence of the value and discreteness might come instead from the observation of large BHs of 10^8-10^{10} $M_\odot$ in AGN. For instance, in the case of M 87*, for fiducial parameters $M = 6 \times 10^9$ $M_\odot$, $\alpha = 0.1$, and $B_0 = 10$ G, the inner engine theory predicts a high-energy (GeV) emission with a luminosity of a few 10^{43} erg s^{-1}, with a timescale of up to tenths of seconds (see Table 2). Emission at higher energies (e.g., in the TeV band), would be characterized by a lower luminosity and a longer timescale. The timescale for UHECR emission is instead approximately half a day (see Table 2 and Rueda & Ruffini 2020).

We can therefore conclude, in the light of the results of this article and the previous articles in this series, that all BdHN I are powered by three independent sources of energy. The BdHN I is triggered by the SN explosion originating from the collapse of the CO_{core} generating a νNS. The accretion of the SN onto the νNS (see Sect. 9.2 and Ruffini et al. 2018c; Wang et al. 2019; Rueda et al. 2020), gives origin to the X-ray afterglow observed by *Swift*. The hypercritical accretion of the SN onto the binary companion NS gives origin to the BH as soon as the NS reaches the critical mass. This smooth accretion process is alternative to the direct gravitational collapse of a massive star. This happens in GRB 190114C at $t_{rf} = 1.99$ s. The further accretion of the SN ejecta onto the newly born BH generates the prompt gamma-ray radiation observed in GRB 190114C between 1.99 s and 3.99 s (Moradi et al., in prep.). The further accretion of the SN ejecta onto the newly born BH leads to a process of energy extraction from the inner engine that generates the jetted high-energy ($\gtrsim$GeV) emission. This radiation, as is shown in this article using the Papapetrou-Wald solution (see Sect. 2), is emitted close to the BH horizon and within an angle of nearly 60° from the BH rotation axis (see Sect. 5 and Fig. 3).

References

Bardeen, J. M. 1970, ApJ, 162, 71
Bardeen, J. M., Press, W. H., & Teukolsky, S. A. 1972, ApJ, 178, 347
Becerra, L., Cipolletta, F., Fryer, C. L., Rueda, J. A., & Ruffini, R. 2015, ApJ, 812, 100
Becerra, L., Bianco, C. L., Fryer, C. L., Rueda, J. A., & Ruffini, R. 2016, ApJ, 833, 107
Becerra, L., Ellinger, C. L., Fryer, C. L., Rueda, J. A., & Ruffini, R. 2019, ApJ, 871, 14
Beniamini, P., Giannios, D., & Metzger, B. D. 2017, MNRAS, 472, 3058
Bianco, C. L., Ruffini, R., & Xue, S.-S. 2001, A&A, 368, 377
Blandford, R. D., & McKee, C. F. 1976, Phys. Fluids, 19, 1130
Blandford, R. D., & Znajek, R. L. 1977, MNRAS, 179, 433
Christodoulou, D. 1970, Phys. Rev. Lett., 25, 1596
Christodoulou, D., & Ruffini, R. 1971, Phys. Rev. D, 4, 3552
Damour, T., & Ruffini, R. 1975, Phys. Rev. Lett., 35, 463
Daugherty, J. K., & Harding, A. K. 1983, ApJ, 273, 761
de Jager, O. C., Harding, A. K., Michelson, P. F., et al. 1996, ApJ, 457, 253
DeWitt, C., & DeWitt, B. S. 1973, in Proceedings, Ecole d'Eté de Physique Théorique: Les Astres Occlus (New York, NY: Gordon and Breach), Les Houches Summer School, 23
Fryer, C. L., Rueda, J. A., & Ruffini, R. 2014, ApJ, 793, L36
Hawking, S. W. 1971, Phys. Rev. Lett., 26, 1344
Hawking, S. W. 1972, Commun. Math. Phys., 25, 152
Kelner, S. R., Prosekin, A. Y., & Aharonian, F. A. 2015, AJ, 149, 33
Kerr, R. P. 1963, Phys. Rev. Lett., 11, 237
Landau, L. D., & Lifshitz, E. M. 1975, The Classical Theory of Fields (Oxford: Pergamon Press)
Liang, L., Ruffini, R., Rueda, J. A., et al. 2019, ArXiv e-prints [arXiv:1910.12615]
MacDonald, D., & Thorne, K. S. 1982, MNRAS, 198, 345
MAGIC Collaboration (Acciari, V. A., et al.) 2019a, Nature, 575, 455
MAGIC Collaboration (Acciari, V. A., et al.) 2019b, Nature, 575, 459
Mészáros, P., & Rees, M. J. 1997, ApJ, 482, L29
Metzger, B. D., Giannios, D., Thompson, T. A., Bucciantini, N., & Quataert, E. 2011, MNRAS, 413, 2031
Mirzoyan, R., Noda, K., Moretti, E., et al. 2019, GCN Circ., 23701, 1
Nakar, E. 2015, ApJ, 807, 172
Nakar, E., & Piran, T. 2017, ApJ, 834, 28
Newman, E. T., Couch, E., Chinnapared, K., et al. 1965, J. Math. Phys., 6, 918
Nousek, J. A., Kouveliotou, C., Grupe, D., et al. 2006, ApJ, 642, 389
Papapetrou, A. 1966, Annales de L'Institut Henri Poincare Section (A) Physique Theorique, 4, 83
Ramirez-Ruiz, E., Celotti, A., & Rees, M. J. 2002, MNRAS, 337, 1349
Rees, M. J., & Meszaros, P. 1992, MNRAS, 258, 41P
Ruderman, M. A., & Sutherland, P. G. 1975, ApJ, 196, 51
Rueda, J. A., & Ruffini, R. 2012, ApJ, 758, L7
Rueda, J. A., & Ruffini, R. 2020, Eur. Phys. J. C, 80, 300
Rueda, J. A., Ruffini, R., Karlica, M., Moradi, R., & Wang, Y. 2020, ApJ, 893, 148
Ruffini, R., & Wheeler, J. A. 1971a, Phys. Today, 24, 30
Ruffini, R., & Wheeler, J. A. 1971b, ESRO, 52, 45
Ruffini, R., & Wilson, J. R. 1975, Phys. Rev. D, 12, 2959
Ruffini, R., Salmonson, J. D., Wilson, J. R., & Xue, S.-S. 1999, A&AS, 138, 511
Ruffini, R., Salmonson, J. D., Wilson, J. R., & Xue, S.-S. 2000, A&A, 359, 855
Ruffini, R., Wang, Y., Enderli, M., et al. 2015, ApJ, 798, 10
Ruffini, R., Wang, Y., Aimuratov, Y., et al. 2018a, ApJ, 852, 53
Ruffini, R., Becerra, L., Bianco, C. L., et al. 2018b, ApJ, 869, 151
Ruffini, R., Karlica, M., Sahakyan, N., et al. 2018c, ApJ, 869, 101
Ruffini, R., Moradi, R., Rueda, J. A., et al. 2019a, ApJ, 886, 82
Ruffini, R., Melon Fuksman, J. D., & Vereshchagin, G. V. 2019b, ApJ, 883, 191
Ruffini, R., Moradi, R., Rueda, J. A., et al. 2021, MNRAS, in press [arXiv:2103.09142]
Sari, R. 1997, ApJ, 489, L37
Sari, R., & Piran, T. 1995, ApJ, 455, L143
Sari, R., Piran, T., & Narayan, R. 1998, ApJ, 497, L17
Sturrock, P. A. 1971, ApJ, 164, 529
Tursunov, A., & Dadhich, N. 2019, Universe, 5, 125
Wald, R. M. 1974, Phys. Rev. D, 10, 1680
Wang, Y., Rueda, J. A., Ruffini, R., et al. 2019, ApJ, 874, 39
Waxman, E., & Piran, T. 1994, ApJ, 433, L85
Wijers, R. A. M. J., Rees, M. J., & Meszaros, P. 1997, MNRAS, 288, L51
Woosley, S. E. 1993, ApJ, 405, 273
Zhang, B. 2018, The Physics of Gamma-ray Bursts (Cambridge: Cambridge University Press)
Zhang, B., Fan, Y. Z., Dyks, J., et al. 2006, ApJ, 642, 354